SCUOLA DI DOTTORATO
UNIVERSITÀ DEGLI STUDI DI MILANO-BICOCCA

Department of Physics G. Occhialini

PhD program in Physics Cycle XXXIII

Curriculum in Physics and Astronomy

IMPROVING THE EOB TOOLBOX FOR GRAVITATIONAL WAVE DATA ANALYSIS

Surname: Messina Name: Francesco

Registration number: 827251

Tutor: Prof. Monica Colpi

Co-tutor: Dott. Alessandro Nagar

Coordinator: Prof. Marta Calvi

ACADEMIC YEAR 2019/2020

Organization of the dissertation

This dissertation is organized as follows: Chapters from 1 to 4 are a detailed introduction to the original works that are exposed from Chapt. 5 to Chapt. 9. The introductive Chapters are based on the existing literature cited in the references. The conlcusions of the papers presented from Chapt. 5 to Chapt. 9 are summarized in Chapt. 10. The original papers presented in this PhD thesis are the following:

- **Chapter 5, Ref. [1]:** *Time-domain effective-one-body gravitational waveforms for coalescing compact binaries with nonprecessing spins, tides and self-spin effects*, by Alessandro Nagar (Enrico Fermi Ctr., Rome & INFN, Turin & IHES, Bures-sur-Yvette), Sebastiano Bernuzzi (Jena U., TPI & INFN, Parma & Parma U.), Walter Del Pozzo (INFN, Pisa & Pisa U.), Gunnar Riemenschneider (INFN, Turin & Turin U.), Sarp Akcay (Jena U., TPI), Gregorio Carullo (INFN, Pisa & Pisa U.), Philipp Fleig (Munich, Max Planck Inst.), Stanislav Babak (APC, Paris), Ka Wa Tsang (NIKHEF, Amsterdam), Marta Colleoni (Balearic Islands U.), Francesco Messina (Milan Bicocca U. & INFN, Milan Bicocca), Geraint Pratten (Balearic Islands U.), David Radice (Princeton U., Astrophys. Sci. Dept. & Princeton, Inst. Advanced Study), Piero Rettegno (INFN, Turin & Turin U.), Michalis Agathos (Cambridge U., DAMTP), Edward Fauchon-Jones, Mark Hannam (Cardiff U.), Sascha Husa (Balearic Islands U.), Tim Dietrich (Gottingen U. & NIKHEF, Amsterdam), Pablo Cerdá-Duran (Valencia U., Astro. Astrophys.), José A. Font (Valencia U., Astro. Astrophys. & Valencia U., IFIC), Francesco Pannarale (Cardiff U.), Patricia Schmidt (Nijmegen U., IMAPP), Thibault Damour (IHES, Bures-sur-Yvette). **Published in Phys. Rev., D98(10):104052, 2018**

- **Chapter 6, Ref. [2]:** *Nonlinear-in-spin effects in effective-one-body waveform models of spin-aligned, inspiralling, neutron star binaries*, by Alessandro Nagar (Enrico Fermi Ctr., Rome & INFN, Turin & IHES, Bures-sur-Yvette), Francesco Messina (Milan Bicocca U. & INFN, Milan Bicocca), Piero Rettegno (INFN, Turin & Turin U.), Donato Bini (CNR, Italy & INFN, Rome3), Thibault Damour (IHES, Bures-sur-Yvette), Andrea Geralico (CNR, Italy), Sarp Akcay, Sebastiano Bernuzzi (Jena U.). **Published in Phys.Rev. D99 (2019) no.4, 044007**

- **Chapter 7, Ref. [3]:** *Quasi-5.5PN TaylorF2 approximant for compact binaries: point-mass phasing and impact on the tidal polarizability inference*, by Francesco Messina (Milan Bicocca U. & INFN, Milan Bicocca), Reetika Dudi (Jena U.), Alessandro Nagar (Enrico Fermi Ctr., Rome & INFN, Turin & IHES, Bures-sur-Yvette), Sebastiano Bernuzzi (Jena U.). **Published in Phys.Rev. D99 (2019) no.12, 124051**

- **Chapter 8, Ref. [4]:** *Factorization and resummation: A new paradigm to improve gravitational wave amplitudes. II: the higher multipolar modes*, by Francesco Messina (Milan Bicocca U. & INFN, Milan Bicocca), Alberto Maldarella (Turin U.), Alessandro Nagar (Enrico Fermi Ctr., Rome & INFN, Turin & IHES, Bures-sur-Yvette). **Published in Phys.Rev. D97 (2018) no.8, 084016**

- **Chapter 9, Ref. [5]:***Factorization and resummation: A new paradigm to improve gravitational wave amplitudes. III: the spinning test-body terms*, by Alessandro Nagar (Enrico Fermi Ctr., Rome & INFN, Turin & IHES, Bures-sur-Yvette), Francesco Messina (Milan Bicocca U. & INFN, Milan Bicocca), Chris Kavanagh (IHES, Bures-sur-Yvette & Potsdam, Max Planck Inst.), Georgios Lukes-Gerakopoulos (Astron. Inst., Praque), Niels Warburton (University Coll., Dublin), Sebastiano Bernuzzi, Enno Harms (Jena U., TPI). **Published in Phys.Rev. D100 (2019) no.10, 104056**

Other papers in which I'm an author but are only cited (or briefly exposed) here are:

- **Ref. [4]:** *Parametrized-4.5PN TaylorF2 approximants and tail effects to quartic nonlinear order from the effective one body formalism*, by Francesco Messina (Turin U.), Alessandro Nagar (INFN, Turin & IHES, Bures-sur-Yvette & Enrico Fermi Ctr., Rome). **Published in Phys.Rev. D95 (2017) no.12, 124001**

- **Ref. [6]:***Effective-one-body multipolar waveform for tidally interacting binary neutron stars up to merger*, by Sarp Akcay, Sebastiano Bernuzzi (U. Jena (main)), Francesco Messina (Milan Bicocca U. & INFN, Milan Bicocca), Alessandro Nagar (Enrico Fermi Ctr., Rome & INFN, Turin & IHES, Bures-sur-Yvette), Néstor Ortiz (U. Jena (main)), Piero Rettegno (INFN, Turin & Turin U.). **Published in Phys.Rev. D99 (2019) no.4, 044051**

- **Ref. [7]:** *A multipolar effective one body waveform model for spin-aligned black hole binaries*, by Alessandro Nagar, Gunnar Riemenschneider, Geraint Pratten, Piero Rettegno, Francesco Messina. **2020, To be published**

Abstract

The parameter estimation of gravitational wave (GW) events detected by LIGO and Virgo relies on analytical waveform models, possibly calibrated (or informed) by Numerical Relativity simulations. The effective-one-body (EOB) model is one of the main analytical models available that can be efficiently used for analyzing both black hole and neutron star binaries. In this script we I) improve it in its various sectors, with the final aim to build a model that includes all the physical information available: in particular, the higher subdominant multipole information, that is useful to optimize GW data analysis' angular resolution [1, 4, 5, 7]; II) use it to develop high-order fast PN approximants for Bayesian analysis in LIGO and Virgo pipelines [3]; III) use it to study the self-spin effects of binary Neutron Stars on their own waveform [2]. One of the central building blocks of the EOB model is the factorized and resummed (circularized) multipolar post-Newtonian (PN) waveform introduced in Ref. [8] for nonspinning binaries. In Ref. [4], we extend up to $\ell = 6$ (i.e. to high multipoles) the resummation approach of Nagar and Shah [9], since it has a better analytical/numerical relativity agreement than its precursor [8]. Ref. [4], updated to the case of a spinning particle of Schwarzschild problem in Ref. [5], has been used in order to update the spin-aligned, quadrupolar EOB model `TEOBResumS`, a `C` code [1] available in the LIGO Advanced Library (`LAL`) and cited in the GW catalogue [10], to a multipolar version [7]. Therefore, following the EOB-PN expansion technique defined in [11], Ref. [3] leads to a fast and accurate 5.5PN phenomenological approximant that, by including more point-mass information than the standard 3.5PN one, optimizes the tidal-parameter estimation of BNS data analysis. In Ref [2], we incorporate the EOS-dependent self-spin terms in `TEOBResumS` at next-to-next-to-leading (NNLO) order, together with other (bilinear, cubic and quartic) nonlinear-in-spin effects (at leading order, LO). Here, with the same toolbox used in Ref. [3], we study the EOS dependence of the self-spin effects and show that the next-to-leading order (NLO) and NNLO monopole-quadrupole corrections yield increasingly phase-accelerating effects compared to the corresponding LO contribution; that the standard TaylorF2 post-Newtonian (PN) treatment of NLO (3PN) EOS-dependent self-spin effects makes their action stronger than the corresponding EOB description; and, finally, we obtain a tail-augmented TaylorF2 approximant that yields an analytically simplified, EOB-faithful, representation of the EOS-dependent self-spin phasing that can be useful to improve current PN-based (or phenomenological) waveform models for inspiralling neutron star binaries.

Main notation and conventions

GW: Gravitational Wave

GR: General Relativity

NR: Numerical Relativity

PN: Post-Newtonian

PM: Post-Minkowsian

MPM: Multipolar Post-Minkowskian

BH: Black Hole

EOB: Effective-One Body

IMR: Inspiral-Merger-Ringdown

LO: Leading Order

NLO: Next-to-Leading Order

NNLO: Next-to-Next-to-Leading Order

BBH: Binary Black Hole

BNS: Binary Neutron Star

ODE: Ordinary Differential Equation

PDE: Partial Differential Equation

SPA: Stationary Phase Approximation

STF: Symmetric Traceless Free

CMM: Campbell Macek Morgan

ADM: Arnowitt Deser Misner

RWZ: Regge Wheeler Zerilli

TOV: Tolman Oppenheimer Volkoff

EOS: Equation of State

CFL: Courant Friedrichs Lewy

NP: Newman Penrose

HH: Hawking Hartle

FP: Finite Part

QNMs: Quasi-Normal Modes

ISCO: Innermost Stable Circular Orbit

LSO: Last Stable Orbit

NQC: Next-to-Quasi Circular

Res: Residue

SCRI: Null infinity

Vectorial notation: bold letters ($\vec{v} \equiv \boldsymbol{v}$), latin indexes. Versors normal to a surface are indicated as $\boldsymbol{n}$. In this work, the hat symbol $\hat{}$ on a letter marks the STF projection (2.28) of the vector; it is not a versor notation.

Partial derivative

$$\frac{\partial}{\partial x^{\mu}} \equiv \partial_{\mu} \equiv_{,\mu} \tag{1}$$

Minkowski Metric Tensor

$$\eta_{\mu\nu} \equiv diag(-,+,+,+) \tag{2}$$

Laplacian (in Cartesian coordinates)

$$\nabla^2 = (\partial_x, \partial_y, \partial_z) \tag{3}$$

D'Alambert operator

$$\Box = \eta^{\mu\nu}\partial_{\mu}\partial_{\nu} \tag{4}$$

GR Metric

$$ds^2 = g_{\mu\nu} dx^\mu dx^\nu \tag{5}$$

Affine Connection

$$\Gamma^\lambda_{\mu\nu} = \frac{1}{2} g^{\lambda\sigma} (\partial^\mu g_{\nu\sigma} + \partial^\nu g_{\mu\sigma} - \partial_\sigma g_{\mu\nu}) \tag{6}$$

Riemann Tensor

$$R^\sigma_{\mu\eta\nu} = \partial_\eta \Gamma^\sigma_{\mu\nu} - \partial_\nu \Gamma^\sigma_{\mu\eta} + \Gamma^\sigma_{\gamma\eta} \Gamma^\gamma_{\mu\nu} - \Gamma^\sigma_{\gamma\nu} \Gamma^\gamma_{\mu\eta} \tag{7}$$

Ricci Tensor

$$R_{\mu\nu} = R^\lambda{}_{\mu\lambda\nu} \tag{8}$$

Ricci Scalar

$$R = g^{\mu\nu} R_{\mu\nu} \tag{9}$$

Stress-energy Tensor

$$T_{\mu\nu} = m \int \frac{d\tau}{\sqrt{-g}} u_\mu u_\nu \delta^4(x^\alpha - X^\alpha(\tau)) \tag{10}$$

where m is the mass of a point particle, τ the proper time, $X^\alpha(\tau)$ the particle's wordline and $u^\alpha(\tau) = \frac{dX^\alpha}{d\tau}$ the 4-velocity.

Einstein field equations

$$R_{\mu\nu} - \frac{1}{2} g_{\mu\nu} R = 8\pi T_{\mu\nu} \tag{11}$$

Covariant Derivative of a rank 2 Tensor

$$h^{\alpha\beta}_{;\sigma} = \partial_\sigma h^{\alpha\beta} + \Gamma^\alpha_{\sigma\eta} h^{\eta\beta} + \Gamma^\beta_{\sigma\eta} h^{\alpha\eta} \tag{12}$$

Euler Gamma Function

$$\Gamma(z) = \int_0^\infty e^{-t} t^{z-1} dt \tag{13}$$

Euler logarithm

$$\text{eulerlog}_m(x) \equiv \gamma_E + \log 2 + \frac{1}{2}\log x + \log m \tag{14}$$

where $\gamma_E = 0.57721...$ is the Euler-Mascheroni constant.

Hypergeometric function

$${}_pF_q(a_1, ..., a_p; b_1, ..., b_q; z) = \sum_{n=0}^{\infty} \frac{\beta_n z^n}{n!} \tag{15}$$

with $\beta_0 = 1$ and

$$\frac{\beta_{n+1}}{\beta_n} = \frac{(n + a_1)(n + a_2)...(n + a_p)}{(n + b_1)(n + b_2)...(n + b_q)} \tag{16}$$

Total mass of a binary

$$M = m_1 + m_2 \tag{17}$$

Reduced mass of a binary

$$\mu = \frac{m_1 m_2}{M} \tag{18}$$

Mass ratio of a binary

$$q = \frac{m_2}{m_1} \tag{19}$$

Symmetric mass ratio of a binary

$$\nu \equiv \frac{\mu}{M} = \frac{m_1 m_2}{(m_1 + m_2)^2} \tag{20}$$

Taylor-expansion of order n

$$T_n$$

Magnitude of the spins of the constituent binary

$$S_{1,2}$$

Dimensionless binary spin notation

$$\begin{aligned}
\chi_{1,2} &\equiv \frac{S_{1,2}}{m_{1,2}} \\
\chi_{S/A} &\equiv \frac{1}{2}(\chi_1 \pm \chi_2) \\
X_{1/2} &\equiv \frac{m_{1,2}}{M} = \frac{1}{2}(1 \pm \sqrt{1-4\nu}) \\
\tilde{a}_{1,2} &\equiv X_{1,2}\chi_{1,2} \\
\hat{a}_0 &\equiv \tilde{a_1} + \tilde{a}_2 \\
\tilde{a}_{12} &\equiv \tilde{a_1} - \tilde{a_2}
\end{aligned}$$

Test mass/particle limit of a binary

$$\begin{aligned}
\nu &\to 0 \\
m_1 &\gg m_2 \\
\tilde{a}_2 &\to 0
\end{aligned}$$

Therefore, the body 2 becomes a *test particle* (i.e. an idealized model of a small object whose mass is so small that it does not appreciably disturb the ambient gravitational field).

Contents

Chapter 1

Preliminary overview

1.1 Introduction

General Relativity [12], the actual theory of gravitation, which incorporates the Newtonian laws as a weak-field limit, predicts the existence of gravitational waves (GWs). In analogy with the theory of electromagnetism, these perturbations occur when a mass that moves in spacetime, which is comparable to an elastic medium, accelerates. The first theoretical prediction of gravitational waves was made by Einstein himself in 1916 [13]. From the experimental point of view, the first, unsuccessful, attempts to detect gravitational waves were made by Weber in the 1960s [14, 15, 16].
Thanks to the progress of experimental radio astronomy and to the theoretical work of Damour and Deruelle [17, 18], the first observational proof of the existence of GWs was given by the observations of the energy loss of the binary pulsar system PSR B1913+16 made by Taylor and Weisberg in 1982 [19, 20]. This discovery opened deeper theoretical studies regarding GWs: if one wants to detect a "pure" gravitational wave signal from a binary merger[1], then he must deal with the intrinsic complexity of General Relativity, finding solutions that go beyond Einstein's quadrupole formula [13]. In order to do that, during the 1980s and the 1990s, Damour, Blanchet and collaborators led important advances in the Post-Newtonian (PN), Post-Minkowskian (PM) and Multipolar Post-Minkowskian (MPM) frameworks [21, 22, 23, 24, 25, 26]. This kind of computations are *analytical*.

[1]Black Hole (BH) and Neutron Star (NS) mergers are the ideal candidates for GW detections since gravity is a very weak force compared to electromagnetism.

Having said that, another way to deal with strong gravity is Numerical Relativity (NR): in this case, spacetime is discretized and Einstein's equations (Eq. 11) are solved using a supercomputer. A NR simulation with $\sim$30 GW cycles can take $\mathcal{O}(10^5 - 10^6)$ CPU-hours, so it is much more expensive than analytical techniques. But it takes precisely into account the strong-curvature and high-velocity effects that enter into play during binary mergers, that are the most (known) violent events in the universe.
NR is very complex, and the first *complete up to ringdown* non-axisymmetric Inspiral-Merger-Ringdown (IMR)[2] simulation was made by Pretorius in 2005 [27]. Almost five years before this important achievement, after some great experimental efforts, LIGO in the United States and VIRGO in Italy were completed. These ground-based experiments, with limited sensitivity, needed hundred of thousands of GW templates almost as fast as an analytical formula[3], but also precise in the high-velocity field regime (i.e. where PN theory, built around low-velocity approximation, fails). The Effective one-Body (EOB) formalism by Buonanno and Damour (1998) [28], which consist into a mapping of resummed PN expressions into a simpler, "one-body" problem, provided the first complete IMR *analytical* GW template in 2000 [29]. The EOB model, that is the main topic of this PhD thesis, is a very flexible toolbox, since it can be informed with NR waveforms or new additional PN, PM or gravitational self-force information; or be used to build phenomenological [30] or PN approximants[4] [11, 3]. A constant improvement of this model, since its numerical-calibrated/informed versions [31, 32, 33, 30, 34, 35, 36, 37] are fundamental in the parameter estimation of GW events [38, 39, 40, 41, 42, 43, 10], is *necessary* in order to improve future events' data analysis.

1.2 What is a gravitational wave?

According to GR, gravitation is curvature. Intuitively, a GW is a ripple in the curvature of spacetime, that is a dynamical structure affected by the matter and energy within it. The interaction between matter, energy and

[2] In Fig.1.1 we can see the three phases of a binary coalescence: I) a slow inspiral phase; II) a merger phase, that is defined as the peak of the dominant-quadrupolar GW signal; III) a ringdown phase (BH only), that is characterized by the dumped gravitational oscillations emitted by the final BH.

[3] See Sec. 1.5 for details.

[4] See chapter 7.

spacetime is mathematically described by the field equation

$$R_{\mu\nu} - \frac{1}{2}Rg_{\mu\nu} = 8\pi T_{\mu\nu} \tag{1.1}$$

where $g_{\mu\nu}$ is the metric tensor, $R_{\mu\nu}$ is the Ricci tensor (a function of the metric and its first and second derivatives) and R is the Ricci scalar, the contraction of the Ricci tensor. $T_{\mu\nu}$ is the stress-energy tensor, which describes the distribution of matter and energy within the spacetime. If the distribution of matter and energy varies in time, then the curvature, as described by the metric $g_{\mu\nu}$, also varies in time. This variation in the metric will propagate outward from the varying matter and energy distribution through the rest of spacetime as GWs which stretch and squeeze spacetime itself, causing the measured distance between two points to grow and shink at different times. The *strain*, or fractional change in length, is used to quantify the effect of GWs in time. Let's consider two freely falling reference points separated by a distance L. When a gravitational strain h passes by, the wave will produce a time-dependent variation in L, $\triangle L(t) = h(t)L$. So, if one can measure the distance between two points to high enough precision, filtering the noise due to other factors, this may be the evidence of a GW. The most important way to "control noise" in this case is to perform these distance measurement experiments at two or more widely separated locations. We then require that multiple sites measure a strain at the same time (within some coincidence window to allow for the fact that a GW can arrive at the different locations at slightly different times), and that the measured strains are all of consistent strength and functional form $h(t)$.

In electrodynamics, one can describe the electromagnetic waves emitted from a source electromagnetic potential by expanding the potential in multipoles. If these multipoles vary in time, they can create electromagnetic radiation. Because electromagnetic charge is conserved, the electric monopole (i.e. total charge) will not vary and cannot produce electromagnetic waves. However, if the electric dipole of the potential varies in time, this will produce radiation. Higher derivatives of higher multipoles can also contribute to it. In GR, one can use an analogous approach to describe GWs in terms of multipoles of the stress-energy tensor (the analogue of the source in the electromagnetic formalism) of a source. Because mass-energy (mass monopole), linear momentum (mass dipole) and angular momentum (current dipole) are conserved, they cannot contribute to GWs. So, the second time derivative

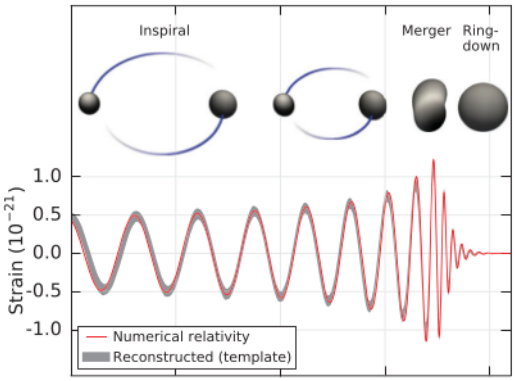

Figure 1.1: *Estimated gravitational-wave strain amplitude from GW150914. This shows the full bandwidth of the waveforms, and the inset images show numerical relativity models of the black-hole horizons as the black holes coalesce (source: Ref [38])*

of the mass quadrupole is the lowest order contribution to radiation. This represents the dominant contribution to GWs, with higher time derivatives of higher order multipoles giving smaller corrections.
Gravity is much weaker than the other fundamental forces of nature, so one must have very large masses undergoing extreme accelerations to produce detectable GWs. Here emerges the importance of compact binaries (like a pair of BHs, a pair of neutron stars (NSs) or a BH and a NS, inspiralling and merging each other to form a final object) as candidates for gravitational laser interferometers. To see quantitatively how difficult it is to detect GWs and why we do not see them without a complex and expansive experimental and data-analysis work, let's consider the leading order expression for the strain of GWs emitted by the Hulse-Taylor binary [14]

$$h(t) \sim 2.3610^{-22} \left(\frac{M}{10M_{\odot}}\right)^{\frac{5}{3}} \left(\frac{\nu}{0.25}\right) \left(\frac{F_{orb}}{100Hz}\right)^{\frac{2}{3}} \left(\frac{100Mpc}{D_{eff}}\right) \tag{1.2}$$

where $M = m_1 + m_2$ is the total mass of the binary, $\nu = \frac{m_1 m_2}{M^2}$ the symmetric mass ratio, F_{orb} the orbital frequency of the binary and D_{eff} the effective distance between the binary and detector. For the example in the above equation we get a strain $\mathcal{O}(10^{-22})$. If a $\sim 2m$ long freely falling test apparatus is impinged upon by a GW from our example source, it will be stretched and squeezed by $\mathcal{O}(10^{-22})m$. Considering the closest extra-solar

stars from Earth ($\sim$1 pc away), then the GWs would only warp our apparatus by $\mathcal{O}(10^{-14})m$. This should make it quite clear that GWs' amplitudes from astrophysical sources are very weak and can be only detected by high-precision experiments.

1.3 Linearized theory of gravity

1.3.1 Einstein's equations in flat space

Linearized gravity theory is the weak field limit of General Relativity. In this approximation the spacetime is made up by a flat background described by the Minkowski metric $\eta_{\mu\nu} = diag(-1, 1, 1, 1)$. In this context the gravitational wave that propagates in the spacetime is represented by a small perturbation $h_{\mu\nu}$. So we can write the metric as

$$g_{\mu\nu} = \eta_{\mu\nu} + h_{\mu\nu}, \tag{1.3}$$

with $|h_{\mu\nu}| << 1$. Since $h_{\mu\nu} \to h_{\mu'\nu'} = \Lambda^{\mu'}_{\mu}\Lambda^{\nu'}_{\nu}h_{\mu\nu}$, where Λ is a Lorentz transformation, $h_{\mu\nu}$ is a rank 2 tensor. Starting from the perturbed metric 1.3, one can compute the linearized Einstein field equations. Firstly, Christoffel symbols (6), by substituting Eq. (1.3) and ignoring the second order terms in the perturbation, can be written as

$$\Gamma^{\lambda}_{\mu\nu} = \frac{1}{2}(\partial_\nu h^{\lambda}_{\mu} + \partial_\mu h^{\lambda}_{\nu} - \partial^{\lambda} h_{\mu\nu}). \tag{1.4}$$

Secondly, neglecting the quadratic terms in $h_{\mu\nu}$ as before, the Ricci tensor (8) becomes

$$R_{\mu\nu} = \partial_\eta \Gamma^{\eta}_{\mu\nu} - \partial_\nu \Gamma^{\eta}_{\mu\eta}. \tag{1.5}$$

Using Christoffel symbols and the simmetry of the second derivatives one obtains

$$\begin{aligned} R_{\mu\nu} &= \frac{1}{2}[\partial_\eta\partial_\mu h^{\eta}_{\nu} + \partial_\eta\partial_\nu h^{\eta}_{\mu} - \partial_\eta\partial^{\eta} h_{\mu\nu} - (\partial_\nu\partial_\mu h^{\eta}_{\eta} + \partial_\nu\partial_\eta h^{\eta}_{\mu} - \partial_\nu\partial^{\eta} h_{\mu\eta})] \\ &= \frac{1}{2}(\partial_\eta\partial_\mu h^{\eta}_{\nu} + \partial_\nu\partial^{\eta} h_{\mu\eta} - \partial_\eta\partial^{\eta} h_{\mu\nu} - \partial_\nu\partial_\mu h^{\eta}_{\eta}). \end{aligned} \tag{1.6}$$

Calling $h \equiv h^{\eta}_{\eta}$ and $\Box \equiv \partial^{\eta}_{\eta}$ we have that

$$R_{\mu\nu} = \frac{1}{2}(\partial_\mu\partial_\eta h^{\eta}_{\nu} + \partial_\nu\partial_\eta h^{\eta}_{\mu} - \Box h_{\mu\nu} - \partial_\mu\partial_\nu h). \tag{1.7}$$

Rewriting all terms apart from $\Box h_{\mu\nu}$ as derivatives of the vector

$$V_\mu = \partial_\eta h^\eta_\mu - \frac{1}{2}\partial_\mu h, \tag{1.8}$$

one obtains

$$R_{\mu\nu} = \frac{1}{2}(-\Box h_{\mu\nu} + \partial_\mu V_\nu + \partial_\nu V_\mu). \tag{1.9}$$

Using the harmonic gauge condition $V_\mu = \partial_\eta h^\eta_\mu - \frac{1}{2}\partial_\mu h = 0$, the previous equations becomes a linear wave equation in vacuum that holds for all ten independent components of $h_{\mu\nu}$:

$$\Box h_{\mu\nu} = 0. \tag{1.10}$$

Plane waves $h = \exp\{ikx\}$ with speed of light c are solutions of 1.10, but since the components of $h_{\mu\nu}$ can't be all equal to zero in order to have a gravitational propagation, necessarily $k_\eta k^\eta = 0 \rightarrow \frac{\omega^2}{c^2} = |\vec{h}|^2$. One can also generalize this result with sources, including the RHS of Einstein's equations (Eq. 11). Since we have found that $2R_{\mu\nu} = -\Box h_{\mu\nu}$, that by contraction with the metric becomes $2R = -\Box h$, we can write that

$$\begin{aligned} \Box\left(h_{\mu\nu} - \frac{1}{2}\eta_{\mu\nu}h\right) &= -2(R_{\mu\nu} - \frac{1}{2}\eta_{\mu\nu}R) \\ &= -2\kappa T_{\mu\nu}, \end{aligned} \tag{1.11}$$

where $\kappa = 8\pi$ (in Eq. 11 we have adopted that $G = 1$). Defining $\bar{h}_{\mu\nu} \equiv h_{\mu\nu} - \frac{1}{2}\eta_{\mu\nu}h$, the harmonic gauge condition becomes $\partial^\mu \bar{h}_{\mu\nu} = 0$, and the linearized Einstein equation yields

$$\Box \bar{h}_{\mu\nu} = -2\kappa T_{\mu\nu}. \tag{1.12}$$

1.3.2 Polarizations of gravitational waves

We now consider a plane wave $h_{\mu\nu} = C_{\mu\nu}\exp\{ikx\}$, where the symmetric matrix $C_{\mu\nu}$ is defined as the polarization tensor. We now define the *transverse traceless* (TT) gauge setting, along with the harmonic gauge condition $\partial^\mu \bar{h}_{\mu\nu} = 0$ (that constraints the polarization tensor along with the wave equation), the two constraints $h_{0a} = 0$ and $h = 0$, with $a = 1, 2, 3$ (we denote

roman letters as 3-dimensional indices).
The harmonic gauge condition then becomes

$$V_0 = \partial_\mu h_0^\mu = \partial_0 h_0^0 = -i\omega C_{00} e^{ikx} = 0 \tag{1.13}$$

$$V_a = \partial_\mu h_a^\mu = \partial_b h_a^b = -ik^b C_{ab} e^{ikx} = 0. \tag{1.14}$$

From the equations of above, we deduce that $C_{00} = 0$ and $k^b C_{ab} = 0$, i.e. the transversality of the polarization tensor. If we choose the plane wave propagating in the z direction, $\vec{k} = k\vec{e}_z$, the z row and column of the polarization tensor vanishes too. Accounting for $h = 0$ and $C_{\mu\nu} = C_{\nu\mu}$, only two independent elements are left,

$$C = \begin{pmatrix} 0 & 0 & 0 & 0 \\ 0 & C_{11} & C_{12} & 0 \\ 0 & C_{12} & -C_{11} & 0 \\ 0 & 0 & 0 & 0 \end{pmatrix} \tag{1.15}$$

For a plane wave that propagates on the z axis, the two independent components C_{11} and C_{12}, that are usually denoted as h_+ and $h_\times$, characterize completely the wave along with the frequency ω, and represent the two degrees of freedom of the gravitational field in the vacuum. Since we can always find a system of coordinates in which a single particle is stationary at the first order in $h_{\mu\nu}$, we will consider a systems of two near particles A and B, with a 4-velocity described by the vectorial field $U^\mu(x)$ and with a separation vector S^μ. The geodesic deviation equation of the system, which describes how much the two objects A and B distance themselves under the oscillating gravitational field of the wave, is

$$\frac{D^2}{d\tau^2} S^\mu = R^\mu_{\nu\rho\sigma} U^\nu U^\rho S^\sigma. \tag{1.16}$$

At the first order in $h^{TT}_{\mu\nu}$, $D \to \partial$, where $D/d\tau$ is the derivative with respect to the proper time of the particle. If the particles are in slow motion, one can write $U^\mu = (1, 0, 0, 0)$ plus correction of order $h^{TT}_{\mu\nu}$ and beyond. Since Eq. 7 is of the first order, such corrections are negligible and in the equations for $(\nu, \rho) \neq (0, 0)$ RHS is equal to zero. Besides that, since we are in a slow motion approximation, $\tau = x_0 = t$, so

$$\frac{\partial^2 S^\mu}{\partial t^2} = R^\mu_{00\sigma} S^\sigma. \tag{1.17}$$

The components of the Riemann tensor in this case will be

$$R_{\mu 00\sigma} = \frac{1}{2}(\partial_0\partial_0 h^{TT}_{\mu\sigma} + \partial_\sigma\partial_\mu h^{TT}_{00} - \partial_\sigma\partial_0 h^{TT}_{\mu 0} - \partial_\mu\partial_0 h^{TT}_{\sigma 0}). \tag{1.18}$$

Since $h^{TT}_{\mu 0} = 0$, the terms beyond the first in the equation from above vanish. So Eq. 1.16 for two slow particles at the first order is

$$\frac{\partial^2 S^\mu}{\partial t^2} = \frac{1}{2} S^\sigma \frac{\partial^2}{\partial t^2} h^{TT\mu}_\sigma. \tag{1.19}$$

From here we deduce that, if the gravitational wave popagates along the z-axis, the separation along t and z between the two particles is not altered, since

$$h^{TT\mu}_\sigma = C^\mu_\sigma e^{-i\omega(t-z)} = \begin{pmatrix} 0 & 0 & 0 & 0 \\ 0 & h_+ & h_\times & 0 \\ 0 & h_\times & -h_+ & 0 \\ 0 & 0 & 0 & 0 \end{pmatrix} e^{-i\omega(t-z)} \tag{1.20}$$

implies

$$\frac{\partial^2 S^0}{\partial t^2} = \frac{1}{2} S^\sigma \frac{\partial^2}{\partial t^2} h^{TT0}_\sigma = 0 \tag{1.21}$$

$$\frac{\partial^2 S^3}{\partial t^2} = \frac{1}{2} S^\sigma \frac{\partial^2}{\partial t^2} h^{TT3}_\sigma = 0. \tag{1.22}$$

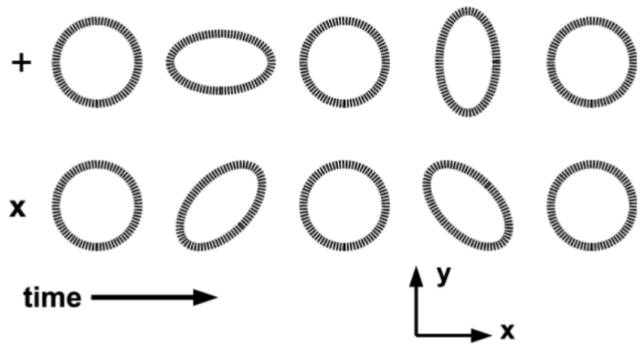

Figure 1.2: *The effects of the two polarizations, h_+ and $h_\times$, on a ring of particles in the plane orthogonal to the direction of propagation.*

Now we analyze separately the effects of the two polarizations h_+ and $h_\times$. Two particles that are initially separated in the direction $x^1(x^2)$ oscillate in the direction $x^1(x^2)$ if perturbed by a gravitational wave with $h_\times = 0$:

$$\frac{\partial^2 S^1}{\partial t^2} = \frac{1}{2} S^1 \frac{\partial^2}{\partial t^2}(h_+ e^{-i\omega(t-z)}) = 0 \rightarrow S^1(t) = \left(1 + \frac{1}{2} h_+ e^{-i\omega(t-z)}\right) S^1(0), \tag{1.23}$$

$$\frac{\partial^2 S^2}{\partial t^2} = \frac{1}{2} S^2 \frac{\partial^2}{\partial t^2}(h_+ e^{-i\omega(t-z)}) = 0 \rightarrow S^2(t) = \left(1 + \frac{1}{2} h_+ e^{-i\omega(t-z)}\right) S^2(0). \tag{1.24}$$

Viceversa, two particles that are initially separated in the direction $x^1(x^2)$ oscillate in the direction $x^2(x^1)$ if perturbed by a gravitational wave with $h_+ = 0$:

$$S^1(t) = S^1(0) + \frac{1}{2} h_\times e^{-i\omega(t-z)} S^2(0), \tag{1.25}$$

$$S^2(t) = S^2(0) + \frac{1}{2} h_\times e^{-i\omega(t-z)} S^1(0). \tag{1.26}$$

The quantities h_+ and $h_\times$ are two independent linear polarization modes of the gravitational waves. One can define the clockwise and counterclockwise circular polarizations as

$$h_R = \frac{1}{\sqrt{2}}(h_+ + i h_\times), \tag{1.27}$$

$$h_L = \frac{1}{\sqrt{2}}(h_+ - i h_\times). \tag{1.28}$$

The effect of a gravitational wave perturbation on a bunch of particles disposed on a ring is shown at Fig. 1.2. These particles assume an elliptical form that seems to rotate[5] clockwise (h_R) or counterclockwise (h_L).

1.4 Detecting gravitational waves

GW astronomy exploits multiple, widely separated detectors to distinguish GWs from local instrumental and environmental noise to provide source sky

[5]More precisely, the particles move with small epycicles around their initial position. It is their collective motion that gives the impression of a real rotation.

localization and to measure wave polarizations. Each LIGO site operates a single Advanced LIGO detector, a modified Michelson interferometer that measures GW strain as a difference in length of its orthogonal arms. Each arm is formed by two mirrors, acting as test masses, separated by 4 km. The differential length variation $\triangle L(t) = \delta L_x - \delta L_y = h(t)L$ alters the phase difference between the two light fields returning to the beam splitter, transmitting an optical signal proportional to the GW strain to the output photodetector.

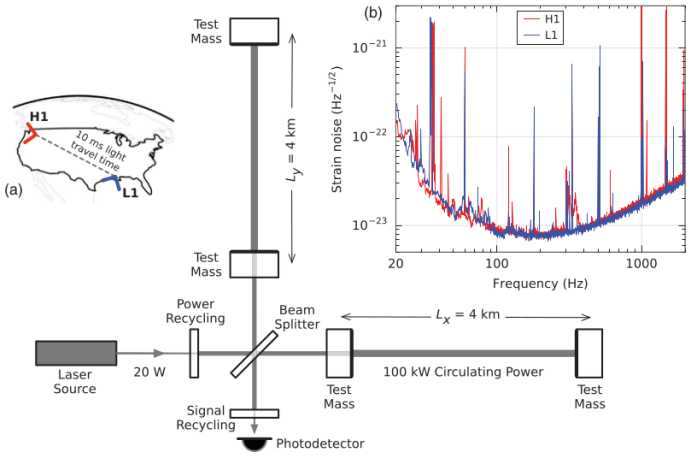

Figure 1.3: *Simplified diagram of an Advanced LIGO detector (not to scale). A gravitational wave propagating orthogonally to the detector plane and linearly polarized parallel to the 4-Km optical cavities will have the effect of lengthening one 4-Km arm and shortening the other during one half-cycle of the wave; these length changes are reversed during the other half-cycle.The output photodetector records these differential Fabri-Perot cavity length variations. Inset (a): Location and orientation of the LIGO detectors at Hanford, WA (H1) and Livingston, LA (L1). Inset (b): The instrument noise for each detector near the time of the signal detection; this is an amplitude spectral density, expressed in terms of equivalent gravitational-wave strain amplitude (source: Ref [38]).*

In order to achieve sufficient sensitivity to measure GWs, the detectors include several enhancements to the basic Michelson interferometer. For further technical details about this experimental subject, the main reference is Ref. [38], that we have closely followed in order to write this (purely informative) section.

1.5 The data analysis of gravitational wave experiments

1.5.1 A little remark

The aim of this section, in which we will briefly summarize Bayesian data analysis, is to motivate the necessity of continuous analytical model improvement in the context of gravitational wave experiments. In ground-based interferometers like LIGO and Virgo, the signal to noise ratio

$$\langle output|h_{template}\rangle = \int \frac{df}{S_n(f)} o(f) h^*_{template}(f), \tag{1.29}$$

where $o(f)$ is the detector's output, $S_n(f)$ the broadband noise of the detector and $h_{template}$ the template of the expected signal, is very low. This means that the gravitational signal that we want to observe is buried into the noise. In order to extract it, along with the values of the parameters that it intrinsecally contains, hundreds of thousands of templates of a "more truthful as possible" model are needed. In Bayesian analysis, the prior hypothesis, the model, must be of a "certain level of truth" to be plausible when compared to the data. This is evident from Fig. 1.4, where we can see a comparison between the data and two waveform models with different "levels of truth". The model with more physics (cyan), i.e. that is a better approximation of General Relativity - that is our theoretical "truth" for what concerns gravitation - represents a more tight and precise waveform than the dummy, unphysical one (blue).

1.5.2 Bayesian Analysis

Considering the LIGO and Virgo experimental framework, complete information about parameter estimation and model selection[6] is given in Refs. [45] and [46], that we follow in this short overview.

[6]Parameter estimation means to use the experimental data in order to estimate the unknown parameters of the source, whereas model selection means to decide which of several models is more probable in light of the observed data.

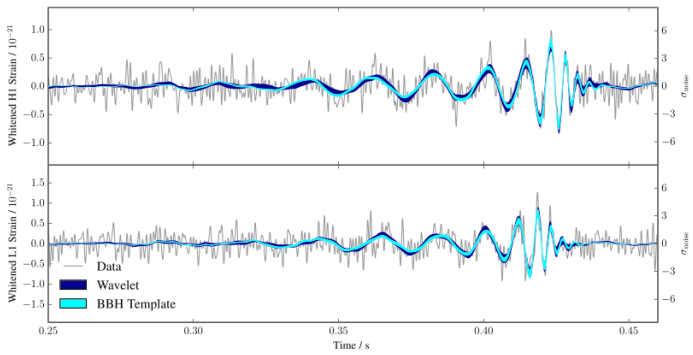

Figure 1.4: *For illustrative purposes, the figure shows the time-domain data (sampled at 2048 Hz) and reconstructed waveforms of GW150914, whitened by the noise power spectral density for the H1 (top) and L1 (bottom) detectors. The lighter, narrower shaded region (cyan) is the result from the modeled analyses using IMRPhenom and EOBNR template waveforms. The cyan region is tighter with respect to a damped-gaussian model (blue). The uncertainty is greater for this minimal-assumption reconstruction due to greater flexibility in its waveform model. The agreement between the reconstructed waveforms using the two models is found to be* $94^{+2}_{-3}\%$*, and is consistent with expectations for the SNR at which GW150914 was observed (source: Ref. [44]).*

Bayesian inference describes the state of knowledge about an uncertain hypothesis H as a probability, denoted $P(H) \in [0, 1]$, or about an unknown parameter as a probability density, denoted $p(\theta|H)$, where $\int p(\theta|H)d\theta = 1$. The relation between the prior distribution $p(\theta|H)$ and the posterior distrubution $p(\theta|d, H)$, where d is the data given by the experiment, is given by

$$p(\theta|d, H) = \frac{p(\theta|H)p(d|\theta, H)}{p(d|H)}. \tag{1.30}$$

This equation is named as Bayes theorem, and is the heart of Bayesian inference. Since models have many parameters, it is more correct to define an array of parameters $\boldsymbol{\theta} = \{\theta_1, \theta_2, ..., \theta_N\}$. In this case, the joint probability distribution $p(\boldsymbol{\theta}|d, H)$ describes the collective knowledge about all parameters as well as their relationships. Results for a specific parameter are found

by marginalising over the unwanted parameters,

$$p(\theta_1|d,H) = \int d\theta_2 ... d\theta_N p(\boldsymbol{\theta}|d,H). \tag{1.31}$$

The probability distribution can be used to find the mean

$$\langle \theta_i \rangle = \int \theta_i p(\theta_i|d,H) d\theta_i. \tag{1.32}$$

Model selection is performed by comparing the fully marginalized likelihood, or "evidence", for different models. This quantity is denoted as Z and is defined as the integral of the likelihood $\mathcal{L}(d|\boldsymbol{\theta})$ multiplied by the prior over all parameters of the model H:

$$Z = p(d|H) = \int d\theta_1 ... d\theta_N p(d|\boldsymbol{\theta},H) p(\boldsymbol{\theta}|H). \tag{1.33}$$

One can compare two competing models computing the ratio of posterior probabilities

$$O_{ij} = \frac{P(H_i|d)}{P(H_j|d)} = \frac{P(H_i)Z_i}{P(H_j)Z_j}, \tag{1.34}$$

where $B_{ij} = Z_i/Z_j$ is the "Bayes factor" between the two models i and j, which shows how much more likely the observed data d is under model i rather than model j. The choice of two competing *a priori* hypothesis is common in bayesian model selection since one cannot exhaustively enumerate the set of exclusive models describing the data.
The Bayesian analysis concepts that we have described above are simple. But in practice, dealing with large amount of data in a multi-dimensional model framework (like gravitational interferometers or particle physics experiments), requires to stochastically sample the parameter space. So parameter estimation or model selection must be done using Markov chain Monte Carlo (MCMC) and Nested Sampling techniques. Besides that, an accurate description of these methods is not in the aims of this PhD thesis.

1.5.3 Waveform models

In gravitational wave experiments, the Bayesian inference is made with different models of the GW signal that is expected to be emitted during a

compact-binary merger. These models differ in their computational complexity, the physics they simulate, and their regime of applicability. The ramification of the Ligo Advanced Library (`LAL`) that interfaces with waveform models for data analysis is called `LALInference`.
Each waveform model takes as input a parameter vector $\boldsymbol{\theta}$ and produces as output $\boldsymbol{h}_{+,\times}(\boldsymbol{\theta})$, either a time domain $h(\boldsymbol{\theta}; t)$ or frequency-domain $h(\boldsymbol{\theta}; f)$ signal. The parameter vector $\boldsymbol{\theta}$ contains at least the following parameters:

- Masses of the two components of the binary, m_1 and m_2. One can define a reparametrization of the mass plane into the chirp mass, that is
$$\mathcal{M} = \frac{(m_1 m_2)^{3/5}}{(m_1 + m_2)^{1/5}}. \tag{1.35}$$
Assuming that $m_1 \geq m_2$, one can define the *mass ratio*
$$q = \frac{m_2}{m_1}, \tag{1.36}$$
and the *symmetric mass ratio*
$$\nu = \frac{m_1 m_2}{(m_1 + m_2)^2}. \tag{1.37}$$
The objects (1.35) and (1.36) are easy to sample in a data analysis process since they are less correlated, while (1.37) has a crucial role in the EOB model (see Chapt. 4), but since its Jacobian is singular at $m_1 = m_2$, it is not used to sample the distribution of masses in the parameter space.

- The luminosity distance to the source d_L;

- The right ascension α and declination δ of the source;

- The inclination angle ι between the system's orbital angular momentum and the line of sight.

- The polarization angle ψ which describes the orientation of the projection of the binary's orbital momentum vector onto the plane on the sky.

- The time of coalescence of the binary t_c;

- The orbital phase ϕ_c of the binary at the reference time t_c.

So nine parameters are necessary to describe a circular non-spinning binary. If we wish to add the spin in our models, six additional parameters are included:

- Dimensionless spin magnitudes a_i, defined as $a_i \equiv \frac{|\boldsymbol{S}_i|}{m_i^2}$ and in the range [0,1], where $\boldsymbol{S}_i$ is the spin vector of the object i;
- Two angles for each $\boldsymbol{S}_i$ specifying its orientation with respect to the plane defined by the line of sight and the initial orbital angular momentum.

If we assume that the spin vectors are aligned or anti-aligned with the orbital angular momentum, the spin-orientation angles are fixed, and the spin magnitudes alone are used, with positive/negative signs corresponding to aligned/anti-aligned configurations (11 parameters). We stress that in this PhD thesis we will always assume that the spins are aligned, neglecting the precession modelization.
Some examples of models that one can find in `LALInference` are:

- Time-domain and frequency-domain inspiral-only post-Newtonian approximants (see Sec. 2.7).
- Frequency-domain inspiral-merger-ringdown phenomenological waveform model calibrated to Numerical Relativity, like IMRPhenomD [30].
- Time-domain inspiral-merger-ringdown effective-one-body (EOB) models calibrated to numerical relativity, that will be the main subject of this PhD dissertation starting from Chapt. 4.

We stress that many of these waveform models have additional options, such as varying the post-Newtonian order of amplitude or phase terms.

1.6 The gravitational self-force

The gravitational self-force (GSF) describes the effect of a particle's own gravitational field on its motion. In this section we would like to remind the

physical aspects of Self-Force, since it is a non-negligible effect for the modelization of compact binary systems [47]. A detailed overview of the subject is given in Ref. [48].
While the motion is geodesic in the test-mass limit, in the GSF formalism it is accelerated to the first order of particle's mass. So GSF is fundamental for the Laser Interferometer Space Antenna (LISA), which will be sensitive to low-frequency gravitational waves. Among the sources for this detector is the motion of small compact objects around massive (galactic) black holes. To calculate waves emitted by such systems requires a detailed understanding of the motion, beyond test-mass approximation. This first step was solved by Mino, Sasaki and Tanaka [49], and then by Quinn and Wald [50]. The equations of motion are now known as the MiSaTaQuWa equations. Sophisticated calculations that are similar - but more complex, since we must take into account the nonlinearities of spacetime - to QFT's regularization processes for the self-energy of an electron are necessary in order to obtain an analytical GSF expansion for a binary system. Since some PN GSF information enters into the EOB formalism as a "more physics to take into account" ingredient for its dynamical sector (see Sec. 4.2), we give here, for completeness, a Newtonian description of self-force (we closely follow Sec. V of Ref. [48]), which is useful to introduce it to the reader without getting lost into very deep and complex technical arguments that are not in the aim of this thesis.
Let's consider, in Newtonian theory, a large mass M at position $\boldsymbol{\rho}(t)$ relative to the centre of mass, and a small mass m at position $\boldsymbol{R}(t)$. We assume that $m \ll M$ and the centre of mass condition reads $m\boldsymbol{R} + M\boldsymbol{\rho} = \boldsymbol{0}$. We denote the position of an arbitrary field point by $\boldsymbol{x}$, and $r \equiv \boldsymbol{x}$ is its distance from the centre of mass. We shall also let $R \equiv |\boldsymbol{R}|$ and $\rho \equiv |\boldsymbol{\rho}|$.
In a test-mass description of the problem, the smaller mass moves in the gravitational field of the larger mass, which is placed at the origin of the coordinate system. The background Newtonian potential is

$$\Phi_0(\boldsymbol{x}) = -\frac{M}{r} \tag{1.38}$$

and the background gravitational field is $\boldsymbol{g_0} = -\boldsymbol{\nabla}\Phi_0 = -M\boldsymbol{x}/r^3$. In this description, the smaller mass m moves according to $d^2\boldsymbol{R}/dt^2 = \boldsymbol{g_0}(\boldsymbol{x} = \boldsymbol{R})$. If the motion is circular, the angular velocity of the small body is $\Omega_0^2 = M/R^3$, where R is the orbital radius. These results are in close analogy with a relativistic description in which the smaller mass is taken to move on a

geodesic of the background spacetime, in a test-mass approximation.
The Newtonian potential that takes into account the gravitational effects produced by the smaller mass is

$$\Phi(\boldsymbol{x}) = -\frac{M}{|\boldsymbol{x}-\boldsymbol{\rho}|} - \frac{m}{\boldsymbol{x}-\boldsymbol{R}}, \tag{1.39}$$

and for $m \ll M$ this can be expressed as $\Phi(\boldsymbol{x}) = \Phi_0(\boldsymbol{x}) + \delta\Phi(\boldsymbol{x})$, with a perturbation given by

$$\delta\Phi(\boldsymbol{x}) = -\frac{M}{|\boldsymbol{x}-\boldsymbol{\rho}|} + \frac{M}{r} - \frac{m}{\boldsymbol{x}-\boldsymbol{R}}. \tag{1.40}$$

This gives rise to a field perturbation $\delta\boldsymbol{g}$ that exerts a force on the smaller mass. This is the particle's "bare" self-acceleration, and there is a correspondence with the analogous relativistic problem. The last term on the right-hand side of Eq. (1.40) diverges at the position of the smaller mass. But since the gravitational field produced by this term is isotropic around $\boldsymbol{R}(t)$, we know that this field will exert no force on the particle. This term can be identified as the singular "S" part of the perturbation,

$$\Phi_{\rm S}(\boldsymbol{x}) = -\frac{m}{|\boldsymbol{x}-\boldsymbol{R}|}, \tag{1.41}$$

and the remainder as the regular "R" potential,

$$\Phi_{\rm R}(\boldsymbol{x}) = -\frac{M}{|\boldsymbol{x}-\boldsymbol{\rho}|} + \frac{M}{r}. \tag{1.42}$$

The full perturbation is given by $\delta\Phi(\boldsymbol{x}) = \Phi_{\rm S}(\boldsymbol{x}) + \Phi_{\rm R}(\boldsymbol{x})$, and only the "R" potential affects the motion of the smaller mass. These physical consideration and the split between a regular and singular have again a correspondence with the relativistic problem.
One can check that at the first order in m/M Eq. (1.42) simplifies to

$$\Phi_{\rm R}(\boldsymbol{x}) = m\frac{\boldsymbol{R}\cdot\boldsymbol{x}}{r^3}. \tag{1.43}$$

This simplification occurs because of the centre-of-mass condition, which implies that $\boldsymbol{\rho}$ is formally of order $m/M \ll 1$. The "R" part of the field perturbation is then

$$\boldsymbol{g}_{\rm R}(\boldsymbol{x}) = m\frac{3(\boldsymbol{R}\cdot\boldsymbol{x})\boldsymbol{x} - r^2\boldsymbol{R}}{r^5}, \tag{1.44}$$

and evaluating this at the particle's position yields a correction to the background field $\boldsymbol{g}_0(\boldsymbol{x} = \boldsymbol{R}) = -M\boldsymbol{R}/R^3$ given by $\boldsymbol{g}_{\rm R}(\boldsymbol{x} = \boldsymbol{R}) = 2m\boldsymbol{R}/R^3$. The force still points in the radial direction but the active mass has been shifted from M to $M-2m$. The angular velocity becomes $\Omega^2 = (M-2m)/R^3$. This can be cast in a more recognizable form if we express the angular velocity in terms of the total separation $s \equiv R + \rho = (1 + m/M)R$ between the two masses. To first order in m/M we obtain $\Omega^2 = (M + m)/s^3$, which is Kepler's third law. So the "R" part of the perturbation is responsible for the finite-mass correction to the angular velocity.

Chapter 2

Approximation Methods for General Relativity

2.1 Preamble

Due to its complexity, GR cannot be exactly solved. So, in order to do GW theory, one must juggle between different approximation approaches, which are very technical and hystorically ramified, at the point that each of them is a research area on its own. In short, they are:

- Post Newtonian Approximation (PN): It was introduced in 1916 by Einsten, Droste and Lorentz. It provides an excellent computation tool when the physical systems are slow-moving ($\frac{v}{c} \ll 1$) with a weak gravitational field inside the source ($\frac{GM}{rc^2} \ll 1$). Both of these quantities are treated as a small parameter, and the gravitational field equations are solved iteratively. A PN series is a Taylor series with n PN orders (beyond the leading order term), therefore "n-PN series" means that the series will stop at the n-th power of the velocity parameter. (see Sec. 2.2).

- Post Minkowskian Approximation (PM): Again, this method was introduced by Einstein himself in 1916. It consists of an approximation of the metric $g_{\mu\nu}$ in a postlinear way, i.e. by adding small curvature corrections to the leading order (LO) flat spacetime represented by the Minkowski metric $\eta_{\mu\nu}$. The small parameter of the expansion in this case will be Newton's coupling constant G. The first attempt to

use this kind of expansion to go beyond linearity in the solution of Einsten's Equations 11 was made by Bertotti and Plebanski [51]. Then the method was refined and pulled up to 1PM order (that is equivalent to the 2.5PN order [52]) by Damour and Deruelle [17, 18], and this was the main theoretical contribution to the discovery of PSR B1913+16 [19].

- Multipole Expansions: These expansions do not require a small parameter since they are expected to converge. This topic is very natural to approach given the structural affinities between electromagnetism and gravity as gauge field theories [53].

- Multipolar Post-Minkowskian Approximation (MPM): Since approximation methods for GR can't be applied to arbitrary sources, but have limited validity in space and time, by merging the PM formalism with a multipolar expansion one solves the problem and gets a very powerful analytical tool for the study of GR [22, 21, 54].

- W.K.B. Approximation (WKB): This is the well known high frequency or shortwave approximation [55, 56].

- Small Perturbations: This is an expansion about an arbitrary curved background rather than flat Minkowski spacetime. This topic is subdivided into two problems that lead to two different master equations: the test particle on Schwartzschild one [57, 58] and the test particle on Kerr one [59]. These equations can be solved numerically [60, 61] or with PN expansions [62].

- Numerical Methods: These may be viewed as expansions in a parameter determined by the ratio of the grid size to the typical length or time scale in the problem. If one uses numerical methods to solve Eqs. (11) directly, then we are speaking about numerical relativity (NR) [63]; if one uses a numerical method to solve approximate equations like the ones for the test particle case, then the name "NR" is not suitable.

In this thesis we will review the approaches that are useful for the GW modelization framework (i.e. the ones that are related to the EOB approach of Chapt. 4), that is one of the "last steps" in interfacing GR with GW data analysis experiments. Therefore, from the above topics, we will not consider the PM formalism and the WKB approximation, that are beyond the work done in this dissertation.

2.2 Post-Newtonian approximation

Let's start from the virial theorem ($\langle E\rangle_{kin} = \frac{1}{2}\langle V\rangle$). It is easy to obtain from it the relation

$$v^2 = \frac{GM}{r}. \tag{2.1}$$

Commonly, when we speak about a n-PN order approximation, this means that up to the parameter $(\frac{v}{c})^{2n}$ and $(\frac{GM}{rc^2})$ beyond the leading order (LO) have been retained and higher order terms have been discarded. From this point of view, is necessary to consider the Kepler law at the LO

$$(r\omega)^2 = \frac{GM}{r}, \tag{2.2}$$

that in PN expanded form becomes

$$(r\omega)^2 = \frac{GM}{r}\left[1 + a_1\left(\frac{GM}{r}\right) + a_2\left(\frac{GM}{r}\right)^2 + a_3\left(\frac{GM}{r}\right)^3 + O\left(\frac{GM}{r}\right)^4\right], \tag{2.3}$$

which is truncated at 3PN order. The values of coefficients are usually written in the harmonic gauge. Besides that, the important thing for us is that, using Eq. (2.3), it is possible to compute any relevant quantity as a power series either of the orbital frequency or the radius. Usually Eq. (2.3) is expandend defining the parameter

$$v = \left(\frac{GM\omega}{c^3}\right)^{1/3} \tag{2.4}$$

that, considering the gauge-invariant parameter in natural units $x = (M\omega)^{\frac{2}{3}}$, gives

$$v = x^{1/2}. \tag{2.5}$$

This quantity is really useful because it trasforms the PN expansions in gauge-invariant ones that do not depend on the radius and the orbital velocity.
The PN approximation, besides, is an asymptotic expansion that is non-convergent. Its validity is near the source, and far away from the source it presents divergencies.

2.3 Multipole Expansions

2.3.1 The quadrupole moment formalism

We mainly refer to Ref. [64] for the discussion of this topic. The lowest-order wave generation formalism is the quadrupole formalism of Einstein [13] and Landau & Lifshitz [65]. This formalism applies to a general isolated matter source which is PN in the sense of existence of the small parameter $\epsilon \equiv \frac{1}{c}$. However, the quadrupole formalism is valid in the Newtonian limit $\epsilon \to 0$; it can rightly be qualified as "Newtonian" because the quadrupole moment of the matter source is Newtonian and its evolution obeys Newton's laws of gravity. In this formalism the gravitational field h_{ij}^{TT} is expressed in a transverse and traceless (TT) coordinate system covering the far zone of the source at retarded times, as

$$h_{ij}^{TT} = \frac{2G}{c^4 R}\mathcal{P}_{ijab}(\boldsymbol{n})\left\{\frac{d^2 Q_{ab}}{dT^2}\left(T - \frac{R}{c}\right) + \mathcal{O}\left(\frac{1}{c}\right)\right\} + \mathcal{O}\left(\frac{1}{R^2}\right) \tag{2.6}$$

where $R = |\boldsymbol{X}|$ is the distance to the source, $T - \frac{R}{c}$ is the retarded time, $\boldsymbol{n} = \frac{\boldsymbol{X}}{R}$ is the unit direction from the source to the far away observer, and $\mathcal{P}_{ijab} = \mathcal{P}_{ia}\mathcal{P}_{jb} - \frac{1}{2}\mathcal{P}_{ij}\mathcal{P}_{ab}$ is the TT projection operator, with $\mathcal{P}_{ij} = \delta_{ij} - n_i n_j$ being the projector onto the plane orthogonal to $\boldsymbol{n}$.
The source's quadrupole moment is

$$Q_{ij}(t) = \int d^3\boldsymbol{x}\rho(\boldsymbol{x}, t)\left(x_i x_j - \frac{1}{3}\delta_{ij}|\boldsymbol{x}|^2\right) \tag{2.7}$$

where ρ is the Newtonian mass density. The total gravitational power emitted by the source in all directions around it is given by the Einstein quadrupole formula

$$\mathcal{F} \equiv \left(\frac{dE}{dT}\right)^{GW} = \frac{G}{c^5}\left\{\frac{1}{5}\frac{d^3 Q_{ab}}{dT^3}\frac{d^3 Q_{ab}}{dT^3} + \mathcal{O}\left(\frac{1}{c^2}\right)\right\} \tag{2.8}$$

where $\mathcal{F}$ stands for the total gravitational energy flux or gravitational "luminosity" of the source. The total angular momentum flux is given by

$$\mathcal{G}_i \equiv \left(\frac{dJ_i}{dT}\right)^{GW} = \frac{G}{c^5}\left\{\frac{2}{5}\epsilon_{iab}\frac{d^2 Q_{ac}}{dT^2}\frac{d^3 Q_{bc}}{dT^3} + \mathcal{O}\left(\frac{1}{c^2}\right)\right\} \tag{2.9}$$

where ϵ_{abc} denotes the Levi-Civita symbol.
The gravitational analogue of the damping force of electromagnetism, which

reacts on the source's dynamics in consequence of the emission of GWs, is given by

$$F_i^{reac} = \frac{G}{c^5}\left\{-\frac{2}{5}x^a\frac{d^5Q_{ia}}{dt^5} + \mathcal{O}\left(\frac{1}{c^2}\right)\right\}. \tag{2.10}$$

It is relevant to remember that the gravitational radiation reaction is gauge-dependent, so the expression of the force depends on the coordinate system which is used. Let's now consider the energy and angular momentum of a matter system made of some perfect fluid:

$$E = \int d^3\boldsymbol{x}\ \rho\left[\frac{|\boldsymbol{v}|^2}{2} + \Pi - \frac{U}{2}\right] + \mathcal{O}\left(\frac{1}{c^2}\right) \tag{2.11}$$

$$J_i = \int d^3\boldsymbol{x}\ \rho\epsilon_{iab}x^a v^b + \mathcal{O}\left(\frac{1}{c^2}\right) \tag{2.12}$$

The specific internal energy of the fluid is denoted Π, and obeys the usual thermodynamic relation $d\Pi = -Pd(\frac{1}{\rho})$ where P is the pressure and ρ the mass density; the gravitational potential obeys Poisson equation $\nabla U = -4\pi G\rho$. Using the usual equation of motion $\rho\frac{dv^i}{dt} = -\partial_i P + \rho\partial_i U + F_i^{reac}$ and continuity equation $\partial_t\rho + \partial_i(\rho v^i) = 0$, one can compute the mechanical losses of energy and angular momentum from the time derivatives of E an J_i. The conservative PN corrections are neglected, but the radiation-reaction contribution F_i^{reac} is added in order to be consistent with the physics of the process. The result is

$$\frac{dE}{dt} = \int d^3\boldsymbol{x}\ v^i F_i^{reac} = -\mathcal{F} + \frac{df}{dt}, \tag{2.13}$$

$$\frac{dJ_i}{dt} = \int d^3\boldsymbol{x}\ \epsilon_{iab}x_a F_b^{reac} = -\mathcal{G}_i + \frac{dg_i}{dt}, \tag{2.14}$$

where the total time derivatives of f and g_i are made of quadratic products of derivatives of the quadrupole moment. Looking only for secular effects, one can apply an average over time on a typical period of variation of the system, obtaining

$$\langle\frac{dE}{dt}\rangle = -\langle\mathcal{F}\rangle, \tag{2.15}$$

$$\langle\frac{dJ_i}{dt}\rangle = -\langle\mathcal{G}_i\rangle, \tag{2.16}$$

where the brackets denote the time averaging over an orbit. These balance equations encode the secular decreases of energy and angular momentum by gravitational radiation emission. Using the binary's Newtonian energy and angular momentum,

$$E = -\frac{Gm_1m_2}{2a} \tag{2.17}$$

$$J = m_1m_2\sqrt{\frac{Ga(1-e^2)}{m_1+m_2}}, \tag{2.18}$$

where a and e are the semi-major axis and eccentricity of the orbit and m_1 and m_2 are the two masses, from the energy balance equation (2.17) one obtains the secular evolution of a and, changing from a to the orbital period P using Kepler's third law[1], the secular evolution of the orbital period P, namely

$$\langle\frac{dP}{dt}\rangle = -\frac{192\pi}{5c^5}\left(\frac{2\pi G}{P}\right)^{5/3}\frac{m_1m_2}{(m_1+m_2)^{1/3}}\frac{1+\frac{73}{24}e^2+\frac{37}{96}e^4}{(1-e^2)^{7/2}}. \tag{2.19}$$

The last factor, depending on the eccentricity, comes out from the orbital average and is known as the Peters & Mathews [66] "enhancement" factor. The secular evolution of the eccentricity e is deduced from the angular momentum balance equation (2.18), as

$$\langle\frac{de}{dt}\rangle = -\frac{608\pi}{15c^5}\frac{e}{P}\left(\frac{2\pi G}{P}\right)^{5/3}\frac{m_1m_2}{(m_1+m_2)^{1/3}}\frac{1+\frac{121}{304}e^2}{(1-e^2)^{5/2}}. \tag{2.20}$$

Interestingly, the system of equations (2.19)-(2.20) can be thoroughly integrated in closed analytic form. This yields the evolution of the eccentricity [67]:

$$\frac{e^2}{(1-e^2)^{19/6}}\left(1+\frac{121}{304}e^2\right)^{145/121} = c_0P^{19/9}, \tag{2.21}$$

where c_0 denotes an integration constant to be determined by the initial conditions at the start of the binary evolution. When $e << 1$ the latter relation gives approximately $e^2 \sim c_0P^{19/9}$.

It is important to stress that if for a long while it was thought that the

[1] $GM = \Omega^2a^3$, where $M = m_1 + m_2$ is the total mass and $\Omega = \frac{2\pi}{P}$ is the orbital frequency.

quadrupole formalism was sufficient for the observation of *all* compact binaries, it is only the *first order* approximation of a more complex PN multipole series that contains (part of) the theoretical information necessary to advanced detectors and strong-field regime sources [68, 69, 70]. Having said that, the quadrupole formalism contains the basic physical properties of coalescing compact binaries. Looking at Eq. (2.19) and Eq. (2.20), one can deduce that the two compact binaries steadily lose their orbital binding energy by emission of gravitational radiation; as a result, the orbital separation between them decreases, and the orbital frequency increases. Thus, the frequency of the GW signal, which equals twice the orbital frequency for the dominant harmonics, "chirps" in time (i.e. the signal becomes higher and higher pitched) until the two objects collide and merge, as what was predicted for the first time by Dyson [71]. The orbit of most inspiralling compact binaries can be considered to be *circular*, apart from the gradual inspiral, because the gravitational radiation reaction forces tend to circularize the motion rapidily. This effect is due to the emission of angular momentum by GWs, resulting in a secular decrease of the eccentricity of the orbit. That being said, the main point about modelling the inspiralling compact binary is that a model made of two structureless point particles, characterized solely by two mass parameters m_a and possibly two spins S_a, with $a = 1, 2$, is sufficient in first approximation. Indeed, most of the non-gravitational effects usually plaguing the dynamics of binary star systems, such as the effects of a magnetic field of an interstellar medium, are dominated by gravitational effects. The main reason for a model of point particles is that the effects due to the finite size of the compact bodies are small.

2.3.2 STF tensor approach

Before introducing the multipolar expansion of the gravitational field, which is the "next natural step" after the definition of the quadrupolar approximation, we review the "language" in which this expansion is written.
The multipole expansions of a field are common objects that are used in different fields of physics (see for example electromagnetism [72]), and for what concerns GWs, it was introduced by Thorne [53] in 1980 and refined by Damour and Iyer [26] ten years after. In this PhD thesis we'll always refer to the latter approach, that is briefly overviewed here following the more detailed Ref. [73].
Firstly, let's remind that $A_L B^L = \sum_{i_1 \dots i_\ell} A_{i_1 \dots i_\ell} B^{i_1 \dots i_\ell}$; $\delta_{ij} = \delta^{ij} = diag(+1, +1, +1)$;

$x^L = x^{i_1}...x^{i_\ell}$; $n^i = \frac{x^i}{r}$ (unit radial vector); $n^L = n^{i_1}...n^{i_\ell}$; $\partial_L = \partial_{i_1...i_\ell}$; $\ell!! = \ell(\ell-2)(\ell-4)...2$ or 1.
Let's consider a Cartesian tensor

$$A_L = A_{(i_1....i_\ell)} = \frac{1}{\ell!}\sum_\sigma A_{i_{\sigma(1)}...i_{\sigma(\ell)}} \tag{2.22}$$

its symmetric part is denoted by (...) parenthesis, and σ runs over all the $\ell!$ permutations of $(1, 2, 3...\ell)$. Usually, the STF part of a tensor is denoted by angular brackets $A_{<L>}$ (as in the previous Poisson PDE example) or by a more explicit STF_L. The STF part of a tensor, which is not STF, is obtained computing its symmetric part

$$S_L = \frac{1}{\ell!}\sum_\sigma A_{i_{\sigma(1)}...i_{\sigma(\ell)}} \tag{2.23}$$

and removing all traces

$$A_{<L>} = \sum_{n=0}^{\left[\frac{\ell}{2}\right]} a_n^l \delta_{(i_1 i_2}\delta_{i_3 i_4}...\delta_{i_{2n-1}i_{2n}}S_{i_{2n+1}...i_\ell)j_1 j_1...j_n j_n} \tag{2.24}$$

where

$$a_n^\ell = \frac{(-)^n \ell!(2\ell-2n-1)!!}{(\ell-2n)!(2\ell-1)!!(2n)!!} \tag{2.25}$$

and $\left[\frac{\ell}{2}\right]$ is the largest integer less than or equal to $\frac{\ell}{2}$. The first term in (2.24) is S_L ($a_0^\ell = 1$), and the subsequent terms are obtained by tracing S_L over one, two... $\left[\frac{\ell}{2}\right]$ pair of indeces. For $\ell = 2$ and $\ell = 3$ is simple to obtain

$$A_{<i_1 i_2>} = \frac{1}{2}(A_{i_1 i_2} + A_{i_2 i_1}) - \frac{1}{3}\delta_{i_1 i_2}A_{jj} \tag{2.26}$$

and

$$A_{<i_1 i_2 i_3>} = A_{(i_1 i_2 i_3)} - \frac{1}{5}(\delta_{i_1 i_2}A_{(jji_3)} + \delta_{i_2 i_3}A_{jji_1} + \delta_{i_3 i_1}A_{jji_2}) \tag{2.27}$$

The proof of Eq. (2.24) follows by noting that the STF tensor is constructed by tracing successively over 0,1,2... pairs of indices. The coefficient of each of these type of terms is determined by tracing both sides of Eq. (2.24) over a pair of indices, two pairs etc. The left hand side yields zero, while a

contraction on the k^{th} term on the right hand side yields a S contracted (k) times or $(k+1)$ times. Consequently, cancellation of terms after contraction will occur only between successive terms, leading to a relative sign between them. Thus, if

$$\hat{S}_{i_1...i_n} = S_{i_1...i_n} - a_2\delta_{(i_1i_2}S_{i_3i_4...i_n)j_1j_1} + a_4\delta_{(i_1i_2}\delta_{i_3i_4}S_{i_5i_6...i_n)j_1j_1j_2j_2} \\ + ... + (-)^k a_{2k}\delta_{(i_1i_2}\delta_{i_3i_4}...\delta_{i_{2k-1}i_{2k}}S_{i_{2k+1}...i_n)j_1j_1...j_kj_k}... \tag{2.28}$$

nothing that $(a^\ell_k = (-)^k a_{2k})$, after some algebra we obtain

$$a_{2(k+1)} = \frac{(n-2k)(n-2k-1)}{2(k+1)(2n-2k-1)}a_{2k}, \tag{2.29}$$

which using $a_0 = 1$ yields

$$a_{2k} = \frac{\binom{n}{2k}\binom{n}{k}}{\binom{2n}{2k}}. \tag{2.30}$$

This leads directly to (2.25) determining the a^ℓ_n.
In general, the set of all STF Cartesian tensors of rank ℓ generates an irreducible representation of weight ℓ and dimension $(2\ell+1)$ of the group of proper rotations $SO(3)$, and any reducible tensor of rank p can be decomposed in a sum of pieces each of which belongs to an irreducible representation and hence is expressible in terms of some building brick STF tensor of rank less than or equal to p.
If e_i denotes the Cartesian basis vectors, the basis of the $(2\ell+1)$-dimensional vector space of STF rank ℓ-tensors is made of the STF parts of the ℓ-fold tensorial products

$$(e_1 + ie_2) \otimes (e_1 + ie_2)... \otimes (e_1 + ie_2) \otimes e_3 \otimes e_3... \otimes e_3 \tag{2.31}$$

And their complex conjugates. Remembering that $e^j_i = \delta^j_i$ and defining $\delta^+_{i_m} \equiv \delta^1_{i_m} + \delta^2_{i_m}$, for $m > 0$ one can choose a basis

$$\hat{\mathcal{Y}}^{\ell m}_L = A^{\ell m} E^{\ell m}_{<L>} \tag{2.32}$$

where

$$E^{\ell m}_L = \delta^+_{i_1}\delta^+_{i_2}...\delta^+_{i_m}\delta^3_{i_{m+1}}...\delta^3_{i_\ell} \tag{2.33}$$

and

$$A^{\ell m} = (-)^m(2\ell-1)!!\sqrt{\frac{2\ell+1}{4\pi(\ell-m)!(\ell+m)!}}. \tag{2.34}$$

This constant is chosen in order to respect the orthonormality relation

$$\sum_{i_1 \ldots i_\ell} \hat{\mathcal{Y}}_L^{\ell m} (\hat{\mathcal{Y}}_L^{\ell m'})^* = \frac{(2\ell+1)!!}{4\pi \ell!} \delta_{mm'}. \tag{2.35}$$

This is consistent with the standard normalization rule for the spherical harmonics $Y_{\ell m}$

$$\int d\Omega Y_{\ell m} Y^*_{\ell' m'} = \delta_{\ell \ell'} \delta_{mm'}. \tag{2.36}$$

If

$$Y_{lm} = \hat{\mathcal{Y}}_L^{\ell m} n_L, \tag{2.37}$$

for $m < 0$

$$\hat{\mathcal{Y}}_L^{\ell m} = (-)^m (\hat{\mathcal{Y}}_L^{\ell |m|})^*. \tag{2.38}$$

The (2.37) formula is very important because it allows to easily compute the usual spherical harmonics by the canonical basis of the vector space of STF tensors $\hat{\mathcal{Y}}_L^{\ell m}$. Starting from Eq. (2.24) and using Eq. (2.33), a straightforward calculation shows that

$$E^{\ell m}_{<L>} = \frac{(\ell - m)!}{(2\ell - 1)!!} \sum_{k=0}^{\left[\frac{\ell - m}{2}\right]} \frac{(-)^k (2\ell - 2k - 1)!!}{(2k)!! (\ell - m - 2k)!} \delta_{(i_1 i_2 \ldots} \tag{2.39}$$
$$\delta_{i_{2k-1} i_{2k}} \delta^+_{i_{2k-1}} \ldots \delta^+_{i_{2k+m}} \delta^3_{i_{2k+m+1}} \ldots \delta^3_{i_\ell)}.$$

Hence, one can obtain an alternative canonical basis expression

$$\hat{\mathcal{Y}}_L^{\ell m} = c_{\ell m} \sum_{k=0}^{\left[\frac{\ell - m}{2}\right]} a_{\ell m k} \delta_{(i_1 i_2} \ldots \delta_{i_{2k-1} i_{2k}} \delta^+_{i_{2k-1}} \ldots \delta^+_{i_{2k+m}} \delta^3_{i_{2k+m+1}} \ldots \delta^3_{i_\ell)}, \tag{2.40}$$

where

$$c_{\ell m} = (-)^m \sqrt{\frac{(2\ell+1)(\ell - m)!}{4\pi (\ell + m)!}} \tag{2.41}$$

and

$$a_{\ell m k} = \frac{(-)^k (2\ell - 2k)!}{2^\ell k! (\ell - k)! (\ell - m - 2k)!}. \tag{2.42}$$

Now, a deeper insight to the relation beetween $\hat{\mathcal{Y}}_L^{\ell m}$ is useful in this discussion. For $m \geq 0$, the usual spherical harmonics can be written as

$$Y^{\ell m} = c_{\ell m} e^{im\phi} P_{\ell m}(\cos\theta), \tag{2.43}$$

where

$$P^{\ell m}(\cos\theta) = (\sin\theta)^m \sum_{j=0}^{\left[\frac{\ell-m}{2}\right]} a_{\ell m j}(\cos\theta)^{\ell-m-2j}. \tag{2.44}$$

The $Y^{\ell m}$'s generate an irreducible representation of the rotation group of weight ℓ and dimension $(2\ell+1)$. As previously seen, the set of all STF tensors of rank ℓ is also an irreducible representation of dimension $(2\ell+1)$. To exhibit the one-one mapping between the spherical harmonics and the STF tensors as written by Thorne [53], one can express the cartesian components of the unit radial vector $\hat{n}$ as

$$\begin{aligned} n_x + i n_y &= \sin\theta\cos\phi + i\sin\theta\cos\phi = \sin\theta e^{i\phi} \\ n_z &= \cos\theta, \end{aligned} \tag{2.45}$$

and rewrite

$$Y^{\ell m} = c_{\ell m} \sum_{j=0}^{\left[\frac{\ell-m}{2}\right]} a_{\ell m j}(n_x + i n_y)^m n_z^{\ell-m-2j}. \tag{2.46}$$

This is consistent with Eq. (2.37). The above formula allows one to use either the spherical harmonics or the STF tensors to expand any function of θ and ϕ on the unit sphere centered on the coordinate origin. One can have

$$f(\theta,\phi) = \sum_{\ell=0}^{\infty} \sum_{m=-\ell}^{m=\ell} F^{\ell m} Y_{\ell m}(\theta,\phi) \tag{2.47}$$

or

$$f(\theta,\phi) = \sum_{\ell=0}^{\infty} \mathcal{F}_L n_L. \tag{2.48}$$

The expansion coefficients in both schemes are related via

$$\mathcal{F}_L = \sum_{m=-\ell}^{m=\ell} F^{\ell m} \hat{\mathcal{Y}}_L^{\ell m} \tag{2.49}$$

or

$$F^{\ell m} = 4\pi \left(\frac{\ell!}{(2\ell+1)!}\right) \mathcal{F}_L \hat{\mathcal{Y}}_L^{\ell m *}. \tag{2.50}$$

Let's now consider an arbitrary reducible tensor T_P; one can decompose it into a finite sum of terms in the form $A_P^L \hat{B}_L$, where A_P^L is a tensor invariant

under $SO(3)$, made up of products of ϵ_{ijk} and δ_{ij}, and $\hat{B}_L$ is an irreducible STF ℓ-tensor of rank $\ell \leq p$ obtained by first contracting T_P with δ's and ϵ's before applying the STF projection. This decomposition corresponds to expressing the repeated direct product of representations in term of direct sums of irreducible representations

$$\mathcal{D}_s \otimes \mathcal{D}_\ell = \mathcal{D}_{|\ell-s|} \oplus \mathcal{D}_{|\ell-s+1|} \oplus ... \oplus \mathcal{D}_{\ell+s}, \tag{2.51}$$

that is common in group theory textbooks as an example involving the quantum mechanics angular momentum addition rule $\boldsymbol{J} = \boldsymbol{L} + \boldsymbol{S}$.
The consideration from above is a generalization of the decomposition of an arbitrary matrix into its trace, antisimmetric part and symmetric traceless part

$$T_{ab} = T_{<ab>} + T_{[ab]} + \frac{1}{3}\delta_{ab}T. \tag{2.52}$$

The only two possible contractions of T_{ab} with invariant tensors in this case are $T = \delta_{ab}T^{ab}$ and $\tilde{T}^a = \frac{1}{2}\epsilon^{abc}T_{bc}$, and (2.52) is equivalent to a sum of irreducible pieces since $T_{[ab]} = \epsilon_{abc}\tilde{T}_c$.

2.3.3 Application to linearized gravity

In the following, we will use capital letters (for example $\boldsymbol{X}$) in order to distinguish the coordinates in the region outside the source with the ones inside the source (lowercase letters). This means that one arbitrary radiation source $S(\boldsymbol{x}, t)$ is spatially confined to the region $|\boldsymbol{x}| < r_0$, i.e. $S(\boldsymbol{x}, t) = 0$ if $|\boldsymbol{x}| > r_0$.
The vacuum field equations of linearized gravity in the harmonic gauge (1.10) may be conveniently written, considering also the R.H.S. of Eq. (11) as

$$\Box\bar{h}_{\mu\nu}(\boldsymbol{X}, T) = -\frac{16\pi G}{c^4}T_{\mu\nu}(\boldsymbol{X}, T). \tag{2.53}$$

If the source $T^{\mu\nu}$ is compact supported in the region exterior to the source we have the following multipole expansions for $\bar{h}_{\mu\nu}$ [73]:

$$\bar{h}^{00}(\boldsymbol{X}, T) = \frac{4G}{c^4}\sum_{\ell=0}^{\infty}\frac{(-)^\ell}{\ell!}\partial_L\left(\frac{F_L(U)}{R}\right) \tag{2.54}$$

$$\bar{h}^{0i}(\boldsymbol{X}, T) = \frac{4G}{c^4}\sum_{\ell=0}^{\infty}\frac{(-)^\ell}{\ell!}\partial_L\left(\frac{G_{iL}(U)}{R}\right) \tag{2.55}$$

$$\bar{h}^{ij}(\boldsymbol{X},T)=\frac{4G}{c^4}\sum_{\ell=0}^{\infty}\frac{(-)^\ell}{\ell!}\partial_L\left(\frac{H_{ijL}(U)}{R}\right), \tag{2.56}$$

where

$$F_L(U)\equiv\int d^3x\hat{x}_L\int_{-1}^{1}dz\delta_\ell(z)\tilde{T}^{00} \tag{2.57}$$

$$G_{iL}(U)\equiv\int d^3x\hat{x}_L\int_{-1}^{1}dz\delta_\ell(z)\tilde{T}^{0i} \tag{2.58}$$

$$H_{ijL}(U)\equiv\int d^3x\hat{x}_L\int_{-1}^{1}dz\delta_\ell(z)\tilde{T}^{ij}, \tag{2.59}$$

where $\tilde{T}^{\mu\nu}=T^{\mu\nu}(\boldsymbol{x},U+\frac{rz}{c})$. Since G_{iL} is reducible, it may be decomposed into three irreducible pieces (for convenience the numerical factors are absorbed in the "bricks"):

$$G^{(+)}_{L+1}\equiv G_{<L+1>} \tag{2.60}$$

$$G^{(0)}_{L}\equiv\frac{\ell}{\ell+1}G_{ab<L-1}\epsilon_{i_L>ab} \tag{2.61}$$

$$G^{(-)}_{L-1}\equiv\frac{2\ell-1}{2\ell+1}G_{aaL-1} \tag{2.62}$$

such that

$$G_{iL}=G^{(+)}_{iL}+\epsilon_{ai<i_\ell}G^{(0)}_{L-1>a}+\delta_{i<i_\ell}G^{(-)}_{L-1>}. \tag{2.63}$$

Similarly, H_{ijL} is also reducible and can be decomposed into six irreducible pieces:

$$H^{(+2)}_{L+2}\equiv H_{<L+2>} \tag{2.64}$$

$$H^{(+1)}_{L+1}\equiv\frac{2\ell}{\ell+2}STF_{L+1}(H_{<ci_\ell>dL-1}\epsilon_{i_{\ell+1}cd}) \tag{2.65}$$

$$H^{(0)}_{L}\equiv\frac{6\ell(2\ell-1)}{(\ell+1)(2\ell+3)}STF_{L}(H_{<ai_\ell>aL-1}) \tag{2.66}$$

$$H^{(-1)}_{L-1}\equiv\frac{2(\ell-1)(2\ell-1)}{(\ell+1)(2\ell+1)}STF_{L-1}(H_{<ca>bcL-2}\epsilon_{i_{\ell-1}ab}) \tag{2.67}$$

$$H^{(-2)}_{L-2}\equiv\frac{2\ell-3}{2\ell+1}H_{<ac>acL-2} \tag{2.68}$$

$$K_L\equiv\frac{1}{3}H_{aaL} \tag{2.69}$$

such that

$$H_{ijL} = H^{(+2)}_{ijL} + STF_L STF_{ij}(\epsilon_{aii_\ell} H^{(+1)}_{ajL-1} + \delta_{ii_\ell} H^{(0)}_{jL-1} + \delta_{ii_\ell}\epsilon_{aji_{\ell-1}} H^{(-1)}_{aL-2} + \delta_{ii_\ell}\delta_{ji_{\ell-1}} H^{(-2)}_{L-2}) + \delta_{ij} K_L. \tag{2.70}$$

By neglecting the technical details and long calculations of Ref. [26], at this point the crucial step is to perform the gauge transformation that preserves harmonicity; then, by using the conservation laws for mass, center of mass and angular momentum of the source, one obtains that $\bar{h}^{\alpha\beta}$ in the canonical gauge is determined by two sets of unknown functions $\mathcal{M}_L = \{M_L, S_L\}$ and given by

$$\bar{h}^{00}_{can}(\boldsymbol{X}, T) = \frac{4}{c^2}\left[\sum_{\ell=0}^{\infty} \frac{(-)^\ell}{\ell!} \partial_L \left(\frac{M_L(U)}{R}\right)\right] \tag{2.71}$$

$$\bar{h}^{0i}_{can}(\boldsymbol{X}, T) = -\frac{4}{c^3}\left\{\sum_{\ell=1}^{\infty} \frac{(-)^\ell}{\ell!}\left[\partial_{L-1}\left(\frac{\dot{M}_{iL-1}(U)}{R}\right) + \frac{\ell}{\ell+1}\epsilon_{iab}\partial_{aL-1}\left(\frac{S_{bL-1}(U)}{R}\right)\right]\right\} \tag{2.72}$$

$$\bar{h}^{ij}_{can}(\boldsymbol{X}, T) = \frac{4}{c^4}\left\{\sum_{\ell=2}^{\infty} \frac{(-)^\ell}{\ell!}\left[\partial_{L-2}\left(\frac{\ddot{M}_{ijL-2}(U)}{R}\right) + \frac{2\ell}{\ell+1}\partial_{aL-2}\left(\frac{\epsilon_{ab(i}\dot{S}_{j)bL-2}(U)}{R}\right)\right]\right\}, \tag{2.73}$$

where the "mass multipole moments" (that in this case substitute the charge multipole moments of electromagnetism) for $\ell \geq 0$ are given by

$$M_L(U) = G\int d^3x \int_{-1}^{1} dz \left\{\delta_\ell \hat{x}_L \tilde{\sigma} - \frac{4(2\ell+1)}{c^2(\ell+1)(2\ell+3)}\delta_{\ell+1}\hat{x}_{aL}\frac{\partial}{\partial U}\tilde{\sigma}^a + \frac{2(2\ell+1)}{c^4(\ell+1)(\ell+2)(2\ell+5)}\delta_{\ell+2}\hat{x}_{abL}\frac{\partial^2}{\partial U^2}\tilde{T}^{ab}\right\} \tag{2.74}$$

and the "spin multipole moments" (that in gravity substitute the magnetic multipole moments of electromagnetism) for $\ell \geq 1$ are given by

$$S_L(U) = GSTF_L \int d^3x \int_{-1}^{1} dz \Bigg\{ \delta_\ell \hat{x}_{L-1} \epsilon_{i\ell ab} x^a \tilde{\sigma}^b - \frac{2\ell+1}{c^2(\ell+2)(2\ell+3)} \delta_{\ell+1} \epsilon_{i\ell ab} \hat{x}_{acL-1} \frac{\partial}{\partial U} \tilde{T}^{bc} \Bigg\}, \tag{2.75}$$

where $\sigma \equiv \frac{T^{00}+T^{ss}}{c^2}$, $\sigma^a \equiv \frac{T^{0a}}{c}$ and the tilde has the same meaning as before. For some interesting analogies between Einstein's theory of gravity and electromagnetism - i.e. the "gravitomagnetism" topic -, see Sec. 3.1.2 of this dissertation.
Let's now consider $\ell = 0$. By STF-decomposing Eq. (2.75) we obtain the following expression which is equivalent to the static multipole

$$\begin{aligned} Mc^2 &= \int d^3x \int_{-1}^{1} dz \delta_0 (\tilde{T}^{00} - z n^a \tilde{T}^{0a}) \\ &= \int d^3x T^{00}(\boldsymbol{x}, t) \end{aligned} \tag{2.76}$$

and for $\ell = 1$

$$\begin{aligned} M_i &= \int d^3x \int_{-1}^{1} dz \delta_1 [x^i (\tilde{T}^{00} - z n^a \tilde{T}^{0a}) - r z (\tilde{T}^{0i} - z n_b \tilde{T}^{ib})] \\ &= \int d^3x x^i T^{00}(\boldsymbol{x}, t). \end{aligned} \tag{2.77}$$

Considering also Eq. (2.76),

$$\begin{aligned} S_i &= \int d^3x \int_{-1}^{1} dz \delta_1 \epsilon_{iab} x_a (\tilde{T}^{0b} - z n_c \tilde{T}^{bc}) \\ &= \epsilon_{iab} \int d^3x x^a T^{0b}(\boldsymbol{x}, t). \end{aligned} \tag{2.78}$$

Therefore, in the linearized gravity case, the efficiency of the STF techniques has allowed to obtain closed form expressions for the spin and mass moments in terms of the stress energy distribution of the source. Furthermore, it encompasses the static moment as well. It is important to keep in mind that M_L and S_L are the *canonical* multipolar moments, whereas the *source*

moments, which are written in terms of the source variables in a consistent way with Eqs (2.75) and (2.76), are

$$I_L(U) = \int d^3x \int_{-1}^{1} dz \Bigg\{ \delta_\ell \hat{x}_L \Sigma - \frac{4(2\ell+1)}{c^2(\ell+1)(2\ell+3)} \delta_{\ell+1} \hat{x}_{aL} \frac{\partial}{\partial U} \Sigma^a + \frac{2(2\ell+1)}{c^4(\ell+1)(\ell+2)(2\ell+5)} \delta_{\ell+2} \hat{x}_{abL} \frac{\partial^2}{\partial U^2} \Sigma^{ab} \Bigg\} (\boldsymbol{x}, u + \frac{zr}{c}) \tag{2.79}$$

and

$$J_L(U) = STF_L \int d^3x \int_{-1}^{1} dz \Bigg\{ \delta_\ell \hat{x}_{L-1} \epsilon_{i_\ell ab} x^a \Sigma^b - \frac{2\ell+1}{c^2(\ell+2)(2\ell+3)} \delta_{\ell+1} \epsilon_{i_\ell ab} \hat{x}_{acL-1} \frac{\partial}{\partial U} \Sigma^{bc} \Bigg\} (\boldsymbol{x}, u + \frac{zr}{c}), \tag{2.80}$$

where the source densities are defined from the PN expansion (denoted by an overbar) of the pseudo-tensor $\tau^{\mu\nu}$ by

$$\Sigma = \frac{\bar{\tau}^{00} + \bar{\tau}^{ii}}{c^2}, \tag{2.81}$$

$$\Sigma_i = \frac{\bar{\tau}^{0i}}{c}, \tag{2.82}$$

and

$$\Sigma_{ij} = \bar{\tau}^{ij}. \tag{2.83}$$

Source multipoles are valid in the "near zone" (distances from the source that are short compared to the gravitational wavelength), while radiative multipoles (that we will discuss in the next section) are valid in the "far zone" (distances that are large compared to the physical size of the source).

2.3.4 The radiative multipole moments

If one moves far away from the source, the emitted spherical waves will become like plane waves. GWs are transversal in respect to the direction of propagation, therefore, there is a symmetric and traceless tensor in the local plane tangent to the field irradiated in form of spherical wavefronts and orthogonal to the versor $\boldsymbol{n}$ normal to them. We want to project the

wave on this plane in a STF form. Given the direction $\boldsymbol{n}$, one can define the projection operation

$$P_{ij}(\boldsymbol{n}) = \delta_{ij} - n_i n_j. \tag{2.84}$$

Doing twice this operation it is easy to obtain the TT projection operator

$$P_{ijab} = P_{ia}(\boldsymbol{n})P_{jb}(\boldsymbol{n}) - \frac{1}{2}P_{ij}(\boldsymbol{n})P_{ab}(\boldsymbol{n}). \tag{2.85}$$

Using Eqs (2.71),(2.73) and (2.74) one can define

$$h_{ij}^{TT} = \frac{4G}{c^2 R}P_{ijab}(\boldsymbol{n})\sum_{\ell=2}^{\infty}\frac{1}{c^\ell \ell!}\left\{n_{L-2}U_{abL-2}(U) - \frac{2\ell}{c(\ell+1)}n_{cL-2}\epsilon_{cd<a}V_{b>dL-2}(U)\right\}, \tag{2.86}$$

where $U_L(U)$ are the mass-type radiative multipole moments and $V_L(U)$ the current-type radiative multipole moments. Radiative coordinates are such that the retarded time $U \equiv T - \frac{R}{c}$ becomes asymptotically a null coordinate at future null infinity. The multipole decomposition from above represents the generalization of quadrupole formalism and at this point it is necessary to put it in relation with the source parameters. At Newtonian level, the mapping between radiative multipole moments and source parameters is

$$U_{ij}(U) = Q_{ij}^{(2)}(U) + \mathcal{O}\left(\frac{1}{c^2}\right), \tag{2.87}$$

where Q_{ij} is the Newtonian quadrupole moment. In linearized gravity, generalizing this case,

$$U_L = I_L^{(\ell)} \tag{2.88}$$

and

$$V_L = J_L^{(\ell)}. \tag{2.89}$$

Keeping in mind Eqs (2.79) and (2.80), (2.86) becomes

$$h_{ij}^{TT} = \frac{4G}{c^2 R}P_{ijab}\left\{I_{ab}^{(2)} + \frac{1}{3c}I_{abc}^{(3)}n^c + \frac{4}{3c}\epsilon_{cd<a}J_{b>c}^{(2)}n^d + \frac{1}{12c^2}I_{abcd}^{(4)}n^c n^d + ...\right\}, \tag{2.90}$$

where $I_{ab}^{(2)} \equiv Q_{ab}^{(2)}$. It is possible to compute the energy flux from the radiative multipole moments using the formula

$$\mathcal{F} = \sum_{\ell=2}^{\infty}[(\dot{U}_L)^2 + (\dot{V}_L)^2], \tag{2.91}$$

that in terms of the source multipole moments becomes

$$\mathcal{F} = \sum_{\ell=2}^{\infty} \frac{1}{c^{2\ell}} \left[(I_L^{(\ell+1)})^2 + \frac{1}{c^2} (J_L^{(\ell+1)})^2 \right]. \tag{2.92}$$

Let's now introduce two unit polarization vectors $\boldsymbol{p}$ and $\boldsymbol{q}$, orthogonal and transverse to the direction of propagation $\boldsymbol{n}$. Then the two "plus" and "cross" polarization states of the asymptotic waveform are defined by

$$h_+ = \frac{1}{2}(p_i p_j - q_i q_j) h_{ij}^{TT} \tag{2.93}$$

and

$$h_\times = \frac{1}{2}(p_i q_j + p_j q_i) h_{ij}^{TT}. \tag{2.94}$$

Although the multipole decomposition (2.86) is completely general, it will also be important, having in view the comparison between PN and numerical results, to consider separately the various modes (ℓ, m) of the asymptotic waveform as defined with respect to a basis of spin-weighted spherical harmonics of weight -2. Those harmonics are function of the spherical angles (θ, ϕ) defining the direction of propagation $\boldsymbol{n}$, and given by

$$Y^{\ell m}_{(-2)} = \sqrt{\frac{2\ell+1}{4\pi}} d^{\ell m}(\theta) e^{im\phi}, \tag{2.95}$$

where

$$d^{\ell m} = \sum_{k=k_1}^{k_2} \frac{(-)^k}{k!} e_k^{\ell m} \left(\cos\frac{\theta}{2}\right)^{2\ell+m-2k-2} \left(\sin\frac{\theta}{2}\right)^{2k-m+2} \tag{2.96}$$

with

$$e_k^{\ell m} = \frac{\sqrt{(\ell+m)!(\ell-m)!(\ell+2)!(\ell-2)!}}{(k-m+2)!(\ell+m-k)!(\ell-k-2)!}, \tag{2.97}$$

where $k_1 = max(0, m-2)$ and $k_2 = min(\ell+m, \ell-2)$. Thus we decompose h_+ and $h_\times$ onto the basis of such spin-weighted spherical harmonics, which means

$$h_+ - i h_\times = \sum_{\ell=2}^{\infty} \sum_{m=-\ell}^{\ell} h^{\ell m} Y^{\ell m}_{-2}(\theta, \phi). \tag{2.98}$$

Using the orthonormality properties of these harmonics we can invert the latter decomposition and obtain the separate modes $h^{\ell m}$ from a surface integral,

$$h^{\ell m} = \int d\Omega [h_+ - i h_\times] \bar{Y}^{\ell m}_{-2}(\theta, \phi), \tag{2.99}$$

where the overbar refers to the complex conjugation. We can also relate $h^{\ell m}$ to the radiative multipole moments U_L and V_L. The result is

$$h^{\ell m} = -\frac{G}{\sqrt{2} R c^{\ell+2}} \left[U^{\ell m} - \frac{i}{c} V^{\ell m} \right], \tag{2.100}$$

where $U^{\ell m}$ and $V^{\ell m}$ denote the radiative mass and current moments in standard (non-STF) guise. These are related to the STF moments by

$$U^{\ell m} = \frac{4}{\ell!} \sqrt{\frac{(\ell+1)(\ell+2)}{2\ell(\ell-1)}} \alpha^{\ell m}_L U_L \tag{2.101}$$

and

$$V^{\ell m} = -\frac{8}{\ell!} \sqrt{\frac{\ell(\ell+2)}{2(\ell+1)(\ell-1)}} \alpha^{\ell m}_L V_L. \tag{2.102}$$

Here $\alpha^{\ell m}_L$ denotes the STF tensor connecting together the usual basis of spherical harmonics $Y^{\ell m}$ to the set of STF tensors $\hat{n}_L = n_{<i_1} ... n_{i_\ell>}$. Both $Y^{\ell m}$ and $\hat{n}_L$ are basis related by

$$\hat{n}_L(\theta, \phi) = \sum_{m=-\ell}^{l} \alpha^{\ell m}_L Y^{\ell m}(\theta, \phi) \tag{2.103}$$

and

$$Y^{\ell m}(\theta, \phi) = \frac{(2\ell+1)!!}{4\pi \ell!} \bar{\alpha}^{\ell m}_L \hat{n}_L(\theta, \phi). \tag{2.104}$$

Remembering (2.37), $\mathcal{Y}^{\ell m}_L = \frac{(2\ell+1)!!}{4\pi\ell!} \bar{\alpha}^{\ell m}_L$, and the tensorial coefficient $\alpha^{\ell m}_L$ can be computed as $\alpha^{\ell m}_L = \int d\Omega \hat{n}_L \bar{Y}^{\ell m}$.

2.4 The MPM approach

The multipolar post-Minkowskian (MPM) expansion [22] is an algorithmic procedure for generating iteratively the most general solution to Eq. (11)

in the form of a post-Minkowskian (or non-linearity) expansion whose coefficients are themselves given by a multipole expansion that is physically valid outside the compact support of the source. A MPM metric is a formal series in powers of G:

$$\mathcal{G}^{\alpha\beta} \equiv \sqrt{g}g^{\alpha\beta} = \eta^{\alpha\beta} + Gh_1^{\alpha\beta} + G^2h_2^{\alpha\beta} + ...G^nh_n^{\alpha\beta} + ... \tag{2.105}$$

such that each term $h_n^{\alpha\beta}$ admits a multipolar expansion associated with the $SO(3)$ group of rotations

$$h_n^{\alpha\beta} = \sum_{\ell\geq 0} h_{nL}^{\alpha\beta}\hat{n}^L(\theta,\phi), \tag{2.106}$$

where $\hat{n}_L$ is the STF part of n_L. This expansion is equivalent to an expansion in $Y_{\ell m}$. Inserting the PM expansion into the Einstein tensor density

$$2g\left(R^{\alpha\beta} - \frac{1}{2}g^{\alpha\beta}R\right) = 2gT^{\alpha\beta} \tag{2.107}$$

in vacuum, one has the following hierarchy of equations:

$$\Box_f h_n^{\alpha\beta} = \partial^\alpha H_n^\beta + \partial^\beta H_n^\alpha - \eta^{\alpha\beta}\partial_\mu H_n^\mu + N_n^{\alpha\beta}(h_1h_2...h_{n-1}) \tag{2.108}$$

where $H_n = \partial_\beta h_n^{\alpha\beta}$ is the harmonicity of $h_n^{\alpha\beta}$ and $N_n^{\alpha\beta}$ is a non-linear function of previous h_n and its first and second derivatives. Choosing harmonic coordinates such that $H_n^\alpha = 0$, one must select the MPM metrics which are stationary in the past and Minkowskian at spatial infinity, so for $t \leq -T$ $\frac{\partial h_n^{\alpha\beta}}{\partial t} = 0$ and $\lim_{r\to\infty} h_n^{\alpha\beta} = 0$. This allows for a well-defined iteration at any order incorporating Fock's no incoming radiation condition. Note that

$$N_1 = 0 \tag{2.109}$$

$$N_2 \sim h_1\partial_1^2 + \partial h_1 \partial h_1 \tag{2.110}$$

$$N_n = \sum_{a=2}^{n} \sum_{m_1+m_2+...m_a=n; m_b<n} \text{“}\partial\partial\text{”} h_{m_1}h_{m_2}...h_{m_a} \tag{2.111}$$

where the two partial derivatives have to be distributed among the $h_n's$ with possible repetition (the quote marks are there to highlight this fact).
To construct the most general solution of the above equation one can proceed as follows:

1. Take the more general gauge transformation of the solution maintaining the harmonic-gauge condition and satisfying $\Box\omega_1^\mu = 0$, with ω_1^α arbitrary gauge vector,

$$h_1^{\alpha\beta}[\mathcal{M}\mathcal{W}] = h_{can1}^{\alpha\beta}[\mathcal{M}] + \partial^\alpha\omega_1^\beta[\mathcal{W}] + \partial^\beta\omega_1^\alpha[\mathcal{W}] - \eta^{\alpha\beta}\partial_\mu\omega_1^\mu[\mathcal{W}], \quad (2.112)$$

with

$$h_{can1}^{00}[\mathcal{M}] = -\frac{4}{c^2}\left[\sum_{\ell=0}^{\infty}\frac{(-)^\ell}{\ell!}\partial_L\left(\frac{M_L(u)}{r}\right)\right] \quad (2.113)$$

$$h_{can1}^{0i}[\mathcal{M}] = \frac{4}{c^3}\left\{\sum_{\ell=1}^{\infty}\frac{(-)^\ell}{\ell!}\left[\partial_{L-1}\left(\frac{\dot{M}_{iL-1}(u)}{r}\right) + \frac{\ell}{\ell+1}\epsilon_{iab}\partial_{aL-1}\left(\frac{S_{bL-1}(u)}{r}\right)\right]\right\} \quad (2.114)$$

$$h_{can1}^{ij}[\mathcal{M}] = -\frac{4}{c^4}\left\{\sum_{\ell=2}^{\infty}\frac{(-)^\ell}{\ell!}\left[\partial_{L-2}\left(\frac{\ddot{M}_{ijL-2}(u)}{r}\right) + \frac{2\ell}{\ell+1}\partial_{aL-2}\left(\frac{\epsilon_{ab(i}\dot{S}_{j)bL-2}(u)}{r}\right)\right]\right\}, \quad (2.115)$$

where $u = t - \frac{r}{c}$, and

$$\omega_1^0 = \frac{4}{c^2}\left[\sum_{\ell=0}^{\infty}\frac{(-)^\ell}{\ell!}\partial_L\left(\frac{W_L(u)}{r}\right)\right], \quad (2.116)$$

$$\omega_1^i = -\frac{4}{c^3}\left\{\sum_{\ell=1}^{\infty}\frac{(-)^\ell}{\ell!}\left[\partial_{iL}\left(\frac{X_L(u)}{r}\right)\right.\right. \quad (2.117)$$
$$\left.\left. - \frac{4}{c^3}\left\{\sum_{\ell=1}^{\infty}\frac{(-)^\ell}{\ell!}\left[\partial_{L-1}\left(\frac{Y_{iL-1}(u)}{r}\right) + \frac{\ell}{\ell+1}\epsilon_{iab}\partial_{aL-1}\left(\frac{Z_{bL-1}(u)}{r}\right)\right]\right\}\right.,$$

where $\mathcal{W} = \{W_L, X_L, Y_L, Z_L\}$ are the gauge multipole moments that parametrize our general MPM solution and $\mathcal{M} = \{M_L(t), S_L(t)\}$ a set of two time-varying tensors that does not have physical meaning except the time-independent M, which is the ADM mass of the system (i.e. the mass at infinity).

2. Starting with $h_1^{\alpha\beta}[\mathcal{M}]$ one computes the effective non-linear source $N_2(h_1)$ for h_2. The inhomogenous wave equation for h_2 cannot be solved by the ordinary retarded (ret) integral since the domain of definition of the right hand side is not R^4 but the open domain $D(r > r_0)$. Instead of using a truncated retarded integral, the explicit solution is given by complex analytic continuation. Each term in the multipolar expansion of N_2 in the exterior region $r > r_0 > 0$ is a function of r which can be analytically continued for $0 \leq r_0$ and has a tempered singularity at $r = 0$ (less than some r^{-k} where k is a positive integer). Since $N_2 \to \infty$ as $r \to 0$, one still cannot use the ordinary retarded integral to solve wave equation. This problem is solved choosing a complex number B such that $Re(B)$ is large enough that $\left(\frac{r}{r_0}\right)^B N_2$ is a continuous function on R^4 (r_0 is an arbitrary length scale). The ordinary retarded integral of this quantity is well-defined for B and can be analytically continued all over the complex plane except for multiple poles at integer values of B. If one denotes

$$I(B) = \Box_{ret}^{-1}\left(\frac{r}{r_0}\right)^B N_2, \tag{2.118}$$

then the Laurent expansion of this function near $B = 0$ defines two quantities: $p_2^{\alpha\beta}$, the finite part of the Laurent expansion of $I(B)$ near $B = 0$, and $q_2^{\alpha\beta}$, a particular solution of the homogeneous wave equation such that $p_2^{\alpha\beta} + q_2^{\alpha\beta}$ satisfies the harmonicity condition.

3. Generalizing to higher orders one has

$$h_n^{\alpha\beta} = p_n^{\alpha\beta} + q_n^{\alpha\beta} \tag{2.119}$$

$$p_n^{\alpha\beta} = FP_{B=0}\left\{\Box_{ret}^{-1}\left(\frac{r}{r_0}\right)^B N_n(h_1, h_2, ...h_{n-1})\right\} \tag{2.120}$$

$$\partial_\beta q_n^{\alpha\beta} = -Res_{B=0}\left\{\Box_{ret}^{-1}\left(\frac{r}{r_0}\right)^B \frac{n_i}{r} N_n^{i\alpha}\right\}, \tag{2.121}$$

where the operator $FP\Box_{ret}^{-1}$ (FP means "finite part") is a convenient generalization of the usual retarded integral operator $\Box_{ret}^{-1}$ when dealing with singular sources.

The full solution of vacuum Einstein field equations in the form of the post-Minkowskian expansion series is then[2]

$$h^{\alpha\beta} = \sum_{n=1}^{\infty} G^n h_n^{\alpha\beta}[M_L, S_L, W_L, X_L, Y_L, Z_L]. \tag{2.122}$$

At this point, the solution from above still does not have any physical meaning. In particular, M_L and S_L are arbitrary functional parameters that have been inserted in order to mediate between the source (that is described by the "source" multipole moments (2.79) and (2.80)) and the radiation in the exterior zone (see Eq. (2.86)), where the PN approximation loses validity. More precisely, in the near zone $r << \lambda$, $r > r_{source}$, each h_n admits an asymptotic expansion for $c \to \infty$ on scale functions $(\log c)^p c^{-q}$. This is a near zone expansion of the exterior field or a PN expansion of the PM field. The PN assumption according to which h_n admits a PN expansion along simple powers of c^{-1} is inconsistent with the non-linear structure of GR. In the far zone $r \to \infty$, $t - \frac{r}{c}$ fixed, one has an asymptotic expansion along scale functions $(\log r)^p r^{-q}$. This does not imply absence of asymptotic simplicity, since we are in the harmonic coordinates which are not good radiative coordinates (this is why in section (2.6) the radiative multipole moments have been chosen with the so-called *radiative coordinates*).
Let's now consider Eq. (2.122). The most general solution is parametrized by *two and only two* sets of moments. The simplest MPM construction, here referred to as "canonical", is obtained by annulling all the gauge moments in Eq. (2.122):

$$h_{can}^{\alpha\beta} = \sum_{n=1}^{\infty} G^n h_n^{\alpha\beta}[M_L, S_L, 0, 0, 0, 0]. \tag{2.123}$$

This means that the iteration now begins at linearized order with the solution $h_{can1}[M_L, S_L]$. To preserve the non-linear effects on subsequent iterations, the two canonical moments must be related to the source and gauge moments. In order to do this, one posits that Eqs (2.122) and (2.123) have to be *isometric* (i.e. to differ by a coordinate trasformation). It can be shown that this yields

[2]The explicit MPM construction leading to (2.122) is quite complicated in practice but now entirely performed with the software Mathematica together with the tensor package *xAct*.

unique relations of the type

$$M_L = I_L + \mathcal{M}_L[I, J, W, X, Y, Z] \tag{2.124}$$
$$S_L = J_L + \mathcal{S}_L[I, J, W, X, Y, Z], \tag{2.125}$$

where $\mathcal{M}_L$ and $\mathcal{S}_L$ denote some non-linear functionals of the source and gauge moments that are at least quadratic and start only at 2.5PN order. When the relations from above are satisfied, the two sets of moments $\mathcal{M} = \{M_L, S_L\}$ and $\{I, J, W, X, Y, Z\}$ describe the same matter source. Since only the radiative moments (2.86) or their derivatives have physical meaning in terms of quantities measurable by an array of detectors, the canonical moments are then matched with the radiative ones (here denoted by $\mathcal{M}^{rad} \equiv \{U_L, V_L\}$):

$$\mathcal{M}^{rad} = \mathcal{M}^{rad}[\mathcal{M}]. \tag{2.126}$$

Now the radiative multipole moments are correlated with the source ones, and the non-linearities of GR are preserved in the iterations. The complex non-linear equations resulting from the matching procedure are contained in Blanchet's review [64]. At a conceptual level, it is fundamental to observe that, doing the multipolar expansion of $h^{\alpha\beta}$ under the hypothesis of matching (Th. 5 of Ref. [64]), the source and gauge moments can be computed in the form of integrals over the source (Eq. (106) of Ref. [64]), obtaining some non-linear PN series that are valid even far away from the source. Once the multipoles at a certain level of approximation are computed, one can obtain the energy flux emitted by the source using the formula

$$\mathcal{F} = \sum_{\ell=2}^{\infty} \frac{G}{c^{2\ell+1}} \left[\frac{(\ell+1)(\ell+2)}{(\ell-1)\ell\ell!(2\ell+1)!!} \dot{U}_L^2 + \frac{4\ell(\ell+2)}{c^2(\ell-1)(\ell+1)!(2\ell+1)!!} \dot{V}_L^2 \right]. \tag{2.127}$$

The flux from above has been exactly computed using MPM methods up to 4.5PN for the orbital, comparable-mass case [74], and up to 3.5PN for the comparable-mass, quadratic-in-spin [75][11] case, that includes a LO cubic-in-spin 3.5PN piece [76]. This information, beyond its fundamental theoretical importance, is useful in order to build PN approximants for GW experiments (see Sec. 2.7). In Ref. [11] and Chapt. 7, it is used for this purpose with some extra-phenomenological terms that have been computed with the EOB approach (see Chapt. 4).

2.4.1 Tail effects in generation of gravitational radiation

The phenomenon of tail effects in gravity (i.e. the backscattering of GWs into the curved spacetime), that has an analogue in covariant Maxwell theory on a differentiable, curved, manifold, has been studied in detail by Blanchet and Damour [24]. Tails are the consequence of the non-locality of spacetime: gravity generates gravity, and this fact influences the propagation of gravity even from the remote past of a source. In other words, the gravitational field backscatters off the curvature of spacetime which is nothing more than the wave-field itself. From a (curved) light-cone point of view, the propagation proceeds not only along the cone's "velocity of light borders", but also within it (this is the "scattered propagation" or "tail" into the spacetime). The effect has various orders: if gravity generates gravity that generates gravity, we will have a *tail-of-tail* term into our PN expansion. In this context, the non-linearities in the MPM formalism enter through higher-order istantaneous interactions between multipoles and by hereditary contributions. For the purposes of this dissertation, let's consider the tail terms only, which correspond to quadratic interactions and arise at 1.5 PN order. The tails come from the interaction between the mass monopole M and a non-static multipole M_L or S_L (with $\ell \geq 2$). The MPM formalism gives the following contributions, which have to be added to any mass and current multipole momements,

$$U_L^{tail}(T_R) = \frac{2GM}{c^3} \int_{-\infty}^{T_R} M_L^{(\ell+2)}(\tau) \left[\log\left(\frac{T_R - \tau}{2b} \right) + \kappa_\ell \right] \tag{2.128}$$

$$V_L^{tail}(T_R) = \frac{2GM}{c^3} \int_{-\infty}^{T_R} S_L^{(\ell+2)}(\tau) \left[\log\left(\frac{T_R - \tau}{2b} \right) + \pi_\ell \right], \tag{2.129}$$

where $T_R = t - \frac{r}{c} - \frac{2GM}{c^3} \log\left(\frac{r}{cb}\right) + \mathcal{O}\left(\frac{1}{r}\right)$ is a relation that takes into account the logarithmic deviation of the MPM solutions at infinity. Besides that, b is an arbitrary costant time scale unrelated to the r_0 introduced in Eq. (2.118); κ_ℓ and π_ℓ are two numerical constants depending on ℓ; M is the ADM mass (i.e. the mass of the physical system at infinity).
In the two integrals the matching between the radiative multipoles and the canonical ones is explicit. The calculation of hereditary integrals requires knowing the dynamics of the binary system in the past: for example, in Ref. [77] it was assumed that at very early times the binary system was

formed from freely falling BHs moving initially on some hyperbolic-like orbits (this ensures the convergence of the integrals). As it was discussed in section 2.4, computing these integrals can lead to the tail term in the source's energy flux. It is important to stress that tail terms can also be computed by expanding the waveform sector of the EOB formalism (See Chapt. 4 and Ref. [11] for details).

2.5 Small Perturbations

2.5.1 Perturbation theory on a Schwarzschild background

Following Ref. [57], let's consider a background metric $g_{\mu\nu}$ with a small perturbation $h_{\mu\nu}$. The contracted Ricci tensor of Eq. (11) will be, as usual, called $R_{\mu\nu}$ if calculated from $g_{\mu\nu}$ and $R_{\mu\nu}+\delta R_{\mu\nu}$ if calculated from $g_{\mu\nu}+h_{\mu\nu}$, where

$$\delta R_{\mu\nu} = -\delta\Gamma^{\beta}_{\mu\nu;\beta} + \delta\Gamma^{\beta}_{\mu\beta;\nu} \tag{2.130}$$

with

$$\delta\Gamma^{\alpha}_{\beta\gamma} = \frac{1}{2}g^{\alpha\nu}(h_{\beta\nu;\gamma} + h_{\gamma\nu;\beta} - h_{\beta\gamma;\nu}). \tag{2.131}$$

From the condition $\delta R_{\mu\nu} = 0$ one gets a second-order differential equation on the $h_{\mu\nu}$. This equation is a generalization in a curved space of the known Schrödinger equation for a massless particle of spin 2 (the graviton) in a flat space. When the background metric is given by the ordinary Schwarzschild one around a fixed spherically symmetrical center of mass

$$ds^2 = \left(1-\frac{2M}{r}\right)dt^2 - \left(1-\frac{2M}{r}\right)^{-1}dr^2 - r^2d\theta^2 - r^2\sin^2\theta d\phi^2, \tag{2.132}$$

where M is the mass of the source in natural units and $x^0 = t$, $x^1 = r$, $x^2 = \theta$ and $x^3 = \phi$, then $R_{\mu\nu} = 0$. In general, one can do perturbation theory nearby a given exact metric $g_{\mu\nu}$ substituting the expansion

$$g'_{\mu\nu} = g_{\mu\nu} + \epsilon h_{\mu\nu} + \epsilon^2 h^{(2)}_{\mu\nu} + ... \tag{2.133}$$

with $\epsilon << 1$ in $R_{\mu\nu} = 0$, choosing an opportune gauge transformation and keeping terms order by order in ϵ. Returning to our Schwarzschild-background Schrödinger-like equation and working only at first order, it

makes sense to expand the perturbations in spherical (tensor) harmonics. The symmetry of the metric allows angular momentum[3] to be defined. The angular momentum is investigated by studying rotations on the two-dimensional manifold $x^0 = t$ = constant, $x^1 = r$ = constant. Under a rotation of the frame around the origin, the ten components of the perturbing tensor transform like 3 scalars (h_{00}, h_{01}, h_{11}), 2 vectors $(h_{02}, h_{03}; h_{12}, h_{13})$, and a rank-two tensor, when considered as covariant quantities on the sphere. A typical scalar function has the form

$$\phi_{\ell m} = \text{constant} \times Y_{\ell m}(x_2, x_3) = \text{constant} \times Y_{\ell m}(\theta, \phi), \tag{2.134}$$

with wave parity $(-)^\ell$ and "angular momentum" ℓ, whose projection on the z-axis is m. For vectors we have two distinct types with opposite parity: for parity $(-)^\ell$ we have

$$\varphi_{\ell m,\mu} = \text{constant} \times \frac{\partial}{\partial x^\mu} Y_{\ell m}(x_2, x_3), \tag{2.135}$$

while for parity $(-)^{\ell+1}$ we have

$$\phi_{\ell m,\mu} = \text{constant} \times \epsilon_\mu^\nu \frac{\partial}{\partial x^\nu} Y_{\ell m}(x_2, x_3). \tag{2.136}$$

Here the labels μ and ν run over the values 2 and 3, and the object ϵ_μ^ν has the values $\epsilon_2^2 = \epsilon_3^3 = 0$, $\epsilon_2^3 = -\frac{1}{\sin x^2}$ and $\epsilon_3^2 = \sin x^2$. For tensors we have, for parity $(-)^\ell$,

$$\psi_{\ell m\mu\nu} = \text{constant} \times Y_{\ell m;\mu\nu} \tag{2.137}$$

$$\phi_{\ell m\mu\nu} = \text{constant} \times \gamma_{\mu\nu} Y_{\ell m}, \tag{2.138}$$

where $\gamma_{22} = 1$, $\gamma_{23} = \gamma_{32} = 0$ and $\gamma_{33} = \sin^2 x^2$, and, for parity $(-)^{\ell+1}$,

$$\chi_{\ell m\mu\nu} = \frac{1}{2}\text{constant} \times [\epsilon_\mu^\lambda \psi_{\ell m\lambda\nu} + \epsilon_\nu^\lambda \psi_{\ell m\lambda\mu}]. \tag{2.139}$$

Anyone of these terms can be multiplied by an arbitrary function of r and t, without changing its trasformation properties under a rotation. The trace of $\psi_{\ell m\mu\nu}$ has the value $g^{\mu\nu}\psi_{\ell m\mu\nu} = -\ell(\ell+1)Y_{\ell m}(\theta, \psi) \times$ constant. From

[3]Regge labels ℓ as angular momentum because in fact he is applying the quantum mechanic formalism to a classical problem. In reality, ℓ labels the *multipole* of the expansion, like what has been explained in Sec. 2.3.3

the results from above, it follows that the most general perturbation with parity $(-)^{\ell+1}$ is of the form of Eq. (12) of Ref. [57], while the $(-)^{\ell}$ one is of the form of Eq. (13) of the same Ref. Since these expressions are too complicated, one can reduce them to a more suitable form choosing a suitable gauge transformation. Following the mathematical analogies between covariant electromagnetism and GR, one can define the Regge-Wheeler gauge transformation

$$h'_{\mu\nu} = h_{\mu\nu} + \xi_{\mu;\nu} + \xi_{\nu;\mu}, \tag{2.140}$$

which is very similar to the well-known gauge transformation for the electromagnetic field. The gauge vector ξ^{α} is chosen in order to simplify each wave consistently with the properties of the spherical harmonics previously discussed. The results are, for the odd parity wave of total "angular momentum" ℓ and projection $m = 0$[4],

$$h^{\text{odd}}_{\mu\nu} = \begin{pmatrix} 0 & 0 & 0 & h_0(r) \\ 0 & 0 & 0 & h_1(r) \\ 0 & 0 & 0 & 0 \\ \text{Sym} & \text{Sym} & 0 & 0 \end{pmatrix} \times \exp(-ikt) \left(\sin\theta \frac{\partial}{\partial\theta}\right) P_{\ell}(\cos\theta), \tag{2.141}$$

while, for the even-parity wave

$$h^{\text{even}}_{\mu\nu} = \begin{pmatrix} H_0\left(1-\frac{2M}{r}\right) & H_1 & 0 & 0 \\ H_1 & H_2\left(1-\frac{2M}{r}\right)^{-1} & 0 & 0 \\ 0 & 0 & r^2K & 0 \\ \text{Sym} & \text{Sym} & 0 & r^2K\sin\theta \end{pmatrix} \times \exp(-ikt) P_{\ell}(\cos\theta), \tag{2.142}$$

where $P_{\ell}(\cos\theta)$ are the Legendre polynomials of grade ℓ; H_0, H_1, H_2 and K some t and r-dependent arbitrary gauge functions; $k = \frac{\omega}{c}$ the propagation constant of the perturbation with frequency ω. Let's now substitute (2.141) and (2.142) in Einstein's equations $R_{\mu\nu} = 0$. For $R_{23} = 0$ and $R_{13} = 0$[5], eliminating h_0, defining $Q \equiv \frac{(1-2M)h_1}{r}$ and choosing the "tortoise coordinates"

[4]Since we are working in the vacuum case, m can be fixed to 0 in order to eliminate the angular component ψ from the equations. Once the wave equation in the vacuum will be obtained, a source term $S^{(\text{even/odd})}_{\ell m}$ can be put in the right part of the equation. In this case, *a posteriori* one has $m \neq 0$.

[5]The equation resulting from $R_{03} = 0$ is a combination of the first two.

$r_* = r + 2M \log\left(\frac{r}{2M} - 1\right)$, one gets

$$\frac{d^2Q}{dr_*^2} + V_{\rm eff,odd}(r)Q = 0, \tag{2.143}$$

or, in the time domain,

$$(\Box + V_{\rm odd}(r))\Psi_{\rm odd} = 0, \tag{2.144}$$

with $\Box = \partial_{r_*}^2 - \partial_t^2$ and $V_{\rm odd}(r) = \left[-\frac{\ell(\ell+1)}{r^2} + \frac{6M}{r^3}\right]\left(1 - \frac{2M}{r}\right)$. This is known as the Regge-Wheeler equation. The even parity one, known as the Zerilli equation [58], has generically the same form,

$$(\Box + V_{\rm even}(r))\Psi_{\rm even} = 0, \tag{2.145}$$

but the potential is different: $V_{\rm even}(r) = \left(\frac{1-2M}{r}\right)\frac{2\lambda^2(\lambda+1)r^3+6\lambda^2Mr^2+18\lambda M^2r+18m^3}{r^3(\lambda r+3M)^2}$, with $\lambda = \frac{1}{2}(\ell-1)(\ell+2)$. The Zerilli and Regge-Wheeler equations each describe one of the two degrees of freedom of linearized gravity propagating in a (non-rotating) BH background. With minor modifications they also describe electromagnetic and scalar fields. The derivations we followed were in the Regge-Wheeler gauge (2.140), but the quantities of interest, the Ψ's, are gauge invariant quantities that can be expressed in terms of the metric perturbations in any gauge. It is worthwhile mentioning that approaches that are "manifestly gauge invariant" to these equations can be constructed [78]. Let's now consider for illustrative purposes the Green's function solution for the Regge-Wheeler-Zerilli (RWZ) equation ($\Psi_{\rm even/odd} \equiv \Psi$),

$$\Psi(x,t) = \int dy[G(x,y;t)\dot{\Psi}(y,0) + \dot{G}(x,y,t)\Psi(y,0)], \tag{2.146}$$

where $G(x,y;t)$ is the Green function of the time-domain RWZ equation. It can be obtained via Fourier transform from the frequency domain Green's function, which is easier to obtain,

$$\tilde{G}(x,y;t) = \int_0^\infty dt G(x,y;t)e^{i\omega t}. \tag{2.147}$$

One way of obtaining the frequency-domain Green's function is by contructing two independent solutions $f(\omega,x)$ and $g(\omega,y)$ to the homogeneous equation, one of them satisfying the left boundary condition and the other one

the right boundary condition, multiplying and dividing by the Wronskian,

$$\tilde{G}(x,y;t) = \begin{cases} \frac{f(\omega,x)g(\omega,y)}{W(f,g)}, x < y \\ \frac{f(\omega,y)g(\omega,x)}{W(f,g)}, y < x, \end{cases} \tag{2.148}$$

where $W(f,g) = f'g - g'f$. To construct the time-domain Green's function we use the inverse Fourier transform, which for $t > 0$ requires following a contour encircling the lower half of the complex ω plane. Examining the singularity structure of the Green's function in that domain we can see that

1. The Green's function will have poles wherever the Wronskian vanishes. At these points, f and g are linearly dependent, meaning that one is finding a solution that satisfies outgoing boundary conditions at both the horizon and at infinity. Such solutions are the *quasinormal modes* (QNMs)of the system and have complex frequency with negative imaginary part. There is generally an infinite collection of such periodic solutions, and the "most general solution" can be expressed as a superposition of QNMs

$$\Psi = \sum_{n=1}^{\infty} \Lambda_n e^{i\omega_n t}, \tag{2.149}$$

   where Λ_n is an unknown complex amplitude (or real amplitude and a phase constant), ω_n the complex frequency labeled by the tones n ($n = 0$ is the fundamental one and for $n > 1$ we have an infinite number of overtones) emitted by a BH when perturbed by a test-particle falling inside it (i.e. after the plunge phase). Physically speaking, after crossing the light-ring the QNMs are excited (see Fig. 2.1), and the BH "sounds like a bell". This is the reason why the last phase of a binary BH collision (i.e. after the plunge and the merger) is called the "ringdown" phase. At this point, the inspiral-merger-ringdown process illustrated in Fig. 1.1 is more clear. Finally, it is important to stress that one can do a ringdown analysis fitting appropriately Eq. (2.149) to numerical and/or experimental data.

2. If the potential is of compact support in x, one can impose the outgoing boundary condition immediately outside the domain of the potential. One can then integrate the differential equation for a finite amount of x range to obtain f and g. Therefore, these two functions cannot have singularities. This is also true if the potential decays fast with

x. If the potential has a slower than exponential tail, f and g will have singularities in the complex plane. These singularities have the form of a branch cut along the negative imaginary ω axis. When these singularities reach ω=0, they produce the *power-law tails* examined in Sec. 2.4.1. As the PN/MPM formalism, perturbation theory tells to us that tails are induced by the non-linearity of spacetime (roughly speaking, GWs meet a potential wall and then backscatter).

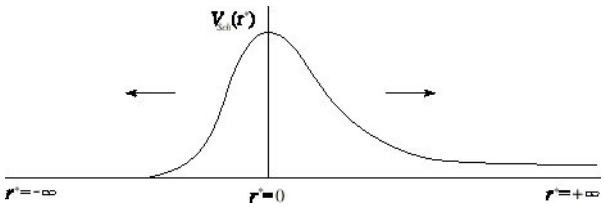

Figure 2.1: *Plot of the Zerilli potential for a fixed multipole ℓ in function of the tortoise coordinates r_*. At the peak located in $r_* = 0$, which corresponds to the value $3M$, the test-particle falling radially into the BH will begin to excite the QNMs of the BH. The peak is located at the light-ring (i.e. at the innermost unstable circular photon orbit) of the Schwarzschild BH . The "ringdown" phase can be viewed as waves bouncing around the potential wall of the Zerilli potential, like indicated by the arrows in the figure.*

2.5.2 Perturbations of rotating black holes

The analogue of RWZ equations 2.144 and 2.145 for a Kerr BH, which is the most interesting case for experimental studies, was deduced by Teukolsky in 1973 [59]. In order to obtain a perturbative equation like the RWZ one, doing a spherical-harmonics expansion like in the nonspinning case is impossible, since the Kerr metric does not have spherical symmetry. The solution of the problem was to use the Newman-Penrose (NP) formalism in order to get a separable wave equation for a Kerr BH [59]. We will not overview here the derivation of Teukolsky's master equation because it is strictly related to the use of the NP formalism (which is, roughly speaking, spinor calculus applied to GR), which is beyond the purposes of this thesis. Following the

computations of Ref. [59] one can derive

$$\left[\frac{(r^2+a^2)^2}{\triangle}-a^2\sin^2\theta\right]\frac{\partial^2\psi}{\partial t^2}+\frac{4Mar}{\triangle}\frac{\partial^2\psi}{\partial t\partial\phi}+\left[\frac{a^2}{\triangle}-\frac{1}{\sin^2\theta}\right]\frac{\partial^2\psi}{\partial\phi^2} \tag{2.150}$$
$$-\triangle^{-s}\frac{\partial}{\partial r}\left(\triangle^{s+1}\frac{\partial\psi}{\partial r}\right)-\frac{1}{\sin\theta}\frac{\partial}{\partial\theta}\left(\sin\theta\frac{\partial\psi}{\partial\theta}\right)-2s\left[\frac{a(r-M)}{\triangle}+\frac{i\cos\theta}{\sin^2\theta}\right]\frac{\partial\psi}{\partial\phi}$$
$$-2s\left[\frac{M(r^2-a^2)}{\triangle}-r-ia\cos\theta\right]\frac{\partial\psi}{\partial t}+(s^2\cot^2\theta-s)\psi=4\pi\Sigma T.$$

Here s is the "spin weight" of the field. It is equal to 0 for a test scalar field; to ±1 for a test electromagnetic field; to ±2 for a gravitational perturbation, which is the case of our interest.
Eq. (2.150) is considerably more involved to handle than the nonspinning (2.144) and (2.145) ones. To begin with, let's consider first the vacuum case ($T=0$). The master equation can be separated by writing

$$\psi\to e^{-i\omega t}e^{im\phi}S(\theta)R(r). \tag{2.151}$$

The equations for R and S are

$$\triangle^{-s}\frac{d}{dr}\left(\triangle^{s+1}\frac{d\psi}{dr}\right)+\left(\frac{K^2-2is(r-M)K}{\triangle}+4is\omega r-\lambda\right)R=0 \tag{2.152}$$

and

$$\frac{1}{\sin\theta}\frac{d}{d\theta}\left(\sin\theta\frac{dS}{d\theta}\right) \tag{2.153}$$
$$+\left(a^2\omega^2\cos^2\theta-\frac{m^2}{\sin^2\theta}-2a\omega s\cos\theta-\frac{2ms\cos\theta}{\sin^2\theta}-s^2\cot^2\theta+s+A\right)S=0,$$

where $K\equiv(r^2+a^2)\omega-am$ and $\lambda\equiv A+a^2\omega^2-2am\omega$. Eq. (2.153), together with boundary conditions of regularity at $\theta=0$ and π, constitutes a Sturm-Liuville eigenvalue problem for the separation constant $A=_s A_{\ell m}(a\omega)$. For fixed s, m and $a\omega$, we label the eigenvalues by ℓ. The smallest eigenvalue has $\ell=max(|m|,|s|)$. From Sturm-Liuville theory, the eigenfunctions ${}_sS_{\ell m}$ are complete and orthogonal on $0\le\theta\le\pi$ for each m, s and $a\omega$. When $s=0$, the eigenfunctions are the spheroidal wave functions $S_{\ell m}(-a^2\omega^2,\cos\theta)$ [79]. When $a\omega=0$, the eigenfunctions are the spin-weighted spherical harmonics ${}_sY_{\ell m}=_s S_{\ell m}(\theta)e^{im\phi}$, and $A=(\ell-s)(\ell+s+1)$ [80]. In the general case,

the eigenfunctions are "spin-weighted spheroidal harmonics", which are different from the more common spherical harmonics used in the nonspinning approach, because they contain implicitily the spin-information of the physical system.
When the sources are present ($T \neq 0$), we can use the eigenfunctions of Eq. (2.153) to separate Eq. (2.150) by expanding

$$4\pi\Sigma T = \int d\omega \epsilon_{\ell m}(r) {}_sS_{\ell m}(\theta) e^{-i\omega t}, \tag{2.154}$$

$$\psi = \int d\omega \psi_{\ell m}(r) {}_sS_{\ell m}(\theta) e^{-i\omega t}. \tag{2.155}$$

Then $\psi_{\ell m}$ satisfies Eq. (2.152) with $\epsilon_{\ell m}(r)$ as source term on the right-hand side. So the full master equation is separable only in the frequency demain. If one is interested to compute the energy flux carried off by outgoing GWs, the process, as outlined in Ref. [62], is the following. The radial functions $\psi_{\ell m}(r)$ then satisfy a second order ordinary differential equation

$$\mathcal{D}\psi_{\ell m}(r) = 4\pi T_{\ell m}(r). \tag{2.156}$$

In the case of a spinning particle on a circular orbit around a Schwarzschild black hole, the source term here takes the schematic form

$$\begin{aligned} T_{\ell m} =& A_0\delta(r-r_p) + A_1\delta'(r-r_p) + A_2\delta''(r-r_p) \\ &+ A_3\delta'''(r-r_p). \end{aligned} \tag{2.157}$$

If we have a pair of homogeneous solutions satisfying retarded boundary conditions at the horizon and at infinity, $R^-_{\ell m}$ and $R^+_{\ell m}$ respectively, then the general solution to this equation is given by

$$\psi_{\ell m}(r) = C^+_{\ell m} R^+_{\ell m}(r) + C^-_{\ell m} R^-_{\ell m}(r), \tag{2.158}$$

where

$$\begin{aligned} C^\pm_{\ell m} &= \frac{1}{W}\int R^\mp_{\ell m} T_{\ell m} \Delta^{-2} dr \\ &= B_0 R^\mp_{\ell m}(r_p) + B_1 R^{\mp\,\prime}_{\ell m}(r_p) + B_2 R^{\mp\,\prime\prime}_{\ell m}(r_p) \\ &\quad + B_3 R^{\mp\,\prime\prime\prime}_{\ell m}(r_p). \end{aligned} \tag{2.159}$$

The $B_i = B_i(r_p, \sigma)$ are determined by completing the integral, W is the invariant Wronskian of the two solutions and $\Delta = r(r-2M)$. Normalizing

the homogeneous solutions so that $R_+ \sim r^3 e^{i\omega r^*}$ as $r \to \infty$, the energy flux emitted at radial infinity is given simply by

$$\frac{dE^\infty}{dt} = \sum_{\ell m} F_{\ell m} = \sum_{\ell m} \frac{|C^+_{\ell m}|^2}{4\pi m^2 \Omega^2} \tag{2.160}$$

where Ω is the orbital frequency given in Eq. (9.4).

2.6 Numerical Methods

2.6.1 Numerical Relativity (NR) simulations for Binary Black Holes

In this subsection, following Sec. 9 of Ref. [81], we will overview the recipe that enabled Frans Pretorius [27] to simulate successfully in 2005 the last plunging orbit, leading to merger and ringdown, of a BBH, and to extract the corresponding waveform.

Of particular importance for the mathematical development of NR was Ref. [82], in which Choquet-Bruhat proved the existence of local-in-time solutions to the harmonic-coordinates-reduced Einstein's equations, and from here showed how to construct solutions of the full field equations (11) i) by solving, on an initial Cauchy hypersurface, the harmonic coordinates version of the constraints of Einstein's equations; ii) by proving that these constraints homogeneously propagate off the initial Cauchy hypersurface. More precisely, the harmonic-coordinates condition used in Ref. [82] was of the form

$$C^{(0)}_\mu = 0, \tag{2.161}$$

where $C^{(0)}_\mu \equiv -g_{\mu\nu}\Box x^\nu$, with $\Box x^\mu \equiv \frac{1}{\sqrt{g}}\partial_\nu(\sqrt{g}g^{\nu\eta}\partial_\eta x^\mu)$. Then the harmonic-coordinates-reduced Einstein equations for the evolution of $g_{\mu\nu}$ read

$$\frac{1}{2}g^{\eta\sigma}g_{\mu\nu;\eta\sigma} + g^{\eta\sigma}_{(;\mu}g_{\nu)\sigma;\eta} + \Gamma^\eta_{\nu\sigma}\Gamma^\sigma_{\mu\eta} = -8\pi\left(T_{\mu\nu} - \frac{1}{2}g_{\mu\nu}T\right). \tag{2.162}$$

The diagonal-hyperbolic nature of the second-derivative term $\frac{1}{2}g^{\eta\sigma}g_{\mu\nu;\eta\sigma}$ allowed Fourès-Bruhat to prove the existence of local-in-time solutions of Eqs. (2.162). To get then the solutions of Eqs. (11), one further needs to show how to satisfy, in addition, the conditions (2.161) everywhere in spacetime. This leads to the wave equation

$$\Box C^\mu_{(0)} = -R^\mu_\nu C^\nu_{(0)}. \tag{2.163}$$

The latter propagation equation for the constraints is homogeneous. Therefore, if $C_\mu^{(0)}$, and their time-derivatives, vanish on some initial time Cauchy hypersurface $t = x^0 = 0$, they will continue to vanish for all times [82].
The system obtained from writing Einstein equations in harmonic coordinates, i.e. Eqs. (2.162), besides its mathematical consistency, is not numerically satisfactory, since the original harmonic coordiante conditions can sometimes develop "coordinate patologies" of their own. An in-principle remedy for avoiding such patologies was advocated by Garfinkle [83] and, earlier, by Friedrich [84], but with a different motivation. It consists in generalizing the harmonic-coordinates condition $\Box x^\mu = 0$ to a generalized form $\Box x^\mu = H^\mu(x)$, where the $H^\mu(x)$ are some suitable "source functions". One must then either specify the $H^\mu(x)$'s as explicit functions of the four spacetime coordinates, or give dynamical equations determining their evolution (and helping in avoiding coordinate patologies). Besides that, a second modification of the standard harmonic-coordinate approach was introduced in 2005 in order to simulate with success the BBH coalescence [27]. This additional modification was requested because the numerical evolution of Einstein's equations in generalized harmonic coordinates was generally numerically unstable. When using Friedrich-Garfinkle 's generalized harmonic coordinates the constraints (2.161) are replaced by

$$C_\mu \equiv g_{\mu\nu}(H^\mu - \Box x^\mu) = 0. \tag{2.164}$$

Pretorius' additional modification [27] consists in adding extra terms proportional to the constraints C_μ in Einstein's equations (2.162):

$$\begin{aligned} &\frac{1}{2}g^{\eta\sigma}g_{\mu\nu;\eta\sigma} + g^{\eta\sigma}_{(;\mu}g_{\nu)\sigma;\eta} + H_{(\mu,\nu)} - H_\sigma\Gamma^\sigma_{\mu\nu} + \Gamma^\eta_{\nu\sigma}\Gamma^\sigma_{\mu\eta} \\ &+ \kappa(n_{(\mu}C_{\nu)} - \frac{1}{2}g_{\mu\nu}n^\sigma C_\sigma) = -8\pi\left(T_{\mu\nu} - \frac{1}{2}g_{\mu\nu}T\right). \end{aligned} \tag{2.165}$$

Here $n^\mu \equiv g^{\mu\nu}n_\nu$ denotes the unit timelike vector normal to the $t =$ constant hypersurfaces, and κ denotes an adjustable parameter. If the metric is evolved using (2.165), the constraints $C^\mu \equiv g^{\mu\nu}C_\nu$ will satisfy

$$\Box C^\mu = -R^\mu_\nu C^\nu + 2\kappa\nabla_\nu n^{(\nu}C^{\mu)}, \tag{2.166}$$

which generalizes Eq. (2.163). When $\kappa > 0$, the extra κ-dependent terms in (2.166) tend to damp the evolution of the constraints C^μ[6]. For this rea-

[6]This means that they tend to make them tend exponentially towards zero when evolving them in the future of the initial Cauchy hypersurface.

son, the extra-terms proportional to κC_μ are called *constraint damping terms*. It is important to stress that this idea, that was the key for the success of Pretorius's BBH IMR simulation, was already surfaced in Refs. [85] and [86]. The landmark paper [27] had a huge impact in NR waveform development, but some groups, like the authors of Refs. [87] and [88], did not use the same mix of methods of Ref. [27], but Brugmann [89]'s trick to represent BHs as "punctures" of the spacetime to move across the numerical grid, without the need of the BH horizon-excision method used by Pretorius. They also used a different formulation of Eqs. (11) going under the name of BSSN, for Baumgarte-Shapiro-Shibata-Nakamura.
On the other hand, the Caltech-Cornell group, the main provider of accurate BBH waveforms for LIGO, did use a mix of methods comparable to Pretorius' one, with generalized harmonic coordinates, excision and a constraint damping method similar to the one used in Ref. [27]. The Caltech-Cornell Spectral code (SPEC) was constructed in a sequence of works, and notably in Refs. [90], [91] and [92].

2.6.2 Numerical resolution of Teukolsky's equation: time domain (TD) approach

For the purposes of this thesis, i.e. for the analytical work done in Chapter 9, two codes where employed to solve Eq. 2.150, a time-domain (TD) one and a frequency domain (FD) one. In Chapter 8, where we do almost the same resummation work of Chapter 9, but in the nonspinning test-particle case, we use numerical Teukolsky waveforms provided directly by Hughes [93], which has used its own time-domain code. These kind of resolution methods are very similar; therefore, for simplicity, here we give an overview of the "most common" TD approach, leaving the details about an FD code in Chapter. 9. For a more complete treatment of Hughes' code, the reader should refer to Ref [93] and references therein.
Firstly, we observe that Eq. (2.150) is separable in the frequency domain. The first numerical computation of gravitational perturbations of Kerr spacetime in the time domain is by Krivan et al. in 1997 [94]. They use Boyer-Lindquist coordinates and solve Eq. (2.150) as a fully first-order system in 2+1 dimensions after a decomposition into azimuthal angular modes. The system is discretized using a second-order convergent Lax-Wendroff scheme which has favorable dissipative properties for numerical stability. The com-

putational boundaries are placed at finite radii and close to the horizon using a tortoise transformation of the radial coordinate. The errors from the boundaries are mitigated by using a large computational domain.
In Ref. [60], a better approach to this problem is discovered (i.e. the *Teukode* in its first incarnation is born). The idea is to use a spacelike foliation that penetrates the horizon in a regular way and asymptotically approaches null infinity so that one can compute both the ingoing and the outgoing radiation. This technique removes the two largest systematic uncertainties of Krivan's method (and of any other based only on Boyer-Lindquist coordinates), namely (i) the inner and outer numerical boundary errors, and (ii) finite-radius-extraction (and/or interpolation) errors. On the computational side, this approach is efficient because the computational domain is much smaller than the one needed in standard Boyer-Lindquist tortoise coordinates. In Ref. [61] a new foliation of Kerr spacetime which leads to more efficient numerical computations than [60] is introduced (in this paper an upgraded *Teukode* is presented). A general framework for the construction of explicit, hyperboloidal coordinates with scri-fixing (i.e. fixing the spatial coordinate location of null infinity) for stationary, weakly asymptotically flat spacetimes (including BH spacetimes) was presented in Ref. [95]. The transformation from standard coordinates $\{t, r\}$ to hyperboloidal coordinates $\{\bar{t}, \bar{r}\}$ can be written as

$$\begin{aligned} t &= \bar{t} + h(\bar{r}), \\ r &= \frac{\bar{r}}{\Omega(\bar{r})}, \end{aligned} \tag{2.167}$$

where $h(\bar{r})$ is the height function and the explicitly prescribed $\Omega(\bar{r})$ acts both as a radial compactification and a conformal factor. Asymptotic conditions derived in Ref. [95] make sure that the resulting metric is regular.
The steps to build the latest *Teukode* version are the following:

1. One chooses as hyperboloidal coordinates (2.167) the "HH"" coordinates $\{\tau, \rho\}$, which are constructed from the metric in Boyer-Lindquist coordinates by imposing the ingoing coordinates boundary[7], and demanding invariance of the coordinate expression for outgoing characteristics in spatially compactifying coordinates [96]. This requirement

[7]The ingoing (iK) Kerr coordinates $\{\tilde{t}, r, \theta, \varphi\}$ are obtained through the transformation $d\tilde{t} = dt + \frac{2Mr}{\triangle}dr$, $d\varphi = d\phi + \frac{a}{\triangle}dr$.

is given by

$$\tilde{t} - (r + 4M \log r) = \tau - (\rho + 4M \log \rho). \tag{2.168}$$

For any choice of spatial compactification through ρ, the above requirement determines the foliation. Then one chooses the simplest conformal factor with a variable scri location S and set

$$\begin{aligned} h(\rho) &= \frac{\rho}{\Omega} - \rho - 4M \log \Omega \\ \Omega(\rho) &= 1 - \frac{\rho}{S}. \end{aligned} \tag{2.169}$$

The event horizon ρ_+ is located at

$$\rho_+ = \frac{a^2 S + MS^2 + \sqrt{M^2 S^4 - a^2 S^4}}{a^2 + 2MS + S^2}. \tag{2.170}$$

The HH coordinates with a specific choice of S are denoted HH_S coordinates. For computational purposes, the most efficient value of S is $S = 10$ [61].

2. Since GWs propagate along null geodesics and their structure in the Kerr spacetime is rather complicated, they are approximated by Schwarzschild null geodesics. The retarded and advanced time coordinates in Schwarzschild spacetime, u and v, are defined by $u = t - r_*$ and $v = t + r_*$, where r_* is the tortoise coordinate defined in Sec. 2.5.1. These coordinates in Kerr spacetime are used to connect the particle's dynamics with the measured gravitational radiation. This approximation agrees with the general practice in NR, where null geodesics in a binary BH spacetime are approximated by their Schwarzschild counterparts for extrapolationg gravitational waveforms [97]. For the retarded coordinate one gets

$$u(\tau, \rho) = \tau - \rho - 4M \log \left(\frac{S\rho + 2M\rho - 2MS}{S} \right) + 2M \log(2M), \tag{2.171}$$

and for the advanced coordinate

$$v(\tau, \rho) = \tau + \rho \frac{S + \rho}{S - \rho} - 4M \log \left(\frac{S - \rho}{S} \right) - 2M \log(2M). \tag{2.172}$$

3. One substituses the formulas (2.167) in the master equation (2.150), rescaling suitably the unknown variable for regularity of the coefficients at the horizon and at null infinity [61]. Eq. (2.150) is then transformed in 2+1 form separating each Fourier m-mode in the azimuthal direction. The resulting equation has the general form

$$C_{\tau\tau}\partial_{\tau\tau}\psi+C_{\tau\rho}\partial_{\tau\rho}\psi+C_{\rho\rho}\partial_{\rho\rho}\psi+C_{\theta\theta}\partial_{\theta\theta}\psi+C_{\tau}\partial_{\tau}\psi+C_{\theta}\partial_{\theta}\psi+C_{\rho}\partial_{\rho}\psi+C_0\psi = S_s, \tag{2.173}$$

with coefficients $C(\rho,\theta;m,s)$ depending on the background coordinates, the spin weight s, and the azimuthal mode-index m. The index m in the variable ψ_m has been suppressed for brevity. The source term S_s depends on the spin-weight s, the background metric, and the stress-energy tensor $T_{\mu\nu}$ of the matter perturbation. The method to compute it in the time domain, which is different from the one in the frequency domain that we presented in Sec. 2.5.2, is illustred in Sec 3.2 of Ref. [61].
In the time domain, the GW strain $h = h_+ - ih_\times$ (where the polarizations h_+ and $h_\times$ are defined in Eqs (2.93) and (2.94)) is found by integrating the asymptotic relation

$$\ddot{h} = 2\psi_4 \tag{2.174}$$

for each m-mode. The integration gives $rh_m(u,\theta)$ along scri. One can also compute the (spin weighted with $s=-2$) multipoles $rh_{lm}(u)$, defined through Eq. (2.99)

$$rh = \sum_{\ell=2,m} rh_{\ell m-2}Y_{\ell m}(\theta,\phi) = \sum_{\ell=2,m}\sqrt{\frac{(\ell+2)!}{(\ell-2)!}}\Psi_{\ell m-2}Y_{\ell m}(\theta,\phi), \tag{2.175}$$

by mode-projecting $rh_m(u,\theta)$ in the θ-direction. The complex quantities $\Psi_{\ell m} = \Psi^{even}_{\ell m} + i\Psi^{odd}_{\ell m}$ in Eq. (2.175) are the RWZ variables of Eqs (2.144) and (2.145). The energy flux at scri is given by

$$\dot{E} = \frac{1}{16\pi}\int_{S_2} d\Omega |r\dot{h}|^2 = \frac{1}{16\pi}\sum_m \int_{-1}^{1} d\xi |r\dot{h}_m|^2, \tag{2.176}$$

where $\xi = \cos\theta$ and the mode decomposition of h express the flux in terms of the 2+1 fields. The angular momentum $\vec{J} = (J_x, J_y, J_z)$ flux is given by

$$\dot{J}_i = -\frac{1}{16\pi} Re\left\{\int_{S_2} d\Omega (r\dot{h})^* \mathcal{J}_i(rh)\right\}, \tag{2.177}$$

where $\mathcal{J}_i$ are the spin 2 quantum mechanical operators, in particular $\mathcal{J}_z = \partial_\phi$. For equatorial orbits $J_x = J_y = 0$, so the relevant quantity is

$$\dot{J}_z = \frac{1}{16\pi} Im\left\{ \sum_m m \int_{-1}^{1} d\xi (r\dot{h}_m)^* (r h_m) \right\}. \tag{2.178}$$

At the horizon one must follow the Hawking-Hartle method [98], like in the frequency domain case, to obtain the variation of the horizon mass and, if desidered, of the horizon angular momentum (see Eqs (37) and (38) of Ref. [61]).

4. Finally, for numerical integration Eq. (2.173) is written as a first-order in time, and second order in space system with reduction variables $u = \{\psi, \partial_\tau \psi\}$. The domain $(x, \theta) \in [x_+, x_S] \times (0, \pi)$, where x is the radial coordinate and $x_+(x_S)$ is the location of the horizon (null infinity), is uniformly discretized with $N_x \times N_\theta$ points. The spatial derivatives are represented by finite differences up to eighth order of accuracy. The stencils in the radial direction are centered in the bulk of the domain and lopsided/sided at the boundaries. The angular grid is staggered and ghost points are employed to implement the boundary conditions on the axis. The ghost points are filled according to the parity condition $\pi = (-1)^{m+s}$.
   A standard fourth order Runge-Kutta integrator is employed for time advancing the solution. The time step is chosen according to a Courant-Friedrichs-Lewy (CFL) condition of type $\triangle t = C_{CFL} min(h_x, h_\theta)$, where h_x is the grid spacing in direction x and the factor C_{CFL} accounts for the maximum coordinate speed of the PDE system. The angular integrals for l-mode projections are computed with the Simpson rule, while integrals in time with the trapezoidal rule. The δ-functions appearing in the stress-energy tensor are discretized for simulating a source that is effectively *not* moving on the computational domain. In cases like inspiral-plunge the δ-functions are used in their gaussian representation (See Sec. 4.3 of Ref. [61]).

2.7 Post-Newtonian approximants

We firstly remark that this is not a *direct* approximation method for GR, but, instead, it is an approximation method for the PN series itself, that

has a rough and practical use in GW data analysis (see Subsec. 1.5.3). In fact, we have not considered it in the preamble of this chapter, but since it is fundamental in the papers presented in Chapters 6 and 7 of this thesis, we will give here a complete overview of the topic, following Ref. [99].
Given PN expansions of the motion and gravitational radiation from a small binary system with $M < 4M_\odot$, one needs to compute an accurate mathematical model for the evolution of the GW phase $\phi^{GW} = p[t; \lambda_i]$, involving the set of parameters $\{\lambda_i\}$ carrying information about the emitting binary system. In the adiabatic approximation the *phasing formula* is easily derived from the energy and flux functions. Indeed, the standard energy-balance equation $\frac{dE_{tot}}{dt} = -\mathcal{F}$ gives the following parametric representation of the phasing formula:

$$t(v) = t_{ref} + M \int_v^{v_{ref}} dv \ \frac{E'(v)}{\mathcal{F}(v)}, \tag{2.179}$$

$$\phi(v) = \phi_{ref} + 2 \int_v^{v_{ref}} dv \ v^3 \frac{E'(v)}{\mathcal{F}(v)}, \tag{2.180}$$

where t_{ref} and ϕ_{ref} are integration constants and v_{ref} an arbitrary reference velocity. From the view point of computational purposes it is more efficient to work with the following pair of coupled, non-linear, ordinary differential equations (ODE's) that are equivalent to the above parametric formulas:

$$\frac{d\phi}{dt} - \frac{2v^3}{M} = 0, \tag{2.181}$$

$$\frac{dv}{dt} + \frac{\mathcal{F}(v)}{ME'(v)} = 0. \tag{2.182}$$

The energy and flux n^{th} order *PN Taylor approximants* are denoted by E_{T_n} and $\mathcal{F}_{T_n}$, and defined by

$$E_{T_n} \equiv E_N(x) \sum_{k=0}^{n} \hat{E}_k(\nu) x^k, \tag{2.183}$$

$$\mathcal{F}_{T_n} \equiv \mathcal{F}_N(x) \left[\sum_{k=0}^{n} \hat{\mathcal{F}}_k(\nu) v^k + \sum_{k=6}^{n} \hat{L}_k(\nu) \log\left(\frac{v}{v_0}\right) v^k \right], \tag{2.184}$$

where $E_N(x) = -\frac{1}{2}\nu x$ and $\mathcal{F}_N(x) = \frac{32}{5}\nu^2 x^5$ are the Newtonian-order prefactors, $\nu \equiv \frac{m_1 m_2}{M^2}$ is the symmetric mass ratio of the binary with total mass

$M = m_1 + m_2$. The problem is to construct a sequence of approximate waveforms $h_n^A(t;\lambda_k)$, starting from the PN expansions of $E(v)$ and $\mathcal{F}(v)$. There are at least three ways of doing that:

1. **Taylor T1:** One can retain the rational polynomial $\frac{\mathcal{F}_{T_n}}{E_{T_n}}$ and integrate the two ODE's numerically. The phase formula so obtained is then denoted by $\phi^{(1)}_{T_n}(t)$:
$$\frac{d\phi^{(1)}}{dt} - \frac{2v^3}{M} = 0, \tag{2.185}$$
$$\frac{dv}{dt} + \frac{\mathcal{F}_{T_n}(v)}{ME'_{T_n}(v)} = 0. \tag{2.186}$$

2. **Taylor T2:** One can re-expand the rational function $\frac{\mathcal{F}_{T_n}}{E_{T_n}}$ appearing in the phasing formula and truncate it at order v^n, in which case the integrals (2.179) and (2.180) can be worked out analytically, to obtain a parametric representation of the phasing formula in terms of polynomial expressions in the auxiliary variable v
$$\phi^{(2)}_{T_n}(v) = \phi^{(2)}_{ref} + \phi^v_N(v)\sum_{k=0}^{n}\hat{\phi}^v_k v^k, \tag{2.187}$$
$$t^{(2)}_{T_n}(v) = t^{(2)}_{ref} + t^v_N(v)\sum_{k=0}^{n}\hat{t}^v_k v^k, \tag{2.188}$$
where the subscript v in the coefficients indicates that v is the expansion parameter.

3. **Taylor T3:** Finally, the second of the polynomials in the Taylor T2 equations can be inverted and the resulting polynomial for v in terms of t can be substituted in $\phi^{(2)}(v)$ to arrive at an explicit time-domain phasing formula
$$\phi^{(3)}_{T_n}(t) = \phi^{(3)}_{ref} + \phi^t_N\sum_{k=0}^{n}\hat{\phi}^t_k\theta^k \tag{2.189}$$
$$F^{(3)}_{T_n}(t) = F^t_N\sum_{k=0}^{n}\hat{F}^t_k\theta^k, \tag{2.190}$$
where $\theta = \left[\frac{\nu(t_{ref}-t)}{(5M)}\right]^{-1/8}$ and $F \equiv \frac{d\phi}{2\pi dt} = \frac{v^3}{\pi M}$ is the instantaneous GW frequency.

The coefficients of these expansions are obviously determinated by substituting the PN energy and the flux at a certain PN order in the formal expressions and doing the respective computations.

Stationary Phase Approximation and Taylor F2

The most commonly used Taylor approximant is the Fourier representation computed using the *stationary phase approximation* (SPA) for chirp signals. Let's consider a signal of the form

$$h(t) = 2a(t)\cos\phi(t) = a(t)[e^{-i\phi(t)} + e^{i\phi(t)}], \tag{2.191}$$

where $\phi(t)$ is the implicit solution of one of the phasing formulas of the above Taylor approximants. The quantity $2\pi F(t) = \frac{d\phi(t)}{dt}$ defines the instantaneous GW frequency $F(t)$, and is assumed to be continuously increasing ($F(t) > 0$). Now the Fourier transform of $h(t)$ is defined by

$$\tilde{h}(f) \equiv \int_{-\infty}^{\infty} dt e^{2\pi i f t} h(t) = \int_{-\infty}^{\infty} a(t)[e^{2\pi f t - \phi(t)} + e^{2\pi f t + \phi(t)}]. \tag{2.192}$$

For positive frequencies only the first term on the right contributes and yields the following usual SPA:

$$\tilde{h}^{uspa}(f) = \frac{a(t_f)}{\sqrt{\dot{F}(t_f}} e^{i[\varphi_f(t_f) - \frac{\pi}{4}]}, \tag{2.193}$$

where $\varphi_f(t) \equiv 2\pi f t - \phi(t)$ and t_f is the saddle point defined by solving for t the condition $\frac{d\varphi_f(t)}{dt} = 0$, i.e. the time t_f when the GW frequency $F(t)$ becomes equal to the Fourier variable f. Eq. (2.179) yields for t_f the value

$$t_f = t_{ref} + M \int_{v_f}^{v_{ref}} dv \frac{E'(v)}{\mathcal{F}(v)}, \tag{2.194}$$

where $v_f \equiv (\pi M f)^{1/3}$. Using the above equation and $\phi(t_f)$ in eq. (2.196) one finds that

$$\psi_f(t_f) = 2\pi f t_{ref} - \phi_{ref} + 2\int_{v_f}^{v_{ref}} (v_f^3 - v^3) \frac{E'(v)}{\mathcal{F}(v)} dv. \tag{2.195}$$

The computational advantage of Eq. (2.195) is that in the frequency domain there are no equations to solve iteratively; the Fourier amplitudes are given

as explicit functions of frequency. The Taylor F2 method consist in using PN expansions of the energy and flux, but re-expanding the ratio $\frac{E'(v)}{\mathcal{F}(v)}$ in Eq. (2.195) in which case the integral can be solved explicitly. This leads to the following Taylor-like, Fourier domain phasing formula:

$$\psi_f(t_f) = 2\pi f t_{ref} - \phi_{ref} + \tau_N \sum_{k=0}^{5} \hat{\tau}_k (\pi M f)^{(k-5)/3}, \tag{2.196}$$

where τ_N is the Newtonian prefactor $\tau_N = \frac{3}{128\nu}$.

Chapter 3

Tidal properties of Neutron Stars

3.1 Tidal responses of a Neutron Star

3.1.1 Newtonian Tidal Force

When a very big object undergoes the gravitational force from another body, this force may significantly vary on its surface. Therefore, the form of the object is deformed without any volume variation. If we suppose that the giant body is spherical, tidal forces will stress it into an ellipsoid, with the major axis aligned to the object that produces the force of gravity.
Tidal laws follow the $\frac{1}{r^3}$ rule. Let's consider two bodies in orbit around each other. It is possible to approximate tidal force to a Newtonian level by differentiating Newton's law of gravity with respect to the distance:

$$dF = \frac{2GMm}{r^3} dr \ll r, \tag{3.1}$$

where M is the mass of the principal body, m the mass of the orbiting body and r the radius of the orbit.
In this case the tidal forces will be $2dF$ to the axis that binds the two center of mass of the bodies, and since the sign is positive, they will be directed to the external part of the body; on the contrary, on the plane perpendicular to the binding axis, the force is internal, and defined as $-dF$.
In General Relativity, the exact tidal force in each point of a body's surface is described by Weyl's tensor, which is obtained by subtracting the trace to

Riemann's tensor (7):

$$C_{\mu\nu\rho\sigma} = R_{\mu\nu\rho\sigma} - \frac{1}{2}R_{\mu\rho}g_{\nu\sigma} + \frac{1}{2}R_{\mu\sigma}g_{\nu\rho} + \frac{1}{2}R_{\nu\rho}g_{\mu\sigma} - \frac{1}{2}R_{\nu\sigma}g_{\mu\rho} + \frac{1}{6}R(g_{\mu\rho}g_{\nu\sigma} - g_{\mu\sigma}g_{\nu\rho}). \tag{3.2}$$

This tensor, which describes the tidal deformation of a body without volume variations, vanishes when contracted with a pair of indexes $(\mu\rho)$ or $(\nu\sigma)$. Using the antisymmetric tensor notation $A_{[\mu\nu]} \equiv \frac{1}{2}(A_{\mu\nu} - A_{\nu\mu})$, we can write Weyl's tensor in a more compact form:

$$C_{\mu\nu\rho\sigma} = R_{\mu\nu\rho\sigma} - R_{\mu[\rho}g_{\sigma]\nu} + R_{\nu[\rho}g_{\sigma]\mu} + \frac{1}{3}Rg_{\mu[\rho}g_{\sigma]\nu}. \tag{3.3}$$

3.1.2 Gravitomagnetism

The term "gravitomagnetism" [100, 101](GM) commonly indicates the collection of those gravitational phenomena regarding orbiting test particles, precessing gyroscopes, moving clocks and atoms and propagating electromagnetic waves [102, 103] which, in the framework of GR, arise from non-static distributions of matter and energy.
Let's consider, in the weak-field and slow motion approximation, the "matching" multi-chart approach developed by Damour, Soffel and Xu [104, 105, 106, 107] in the nineties. Here the motion and radiation of a compact body is splitted into an *inner* problem, where the worldine $\mathcal{L}_A$[1] is "skeletonized", and into an *outer* problem, where we have a worldtube $\tau_A \subset V_4$ that wraps $\mathcal{L}_A$ (V_4 is the atlas where all the considered bodies move). The two problems are then matched after a multipolar expansion. The local system of coordinates, that is bound to the bodies, is defined as a chart $X^\alpha_A : \tau_A \to \Re$. In short, in the *outer* problem one solves field equations in which the worldlines are provided with some global characteristics such as mass, spins and higher multipole moments, while in the *inner* problem one obtains the near-wordline behavior of the outer solution from a study of the influence of the other bodies on the structure of the fields in an inner world tube around each body. The resulting metric parametrization for the local chart at 1PN, using the

[1] The index A refers to the number of bodies that we are considering. If we are interested in a binary system, then $A = 2$.

DSX notation where $T \equiv X^0_A/c$, is the following:

$$G^A_{00}(X) = -\exp\left(-\frac{2W^A}{c^2}\right), \tag{3.4}$$

$$G^A_{0a}(X) = -\frac{4}{c^3}W^A_a, \tag{3.5}$$

$$E^A_a(X) = \partial_a W^A + \frac{4}{c^2}\partial_T W^A_a, \tag{3.6}$$

$$B^A_a(X) = \epsilon_{abc}\partial_b(-4W^A_c), \tag{3.7}$$

where $a, b, c = 1, 2, 3$. The gauge-invariant fields E, B and W satisfy the familiar equations[2]

$$\boldsymbol{\nabla}\cdot\boldsymbol{B} = \mathbf{0}, \tag{3.8}$$

$$\boldsymbol{\nabla}\times\boldsymbol{E} = -\frac{1}{c^2}\partial_T\boldsymbol{B}, \tag{3.9}$$

$$\boldsymbol{\nabla}\cdot\boldsymbol{E} = -\frac{3}{c^2}\partial^2_T W + O\left(\frac{1}{c^4}\right), \tag{3.10}$$

$$\boldsymbol{\nabla}\times\boldsymbol{B} = 4\partial_T\boldsymbol{E} + O\left(\frac{1}{c^2}\right). \tag{3.11}$$

We can naturally define the vector $\boldsymbol{B}$ as the gravitomagnetic field, and the vector $\boldsymbol{E}$ as the gravitoelectric field. The metric potential $W_\mu = (W, W_i)$ is related to the gravitational quadripotential A_μ by the relation $A_\mu \equiv (A_0, A_i) \equiv (cW, -4W_i)$. Defining $\Lambda(X)$ as an arbitrary function, this potential has the same gauge invariance of its electromagnetic analogue:

$$W' = W - \frac{1}{c^2}\partial_t\Lambda \tag{3.12}$$

$$W'_i = W_i + \frac{1}{4}\partial_i\Lambda. \tag{3.13}$$

The gravitational force density will be defined as analogue of electromagnetism's Lorentz force,

$$\boldsymbol{F} \equiv \Sigma\boldsymbol{E} + \frac{1}{c^2}\boldsymbol{\Sigma}\times\boldsymbol{B}, \tag{3.14}$$

[2]Gravitomagnetic Maxwell's equations are defined as Eqs. (3.8),(3.9), (3.10) and (3.11) at 1PN order, in the flat spacetime. This means that the curvature effects typical of GR are contained in the corrections $O\left(\frac{1}{c^4}\right)$ and $O\left(\frac{1}{c^2}\right)$.

where the quadrivector Σ_μ is related to the stress-energy tensor by

$$\Sigma(T, \boldsymbol{X}) \equiv \frac{T^{00} + T^{bb}}{c^2} \tag{3.15}$$

and

$$\Sigma^a(T, \boldsymbol{X}) \equiv \frac{T^{0a}}{c}. \tag{3.16}$$

Looking at the equation (3.14), we can say that the tidal force is split into two compenents, a gravitomagnetic one, proportional to the current density (3.16), and a gravitoelectric one, proportional to charge density (3.15)[3]. In the case of a multipolar expansion using spherical harmonics ($Y_{\ell m}$), the even-parity part ($\ell + m =$ even) is related to the mass/charge, so it can be defined as "electric", while the odd parity part ($\ell + m =$ odd), is related to the angular momentum/current, so it can be defined as "magnetic". In Ref. [6], we compare the effects of gravitomagnetic and gravitoelectric tides using the EOB formalism and we find, like what was previously hinted in Ref. [108], that they are $\sim \mathcal{O}(10^{-2})$ orders of magnitude negligible for data analysis purposes (see Fig. 2 there).

3.1.3 Love Numbers theory

Having in mind Eqs. (3.4), (3.5), (3.6) and (3.7), following Ref. [108] one defines, in the local frame of each body A, two sets of gravitoelectric and gravitomagnetic relativistic tidal moments, G_L^A and H_L^A, as

$$G_L^A(T) \equiv [\partial_{\langle L-1} E_{a_\ell\rangle}^{A,\mathrm{ext-gen}}(T, \boldsymbol{X})]_{X^a \to 0}, \tag{3.17}$$

$$H_L^A(T) \equiv [\partial_{\langle L-1} B_{a_\ell\rangle}^{A,\mathrm{ext-gen}}(T, \boldsymbol{X})]_{X^a \to 0}, \tag{3.18}$$

where $E_a^{A,\mathrm{ext-gen}}$ and $B_a^{A,\mathrm{ext-gen}}$ denote the externally-generated parts of the local gravitoelectric and gravitomagnetic fields E_a^A and B_a^A, while the angular brakets on the indexes refer to the STF notation that we have introduced in Sec. 2.3.3. The formal limit $X^a \to 0$ refers to the "skeletonized"[4] matching performed in the *outer* problem [104]. The multipole moments of the *inner* zone, that are internally generated, are the symmetric traceless free

[3] T^{bb} is the trace of the spatial part of $T^{\mu\nu}$.

[4] $X^A_{\mathrm{outer}} \to 0$ can be visualized as the limit in which the world tube is large with respect to the radius of the body A.

(STF) tensors $M_L^A(T)$ (mass moments) and $S_L^A(T)$ (spin moments). They asymptotically decrease as $R \equiv |\boldsymbol{X}| \to \infty$, and in the stationary case they are related with the internally-generated metric potentials by the multipolar expansions

$$W^{\rm int-gen,A}(X) = G \sum_{\ell \geq 0} \frac{(-)^\ell}{\ell!} \partial_L \left(\frac{M_L^A}{R} \right), \tag{3.19}$$

$$W_a^{\rm int-gen,A}(X) = G \sum_{\ell \geq 1} \frac{\ell}{\ell+1} \frac{(-)^\ell}{\ell!} \epsilon_{abc} \partial_{bL-1} \left(\frac{S_{cL-1}^A}{R} \right) - \frac{1}{4} \partial_a (\Lambda^A - \lambda), \tag{3.20}$$

where $\Lambda^A - \lambda$ is a gauge transformation[5]. Substantially, the matching between the outer (Eqs. (3.17) and (3.18)) and the inner problem (Eqs. (3.19) and (3.20)) leads to the following equations:

$$M_L^A = \mu_\ell^A G_L^A \tag{3.21}$$

$$S_L^A = \sigma_\ell^A H_L^A. \tag{3.22}$$

Here we have defined two tidal-polarizability coefficients μ_ℓ (gravitoelectric, even parity) and σ_ℓ (gravitomagnetic, odd parity), as previously done in the DSX formalism [104]. These coefficients relate the tidal induced multipole moments M_L^A and S_L^A to the corresponding external tidal fields G_L^A and H_L^A. More practically, μ_2 is the tidal polarizability associated to the quadrupole moment, and is equivalent to Hinderer's λ coefficient [109, 110], while σ_2 is the analogue of Favata's γ coefficient [111].
In terms of the finite-size corrections to the leading point-particle effective action $S_{\rm pointmass} = -\sum_A \int M_A ds_A$, the two tidal effects parametrized by μ_ℓ and σ_ℓ correspond to nonminimal wordline couplings proportional to the quantities

$$S_{\rm pointmass,electric} \sim \mu_\ell^A \int ds_A (G_L^A)^2, \tag{3.23}$$

$$S_{\rm pointmass,magnetic} \sim \sigma_\ell^A \int ds_A (H_L^A)^2. \tag{3.24}$$

[5]This transformation can be gauged-away by considering the internal-produced magnetic field of the binary.

These leading quadrupolar corrections can be reproduced (see Refs [112, 104]) as the following nonminimal coupling involving the Weyl tensor (Eq. (3.3)):

$$S_{\rm pointmass,electric} \sim \mu_2 \int ds \mathcal{E}_{\alpha\beta}\mathcal{E}^{\alpha\beta}, \tag{3.25}$$

$$S_{\rm pointmass,magnetic} \sim \sigma_2 \int ds \mathcal{B}_{\alpha\beta}\mathcal{B}^{\alpha\beta}, \tag{3.26}$$

where $\mathcal{E}_{\alpha\beta} \equiv u^\mu u^\nu C_{\mu\alpha\nu\beta}$ and $\mathcal{B}_{\alpha\beta} \equiv u^\mu u^\nu C^*_{\mu\alpha\nu\beta}$, with $u = dz^\mu/ds$ and $C^*_{\mu\alpha\nu\beta} \equiv \frac{1}{2}\epsilon_{\mu\nu}{}^{\rho\sigma}C_{\rho\sigma\alpha\beta}$ (i.e. the dual of Eq. (3.3)).
Considering a strongly self-gravitating NS, one wants then to determine μ_ℓ^A and σ_ℓ^A as functions of the compactness $\mathcal{C}_A \equiv \left(\frac{GM}{c^2R}\right)_A$. The starting point of the process, Eqs. (3.21) and (3.22), are the most general coefficients that can exist in the (parity preserving) case of a nonspinning NS. The tidal properties of a spinning NS will involve other tidal coefficients, proportional to the spin, and associated to a mixing between gravitoelectric and gravitomagnetic effects. They would correspond, for example in the quadrupolar case, to nonminimal worldline couplings quadratic in the Weyl tensor and linear in the spin tensor $S^A_{\mu\nu}$.
Up to now we have only considered tidal coefficients with a direct dynamical meaning. For completeness, we stress that there exist also a "shape" Love number h_ℓ that measures the proportionality between the external tidal influence and the deformation of the geometry of the surface of the considered NS. It is defined as

$$\left(\frac{\delta R}{R}\right)_\ell = h_\ell \frac{U_\ell^{\rm disturb}(R)}{gR}, \tag{3.27}$$

where the L.H.S. of the equation is proportional to the Legendre polynomial $P_\ell(\cos\theta)$, which represents the fractional deformation of the areal radius R of the NS. The quantity $U_\ell^{\rm disturb}(R) \propto R^\ell P_\ell(\cos\theta)$ represents the usual, external, Newtonian tidal potential deforming the star, formally evaluated at the radius of the star, whereas $g \equiv GM/R^2$ represents the usual Newtonian surface gravity of the body. For a more complete treatment of the shape Love number, that is not in the aims of this PhD thesis, the reader should refer to Refs. [108] and [113].

3.1.4 Computing μ_ℓ and σ_ℓ

Following Ref. [108], let's consider the metric of an isolated, nonrotating NS,

$$G^{A(0)}_{\alpha\beta} dX^\alpha dX^\beta = -e^{\nu(r)} dt^2 + e^{\lambda(r)} dr^2 + r^2 d\Omega^2, \tag{3.28}$$

where the index (0) reminds us that the body is not perturbed. The local spherical coordinates of the A-body frame are denoted by (t, r, θ, φ), with $d\Omega^2 \equiv d\theta^2 + \sin^2\theta d\varphi^2$. Introducing the radial dependent mass parameter $m(r)$ by

$$e^{\lambda(r)} \equiv \left(1 - \frac{2m(r)}{r}\right)^{-1}, \tag{3.29}$$

and considering a perfect fluid energy-momentum tensor

$$T_{\mu\nu} = (e + p) u_\mu u_\nu + p g_{\mu\nu}, \tag{3.30}$$

the spherically symmetric metric coefficients $\nu(r)$, $m(r)$ and the pressure $p(r)$ satisfy the Tolman-Oppenheimer-Volkoff (TOV) equations of stellar equilibrium

$$\frac{dm}{dr} = 4\pi r^2 e, \tag{3.31}$$

$$\frac{dp}{dr} = -(e + p)\frac{m + 4\pi r^3 p}{r^2 - 2mr}, \tag{3.32}$$

$$\frac{d\nu}{dr} = \frac{2(m + 4\pi r^3 p)}{r^2 - 2mr}. \tag{3.33}$$

These equations are integrated from the center outward once that a baritropic EOS relating p to e is provided (see Subsec. 3.1.5 for comparisons between models of various EOS).
Since the background geometry of the problem is spherical, the metric perturbation

$$G^A_{\alpha\beta}(X) = G^{A(0)}_{\alpha\beta}(X) + H_{\alpha\beta}(X), \tag{3.34}$$

can be decomposed into spherical harmonics. The metric is expanded in even-parity and odd-parity tensor harmonics as

$$H_{\alpha\beta} = H^{\text{even}}_{\alpha\beta} + H^{\text{odd}}_{\alpha\beta}. \tag{3.35}$$

In the Regge-Wheeler gauge $H_{\mu\nu} \to H_{\mu\nu} + \xi_{\mu;\nu} + \xi_{\nu;\mu}$, where ξ^μ is a gauge vector, and following standard definitions for the expansion coefficients and the sign conventions, for the even parity case one obtains

$$H^{\rm even}_{\alpha\beta} dX^\alpha dX^\beta = -[e^\nu H_0^{\ell m} dt^2 + 2H_1^{\ell m} dt dr + H_2^{\ell m} e^\lambda dr^2 + r^2 K^{\ell m} d\Omega^2] Y_{\ell m}. \tag{3.36}$$

For what concerns the odd parity case, the nonvanishing components of $H^{\rm odd}_{\alpha\beta}$ are $H^{\rm odd}_{tA} = h_0 \epsilon^B_A \nabla_B Y_{\ell m}$ and $H^{\rm odd}_{rA} = h_1 \epsilon^B_A \nabla_B Y_{\ell m}$ where $(A, B) = (\theta, \varphi)$ and where ϵ^B_A is the mixed form of the volume form on the sphere S^2_r. The next step is, considering the *adiabatic* tides case (i.e. the perturbations are stationary), to solve Einstein's Equations (11) together with the perturbed hydrodynamical equations $\nabla^\alpha \delta T_{\alpha\beta}[e, p] = 0$, so as to describe a star deformed by an external tidal field.
The problem to compute gravitomagnetic and gravitoelectric Love numbers is different for the even and the odd parity perturbations. Let's consider them separately.

- **Even parity case:** The metric perturbations reduce to two functions $H = H_0 = H_2$, and K (with $H_1 = 0$). The fluid perturbations are described by the logarithmic enthalpy function $h = \delta p/(e + p)$. The relation, in absence of entropy, with the metric function H is given by $\delta h = \frac{1}{2} H$. Then the problem to convert the first order radial differential eqations relating H', K', H and K to a single second order master equation was solved by Lindblom, Mendell and Ipser [114]:

  $$H'' + C_1 H' + C_0 H = 0. \tag{3.37}$$

  Taking the stationary limit ($\omega \to 0$) of the results given in Appendix A of Ref. [114] one obtains the coefficients $C_1 = C_1(r; \nu, \lambda, m, p, e)$ and $C_0 = C_0(\ell; \nu, \lambda, p, e)$, that are given in Eqs. (28) and (29) of Ref. [108]. Eq. (3.37) generalizes the quadrupolar Eq. (15) of Ref. [110] to higher multipolar orders (in fact the coefficient C_0 is ℓ-dependent).
  The metric variable K can be expressed as a linear combination of H and H', namely

  $$K = \alpha_1 H' + \alpha_2 H, \tag{3.38}$$

  where the coefficients α_1 and α_2 can be computed by taking the stationary limit of the results given in Appendix A of Ref. [114].
  The electric-type tidal response coefficient μ_ℓ, defined by Eq. (3.21),

can be obtained by going through three steps: **i)** numerically solving Eq. (3.37) within the NS; **ii)** analytically solving the same equation in the exterior of the star; **iii)** matching the interior and exterior solutions across the star surface, taking into account the definition (3.21) to normalize the ratio between the two parts of $H(r)$, $H^{\rm growing} \sim r^\ell$ and $H^{\rm decreasing} \sim \mu_\ell r^{-(\ell+1)}$.

- **i)** Eq. (3.37) is numerically integrated, along with TOV equations (3.31) (3.32) (3.33), from the center $r_0 \sim 10^{-6}$ outwards, starting with some central values of m, p, ν, H and H'. For H, one obviously takes starting values at $H(r_0) = r_0^\ell$ and $H'(r_0) = \ell r_0^{\ell-1}$. The latter boundary conditions follow from the analysis of Eq. (3.37) around $r = 0$, which shows that $H(r) \simeq r^\ell$ is the most general regular solution around $r = 0$. The internal integration's output is the value, for each ℓ, of the internal logarithmic derivative

$$y^{\rm int}(r) \equiv \frac{rH'}{H} \tag{3.39}$$

  at the star's surface $r = R$,

$$y_\ell \equiv y^{\rm int}(R). \tag{3.40}$$

- **ii)**The exterior form of Eq. (3.37) with $e = p = 0$ and $m(r) = M$ can be rewritten as an associated Legendre equation with $\ell = \ell$ and $m = 2$ [57, 58]:

$$(x^2-1)H'' + 2xH' - \left(\ell(\ell+1) + \frac{4}{x^2-1}\right) H = 0, \tag{3.41}$$

  where $x \equiv r/M - 1$. The general solution of this equation can be written as

$$H = a_P \hat{P}_{\ell 2}(x) + a_Q \hat{Q}_{\ell 2}(x), \tag{3.42}$$

  where the hat indicates that the Legendre functions have been normalized so that $\hat{Q}_{\ell 2} \simeq 1/x^{\ell+1} \simeq (M/r)^{\ell+1}$ and $\hat{P}_{\ell 2} \simeq x^\ell \simeq (r/M)^\ell$ when $x \to \infty$ or $r \to \infty$. The integration constants a_Q and a_P are determinated by matching to the internal solution. Defining $a_\ell \equiv a_Q/a_P$ the exterior logarithmic derivative $y^{\rm ext} \equiv rH'/H$ reads

$$y_\ell^{\rm ext}(x) = (1+x)\frac{\hat{P}'_{\ell 2}(x) + a_\ell \hat{Q}'_{\ell 2}(x)}{\hat{P}_{\ell 2}(x) + a_\ell \hat{Q}_{\ell 2}(x)}. \tag{3.43}$$

– **iii)**When $\gamma < \infty$, it is correct to impose the continuity of H and H' at the star's surface $r = R$ (the incompressible limit $\gamma \to \infty$ is singular at that point). This continuity implies the continuity of the logarithmic derivative rH'/H. This leads to the condition $y^{\rm ext}(R) = y^{\rm int}(R) = y_\ell$, which determines the value of the ratio $a_\ell = a_Q/a_P$ in terms of the compactness $\mathcal{C} = M/R$ of the star

$$a_\ell = -\left(\frac{\hat{P}'_{\ell 2}(x) - \mathcal{C} y_\ell \hat{P}_{\ell 2}(x)}{\hat{Q}'_{\ell 2}(x) - \mathcal{C} y_\ell \hat{Q}_{\ell 2}(x)}\right)_{x=1/\mathcal{C}-1}. \tag{3.44}$$

The ratio $a_\ell \equiv a_Q/a_P$ can be related to the tidal coefficient μ_ℓ by comparing (modulo an overall factor -2)

$$H^{\rm growing}(r) = a_p \hat{P}_{\ell 2}(x) Y_{\ell m} \simeq a_P \left(\frac{r}{M}\right)^\ell Y_{\ell m}, \tag{3.45}$$

$$H^{\rm decreasing}(r) = a_Q \hat{Q}_{\ell 2}(x) Y_{\ell m} \simeq a_Q \left(\frac{r}{M}\right)^{-(\ell+1)} Y_{\ell m}, \tag{3.46}$$

respectively to

$$W^{\rm ext-gen} = \frac{1}{\ell!}\hat{X}^L G^A_L = \frac{1}{\ell!} r^\ell \hat{n}^L G^A_L \tag{3.47}$$

and Eq. (3.19). The radial unit vector from above is defined as $n^a \equiv X^a/r$. Since

$$\partial_L r^{-1} = (-)^\ell (2\ell-1)!! \hat{n}^L r^{-(\ell+1)}, \tag{3.48}$$

and $M_L = \mu_\ell G_L$ and $G_L \hat{n}^L \propto Y_{\ell m}(\theta, \varphi)$, we see that

$$(2\ell-1)!! G\mu_\ell = \frac{a_Q}{a_P}\left(\frac{GM}{c^2}\right)^{2\ell+1} = a_\ell \left(\frac{GM}{c^2}\right)^{2\ell+1}. \tag{3.49}$$

The dimensions of $G\mu_\ell$ are $[\text{length}]^{2\ell+1}$. By scaling this quantity by the $(2\ell+1)$-th power of the star radius R we have

$$(2\ell-1)!! \frac{G\mu_\ell}{R^{2\ell+1}} \equiv 2k_\ell = a_\ell \mathcal{C}^{2\ell+1}. \tag{3.50}$$

This is the traditional "Newtonian" way of proceeding, and leads to the introduction of the dimensionless "second tidal Love number" k_ℓ.

One can finally write k_ℓ as

$$k_\ell = \frac{1}{2}\mathcal{C}^{2\ell+1} a_\ell \tag{3.51}$$

$$= -\frac{1}{2}\mathcal{C}^{2\ell+1}\left(\frac{\hat{P}'_{\ell 2}(x) - \mathcal{C} y_\ell \hat{P}_{\ell 2}(x)}{\hat{Q}'_{\ell 2}(x) - \mathcal{C} y_\ell \hat{Q}_{\ell 2}(x)}\right)_{x=1/\mathcal{C}-1} . \tag{3.52}$$

The dimensionless Love number has the advantage of having a weaker sensitivity on the compactness $\mathcal{C} \equiv GM/c^2R$. Besides that, the dimensionless quantity which will most directly enter the gravitational-wave phase of a BNS is $G\mu_\ell/(GM/c^2)^{2\ell+1} \sim a_\ell \sim \mathcal{C}^{-(2\ell+1)}k_\ell$. Using the Legendre polynomial formulas that are present in common literature one can solve Eq. (3.51) for $2 \leq \ell \leq 4$, that are reported in Eqs. (50), (51) and (52) of Ref. [108].

- **Odd parity case:** The gravitational potential well generated by the stress-energy tensor of a star does affect the radial propagation of the external odd-parity tidal fields, and adds an asymptotically decreasing tidal response to the incoming tidal field. This phenomenon is decribed by the static limit of Cummingham, Price and Moncrief equation [115, 116]. In the stationary limit this equations reads

$$\psi'' + \frac{e^\lambda}{r^2}[2m + 4\pi r^3(p-e)]\psi' - e^\lambda\left[\frac{\ell(\ell+1)}{r^2} - \frac{6m}{r^3} + 4\pi(e-p)\right]\psi = 0. \tag{3.53}$$

In terms of the variables (h_0, h_1) entering the odd parity perturbations, the odd-parity master function ψ can be taken to be either $e^{(\nu-\lambda)/2}h_1/r$, or the combination $r\partial_t h_1 - r^3\partial_r(h_0/r^2)$. Since h_1 vanishes in the stationary limit, ψ yields

$$\psi = r^3\partial_r\left(\frac{h_0}{r^2}\right) = rh'_0 - 2h_0. \tag{3.54}$$

The magnetic-type tidal coefficient σ_ℓ can be obtained in three steps that are analogue to the even-parity case from above.

  - **i)** The internal value of the odd-parity master function ψ is obtained by numerically integrating Eq. (3.53), together with TOV

equations. The boundary condition in this case are obtained from the behavior $\psi \propto r^{\ell+1}$ of the general regular solutions in $r = 0$. Like the previous case, the main output of the internal integration procedure is to compute, for each value of ℓ, the value of the internal logarithmic derivative of ψ at the star surface:

$$y_\ell^{\rm odd} \equiv y_\ell^{\rm int}(R) \equiv \left[\frac{r\psi'_{\rm int}}{\psi_{\rm int}}\right]_{r=R}. \tag{3.55}$$

– **ii)** Similar to the even-parity case, there exist two types of exterior solutions: a growing one and a decreasing one. We respectively normalize them in order to have $\psi_P(\hat{r}) \simeq \hat{r}^{\ell+1}$, and $\psi_Q(\hat{r}) \simeq \hat{r}^{-\ell}$ as $\hat{r} \to \infty$, where $\hat{r} \equiv r/M$. In the quadrupolar case the growing analytical exterior solution of Eq. (3.53) is the polynomial

$$\psi_P^{\ell=2}(\hat{r}) = \hat{r}^3, \tag{3.56}$$

while the decreasing one can be expressed in terms of an hypergeometric function $F(a, b; c; z)$ (15) as

$$\psi_Q^{\ell=2}(\hat{r}) = -\frac{1}{4}\hat{r}^3\partial_{\hat{r}}\left[\hat{r}^{-4}F\left(1, 4; 6; \frac{2}{\hat{r}}\right)\right]. \tag{3.57}$$

The normalization of $\psi_Q(\hat{r})$ is such that $\psi_Q(\hat{r}) \simeq \hat{r}^{-2}$ as $r \to \infty$. For $a = 1, b = 4$ and $c = 6$ one can rewrite the hypergeometric function as a polynomial with the form

$$\psi_Q^{\ell=2}(\hat{r}) = A_3\hat{r}^3\log\left(\frac{\hat{r}-2}{\hat{r}}\right) + A_2\hat{r}^2 + A_1\hat{r} + A_0 + A_{-1}\hat{r}^{-1}. \tag{3.58}$$

For an arbitrary ℓ, the general exterior solution of Eq. (3.37) can be written as

$$\psi^{\rm ext} = b_P\psi_P(\hat{r}) + b_Q\psi_Q(\hat{r}), \tag{3.59}$$

which is the analogue of the even-parity one (3.42). This result allows one to compute the logarithmic derivative $y^{\rm odd} = r\psi'/\psi$ of ψ in the exterior domain, namely

$$y_{\rm odd}^{\rm ext}(\hat{r}) = \hat{r}\frac{\psi'_P(\hat{r}) + b_\ell\psi'_Q(\hat{r})}{\psi_P(\hat{r}) + b_\ell\psi_Q(\hat{r})}, \tag{3.60}$$

where $b_\ell \equiv b_Q/b_P$.

– **iii)** Similarly to the even-parity case, by imposing the continuity of ψ, ψ' and therefore $y^{\rm odd} = r\psi'/\psi$ at the star's surface, one obtains

$$b_\ell = -\left(\frac{\psi'_P(\hat{r}) - \mathcal{C} y_{\rm odd}\psi_P(\hat{r})}{\psi'_Q(\hat{r}) - \mathcal{C} y_{\rm odd}\psi_Q(\hat{r})}\right)_{\hat{r}=1/\mathcal{C}}, \tag{3.61}$$

that is the odd-parity analogue of a_ℓ. In the present odd-parity case, the tidal response coefficient $G\sigma_\ell$ has the dimension $[\text{length}]^{2\ell+1}$, like a_ℓ, and for a general ℓ we have $b_\ell \sim G\sigma_\ell (GM/c^2)^{-(2\ell+1)}$. The odd parity analogue of k_ℓ will be obtained by scaling $G\sigma_\ell$ by the $(2\ell+1)$-th power of the star radius R, and will therefore involve the new dimensionless combination

$$\begin{aligned} j_\ell &\equiv \mathcal{C}^{2\ell+1} b_\ell \\ &= -\mathcal{C}^{2\ell+1}\left(\frac{\psi'_P(\hat{r}) - \mathcal{C} y_{\rm odd}\psi_P(\hat{r})}{\psi'_Q(\hat{r}) - \mathcal{C} y_{\rm odd}\psi_Q(\hat{r})}\right)_{\hat{r}=1/\mathcal{C}}. \end{aligned} \tag{3.62}$$

The Regge-Wheeler metric function h_0 entering Eq. (3.54) parametrizes the the time $\times$ angle off diagonal component of the metric perturbation

$$H_{0A} \propto h_0(r)\epsilon^B_A \nabla_B Y_{\ell m}(\theta,\varphi), \tag{3.63}$$

where $A, B = 2, 3 = \theta, \varphi$ are indices on the background coordinate sphere S^2_r of radius r. The metric on S^2_r is $\gamma_{AB}dx^A dx^B = r^2 d\Omega^2$, while $\epsilon^B_A \equiv \gamma^{BC}\epsilon_{AC}$ denotes the mixed form of the volume form $\frac{1}{2}\epsilon_{AB}dx^A \wedge dx^B = r^2 \sin\theta d\theta \wedge d\varphi$ on S^2_r. Let's now consider the 3-dimensional component of the gravitomagnetic field $B_a \propto \epsilon_{abc}\partial_b H_{0c}$. Its radial component is the pseudoscalar

$$\boldsymbol{n}\cdot\boldsymbol{B} = n^a B_a \propto n^a \epsilon_{abc}\partial_b H_{0c} \propto \epsilon^{AB}\nabla_A H_{0B}. \tag{3.64}$$

By substituting Eq. (3.63) this equation yields

$$\boldsymbol{n}\cdot\boldsymbol{B} \propto -h_0(r)\epsilon^{AB}\epsilon^C_A \nabla_B \nabla_C Y_{\ell m} = \ell(\ell+1)\frac{h_0(r)}{r^2}Y_{\ell m}, \tag{3.65}$$

where one used $\epsilon^{AB}\epsilon^C_A = \gamma^{BC}\epsilon^{BC}$ and the fact that $\gamma^{AB}\nabla_A\nabla_B Y_{\ell m} = -\ell(\ell+1)r^{-2}Y_{\ell m}$, where the factor r^{-2} comes from the fact that

γ_{AB} is the metric on a sphere of radius r, than an unit sphere. This leads to

$$\psi = r^3 \partial_r \left(\frac{h_0}{r^2} \right) \propto r^3 \partial_r (\boldsymbol{n} \cdot \boldsymbol{B}). \tag{3.66}$$

Focusing on the growing or decreasing asymptotic terms in the odd-parity metric, we can now compare the definition of b_ℓ, namely

$$\psi \propto \left[r^{\ell+1} + b_\ell \left(\frac{GM}{c^2} \right)^{2\ell+1} r^{-\ell} \right] Y_{\ell m}(\theta, \varphi), \tag{3.67}$$

to the stationary limit of the general gravitomagnetic fields in a local A frame (that are shown in Eqs. (2.19) and (4.16) of Ref. [105]),

$$\begin{aligned} B_a &= B_a^{\rm ext-gen} + B_a^{\rm int-gen} \\ &= \sum_\ell \frac{1}{\ell!} X^L H_{aL} + \sum_\ell 4G \frac{(-)^\ell}{\ell!} \frac{\ell}{\ell+1} \partial_{aL} \left(\frac{S_L}{r} \right). \end{aligned} \tag{3.68}$$

Inserting now $S_L = \sigma_\ell H_L$, contracting B_a with n^a, and recalling that one has $n^a \partial_a = \partial_r$ and $\partial_L (r^{-1}) = (-)^\ell \times (2\ell - 1)!! r^{-(\ell+1)}$, one finds

$$\begin{aligned} \boldsymbol{n} \cdot \boldsymbol{B} &= \sum_\ell \frac{1}{(\ell-1)!} r^{\ell-1} H_L n^L + \sum_\ell 4G\sigma_\ell \frac{(-)^\ell}{\ell!} \frac{\ell}{\ell+1} \partial_r \partial_L \left(\frac{H_L}{r} \right) \\ &= \sum_\ell \frac{1}{(\ell-1)!} \left[r^{\ell+1} - 4G\sigma_\ell (2\ell-1)!! \frac{1}{r^{\ell+2}} \right] n_L H_L, \end{aligned} \tag{3.69}$$

so that

$$r^3 \partial_r (\boldsymbol{n} \cdot \boldsymbol{B}) = \sum_\ell \frac{1}{(\ell-2)!} \left[r^{\ell+1} + 4G\sigma_\ell (2\ell-1)!! \frac{\ell+2}{\ell-1} \frac{1}{r^\ell} \right] n_L H_L. \tag{3.70}$$

The comparison with Eq. (3.67) yields the final result

$$G\sigma_\ell = \frac{\ell-1}{4(\ell+2)} \frac{j_\ell}{(2\ell-1)!!} R^{2\ell+1}, \tag{3.71}$$

where $j_\ell \equiv \mathcal{C}^{2\ell+1} b_\ell$. In the $\ell = 2$ quadrupolar case we have

$$G\sigma_2 = \frac{1}{48} j_2 R^5 = \frac{1}{48} b_2 \left(\frac{GM}{c^2} \right)^5, \tag{3.72}$$

where the explicit expression of j_2 is given by Eq. (73) of Ref. [108].

3.1.5 Polytropic Equations of State

The Equation of State (EOS) framework is mainly discussed in Refs. [117, 118] and references therein. In this section, following the references from above, we briefly overview this topic in order to clarify what is explained in Chapters 5 and 6.
Since the temperature of Neutron Stars (NS) is far below the Fermi energy of their constituent particles, their matter is described by the one-parameter EOS that governs cold matter above nuclear density. This EOS, besides being the correct choice, has a large uncertainty, since the pressure p as a function of the mass density ρ is uncertain by as much as an order of magnitude above nuclear density. The phase of the matter in the core of a NS is similarly uncertain, so there exists various models of EOS that depend from physical models of the nucleus. The correspondigly large number of fundamental parameters needed to accomodate the models' Lagrangians has meant that studies of astrophysical constraints have induced a separation between "allowed" and "excluded" EOS lists. In Ref. [117] it is shown that if one uses phenomenological rather than fundamental parameters, one can obtain a parametrized EOS in which the astrophysical constraints are described as constraints on the parameter space. This implies that the number of parameters are smaller than the number of the "true" NS properties, but at the same time large enough to accurately approximate the EOS candidates.
One can define a parametrized EOS by specifying the stiffness of the star in three density intervals, measured by the adiabatic index

$$\Gamma = \frac{d \log p}{d \log \rho}. \tag{3.73}$$

A fourth parameter translates the $p(\rho)$ curve up or down, adding a constant pressure or, equivalently, fixing the pressure at the endpoint of the first density interval. The EOS is then matched below nuclear density to the (presumed known) EOS. An EOS with Γ = constant is a polytrope, so a parametrized EOS is still polytropic, but with different *polytropic intervals*. Several studies [119, 120, 121, 122, 123] have considered piecewise polytropic equations to approximate NS EOS candidates. Ref. [117] uses a small number of parameters to fit a wide variety of fundamental EOS. In literature these candidates are usually the following:

- Potential-method EOSs, as PAL6 [124] and Sly [125];

- Variational-method EOSs like AP1-4 [126], FPS [127] and WFF1-3 [128];
- Brueckner-Hartree-Fock EOSs, that are subdivided in nonrelativistic (BBB2 [129]) and relativistic (BPAL12 [130], ENG [131] and MPA1 [132]) ones;
- Relativistic mean-field theory EOSs: MS1-2 and MS1b, which is identical to MS1 except with a low simmetry energy of 25 MeV [133]).

A polytropic EOS has the form

$$p(\rho) = K\rho^{\Gamma}, \tag{3.74}$$

where ρ is the rest-mass density, K a constant of proportionality and Γ the adiabatic index. The energy density ϵ is fixed by the first law of thermodynamics ($c \equiv 1$):

$$d\frac{\epsilon}{\rho} = -pd\frac{1}{\rho}. \tag{3.75}$$

The integral of Eq. (3.75) given Eq. (3.74) is

$$\frac{\epsilon}{\rho} = (1+a) + \frac{1}{\Gamma - 1}K\rho^{\Gamma-1}, \tag{3.76}$$

where $a =$ constant. But since $\lim_{\rho\to 0}\frac{\epsilon}{\rho} = 1$, $a = 0$ and

$$\epsilon = \rho + \frac{1}{\Gamma - 1}p. \tag{3.77}$$

A parametrized EOS like the one introduced in Ref. [117] is a piecewise polytrope above a density ρ_0, satisfying Eqs. (3.74) and (3.76) on a sequence of density intervals, each with its own K_i and Γ_i. An EOS is piecewise polytropic for $\rho \geq \rho_0$ if, for a set of dividing densities $\rho_0 < \rho_1 < \rho_2 < ...$, the pressure and energy density are everywhere continuous and satisfy the conditions

$$\begin{aligned} p(\rho) &= K_i\rho^{\Gamma_i}, \\ d\frac{\epsilon}{\rho} &= -pd\frac{1}{\rho} \\ \rho_{i-1} &\leq \rho \leq \rho_i. \end{aligned} \tag{3.78}$$

Then, for $\Gamma \neq 1$,

$$\epsilon(\rho) = (1 + a_i)\rho + \frac{K_i}{\Gamma_i - 1}\rho^{\Gamma_i} \tag{3.79}$$

with

$$a_i = \frac{\epsilon(\rho_{i-1})}{\rho_{i-1}} - 1 - \frac{K_i}{\Gamma_i - 1}\rho_{i-1}^{\Gamma_i - 1}. \tag{3.80}$$

The *specific enthalpy* h is defined as $(\epsilon + p)/\rho$ and is given in each density interval by

$$h(\rho) = 1 + a_i + \frac{\Gamma_i}{\Gamma_i - 1}K_i\rho^{\Gamma_i - 1}. \tag{3.81}$$

The internal energy $e = \frac{\epsilon}{\rho} - 1$ is then

$$e(\rho) = a_i + \frac{K_i}{\Gamma_i - 1}\rho^{\Gamma_i - 1} \tag{3.82}$$

and the sound velocity v_s is

$$v_s(\rho) = \sqrt{\frac{dp}{d\epsilon}} = \sqrt{\frac{\Gamma_i p}{\epsilon + p}} \tag{3.83}$$

Each piece of a piecewise polytropic EOS is specified by three parameters: the initial density, the coefficient K_i, and the adiabatic index Γ_i. However, when the EOS at lower density has already been specified up to the chosen ρ_i, continuity of pressure restricts K_{i+1} to the value

$$K_{i+1} = \frac{p(\rho_i)}{\rho_i^{\Gamma_i + 1}} \tag{3.84}$$

Thus each additional region requires only two parameters, ρ_i and Γ_{i+1}.
The fitting procedure for piecewise polytropic equations (see Sec. IV of Ref. [117]) is beyond the aim of this work; the important thing to stress is that there is a general agreement on the low density EOS for cold matter, so each choice of a piecewise polytropic EOS above nuclear density is matched to a SLy equation [125] in order to get a "realistic" fitted equation. These phenomenological equations can be employed in comparisons between numerical and analytical models; in this case there are shown some tables with the different adiabatic indexes Γ_i associated to each polytropoc interval, the dividing density (ρ_0) between the low density part of the EOS (the "crust")

and the high density one; the gravitoelectric Love Numbers associated to the EOS. For preliminary or theoretical-oriented works, a rather good representation of the overall characteristics of NSs for a polytropic equation like (3.74) is $\Gamma \sim 2$ [108].

3.2 Quadrupole-monopole responses of a Neutron Star

In a BNS system, the spinning motion of the body A induces a distortion in its mass distribution which creates another distortion in the gravitational field outside the star, measured by the STF tensor C_{QA}^{ab}. The quadrupole term in the gravitational potential affects the orbital motion of the companion, and this effect can modify the rate of the inspiral of a spinning BNS (i.e. it enters in the phase of our gravitational signal, see Chapt. 6). In literature this interaction is often named "quadrupole-monopole" effect, as it was introduced by Poisson [134].
Assuming that the spinning body A is axially symmetric about the direction of $\hat{\boldsymbol{S}}_A$, where the hat indicates an unit vector, the quadrupole-moment tensor can be expressed as

$$Q_A^{ab} = C_{QA}(\hat{s}^a \hat{s}^b - \frac{1}{3}\delta^{ab}), \tag{3.85}$$

where $C_{QA} \neq 1$ for a NS and $C_{QA} = 1$ for a BH (so in the latter case we get the standard formula (2.7)). In Newtonian theory this is given in terms of the mass density ρ by $Q_A = \int_A \rho(\boldsymbol{x})|\boldsymbol{x}|^2 P_2(\hat{\boldsymbol{s}}\cdot\hat{\boldsymbol{x}})d^3x$, where $P_2(x) = \frac{1}{2}(3x^2-1)$. In GR, C_{QA} is defined in a coordinate-invariant manner in terms of the falloff behavior of the metric outside the star. The general relativistic definition reduces to the Newtonian one when the gravitational field is weak everywhere inside the star. The LO quadrupole-moment contribution computed by Poisson [134] reads

$$\sigma_{qm} = -\frac{5}{2}\sum_A C_{QA}\frac{\chi_A^2 m_A^2}{M^2}[3(\hat{\boldsymbol{L}}\cdot\hat{\boldsymbol{S}}_A)^2 - 1], \tag{3.86}$$

and has been studied in a data analysis context in Ref. [135]. We refer the reader to Chapt. 6 for an original study of the effects on the phase of NLO and NNLO quadrupole-monopole terms [136].
Finally, for the purposes of this work, it is useful to remind that there exist

some phenomenological correlations between the mass, the moment of inertia and the quadrupole moment of a BNS [137]. Roughly speaking, the moment of inertia I quantifies how fast a NS can spin given a fixed spin angular momentum S; the quadrupole moment Q describes how much a NS is deformed away from sphericity, and the Love number characterizes how easy or difficult it would be to deform a NS. The quadrupole moment scalar defined as $Q_{\rm spin} \approx -C_Q(m, EOS)\chi^2$ depends from the equation of state, and so from the Love Number. The (phenomenological) relation that binds these quantities allowing us to compute the $C_Q(\lambda)$ scalar that enters at the quadratic-order in the spin given a Love number λ (and so an EOS) is the fitting formula [137]

$$\log y_i = a_i + b_i \log x_i + c_i(\log x_i)^2 + d_i(\log x_i)^3 + e_i(\log x_i)^4, \qquad (3.87)$$

where the coefficients are given by Table 3.1

Table 3.1: Estimated numerical coefficients for the fitting formula of the I-Love, I-Q and Q-Love (dimensionless) relations given in Ref [137] for Eq. (3.87).

y_i	x_i	a_i	b_i	c_i	d_i	e_i
I	λ	1.47	0.0817	0.0149	2.87×10^{-4}	-3.64×10^{-5}
I	Q	1.35	0.697	-0.143	9.94×10^{-2}	-1.24×10^{-2}
Q	λ	0.194	0.0936	0.0474	-4.21×10^{-3}	1.23×10^{-4}

For gravitational-wave modelization we are interested to the last row of the table, where we can see the relation between the quadrupole-monopole coefficients $C_Q(\lambda)$ and the Love number λ of the associated EOS (see Chapt. 5). It is important to stress that Yunes and Yagi's relations (3.87) do not depend sensitively on the NS's internal structure. They are "universal" in the sense that phenomenologically they depend most sensitively on the internal structure far from the core, where *all* realistic EOS mostly approach each other. Beyond that, as the NS compactness increases, the fitting formula approaches the parameter configuration of a BH, which does not have an internal-structure dependence.

Chapter 4

The Effective one-Body model

4.1 Introduction and motivations

In this Chapter, we mainly follow one of the best seminars on the topic, i.e. Damour's 2016 Séminaire Poincaré session [81], updating it with the actual state-of-the-art EOB developments when necessary.
High-order PN-expanded analytical results, if used as they are, are insufficient for allowing one to describe the last orbits, and the merger of BBHs or BNSs. The issue is that the velocity parameter $\epsilon = v/c \equiv x^{1/2} \equiv (GM\Omega/c^3)^{\frac{1}{3}}$ becomes of order unity near the end of the inspiral, so that the various PN-expanded representations of both the dynamics, and the GW emission, of the type $c_0 + c_1 v/c + c_2 v^2/c^2 + c_3 v^3/c^3 + ... + c_n v^n/c^n$, become numerically useless before one can reach the merger. Some authors, led by Thorne, suggested in 1998 that only NR will have solved the problem: near the merger, one must use NR simulations only [138], even if that method is slow and incompatible with bayesian analysis' high number of template requirements. On the other hand, the same year Damour and collaborators proposed to simply use resummation to 'cure" the divergent PN results' pathologies [139].
A resummation method consists in replacing a Taylor-like truncated expansion by some non-polynomial funtion of v/c, defined so as to incorporate some of the expected non-perturbative features of the exact results. In 1999-2000 a new approach to the resummation of the conservative dynamics of binary systems was introduced [28, 140, 141]. This approach, named "Effective one-Body (EOB) model", is constituted by three different bricks: the dynamical sector, which was inspired by an approach to electromagnetically

interacting quantum two-body systems introduced by Brézin, Itzykson and Zinn-Justin [142]; the radiation-reaction force $\mathcal{F}$ sector, that was initially inspired by the Padé resummation of the flux function introduced in Ref. [139] and then improved (along with the waveform, which is the square-root of the flux) in Refs. [8, 143, 9], and by Chapters 8 and 9 of this work; a waveform sector inspired by the work of Davis, Ruffini and Tiomno [144], which discovered the transition between the plunge signal and a ringing tail when a particle falls into a BH. Additional motivation for the EOB treatment of the transition from plunge to ringdown for a BBH came from Ref. [145].

4.2 EOB dynamics

The EOB is a general-relativistic generalization of the Newtonian fact that the relative dynamics of a two-body system with masses m_1, m_2 and potential $V(\boldsymbol{x_1}-\boldsymbol{x_2})$, is equivalent to the dynamics of a test-particle of mass $\mu=m_1m_2/|\boldsymbol{x_1}-\boldsymbol{x_2}|$ and position $\boldsymbol{x}=\boldsymbol{x_1}-\boldsymbol{x_2}$ subject to the same potential $V(\boldsymbol{x})$. In a gravitational two-body interaction, since $V(\boldsymbol{x_1}-\boldsymbol{x_2})=-Gm_1m_2/|\boldsymbol{x_1}-\boldsymbol{x_2}|$, the identity $m_1m_2\equiv\mu M$ (where $M\equiv m_1+m_2$) means that the gravitational two-body Newtonian interaction is equivalent to the dynamics of a test-particle mass μ attracted by a larger, central mass $GM=G(m_1+m_2)$. This fact is generalized into a GR framework by considering an "effective" metric $g^{\rm eff}_{\mu\nu}(x^\lambda;GM,\nu)$ such that the geodesic dynamics of a test-particle of mass μ within it is equivalent, when Taylor-expanded in powers of c^2, to the original, relative PN-expanded dynamics, which is described by the PN-expanded Hamiltonian in the ADM formalism [146, 147]. Looking at Appendix E of Ref. [146], one can observe that the full 4PN Hamiltonian is very complex, and that it takes several sheets of paper. The EOB approach to the relativistic two-body problem introduces strong simplifications thanks to mapping of the *real* comparable-mass binary system dynamics into the *effective* test-particle one.

Let's now explain the idea, proposed in Ref. [28], which defines the EOB approach. It consists, like what was emphasized by John Wheeler, in thinking "quantum mechanically" into a classical mechanics framework. Instead of thinking in terms of a classical Hamiltonian $H(\boldsymbol{q},\boldsymbol{p})$, and of its classical bound orbits, we can think in terms of the quantized energy levels $E(n,\ell)$ of the quantum bound states of the Hamiltonian operator $H(\hat{\boldsymbol{q}},\hat{\boldsymbol{p}})$. Here ℓ will be the discrete angular momentum quantum number (we remind

that $\boldsymbol{L}^2 = \hbar\ell(\ell+1)$), while n represents the principal quantum number $n = \ell + n_r + 1$, where n_r (the radial quantum number) denotes the number of nodes in the radial wave function. The third quantum number m (which satisfy the constraint $-\ell \leq m \leq \ell$) does not enter the energy levels because of the spherical symmetry of the two-body interaction in the center of mass frame. By considering the rescaled (i.e. $\hat{H} \equiv H/\mu$) non-relativistic Newtonian Hamiltonian

$$\hat{H}_N(\boldsymbol{r}, \boldsymbol{p}) = \frac{\boldsymbol{p}^2}{2} - \frac{1}{r}, \tag{4.1}$$

where the scaled variables are defined as $\boldsymbol{r} = (\boldsymbol{x_1} - \boldsymbol{x_2})/GM$ and $\boldsymbol{p} = \boldsymbol{p_1}/\mu = -\boldsymbol{p_2}/\mu$, one obtains the well-known eigenvalue

$$E_0(n, \ell) = -\frac{1}{2}\mu \left(\frac{GM\mu}{n\hbar}\right)^2, \tag{4.2}$$

which depends only on n. When considering the PN corrections to H_0 one gets a more complicated expression of the form

$$E^{\text{relative}}_{\text{PN}}(n, \ell) = -\frac{1}{2}\mu\frac{\alpha^2}{n^2}\Bigg[1 + \frac{\alpha^2}{c^2}\left(\frac{c_{11}}{n\ell} + \frac{c_{20}}{n^2}\right) + \frac{\alpha^4}{c^4}\left(\frac{c_{13}}{n\ell^3} + \frac{c_{22}}{n^2\ell^2} + \frac{c_{31}}{n^3\ell} + \frac{c_{40}}{n^4}\right) + \frac{\alpha^6}{c^6}\left(\frac{c_{15}}{n\ell^5} + ... + \frac{c_{60}}{n^6} + ...\right)\Bigg], \tag{4.3}$$

where $\alpha \equiv GM\mu/\hbar = Gm_1m_2/\hbar$, and where the "classical" limit where the quantum numbers n and ℓ are large is considered. The 2PN version of Eq. (4.3) had been derived in Ref. [148], while the 3PN one in Ref. [149]. The dimensionless coefficients c_{pq} are functions of the symmetric mass ratio (1.37), for instance $c_{40} = \frac{1}{8}(145 - 15\nu + \nu^2)$. This kind of Hamiltonian in classical mechanics ($n, \ell \to \infty$) is called "Delaunay Hamiltonian". It is expressed in terms of the action variables $J = \ell\hbar = \frac{1}{2\pi}\oint p_\varphi d\varphi$, and $N = n\hbar = I_r + J$, with $I_r = \frac{1}{2\pi}\oint p_r dr$.

The PN-expanded energy levels (4.3) encode, in a gauge invariant way, the relative dynamics of a *real* binary. Therefore, at this point one must analyze the *effective* dynamics of a test-particle body of mass μ and then find a mapping between the two. Let's consider the *effective* ν-deformed geodesic equation in some external Schwartzschild metric with spherical symmetry

$$g^{\text{eff}}_{\mu\nu}dx^\mu dx^\nu = -A(R;\nu)c^2dT^2 + B(R;\nu)dR^2 + R^2(d\theta^2 + \sin\theta d\varphi^2), \tag{4.4}$$

where the a priori unknown metric functions $A(R;\nu)$ and $B(R;\nu)$ will be constructed in the form of expansions in the parameter GM/c^2R,

$$A(R;\nu) = 1 + \tilde{a}_1\frac{GM}{c^2R} + \tilde{a}_2\left(\frac{GM}{c^2R}\right)^2 + \tilde{a}_3\left(\frac{GM}{c^2R}\right)^3 + \tilde{a}_4\left(\frac{GM}{c^2R}\right)^4 + ...,$$
$$B(R;\nu) = 1 + \tilde{b}_1\frac{GM}{c^2R} + \tilde{b}_2\left(\frac{GM}{c^2R}\right)^2 + \tilde{b}_3\left(\frac{GM}{c^2R}\right)^3 + ..., \tag{4.5}$$

where the dimensionless coefficients $\tilde{a}_n$, $\tilde{b}_n$ depend on ν. The Newtonian limit constraint is $\tilde{a}_1 = -2$. It is important to stress that since ν can be viewed as a deformation parameter away from the test-mass limit, the effective metric (4.5) must reduce to the standard Schwartzschild metric for $\nu \to 0$:

$$A(R;\nu=0) = 1 - \frac{2GM}{c^2R} = B^{-1}(R;\nu=0). \tag{4.6}$$

By requiring that the dynamics of the *effective* body of mass μ satisfy the mass-shell condition

$$g^{\mu\nu}_{\rm eff}p^{\rm eff}_\mu p^{\rm eff}_\nu + \mu^2c^2 + Q(p^{\rm eff}_\mu) = 0, \tag{4.7}$$

where Q(p) is at least quartic in p, and then by solving the corresponding Hamilton-Jacobi equation

$$g^{\mu\nu}_{\rm eff}\frac{\partial S_{\rm eff}}{\partial x^\mu}\frac{\partial S_{\rm eff}}{\partial x^\nu} + \mu^2c^2 + Q\left(\frac{\partial S_{\rm eff}}{\partial x^\mu}\right) = 0,$$
$$S_{\rm eff} = -\mathcal{E}_{\rm eff}t + J_{\rm eff}\varphi + S_{\rm eff}(R), \tag{4.8}$$

one can compute in the $n, \ell \to \infty$ limit the effective Delaunay Hamiltonian $\mathcal{E}_{\rm eff}(N_{\rm eff}, J_{\rm eff})$, with $N_{\rm eff} = n_{\rm eff}\hbar, J_{\rm eff} = \ell_{\rm eff}\hbar$ (where $N_{\rm eff} = J_{\rm eff} + I^{\rm eff}_R$, with $I^{\rm eff}_R = \frac{1}{2\pi}\oint p^{\rm eff}_R dR$, $P^{\rm eff}_R = \partial S_{\rm eff}(R)/dR$). This yields a result in the form

$$\mathcal{E}_{\rm eff}(n_{\rm eff},\ell_{\rm eff}) = \mu c^2 - \frac{1}{2}\mu\frac{\alpha^2}{n^2_{\rm eff}}\Bigg[1 + \frac{\alpha^2}{c^2}\left(\frac{c^{\rm eff}_{11}}{n_{\rm eff}\ell_{\rm eff}} + \frac{c^{\rm eff}_{20}}{n^2_{\rm eff}}\right)$$
$$+ \frac{\alpha^4}{c^4}\left(\frac{c^{\rm eff}_{13}}{n_{\rm eff}\ell^3_{\rm eff}} + \frac{c^{\rm eff}_{22}}{n^2_{\rm eff}\ell^2_{\rm eff}} + \frac{c^{\rm eff}_{31}}{n^3_{\rm eff}\ell_{\rm eff}} + \frac{c^{\rm eff}_{40}}{n^4_{\rm eff}}\right)$$
$$+ \frac{\alpha^6}{c^6}\left(\frac{c^{\rm eff}_{15}}{n_{\rm eff}\ell^5_{\rm eff}} + ... + \frac{c^{\rm eff}_{60}}{n^6_{\rm eff}}\right) + ..\Bigg], \tag{4.9}$$

where the dimensionless coefficients $c_{pq}^{\rm eff}$ are now functions of the unknown *external* metric coefficients $\tilde{a}_n$ and $\tilde{b}_n$.
At this point, one needs a rule to correlate the *real* two-body dynamics, summarized by Eq. (4.3), and the *effective one-body* one, summarized in Eq. (4.9). Since in quantum mechanics the action variables are quantized ($N_{\rm real} = n\hbar$, $N_{\rm eff} = n_{\rm eff}\hbar$, etc.) it is natural to identify $n = n_{\rm eff}$ and $\ell = \ell_{\rm eff}$. Starting from this observation, Ref. [28] proposed a genaral map between the real energy levels and the effective ones, namely

$$\frac{\mathcal{E}_{\rm eff}}{\mu c^2} - 1 = f\left(\frac{E_{\rm real}^{\rm relative}}{\mu c^2}\right) = \frac{E_{\rm real}^{\rm relative}}{\mu c^2}\left[1 + \alpha_1 \frac{E_{\rm real}^{\rm relative}}{\mu c^2} + \alpha_2 \left(\frac{E_{\rm real}^{\rm relative}}{\mu c^2}\right)^2 + \alpha_3 \left(\frac{E_{\rm real}^{\rm relative}}{\mu c^2}\right)^3 + ...\right]. \tag{4.10}$$

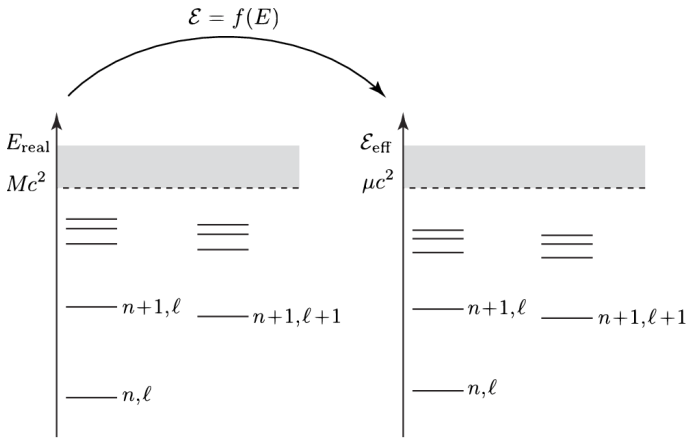

Figure 4.1: *Sketch, due to Damour* [81]*, of the correspondance between the quantized energy levels of the real and effective conservative dynamics. n denotes the principal, "energy" quantum number, while ℓ denotes the relative orbital angular momentum. Though the EOB method is purely classical, it uses the Bohr-Sommerfield quantization conditions of the action variables I_R and J to motivate the identification between n and ℓ in the two dynamics.*

The identification of $\mathcal{E}_{\rm eff}(n,\ell)/\mu c^2$ with $1 + f(E_{\rm real}^{\rm relative}(n,\ell)/\mu c^2)$ yields a system of equations for determining the unknown EOB coefficients $\tilde{a}_n, \tilde{b}_n, \alpha_n$, as well as the coefficients parametrizing a general quartic mass-shell deformation Q (which is introduced at the 3PN order [141]). In Ref. [141] this

system of equations was solved, for example, at 3PN order. Here the three EOB potentials A, D and Q describing the two-body dynamics where given by very simple functions of the EOB "gravitational potental" $u \equiv GM/c^2R$, i.e.

$$\begin{aligned} A_{\rm 3PN}(R) &= 1 - 2u + 2\nu u^3 + a_4 \nu u^4, \\ D_{\rm 3PN}(R) \equiv (A(R)B(R))_{\rm 3PN} &= 1 - 6\nu u^2 + 2(3\nu - 26)\nu u^3, \\ Q_{\rm 3PN}(\boldsymbol{q}, \boldsymbol{p}) &= \frac{1}{c^2} 2(4 - 3\nu)\nu u^2 \frac{p_r^4}{\mu^2}, \end{aligned} \tag{4.11}$$

where

$$a_4 = \frac{94}{3} - \frac{41}{32}\pi^2 \simeq 18.6879027, \tag{4.12}$$

as computed in Ref. [141]. Eqs. (4.11) remarkably condense the information of the (complex) 3PN ADM Hamiltonian [150, 151] into simple equations. This is due not only to the reformulation of the PN-expanded Hamiltonian into an effective dynamics, but also follows from several remarkable cancellations taking place in the ν-dependence of the EOB $A(u;\nu)$ potential.
The map between the *real* center-of-mass energy of the binary system $E_{\rm real}^{\rm relative} = H^{\rm relative} = \mathcal{E}_{\rm relative}^{\rm tot} - Mc^2$ and the effective one $\mathcal{E}_{\rm eff}$ is found to have the compact form

$$\frac{\mathcal{E}_{\rm eff}}{\mu c^2} = 1 + \frac{E_{\rm real}^{\rm relative}}{\mu c^2}\left(1 + \frac{\nu}{2}\frac{E_{\rm real}^{\rm relative}}{\mu c^2}\right) = \frac{s - m_1^2c^4 - m_2^2c^4}{2m_1m_2c^4}, \tag{4.13}$$

where $s = (\mathcal{E}_{\rm real}^{\rm tot})^2 \equiv (Mc^2 + E_{\rm real}^{\rm relative})^2$ is Mandelstam's invariant $s = -(p_1 + p_2)^2$.
It is important to stress that the large value of the a_4 coefficient prevents the PN-expanded, deformed potential $A_{\rm 3PN}$ to be qualitatively similar, as $\nu \to 1/4$, to the Schwarzschild potential $A_{\rm Schwarz}(u) = 1 - 2u$ in exhibiting an "horizon" zero (i.e. the $\nu = 1/4$ case was not smoothly connected with the $\nu = 0$ case) . This disagreement was solved in Ref [141] by Padé-resumming the potential, i.e. by replacing $A_{\rm 3PN}$ with the rational function

$$A_3^1(R) \equiv P_3^1[A_{\rm 3PN}(R)] = \frac{1 + n_1 u}{1 + d_1 u + d_2 u^2 + d_3 u^3}, \tag{4.14}$$

where P_m^n denotes a Padé approximant of order (n, m) and the coefficients n_1 and (d_1, d_2, d_3), as prescribed by the theory of Padé resummation, are

determined by the condition that the first four terms of the Taylor expansion of A_3^1 in powers of u coincide with $A_{3\rm PN}$.
The full analytical EOB potential, since the 4PN ADM Hamiltonian is known [146], is

$$A_{4\rm PN}(u;\nu) = A_{3\rm PN} + \nu(a_5^c(\nu) + a_5^{\log}(\nu)\log u)u^5, \tag{4.15}$$

where the value of the 4PN-level logarithmic coefficient

$$a_5^{\log}(\nu) = \frac{64}{5}, \tag{4.16}$$

was derived in Refs [47, 152, 153] using the results of Ref. [154]. The value of the $a_5^c(\nu) = a_5^{c0} + \nu a_5^{c1}$ piece, where

$$\begin{aligned} a_5^{c0} &= -\frac{4237}{60} + \frac{2275}{512}\pi^2 + \frac{256}{5}\log 2 + \frac{128}{5}\gamma, \\ a_5^{c1} &= -\frac{221}{6} + \frac{41}{32}\pi^2, \end{aligned} \tag{4.17}$$

was derived in Ref. [155]. The existence of this term is related to the tail effects discussed in Sec. 2.4.1; the second, ν-dependent, term of Eq. (4.17) was derived by Bini and Damour from the 4PN infra-red convergent near-zone computation of Ref. [156], while the first $\nu \to 0$ term a_5^{c0}, that is connected with the infrared-divergent effects in the far zone, was not under control in the result of Ref. [156]. Therefore, in Ref. [155] a mix of techniques using the RWZ and GSF approaches were used [62].
At this point, following Ref. [157], the resummed, full analytical point-mass EOB potential is given by

$$A_0(u;\nu) = P_5^1[A_{4\rm PN}(u;\nu)]. \tag{4.18}$$

4.3 EOB waveform and radiation reaction during the inspiral phase

In the previous section we have described how the EOB method encodes the conservative part of the relative orbital dynamics into the dynamics of an "effective" particle. Let us now briefly discuss how to complete the EOB dynamics by defining some *resummed* expressions describing radiation reaction effects, and the corresponding waveform emitted at infinity. We are interested *circularized* binaries, which have lost their initial eccentricity under the

influence of radiation reaction. The relative dynamics is evolved using phase space dimensionless variables $(r, p_r, \varphi, p_\varphi)$, associated to polar coordinates in the equatorial plane $\theta = \pi/2$. We denote by r the relative separation. Its conjugate momentum, p_r is replaced by $p_{r_*} = (A/B)^{1/2}\, p_r$, with respect to the "tortoise" (dimensionless) radial coordinate $r_* = \int dr (A/B)^{-1/2}$, where A and B are the EOB potentials. The real EOB Hamiltonian is obtained by first solving Eq. (4.13) to get $H^{\rm total}_{\rm real} = \sqrt{s}$ in terms of $\mathcal{E}_{\rm eff}$, and then by solving the effective Hamilton-Jacobi equation to get $\mathcal{E}_{\rm eff}$ in terms of the effective phase space coordinates $\boldsymbol{q}_{\rm eff}$ and $\boldsymbol{p}_{\rm eff}$. The result, which represents the heart of the EOB formalism, is given by two nested square roots (it is common to put $c = 1$ here):

$$\hat{H}_{\rm EOB} = \frac{H^{\rm real}_{\rm EOB}}{\mu} = \frac{1}{\nu}\sqrt{1 + 2\nu\big(\hat{H}_{\rm eff} - 1\big)}. \tag{4.19}$$

At this point we are interested in the form of $\hat{H}_{\rm eff}$ for the more general case of a spinning binary system. The EOB Hamiltonian for the coalescence of two spinning BHs was introduced by Damour in Ref. [158]. Here the crucial functions, which determine the strength of the spin-orbit coupling, are the gyro-gravitomagnetic functions G_S and G_{S_*}, that account for the spin-orbit interaction and are ν-dependent deformations, properly resummed, of the corresponding functions entering the Hamiltonian of a spinning particle in Kerr background [159]. The spin-spin coupling was inserted, at next-to-leading order, in a special resummed form involving the centrifugal radius r_c [159] that mimics the same structure present in the Hamiltonian of a test particle on a Kerr spacetime.

The dimensionless phase-space variables are related to the dimensional ones $(R, P_R, \varphi, P_\varphi)$ by

$$r = \frac{R}{GM},\ p_{r_*} = \frac{P_{R_*}}{\mu},\ p_\varphi = \frac{P_\varphi}{\mu GM},\ t = \frac{T}{GM}. \tag{4.20}$$

The spin dependence in the spin-orbit sector of the EOB dynamics is expressed using the following combinations of the individual spins

$$S = S_A + S_B, \tag{4.21}$$

$$S_* = \frac{M_B}{M_A} S_A + \frac{M_A}{M_B} S_B. \tag{4.22}$$

With these definitions in hand, we can split the full effective Hamiltonian as

$$\hat{H}_{\rm eff}^{\rm SO} = \hat{H}_{\rm eff}^{\rm orb} + \hat{H}_{\rm eff}^{\rm S} \tag{4.23}$$

with

$$\hat{H}_{\rm eff}^{\rm orb} = \sqrt{p_{r_*}^2 + A\left(1 + \frac{p_\varphi^2}{r_c^2} + z_3 \frac{p_{r_*}^4}{r_c^2}\right)} \tag{4.24}$$

for what concerns the orbital case, and

$$\hat{H}_{\rm eff}^{\rm SO} = p_\varphi\big(G_S \hat{S} + G_{S_*} \hat{S}_*\big) \tag{4.25}$$

for the spin-orbit coupling. Here, we introduced the dimensionless spin variables $\hat{S} \equiv S/M^2$, $\hat{S}_* \equiv S_*/M^2$, $z_3 = 2\nu(4-3\nu)$ and r_c is the centrifugal radius [159] that incorporates next-to-leading (NLO) spin-spin terms [160]. It formally reads

$$r_c^2 = r^2 + \hat{a}_0^2\left(1 + \frac{2}{r}\right) + \delta\hat{a}^2, \tag{4.26}$$

where $\hat{a}_0$ is the dimensionless effective Kerr parameter

$$\hat{a}_0 \equiv \hat{S} + \hat{S}_* = X_A\chi_A + X_B\chi_B = \tilde{a}_A + \tilde{a}_B \ , \tag{4.27}$$

and the NLO spin-spin contribution is included in the function $\delta\hat{a}^2$ that explicitly reads [161, 159]

$$\begin{aligned}\delta\hat{a}^2 =& \frac{1}{r}\Bigg\{\frac{5}{4}(\tilde{a}_A - \tilde{a}_B)\hat{a}_0 X_{AB} - \left(\frac{5}{4} + \frac{\nu}{2}\right)\hat{a}_0^2 \\ &+ \left(\frac{1}{2} + 2\nu\right)\tilde{a}_A\tilde{a}_B\Bigg\}.\end{aligned} \tag{4.28}$$

Following Refs. [162, 159], the latest EOB model by Nagar, Damour and collaborators, which is presented in detail in Chapter 5, works at next-to-next-to-leading order (NNLO) [163] in the spin-orbit coupling and uses the Damour-Jaranowski-Schäfer gauge [164, 162], so that (G_S, G_{S_*}) are only functions of $(r, p_{r_*}^2)$ and *not* of the angular momentum p_φ. This simplifies

Hamilton's equations[1], which formally read

$$\frac{d\varphi}{dt} = \Omega = \frac{\partial \hat{H}_{\rm EOB}}{\partial p_\varphi}, \tag{4.29a}$$

$$\frac{dr}{dt} = \Big(\frac{A}{B}\Big)^{1/2} \frac{\partial \hat{H}_{\rm EOB}}{\partial p_{r_*}}, \tag{4.29b}$$

$$\frac{dp_\varphi}{dt} = \hat{\mathcal{F}}_\varphi, \tag{4.29c}$$

$$\frac{dp_{r_*}}{dt} = -\left(\frac{A}{B}\right)^{1/2} \frac{\partial \hat{H}_{\rm EOB}}{\partial r}, \tag{4.29d}$$

and explicitly become

$$\frac{d\varphi}{dt} = \Omega = \frac{1}{\nu \hat{H}_{\rm EOB} \hat{H}^{\rm orb}_{\rm eff}} \Big[A \frac{p_\varphi}{r_c^2} + \hat{H}^{\rm orb}_{\rm eff} \big(G_S \hat{S} + G_{S_*} \hat{S}_* \big) \Big], \tag{4.30a}$$

$$\begin{aligned} \frac{dr}{dt} = & \left(\frac{A}{B}\right)^{1/2} \frac{1}{\nu \hat{H}_{\rm EOB} \hat{H}^{\rm orb}_{\rm eff}} \Big[p_{r_*} \Big(1 + 2 z_3 \frac{A}{r_c^2} p_{r_*}^2 \Big) + \\ & + \hat{H}^{\rm orb}_{\rm eff} p_\varphi \Big(\frac{\partial G_S}{\partial p_{r_*}} \hat{S} + \frac{\partial G_{S_*}}{\partial p_{r_*}} \hat{S}_* \Big) \Big], \end{aligned} \tag{4.30b}$$

$$\frac{dp_\varphi}{dt} = \hat{\mathcal{F}}_\varphi, \tag{4.30c}$$

$$\begin{aligned} \frac{dp_{r_*}}{dt} = & -\left(\frac{A}{B}\right)^{1/2} \frac{1}{2\nu \hat{H}_{\rm EOB} \hat{H}^{\rm orb}_{\rm eff}} \Big[A' + p_\varphi^2 \Big(\frac{A}{r_c^2} \Big)' + \\ & + z_3 \, p_{r_*}^4 \Big(\frac{A}{r_c^2} \Big)' + 2 \hat{H}^{\rm orb}_{\rm eff} p_\varphi \Big(G'_S \hat{S} + G'_{S_*} \hat{S}_* \Big) \Big], \end{aligned} \tag{4.30d}$$

where the prime indicates the partial derivative with respect to r, i.e. $(\cdots)' \equiv \partial_r (\cdots)$. Above, $\hat{\mathcal{F}}_\varphi \equiv \mathcal{F}_\varphi / \mu$ denotes the *radiation reaction* force entering the equation of motion of the angular momentum (that is not conserved) and that relies on a special factorization and resummation of the multipolar waveform [8] (see below).

[1]Note that this gauge choice is not made in the tidal EOB model by Buonanno and collaborators, which is named `SEOBNRv4T` and follows Ref. [165].

4.4 EOB waveform and radiation reaction resummation

Several methods have been tried during the development of the EOB formalism to resum the radiation reaction $\hat{\mathcal{F}}_\varphi$ (starting from the high-order PN-expanded results that have been obtained in the literature). In Refs. [166, 167] it was introduced a *parameter-free* resummation procedure, perfected in Ref. [8] and further investigated, introducing new techniques, in Ref. [9] and Chapters 8 and 9.

The results discussed in Ref. [8] are twofold: on the one hand, the work generalized to a multipolar case the quadrupolar factorized resummed waveform of Refs. [166, 167] by using the currently known (at the time) PN-expanded results of Refs. [168, 169, 170, 171] as well as the higher PN terms which where known in the test-mass limit [172, 173]; on the other hand, it introduced a resummation procedure considering a theoretical quantity, denoted by $\rho_{\ell m}(x)$ and named "relativistic waveform amplitude", which enters into the multipolar waveform only through its ℓ-th power, i.e. $(\rho_{\ell m}(x))^\ell$. Here x is the usual invariant PN-ordering dimensionless frequency parameter $x \equiv (GM\Omega/c^3)^{2/3}$. The main novelty introduced by Ref. [8] is to write the (ℓ, m) multipolar waveform emitted by a circularized compact binary as

$$h^{(\epsilon)}_{\ell m} = \frac{GM\nu}{c^2 R} n^{(\epsilon)}_{\ell m} c_{\ell+\epsilon}(\nu) x^{(\ell+\epsilon)/2} Y^{\ell-\epsilon,-m}\left(\frac{\pi}{2}, \Phi\right) \hat{S}^{(\epsilon)}_{\rm eff} T_{\ell m} e^{i\delta_{\ell m}} \rho^\ell_{\ell m}. \tag{4.31}$$

Here ϵ denotes the parity of $\ell+m$ ($\epsilon = \pi(\ell+m)$), i.e. $\epsilon = 0$ for "even-parity" (mass generated) multipoles ($\ell + m =$ even), and $\epsilon = 1$ for "odd-parity" (current generated generated) ones ($\ell+m =$ odd); the $Y^{\ell m}(\theta, \phi)$ are the usual scalar spherical harmonics (as defined by Eqs. (2.7) and (2.8) of Ref. [53] and Eqs. (4) and (5) of Ref. [169]); $n^{(\epsilon)}_{\ell m}$ and $c_{\ell+\epsilon}(\nu)$ are numerical coefficients; $\hat{S}^{(\epsilon)}_{\rm eff}$ is a μ-normalized effective source; $T_{\ell m}$ is a resummed version [166, 167] of an infinite number of "leading logarithms" entering the tail effects discussed in Sec. 2.4.1, which is based on a work of Asada and Futamase [174]; $\delta_{\ell m}$ is a supplementary phase (which corrects the phase effects not included in the tail factor $T_{\ell m}$, which is a complex number). Now we will give the explicit expression of the terms of Eq. (4.31) as prescribed by Ref. [8]. Firstly, the numerical coefficients are given by

$$c_{\ell+\epsilon}(\nu) = X_2^{\ell+\epsilon-1} + (-)^{\ell+\epsilon} X_1^{\ell+\epsilon-1} \tag{4.32}$$

and

$$n_{\ell m}^{(0)} = (\mathrm{i}m)^{\ell} \frac{8\pi}{(2\ell+1)!!} \sqrt{\frac{(\ell+1)(\ell+2)}{\ell(\ell-1)}} \ , \tag{4.33}$$

$$n_{\ell m}^{(1)} = -(\mathrm{i}m)^{\ell} \frac{16\pi \mathrm{i}}{(2\ell+1)!!} \sqrt{\frac{(2\ell+1)(\ell+2)(\ell^2-m^2)}{(2\ell-1)(\ell+1)\ell(\ell-1)}} \ . \tag{4.34}$$

The Newtonian part of Eq. (4.31) is defined as

$$h_{\ell m}^{(N,\epsilon)} \equiv \frac{GM\nu}{c^2 R} n_{\ell m}^{(\epsilon)} c_{\ell+\epsilon}(\nu) x^{(\ell+\epsilon)/2} Y_{\ell-\epsilon,-m}(\frac{\pi}{2}, \Phi) \ , \tag{4.35}$$

so that (4.31) can be rewritten as

$$h_{\ell m}^{(\epsilon)} = h_{\ell m}^{(N,\epsilon)} \hat{S}_{\rm eff}^{(\epsilon)} T_{\ell m} e^{i\delta_{\ell m}} \rho_{\ell m}^{\ell}, \tag{4.36}$$

where $\hat{h}_{\ell m}^{(\epsilon)} = \hat{S}_{\rm eff}^{(\epsilon)} T_{\ell m} e^{i\delta_{\ell m}} \rho_{\ell m}^{\ell}$ is the Post-Newtonian part of the multiplicative expression. The source factor, like what happens in the RWZ formalism, is given by $\hat{S}_{\rm eff}^{(0)}(x) = \hat{H}_{\rm eff}(x)$ for the even parity case $\ell + m =$ even and by $\hat{S}_{\rm eff}^{(1)}(x) = \hat{j}(x) = x^{1/2} j(x)$ for $\ell + m =$ odd, where, for circular orbits, the angular momentum j is given by

$$j(u) = \frac{A'(u)}{(u^2 A(u))'}, \tag{4.37}$$

where the PN relation between u and x can be found by solving

$$M\Omega(u) = \frac{1}{\mu} \frac{H_{\rm EOB}^{\rm real}}{\partial j} = \frac{MA(u) j(u) u^2}{H_{\rm EOB}^{\rm real} \hat{H}_{\rm eff}}, \tag{4.38}$$

where we remind that the relation between x and the orbital frequency Ω is given by $x = (GM\Omega/c^3)^{2/3}$.
The explicit expression of the tail factor $T_{\ell m}$ is

$$T_{\ell m}(x) = \frac{\Gamma(\ell + 1 - 2i\hat{\hat{k}})}{\Gamma(\ell+1)} e^{(\pi + 2\ln(2kr_0)i)\hat{\hat{k}}} \ , \tag{4.39}$$

where

$$k = m\Omega, \tag{4.40}$$

$$\hat{\hat{k}} = mGH_{\rm EOB}\Omega, \tag{4.41}$$

with $r_0 = 2GM/\sqrt{e}$. For extensions of the nonspinning factorized waveform of Ref. [8] to the spinning case, see Refs. [175, 176, 177]. It is important to stress that the factorized EOB waveform (4.31) absorbs high-order PN-expanded waveform computations, both in the test-particle $\nu \to 0$ (such as the "japanese" ones in Refs. [173, 172, 178, 179]) and comparable mass $\nu \neq 0$ cases (such as the "french" ones in Refs. [171, 75, 180, 181]). In order to maximize the amount of PN waveform information to resum by using (4.31), in Refs like [175] or Chapter 8 , the comparable mass PN series (which usually are at low PN orders) are summed to the test-mass ones (which usually can be found at higher orders). This process is named *hybridization*, and can be visualized, for example, as

$$\hat{h}^{\rm PN,hyb}_{\ell m} = 1 + c^{\ell m}_1(\nu \neq 0)x + c^{\ell m}_{3/2}(\nu \neq 0)x^{3/2} + c^{\ell m}_2(\nu \to 0)x + c^{\ell m}_{5/2}(\nu \to 0)x^3 + ... \tag{4.42}$$

It is important to stress that the case from above is purely indicative, since the amount of comparable mass and/or test particle PN information (i.e. the orders that one can find in literature) depend from the state of knowledge of the PN expansion itself.
The perfomance of the resummed factorized EOB waveform can be seen in Fig. (1) of Ref. [143], that we reproduce here in Fig. 4.2. This figure is a comparison between a very accurate `SpEC` waveform (for equal-mass, non-spinning BBH) and a NR-completed EOB waveform(in which the 5PN-level coefficient $a_6(\nu)$ in the EOB $A(u;\nu)$ potential was NR-fitted, as well as some non-quasi-circular corrections to the $(\ell, m) = (2, 2)$ quadrupolar waveform; see Sec. 4.5 below). The agreement between the red (EOB) and black (NR) curves is remarkably good (they are superposed nearly everywhere, except just after the merger).

Finally, Eq. (4.31) leads to the definition of a resummed radiation reaction force $\mathcal{F}_\varphi$ defined as

$$\mathcal{F}_\varphi = -\frac{1}{\Omega} F^{(\ell_{\rm max})}, \tag{4.43}$$

where the circularized GW flux $F^{(\ell_{\rm max})}$ is defined as

$$F^{(\ell_{\rm max})} = \frac{2}{16\pi G} \sum_{\ell=2}^{\ell_{\rm max}} \sum_{m=1}^{\ell} (m\Omega)^2 |R h_{\ell m}|^2. \tag{4.44}$$

For each multipole, the Newtonian prefactor of the flux can be written in

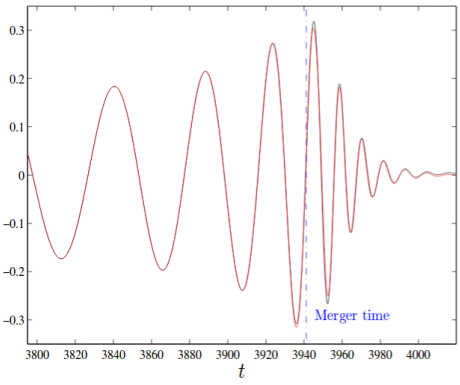

Figure 4.2: *Fig. (1) of Ref.* [143]. *This figure illustrates the agreement between NR (black online) and EOB-based (red online) quadrupolar comparable mass metric waveforms.*

closed form as

$$F_{\ell m}^{(N,\epsilon)} = \frac{1}{8\pi} x^3 m^2 (-)^{\ell+\epsilon} \left| R h_{\ell m}^{(N,\epsilon)} \right|^2 \tag{4.45}$$

4.5 IMR EOB waveforms: merger, ringdown and NR completion

From the very beginning [140], the EOB formalism proposed a specific strategy for desribing the complete waveform emitted during the entire coalescence process, covering inspiral, merger and ringdown. After some time, when numerical simulations where able to describe the late inspiral and the merger of BBHs, this analytical prediction was then confirmed by NR.
Within the EOB theory, the instant of the (effective) merger of the two BHs is the time t_m where the orbital frequency $\Omega(t)$ reaches its maximum. For $t \leq t_m$ the inspiral-plus-plunge (or simply *insplunge*) waveform, $h^{\rm insplunge}(t)$, is built by using the inspiral EOB dynamics illustrated in the previous section. For $t \geq t_m$, the merger-plus-ringdown waveform is described by a superposition of quasi-normal modes (QNM), which are complex frequencies of a final Kerr BH of mass M_f and spin parameter a_f,

$$\left(\frac{Rc^2}{GM}\right) h_{\ell m}^{\rm ringdown}(t) = \sum_N C_N^+ e^{\sigma_N^+ (t-t_m)}, \tag{4.46}$$

where $\sigma_N^+ = \alpha_N + i\omega_N$, and where the label N refers to indices (ℓ, ℓ', m, n), with (ℓ, m) being the Schwarzschild-background multipolarity of the metric waveform $h_{\ell m}$, with $n = 0, 1, 2...$ being the "overtone number" of the considered Kerr-background Quasi-Normal-Mode, and ℓ' the degree of its associated spheroidal harmonics $S_{\ell' m}(a\sigma, \theta)$. The excitation coefficients C_N^+ of the QNM's in Eq. (4.46) are determined by using a simplified representation of the transition between plunge and ringdown obtained by following Ref. [167], i.e. by smoothly matching on a $(2p + 1)$-toothed "comb" $(t_m - p\delta, ..., t_m - \delta, t_m, t_m + \delta, ..., t_m + p\delta)$ centered around the merger and t_m, the inspiral-plus-plunge waveform to the above ringdown waveform.
Finally, one defines a complete, quasi-analytical EOB waveform (covering the full process to inspiral from ringdown) as

$$h_{\ell m}^{\rm EOB} = \theta(t_m - t) h_{\ell m}^{\rm insplunge}(t) + \theta(t - t_m) h_{\ell m}^{\rm ringdown}(t), \tag{4.47}$$

where $\theta(t)$ denotes Heaviside's step function. The final result is a waveform that essentialy depends only on the choice of a resummed EOB A(u) potential, and, less importantly, on the choice of resummation of the main waveform amplitude factor $f_{22} = (\rho_{22})^2$.
The early comparisons between 3PN EOB waveforms and NR-computed waveforms showed a satisfactory agreement between the two, within the relatively large NR uncertainties [182, 183]. Despite that, when NR's uncertainties were reduced, and it started to give highly accurate waveforms, it became clear that the 3PN-level analytical knowledge incorporated in the EOB theory was not accurate enough for providing waveform agreeing with NR ones within the accuracy needed for the upcoming gravitational wave signals' detection and data analysis. This problem was solved by introducing some additional fitting parameter in the unknown analytical terms of EOB potential, i.e. Eq. (4.15) (at the time of the first EOB/NR works the analytical terms up to 4PN of the A-potential were not known). The first EOB/NR attempt was done in Ref. [184], where the (at the time) unknown A-potential parameter $\tilde{a_5}(\nu) = a_5\nu$ entering a Padé resummed 4PN potential $A_4^1(u; a_5, \nu) = P_4^1[A_{\rm 3PN}(u) + \nu a_5 u^5]$ was determined via a fit with NR. This strategy was then pursued in subsequent works. In Ref. [143] it was shown that the introduction of a further 5PN coefficient $\tilde{a_6}(\nu) = a_6\nu$, entering a Padé resummed 5PN-level A-potential like before, gave a closer agreement with accurate NR waveforms. The updated determinations of the EOB A potential are given by Ref. [31] (in the context of the EOB model developed by Buonanno and collaborators) and by Ref. [159] (in the context of

the EOB model developed by Damour itself and collaborators). The dynamical differences of the two existing spin-informed EOB models in their last-updated versions, `SEOBNRv4` [36] and `TEOBResumS` [1] (which is described here in Chapt. 5), are explained for the first time in Ref. [185].
Refs. [166] and [167] have introduced in the EOB/NR context another type of flexibility parameters, which are named next-to-quasi-circular (NQC) corrections. These parameters account for uncalculated modifications of the quasi-circular EOB inspiral waveform, and are linked to the deviations from an adiabatic quasi-circular motion. These parameters are of various types, and subsequent works [186, 187, 143, 188, 189, 176] have explored several ways of introducing them. For each (ℓ, m), these waveform corrections, that we label as $\hat{h}^{\rm NQC}_{\ell m}$, depend on 4 parameters that are NR-informed by requiring *osculation* between, say, the EOB waveform (which will depend from the unknown A-potential coefficients like $\tilde{a}_6$ and obviously by the NQC factors that are defined in the specific problem) and the NR one (as illustrated in Eq. (4.48), one considers the amplitude and frequency, and their first time derivatives) close to merger. Then, for consistency between waveform and flux, the NQC factor also enters the radiation reaction and one iterates the procedure a few times until the procedure converges. We focus here only on the $\ell = m = 2$ waveform mode, as what has been done in Chapt. 5. In this case, the NQC factor reads

$$\hat{h}^{\rm NQC}_{22} = (1 + a_1 n_1 + a_2 n_2) e^{{\rm i}(b_1 n'_1 + b_2 n'_2)}, \tag{4.48}$$

where (a_1, a_2, b_1, b_2) are the free parameters while (n_1, n_2, n'_1, n'_2) are explicit functions of the radial momentum and its time derivative that are listed in Eq. (96) of Ref. [159]. On the EOB time axis, t, the NQC parameters are determined at a time defined as

$$t^{\rm EOB}_{\rm NQC} = t^{\rm peak}_{\Omega_{\rm orb}} - \Delta t_{\rm NQC} \ , \tag{4.49}$$

where $\Omega_{\rm orb}$ was called the *pure orbital frequency* in Ref. [159] (see Eq. (100) there) and is defined, from Eq. (4.30a) of Sec. 4.2, as

$$\Omega_{\rm orb} \equiv \frac{1}{H_{\rm EOB}} \frac{\partial \hat{H}^{\rm eff}_{\rm orb}}{\partial p_\varphi} = \frac{p_\varphi u_c^2 A}{H_{\rm EOB} \hat{H}^{\rm eff}_{\rm orb}}, \tag{4.50}$$

where $u_c = 1/r_c$. In previous work [159, 34, 37], it was found that $\Delta t_{\rm NQC}$ needed to be informed by NR simulations for large, positive spins. In Sec. 5.2.2

of Chapt. 5 it is shown that this was the result of a small, though nonnegligible, implementation mistake, so that here the authors fix $\Delta t_{\rm NQC} = 1$ always, except for some corner cases defined in Ref. [1].
Since EOB waveforms are much faster to compute than NR waveforms (it takes more than a month to compute a reasonably long and accurate NR waveform), LIGO has used several banks of EOB/NR templates (corresponding initially[2] to different versions of spinning EOB/NR models deveoped by the group of Buonanno [31]) for their search and data analysis pipelines. The parameters of these models (See Sec. 1.5.3) are discretized in order to build an adequately dense bank of hundred of thousands of waveforms (~ 250000 for the first detection, GW150914) covering the space of expected physical parameters (up to BH masses to $100 M_\odot$). Since an analytically-defined EOB/NR waveform in the time domain requires a numerical integration of the model's dynamical ODEs, this process may take a minute, some seconds in the best case, but this time, even if very small if compared to the computational times of NR, is still not sufficient for the utilization of Bayesian data analysis (See Sec. 1.5.2). To feed these demands, parametrized, "Reduced Order" Fourier domain versions of the spinning EOB/NR have been obtained [190]. An alternative method to maximize the velocity of EOB/NR templates is the "rush" approximation of the EOB inspiral waveform described in Ref. [191].

[2]Only recently [10] the EOB model of Nagar and collaborators, `TEOBResums` [1], which is described in Chapter. 5, has been added to the LIGO Advanced Library `LAL`

Chapter 5

The TEOBResumS model [1]

5.1 Introduction

The purpose of this work is to introduce `TEOBResumS`, a state-of-the art EOB model, informed by BBH NR simulations, that is fit to describe the dynamics and waveforms from nonprecessing coalescing binaries, both black holes and neutron stars. For BBH binaries, `TEOBResumS` is an improvement of the model of Refs. [37, 34, 159] implementing a refined phenomenological representation of the postmerger waveform (ringdown). The latter is built from an effective fit of many spin-aligned NR waveform data available in the SXS catalog [192] obtained with the `SpEC` code [193, 194, 195, 196, 197, 198, 199, 200, 201, 202, 203] and, notably, also incorporates test-particle results[1]. We show here the performance of the model over the SXS [192] and `BAM` waveform catalogs (the latter consisting of simulations produced using the `BAM` code [204, 205]), and check its robustness also outside NR-covered regions of the parameter space.

For BNSs, we built on our previous efforts [206] (see also [207, 208]) and merged together into a single EOB code, tidal and spin effects, so as to produce a complete waveform model of spinning BNSs. We show that the EOB waveform is accurate up to BNS merger by comparing with state-of-the art, high end, NR simulations. The tidal-and-spin model uses most of the existing analytical knowledge. In particular, we incorporate in the EOB model equation-of-state (EOS) dependent self-spin effects at leading-order (also known as spin-induced quadrupole moment or monopole-

[1] In doing so, we corrected a minor coding error in the numerical implementation that had affected the $\ell = 5$, $m =$ odd flux modes from Ref. [159].

quadrupole couplings [134]). `TEOBResumS` has been the first EOB model to have these effects. As such, it was used for validating the phenomenological waveform model, `PhenomPv2_NRTidal`, that incorporates similar self-spin effects [209] and that was recently used for a detailed study of the parameters of GW170817 [210, 211]. However, while `TEOBResumS` was under internal LVC review, leading-order self-spin effects were also included in `SEOBNRv4T`, though in a different fashion for what concerns the Hamiltonian [36, 212, 213, 214]. A targeted comparison between the two models for BNS configurations is described in Sec. 5.6.

This chapter, in which we reproduce some sections of Ref. [1] for the aims of this thesis, is organized as follows: in Sec. 5.2 we compare the performance of the BBH EOB model against the SXS [192] and `BAM` NR data, test its robustness over a large portion of the parameter space; in Sec. 5.3 we discuss the BNS case, focusing on our analytical strategy to incorporate in a consistent, and resummed, way both tidal and spin effects, including the self-spin ones. In this respect, Sec. 5.4 compares the EOB description with the corresponding nonresummed PN-based expressions. Section 5.6 collects selected comparisons (photon potential and, notably, faithfulness) between `TEOBResumS`, `SEOBNRv4` and `SEOBNRv4T`. To probe our model we also present, in Sec. 5.5, a case study done on the GW150914 event [38]. Since Ref. [1] is complemented by several technical appendices that are beyond the purposes of this thesis, we neglect them and we adress the interested reader to the original paper. Among these, the case of mixed black-hole and neutron-star binaries is discussed in Sec. 5.8.

5.2 Binary Black Holes

5.2.1 Main features

The details about the structure of the `TEOBResumS` model can be found in Ref. [159, 34, 37]. We refer to Sec. 4.2 of Chapt. 4 for the visualization of the dynamical equations of the EOB formalism. Following the choice made in previous work [159], we set $\hat{\mathcal{F}}_{r_*} = 0$ explicitly, so that the radial flux does not appear in the r.h.s. of Eq. (4.29d). Note that the effect of the absorption due to the horizon is explicitly included in the model at leading order (see Eqs. (97)-(98) of [159]). The relative dynamics is initiated using post-post-adiabatic (2PA) initial data [166, 215].

The multipolar waveform strain is computed out of the dynamics with the following convention

$$h_+ - \mathrm{i}h_\times = \frac{1}{\mathcal{R}} \sum_{\ell=2}^{\ell_{\max}} \sum_{\ell=-m}^{\ell+m} h_{\ell m} \, {}_{-2}Y_{\ell m}(\theta, \phi), \tag{5.1}$$

where ${}_{-2}Y_{\ell m}(\theta, \phi)$ are the $s = -2$ spin-weighted spherical harmonics. In the following text, for consistency with previous work, we shall often use the Regge-Wheeler-Zerilli [216] normalized waveform $\Psi_{\ell m} = h_{\ell m}/\sqrt{(\ell+2)(\ell+1)\ell(\ell-1)}$. The strain multipoles $h_{\ell m}$ are written in special factorized and resummed form [8, 175, 159]. Following the notation of [159], they read

$$h_{\ell m} = h_{\ell m}^{(N,\epsilon)} \hat{S}_{\rm eff}^{(\epsilon)} \hat{h}_{\ell m}^{\rm tail} f_{\ell m} \hat{h}_{\ell m}^{\rm NQC}, \tag{5.2}$$

where ϵ denotes the parity of $\ell+m$, $h_{\ell m}^{(N,\epsilon)}$ is the Newtonian (or leading-order) contribution, $\hat{S}_{\rm eff}^{(\epsilon)}$ the effective source, $\hat{h}_{\ell m}^{\rm tail}$ the tail factor, $f_{\ell m}$ the residual amplitude correction and $\hat{h}_{\ell m}^{\rm NQC}$ the next-to-quasi-circular (NQC) correction factor. We recall that $\hat{h}_{\ell m}^{\rm NQC}$ accounts for corrections to the circularized EOB waveform that explicitly depend on the radial momentum and that are relevant during the plunge up to merger [167], see Eq. (4.48) of Sec. 4.5.

On top of the NQC corrections to the waveform, `TEOBResumS` is also NR-informed in the nonspinning and spinning sector of the dynamics. Section IIIA of Ref. [37] gives a comprehensive summary of the *analytical flexibility* of the model, while Sec. IIIB and IIIC of [37] illustrate how the NR information is injected in the model. The nonspinning sector of `TEOBResumS` fully coincides with Sec. IIIB of Ref. [37]: the orbital interaction potential A, taken at formal 5PN order, is Padé resummed with a $(1,5)$ Padé approximant and it incorporates an "effective" 5PN parameter $a_6^c(\nu) = 3097.3\nu^2 - 1330.6\nu + 81.38$ that was determined by EOB/NR comparisons with a set of nonspinning SXS simulations. More precisely this specific functional form dates back to Ref. [34], it was based on the SXS NR simulations publicly available at the time (see Table I of [34]) and never changed after. We address the reader to Sec. III of Ref. [34] for details and in particular to Eq. (1) there for the explicit analytical form of the orbital interaction potential.

The spinning sector of the model is flexed by a single NNNLO effective spin-orbit parameter c_3 that enters both G_S and G_{S_*} (see e.g. Eqs. (19)-(20) of [37]). Finally, the factorized waveform is then complemented by a description of the post-merger and ringdown phase [217, 218]. The model of [37],

though informed by a rather sparse number of NR simulations, proved to be rather accurate, reliable, and robust against a set of 149 public NR simulations by the SXS collaboration [192] (see specifically Tables V-IX therein). It also showed, however, its drawbacks, mostly restricted to the merger and post-merger part that was obtained through fit of only a sparse number (≈ 40) of NR simulations, most of them clustered around the equal-mass, equal-spin case. Here these problems are overcome by making crucial use of *all* the NR information available in order to devise better fits of the NR data to describe the post-merger-ringdown part of the waveform. This will be discussed in the forthcoming section.

5.2.2 Improvement over previous work

The BBH sector of the `TEOBResumS` model improves the version of the one discussed in Ref. [159, 34, 37] on the following aspects: (i) improved (and corrected) $\ell = 5$ flux; (ii) related new determination of the NNNLO spin-orbit parameter c_3; (iii) more robust description of the postmerger and ringdown waveform; (iv) more robust and accurate fits of the NR point used to determine the NQC waveform corrections.

Flux multipoles: the $\ell = 5$, $m = odd$ modes

We start the technical discussion of the BBH sector of `TEOBResumS` by pointing out a coding error in its `Matlab` numerical implementation that has affected (though marginally) the spin-dependent sector of the model as soon as it was conceived back in 2013 [159], with effects on Refs. [159, 34, 37, 209]. We found that there was a missing overall factor $X_{AB} = \sqrt{1-4\nu}$ in the $\ell = 5$, $m =$ odd multipolar waveform amplitudes that, once squared, contributed to the radiation reaction force $\hat{\mathcal{F}}_\varphi$. Such small, though non-negligible, difference in the radiation reaction resulted in an inconsistency between the nonspinning and spinning sector of the model, that are implemented through a different set of routines. The effect of this error was more important for spins of large amplitude, both aligned with the angular momentum. Once this error was corrected, we had to redetermine, through comparison with NR waveform data, the function $c_3(\tilde{a}_A, \tilde{a}_B, \nu)$, that describes the NNNLO spin-orbit effective correction [159, 34, 37]. In doing so, we found that the correct implementation of the $\ell = 5$ modes brings a simplification to the model: there is *no need* of ad-hoc NR-calibrating the additional parameter

$\Delta t_{\rm NQC}$ when $\chi_A = \chi_B > 0.85$, as it was necessary to do in Ref. [34] [see also Sec. IIIC of Ref. [37], Eqs. (24)-(25) therein]. As in the nonspinning case, we can choose $\Delta t_{\rm NQC} = 1$ for all configurations, without any special tweaks needed for the high-spin case.

New determination of c_3

It was possible to inform a new function $c_3(\tilde{a}_A, \tilde{a}_B, \nu)$ with the limited set of 27 SXS NR simulations (see Table 5.1), most of which are the same used in Ref. [37]. The determination of $c_3(\tilde{a}_A, \tilde{a}_B, \nu)$ is based on two steps. First, for each of the 27 SXS configurations of Table 5.1 one determines, tuning it by hand, a value of c_3 such that the dephasing between EOB and NR waveform at merger is within the NR uncertainty. Such first-guess values of c_3 are then globally fitted with a suitable functional form that, as in [37], is chosen to represent a quasi-linear behavior in the spins. More precisely, the new representation of c_3 is given by

$$\begin{aligned} c_3(\tilde{a}_A, \tilde{a}_B, \nu) = p_0 &\frac{1 + n_1 \hat{a}_0 + n_2 \hat{a}_0^2}{1 + d_1 \hat{a}_0} \\ &+ \left(p_1 \nu + p_2 \nu^2 + p_3 \nu^3\right) \hat{a}_0 \sqrt{1 - 4\nu} \\ &+ p_4 \left(\tilde{a}_A - \tilde{a}_B\right) \nu^2, \end{aligned} \tag{5.3}$$

where

$$p_0 = 43.371638, \tag{5.4a}$$
$$n_1 = -1.174839, \tag{5.4b}$$
$$n_2 = 0.354064, \tag{5.4c}$$
$$d_1 = -0.151961, \tag{5.4d}$$
$$p_1 = 929.579, \tag{5.4e}$$
$$p_2 = -9178.87, \tag{5.4f}$$
$$p_3 = 23632.3, \tag{5.4g}$$
$$p_4 = -104.891. \tag{5.4h}$$

Table 5.1 lists, for the configuration chosen, both the first-guess value of c_3, that yields an EOB/NR phase agreement within the NR error at merger, as well as the value obtained from the fit (5.3). The last column lists the relative error $(c_3^{\rm first\ guess} - c_3^{\rm fit})/c_3^{\rm fit}$. As it will be shown below, despite the fact

that for some configurations the first-guess value and the corresponding one obtained from the fit are significantly different, the EOB/NR unfaithfulness (see below) is still considerably smaller than the usually accepted limit of 1%. We note however that the global fit can be further improved, if needed, by incorporating more NR datasets and/or changing the functional form of Eq. (5.3). We shall briefly discuss an example at the end of next section.

Post-merger and ringdown

Let us come now to discussing the improved representation of the post-merger and ringdown, that in [37] relied on the, rather simplified, fits presented in [218]. For completeness, we also recall that the NR-based phenomenological description of the waveform is attached at the inspiral part, NQC-modified, at $t^{\rm EOB}_{\rm NQC}$ given by Eq. (4.49) above. The new fits for the $\ell = m = 2$ merger and postmerger waveform are detailed in Appendix F of Ref. [1]. Let us briefly summarize their new features. First, the major novelty behind the fitting procedure is that it is done by exploiting the rather simple behavior that the merger[2] waveform strain amplitude and frequency $(A^{\rm mrg}_{22}, \omega^{\rm mrg}_{22})$ show when plotted versus the spin-variable $\hat{S} = (S_A + S_B)/M^2$. This allows one to capture the full dependence on mass ratio and spins by means of rather simple two-dimensional fits versus $(\nu, \hat{S})$. In addition, we use a larger set of NR waveforms than in previous work: more precisely, we use 135 spin-aligned NR waveforms[3] from the publicly available SXS catalog [192] obtained with the `SpEC` code [193, 194, 195, 196, 197, 198, 199, 200, 201, 202, 203] whose parameters are summarized in the Tables V-IX of Ref. [37]. These waveforms replace and update the set of 39 waveforms used in [218]. In particular, the SXS waveforms used are corrected for the effect of the spurious motion of the center of mass, as pointed out in Ref. [219] as well as in Sec. V [37]. These SXS waveform data are complemented by 5 `BAM` waveforms with mass ratio $q = 18$, where the heavier BH is spinning with $\chi_A = (-0.8, -0.4, 0, +0.4, +0.8)$ and by test-mass waveform[4] data [61] obtained from new simulations with an improved version of the test-particle radiation reaction, now resummed accord-

[2] As in previous work, the merger time is defined as the peak of the waveform strain amplitude $A_{22} \equiv |h_{22}|$.

[3] Out of the 149 waveforms listed in Ref. [37], 14 are older simulations whose parameters are covered by simulations more recently released. These 14 waveforms were not used in the determination of the new merger and postmerger parameters.

[4] Note that the phenomenological representation of the fit with the template proposed in Refs. [217, 218] is not accurate for high-spin and larger-mass ratio limit waveforms,

ing to Refs. [9, 4]. The model is completed by the fit of the spin and mass of the remnant BH of Ref. [220], and by accurate fits of the quasi-normal-mode (QNM) frequency and inverse-damping times versus the dimensionless spin of the remnant BH. These are fits of the corresponding data extracted from the publicly available tables of Berti *et al.* [221, 222]. This is an improvement with respect to previous work, where the final QNM frequencies were obtained simply by interpolation the publicly available data of Ref. [221, 222]. We address the reader to Appendix F of Ref. [1] for precise technical details.

The NR waveform point used to obtain NQC parameters

Using all available information listed above, it was also possible to obtain more accurate fits of the NR waveform point $\left(A_{22}^{\rm NQC}, \dot{A}_{22}^{\rm NQC}, \omega_{22}^{\rm NQC}, \dot{\omega}_{22}^{\rm NQC}\right)$, used to compute the NQC parameters (a_1, a_2, b_1, b_2) entering the $\ell = m = 2$ NQC waveform correction factor discussed above. These fits replace those of Sec. IVB of [37] for $q \geq 4$ and are listed together with the details of the new improved postmerger fits in Appendix F of Ref. [1].

5.2.3 Comparison with NR data

Let us evaluate the global accuracy of the BBH model that incorporates the new fit for c_3, Eq. (5.3), as well as the new fits for the NQC point and postmerger part. We do this by computing the usual EOB/NR unfaithfulness $\bar{F}$ defined as

$$\bar{F}(M) \equiv 1 - F = 1 - \max_{t_0,\phi_0} \frac{\langle h_{22}^{\rm EOB}, h_{22}^{\rm NR} \rangle}{||h_{22}^{\rm EOB}||\,||h_{22}^{\rm NR}||}, \tag{5.5}$$

where (t_0, ϕ_0) are the arbitrary initial time and phase and $||h|| \equiv \sqrt{\langle h, h \rangle}$. The inner product between two waveforms is defined as

$$\langle h_1, h_2 \rangle \equiv 4\Re \int_{f_{\rm min}^{\rm NR}(M)}^{\infty} \tilde{h}_1(f) \tilde{h}_2^*(f)/S_n(f)\, df, \tag{5.6}$$

where $\tilde{h}(f)$ denotes the Fourier transform of $h(t)$, $S_n(f)$ is the zero-detuned, high-power noise spectral density of Advanced LIGO [223] and $f_{\rm min}^{\rm NR}(M) =$

and needs to be modified, including more parameters, to be more flexible. That is the reason why in the current representation test-mass data are only used to improve the representation of *merger* quantities $(A_{22}^{\rm mrg}, \omega_{22}^{\rm mrg})$, and not of the postmerger ones.

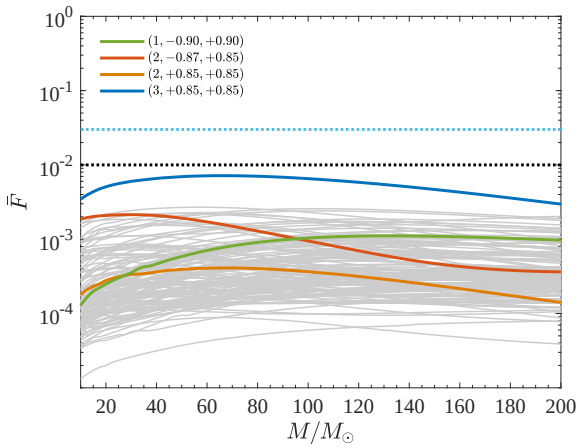

Figure 5.1: Unfaithfulness, Eq. (5.5), comparison between `TEOBResumS` and SXS waveforms, using the design-sensitivity noise curve of Advanced LIGO. This figure is the updated version of Fig. 7 of Ref. [37]. Thanks to the joint action of (i) the correct implementation of the $\ell = 5$, $m =$ odd modes of the radiation reaction and the related new determination of the NNNLO effective spin orbit parameter c_3 and (ii) the improved treatment of the postmerger part of the signal as well as of the improved NQC determination, there are no outliers above the 1% limit. Remarkably, it is found $\max(\bar{F}) \lesssim 2.5 \times 10^{-3}$ all over the SXS catalog except for a single outlier, $(q, \chi_A, \chi_B) = (3, +0.85, +0.85)$, with $\max(\bar{F}) \simeq 7.1 \times 10^{-3}$.

$\hat{f}^{\rm NR}_{\rm min}/M$ is the *starting frequency of the NR waveform* (after the junk radiation initial transient). Both EOB and NR waveforms are tapered in the time domain so as to reduce high-frequency oscillations in the corresponding Fourier transforms. We display $\bar{F}(M)$, for $10M_\odot \leq M \leq 200M_\odot$, in Fig. 5.1 for the 171 SXS waveform data and in Fig. 5.3 for the 18 `BAM` datasets. Let us discuss first the `TEOBResumS`/SXS comparison, Fig. 5.1. To better appreciate the improvement brought by the correct implementation of the $\ell = 5$, $m =$odd flux modes and the post-merger fits, this figure should be compared with Fig. 7 of [37]. Figure 5.1 illustrates that $\max(\bar{F}) \lesssim 2.7 \times 10^{-3}$ all over the waveform database except for a single outlier, $(3, +0.85, +0.85)$, where $\max(\bar{F}) = 7.1 \times 10^{-3}$. Note however that the performance is much better than the minimal accepted limit of 3% (light-blue, dotted, horizontal line) or the more stringent 1% limit (black, dotted, horizontal line) that is taken as a goal by `SEOBNRv4` (see Fig. 2 in [36]); in fact, it is the *low-*

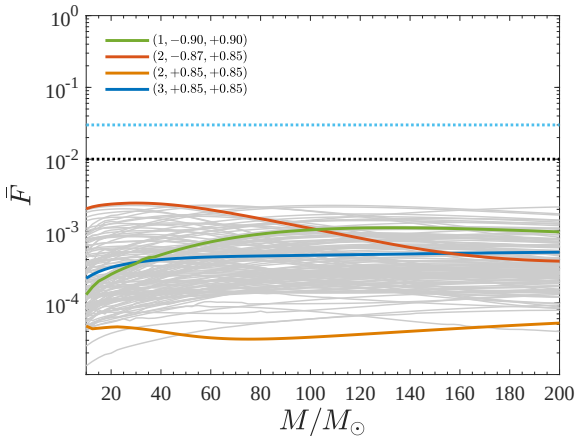

Figure 5.2: Same as Fig. 5.1, but including an additional term proportional to $\nu\hat{a}_0^2\sqrt{1-4\nu}$ in the functional form Eq. (5.3) using to fit the $c_3^{\text{first guess}}$ values of Table 5.1. One has $\max(\bar{F}) < 2.5\times10^{-3}$ all over the SXS catalog of public NR waveforms.

est ever value of $\max\left[\max(\bar{F})\right]$ obtained from SXS/EOB comparisons. We note that the reason why $\bar{F} \simeq 7.1\times10^{-3}$ for $(3,+0.85,+0.85)$ is entirely due to the fact that the global representation of c_3 yielded by Eq. (5.3) is not that accurate in that corner of the parameter space, and yields the value 14.38 instead of 16.5 (see line #23 of Table 5.1). Interestingly, we have verified that, by using the value 16.5, the value of $\bar{F}(M)$ significantly drops, being smaller than 10^{-4} at $M = 10M_\odot$ and just growing up to 2×10^{-4} at $M = 200M_\odot$. This illustrates that our analytical representation of c_3 is actually very conservative. It would be easy, by either incorporating more datasets in the global fit and/or improving the functional form of (5.3) to reduce the discrepancy between the first-guess and fitted value of c_3. As a simple attempt to do so, we slightly changed the functional form of $c_3(\tilde{a}_A,\tilde{a}_B,\nu)$ so as to introduce nonlinear spin-dependence away from the equal-mass, equal-spin case. For example, to introduce such nonlinearities in spin in a simple way, one easily checks that the addition to Eq. (5.3) of only one term *quadratic* in $\hat{a}_0$ of the form $p_5\nu\hat{a}_0^2\sqrt{1-4\nu}$, where p_5 is a further fitting coefficient, is by itself sufficient to obtain $c_3 = 17.28$ for $(3,+0.85,+0.85)$, with a corresponding value of $\max(\bar{F}) = 5\times10^{-4}$ reached at $M = 200M_\odot$. Once this term is included, the new fitting coefficients that parametrize the sector of c_3 away from the equal-mass, equal-spin limit read

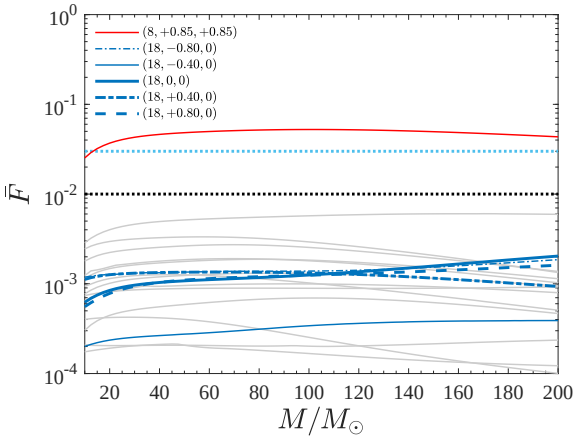

Figure 5.3: Unfaithfulness comparison between `TEOBResumS` and the set of `BAM` waveforms mostly presented in Refs. [224, 30, 225] and listed in Table 5.2 for completeness. The case $(8, +0.85, +0.85)$, where a new, high-resolution, `BAM` waveform was produced explicitly for this work, is meaningfully above the 3% limit and calls for an improvement of the model in that specific corner of the parameter space.

$(p_1, p_2, p_3, p_4, p_5) = (917.59, -8754.35, 20591.0, -78.95, 83.40)$. For completeness, we evaluated again the EOB/NR $\bar{F}$ with this new fit. The result is displayed in Fig. 5.2. It is remarkable to find that $\max(\bar{F}) < 2.5 \times 10^{-3}$ all over the SXS catalog. It is also interesting to note that the two curves for $(3, +0.85, +0.85)$ and $(2, +0.85, +0.85)$ are essentially flat, which illustrates that all the difference with the previous case was coming from the slightly inaccurate representation of the spin-orbit coupling functions, now corrected by the improved representation of c_3.

Let us turn now to discussing `TEOBResumS`/`BAM` comparisons, Fig. 5.3. These waveforms cover a region of the parameter space, for large mass ratios, that is not covered by SXS data (see Table 5.2). Hence, we use them here as a probe of the phasing provided by `TEOBResumS`. In general, `BAM` waveforms in the current database are shorter than the SXS ones and have larger uncertainties. This is also the case for the $(8, +0.85, +0.85)$ configuration, that yields the largest NR/EOB disagreement, $\max(\bar{F}) \simeq 5.2\%$, which is above the usually acceptable level of 3%. However, though this waveform is much longer (≈ 18 orbits) than the one previously used in [37], it was also obtained at higher resolution, so that its error assessment is similar to those

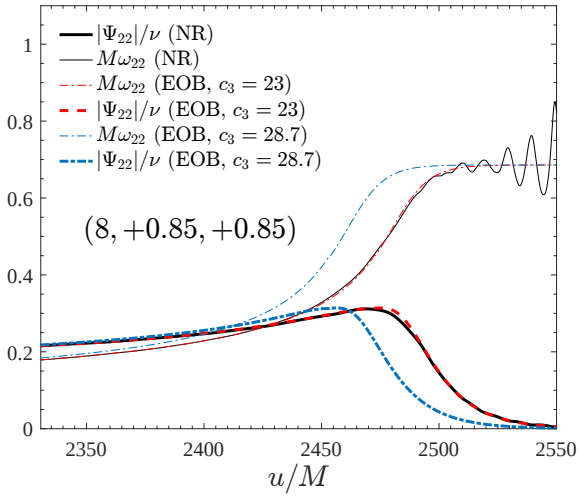

Figure 5.4: Effect of changing the value of the effective NNNLO spin-orbit parameter c_3 for the $(8, +0.85, +0.85)$ configuration. Time-domain evolution of frequency and amplitude. The 5.2% value of $\bar{F}$ in Fig. 5.3 comes entirely from the value $c_3 = 28.7$ obtained by extrapolating from the SXS-based fit of Eq. (5.3). A smaller value of the parameter, $c_3 = 23$, succeeds in getting a good EOB/NR agreement ($\bar{F} \simeq 1.3 \times 10^{-3}$) . Despite this, both the NQC and post-merger sectors are correctly represented by the model because of the robust NR-informed fits.

used for the `IMRPhenomD` waveform model [30, 225], with a mismatch error of less than 10^{-3}. The EOB/NR difference seen in Fig. 5.3, originates then in the EOB model, notably during the inspiral, and not in the NR data. To explicitly see that the origin of such EOB/NR discrepancy comes from the EOB-driven inspiral dynamics and not from the ringdown part[5], we display in Fig. 5.4 the waveform frequency and amplitude versus time. The figure compares three datasets: (i) the `BAM` data (black); (ii) the `TEOBResumS` waveform with the value of $c_3 \approx 28.7$ obtained from Eq. (5.3) (blue, dash-dotted, lines) and $c_3 = 23$. Note that while the $c_3 = 28.7$ waveform was obtained by iterating on NQCs parameter (i.e., the NQC correction is also added to the flux for consistency with the waveform and then an iterative procedure is set until the values of (a_1, a_2) are seen to converge [37]), the $c_3 = 23$ one was not

[5]This is the contrary of what was stated in [37]. The reason for this is that the `BAM` waveform used there was shorter than the one we are using now.

(see below). The waveforms are aligned in the $(0.2, 0.35)$ frequency interval region. The figure clearly illustrates that the simple action of lowering c_3 (i.e. making the spin-orbit interaction less attractive, see discussion in [37]) is effective in getting the `TEOBResumS` waveform closer to the `BAM` one: the waveform becomes longer and the frequency behaviors get qualitatively more similar up to merger. Note also that the postmerger part is perfectly consistent with the NR one. This is a remarkable indication of the robustness of our post-merger fits since the $(8, +0.85, +0.85)$ `BAM` dataset was not used in their construction. We mentioned above that the curves corresponding to $c_3 = 23$ were obtained without iterating on the amplitude NQC parameters (a_1, a_2). The reason for this is that the value of the NQC parameters are rather large because of the lack of robustness of the resummed waveform amplitude in this corner of the parameter space and they effectively tend to compensate the action of c_3, that should be lowered further. The consequence of this is that, when c_3 is chosen to be below 20, (a_1, a_2) become so large that the iteration procedure is unable to converge. The use of the improved factorized and resummed waveform amplitudes of Refs. [9, 4], that display a more robust and self-consistent behavior towards merger for high, positive spins is expected to solve this problem.

To summarize, the message of the analysis illustrated in Fig. 5.4 goes as follows: (i) on the positive side, the figure illustrates that, even if we had not included $(8, +0.85, +0.85)$ data to obtaining the postmerger fit parameters, the resulting model is rather accurate also for this choice of parameters; (ii) on the negative side, it also tells us that the dataset $(8, +0.85, +0.85)$ brings us new, genuine, NR information that is currently not incorporated in the model, but it should be in order to properly capture the correct phasing behavior in this corner of the parameter space[6]. In principle, improving the model would be rather straightforward, as it would just amount to adding a new value of c_3 in Table 5.1, corresponding to an acceptable `BAM`/EOB phasing up to merger, and redoing the global fit. However, because of the aforementioned problems in obtaining a consistent determination of the NQC parameters, we shall postpone this to a forthcoming study that will (partly) use the factorized and resummed waveform amplitudes of Ref. [4].

Finally, Fig. 5.5 illustrates another difference between `TEOBResumS` and `BAM` waveforms. The figure compares the analytical and numerical frequen-

[6]We note in passing that `SEOBNRv4` also used `BAM` datasets with $(8, +0.85, +0.85)$, though different from the one we used here, for its calibration.

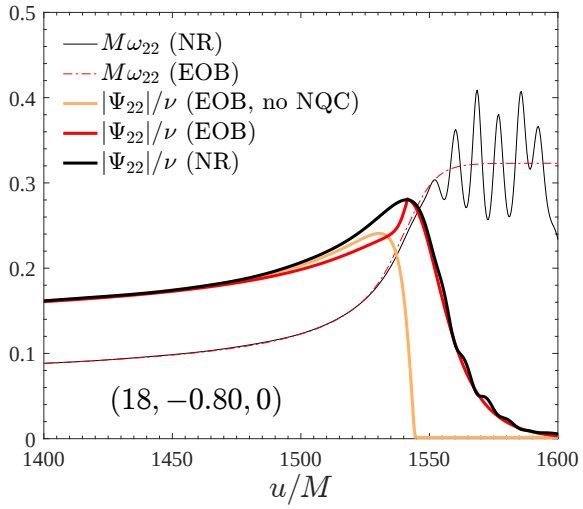

Figure 5.5: Frequency and amplitude comparison between `TEOBResumS` and `BAM` for $(18, -0.80, 0)$. The full waveform amplitude develops a slightly unphysical feature due to the action of the NQC parameters. The frequency (as well as $\bar{F}$) is unaffected by this.

cies and amplitudes for $(18, -0.80, 0)$. The waveforms are aligned around merger. Although the frequencies are perfectly consistent, the analytical amplitude (red line) shows a qualitatively incorrect behavior before merger. Although such feature in the amplitude might be interpreted as due to an incorrect determination of the NQC corrections, it is actually of dynamical origin. More precisely, it comes from the orbital frequency Ω crossing zero and then becoming negative due to a somewhat large values of the gyro-gravitomagnetic functions (G_S, G_{S_*}) for small values of the EOB radial separations. Since the spins are negative, the spin-orbit part of the orbital frequency progressively compensates the orbital one, until dominating over it so that $\Omega < 0$ around merger time. We have tracked back the origin of this problem to the fact that, following Ref. [159], the argument of the functions $(\hat{G}_S, \hat{G}_{S_*})$ (see Eqs. (36)-(37) of [159]) were chosen, by construction, to be $1/r_c$, instead of of $1/r$, so as to effectively incorporate higher-order spin-orbit corrections. Although it is not our intention to discuss this subject in more detail here, we have actually verified that going back to the standard $1/r$ dependence of these functions is sufficiently to reduce and/or cure completely (as it is the case for the configuration $(11, -0.95, -0.50)$ discussed below)

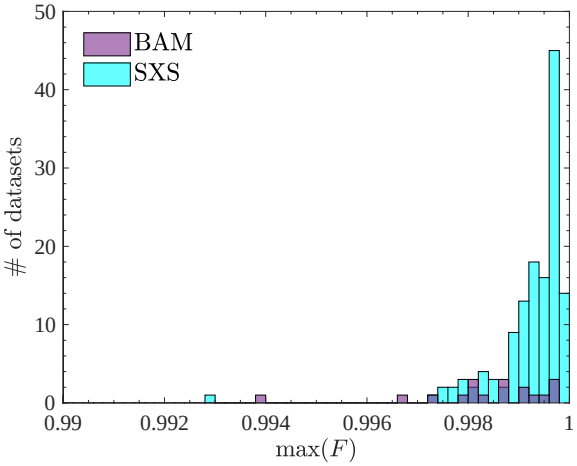

Figure 5.6: Global picture of the maximum value of the EOB/NR faithfulness F, Eq. (5.5) over SXS and `BAM` NR data. The only outlier above 3%, (8,+0.85,+0.85), is omitted from the figure.

this somewhat unphysical feature[7]. Although the behavior of the modulus in Fig. 5.5 has not practical consequences, it is important to mention that similar features may occur systematically for binaries with large q and large spins, anti-aligned with the orbital angular momentum. This statement will be recalled below when discussing the performance of the model outside the NR-covered region of the parameter space. Finally, a global representation of the results of Figs. 5.1-5.3 is given in Fig. 5.6, that displays the maximum value of the EOB/NR *faithfulness* F, reached for each dataset varying the total mass M, all over the SXS and `BAM` waveform catalogs, only excluding the $(8, +0.85, +0.85)$ outlier for readability.

[7]Please note, however, that, likewise the case of a test-particle plunging over a highly spinning black hole whose spin is anti-aligned with the orbital angular momentum [61, 226], by continuity there might exist BBH configurations where the orbital frequency is actually due to change its sign while approaching merger. This is however not the case of the $(18, -0.80, 0)$ binary under consideration, since the positive-frequency QNMs branch is still more excited than the negative frequency one. The contribution of this latter is not, however, negligible, as illustrated by the large amplitude oscillation in the NR frequency displayed in Fig. 5.5.

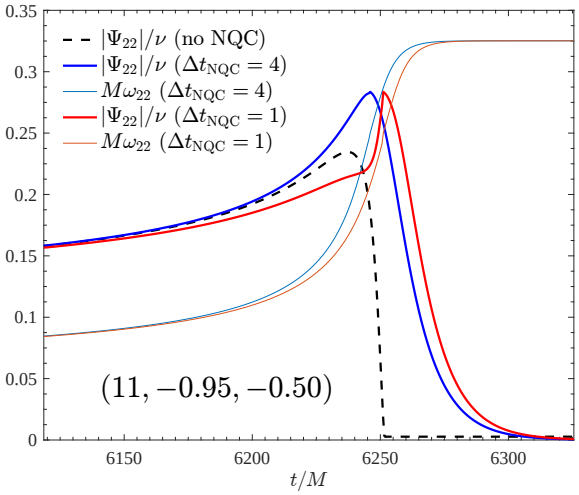

Figure 5.7: Comparing the effect of using $\Delta t_{\rm NQC}=1$ and $\Delta t_{\rm NQC}=4$ for $(q,\chi_1,\chi_2)=(11,-0.95,-0.50)$. The use of $\Delta t_{\rm NQC}=4$ makes the behavior of the waveform amplitude at merger consistent with the NR-fitted postmerger behavior.

5.2.4 Waveform robustness outside the NR-covered region of parameter space

The model was tested to be robust in the most demanding corners of the parameter space, notably for large mass ratios (though we limit ourselves to $q\leq 20$) and large values of the spin magnitudes. In particular, no obvious problem was found for large mass ratios and when the spins are positive. The absence of ill-defined behaviors in the waveform is mostly due to the use of robust fits across the whole parameter space and to the fact that the NQC corrections are able to effectively reduce the residual inaccuracies in the EOB waveform. However, this comes at the price of large NQC parameters (far from being order unity, as noted above for the specific case of $(8,+0.85,+0.85)$) since they have to strongly correct a waveform in a regime where the radial momenta are small. Large NQC parameters prevent the necessary iterative procedure of recomputing the flux from converging. We thus remove the NQC corrections to the flux, although in this way it becomes mildly inconsistent with the waveform.

As anticipated above, when the mass ratio is moderately large ($q\geq 8$) and spins are equally large but anti-aligned with the angular momentum,

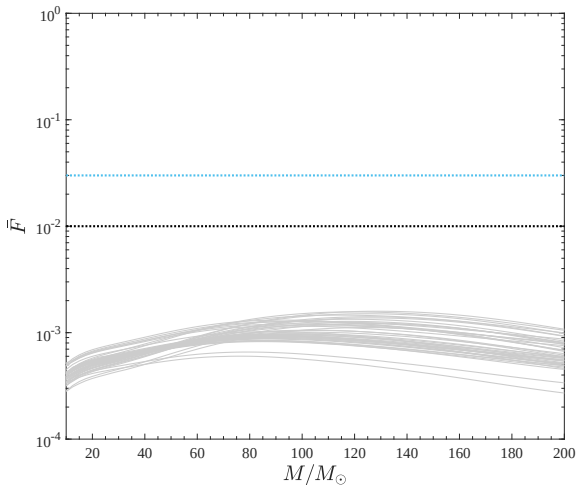

Figure 5.8: Calculation of $\bar{F}$ between EOB waveforms with $\Delta t_{\rm NQC} = 1$ and $\Delta t_{\rm NQC} = 4$ at the boundary of the region of the parameter space defined by Eqs. (5.7)-(5.8). The consistency between the two types of waveforms is excellent.

the waveform amplitude may develop artifacts prompted by the underlying orbital frequency being small and eventually crossing zero (and thus strongly affecting the NQC amplitude correction factor) as we found for the $(8, -0.80, 0)$ configuration. For example, Fig. 5.7 illustrate the type of qualitatively incorrect features that the waveform can develop towards merger due to the incorrect action of the NQC factor. In the figure we show, with a red and an orange line, the amplitude and frequency for $(11, -0.95, -0.50)$ as generated by the model described above. The black dashed line is the *bare* EOB-waveform amplitude, without the NQC factor. We have explicitly verified that Ω crosses zero also in this case. Although, as we mentioned above, the theoretically correct way of solving this problem is to modify the spin-orbit sector of `TEOBResumS`, one finds that, if the standard value $\Delta t_{\rm NQC} = 1$ is increased to $\Delta t_{\rm NQC} = 4$, the weird behavior disappears and the inspiral EOB waveform amplitude can be connected smoothly to the postmerger part obtained via the global fit of the NR waveform data. The same kind of EOB/NR inconsistency also appears for configurations with even higher mass ratios and large, negative, spins. In some extreme situations, it can also affect the frequency. We performed a thorough scan of the parameter space and we concluded that a pragmatical approach to solve this problem

is simply to impose $\Delta t_{\rm NQC} = 4$ for a certain sample of configurations. More precisely, we found that the ubiquitous $\Delta t_{\rm NQC} = 1$ should be replaced by $\Delta t_{\rm NQC} = 4$ when

$$8 < q < 11 \text{ and } \chi_A < -0.9, \tag{5.7}$$

$$11 < q < 19 \text{ and } \chi_A < -0.8. \tag{5.8}$$

Note that, despite being independent of the value of χ_B, such simplified conditions allow to generate waveforms that present a sufficiently sane and smooth behavior around the merger up to mass ratio $q = 20$ and spins $\chi_A = \chi_B = \pm 0.95$. Finally, the last question is about the magnitude of the uncertainty that one introduces by choosing $\Delta t_{\rm NQC} = 4$ instead of $\Delta t_{\rm NQC} = 1$ at the boundary of the region of the parameter space defined by Eqs. (5.7)-(5.8). We evaluated this by (i) choosing several configurations at the interface, on the (ν, χ_A) square, and by computing $\bar{F}$ between EOB waveforms with $\Delta t_{\rm NQC} = 1$ and $\Delta t_{\rm NQC} = 4$. We find values of $\bar{F}$ (see Fig. (5.8)) on average around 10^{-3}, which means that having a discontinuous transition has in fact no practical consequences. Evidently, the radical solution to this problem will eventually be to change the argument of the gyro-gravitomagnetic functions $(\hat{G}_S, \hat{G}_{S_*})$ as mentioned above. In this respect, we have checked that doing so for the case $(11, -0.95, -0.50)$ of Fig. 5.7 allows one to (i) avoid the orbital frequency Ω crossing zero and (ii) consequently recovering a qualitatively excellent modulus around merger simply keeping $\Delta t_{\rm NQC} = 1$. Since such an improved `TEOBResumS` model will have also to rely on a different determination of c_3 to be consistent with all NR simulations, we postpone a detailed treatment to future work.

Finally, we test the robustness of the merger waveform provided by `TEOBResumS` on several specific configurations. In Fig. 5.9 we cover that portion of the parameter space listed in Table I of Ref. [36] (and notably covered by nonpublic SXS NR simulations). In addition, Figs. 5.10-5.11 systematically explore several configurations corresponding to the conditions given by Eqs. (5.7)-(5.8). The figure stresses that neither the amplitude nor the frequency show any evident pathological behavior around merger. This makes us confident that `TEOBResumS` waveforms should provide a reasonable approximation to the actual waveform for that region of the parameter space. Evidently, like the case of (8,+0.85,+0.85) mentioned above, this does not a priori guarantee that, had we at hand long NR simulations for such parameters, we would get a phasing consistent with the numerical error, since modifications of c_3

might be needed. However, we think that constructing a waveform without evident pathologies is already a good achievement seen the lack of NR-based complementary information in these corners of the parameter space.

5.3 Binary Neutron Stars

General relativity predicts that the GW signal emitted by the quasi-circular inspiral and plunge of BNSs is a chirp-like signal qualitatively similar to that of a BBH system, but modified due to the presence of tidal effects. At leading PN order, the latter arise because the gravitational field of each star induces a multipolar deformation on the companion that makes the binary interaction potential more attractive. This means that, compared to the pure space-time BBH process, the coalescence process is faster. Quadrupolar leading-order tidal interactions enter the dynamics at the 5th post-Newtonian order [227, 106, 228, 229, 157, 230]. The impact on the phase evolution, however, is significant already at GW frequencies $f_{\rm GW} \gtrsim 150$Hz [231] and becomes the dominant effect towards the end of the inspiral [232]. The magnitude of the tidal interaction is quantified by a set of dimensionless tidal polarizability coefficients for each star. The dominant one is usually addressed in the literature as "tidal deformability" and is defined as

$$\Lambda_2 = \frac{2}{3} k_2 \left(\frac{c^2}{G} \frac{R_*}{M_*} \right)^5 , \tag{5.9}$$

where k_2 is the quadrupolar gravito-electric Love number (see Sec. 3.1.4 and Chapt. 3 in general for details about the tidal phenomenology of NSs) and (R_*, M_*) are the NS areal radius and mass [110, 108, 233].

5.3.1 Main features

Our starting point for describing the BNS evolution up to the merger is the model discussed in Ref. [206], where the point-mass A_0 potential (formerly denoted as $A(r)$ and discussed in Sec. 4.2 of this thesis) is augmented by a gravitational self-force (GSF)-informed tidal contribution [234]. Following [157], the complete EOB potential is written as

$$A = A_0 + A_T^{(+)} , \tag{5.10}$$

where

$$A_T^{(+)}(u;\nu) \equiv -\sum_{\ell=2}^{4}\left[\kappa_A^{(\ell)} u^{2\ell+2}\hat{A}_A^{(\ell^+)} + (A \leftrightarrow B)\right] \tag{5.11}$$

models the gravito-electric sector of the interaction, with $u \equiv 1/r$. In the expression above, the $\ell = 2, 3, 4$ tidal coupling constants are defined as

$$\kappa_A^{(\ell)} = 2\frac{X_B}{X_A}\left(\frac{X_A}{\mathcal{C}_A}\right)^{2\ell+1} k_\ell^A \ , \tag{5.12a}$$

$$\kappa_B^{(\ell)} = 2\frac{X_A}{X_B}\left(\frac{X_B}{\mathcal{C}_B}\right)^{2\ell+1} k_\ell^B \ , \tag{5.12b}$$

in which $\mathcal{C}_{A,B} = M_{A,B}/R_{A,B}$ are the compactness of the two stars, $R_{A,B}$ their areal radii, while $k_\ell^{A,B}$ are the dimensionless relativistic Love numbers [227, 110, 108, 233, 231].

At leading order, tidal interactions are fully encoded in the total dimensionless *quadrupolar* tidal coupling constant

$$\kappa_2^T \equiv \kappa_A^{(2)} + \kappa_B^{(2)}. \tag{5.13}$$

The above parameter is key to discovering and to interpreting EOS quasi-universal relations for BNS merger quantities [232, 235, 236]. In GW experiments, however, one often measures separately (Λ^A, Λ^B) and the masses [237, 238, 43]. The expression relating κ_2^T to $(\nu, \Lambda_2^A, \Lambda_2^B)$ can be easily obtained by inserting Eq. (5.9) into Eq. (5.13) and reads

$$\begin{aligned}\kappa_2^T\left(\nu;\Lambda_2^A,\Lambda_2^B\right) = \frac{3}{8}\nu\Big[&\left(\Lambda_2^A+\Lambda_2^B\right)\left(1+3X_{AB}^2\right)\\ &+\left(\Lambda_2^A-\Lambda_2^B\right)X_{AB}\left(3+X_{AB}^2\right)\Big] \ .\end{aligned} \tag{5.14}$$

The relativistic correction factors $\hat{A}_A^{(\ell^+)}$ formally include all the high PN corrections to the leading-order tidal interaction. The particular choice of $\hat{A}_A^{(\ell^+)}$ defines a particular `TEOB` model. For example, the PN-expanded next-to-next-to-leading-order (NNLO) tidal model is given by the, fractionally 2PN accurate, expression

$$\hat{A}_A^{(\ell^+)}(u) = 1 + \alpha_1^{(\ell)} u + \alpha_2^{(\ell)} u^2 \quad [\text{NNLO}] \ , \tag{5.15}$$

with $\alpha^{(2),(3)}_{1,2} \neq 0$ computed analytically and $\alpha^{(4)}_{1,2} = 0$ [239]. This `TEOBNNLO` model has been compared against NR simulations in [240, 206]. Significant deviations are observed during the last 2-3 orbits before merger at dimensionless GW frequencies $M\omega_{22} \gtrsim 0.8$, that roughly correspond to the GW frequency of the stars' contact.

The `TEOBResum` model is defined from `TEOBNNLO` by replacing the $\ell = 2$ term in (5.15) with the expression

$$\hat{A}^{(2^+)}_A(u) = 1 + \frac{3u^2}{1 - r_{\rm LR}u} + \frac{X_A \tilde{A}^{(2^+)1{\rm SF}}_1}{(1 - r_{\rm LR}u)^{7/2}} + \frac{X^2_A \tilde{A}^{(2^+)2{\rm SF}}_2}{(1 - r_{\rm LR}u)^p}, \tag{5.16}$$

where $p = 4$ and the functions $\tilde{A}^{(2^+)1{\rm SF}}_1(u)$ and $\tilde{A}^{(2^+)2{\rm SF}}_2(u)$ are given in [234], obtained by fitting to numerical data from [241]. The key idea of `TEOBResum` is to use as pole location in Eq. (5.16) the light ring $r_{\rm LR}(\nu; \kappa^{(\ell)}_A)$ of the `TEOBNNLO` model, i.e., the location of the maximum of $A^{\rm NNLO}(r;\, \nu;\, \kappa^{(\ell)}_A)/r^2$. `TEOBResum` is completed with a resummed waveform [8] that includes the NLO tidal contributions computed in [157, 242, 243]. `TEOBResum` is consistent with state-of-the-art NR simulations up to merger [206]. Consistently with the BBH case, we here conventionally *define* the BNS merger as the peak of the $\ell = m = 2$ amplitude of the strain waveform. The results of [206] span a sample of equation of states (EOS) and consequently a large range of the tidal coupling parameters. Such results were later confirmed by Hotokezaka et al. [244, 245]. Similarly, Ref. [246] showed that `TEOBResum` is consistent with an alternative tidal EOB model that does not incorporate GSF-driven information but instead includes a way of accounting for the f-mode oscillations of the NS excited during the orbital evolution [212]. A ROM version of `TEOBResum` of Ref. [206] exists [247] and it is implemented in `LAL` under the name `TEOBResum_ROM`. In conclusion, despite a certain amount of approximations used to build the model, we take the tidal EOB-model of Ref. [206] as our current best waveform approximant for coalescing nonspinning BNS up to merger. In the next Section, we use `TEOBResum` as a starting point to construct a BNS waveform model that puts together both tidal and spin effects.

5.3.2 EOB formalism for self-spin term

The spins of the two NSs (or in general of two deformable bodies) can be easily incorporated in the formalism of Ref. [159]. Let us describe a two-step

procedure starting from the case where the spin-spin terms are not present. This corresponds to posing the centrifugal radius $r_c = r$ in the framework of Ref. [159], i.e. Eq. (4.26) above. In this case, moving from spinning BBHs to spinning BNSs is procedurally straightforward, since the only trivial change is to replace the point-mass potential with the tidally augmented one. The gyro-gravitomagnetic function G_S and G_{S_*} are the same as in the BBH case, and are resummed taking their Taylor-inverses as discussed in [159]. A choice needs to be made for what concerns the NNNLO effective parameter c_3, that for BBHs was tuned using NR data. Here we decide to simply fix it to zero. The reason behind this choice is that c_3 is an effective correction that depends on spin-square terms that are different in BBHs and BNSs and thus it is safer to drop it here. We have indeed explored the effect of keeping the BBH value of c_3 for $\chi_A = \chi_B = 0.1$ comparing with the BNS NR data corresponding to the SLy EOS and $1.35M_\odot + 1.35M_\odot$. We find that such effect is not significant because it enters at high PN order in a frequency regime that is not really reached in a BNS system.

For what concerns spin-spin effects, it turns out that it is very easy to incorporate them into the EOB model at *leading-order* (LO) also in the presence of matter objects like NSs[8]. When we talk of spin-spin interaction, let us recall that the PN-expanded Hamiltonian is made by three terms: the mutual interaction term, $H_{S_A S_B}$, and the two self-spins ones $H_{S_A S_A}$ and $H_{S_B S_B}$. These two latter terms originate from the interaction of the monopole m_B with the spin-induced quadrupole moment of the spinning black hole of mass m_A and vice versa. For a NS, the same physical effect exists, but the spin-induced quadrupole moment depends on the equation of state (EOS) by means of some, EOS-dependent, proportionality coefficient [134]. As we have seen above, for BBHs, Ref. [159] introduced a prescription to incorporate into the EOB Hamiltonian all three spin-spin couplings (at NLO) in resummed form, by including them inside a suitable centrifugal radius r_c. This quantity mimics, in the general, comparable-mass case, the same quantity that can be defined in the case of the Hamiltonian of a test particle around a Kerr black hole. In this latter case, this takes into account the quadrupolar deformation of the hole due to the black hole rotation. For comparable-mass binaries, this may be thought as a way of incorporating the quadrupolar deformation

[8]Since the spin magnitude of each NS composing the binary is expected to be small ($\chi \lesssim 0.1$), we may a priori expect this order of approximation to be sufficient, although the corresponding Hamiltonian at NLO has been obtained recently with different approaches [248].

of each black hole induced by its rotation. At LO, the definition of the centrifugal radius of Eq. (4.26) simply reads

$$r_c^2 = r^2 + \hat{a}_0^2 \left(1 + \frac{2}{r}\right). \tag{5.17}$$

where we recall that the dimensionless effective Kerr spin is

$$\hat{a}_0 = \tilde{a}_A + \tilde{a}_B \tag{5.18}$$

with $\tilde{a}_{A,B} = X_{A,B}\chi_{A,B}$. The use of these spin variables is convenient for several reasons: (i) the analytical expressions for spin-aligned binaries are nicely simplified and shorter compared to other standard notations [9]; (ii) in the large mass ratio limit $M_B \ll M_A$, one has that $\tilde{a}_A$ becomes the dimensionless spin of the massive black hole of mass $M_A \approx M$, while $\tilde{a}_B$ just reduces to the usual spin-variable of the particle $\sigma \equiv S_B/(M_A M_B)$.

Next-to-leading order spin-spin effects can be incorporated in a different fashion depending on whether the spins are generic or aligned with the orbital angular momentum. This is still ongoing work that needs further investigation [249]. In the case of two NSs the recipe we propose here to include spin-spin couplings at LO is just to replace the definition of the effective spin $\hat{a}_0$ in Eq. (5.17) by the following quadratic form of $\tilde{a}_A$ and $\tilde{a}_B$

$$\hat{a}_Q^2 = C_{QA}\tilde{a}_A^2 + 2\tilde{a}_A\tilde{a}_B + C_{QB}\tilde{a}_B^2 \tag{5.19}$$

where C_{QA} and C_{QB} parametrize the quadrupolar deformation acquired by each object due to its spin [10]. For a black hole, $C_Q = 1$ and in this case Eq. (5.19) coincides with Eq. (5.18). For a NS (or any other "exotic" object different from a black hole, like a boson star [251]) $C_Q \neq 1$ and needs to be computed starting from a certain equation of state (see below). We can then follow Ref. [159] and the EOB Hamiltonian will have precisely the same formal structure of the BBH case. In particular, the complete equatorial A function entering $\hat{H}^{\rm eff}_{\rm orb}$ reads

$$A(r, \nu, S_i, \kappa_i, C_{Qi}) = \left[\frac{1+2u_c}{1+2u} A_{\rm orb}(u_c, \nu, \kappa_i)\right]_{u_c(u,S_i,C_{Qi})}, \tag{5.20}$$

[9] Like, for example, the symmetric $\chi_S \equiv (\chi_A + \chi_B)/2$ and antisymmetric $\chi_S \equiv (\chi_A - \chi_B)/2$ combinations of the dimensionless spins, or $S_\ell \equiv S_A + S_B$ and $\Sigma_\ell = X_B S_B - X_A S_A$ are typically used to express PN results.

[10] The notation C_{Qi} we adopt here is mediated from Ref. [248] and we remind the reader that this quantity is identical to the parameter a in Poisson [134] and C_{ES^2} of Ref. [250]. It is also the same parameter called κ_i in Bohé et al. [75].

where $u_c \equiv 1/r_c$ is obtained from Eq. (5.17) and (5.19) and we indicated explicitly the dependence on the various EOS-dependent parameters. Note that $A_{\rm orb}$ is here depending explicitly on the tidal parameters κ_i, because this is meant to be the sum of the point-mass A function plus the tidal part of the potential used in Ref. [206] but everything is now taken as a function of u_c instead of u. One easily checks that, by PN-expanding the spin-dependent EOB Hamiltonian, as given by Eqs. (23), (24) and (25) of [159], the LO spin-spin term coincides with the corresponding one of the ADM Hamiltonian given in Eqs. (8.15) and (8.16) of [248], that in our notation just rereads as

$$\hat{H}^{\rm ADM}_{\rm ss_{LO}} = -\frac{1}{2r^3_{\rm ADM}} \left\{ C_{QA} \tilde{a}^2_A + 2\tilde{a}_A \tilde{a}_B + C_{QB} \tilde{a}^2_B \right\}, \tag{5.21}$$

i.e $\hat{H}^{\rm ADM}_{\rm ss} = -\hat{a}^2_Q/(2r^3_{\rm ADM})$ using Eq. (5.19). Since at this PN order the useful relation between the ADM radial separation $r_{\rm ADM}$ and the EOB radial separation is just $r = r_{\rm ADM}$, it is immediate to verify the equivalence of the two results.

Incorporating the full LO spin-spin interaction in the waveform, including monopole-quadrupole terms, is similarly straightforward. First, following Ref. [159], Eq. (80) there, we recall that, for BBHs, this is done by including in the residual amplitude correction to the $(2,2)$ waveform a spin-dependent term of the form

$$\rho^{\rm SS_{LO}}_{22} = c^{\rm SS}_{\rm LO} x^2 = \frac{1}{2} \hat{a}^2_0 x^2. \tag{5.22}$$

The monopole-quadrupole effect is then included by just replacing $\hat{a}^2_0$ by $\hat{a}^2_Q$ from Eq. (5.19). One then verifies that, after PN-expanding the resummed EOB flux, the corresponding LO spin-spin term coincides with the LO term for spin-aligned, circularized binaries, given in Eq. (4.12) of Ref. [75]. Such Newton-normalized, spin-spin flux contributions, once rewritten using the $(\tilde{a}_1, \tilde{a}_2)$ spin variables, just gets simplified as

$$\hat{\mathcal{F}}^{\rm LO}_{\rm SS} = \left\{ \tilde{a}^2_A \left(\frac{1}{16} + 2C_{QA} \right) + \frac{31}{8} \tilde{a}_A \tilde{a}_B + \tilde{a}^2_2 \left(\frac{1}{16} + 2C_{QB} \right) \right\} x^2, \tag{5.23}$$

so that the $A \leftrightarrow B$-symmetry is apparent[11]. This can be obtained by directly expanding the EOB-resummed flux as defined in Ref. [159]. Actually, for this

[11] To obtain this result from Eq. (4.12) of Ref. [75] we recall the connection between the notations and spin variables: $\kappa_i = C_{Qi}$; $\kappa_\pm \equiv \kappa_A \pm \kappa_B$; $S_\ell = X_A \tilde{a}_A + X_B \tilde{a}_B$; $\Sigma_\ell = \tilde{a}_B - \tilde{a}_A$; $\delta = X_A - X_B = \sqrt{1-4\nu}$ and thus $X_A = (1+\sqrt{1-4\nu})/2$

specific calculation, it is enough to consider the $(2,2)$ and $(2,1)$ waveform modes, the first at LO in the spin-spin and spin-orbit interaction, while the latter only at LO in the spin-orbit interaction. The corresponding residual amplitudes, taken from Eqs. (79), (84), (86), (89) and (90) of [159], read

$$\rho_{22} = \rho_{22}^{\rm orb} + \rho_{22}^{\rm S}, \tag{5.24}$$

$$X_{AB} f_{21} = X_{AB} \left(\rho_{21}^{\rm orb}\right)^2 + \tilde{f}_{21}^{\rm S}, \tag{5.25}$$

where $\rho_{22}^{\rm S}$ is assumed here to incorporate only the LO spin-orbit and spin-spin contribution

$$\begin{aligned}\rho_{22}^{\rm S} &= c_{\rm SO}^{\rm LO} x^{3/2} + c_{\rm SS}^{\rm LO} x^2 \\ &= -\left[\frac{\hat{a}_0}{2} + \frac{X_{AB}}{6}(\tilde{a}_A - \tilde{a}_B)\right] x^{3/2} + \frac{1}{2}\hat{a}_Q^2 x^2,\end{aligned} \tag{5.26}$$

$$\tilde{f}_{21}^{\rm S} = -\frac{3}{2}(\tilde{a}_A - \tilde{a}_B). \tag{5.27}$$

One verifies that, by keeping the orbital terms consistently, using these expressions in Eq. (74) and (75) of [159], one eventually obtains Eq. (5.23) above. As a further check, we have also verified that the use of Eq. (5.19) is also fully consistent with the calculation of the multipolar waveform amplitude h_{22} that was done by S. Marsat and A. Bohé and kindly shared with us before publication [252].

At this stage, we have a complete analytical model that is able to blend, in a resummed (though approximate) way spin and tidal effects. The model is complete once all the EOS dependent information, schematically indicated by Λ is given. More precisely, the procedure is as follows: for a given choice of the EOS, one fixes the compactness $\mathcal{C}$ (or the mass of the NS), which defines its equilibrium structure. Then, following Ref. [108] (see also Refs. [110, 233, 231]), one computes the corresponding dimensionless Love numbers (k_2, k_3, k_4) as they appear in the EOB potential. At this stage, the only missing piece is the EOS-dependent coefficient C_Q for the two objects. Luckily, this can be obtained easily by taking advantage of the so-called I-Love-Q quasi-universal relations found by Yunes and Yagi [253, 137], that are listed in Table 3.1. We remind to the reader that C_Q is 1 for a BH but it is larger for a NS, depending on the EOS one is expecting a relevance of the monopole-quadrupole interaction terms. This was already pointed out by Poisson long ago [134] and more recently by Harry and Hinderer [135].

5.3.3 Comparison with NR data

We verify the accuracy of `TEOBResumS` against error-controlled NR waveforms obtained from the evolution of spinning and eccentricity reduced initial data using multiple resolutions. Initial data are constructed in the constant rotational velocity formalism using the `SGRID` code [254, 255]. The residual eccentricity of the initial data is reduced to typical values $e \sim 10^{-3} - 10^{-4}$ following the procedure described in [256]. The main properties of the BNS configurations discussed in this work are listed in Table 5.3. The initial data are then evolved with `BAM` [257, 258] using a high-order method for the numerical fluxes of the general-relativistic hydrodynamics solver [259].

The `BAM` waveforms employed here were produced and discussed in [260, 261]. We perform multiple resolution runs, up to grid resolutions that allow us to make an unambiguous assessment of convergence. We find a clear second order convergence in many cases and build a consistent error budget following the convergence tests [259]. For this work we additionally checked some of the waveforms by performing additional simulation with the `THC` code [262, 263]. The comparison with an independent code allows us to check some of the systematics uncertainties that affect BNS simulations [240, 262, 263]. We find that the two codes produce consistent waveforms. Results are summarized in Appendix D of Ref. [1].

Figures 5.12 and 5.13 illustrate EOB/NR phasing comparison. The EOB waveforms are aligned, fixing a relative time and phase shift, to the NR ones in the inspiral region marked by two vertical lines on the left panels that correspond to the same frequency interval (ω_L, ω_R) on both the EOB and NR time series [264]. The alignment frequency intervals are $(\omega_L, \omega_R) = (0.039, 0.05)$ for BAM:0095; $(0.0365, 0.045)$ for BAM:0039 and $(0.038, 0.05)$ for BAM:0064. The shaded areas in the top panels mark the NR phasing uncertainty as estimated in Appendix D of Ref. [1]. For reference, the green, vertical line indicates the time at which the 700 Hz frequency is crossed. The figure clearly illustrates that: (i) EOB and NR waveforms are *fully compatible* up to our conventionally defined merger point, the peak of the $|h_{22}|$ waveform amplitude, over the full range of values of κ_2^T considered as well as for spins. Interestingly, the leftmost panel of Fig. 5.12 also shows that the EOB-NR phase difference towards merger is acceptably small ($<$ 1 rad), but also significantly *larger* than the NR uncertainty. This illustrates that, for the first time, our NR simulations are finally mature to *inform* the analytical model with some new, genuinely strong-field, information that can

be extracted from them. The figures show that for the EOB dynamics, we typically underestimate the effect of tides in the last orbit, since the phase of the NR data is evolving faster (stronger tides). However, the opposite is true for BAM:0095. This result is consistent with the ones of Ref. [206] for the same physical configuration (but different simulations, leftmost panel of Fig. 3) where one had already the indication that for compact NS, tidal effects could be slightly overestimated with respect to the corresponding NR description. Informing `TEOBResumS` with the `BAM` simulations is outside the scope of the current work. However, we want to stress that this is finally possible with our improved simulations.

5.4 Contribution of self-spin terms to BNS inspiral

Now that we could show the consistency between the `TEOBResumS` phasing and state-of-the art NR simulations, let us investigate in more detail the effect of spins on long BNS waveforms as predicted by our model. First of all, let us recall that inspiralling BNS systems are not likely to have significant spins. The fastest NS in a confirmed BNS system has dimensionless spins ~ 0.04 [265]. Another potential BNS system has a NS with spin frequency of 239 Hz, corresponding to dimensionless spin 0.2. The fastest-spinning, isolated, millisecond pulsar observed so far has $\chi = 0.04$ [265]. However, it is known that even a spin of 0.03 can lead to systematic biases in the estimated tidal parameters if not incorporated in the waveform model [266, 267]. Those analyses are based on PN waveform models. A precise assessment of these biases using `TEOBResumS` is given in Chapters 6 and 7. Since the most important theoretical novelty of `TEOBResumS` is the incorporation of self-spin effects in resummed form, our aim here is to estimate their effect in terms of time-domain phasing up to merger [12], notably contrasting the `TEOBResumS` description with the standard PN one.

Before doing so, let us mention that LO, PN-expanded, self-spin terms [134] in the TaylorF2 inspiral approximant (see Sec. 2.7 for details) have been used in parameter-estimation studies by Agathos et al. [238], and, more recently, by Harry and Hinderer [135]. The LO term (2PN accurate) to the

[12]Note that it is currently not possible to reliably extract self-spin information from numerical simulations [268, 260].

frequency-domain phasing was originally computed by Poisson [134]. Currently, EOS-dependent, self-spin information is computed in PN theory up to 3.5PN order, so that one can have the corresponding 3.5PN accurate terms in the TaylorF2 approximant. Let us explicitly review their computation. Given the Fourier transform of the quadrupolar waveform as

$$\tilde{h}_{22} \equiv \tilde{A}(f) e^{-\mathrm{i}\Psi(f)}, \tag{5.28}$$

the frequency domain phasing of the TaylorF2 waveform approximant, that assumes the stationary phase approximation, is obtained solving the integral given by Eq. (3.5) of Ref. [99], that here is given by Eq. (2.195). The C_{Qi}-dependent quadratic-in-spin energy and flux available in the literature at 3.5PN, the maximum PN order actually known in this particular case, are given in Refs. [76] and [75] respectively, where their notation $\kappa_{\pm}$ corresponds to $\kappa_+ = C_{QA} + C_{QB}$ and $\kappa_- \equiv C_{QA} - C_{QB}$. It is important to stress that in Ref. [248] a circularized spin-spin C_{Qi}-dependent Hamiltonian, equivalent to the Multipolar post-Minkowskian (MPM) result of Ref. [76] (see their Appendix D), was computed via effective field theory (EFT) techniques. From Eq. (2.195), by taking into account all the orbital pieces at the consistent PN order [269, 270, 271, 147, 64], one gets that the self-spin contribution is given by the sum of an LO term (2PN) [134], an NLO term (3PN) and a LO tail[13] term (3.5PN)

$$\Psi_{\rm SS}^{\rm PN} = \Psi_{\rm SS}^{\rm PN,LO} + \Psi_{\rm SS}^{\rm PN,NLO} + \Psi_{\rm SS}^{\rm PN,tail}. \tag{5.29}$$

The LO tail term is computed here for the first time. It was obtained by expanding, at the corresponding PN order, the EOB energy and flux adapting the procedure discussed in [11]. These three terms explicitly read

$$\Psi_{\rm SS}^{\rm PN,LO} = -\frac{75}{64\nu}\left(\tilde{a}_A^2 C_{QA} + \tilde{a}_B^2 C_{QB}\right)\left(\frac{\omega}{2}\right)^{-1/3}, \tag{5.30}$$

$$\Psi_{\rm SS}^{\rm PN,NLO} = \frac{1}{\nu}\left[\left(\frac{45}{16}\nu + \frac{15635}{896}\right)(C_{QA}\tilde{a}_A^2 + C_{QB}\tilde{a}_B^2) + \frac{2215}{512} X_{AB}(C_{QA}\tilde{a}_A^2 - C_{QB}\tilde{a}_B^2)\right]\left(\frac{\omega}{2}\right)^{1/3}, \tag{5.31}$$

$$\Psi_{\rm SS}^{\rm PN,tail} = -\frac{75}{8\nu}\pi\left(\tilde{a}_A^2 C_{QA} + \tilde{a}_B^2 C_{QB}\right)\left(\frac{\omega}{2}\right)^{2/3}, \tag{5.32}$$

[13] See Refs. [154] and [24] for a physical insight to memory and tail effects in gravitational radiation.

where $\omega = 2\pi M f$ denotes the circularized quadrupolar gravitational wave frequency.

To quantitatively investigate the differences between the PN-expanded and EOB-resummed treatment of the self-spin contribution to the phase, it is convenient to use the quantity $Q_\omega = \omega^2/\dot{\omega}$, where $\omega = \omega(t)$ is the time-domain quadrupolar gravitational wave frequency, $\omega \equiv d\phi/dt$, where $\phi(t) \equiv \phi_{22}(t)$ is the phase of the time-domain quadrupolar GW waveform $h_{22}(t) = A(t)e^{\mathrm{i}\phi_{22}(t)}$. This function has several properties that will be useful in the present context. First, its inverse can be considered as an adiabatic parameter $\epsilon_{\rm adiab} = 1/Q_\omega = \dot{\omega}/\omega^2$ whose magnitude controls the validity of the stationary phase approximation (SPA) that is normally used to compute the frequency-domain phasing of PN approximants during the quasi-adiabatic inspiral. Thus, the magnitude of Q_ω itself tells us to which extent the SPA delivers a reliable approximation to the exact Fourier transform of the complete inspiral waveform, that also incorporates nonadiabatic effects. Let us recall [243] that, as long as the SPA holds, the phase of the Fourier transform of the time-domain quadrupolar waveform $\Psi(f)$ is simply the Legendre transform of the quadrupolar time-domain phase $\phi(t)$, that is

$$\Psi(f) = 2\pi f t_f - \phi(t_f) - \pi/4, \tag{5.33}$$

where t_f is the solution of the equation $\omega(t_f) = 2\pi f$. Differentiating twice this equation one finds

$$\omega^2 \frac{d^2\Psi(\omega)}{d\omega^2} = Q_\omega(\omega), \tag{5.34}$$

where we identify the time domain and frequency domain circular frequencies, i.e., $\omega_f = \omega(t)$. Second, the integral of Q_ω per logarithmic frequency yields the phasing accumulated by the evolution on a given frequency interval (ω_L, ω_R), that is

$$\Delta\phi_(\omega_L, \omega_R) \equiv \int_{\omega_L}^{\omega_R} Q_\omega d\log\omega. \tag{5.35}$$

Additionally, since this function is free of the two "shift ambiguities" that affect the GW phase (either in the time or frequency domain), it is perfectly suited to compare in a simple way different waveform models [272, 272, 240, 215, 206]. Then, the self-spin contribution to the PN-expanded Q_ω is given by three terms

$$Q_\omega^{\rm PN,SS} = Q_\omega^{\rm SS_{PN,LO}} + Q_\omega^{\rm SS_{PN,NLO}} + Q_\omega^{\rm SS_{PN,tail}}, \tag{5.36}$$

that are obtained from Eqs. (5.30)-(5.32) and read

$$Q_\omega^{\mathrm{SS_{PN,LO}}} = -\frac{25}{48\nu}\left(\tilde{a}_A^2 C_{QA} + \tilde{a}_B^2 C_{QB}\right)\left(\frac{\omega}{2}\right)^{-1/3}, \tag{5.37}$$

$$Q_\omega^{\mathrm{SS_{PN,NLO}}} = -\frac{1}{\nu}\left[\left(\frac{5}{8}\nu + \frac{15635}{4032}\right)(C_{QA}\tilde{a}_A^2 + C_{QB}\tilde{a}_B^2) + \frac{2215}{2304}X_{AB}(C_{QA}\tilde{a}_A^2 - C_{QB}\tilde{a}_B^2)\right]\left(\frac{\omega}{2}\right)^{1/3}, \tag{5.38}$$

$$Q_\omega^{\mathrm{SS_{PN,tail}}} = \frac{25}{12\nu}\pi\left(\tilde{a}_A^2 C_{QA} + \tilde{a}_B^2 C_{QB}\right)\left(\frac{\omega}{2}\right)^{2/3}. \tag{5.39}$$

The corresponding function in `TEOBResumS`, $Q_\omega^{\mathrm{TEOBResumS,SS}}$ is computed, in the time domain, as follows. We perform two different runs, one with $C_{Qi} \neq 0$ another with $C_{Qi} = 0$. In both cases we compute the time-domain Q_ω and finally calculate

$$Q_\omega^{\mathrm{TEOBResumS,SS}} = Q_\omega^{\mathrm{TEOBResumS_{C_{Qi}\neq 0}}} - Q_\omega^{\mathrm{TEOBResumS_{C_{Qi}=0}}}. \tag{5.40}$$

Although the procedure is conceptually straightforward, since it only requires the computation of numerical derivatives of the time-domain phase $\phi(t)$, there are technical subtleties in order to obtain a clean curve to be compared with the PN results. First of all, any oscillation related to residual eccentricity coming from the initial data, though negligible both in $\phi(t)$ or $\omega(t)$, will get amplified in Q_ω making the quantity useless. To avoid this drawback, the use of the 2PA initial data of Ref. [215], discussed in detail in Appendix C of Ref. [1], is absolutely crucial. Second, in order to explore the low-frequency regime one has to get rid of the time-domain oversampling of the waveform, since it eventually generates high-frequency (though low-amplitude) noise in the early frequency part of the curve. To this aim, the raw time-domain phase $\phi(t)$ was suitably downsampled (and smoothed). Since the time-domain output of `TEOBResumS` is evenly sampled in time (but not in frequency) such procedure had to be done separately on different time intervals of the complete signal (e.g. starting from 20Hz) that are then joined together again.

The outcome of this calculation is represented, as a black line, in Fig. 5.14. As case study, we selected the BAM:0095 configuration of Table 5.3 with $\chi_A = \chi_B = 0.1$. To orient the reader, the vertical lines correspond to 400Hz, 700Hz and 1kHz. The figure illustrates two facts: (i) the EOB-resummed

representation of the self-spin phasing is consistent, as it should, with the PN description when going to low-frequencies and (ii) it is stronger during most of the inspiral (i.e. more attractive). More detailed analysis of the self-spin effects in comparison with the various PN truncations displayed in the figure are discussed in Sec. VI of Ref. [209], to which we address the interested reader. One important information enclosed in the figure is that the difference between the EOB and NLO (3PN) description of self-spin effects is nonnegligible. It is likely that most of this difference comes from the bad behavior of the PN-expanded NLO term. Note in fact that $Q_\omega^{\mathrm{SS}_{\mathrm{PN,NLO}}}$ has a quite large coefficient, $15635/4032 \simeq 4$, (see Eq. (5.38)), that, e.g. at $M\omega \sim 0.04$, eventually yields a contribution that is comparable to the LO one in the PN series. For this reason, we are prone to think that the EOB description of self-spin effects, even if it is based only on the (limited) LO self-spin term, is more robust and trustable than the straightforward PN-expanded one. Clearly, to finally settle this question we will need to incorporate in the EOB formalism, through a suitable C_{Qi}-dependent expression of the $\delta\hat{a}^2$ given in Eq. (4.28), EOS-dependent self-spin effects at NLO. This will be discussed extensively in a forthcoming study.

5.5 Case study: Parameter estimation of GW150914

We test the performance and faithfulness of our waveform model in a realistic setting by performing a parameter estimation study on the 4096 seconds of publicly available data for GW150914 [273]. To do so efficiently, we do not iterate on the NQC parameters, so that the generation time of each waveform from 20 Hz is $\sim$ 40 ms using the C++ version of `TEOBResumS`. This worsens a bit the SXS/`TEOBResumS` unfaithfulness, as we illustrate in Fig. 5.15, though the model is still compatible with the $\max \bar{F} \approx 1\%$ limit and below the 3% threshold. The largest value of $\bar{F}$ is in fact $\max \bar{F} \approx 0.018$, that is obtained for $(1, +0.40, +0.80)$. We define θ as the vector of physical parameters necessary to fully characterize the gravitational wave signal. For `TEOBResumS` and binary black hole systems, these are the component masses (M_A, M_B), their dimensionless spin components (χ_A, χ_B) along the direction of the orbital angular momentum, the three-dimensional coordinates in the Universe – sky position angles and luminosity distance –, polarization and inclination angles, and finally time and phase of arrival at the LIGO sites. We operate within the context of Bayesian inference; given k time series of k

detectors' data d, we construct the posterior distribution over the parameters θ as

$$p(\theta|d_1,\ldots,d_k,H,I) = p(\theta|H,I)\frac{p(d_1,\ldots,d_k|\theta,H,I)}{p(d_1,\ldots,d_k|H,I)} \tag{5.41}$$

where we defined our gravitational wave model – `TEOBResumS` – as H and I represents all "background" information which is relevant for the inference problem[14]. For our choice of prior distribution $p(\theta|H,I)$, we refer the reader to Ref. [44]. Finally, we choose the likelihood $p(d_1,\ldots,d_k|\theta,H,I)$ to be the product of k wide sense stationary Gaussian noise distributions characterised entirely by their power spectral density, which is estimated using the procedure outlined in Ref. [273]. We sample the posterior distribution for the physical parameters of GW150914 using the Python parallel nested sampling algorithm in [274]. The `cpnest` model we wrote is available from the authors on request. In Table 5.4 we summarize our results by reporting median and 90% credible intervals. These numbers are to be compared with what reported in Table I in Ref. [44] and Table I in Ref. [275]. We also list them in the last column of Table 5.4 for convenience. As examples, we show the whitened reconstructed waveforms in Fig. 5.16 and the $\mathcal{M}$ and mass ratio posterior distribution in Fig. 5.17. We find our posteriors to be consistent with what published by the LIGO and Virgo collaborations, albeit our inference tends to prefer higher values for the mass parameters. However, no statistically significant difference is found. We find that `TEOBResumS` is fit to perform parameter estimation studies and that on GW150914 it performs as well as mainstream waveform models.

5.6 Selected comparisons with SEOBNRv4 and SEOBNRv4T

To complement the above discussion, let us collect in this section a few selected comparisons between `TEOBResumS` and the only other existing state-of-the-art NR-informed EOB models `SEOBNRv4` and `SEOBNRv4T` [36, 212, 213, 214], that are currently being used on LIGO/Virgo data. The tidal sector of the `SEOBNRv4T` model has been recently improved so as to also include EOS-dependent self-spin terms in the Hamiltonian, though in a form different

[14]For instance, the assumption of stationary Gaussian detector noise is hidden in the definition of I.

from ours, and will be discussed in a forthcoming publication. For the BBH case, our Fig. 5.1, when compared with Fig. 2 of [36], points out the excellent compatibility between the two models at the level of unfaithfulness with the SXS catalog of NR simulations, although the information (or calibration) of the model was done in rather different ways. For `SEOBNRv4` it relies on monitoring a likelihood function that combines together the maximum EOB/NR faithfulness and the difference between EOB and NR merger times (see Sec. IVB of [36]). By contrast, the procedure of informing `TEOBResumS` via NR simulations relies on monitoring the EOB/NR phase differences and choosing (with a tuning by hand that can be performed in little time without the need of a complicated computational infrastructure, as explained in detail in [37]) values of parameters such that the accumulated phase difference at merger is within the SXS NR uncertainty obtained, as usual, by taking the phase difference between the two highest resolutions. This is possible within `TEOBResumS` because of the smaller number of dynamical parameters, i.e. (a_6^c, c_3), and the rather "rigid" structure that connects the peak of the (pure) orbital frequency with the NQC point and the beginning of ringdown, Eq. (4.49).

Once this is done, and in particular once one has determined a global fit for c_3, the EOB/NR unfaithfulness is computed as an additional cross check between waveforms. Here we want to make the point that, even if the models look very compatible among themselves from the phasing and $\bar{F}$ point of view, they may actually hide different characteristics. As a concrete example, we focus on the (effective) photon potential function A/r^2, where A is the EOB central interaction potential. In the test-particle (Schwarzschild) limit, $A = 1 - 2/r$ and A/r^2 peaks at the light ring $r = 3$, which approximately coincides with (i) the peak of the orbital frequency; (ii) the peak of the Regge-Wheeler-Zerilli potential; (iii) the peak of the $\ell = m = 2$ waveform amplitude [167]. The location of the effective light ring (or the peak of the orbital frequency) is a crucial point in the EOB formalism, since, as in the test-particle limit, it marks the beginning of the postmerger waveform part eventually dominated by quasi-normal mode ringing. We recall that `TEOBResumS` and `SEOBNRv4` resum the A potential in different ways: it is a (1,5) Padé approximant for `TEOBResumS`, while it is a more complicated function resummed by taking an overall logarithm for `SEOBNRv4` [276]. Moreover, while `TEOBResumS` includes a 5PN-accurate logarithmic term, `SEOBNRv4` only relies on 4PN-accurate analytic information. In addition, both functions are NR-modified by a single, ν-parametrized function that is deter-

mined through EOB/NR phasing comparison. This is the 5PN effective correction $a_6^c(\nu)$ mentioned above for `TEOBResumS` and the function $K_0(\nu)$ for `SEOBNRv4`. Explicitly, we are using $a_6^c(\nu) = 3097.3\nu^2 - 1330.6\nu + 81.38$ and $K_0 = +267.788247\nu^3 - 126.686734\nu^2 + 10.257281\nu + 1.733598$. As a first comparison, we plot in Fig. 5.18 the $q = 1$ effective photon potential. Right to the point, the figure illustrates that the two potentials are nicely consistent among themselves, although the structure close to merger is different. The figure also includes the potential of the `SEOBNRv2` model [31], a model that has been used on GW150914 and that was characterized by $K_0 = 103.2\nu^3 - 39.77\nu^2 - 1.804\nu + 1.712$. Interestingly, the plot shows that the `*v4` potential peak is closer to the `TEOBResumS` one than the `*v2` one. This finding deserves some mention for several reasons. First, the `TEOBResumS` nonspinning A function behind the photon potential of Fig. 5.18 was NR-informed in Ref. [34] with the same nonspinning SXS NR simulations used for `SEOBNRv2` (plus a $q = 10$ dataset that became available after Ref. [31]). Second, `SEOBNRv2` uses only linear-in-ν 4PN information [152, 155] while `SEOBNRv4` uses the full 4PN information [271, 270], as for `TEOBResumS`. However, to our understanding, the `SEOBNRv4` potential was also calibrated using more nonspinning NR simulations (notably with $q \gtrsim 1$) than for `SEOBNRv2` (see Ref. [36]) and `TEOBResumS`. This suggests that the `TEOBResumS` potential seems able to naturally incorporate some amount of strong-field information that needs to be extracted from NR when a SEOBNRv*-like [276] potential is employed. These findings merit further investigation.

In Fig. 5.19 we display the same comparison (though after omission of the `SEOBNRv2` curve) for different mass ratios, $q = (1, 2, 3, 4, 6, 18)$. One sees that both `TEOBResumS` and `SEOBNRv4` curves are smoothly and consistently connected to the Schwarzschild case. This accomplishes the basic paradigm of the EOB formalism that the dynamics of the two-body problem is a *continuous deformation* of the dynamics of a test-mass on a Schwarzschild black hole [28, 29], so that this limit should be properly incorporated by construction in the model and should be preserved by the addition of NR information. However, the way the Schwarzschild limit is reached is rather different in the two models. This is highlighted very well by the markers in Fig. 5.19. These markers indicate the location of the effective light-ring, $r_{\rm LR}$, that is shown, versus ν, in Fig. 5.20. The figure highlights that, while the $r_{\rm LR}(\nu)$ is approximately linear for `TEOBResumS` (i.e. the Schwarzschild light-ring is reached at constant speed in the space of the nonspinning configurations parametrized by ν) the behavior of the corresponding quantity in `SEOBNRv4` is more com-

plicated, notably it is not monotonic in ν. This is not necessarily a problem from the practical point of view of generating NR-calibrated waveforms that are consistent with NR simulations. However, from the theoretical point of view, this suggests a slight inconsistency within the model, because the location of $r_{\rm LR}$ for $\nu = 0.25$ is the same as for $\nu \approx 0.09$. A priori, as it was pointed out in the foundation of the EOB model [29, 141], one would expect that the location of the LR is simply monotonically pushed to smaller radii (i.e. higher frequency) due to the repulsive effect of the higher PN ν-dependent corrections that exist both at 2PN and at 3PN order. This is also suggested by NR simulations, where one finds that the GW frequency at merger (that in the EOB formalism is connected with the peak of the effective photon potential) is monotonically growing with ν (see e.g. Fig. 3 of [277]). By contrast, `TEOBResumS` seems to consistently incorporate this feature by construction, even with the NR-informed function $a_6^c(\nu)$. However, one sees that $r_{\rm LR}(\nu)$ is a quasi-linear function, though not exactly a straight line. This suggests that it would be interesting to investigate to which extent one can take it as a straight line (since it depends on a_6^c) and how this influences the EOB/NR phasing performances. We hope to address these questions in future work. As a last remark, we note that one can just plug the `SEOBNRv4` A interaction potential within the `TEOBResumS` infrastructure and, without changing anything else in the model, see whether or not the differences of Fig. 5.19 reflect on the waveform. It is easily found that, especially when $q > 1$, the dynamics yielded by the two NR-informed potentials are rather different (and somehow not compatible), non-negligibly affecting the phasing. A detailed comparison of these aspects is interesting, and will be possibly undertaken in future work.

As additional comparison between different EOB-based waveform models, we also computed the faithfulness (or match) F between `TEOBResumS` and `SEOBNRv4T`, i.e., the tidal version of `SEOBNRv4` [212, 213]. It has to be noticed that `SEOBNRv4T` is conceptually different from `TEOBResumS` in that the effects of enhancement of the tidal interaction due to couplings with the internal oscillation f-mode of the stars is incorporated in the model [229, 213]. In addition, it also includes EOS-dependent spin-spin terms, though not in the resummed form involving the centrifugal radius [214]. As above, the match here is the overlap maximized over the time (time shift) and fiducial constant phase [15]. The comparison was done in the part of the parame-

[15] Note that, due to an incorrect flag, these results were obtained omitting, in

ter space that we expect to be astrophysically more relevant, namely, we randomly draw parameters from the uniform distributions in the mass ratio $M_A/M_B \in [1,2]$, the heaviest mass $M_A \in [1,3]M_\odot$, the spins (along orbital angular momentum) $\chi_{A,B} \in [-0.15, 0.15]$, and the tidal parameters for each body $\Lambda_{A,B} \in [2, 1600]$. Each waveform is computed from a nominal initial frequency of 40 Hz. The most representative results are given in Fig. 5.21 where we show the points drawn in the (Λ_A, M_A) and (Λ_B, M_B) planes. The match values, that are very high, are color-coded. The lowest match value found is 0.9898.

To better clarify the meaning of Fig. 5.21 with complementary information, we also depict in Fig. 5.22 the direct time-domain comparison between the two waveforms corresponding to the lowest match value, $F = 0.9898$. The parameters of this binary are $M_A = 2.99173181168$, $M_B = 1.54656708774$, $\chi_A = -0.00403135733793$, $\chi_B = 0.104676230478$, $\Lambda_A^2 = 1595.82370308$, $\Lambda_B^2 = 410.054257357$. The corresponding values the spin-induced quadrupoles are $C_{QA} = 8.47884798$ and $C_{QB} = 5.56870361$. The top panel of Fig. 5.22 shows the two h_+ waveforms without any relative time and phase shift. This is instead done in the bottom panel, with these shifts dictated by the match calculation. One notes that, although the initial GW frequency of the wave is chosen to be 40 Hz for both models (and the waves seem to consistently start in the same way) the initial conditions between the two models are different, as highlighted in Table 5.5. This difference comes from the relation that connects the initial frequency f_0 to the initial radius r_0. For `TEOBResumS`, for simplicity, one is using the simple (though approximate in this context) Newtonian Kepler's law

$$r_0 = \left(\frac{\pi f M G}{c^3}\right)^{-2/3} . \tag{5.42}$$

On the contrary, `SEOBNRv4T` correctly recovers r_0 from Hamilton's equations (see Eqs. (4.8)-(4.9) of Ref. [279]). The difference in r_0 is then responsible for the difference in the other phase-space variable, that is mostly behind the accumulated time-domain relative dephasing between the two waveforms highlighted in Fig. 5.22. By contrast, what is not relevant for this case is the fact that, while `TEOBResumS` implements 2PA initial data [166, 215]

`TEOBResumS`, the 3PN ν-dependent, spin-independent, terms in ρ_{31} and ρ_{33} as computed in Ref. [278]. These terms were however correctly included to obtain all other results presented so far.

SEOBNRv4T only uses the post-adiabatic (PA) approximation [29]. Note that the effect of the 2PA correction is very small at 40 Hz, since $p_\varphi^{\rm circ}$ is only changed at the 7th decimal digit (see first row of Table 5.5). The last row of Table 5.5 illustrates that, if f_0 is slightly changed so to compensate for the relativistic corrections that are not included in Eq. (5.42) and make TEOBResumS start at the same initial radius of SEOBNRv4T, the fractional difference between the angular momenta is $\sim 10^{-7}$ and between the radial momenta is $\sim 10^{-4}$. The TEOBResumS waveform corresponding to the last row of Table 5.5 is now largely more consistent with the SEOBNRv4T *even without* time and phase alignment (see bottom panel of Fig. 5.22). The corresponding value of the match remains unchanged.

Since the C++ implementation of TEOBResumS that was used in [210] was setting up the initial conditions using the simplified relation given by Eq. (5.42) above, we have decided not to modify it in the publicly available version of this code (see Appendix E of Ref. [1]). By contrast, we are using a more correct relation between frequency and radius in the corresponding C implementation of TEOBResumS: the radius is obtained by solving Eq. (4.30a) for a given orbital frequency (assumed to be half of the nominal initial gravitational wave frequency). In this way, we can greatly improve the agreement with the corresponding SEOBNRv4T initial conditions. As an example, considering the case discussed above and detailed in Table 5.5, the initial radius obtained in this way is found to be $r_0 = 50.296014$.

5.7 An extreme BBH configuration: $(8, -0.90, 0)$

The SXS:BBH:1375 [280] dataset of the SXS collaboration with $(8, -0.90, 0)$ is very interesting because it allows us to test TEOBResumS in the most difficult region of the parameter space (i.e., when the spins are anti-aligned with the orbital angular momentum) and, notably, it is marginally outside the portion covered by the BAM simulations of Table 5.2 for $q = 8$. In fact, it has $\hat{S} = -0.7111$, to be compared with $\hat{S} = -0.6821$ corresponding to $(8, -0.85, -0.85)$. The phasing comparison is illustrated in Fig. 5.23. We remark the following. First, one sees that the phase difference (blue line) oscillates around zero. This oscillation reflects the residual eccentricity of the SXS waveform. Though it is rather small (i.e. $\sim 1.1 \times 10^{-3}$) it is visible because the TEOBResumS waveform is started with essentially eccentricity free initial data because of the 2PA approximation (see Appendix C of Ref. [1]).

Second, the two waveforms dephase of about 1 rad up to the NR merger, with the `TEOBResumS` plunging slightly slower than the SXS one. The physical meaning of this plot is, for example, that the spin-orbit coupling in `TEOBResumS` is not strong enough. In our current framework, this is understood as that the value of c_3 deduced by fitting the choices of Table 5.1 might be (slightly) too large. Before pushing this reasoning further, let us focus on Fig. 5.24, that illustrates the nice agreement between the frequency and amplitude when the two waveforms are aligned around merger, on a frequency interval (0.2,0.3).

Note in passing that the oscillation in the frequency is physical and is due to the beating between positive and negative frequency quasi-normal-modes [281]. This well-known feature is currently not included in the EOB model. As a last check, we computed, as usual, the EOB/NR unfaithfulness, Fig. 5.25. One finds that $\max(\bar{F}) = 0.001027$. This makes us conclude that, even if the time-domain analysis suggests that the value of c_3 should be slightly reduced, we are not going to do it now since the value of $\bar{F}$ is already one order of magnitude smaller than the usual target of 0.01.

5.8 Black-hole – Neutron-star binaries

In this section we discuss the performances of `TEOBResumS` for the description of BH-NS waveforms. We stress that the model has not been developed for this type of waveforms and that this comparison is preliminary to a forthcoming investigation. We focus on the two public SXS datasets BHNS:0001 and BHNS:0002 that refer to a $q = 2$ and $q = 6$ nonspinning binaries where the NS is described by a $\Gamma = 2$ polytropic EOS with $K = 101.45$ and $K = 92.12$ respectively. The dimensionless Love numbers are $k_{2,3,4} = (0.07524, 0.0220429, 0.0089129)$ and $k_{2,3,4} = (0.0658832, 0.01873168, 0.007341026)$ and the NS compactness $C_B = 0.144404$ and $C_B = 0.1563007$. The corresponding tidal parameters are $\Lambda_{2,3,4} = (470.8450, 1095.9415, 2511.5797)$ (BHNS:0001) and $\Lambda_{2,3,4} = (798.8698, 2244.6773, 6217.96765)$ (BHNS:0002). The values of the tidal coupling constant are $\kappa_2^T = 0.50426$ for BHNS:0001 and $\kappa_2^T = 19.725$ for BHNS:0002. Given the very small value of κ_2^T for BHNS:0001, and following the reasoning of Ref. [157] (see discussion related to Table I), we expect that dataset to behave essentially like a BBH binary with the same mass ratio.

Let us focus first on the $q = 2$ binary, BHNS:0002 Fig. 5.26. This

binary dynamics is characterized by tidal disruption that suppresses the ringdown oscillation after merger. The left panel of the figure illustrates that `TEOBResumS` *with tides and no NQC* captures well the waveform up to merger, with a phase difference of ~ -0.3 rad there. The "glitch" around $u/M \sim 1300$ is in the Lev3 NR data (notably not in the Lev2 ones), it is perhaps due to a re-gridding, but it is not relevant for our comparison. The phase uncertainty at merger, estimated by just taking the difference between Lev3 and Lev2 resolutions [192], is of the order of 0.1 rad. This is of the order of the error budget at merger estimated in Ref. [212], see Fig. 2 and Fig. 3 there, that is of the order of ± 0.5 rad. Hence, the BHNS waveform obtained with `TEOBResumS` with tides is in agreement with the NR data up to NR merger. Our result is comparable to those presented in Ref. [212], but we stress here that we do not use NQC-calibration and that the model only depends on the single parameter $a_5^c(\nu)$ informed by BBH data; `TEOBResumS` is not fed by any strong-field information extracted from the BHNS:0002.

Figure 5.27 refers to the BHNS binary with larger mass ratio, $q = 6$. To our knowledge, this is the first time an EOB/NR comparison is done for this dataset, as it was not included in Refs. [212, 213]. The phasing analysis (left panel of Fig. 5.27, alignment in the early inspiral) is telling us that the EOB/NR phase difference is around -1.6 rad at NR merger. The right panel illustrates that the `TEOBResumS` tidal waveform (red lines) is sane, notably with value of the merger amplitude very close to the NR one. On the same right panel we also superpose the $q = 6$ BBH `TEOBResumS` amplitude and frequency (orange lines). This waveform has *no tidal effects*, but it is completed by NQC and postmerger-ringdown. Once the `TEOBResumS` BBH waveform is aligned to the SXS, see Fig. 5.28 one appreciates the high compatibility between the two waveforms during the plunge and merger, consistently with the analytical understanding that a BHNS system with $\kappa_2^T = 0.50426$ is *almost* a BBH binary. This brings also us to the conclusion that *most* of the EOB/NR dephasing found in the phasing comparison of Fig. 5.27 is very likely not physical, but of numerical origin. Due to the lack of different resolutions in the SXS catalog (notably the Lev2 dataset was incomplete) we could not compute and estimate of the numerical error on the BHNS:0001 waveform.

We conclude that the current design of `TEOBResumS` is very robust and does not lead to unphysical features in extreme regions of the binary parameters. Hence, `TEOBResumS` is a good starting points for future BH-NS development. We also suggest that, lacking an accurate model for BH-NS,

`TEOBResumS` can be used for the analysis of BH-NS by turning on tides in the regime $1 \leq q \lesssim 4-6$ while simply using the BBH waveform for larger mass-ratios.

Table 5.1: First-guess values of c_3 compared with the values obtained from the interpolating fit for the sample of 27 SXS NR datasets used to construct the fit itself. The last column also lists the spin combination $\hat{S}$, helpful in characterizing the gravitational wave frequency at merger.

#	(q, χ_A, χ_B)	$c_3^{\text{first guess}}$	c_3^{fit}	$\Delta c_3/c_3^{\text{fit}}[\%]$	$\hat{S}$
1	$(1, -0.95, -0.95)$	93.0	92.31	0.75	-0.4750
2	$(1, -0.90, -0.90)$	89.0	89.44	-0.49	-0.4500
3	$(1, -0.80, -0.80)$	83.0	83.78	-0.93	-0.4000
4	$(1, -0.60, -0.60)$	73.5	72.83	0.92	-0.3000
5	$(1, -0.44, -0.44)$	64	64.45	-0.70	-0.2200
6	$(1, +0.20, +0.20)$	35	34.85	0.43	$+0.1000$
7	$(1, +0.60, +0.60)$	20.5	20.17	1.64	$+0.3000$
8	$(1, +0.80, +0.80)$	13.5	14.15	-4.59	$+0.4000$
9	$(1, +0.90, +0.90)$	11.5	11.52	-0.17	$+0.4500$
10	$(1, +0.99, +0.99)$	9.5	9.39	1.17	$+0.4950$
11	$(1, +0.994, +0.994)$	9.5	9.30	2.15	$+0.4970$
12	$(1, -0.50, 0)$	61.5	56.62	8.62	-0.1250
13	$(1, +0.90, 0)$	25.5	22.33	14.20	$+0.2250$
14	$(1, +0.90, +0.50)$	17.0	15.73	8.07	$+0.3500$
15	$(1, +0.50, 0)$	32.0	31.20	2.56	$+0.1250$
16	$(1.5, -0.50, 0$	62.0	57.97	6.95	-0.1800
17	$(2, +0.60, 0)$	29.0	26.71	8.57	$+0.2\bar{6}$
18	$(2, +0.85, +0.85)$	15.0	14.92	0.54	$+0.47\bar{2}$
19	$(3, -0.50, 0)$	63.0	61.15	3.03	-0.28125
20	$(3, -0.50, -0.50)$	70.5	66.63	5.81	-0.3125
21	$(3, +0.50, 0)$	28.0	28.02	-0.07	$+0.28125$
22	$(3, +0.50, +0.50)$	26.5	24.44	8.43	$+0.3125$
23	$(3, +0.85, +0.85)$	16.5	14.38	14.74	$+0.53125$
24	$(5, -0.50, 0)$	62.0	59.84	3.61	$-0.347\bar{2}$
25	$(5, +0.50, 0)$	30.5	29.01	5.14	$+0.347\bar{2}$
26	$(8, -0.50, 0)$	57.0	56.48	0.92	-0.3951
27	$(8, +0.50, 0)$	35.0	33.68	3.92	$+0.3951$

Table 5.2: Portion of the parameter space covered by BAM NR simulations.

#	(q, χ_A, χ_B)	$\hat{S}$
1	$(2, +0.75, +0.75)$	0.4167
2	$(2, +0.50, +0.50)$	0.2778
3	$(3, +0.50, +0.50)$	0.3125
4	$(4, +0.75, +0.75)$	0.51
5	$(4, +0.50, +0.50)$	0.34
6	$(4, +0.25, +0.25)$	0.17
7	$(4, 0, 0)$	0
8	$(4, -0.25, -0.25)$	-0.17
9	$(4, -0.50, -0.50)$	-0.34
10	$(4, -0.75, -0.75)$	-0.51
11	$(8, +0.85, +0.85)$	0.6821
12	$(8, +0.80, 0)$	0.6321
13	$(8, -0.85, -0.85)$	-0.6821
14	$(10, 0, 0)$	0
15	$(18, +0.80, 0)$	0.7180
16	$(18, +0.40, 0)$	0.3590
17	$(18, 0, 0)$	0
18	$(18, -0.40, 0)$	-0.3590
19	$(18, -0.80, 0)$	-0.7180

Table 5.3: Equal-mass BNS configurations considered in this work. From left to right the column reports: the EOS, the gravitational mass of each star, the compactness, the quadrupolar dimensionless Love numbers, the leading-order tidal coupling constant κ_2^T, the corresponding value of the quadrupolar "tidal deformability" for each object, $\Lambda_2^{A,B}$, Eq. (5.9), the dimensionless spin magnitude and the spin-induced quadrupole momenta $C_{QA,QB}$.

name	EOS	$M_{A,B}[M_\odot]$	$C_{A,B}$	$k_2^{A,B}$	κ_2^T	$\Lambda_2^{A,B}$	$\chi_{A,B}$	$C_{QA,QB}$
BAM:0095	SLy	1.35	0.17	0.093	73.51	392	0.0	5.491
BAM:0039	H4	1.37	0.149	0.114	191.34	1020.5	0.141	7.396
BAM:0064	MS1b	1.35	0.142	0.134	289.67	1545	0.0	8.396

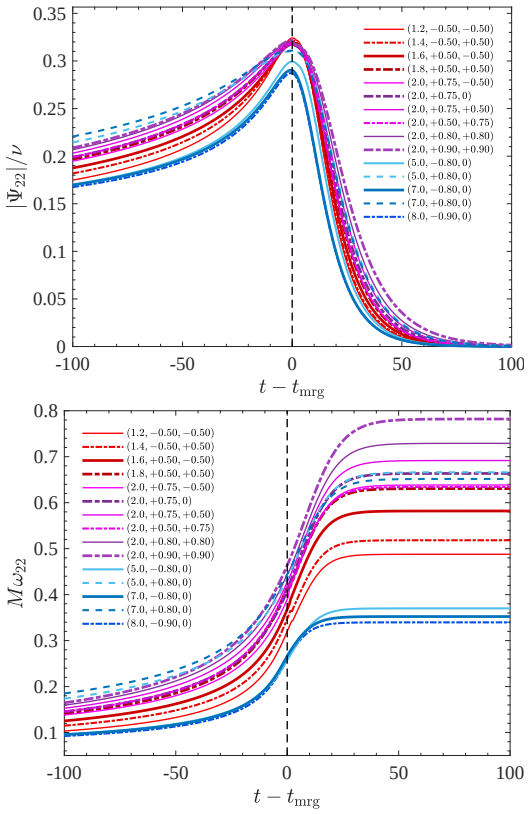

Figure 5.9: Sanity check of EOB waveform modulus (top) and frequency (bottom) on the configurations considered in Table I of Bohé et al. [36]. Differently from what we do here, NR waveform data for these configurations were used in [36] to calibrate `SEOBNRv4`. The behavior of both functions look qualitatively and quantitatively consistent and robust. Waveforms are time-shifted to be all aligned at merger time.

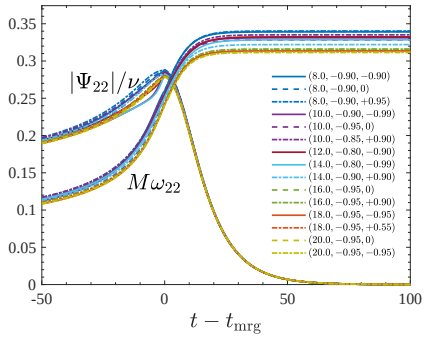

Figure 5.10: Sanity check of EOB waveforms for large mass ratios and large spins anti-aligned with the angular momentum. The good qualitative behavior of the waveform around merger is guaranteed by the value of $\Delta t_{\rm NQC}$ given by Eq. (5.7)-(5.8).

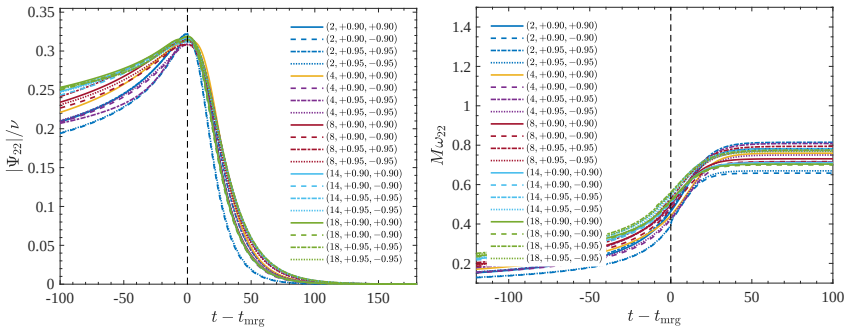

Figure 5.11: Sanity check of EOB waveforms amplitude (top) and frequency (bottom) for several mass ratios and large spins aligned with the orbital angular momentum. The global consistency is highly satisfactory for both amplitude and frequency.

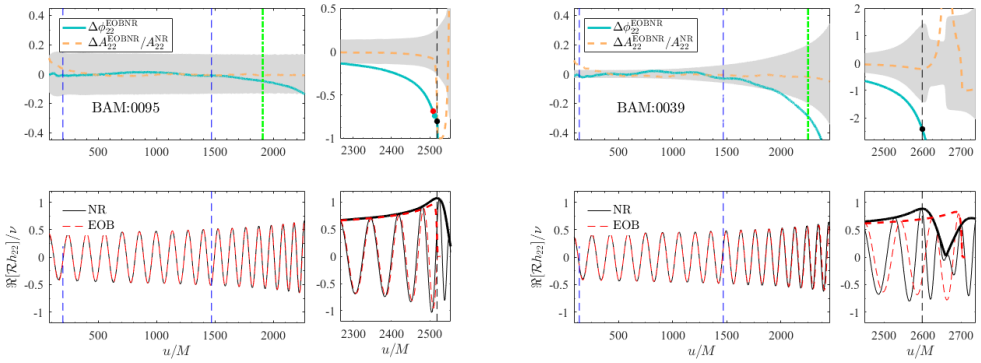

Figure 5.12: Phasing comparison between `BAM` and `TEOBResumS` waveforms for the SLy and Ms1b equal-mass BNS configurations of Table 5.3. The EOB and NR waveforms, once aligned during the early inspiral (approximately over the first $1500M$ of evolution), are compatible, within the NR uncertainty (gray area in the figures) essentially up to the NR merger point, defined as the peak of the waveform amplitude $|h_{22}|$. Note however that the errors are *larger* for the MS1b configuration. The time marked by the vertical green line corresponds to 700Hz.

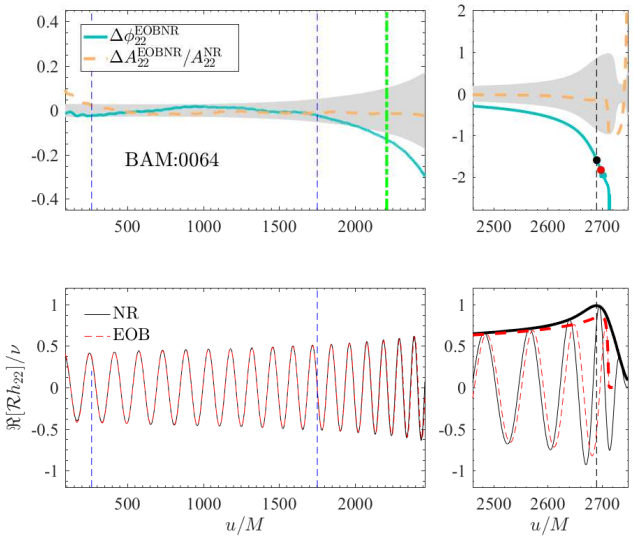

Figure 5.13: Phasing comparison between `BAM` and `TEOBResumS` waveforms, effect of spin (H4 EOS, see Table 5.3). The figure refers to spinning binary with dimensionless spins $\chi_A = \chi_B \approx 0.14$. NR and EOB waveforms are still compatible, within the NR uncertainty (gray area in the figures), up to the NR merger point. The time marked by the vertical green line corresponds to 700Hz.

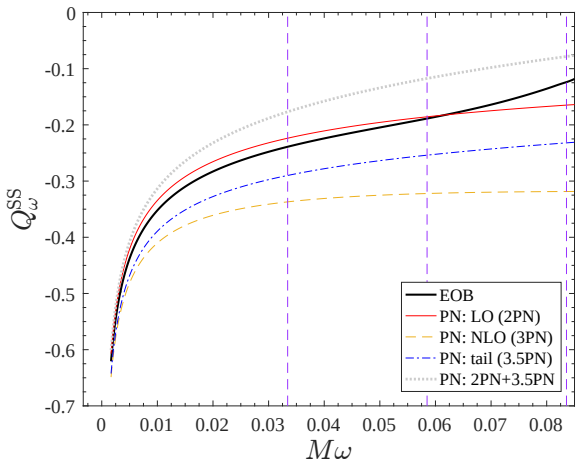

Figure 5.14: EOS-dependent self-spin effects on the phasing through the $Q_\omega^{\rm SS}$ diagnostics. The figure contrasts the EOB description (incorporating LO dynamical and dissipative effects) with various PN approximations (see text) for the BAM:0095 tidal configuration with however $\chi_A = \chi_B = 0.1$. The vertical lines mark respectively 400Hz, 700Hz and 1kHz. The EOB resummed description enhances the effect during most of the inspiral, though it reduces it towards merger. Consistency with all PN approximants is found in the low frequency regime (20Hz), though the PN regime is not yet reached there.

Table 5.4: Summary of the parameters that characterize GW150914 as found by `cpnest` and using `TEOBResumS` as template waveform, compared with the values found by the LVC collaboration [44]. We report the median value as well as the 90% credible interval. For the magnitude of the dimensionless spins $|\chi_A|$ and $|\chi_B|$ we also report the 90% upper bound. Note that we use the notation $\chi_{\rm eff} \equiv \hat{a}_0$ for the effective spin, as introduced in Eq. (4.27).

	`TEOBResumS`	LVC
Detector-frame total mass $M/M_\odot$	$73.6^{+5.7}_{-5.2}$	$70.6^{+4.6}_{-4.5}$
Detector-frame chirp mass $\mathcal{M}/M_\odot$	$31.8^{+2.6}_{-2.4}$	$30.4^{+2.1}_{-1.9}$
Detector-frame remnant mass $M_f/M_\odot$	$70.0^{+5.0}_{-4.6}$	$67.4^{+4.1}_{-4.0}$
Magnitude of remnant spin $\hat{a}_f$	$0.71^{+0.05}_{-0.07}$	$0.67^{+0.05}_{-0.07}$
Detector-frame primary mass $M_A/M_\odot$	$40.2^{+5.1}_{-3.7}$	$38.9^{+5.6}_{-4.3}$
Detector-frame secondary mass $M_B/M_\odot$	$33.5^{+4.0}_{-5.5}$	$31.6^{+4.2}_{-4.7}$
Mass ratio M_B/M_A	$0.8^{+0.1}_{-0.2}$	$0.82^{+0.20}_{-0.17}$
Orbital component of primary spin χ_A	$0.2^{+0.6}_{-0.8}$	$0.32^{+0.49}_{-0.29}$
Orbital component of secondary spin χ_B	$0.0^{+0.9}_{-0.8}$	$0.44^{+0.50}_{-0.40}$
Effective aligned spin $\chi_{\rm eff}$	$0.1^{+0.1}_{-0.2}$	$-0.07^{+0.16}_{-0.17}$
Magnitude of primary spin $\lvert\chi_A\rvert$	≤ 0.7	≤ 0.69
Magnitude of secondary spin $\lvert\chi_B\rvert$	≤ 0.9	≤ 0.89
Luminosity distance $d_{\rm L}$/Mpc	479^{+188}_{-235}	410^{+160}_{-180}

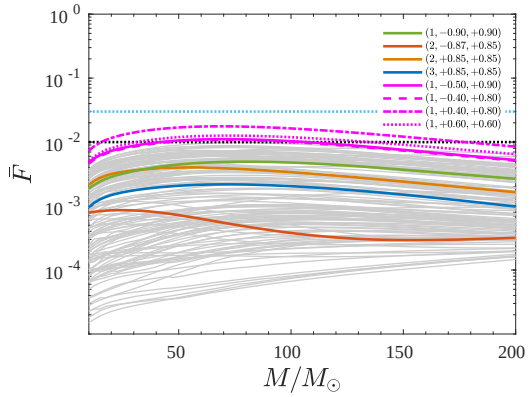

Figure 5.15: Unfaithfulness comparison between `TEOBResumS` and SXS waveforms obtained *without* iterating on the amplitude NQC parameters (a_1, a_2), see Eq. (4.48). The performace of the model, where the parameters (a_6^c, c_3) were NR-tuned *with* the iterative determination of (a_1, a_2) (see Sec. 5.2.1), is slightly worsened with respect to Fig. 5.1, although it is still compatible with the 1% limit. Such simplified version of `TEOBResumS` is used for the parameter estimation of GW150914, with results reported in Table 5.4.

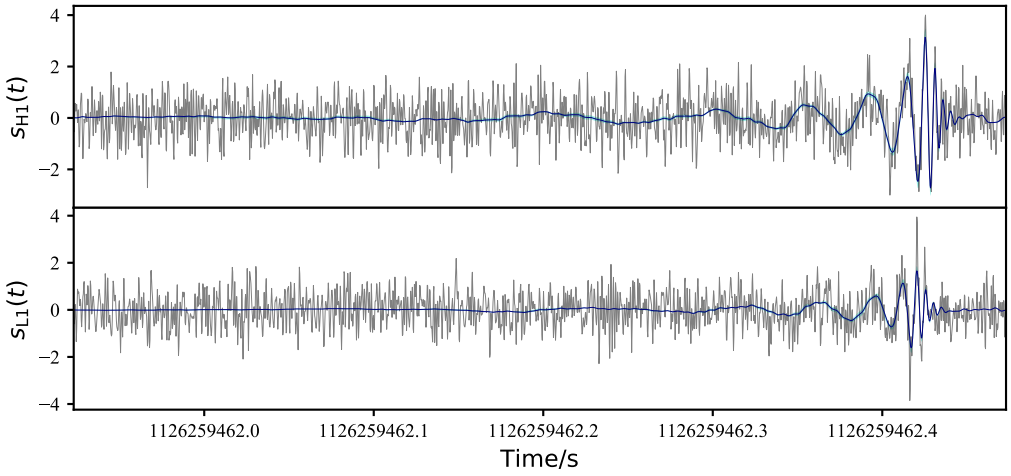

Figure 5.16: Reconstructed whitened GW waveforms in the Hanford (top panel) and in the Livingston (bottom panel) detectors. The solid lines indicate the median recovered waveforms. The cyan bands indicate the 90% credible regions as recovered by our analysis. As a comparison we also overlay the whitened raw strain for the two detectors.

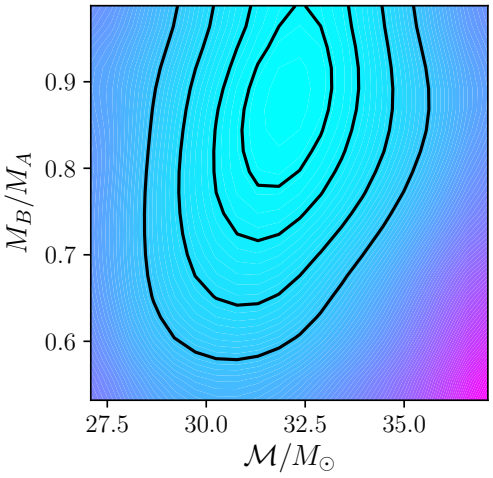

Figure 5.17: Two-dimensional posterior distribution for $\mathcal{M}$ and M_B/M_A for GW150914 as inferred using `cpnest` and `TEOBResumS`. The contours indicate the regions enclosing 90%, 75%, 50% and 25% of the probability.

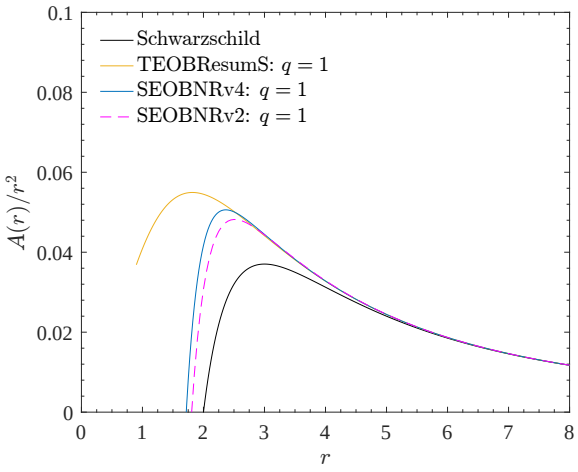

Figure 5.18: Comparison between two flavors of the `SEOBNRv*` model and `TEOBResumS`. The improved NR calibration incorporated in `SEOBNRv4` [36, 212, 213] pushed it closer to the `TEOBResumS` curve than the `SEOBNRv2` one [31].

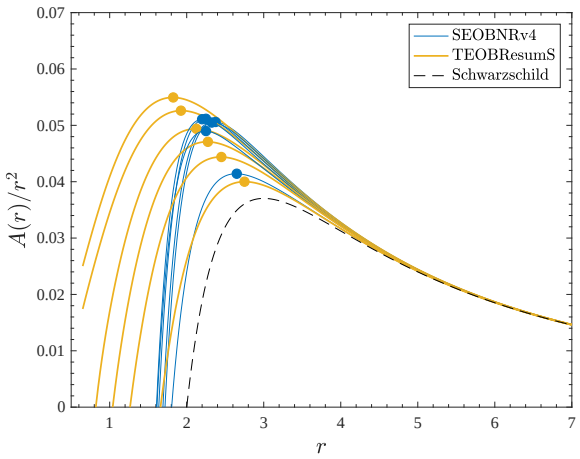

Figure 5.19: EOB effective photon potential $A(r)/r^2$ for `SEOBNRv4` and `TEOBResumS` for mass ratios $q = (1, 2, 3, 4, 6, 18)$. The potentials are consistent, though different at the peak, also for medium mass ratios. The highest consistency is found for $q = 18$. The markers highlight the peaks of the functions, i.e. the locations of the effective light-rings

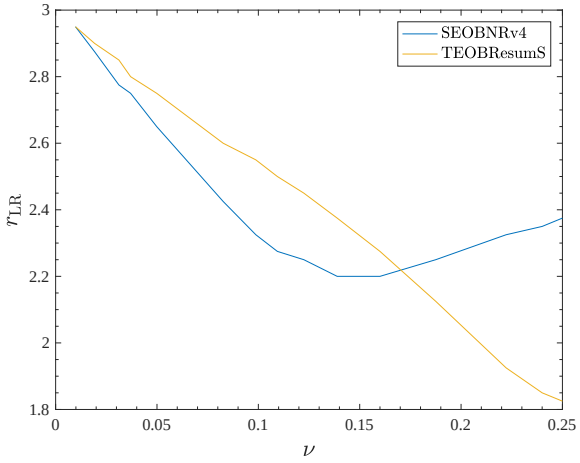

Figure 5.20: Dependence of the effective light-ring position, $r_{\rm LR}$, i.e. the peak of $A(r)/r^2$ in Fig. 5.19, versus ν. The behavior of the `TEOBResumS` effective light-ring tends quasi-linearly to $r = 3$, while the structure of the corresponding `SEOBNRv4` function is more complex.

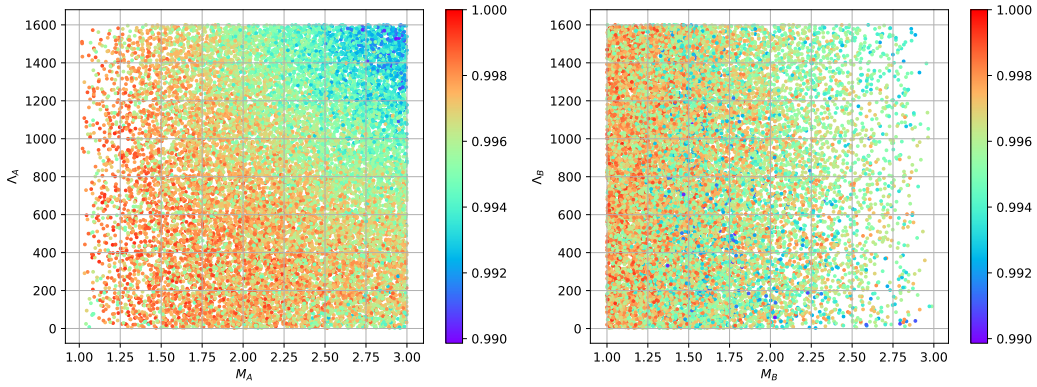

Figure 5.21: The match computed between `SEOBNRv4T` and `TEOBResumS`. The match values are color-coded. Based on 17300 randomly chosen points. The plot highlights the high compatibility between the two models.

Table 5.5: Initial conditions used to start the two EOB dynamics behind the waveforms of Fig. 5.22 which yield the lowest match value 0.9898. The initial frequency was nominally fixed to be 40Hz in both models. From left to right we have: the name of the model; the initial relative separation; the corresponding value of the angular momentum; the corresponding value of the *circular* angular momentum and the value of the radial momentum. The initial values of the phase-space variables corresponding to 40Hz are slightly different in the two models. Due to the Newtonian relation between frequency and radius that we use in `TEOBResumS`, Eq. (5.42), the consistency between initial configurations is recovered thanks to a slight modification in the initial nominal frequency of `TEOBResumS` so that the values of r_0/M coincide up to the 5th decimal digit. See text for details.

Model	f_0 [Hz]	r_0	p_φ	$p_\varphi^{\rm circ}$	p_r
`TEOBResumS`	40.000000	50.230212	7.3060375	7.3060378	-2.2938×10^{-5}
`SEOBNRv4T`	40.000000	50.296059	7.3105268	7.3105268	-2.2856×10^{-5}
`TEOBResumS`	39.921474	50.296059	7.3105277	7.3105279	-2.2848×10^{-5}

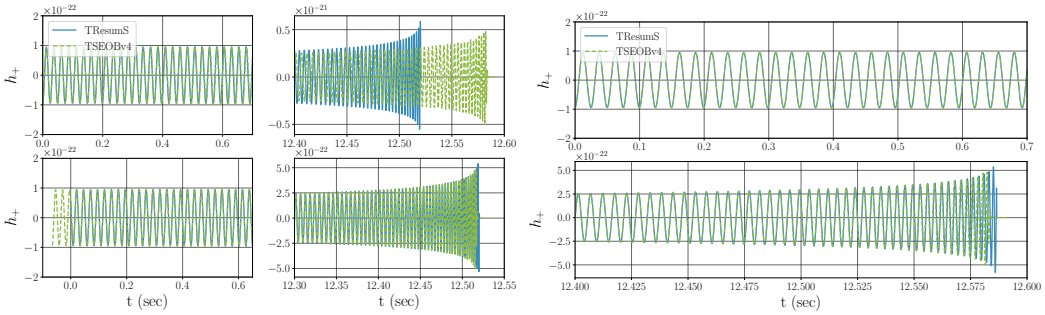

Figure 5.22: Time-domain comparison between `SEOBNRv4T` and `TEOBResumS` for the case that delivers the lowest match, $F = 0.9898$. Top panel: same initial nominal frequency, first two lines of Table 5.5, the two waveforms are aligned by choosing a suitable relative time and phase shift. The first two rows of the plot show the waveforms before alignment, while the second ones after the alignment. Bottom panel: initial data for `TEOBResumS` consistent with those of `SEOBNRv4T`, see second and third row of Table 5.5. The two waveforms nicely agree directly, without the need of the additional alignment.

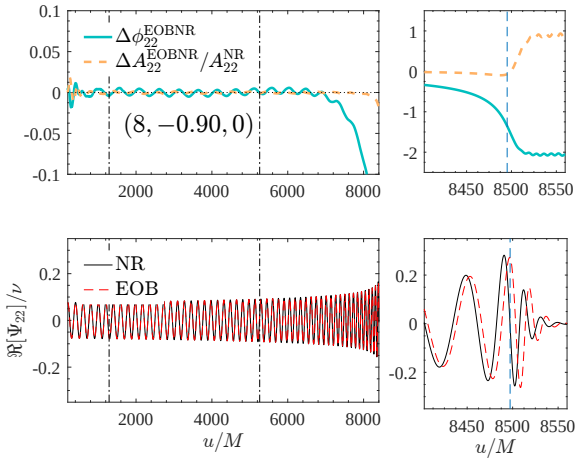

Figure 5.23: Phasing comparison between `TEOBResumS` and SXS dataset SXS:BBH:1375. Alignment in the early inspiral (vertical lines). A EOB-NR phase difference of -1.3 rad is accumulated up to NR merger.

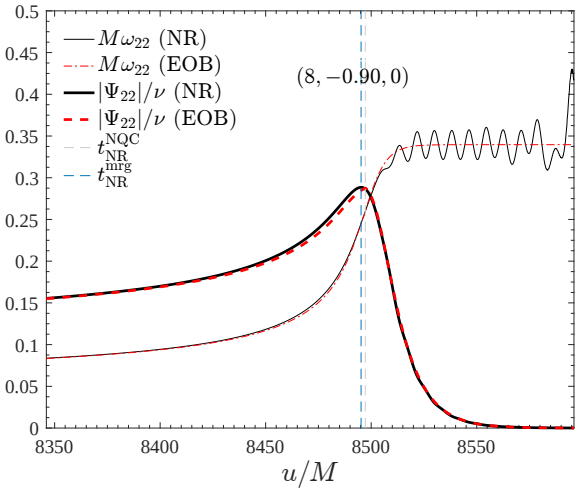

Figure 5.24: Complement to Fig. 5.23: excellent agreement between amplitude and frequency once the `TEOBResumS` and SXS waveforms are aligned around merger.

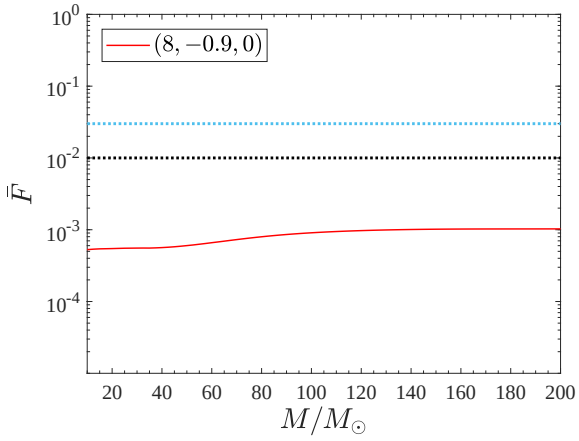

Figure 5.25: Unfaithfulness calculation for the system of Fig. 5.23. One finds that $\max(\bar{F}) = 0.001027$

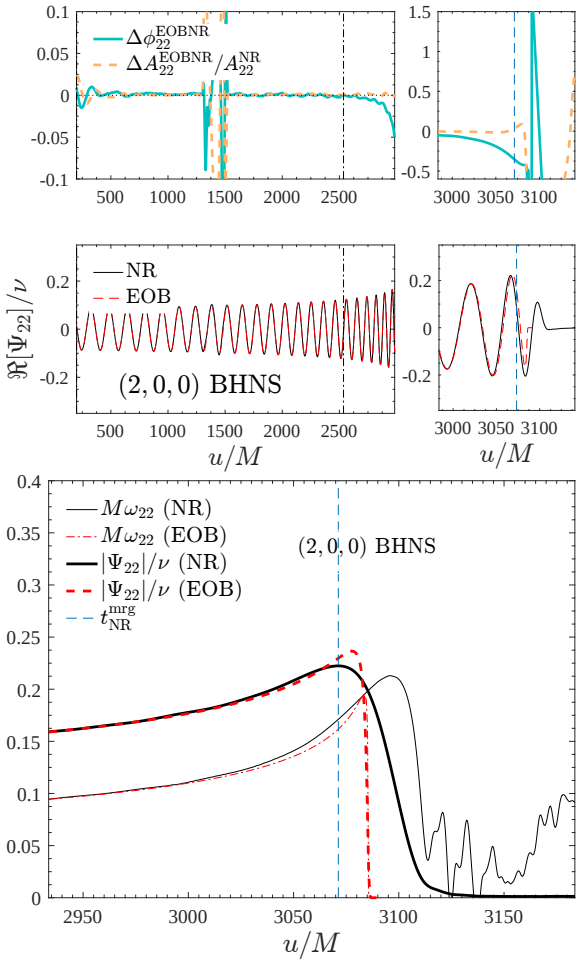

Figure 5.26: Phasing (left) and amplitude and frequency comparison (right) between `TEOBResumS` and BHNS:0002 waveform for a BHNS merger with mass ratio $q = 2$, with $M_B = 1.4M_\odot$. Reference [212] indicates that the accumulated phase errors to merger are about$\sim \pm 0.5$ rad. The `TEOBResumS` tidal waveform is well consistent with the NR one up to merger, even in the presence of tidal disruption.

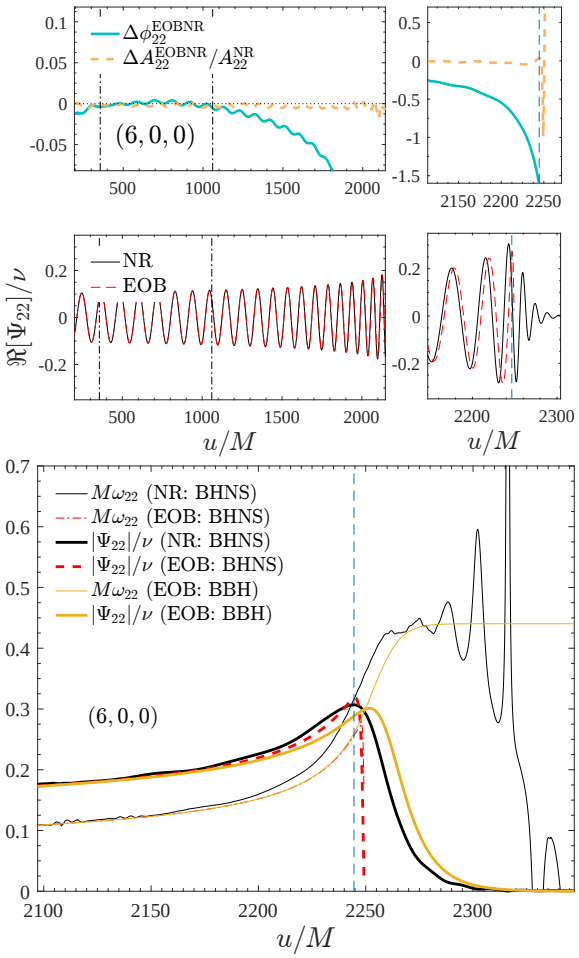

Figure 5.27: Left panel: `TEOBResumS` and NR phasing for BHNS:0001, with $q = 6$ and $M_B = 1.4M_\odot$. A phase difference of $\simeq -1.6$ rad is accumulated up to merger. Right panel: frequency and amplitude plot. The orange line corresponds to the `TEOBResumS` BBH (point-mass, no tides) waveform completed with NQC corrections and ringdown. Note that the frequency growth with tides (red-dashed) is almost indistinguishable from the corresponding curve without tides.

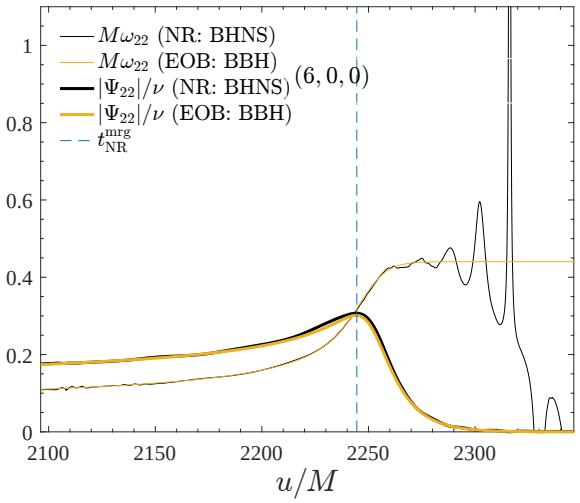

Figure 5.28: Comparison between SXS BHNS waveform (black) with the `TEOBResumS` BBH waveform (orange) *without* tides. Waveforms are aligned around merger. The suppression of the tidal interaction due to the effect of the large mass ratio is such that very little differences between the frequency and amplitude are seen.

Chapter 6

Nonlinear-in-spin effects in EOB waveform models of spin-aligned inspiralling BNS [2]

6.1 Introduction

Gravitational wave (GW) signals of BNS can be used to put constraints on the equation of state (EOS) of degenerate matter in these extreme environments. In fact, when a NS is part of a binary system, their mutual tidal interaction deform the stars, affecting the dynamics of the system and the emitted GWs. On August 17, 2017, the first binary neutron star (BNS) inspiral has been detected by the LIGO-Virgo interferometers [43]. One of the important outcomes of this discovery was the measurement of the neutron star radii and EOS from the GW signal [210, 211] obtained by extracting from the data the tidal polarizabilities (or deformabilities) related to the NS Love numbers [227, 229, 108, 243].

When NSs are spinning, the rate of the inspiral can be modified by an additional EOS-dependent effect, since each NS acquires a quadrupole moment due to its own rotation, as explained in Sec. 5.4. The importance of such spin-induced-monopole-quadrupole effects on BNS inspirals was pointed out long ago [134] and recently revived [135] in a data-analysis context, emphasizing that it is important to incorporate such self-spin terms in BNS

waveform templates to avoid parameter biases in the case of highly spinning BNS systems. In addition, it was also recently pointed out that self-spin effects might be useful to test the binary black hole nature of the compact objects [282, 283]. Consistently with these findings, the analysis of GW170817 was done with waveform models that *do* include EOS-dependent self-spin effects. These were incorporated in resummed form in the `SEOBNRv4T` [213] and `TEOBResumS` [1] effective one body (EOB) models and in TaylorF2-like post-Newtonian (PN) form in the `PhenomPv2NRTidal` model [260, 209]. Both descriptions have their drawbacks and can be improved. On the one hand, the `PhenomPv2NRTidal` description is incorporating self-spin terms up to next-to-leading order (NLO), but it is biased by the fact that the PN approximation breaks down at some stage in the relativistic regime close to merger. On the other hand, the EOB description is robust up to merger, but only the leading order (LO) self-spin effects (both in the EOB Hamiltonian and flux) were included in the models. Although one of the main results of Ref. [209] was to show good consistency between `TEOBResumS` and `PhenomPv2NRTidal`, this was not a precise apple-with-apple comparison because of the additional NLO self-spin effects included in `PhenomPv2NRTidal` and not in `TEOBResumS`. Furthermore `TEOBResumS` actually takes into account an infinite number of self-spin tail terms (in the waveform and flux), that are absent in `PhenomPv2NRTidal`, so that the precise question about which model is analytically more complete requires an elaborate study. In particular, none of the current waveform models that use a 3.5PN-accurate inspiral description (like TaylorF2 or `PhenomPv2NRTidal` [209]) are using the EOS-dependent 3.5PN-accurate self-spin tail term, although it is available analytically [1]. Such a term can be obtained by suitably expanding the EOB energy and flux along circular orbits, adapting the procedure of Ref. [11] (see also [243]), that allowed one to cross check the 4.5PN, nonspinning, tail term in the flux formerly obtained from an *ab initio* PN calculation [74]. Finally, we mention that state-of-the-art NR simulations of coalescing BNSs [284, 240, 263, 206, 285, 259, 286] are currently barely able to resolve spin-quadratic effects close to merger [287, 268] and are too short to measure their cumulative effect during many inspiral orbits. As a consequence, we can only rely on analytical models for their description for LIGO/Virgo targeted analyses.

The purpose of this work is then to address and answer the questions that remained open in Refs. [1, 209]. We do so by extending the EOS-dependent self-spin sector of `TEOBResumS` to NLO and next-to-next-to-leading order

(NNLO), suitably recasting in EOB form recent PN calculations of Levi and Steinhoff [288, 289, 136]. For simplicity, this is done in the circular approximation by exploiting the gauge-invariant relation between energy and angular momentum rather than by deriving the explicit canonical transformation that maps the Arnowitt-Deser-Misner (ADM) Hamiltonian [290] into the EOB Hamiltonian. This new knowledge allows us to produce a consistent phasing comparison with the TaylorF2 approximant. We find that the phase accelerating effect of the spin-induced quadrupole moment terms is *enhanced* by the NLO contribution, although the magnitude of the effect as predicted by `TEOBResumS` is always *smaller* than in the corresponding TaylorF2 description. Remarkably, a TaylorF2 approximant that also incorporates the LO self-spin tail effect yields a self-spin phasing that is essentially equivalent to the NLO `TEOBResumS` one up to frequency $M\omega \simeq 0.05$ independently of the EOS choice. We also show that the LO quartic-in-spin effects entering the circularized Hamiltonian recently computed by Levi and Steinhoff [136] are already contained in the `TEOBResumS` Hamiltonian of Ref. [159] in the black-hole (BH) case, due to the use of the centrifugal radius. The corresponding correction to the centrifugal radius yielded by the octupolar and hexadecapolar EOS-dependent spin-induced effects (in the non binary BH case) is explicitly obtained.

6.2 Nonlinear-in-spin effects within TEOBResumS

The EOS-dependent self-spin contribution at LO in `TEOBResumS` was discussed extensively in Sec. 5.3.2. We consider binary systems in which the two bodies are labeled by (A, B). Their masses and dimensional spins are denoted $M_{A,B}$ (with $M_A \geq M_B$) and $S_{A,B} \equiv M_{A,B} a_{A,B}$ respectively. The total mass is $M = M_A + M_B$ and the reduced mass $\mu = (M_A M_B)/M$. We also remind the reader the following notation: the mass ratio $q \equiv M_A/M_B \geq 1$, the symmetric mass ratio $\nu = \mu/M$, the mass fractions $X_{A,B} \equiv M_{A,B}/M$ and the shorthand $X_{AB} \equiv X_A - X_B = \sqrt{1-4\nu}$. Finally, we make use of the dimensionless spin variables $\tilde{a}_i \equiv a_i/M \equiv S_i/(M_i M)$ together with their symmetric and antisymmetric combinations[1] $\tilde{a}_0 = \tilde{a}_A + \tilde{a}_B$ and $\tilde{a}_{AB} = \tilde{a}_A - \tilde{a}_B$.

[1]Note the difference between $\tilde{a}_i \equiv a_i/M$ and the usually introduced dimensionless spin $\hat{a}_i \equiv \chi_i \equiv a_i/M_i$. Note also that in Refs [9, 4, 1] we had denoted $\tilde{a}_0$ as $\hat{a}_0$.

6.2.1 Hamiltonian: quadratic-in-spin terms

In `TEOBResumS` [217, 1], which is limited to the case of spin-aligned (non-precessing) binaries, spin-quadratic effects are treated introducing the "centrifugal radius" r_c, considered as a function of the Boyer-Lindquist-type EOB radial variable r, and of the spin variables. For BBHs, the function $r_c(r, \tilde{a}_A, \tilde{a}_B)$ incorporates both LO and NLO spin-quadratic effects [160, 161, 217]; by contrast only LO spin-quadratic effects were considered for extended objects like NSs [1]. We hence start by generalizing the expression of the centrifugal radius in order to take into account both NLO and NNLO, EOS-dependent, self-spin effects, exploiting the PN-expanded results of Refs. [288, 289, 136]. The generalized formula for the centrifugal radius (4.26) that formally takes into account both NLO and NNLO spin-quadratic effects reads

$$r_c^2(r, \tilde{a}_A, \tilde{a}_B)^{\rm NNLO} = r^2 + \tilde{a}_Q^2 \left(1 + \frac{2}{r}\right) + \frac{\delta a^2_{\rm NLO}}{r} + \frac{\delta a^2_{\rm NNLO}}{r^2}, \tag{6.1}$$

where we are using a dimensionless radial coordinate $r \equiv \frac{R}{M}$, and we introduced the effective spin variable

$$\tilde{a}_Q^2 \equiv C_{QA}\tilde{a}_A^2 + 2\tilde{a}_A\tilde{a}_B + C_{QB}\tilde{a}_B^2. \tag{6.2}$$

C_{QA} and C_{QB} are coefficients that parametrize the quadrupolar deformation acquired by the NSs due to their own rotation. For binary black holes, $C_{Qi} = 1$, so $\tilde{a}_Q^2$ reduces to $\tilde{a}_0^2$. The parameters $\delta a^2_{\rm NLO}$ and $\delta a^2_{\rm NNLO}$ encode the NLO and NNLO spin-spin information respectively. As mentioned above, working in the circular approximation for simplicity, we compute them exploiting the functional relation between binding energy and orbital angular momentum, that is explicitly given, in PN-expanded form, in Refs. [288, 289, 136]. In practice, one computes the PN-expanded EOB dynamics along circular orbits, that will explicitly depend on $(\delta a^2_{\rm NLO}, \delta a^2_{\rm NNLO})$, and then fixes these coefficients by comparison with the PN-expanded relation of Ref. [136].

The main elements of the Hamiltonian of `TEOBResumS` that are useful for this calculation are augmented in detail in Sec. 4.2. Since we are considering nonprecessing systems, the dynamics is described by the dimensionless phase-space variables $(r, p_{r_*}, \varphi, p_\varphi)$. We use φ to denote the orbital phase, while the (dimensionless) radial and angular momentum are respectively defined as $p_{r_*} = P_{R_*}/\mu$ and $p_\varphi = P_\varphi/(\mu M)$. The μ-rescaled EOB Hamiltonian

is given by Eq. (4.19). The explicit expressions of (G_S, G_{S_*}) can be found in Refs. [162, 217]. These expression only retain, in the spin-orbit part of the Hamiltonian, terms that are *linear* in the spins. However, the complete `TEOBResumS` model is based on the prescription of Refs. [159, 34, 1] to effectively incorporate, in resummed form, also higher odd-powers of the spins (spin-cubed, spin^5 etc.) by suitably replacing the u-dependence of the functions (G_S, G_{S_*}) with dependence on u_c. We shall see in Sec. 6.2.2 below that `TEOBResumS` delivers a reasonable approximation to the actual LO spin-cubic part of the ADM Hamiltonian of Ref. [136]. In Sec. 6.5 we give possible EOB transcriptions of the results of [136].

The orbital part of the effective Hamiltonian is given by Eq. (4.24). Here A is the effective metric potential, whose PN expansion in the non-spinning limit is given by Eq. (4.15), with coefficients (4.12), (4.16) and (4.17). In `TEOBResumS`, this effective metric is resummed using a Padé approximant, namely (4.18). When spins are present, the metric is built upon the Kerr one and reads

$$A(u; S_i) = \frac{1+2u_c}{1+2u} A_{\rm orb}(u_c). \tag{6.3}$$

We hence start considering circular orbits ($p_{r_*} = 0$) and compute the circular angular momentum, j, using the condition $\partial_u \hat{H}_{\rm eff} = 0$, that yields the following equation

$$\begin{aligned} &\left\{ \left[\left(A u_c^2\right)' \right]^2 - 4 A u_c^2 \left(\tilde{G}'\right)^2 \right\} j^4 \\ &+ \left[2A' \left(A u_c^2\right)' - 4A \left(\tilde{G}'\right)^2 \right] j^2 + \left(A'\right)^2 = 0, \end{aligned} \tag{6.4}$$

where the prime indicates $(\cdot)' \equiv \partial_u (\cdot)$. By expanding the solution of Eq. (6.4)

in series of u and up to the second order in spin one obtains

$$
\begin{aligned}
j(u) = \frac{1}{\sqrt{u}} &+ \frac{3}{2}\sqrt{u} - \frac{3}{8}\left(7\tilde{a}_0 + X_{AB}\tilde{a}_{AB}\right)u + \left[\frac{27}{8} - \frac{3}{2}\nu + \tilde{a}_Q^2\right]u^{3/2} \\
&+ \left[\left(-\frac{87}{16} + \frac{11}{8}\nu\right)\tilde{a}_0 - \left(\frac{33}{16} + \frac{1}{8}\nu\right)X_{AB}\tilde{a}_{AB}\right]u^2 \\
&+ \left[\frac{135}{16} + \left(-\frac{433}{12} + \frac{41}{32}\pi^2\right)\nu + \frac{441}{128}\tilde{a}_0^2 + \frac{1}{2}\tilde{a}_Q^2 + \left(\frac{9}{128} - \frac{9}{32}\nu\right)\tilde{a}_{AB}^2\right. \\
&\left. + \frac{63}{64}X_{AB}\tilde{a}_0\tilde{a}_{AB} + \frac{5}{4}\delta a_{\mathrm{NLO}}^2\right]u^{5/2} \\
&+ \left[\left(-\frac{63}{4} + \frac{505}{16}\nu + \frac{25}{64}\nu^2\right)\tilde{a}_0 + \left(-\frac{63}{8} + \frac{55}{16}\nu - \frac{5}{64}\nu^2\right)X_{AB}\tilde{a}_{AB}\right]u^3 \\
&+ \left[\frac{2835}{128} - \left(\frac{3029}{120} + 32\gamma + \frac{3503}{2048}\pi^2 + 64\log(2) + 16\log(u)\right)\nu + \left(\frac{539}{12} - \frac{205}{128}\pi^2\right)\nu^2\right. \\
&+ \left(\frac{4095}{256} - \frac{231}{64}\nu\right)\tilde{a}_0^2 - \left(\frac{9}{8} - \frac{9}{4}\nu\right)\tilde{a}_Q^2 + \left(\frac{207}{256} - \frac{51}{16}\nu - \frac{3}{16}\nu^2\right)\tilde{a}_{AB}^2 \\
&\left. + \left(\frac{1017}{128} - \frac{3}{16}\nu\right)X_{AB}\tilde{a}_0\tilde{a}_{AB} - \frac{19}{8}\delta a_{\mathrm{NLO}}^2 + \frac{3}{2}\delta a_{\mathrm{NNLO}}^2\right]u^{7/2} + \mathcal{O}\left[u^4\right].
\end{aligned}
\tag{6.5}
$$

This truncated series can be inverted so to obtain $u(j)$, which reads

$$
\begin{aligned}
u(j) = & \frac{1}{j^2} + \frac{3}{j^4} - \frac{3}{4}\left(7\tilde{a}_0 + X_{AB}\tilde{a}_{AB}\right)\frac{1}{j^5} + \left(18 - 3\nu + 2\tilde{a}_Q^2\right)\frac{1}{j^6} \\
& + \left[\left(-\frac{465}{8} + \frac{11}{4}\nu\right)\tilde{a}_0 - \left(\frac{87}{8} + \frac{\nu}{4}\right)X_{AB}\tilde{a}_{AB}\right]\frac{1}{j^7} \\
& + \left[135 + \left(-\frac{311}{3} + \frac{41}{16}\pi^2\right)\nu + \frac{441}{8}\tilde{a}_0^2 + 22\tilde{a}_Q^2 + \left(\frac{9}{8} - \frac{9}{2}\nu\right)\tilde{a}_{AB}^2\right. \\
& \left. + \frac{63}{4}X_{AB}\tilde{a}_0\tilde{a}_{AB} + \frac{5}{2}\delta a_{\rm NLO}^2\right]\frac{1}{j^8} \\
& + \left[\left(-\frac{1269}{2} + \frac{1273}{8}\nu + \frac{25}{32}\nu^2\right)\tilde{a}_0 + \left(-\frac{531}{4} + \frac{103}{8}\nu - \frac{5}{32}\nu^2\right)X_{AB}\tilde{a}_{AB}\right]\frac{1}{j^9} \\
& + \left[1134 - \left(\frac{163063}{120} + 64\gamma - \frac{31921}{1024}\pi^2 + 128\log(2) + 64\log\left(1/j\right)\right)\nu + \left(\frac{1321}{12} - \frac{205}{64}\pi^2\right)\nu^2\right. \\
& + \left(\frac{9009}{8} - \frac{1155}{16}\nu\right)\tilde{a}_0^2 + \left(234 - \frac{45}{2}\nu\right)\tilde{a}_Q^2 + \left(\frac{261}{8} - \frac{2073}{16}\nu - \frac{15}{4}\nu^2\right)\tilde{a}_{AB}^2 \\
& \left. + \left(\frac{1557}{4} - \frac{15}{4}\nu\right)X_{AB}\tilde{a}_0\tilde{a}_{AB} + 29\ \delta a_{\rm NLO}^2 + 3\ \delta a_{\rm NNLO}^2\right]\frac{1}{j^{10}} + \mathcal{O}\left[j^{-11}\right].
\end{aligned}
\tag{6.6}
$$

By placing this expanded expression of u into the EOB Hamiltonian, one can finally obtain the gauge-invariant relation between the binding energy and angular momentum. The binding energy per reduced mass is in fact defined as $E_b = (E - M)/\mu$, where $E = \nu\hat{H}_{\rm EOB}$, and is given as a polynomial in inverse powers of j, i.e.,

$$
E_b(j) = -\frac{1}{2j^2}\left(1 + \sum_{n=1}^{8}\frac{c_n}{j^n} + \mathcal{O}\left[j^{-9}\right]\right). \tag{6.7}
$$

Explicitly, from the expansion of the EOB Hamiltonian along circular orbits we get

$$
\begin{aligned}
E_b(j) = &-\frac{1}{2j^2}\Bigg\{1+\frac{1}{4}(9+\nu)\frac{1}{j^2}-\frac{1}{2}\left(7\tilde{a}_0+X_{AB}\tilde{a}_{AB}\right)\frac{1}{j^3}\\
&+\frac{1}{8}\left[81-7\nu+\nu^2+8\tilde{a}_Q^2\right]\frac{1}{j^4}-\frac{3}{8}\left[(81+\nu)\,\tilde{a}_0+(15+\nu)\,X_{AB}\tilde{a}_{AB}\right]\frac{1}{j^5}\\
&+\left[\frac{3861}{64}-\left(\frac{8833}{192}-\frac{41}{32}\pi^2\right)\nu-\frac{5}{32}\nu^2+\frac{5}{64}\nu^3+\frac{441}{16}\tilde{a}_0^2\right.\\
&\left.+\left(\frac{17}{2}+\frac{\nu}{2}\right)\tilde{a}_Q^2+\left(\frac{9}{16}-\frac{9}{4}\nu\right)\tilde{a}_{AB}^2+\frac{63}{8}X_{AB}\tilde{a}_0\tilde{a}_{AB}+\delta a_{\rm NLO}^2\right]\frac{1}{j^6}\\
&+\frac{1}{16}\left[\left(-4293+822\nu-5\nu^2\right)\tilde{a}_0+\left(-891+42\nu-5\nu^2\right)X_{AB}\tilde{a}_{AB}\right]\frac{1}{j^7}\\
&+\left[\frac{53703}{128}-\left(\frac{989911}{1920}+\frac{128}{5}\gamma-\frac{6581}{512}\pi^2+\frac{256}{5}\log(2)+\frac{128}{5}\log\left(1/j\right)\right)\nu\right.\\
&+\left(\frac{8875}{384}-\frac{41}{64}\pi^2\right)\nu^2-\frac{3}{64}\nu^3+\frac{7}{128}\nu^4+\left(\frac{14679}{32}-\frac{385}{32}\nu\right)\tilde{a}_0^2\\
&+\left(\frac{603}{8}-\frac{29}{8}\nu+\frac{3}{8}\nu^2\right)\tilde{a}_Q^2+\left(\frac{423}{32}-\frac{1669}{32}\nu-\frac{23}{8}\nu^2\right)\tilde{a}_{AB}^2\\
&\left.+\left(\frac{2529}{16}+\frac{53}{16}\nu\right)X_{AB}\tilde{a}_0\tilde{a}_{AB}+\left(\frac{19}{2}+\frac{\nu}{2}\right)\delta a_{\rm NLO}^2+\delta a_{\rm NNLO}^2\right]\frac{1}{j^8}+\mathcal{O}\left[j^{-9}\right]\Bigg\},
\end{aligned}
\tag{6.8}
$$

where we see that the c_6 and c_8 coefficients explicitly depend on $\delta a_{\rm NLO}^2$ and $\delta a_{\rm NNLO}^2$. The corresponding quantities in Eq. (5.3) of Ref. [289], once expressed in our spin variables[2], explicitly read

[2]Note that Ref. [289] uses as dimensionless spin variables some quantities, $S_i^{\rm L-S}$, that correspond to our $S_i/(M_A M_B)$. Furthermore, their deformation coefficients are denoted by $(C_{ES^2}, C_{BS^3}, C_{ES^4})$, in order to highlight the spin order and their electric/magnetic behavior. In our convention, they correspond to $(C_Q, C_{\rm Oct}, C_{\rm Hex})$ respectively, which puts the emphasis on the multipole of the deformation. We also note that the λ constants by Marsat (see Sec. B of Ref. [76]) are the same as Levi and Steinhoff's C_{BS^3} and our $C_{\rm Oct}$'s.

$$\left(c_6^{\rm SS}\right)^{\rm L-S} = \frac{1}{16}\Bigg\{ \left(375+8\nu\right)\tilde{a}_0^2 + 8\left(-23+\nu\right)\tilde{a}_Q^2 + \left(7-52\nu\right)\tilde{a}_{AB}^2 + X_{AB}\left[130\ \tilde{a}_0\tilde{a}_{AB} + 16\left(C_{QA}\tilde{a}_A^2 - C_{QB}\tilde{a}_B^2\right)\right]\Bigg\}, \tag{6.9}$$

$$\left(c_8^{\rm SS}\right)^{\rm L-S} = \frac{1}{112}\Bigg\{ -\left(51369-2743\nu+21\nu^2\right)\tilde{a}_0^2 + \left(13182-1066\nu+42\nu^2\right)\tilde{a}_Q^2 - \left(5205+6292\nu+329\nu^2\right)\tilde{a}_{AB}^2 + X_{AB}\left[13\left(1380+7\nu\right)\tilde{a}_0\tilde{a}_{AB} + \left(1716+56\nu\right)\left(C_{QA}\tilde{a}_A^2 - C_{QB}\tilde{a}_B^2\right)\right]\Bigg\}. \tag{6.10}$$

Comparing Eqs. (6.9) and (6.10) to Eq. (6.8) one obtains

$$\delta a_{\rm NLO}^2 = -\frac{33}{8}\tilde{a}_0^2 + 3\tilde{a}_Q^2 - \frac{1}{8}\left(1+4\nu\right)\tilde{a}_{AB}^2 + X_{AB}\left[\frac{1}{4}\tilde{a}_0\tilde{a}_{AB} + \left(C_{QA}\tilde{a}_A^2 - C_{QB}\tilde{a}_B^2\right)\right], \tag{6.11}$$

and

$$\delta a_{\rm NNLO}^2 = -\left(\frac{4419}{224}+\frac{1263}{224}\nu\right)\tilde{a}_0^2 + \left(\frac{387}{28}-\frac{207}{28}\nu\right)\tilde{a}_Q^2 + \left(\frac{11}{32}-\frac{127}{32}\nu+\frac{3}{8}\nu^2\right)\tilde{a}_{AB}^2 + X_{AB}\Bigg[-\left(\frac{29}{112}+\frac{21}{8}\nu\right)\tilde{a}_0\tilde{a}_{AB} + \frac{163}{28}\left(C_{QA}\tilde{a}_A^2 - C_{QB}\tilde{a}_B^2\right)\Bigg]. \tag{6.12}$$

Binary black hole limit

The BH case is recovered imposing $C_{QA} = C_{QB} = 1$ or, equivalently, $\tilde{a}_Q^2 = \tilde{a}_0^2$ and $(C_{QA}\tilde{a}_A^2 - C_{QB}\tilde{a}_B^2) = \tilde{a}_0\tilde{a}_{AB}$. This yields

$$\delta a^2_{\rm BBH\,NLO} = -\frac{9}{8}\tilde{a}_0^2 - \frac{1}{8}(1+4\nu)\,\tilde{a}_{AB}^2 + \frac{5}{4}X_{AB}\tilde{a}_0\tilde{a}_{AB}, \tag{6.13}$$

$$\begin{aligned}\delta a^2_{\rm BBH\,NNLO} = &-\left(\frac{189}{32}+\frac{417}{32}\nu\right)\tilde{a}_0^2 \\ &+\left(\frac{11}{32}-\frac{127}{32}\nu+\frac{3}{8}\nu^2\right)\tilde{a}_{AB}^2 \\ &+\left(\frac{89}{16}-\frac{21}{8}\nu\right)X_{AB}\tilde{a}_0\tilde{a}_{AB}.\end{aligned} \tag{6.14}$$

Eq. (6.13) agrees with the result for the same quantity obtained in Ref. [217] (see Eq. (60) there) with a different method (see also [249]). The impact of the newly computed $\delta a^2_{\rm NNLO}$ in BBH systems will be analyzed elsewhere.

6.2.2 Hamiltonian: cubic-in-spin terms already included in `TEOBResumS`

The LO cubic-in-spin contribution to the PN-expanded Hamiltonian (and thus on the $E_b(j)$ curve) was derived in Ref. [289]. This contribution is not fully incorporated in the current version of `TEOBResumS`. However, one should be aware that some cubic-in-spin terms *are already included* in the model, because they naturally arise due to the presence of u_c in the gyro-gravitomagnetic functions G_S and G_{S_*} that enter the spin-orbit sector of the Hamiltonian (see Sec. 6.2.1). It is then interesting to check how these terms, that are guessed by the resummed structure of the Hamiltonian, do compare with the exact result of Ref. [289]. We now redo the calculations of Sec. 6.2.1, this time keeping the cubic-in-spin terms, whose LO enters in the coefficient of j^{-9} in the gauge-invariant relation $E_b(j)$. In `TEOBResumS`, the former is given by

$$\left(c_7^{S^3_{\rm LO}}\right)^{\texttt{TEOBResumS}} = -\left(\frac{67}{4}\tilde{a}_0 + \frac{13}{4}X_{AB}\tilde{a}_{AB}\right)\tilde{a}_Q^2. \tag{6.15}$$

By contrast, the PN-expanded result from Ref. [289] reads

$$\begin{aligned}\left(c_7^{S^3_{\rm LO}}\right)^{\rm L-S} =& -\left(2C_{{\rm Oct}A}+15C_{QA}+3X_{AB}C_{QA}\right)\tilde{a}_A^3\\ &-\left[30+21C_{QA}+X_{AB}\left(6-3C_{QA}\right)\right]\tilde{a}_A^2\tilde{a}_B\\ &-\left[30+21C_{QB}-X_{AB}\left(6-3C_{QB}\right)\right]\tilde{a}_A\tilde{a}_B^2\\ &-\left(2C_{{\rm Oct}B}+15C_{QB}-3X_{AB}C_{QB}\right)\tilde{a}_B^3, \end{aligned} \tag{6.16}$$

which is qualitatively different from Eq. (6.15) above because of the presence of the spin-induced octupolar moments $C_{{\rm Oct}A,B}$. Comparing Eqs. (6.15) and (6.16), we see that `TEOBResumS` does not automatically predict (through the definition Eqs. (6.1), (6.2) used to incorporate spin-quadratic couplings) the needed PN LO spin-cubic terms. We have, however, checked that the coefficients entering the two expressions are numerically sufficiently close to lead to nearly equivalent physical predictions. This is especially evident in the BBH case when $C_{{\rm Oct}A,B}=C_{QA,B}=1$. In this case the above equations read

$$\left(c_7^{S^3_{\rm LO}}\right)^{\texttt{TEOBResumS}} = -\left(\frac{67}{4}\tilde{a}_0+\frac{13}{4}X_{AB}\tilde{a}_{AB}\right)\tilde{a}_0^2, \tag{6.17}$$

$$\left(c_7^{S^3_{\rm LO}}\right)^{\rm L-S} = -\left(17\tilde{a}_0+3X_{AB}\tilde{a}_{AB}\right)\tilde{a}_0^2, \tag{6.18}$$

with a fractional difference of $1/68\approx 1.47\%$ between the first coefficients and $1/12\approx 8.3\%$ for second ones. In practice, the Hamiltonian of `TEOBResumS` incorporates this approximate description of cubic-in-spin terms, as well as higher-order odd powers of the spins due to its resummed structure. In Appendix 6.5 we propose possible EOB transcriptions of the full cubic-in-spin information of Ref. [289].

6.2.3 Hamiltonian: quartic-in-spin terms

The quartic-in-spin contribution to the PN-expanded $E_b(j)$ curve was also computed by Levi and Steinhoff [136]. This corresponds to a 4PN effect, i.e., it enters at order $1/j^{10}$. We can thus slightly modify the procedure of Sec. 6.2.1 above so to apply it also to the recovery of the spin-quartic EOS-dependent terms. We introduce a new parameter $\delta a^4_{\rm LO}$ in the definition of r_c^2 that now reads

$$r_c^2 = r^2+\tilde{a}_Q^2\left(1+\frac{2}{r}\right)+\frac{\delta a^2_{\rm NLO}}{r}+\frac{\delta a^2_{\rm NNLO}}{r^2}+\frac{\delta a^4_{\rm LO}}{r^2}. \tag{6.19}$$

We then proceed and compute the same formulas we showed before consistently keeping all the quartic-in-spin term. The LO quartic-in-spin term, $O(1/j^8)$ in $E_b(j)$ reads

$$\left(c_8^{S^4_{\rm LO}}\right)^{\texttt{TEOBResumS}} = 3\tilde{a}_Q^4 + \delta a^4_{\rm LO}. \tag{6.20}$$

The corresponding term from Ref. [288] reads

$$\begin{aligned}\left(c_8^{S^4_{\rm LO}}\right)^{\rm L-S} = &\frac{3}{4}\left(3C_{QA}^2 + C_{{\rm Hex}A}\right)\tilde{a}_A^4 \\ &+ 3\left(3C_{QA} + C_{{\rm Oct}A}\right)\tilde{a}_A^3\tilde{a}_B \\ &+ 9\left(C_{QA}C_{QB} + 1\right)\tilde{a}_A^2\tilde{a}_B^2 \\ &+ 3\left(3C_{QB} + C_{{\rm Oct}B}\right)\tilde{a}_A\tilde{a}_B^3 \\ &+ \frac{3}{4}\left(3C_{QB}^2 + C_{{\rm Hex}B}\right)\tilde{a}_B^4,\end{aligned} \tag{6.21}$$

where $C_{\rm Oct}$ and $C_{\rm Hex}$ are the spin-induced octupolar and hexadecapolar moments quoted above. From these two equation one obtains

$$\begin{aligned}\delta a^4_{\rm LO} = &\frac{3}{4}\left(C_{{\rm Hex}A} - C_{QA}^2\right)\tilde{a}_A^4 \\ &+ 3\left(C_{{\rm Oct}A} - C_{QA}\right)\tilde{a}_A^3\tilde{a}_B \\ &+ 3\left(C_{QA}C_{QB} - 1\right)\tilde{a}_A^2\tilde{a}_B^2 \\ &+ 3\left(C_{{\rm Oct}B} - C_{QB}\right)\tilde{a}_A\tilde{a}_B^3 \\ &+ \frac{3}{4}\left(C_{{\rm Hex}B} - C_{QB}^2\right)\tilde{a}_B^4.\end{aligned} \tag{6.22}$$

To our knowledge C_Q and $C_{\rm Oct}$ have been calculated using numerical approaches [291, 292, 293]; by contrast, current knowledge about $C_{\rm Hex}$ relies on both the slow-rotation approximation (if the NS dimensionelss spin is smaller than 0.3) and on numerical calculations otherwise [294]. All this knowledge (notably recasted in terms of EOS quasi-universal relations [253, 137, 294] with the NS Love numbers [227, 106, 110, 108, 233]) allows us to evaluate also the impact $\delta a^4_{\rm LO}$ on the BNS phasing. Before doing so, we note that in the BH limit (when $C_Q = C_{\rm Oct} = C_{\rm Hex} = 1$) $\delta a^4_{\rm LO}$ vanishes. It is remarkable that the resummed EOB Hamiltonian, thanks to the use of the deformed Kerr structure provided by the EOB centrifugal radius [159], is proven to correctly incorporate, at the LO, the quartic-in-spin behavior. We also point

out, in passing, that the same structure is present also in the EOB Hamiltonian of Refs. [276, 165, 177], and thus the quartic-in-spin terms at LO are also present in the `SEOBNRv4` corresponding EOB model [295]

6.2.4 Waveform and flux

Recently, Marsat and Bohé have also computed several terms quadratic in spin entering the post-Newtonian waveform [252]. Their work is yet unpublished, but they kindly gave us access to their most recent results. We report below the corresponding contributions to the factorized waveform amplitude, as the EOS-dependent generalization of Eqs. (39), (43), (44) and (45) of Ref. [4].

$$\rho_{22}^{\rm SS,LO} = \frac{1}{2}\tilde{a}_Q^2 x^2, \tag{6.23}$$

$$\begin{aligned}\rho_{22}^{\rm SS,NLO} =& \left\{ -\frac{187}{252}\tilde{a}_0^2 + \left(\frac{1}{7}+\frac{27}{56}\nu\right)\tilde{a}_Q^2 + \left(\frac{19}{252}-\frac{5}{18}\nu\right)\tilde{a}_{AB}^2 \right.\\ &\left. + X_{AB}\left[\frac{2}{9}\tilde{a}_0\tilde{a}_{AB} + \frac{55}{84}(C_{QA}\tilde{a}_A^2 - C_{QB}\tilde{a}_B^2)\right]\right\} x^3,\end{aligned} \tag{6.24}$$

$$\tilde{f}_{21}^{\rm SS,LO} = \left[-\frac{19}{8}\tilde{a}_0\tilde{a}_{AB} - (C_{QA}\tilde{a}_A^2 - C_{QB}\tilde{a}_B^2) + X_{AB}\left(-\tilde{a}_0^2 + \frac{3}{2}\tilde{a}_Q^2 - \frac{1}{8}\tilde{a}_{AB}^2\right)\right] x^2, \tag{6.25}$$

$$\tilde{f}_{31}^{\rm SS,LO} = \left[-4(C_{QA}\tilde{a}_A^2 - C_{QB}\tilde{a}_B^2) + \frac{3}{2}X_{AB}\tilde{a}_Q^2\right] x^2, \tag{6.26}$$

$$\tilde{f}_{33}^{\rm SS,LO} = \frac{3}{2}X_{AB}\tilde{a}_Q^2 x^2. \tag{6.27}$$

For this work, all these new terms (due to Marsat and Bohé) are incorporated in the flux and waveform of `TEOBResumS`.

Let us finally comment about the cubic-in-spin terms, that, at leading order, contribute to both the $\ell = m = 2$ and to the $\ell = 2$, $m = 1$ quadrupolar modes. The corresponding contribution to the flux was obtained by S. Marsat in Ref. [76]. In Ref. [4] this information (though restricted to the BBH case) was incorporated in the EOB waveform. Although the results of this paper are obtained by *omitting* such LO spin-cube contribution, let us write here the full terms entering ρ_{22}^S and $\tilde{f}_{21}^S$, that reduce to part of Eqs. (39) and (43)

of Ref. [4] in the black hole limit $C_{QA}=C_{QB}=C_{\mathrm{Oct}A}=C_{\mathrm{Oct}B}=1$.

$$\begin{aligned}\rho_{22}^{S^3} = &\left\{\left(\frac{19}{12}C_{QA}-C_{\mathrm{Oct}A}-\frac{1}{4}C_{QA}X_{AB}\right)\tilde{a}_A^3\right.\\ &+\left[\frac{19}{6}-\frac{17}{12}C_{QA}-\left(\frac{1}{2}-\frac{1}{4}C_{QA}\right)X_{AB}\right]\tilde{a}_A^2\tilde{a}_B\\ &+\left[\frac{19}{6}-\frac{17}{12}C_{QB}+\left(\frac{1}{2}-\frac{1}{4}C_{QB}\right)X_{AB}\right]\tilde{a}_A\tilde{a}_B^2\\ &\left.+\left(\frac{19}{12}C_{QB}-C_{\mathrm{Oct}B}+\frac{1}{4}C_{QB}X_{AB}\right)\tilde{a}_B^3\right\}x^{7/2}, \end{aligned} \tag{6.28}$$

$$\tilde{f}_{21}^{S^3} = \left(\frac{3}{2}\tilde{a}_0^2-\frac{3}{4}\tilde{a}_Q^2\right)\tilde{a}_{AB}\; x^{5/2}. \tag{6.29}$$

6.3 Post-Newtonian phasing description

6.3.1 Reminder on the the TaylorF2 phasing approximant

In the previous section, we have extensively discussed the spin-quadratic (and spin-quartic) contributions in both the Hamiltonian and waveform/flux of `TEOBResumS`. Inspecting the expressions for, e.g., $(\delta a^2_{\rm NLO}, \delta a^2_{\rm NNLO})$ one sees that there are several terms that involve (C_{QA}, C_{QB}) and thus take into account the effect due to the spin-induced quadrupole moments both in the dynamics and in the radiation (cf. Eqs. (8.62)-(6.27)). In this section, we move to the PN-based equivalents of these effects within the TaylorF2 phasing approximant [99], see Sec. 2.7. Although our final goal is to compare the effect of the spin-induced quadrupole moment in TaylorF2 and in `TEOBResumS`, here we aim at being as general as possible. So, for completeness we collect all currently available spin-dependent analytical information that allows us to push the complete spin sector of the TaylorF2 approximant up to 4PN accuracy. This means considering linear and quadratic-in-spin effects that also involve tail terms.

TaylorF2 (see Eq. (2.195)) is typically used at 3.5PN accuracy for the orbital and spin-orbit part, while the spin-spin part is limited to 3PN order. It was used in this form for GW data-analysis purposes (see, e.g., [210, 43]). The complete extension of the approximant at 4PN is currently not possible since the calculation of the ν-dependent part of the energy fluxes is currently

incomplete. However, there are higher-order terms in TaylorF2, those involving the tail terms, that are analytically known. For example, Ref. [11] showed how the 4.5PN-accurate term of the energy flux, that is a pure tail term, can be obtained exactly by PN-expanding the EOB energy flux. Applying the same procedure, one can have access to the 3.5PN-accurate, LO, spin-spin tail term as well as to the 4PN-accurate, NLO, spin-orbit tail term. The spin-spin and spin-orbit tail terms in the flux (and TaylorF2) are presented here for the first time. After the integration of Eq. (2.195) the 4PN-accurate spin-dependent part of the phasing reads

$$\Psi^{\rm F2}_{\rm 4PN,spin}(f) = 2\pi f t_c - \varphi_c - \frac{\pi}{4} + \frac{3}{128\nu}(\pi f M)^{-5/3} \sum_{i=0}^{8} \varphi_i (\pi f M)^{i/3}. \tag{6.30}$$

As mentioned above, the orbital (spin-independent) part has the same structure, but the 4PN term is currently incomplete, so we omit its discussion here. Following the procedure of Ref. [11], we construct the PN-expanded total energy flux starting from the EOB-resummed prescription [8]

$$\mathcal{F} = \sum_{\ell=2}^{\infty} \sum_{\ell=-m}^{m} F^{\rm Newt}_{\ell m} \hat{F}_{\ell m} \tag{6.31}$$

using the orbital dynamical information at the consistent PN order [269, 270, 271, 147, 64], the spin information given in Ref. [75] and the new spin waveform results computed by Marsat (Eqs. (18)-(22) from Sec. 6.2.4, [11, 4, 296]). The relation between the dynamics, the EOB residual relativistic amplitudes (which can be derived from the PN waveforms) and the flux is given in Ref. [8] (it is the square of Eq. (4.36), since the GW flux is the square of the waveform):

$$\hat{F}_{\ell m} = \left(S^{(\epsilon)}_{\rm eff}\right)^2 |T_{\ell m}|^2 (\rho_{\ell m})^{2\ell}. \tag{6.32}$$

In this equation, $S^{(\epsilon)}_{\rm eff}$ is the effective source, that is the effective EOB energy along circular orbits $\hat{E}_{\rm eff}(x) \equiv E_{\rm eff}/\mu$ when $\epsilon = 0$ ($\ell + m$=even) or the Newton-normalized orbital angular momentum when $\epsilon = 1$ ($\ell + m$=odd).

6.3.2 Extracting tail effects from the EOB resummed tail factor $T_{\ell m}$

Of crucial importance for our present purpose is the (complex) tail factor $T_{\ell m}$ that resums an infinite number of leading logarithms (see Sec. 2.4.1, 4.4 and Refs. [8, 278]). This factor automatically incorporates tail effects that can be extracted from it and added to the lower-order PN results.

Expanding the formula (6.32) multipole by multipole and then summing all the contributions up to $\ell = 4$, one obtains the following expression for the 3.5PN spin-quadratic tail term in the flux

$$\hat{\mathcal{F}}^{\rm SS,tail}_{\rm 3.5PN} = \left(8\tilde{a}_Q^2 + \frac{1}{8}\tilde{a}_{AB}^2\right)\pi\, x^{7/2}, \tag{6.33}$$

which reduces to Eq. (26) of Ref. [11] in the BH case, when $\tilde{a}_Q^2 = \tilde{a}_0^2$. Adding this new piece to Eq. (4.14) of Ref. [75], one obtains a full 3.5PN flux that is used, together with the energy given by Eq. (3.33) of the same reference, to compute the 3.5PN accurate spin-spin tail term at NLO (entering the φ_7 coefficient in Eq. (6.30), as detailed below) by solving the integral given by Eq. (2.195).

This resummed tail expansion procedure can be applied also to the spin-orbit analogue of the flux. As we did previously, the fact that the EOB-resummed tail amplitude $T_{\ell m}$ contains and infinite amount of PN information when expanded, using consistently the $\rho_{\ell m}$ and $\tilde{f}_{\ell m}$ information computed from Eqs. (8.62)-(6.27) and the point-mass ones from [4, 296], we can compute again Eq. (6.32), but this time, for what concerns the dynamics, we add to the orbital information of Refs. [147, 271, 270, 269] the spin-orbit one of Refs. [76, 297]. The spinning angular momentum at NLO in the spin-orbit coupling is given by Eq. (3.12) of Ref. [77]. This time we use the spin residual relativistic waveform amplitudes up to $\ell = 4$, and the purely orbital ones from $\ell = 5$ to $\ell = 7$, truncating at the right PN order being careful to account for the relative order of the Newtonian prefactors in the process (see Appendix of [4]). Like in Ref. [11], the $m =$ even flux information of the $\ell = 7$ multipoles is out of one PN order with respect to the result we are searching for, so can be neglected in this computation. The new result

obtained this way yields [3]

$$\mathcal{F}_{5\mathrm{PN}}^{\mathrm{SO,tail}} = \left[\left(\frac{220103}{1512}+\frac{8421757}{72576}\nu-\frac{9491453}{18144}\nu^2\right)\tilde{a}_0 + \left(\frac{55499}{3024}+\frac{1149163}{72576}\nu-\frac{4993897}{36288}\nu^2\right)X_{AB}\tilde{a}_{AB}\right]\pi x^5, \tag{6.34}$$

and gives access to the new 4PN spin-orbit terms in the φ_8 coefficient in the PN-SPA phase.

6.3.3 Final 4PN-accurate TaylorF2 phasing coefficients

The complete calculation, at 4PN-accuracy, gives

$$\varphi_3^{\mathrm{SO}} = \frac{94}{3}\tilde{a}_0+\frac{19}{3}X_{AB}\tilde{a}_{AB}, \tag{6.35}$$

$$\varphi_4^{\mathrm{SS}} = -50\tilde{a}_Q^2-\frac{5}{8}\tilde{a}_{AB}^2, \tag{6.36}$$

$$\varphi_5^{\mathrm{SO}} = -\left[1+\log\left(\pi f M\right)\right]\left[\left(\frac{554345}{2268}+\frac{55}{9}\nu\right)\tilde{a}_0+\left(\frac{6380}{81}+\frac{85}{9}\nu\right)X_{AB}\tilde{a}_{AB}\right], \tag{6.37}$$

$$\varphi_6^{\mathrm{SS;\ SO_{tail}}} = \pi\left(\frac{1880}{3}\tilde{a}_0+130X_{AB}\tilde{a}_{AB}\right)+\left(\frac{15635}{21}+120\nu\right)\tilde{a}_Q^2-\frac{5570}{9}\tilde{a}_0^2 - \left(\frac{40795}{2016}+\frac{1255}{36}\nu\right)\tilde{a}_{AB}^2+X_{AB}\left[-\frac{250}{9}\tilde{a}_0\tilde{a}_{AB}+\frac{2215}{12}\left(C_{QA}\tilde{a}_A^2-C_{QB}\tilde{a}_B^2\right)\right], \tag{6.38}$$

$$\varphi_7^{\mathrm{SS_{tail};\ SO}} = -\pi\left(400\tilde{a}_Q^2+\frac{15}{2}\tilde{a}_{AB}^2\right)+\left(-\frac{8980424995}{1524096}+\frac{6586595}{1512}\nu-\frac{305}{72}\nu^2\right)\tilde{a}_0 + \left(-\frac{7189233785}{3048192}+\frac{458555}{6048}\nu-\frac{5345}{144}\nu^2\right)X_{AB}\tilde{a}_{AB}, \tag{6.39}$$

$$\varphi_8^{\mathrm{SO_{tail}}} = \pi\left[1-\log\left(\pi f M\right)\right]\left[\left(\frac{2388425}{2268}-\frac{9925}{27}\nu\right)\tilde{a}_0+\left(\frac{1538855}{4536}-\frac{19655}{756}\nu\right)X_{AB}\tilde{a}_{AB}\right]. \tag{6.40}$$

[3] By PN consistency, this procedure yields lower PN spin-orbit terms that are well known in literature. Note also that the test-particle limit of (6.34) (in which $\tilde{a}_0=\tilde{a}_{AB}X_{AB}=\tilde{a}_A$) agrees with the result of Ref. [298], namely $\frac{23605}{144}\tilde{a}_A\pi x^5$.

No.	M_A	M_B	q	χ_A	χ_B	Λ_A	Λ_B	C_{QA}	C_{QB}	$M\omega_{\rm mrg}$	$\Delta^{\rm EOB}\phi$
SLy-q1-sA01-sB01	1.35	1.35	1	0.1	0.1	389.96	389.96	5.48	5.48	0.1344	−2.04
SLy-q1-sA005-sB005	1.35	1.35	1	0.05	0.05	389.96	389.96	5.48	5.48	0.13446	−0.51
SLy-q1.2-sA005-sA008	1.6573	1.354	1.224	0.05	0.08	382.7	1312.1	5.45	7.99	0.12155	−1.04
Ms1b-q1-sA01-sB01	1.35	1.35	1	0.1	0.1	1545	1545	8.40	8.40	0.10616	−3.06
Ms1b-q1-sA005-SB005	1.35	1.35	1	0.05	0.05	1545	1545	8.40	8.40	0.10616	−0.76
H4-q1.25-sA005-sB008	1.91	1.528	1.25	0.05	0.08	499.6	1986	5.92	9.06	0.11508	−1.08

Table 6.1: BNS configurations used in this section. From left to right the columns report: the name of the configurations; the individual masses; the mass ratio; the individual spins, tidal parameters and spin-induced quadrupole moments, that are obtained with the universal relations of [253, 137]. Then, $M\omega_{\rm mrg}$ denotes the dimensionless GW frequency at the EOB BNS merger, conventionally defined as the peak of the $\ell = m = 2$ waveform amplitude. The last column lists the accumulated phase from 10 Hz to BNS merger due to the presence of the self-spin effects. For obtaining these numbers only the NLO self-spin terms, both in waveform and Hamiltonian, were included in `TEOBResumS`.

In the above equations, we have explicitly emphasized in the definition of each term its spin-orbit, spin-spin or spin-tail character. Note that φ_6 and φ_7 receive contributions from both tail and non-tail terms. The $(\varphi_7^{\rm SS_{tail}}, \varphi_8^{\rm SO_{tail}})$ terms are computed here from the first time.

6.3.4 Isolating the EOS-dependent quadrupole-monopole terms

From the result above we can finally isolate the EOS-dependent quadrupole-monopole terms (i.e., those proportional to C_{Qi}). These terms are the main focus of the present paper. Multiplying by the Newtonian prefactor (see Sec. 5.4) one obtains, at 3.5PN order, the quadratic-in-spin phase (5.29), which is the sum of the LO, NLO and NNLO contributions (5.30) (5.31) (5.32).

Following previous practice (see Chapt. 5.4) we do so by the Q_ω function (5.34). The integral of Q_ω per logarithmic frequency yields the phasing accumulated by the evolution on a given frequency interval (ω_L, ω_R). The quadrupole-monopole contribution to the PN-expanded Q_ω we are interested in here is given by the three terms given by Eqs. (5.37), (5.38) and (5.39). The aim of the next section will be to investigate how this function compares with the analogous quantity obtained from `TEOBResumS` with all the

spin-dependent information detailed in the previous section.

6.4 Results: gauge-invariant phasing comparisons of the EOS-dependent self-spin effects

In Sec. 5.4 we presented a preliminary comparison between the various PN truncations of the $Q_\omega^{\rm SS_{QM}}$'s and the corresponding quantity computed using from the time-domain waveform generated by `TEOBResumS` including only the self-spin information at LO in both the Hamiltonian and waveform/flux (see Fig. 5.14). The main outcome of this preliminary comparison was to show, for an illustrative BNS configuration, the consistency between the PN and EOB descriptions, especially at low frequencies, with the latter being slightly more phase-accelerating than the former. In this respect, Refs. [1, 209] showed the existence of a nonnegligible difference with respect to the TaylorF2 phasing with NLO (i.e., 3PN) self-spin effects. However, Ref. [209], see Sec. VI there, stressed that a more definitive assessment of the EOB/PN performances would need the incorporation of the NLO information in `TEOBResumS`. We shall do so here, closely following what was done in Sec. 5.4. To start with, we work at NLO in the self-spin within `TEOBResumS`, adding the corresponding terms to both the Hamiltonian and the multipolar waveform amplitude (and flux). For definiteness, we consider a few BNS configurations, that we list in Table 6.1, ranging from stiffer to softer EOS. Similarly, we mainly explore values of the spins that are compatible with those expected for BNSs. However, to stretch the limits of the model, we also consider a fast-spinning configuration, with $\chi_A = 0.8$ and $\chi_B = 0.4$. We note that, although such a configuration is unlikely to exist in a realistic binary system, these spin magnitudes values were considered in the parameter estimation of GW170817 when considering high-spin priors analyses [43, 210].

The $Q_\omega(\omega)$ is computed (from the time-domain phasing) in the same way as briefly described in Ref. [1], though here we pushed the lower frequency limit down to 5Hz, so as to unambiguously identify the frequency region were the EOB and PN curve converge together. The code we used to do so is `TEOBResumS v0.1` that improves over `v0.0` (see Ref. [1]) because of the presence of the nonlinear spin terms discussed here[4] The same terms are also

[4]Note that `v0.1` also implements by default the EOS-dependent quartic-in-spin terms

Table 6.2: Configuration `SLy-q1.2-sA005-sA008` in Table 6.1. Indicative time, τ, obtained with the `v0.1` version of the public implementation of `TEOBResumS`, needed for obtaining the complete waveform, from 5Hz up to merger. To ease the computation (and to reduce the high-frequency noise due to the oversampling of the inspiral part), the waveform is computed joining together three pieces (starting at $r_{\rm max}$ and ending at $r_{\rm min}$) obtained with different sampling rates Δt. Note that the value of τ also takes into account the time needed to actually write the data on disk. Runs on an Intel Core i5-8250 (1.6GHz) and 8GB RAM. The code was compiled with the g++ GNU compiler using O3 optimization.

f_0 [Hz]	$r_{\rm max}$	$r_{\rm min}$	Δt^{-1} [Hz]	$\Delta t/M$	τ [sec]
5	264.11	80	100	674.2	102.177
20	104.81	8	10000	6.742	1.622
200	22.58	merger	100000	0.674	1.4832

implemented in `v1.0` which additionally contains the updated tidal model of Ref. [6] and the post-adiabatic approximation to efficiently compute long inspirals [191] (see Sec. 6.6 for additional details). With `TEOBResumS v0.1` is is easy to compute such a long waveform with reasonable efficiency. In practice, it is convenient to join together the waveforms computed on three different frequency intervals. The intervals are chosen in a way that the two pieces overlap on a common frequency interval. Table 6.2 illustrates our choices for one specific configuration, `SLy-q1.2-sA005-sA008` in Table 6.1, and lists: the different running times τ (including the time needed to write the file on disk); the sampling $\Delta t/M$; and the various intervals (in radius) where the EOB dynamics is evolved. As explained in Sec. 5.4, in order to explore the low-frequency regime one has to avoid the time-domain oversampling of the waveform that naturally occurs from the ODE solver. To remove this, the raw time-domain waveform phase is additionally downsampled and its derivatives smoothed in order to get a clean and nonoscillatory Q_ω function. The procedure is tedious, but straightforward and it is done separately on different frequency intervals, with the final results eventually joined together. To isolate the, C_{Qi}-dependent only, $Q_\omega^{\rm SS}$ contribution within `TEOBResumS` we

of Sec. 6.2.3.

perform, for each configuration, two different runs, one with $C_{Qi} \neq 0$ another one with $C_{Qi} = 0$. In both cases we compute the time-domain Q_ω and finally calculate

$$Q_\omega^{\rm TEOBResumS,SS} = Q_\omega^{\rm TEOBResumS_{C_{Qi}\neq 0}} - Q_\omega^{\rm TEOBResumS_{C_{Qi}=0}}. \tag{6.41}$$

Illustrative results are shown in Fig. 6.1 for the two configurations `SLy-q1-sA01-sB01` (left panel) and `Ms1b-q1-sA01-sB01` (right panel). Each panel is separated into two subpanels: the top part reports $Q_\omega^{\rm SS}$, with the EOB and the three different PN truncations; the bottom panel reports the differences $\Delta Q_\omega^{\rm EOBPN} \equiv Q_\omega^{\rm SS_{EOB}} - Q_\omega^{\rm SS_{PN}}$. To orient the reader, the vertical lines superposed to the plot correspond to 50, 400, 800 and 1200 Hz. As mentioned in Ref. [1] the comparison between the time-domain EOB Q_ω and the frequency domain PN-expanded Q_ω is meaningful as long as the SPA holds. In other words, this is true until the adiabatic parameter given by $1/Q_\omega$ is small enough. We will briefly comment about this at the end of the section.

The main conclusions we draw from figure Fig. 6.1 are: (i) the EOB description of the self-spin effects at NLO is more phase-accelerating than the LO one (both PN or EOB, cf. Fig. 14 of Ref. [1]); (ii) it is however *less phase-accelerating* than the standard TaylorF2 NLO one. This seems to corroborate the suggestion made in Sec. VI of Ref. [209] that part of the phasing accumulated by this approximant is due to its PN-nature. Since, a priori, tidal effects might be degenerate with self-spin effects (since they both accelerate the phasing), the use of the 3PN Taylor-expanded approximant may introduce biases in the measurement of the tidal parameters. This will deserve further investigations in the future; (iii) on the other hand, our comparisons show that the TaylorF2 phasing augmented with the tail factor is fully consistent with the EOB-resummed description up to frequencies ~ 600 Hz. We have checked that the importance of the self-spin tail term in reconciling the TaylorF2 with the EOB phasing description remains essentially the same when changing the BNS model, though it slightly deteriorates when the individual spins are increased. For example Fig. 6.2 refers to the `SLy-q1-sA04-sB08` configuration, with $\chi_A = 0.4$ and $\chi_B = 0.8$, which illustrates the ability of the tail-completed TaylorF2 approximant to reasonably agree with the EOB phasing even in difficult corners of the parameter space.

Let us now explore the implications of the NNLO self-spin correction to r_c. [We recall that the corrections to r_c only enter the Hamiltonian, and do

not concern the waveform.] This is done in Fig. 6.3, which refers to configurations `SLy-q1.2-sA005-sB008`, i.e., an unequal-mass binary with physically motivated values of the spins and medium values of (C_{QA}, C_{QB}). The NNLO term yields an additional acceleration of the phasing. However, the corresponding modification of the NLO curve is *smaller* than the modification of the LO curve brought by the NLO contributions. [This intuitively suggests some type of convergence of the EOB Q_ω curves as the amount of analytical information is increased.] Since the calculation of the self-spin terms in the energy flux (and waveform) is currently not available at NNLO, we cannot include in Fig. 6.3 the corresponding TaylorF2 curve. This raises the issue of knowing to which extent the NNLO curve represents a faithful representation of the complete self-spin effects. We can venture an answer based on the knowledge of what happens at NLO. Indeed, in the latter case one finds that the effect of the NLO waveform amplitude terms is almost negligible: the Q_ω curve obtained by switching off these terms is essentially superposed to the one with the NLO waveform corrections. Based on this finding, we expect that a similar situation will hold at the NNLO level.

Let us finally get an idea of the effect of the complete quartic-in-spin term once included into r_c. This can be done evaluating numerically $C_{\rm Oct}$ and $C_{\rm Hex}$ using the quasi-universal fits of Eq. (90) of Ref. [294] (see Sec. 3.2). Considering again the configuration `SLy-q1.2-sA005-sB008` of Fig. 6.3 above, one notes that the NNLO spin-square effect is determined by the coefficient $\delta a^2_{\rm NNLO} \simeq 0.108$ entering r_c. For the same configuration, the quartic-in-spin LO coefficient of Eq. (6.22), that can be seen as a correction to $\delta a^2_{\rm NNLO}$, numerically reads $\delta a^4_{\rm LO} \simeq 3.05 \times 10^{-4}$, so that its effect would be completely negligible on the phasing analysis of Fig. 6.3. One also easily checks that one would need to have $\chi_A = \chi_B \approx 0.29$ so to have $\delta a^4_{\rm LO} \approx 0.1$, thus yielding a phasing correction, at the Q_ω level, comparable to the $\delta a^2_{\rm NNLO}$ displayed in Fig. 6.3.

6.5 Cubic-in-spin terms within the EOB Hamiltonian

In this Section, we discuss preliminary ways of incorporating in the EOB Hamiltonian the LO cubic-in-spin contributions to the dynamics derived in Ref. [289].

As briefly mentioned in the main text, let us first recall that in `TEOBResumS` some contributions cubic in spin are already incorporated in the EOB Hamiltonian via the presence of $u_c(r,\tilde{a}_i)$-dependent factors in the gyro-gravitomagnetic functions G_S and G_{S_*} parametrizing the spin-orbit sector of the Hamiltonian (see Sec. 6.2.1). Indeed, we have $u_c^2 = u^2(1+(\mathrm{spin}-\mathrm{quadratic})O(u^2))$ so that the linear-in-spin couplings defined by $G_S(u_c)$ and $G_{S_*}(u_c)$ automatically contain some $O(u^5)$ spin-cubic contributions. However, one checks (see main text, Eqs. (6.15)-(6.16)) that the spin-cubic terms thereby already incorporated in the Hamiltonian are not the ones needed from the results of Ref. [289]. This remark suggests a way of incorporating the needed spin-cubic terms in a resummed manner, namely to introduce new definitions of the function $u_c(r,\tilde{a}_i)$ to be used as inputs in modified definitions of the gyro-gravitomagnetic functions G_S and G_{S_*}. Say

$$\begin{aligned} G_S &= 2uu^2_{c,G_S}\hat{G}_S(u_c),\\ G_{S_*} &= \frac{3}{2}(u^2_{c,G_{S_*}})^{3/2}\hat{G}_{S_*}(u_c), \end{aligned} \tag{6.42}$$

where $\hat{G}_S(u_c) = 1+O(u_c)$ and $\hat{G}_{S_*} = 1+O(u_c)$ are PN correcting factors [162, 217]. [The arguments u_c entering $\hat{G}_S(u_c)$ and $\hat{G}_{S_*}(u_c)$ can be taken as being any variable such that $u_c^2 = u^2(1+(\mathrm{spin}-\mathrm{quadratic})O(u^2))$.] We found that this possibility a priori involves six parameters, parametrizing the two different spin-quadratic expressions separately entering the modified definitions of $r^2_{c,G_S} = r^2 + \mathrm{spin}-\mathrm{quadratic}(1+O(u))$ and $r^2_{c,G_{S_*}} = r^2 + \mathrm{spin}-\mathrm{quadratic}(1+O(u))$, modelled on Eqs. (6.1), (6.2). This leaves the freedom to arbitrarily choose two among these six parameters. This freedom of choice can be used to simplify the resulting definitions. We have explored this avenue. However, at this stage we did not find a unique, convincing way of simplifying the two spin-quadratic expressions entering r^2_{c,G_S} and $r^2_{c,G_{S_*}}$. We leave further studies along this avenue to future work.

Without committing ourselves to any specific resummed way of incorporating spin-cubic terms in the EOB Hamiltonian, we wish, however, to display here the full information needed for such definitions. To do this we will parametrize the spin-cubic contributions in the following 4-parameter,

non-committal form

$$H_{\rm SO} = p_\varphi \Bigg[\tilde{G}(u,\tilde{a}_i) + \big(b_{30} \tilde{a}_A^3 + b_{21} \tilde{a}_A^2 \tilde{a}_B + b_{12} \tilde{a}_A \tilde{a}_B^2 + b_{03} \tilde{a}_B^3 \big) u^5 \Bigg], \tag{6.43}$$

where

$$\tilde{G}(u,\tilde{a}_i) = 2u^3 \hat{G}_S(u) \hat{S} + \frac{3}{2} u^3 \hat{G}_{S_*}(u) \hat{S}_*. \tag{6.44}$$

We then follow the procedure described in Section 6.2 to determine the four parameters $b_{30}, b_{21}, b_{12}, b_{03}$ entering this parametrization. By calculating the corresponding modified version of $c_7^{S^3_{\rm LO}}$ and comparing it to Eq. (6.15), we obtain the simple expressions

$$\begin{aligned} b_{30} &= C_{{\rm Oct}A} - 3 C_{QA}, \\ b_{21} &= -6, \\ b_{12} &= -6, \\ b_{03} &= C_{{\rm Oct}B} - 3 C_{QB}. \end{aligned} \tag{6.45}$$

Let us note that if we consider the BH limit where $C_Q = C_{\rm Oct} = 1$ the needed modified spin-orbit coupling takes the very simple form

$$H_{\rm SO\,BBH} = p_\varphi \left[\tilde{G}(u) - 2(\hat{S} + \hat{S}_*)^3 u^5 \right]. \tag{6.46}$$

Let us also note that if we insist on utilizing the full `TEOBResumS` structure, keeping the cubic-in-spin terms that come from the use of $r_c(r,\tilde{a}_i)$, as defined in Eq. (6.1) above, we must modify the expressions of the parameters $b_{30}, b_{21}, b_{12}, b_{03}$ into

$$\begin{aligned} b'_{30} &= C_{{\rm Oct}A} - \frac{7}{8} C_{QA} - \frac{1}{8} X_{AB} C_{QA}, \\ b'_{21} &= -\frac{7}{4} + \frac{17}{8} C_{QA} - X_{AB} \left(\frac{1}{4} - \frac{1}{8} C_{QA} \right), \\ b'_{12} &= -\frac{7}{4} + \frac{17}{8} C_{QB} + X_{AB} \left(\frac{1}{4} - \frac{1}{8} C_{QB} \right), \\ b'_{03} &= C_{{\rm Oct}B} - \frac{7}{8} C_{QB} + \frac{1}{8} X_{AB} C_{QB}. \end{aligned} \tag{6.47}$$

In that case, the BBH case leads to the following very simple correction to the spin-sector implied by the current `TEOBResumS` model:

$$H_{\rm SO\,BBH} = p_\varphi \left[\tilde{G} + \frac{1}{4}(\hat{S} + \hat{S}_*)^2 \hat{S}_* u^5\right]. \tag{6.48}$$

We postpone a comparison of the various avenues mentioned here to a later work.

6.6 Post-adiabatic dynamics

The EOB/PN comparisons done in the main text employ `TEOBResumS v0.1`, that was implemented in C++. An equivalent, though tidally enhanced model (see [6]) and computationally more efficient version of the model (implemented in C) is `v1.0`. All our codes are publicly available at

`https://bitbucket.org/account/user/eob_ihes/projects/EOB`

`TEOBResumS v1.0` optionally implements the post-adiabatic (PA) approximation to efficiently deal with the long inspiral phase [191]. Following the logic of Appendix B of Ref. [6], we here present the performance of the PA evolution in the case of spinning neutron stars. The result presented here are obtained incorporating (i) NLO spin-quadratic information in the waveform and (ii) NNLO spin-quadratic information in the Hamiltonian. This should be considered as the default choice in `TEOBResumS` for what concerns spinning BNS. Optionally, it is possible to switch on the EOS-dependence in the quartic-in-spin correction to r_c, Eq. (6.22), though this does not come as default choice in the code.

Within `TEOBResumS`, the dynamics of a binary system is usually determined by numerically solving the four Ordinary Differential Equations (ODEs) of the Hamiltonian relative dynamics. The time needed to solve these ODEs usually weighs as the main contribution to the waveform evaluation time. Using this C-implementation of `TEOBResumS`, a typical time-domain BNS waveform requires ~ 1 sec to be generated starting from a GW frequency of 10 Hz by means of standard Runge-Kutta integration routines with adaptive step-size that are publicly available through the GNU Scientific Library (`GSL`). Thus, ODE integration as is cannot be used in parameter estimation runs that require the generation of 10^7 waveforms. Reference [191] proposed a method of reducing the evaluation time by making use of the PA

approximation to compute the system dynamics. In Ref. [6] we restricted to non spinning BNS and we showed, for the first time, how a waveform obtained from the complete ODE evolution compares with a waveform obtained by stitching the PA dynamics to the complete dynamics for the last few orbits up to merger (as suggested in [191]). For completeness, we here present the same comparison for two illustrative, spinning, BNS systems.

Let us briefly summarize the approach of Ref. [191]. The PA approximation to the EOB dynamics was introduced in Refs. [28, 29] (and expanded in Refs. [166, 215]) and is currently used to initialize the relative dynamics in `TEOBResumS` with negligible eccentricity. Using this approximation, it is possible to analytically compute the radial and angular momentum of a binary system, under the assumption that the radiation reaction force is small. This is true in the early inspiral phase and progressively loses validity when the two objects get close. The approach starts by considering the conservative system, when the flux is null, and then computes the successive corrections to the momenta. We denote as nPA the n-th order iteration of this procedure. Practically, to compute the PA dynamics, we first build a uniform

f_0 [Hz]	r_0	$r_{\rm min}$	N_r	Δr	$\tau_{\rm 8PA}$ [sec]	$\tau_{\rm ODE}$ [sec]
20	112.81	12	500	0.20	0.03	0.53
10	179.02	12	830	0.20	0.05	1.1

Table 6.3: Performance of `TEOBResumS v1.0` for a BNS system with $1.35M_\odot + 1.35M_\odot$, SLy EOS and $\chi_A = \chi_B = 0.1$. The waveform for the $\chi_A = \chi_B = -0.1$ case is a little shorter but the evaluation times are comparable to the ones showed in the table. f_0 and r_0 denote the initial GW frequency and radial separation. The 8PA dynamics is computed on a grid with N_r points and grid separation Δr that ends at $r_{\rm min}$ and then is completed by the standard ODE one. The evaluation times τ are determined using a standard Intel Core i7, 1.8GHz and 16GB RAM. The code is compiled with the GNU gcc compiler using O3 optimization.

radial grid from the initial radius r_0 to an $r_{\rm min}$ up until which we are sure the approximation holds. We then analytically compute the momenta that correspond to each radius at a chosen PA order. Finally, we determine the full dynamics recovering the time and orbital phase by quadratures. From $r_{\rm min}$ we can then start the usual ODE-based dynamics using the PA quantities as initial data as it is usually done (at 2PA order) in `TEOBResumS`. With

f_0 [Hz]	r_0	$\tau^{\rm int}_{\rm 8PA}$ [sec]	$\tau^{\rm int}_{\rm ODE}$ [sec]
20	112.81	0.10	0.64
10	179.02	0.37	1.70

Table 6.4: Performance of the `TEOBResumS v1.0` when the final waveform is interpolated on a time grid evenly sampled at 1/(4096 Hz). We use the standard spline interpolation routine implemented in the `GSL` library. The considered system coincides with the one of Table 6.3.

this method one can avoid to numerically solving two Hamilton equations (those for the momenta), while the orbital phase and time can be obtained by quadratures over a rather sparse radial grid.

Figure 6.4 displays the performance of the PA approximation (at 8PA order) for two, illustrative, spinning BNS systems with $1.35M_\odot + 1.35M_\odot$ and SLy EOS. The figure shows the distance-normalized waveform strain $h \equiv \mathcal{R}(h_+ - {\rm i}h_\times)$, where we recall that the multipolar decomposition of the waveform reads

$$\mathcal{R}(h_+ - {\rm i}h_\times) = \sum_{\ell=2}^{\ell_{\rm max}} \sum_{m=-\ell}^{\ell} h_{\ell m}\, {}_{-2}Y(\theta, \Phi), \tag{6.49}$$

where $h_{\ell m}$ are the waveform (complex) multipoles and ${}_{-2}Y(\theta, \Phi)$ are the $s = -2$ spin-weighted spherical harmonics (that are here evaluated at $\theta = \Phi = 0$). In fig. 6.4 we evaluate h with $\ell_{\rm max} = 8$, i.e. retaining in the waveform the same 35 multipoles that are used to compute the EOB radiation reaction. For each binary, each subpanel displays the the waveform fractional-amplitude difference (top), phase difference (medium) and real part of the waveform strain. The left columns offer a global view, while the right columns focus on the last few GW cycles up to merger. The vertical dashed line marks the time where the PA evolution is stitched to the ODE evolution for the last orbits where the PA approximation breaks down. Table 6.3 highlights the performances of `TEOBResumS v1.0` for such a case. Note that the initial radius is determined by solving the circular Hamilton's equations instead of relying on the Newtonian Kepler's law, as discussed in Sec. VI of Ref. [1].

The waveform computed using the PA dynamics (completed with the ODE for the last few orbits) only takes around 50 milliseconds to be evaluated. Such a time is comparable to the one needed by the surrogate models

that are currently being constructed in order to reduce waveform evaluation times (see e.g. [247]) and that, typically, only involve the $\ell = m = 2$ mode. Finally, Table 6.4 illustrates the performance of `TEOBResumS` when the waveform of above, which is obtained on a *nonuniform* temporal grid (because the corresponding radial grid is evenly spaced), is interpolated on an evenly spaced time grid, sampled at $\Delta t^{-1} = 4096$ Hz, that is usually neecessary to compute the Fourier transform with standard algorithms. It is remarkable that the generation time of the *full multipolar waveform* is below 1 sec *also* when the starting frequency is 10 Hz. Such interpolation is done with the spline interpolant that is freely available in the `GSL` library and looks to be the main routine responsible for the computational cost of the waveform generation. We expect this can be further speed up exploting vectorization or shared memory parallelization. Similarly, one expects that the number of radial gridpoints needed might be lowered further by adopting a quadrature formula at higher order (now a third-order one is implemented, following Ref. [191]) to recover the orbital phase and time. Such technical improvements will be explored extensively in forthcoming works.

6.7 Using $\hat{S}$ and $\hat{S}_*$ as spin variables.

Finally, for completeness, we report here the results of Sec. 6.2 using $\hat{S}$ and $\hat{S}_*$ as spin variables. First, the newly computed $\delta a^2_{\rm NLO}$ and $\delta a^2_{\rm NNLO}$ are written as quadratic forms in (S, S_*) as

$$\begin{aligned}\delta a^2_{\rm NLO} =&\frac{1}{1-4\nu}\Bigg\{\left[-4+9\nu+(2-5\nu)\left(C_{QA}+C_{QB}\right)+(2-\nu)\,X_{AB}\left(C_{QA}-C_{QB}\right)\right]\hat{S}^2\\&+\left[-\frac{9}{2}+11\nu+(1-\nu)\left(C_{QA}+C_{QB}\right)-(1+\nu)\,X_{AB}\left(C_{QA}-C_{QB}\right)\right]\hat{S}_*^2\\&+\left[-2+22\nu-6\nu\left(C_{QA}+C_{QB}\right)-2\nu X_{AB}\left(C_{QA}-C_{QB}\right)\right]\hat{S}\hat{S}_*\Bigg\},\end{aligned}\tag{6.50}$$

$$\begin{aligned}\delta a^2_{\rm NNLO} =&\frac{1}{1-4\nu}\Bigg\{\Big[-\frac{275}{14}+\frac{561}{14}\nu+\frac{675}{14}\nu^2\\&+\left(\frac{275}{28}-\frac{1633}{56}\nu+\frac{207}{28}\nu^2\right)\left(C_{QA}+C_{QB}\right)+\left(\frac{275}{28}-\frac{533}{56}\nu\right)X_{AB}\left(C_{QA}-C_{QB}\right)\Big]\hat{S}^2\\&+\left[-\frac{153}{8}+\frac{173}{4}\nu+\frac{381}{14}\nu^2+\left(4-\frac{47}{8}\nu+\frac{207}{28}\nu^2\right)\left(C_{QA}+C_{QB}\right)\right.\\&\left.-\left(4+\frac{17}{8}\nu\right)X_{AB}\left(C_{QA}-C_{QB}\right)\right]\hat{S}_*^2\\&+\left[-\frac{25}{2}+\frac{4727}{56}\nu-\frac{163}{14}\nu^2-\left(\frac{387}{14}-\frac{207}{14}\nu\right)\nu\left(C_{QA}+C_{QB}\right)\right.\\&\left.-\frac{163}{14}\nu X_{AB}\left(C_{QA}-C_{QB}\right)\right]\hat{S}\hat{S}_*\Bigg\}.\end{aligned}\tag{6.51}$$

Note that the use of (S, S_*) leads to formally singular terms when $\nu = 1/4$. This singularity is actually reabsorbed by $(\hat{S}, \hat{S}_*)$ when the limit is done carefully taking into account the various mass terms. From these equations, one can obtain the orbital angular momentum j as a function of u, namely

$$
\begin{aligned}
j(u) = {} & \frac{1}{\sqrt{u}} + \frac{3}{2}\sqrt{u} - 3\left(\hat{S} + \frac{3}{4}\hat{S}_*\right)u \\
& + \Bigg\{ -\frac{27}{8} - \frac{3}{2}\nu + \frac{1}{1-4\nu}\left[-2\nu + \left(\frac{1}{2}-\nu\right)(C_{QA}+C_{QB}) + \frac{1}{2}X_{AB}\,(C_{QA}-C_{QB})\right]\hat{S}^2 \\
& + \frac{1}{1-4\nu}\left[-2\nu + \left(\frac{1}{2}-\nu\right)(C_{QA}+C_{QB}) - \frac{1}{2}X_{AB}\,(C_{QA}-C_{QB})\right]\hat{S}_*^2 + \\
& + \frac{2}{1-4\nu}\left[1-2\nu-\nu(C_{QA}+C_{QB})\right]\hat{S}\hat{S}_*\Bigg\}u^{3/2} \\
& + \left[\left(-\frac{15}{2}+\frac{5}{4}\nu\right)\hat{S} + \left(-\frac{27}{8}+\frac{3}{2}\nu\right)\hat{S}_*\right]u^2 + \Bigg\{\frac{135}{16} + \left(-\frac{433}{12}+\frac{41}{32}\pi^2\right)\nu \\
& + \frac{1}{1-4\nu}\Bigg[-\frac{1}{2} - \frac{31}{4}\nu + \left(\frac{11}{4}-\frac{27}{4}\nu\right)(C_{QA}+C_{QB}) \\
& + \left(\frac{11}{4}-\frac{5}{4}\nu\right)X_{AB}\,(C_{QA}-C_{QB})\Bigg]\hat{S}^2 \\
& + \frac{1}{1-4\nu}\Bigg[-\frac{99}{32} + \frac{21}{8}\nu + \left(\frac{3}{2}-\frac{7}{4}\nu\right)(C_{QA}+C_{QB}) \\
& - \left(\frac{3}{2}+\frac{5}{4}\nu\right)X_{AB}\,(C_{QA}-C_{QB})\Bigg]\hat{S}_*^2 \\
& + \frac{1}{1-4\nu}\left[\frac{21}{4} - \frac{3}{2}\nu - \frac{17}{2}\nu\,(C_{QA}+C_{QB}) - \frac{5}{2}\nu\,(C_{QA}-C_{QB})\right]\hat{S}\hat{S}_*\Bigg\}u^{5/2} \\
& + \left[\left(-\frac{189}{8}+35\nu+\frac{5}{16}\nu^2\right)\hat{S} + \left(-\frac{63}{8}+\frac{225}{8}\nu+\frac{15}{32}\nu^2\right)\hat{S}_*\right]u^3 \\
& + \Bigg\{\frac{2835}{128} - \left(\frac{3029}{120}+32\gamma+\frac{3503}{2048}\pi^2+64\log(2)+16\log(u)\right)\nu + \left(\frac{539}{12}-\frac{205}{128}\pi^2\right)\nu^2 \\
& + \frac{1}{1-4\nu}\Bigg[\frac{67}{14} - \frac{3459}{56}\nu + \frac{2319}{28}\nu^2 + \left(\frac{1055}{112}-\frac{3317}{112}\nu+\frac{495}{56}\nu^2\right)(C_{QA}+C_{QB}) \\
& + \left(\frac{1055}{112}-\frac{1207}{112}\nu\right)X_{AB}\,(C_{QA}-C_{QB})\Bigg]\hat{S}^2 + \frac{1}{1-4\nu}\Bigg[-\frac{585}{64} + \frac{35}{16}\nu + \frac{1395}{28}\nu^2 \\
& + \left(\frac{49}{16}-\frac{67}{16}\nu+\frac{495}{56}\nu^2\right)(C_{QA}+C_{QB}) - \left(\frac{49}{16}+\frac{31}{16}\nu\right)X_{AB}\,(C_{QA}-C_{QB})\Bigg]\hat{S}_*^2 \\
& + \frac{1}{1-4\nu}\Bigg[\frac{113}{8} - \frac{2545}{56}\nu + \frac{918}{7}\nu^2 - \left(\frac{699}{28}-\frac{495}{28}\nu\right)\nu\,(C_{QA}+C_{QB}) \\
& - \frac{89}{7}\nu X_{AB}\,(C_{QA}-C_{QB})\Bigg]\hat{S}\hat{S}_*\Bigg\}u^{7/2} + \mathcal{O}\left[u^4\right]. \qquad (6.52)
\end{aligned}
$$

Similarly, the inverse expression can be written as

$$
\begin{aligned}
u(j) = & \frac{1}{j^2} + \frac{3}{j^4} - 6\left(\hat{S} + \frac{3}{4}\hat{S}_*\right)\frac{1}{j^5} \\
& + \Bigg\{ 18 - 3\nu + \frac{1}{1-4\nu}\left[-4\nu + (1-2\nu)\left(C_{QA}+C_{QB}\right) + X_{AB}\left(C_{QA}-C_{QB}\right)\right]\hat{S}^2 \\
& + \frac{1}{1-4\nu}\left[-4\nu + (1-2\nu)\left(C_{QA}+C_{QB}\right) - X_{AB}\left(C_{QA}-C_{QB}\right)\right]\hat{S}_*^2 + \\
& + \frac{4}{1-4\nu}\left[1-2\nu-\nu(C_{QA}+C_{QB})\right]\hat{S}\hat{S}_* \Bigg\}\frac{1}{j^6} + \left[\left(-69+\frac{5}{2}\nu\right)\hat{S} + \left(-\frac{189}{4}+3\nu\right)\hat{S}_*\right]\frac{1}{j^7} \\
& + \Bigg\{ 135 + \left(-\frac{311}{3} + \frac{41}{16}\pi^2\right)\nu \\
& + \frac{1}{1-4\nu}\left[62 - \frac{619}{2}\nu + \left(16-\frac{69}{2}\nu\right)\left(C_{QA}+C_{QB}\right) + \left(16-\frac{5}{2}\nu\right)X_{AB}\left(C_{QA}-C_{QB}\right)\right]\hat{S}^2 \\
& + \frac{1}{1-4\nu}\left[\frac{117}{4} - \frac{375}{2}\nu + \left(\frac{27}{2}-\frac{49}{2}\nu\right)\left(C_{QA}+C_{QB}\right) - \left(\frac{27}{2}+\frac{5}{2}\nu\right)X_{AB}\left(C_{QA}-C_{QB}\right)\right]\hat{S}_*^2 \\
& + \frac{1}{1-4\nu}\left[147 - 465\nu + -59\nu\left(C_{QA}+C_{QB}\right) - 5\nu X_{AB}\left(C_{QA}-C_{QB}\right)\right]\hat{S}\hat{S}_* \Bigg\}\frac{1}{j^8} \\
& + \left[\left(-\frac{3069}{4} + 172\nu + \frac{5}{8}\nu^2\right)\hat{S} + \left(-\frac{2007}{4} + \frac{585}{4}\nu + \frac{15}{16}\nu^2\right)\hat{S}_*\right]\frac{1}{j^9} \\
& + \Bigg\{ 1134 - \left(\frac{163063}{120} + 64\gamma - \frac{31921}{1024}\pi^2 + 128\log(2) + 64\log\left(1/j\right)\right)\nu + \left(\frac{1321}{12} - \frac{205}{64}\pi^2\right)\nu^2 \\
& + \frac{1}{1-4\nu}\Bigg[\frac{19223}{14} - \frac{88953}{14}\nu + \frac{6855}{14}\nu^2 + \left(\frac{5725}{28} - \frac{26753}{56}\nu + \frac{1251}{28}\nu^2\right)\left(C_{QA}+C_{QB}\right) \\
& + \left(\frac{5725}{28} - \frac{3853}{56}\nu\right)X_{AB}\left(C_{QA}-C_{QB}\right)\Bigg]\hat{S}^2 + \frac{1}{1-4\nu}\Bigg[\frac{4653}{8} - \frac{12659}{4}\nu + \frac{5553}{14}\nu^2 \\
& + \left(158 - \frac{2335}{8}\nu + \frac{1251}{28}\nu^2\right)\left(C_{QA}+C_{QB}\right) - \left(158+\frac{193}{8}\nu\right)X_{AB}\left(C_{QA}-C_{QB}\right)\Bigg]\hat{S}_*^2 \\
& + \frac{1}{1-4\nu}\Bigg[\frac{5119}{2} - \frac{503105}{56}\nu + \frac{12555}{14}\nu^2 - \left(\frac{10149}{14} - \frac{1251}{14}\nu\right)\nu\left(C_{QA}+C_{QB}\right) \\
& - \frac{1301}{14}\nu X_{AB}\left(C_{QA}-C_{QB}\right)\Bigg]\hat{S}\hat{S}_* \Bigg\}\frac{1}{j^{10}} + \mathcal{O}\left[j^{-11}\right]. \qquad (6.53)
\end{aligned}
$$

Finally, the gauge-invariant link between the binding energy and the orbital angular momentum becomes

$$
\begin{aligned}
E_b(j) = &-\frac{1}{2j^2}\Bigg\{1+\frac{1}{4}(9+\nu)\frac{1}{j^2}-4\left(\hat{S}+\frac{3}{4}\hat{S}_*\right)\frac{1}{j^3}\\
&+\Bigg\{\frac{1}{8}\left(81-7\nu+\nu^2\right)+\frac{1}{1-4\nu}\left[-2\nu+\left(\frac{1}{2}-\nu\right)\left(C_{QA}+C_{QB}\right)+\frac{1}{2}X_{AB}\left(C_{QA}-C_{QB}\right)\right]\hat{S}^2\\
&+\frac{1}{1-4\nu}\left[-2\nu+\left(\frac{1}{2}-\nu\right)\left(C_{QA}+C_{QB}\right)-\frac{1}{2}X_{AB}\left(C_{QA}-C_{QB}\right)\right]\hat{S}_*^2+\\
&+\frac{2}{1-4\nu}\left[1-2\nu-\nu(C_{QA}+C_{QB})\right]\hat{S}\hat{S}_*\Bigg\}\frac{1}{j^4}+\left[\left(-36-\frac{3}{4}\nu\right)\hat{S}+-\frac{99}{4}\hat{S}_*\right]\frac{1}{j^5}\\
&+\Bigg\{\frac{3861}{64}-\left(\frac{8833}{192}-\frac{41}{32}\pi^2\right)\nu-\frac{5}{32}\nu^2+\frac{5}{64}\nu^3\\
&+\frac{1}{1-4\nu}\Bigg[32-152\nu-\nu^2+\left(\frac{25}{4}-\frac{53}{4}\nu-\frac{\nu^2}{2}\right)\left(C_{QA}+C_{QB}\right)\\
&+\left(\frac{25}{4}-\frac{3}{4}\nu\right)X_{AB}\left(C_{QA}-C_{QB}\right)\Bigg]\hat{S}^2\\
&+\frac{1}{1-4\nu}\Bigg[\frac{63}{4}-87\nu-\nu^2+\left(\frac{21}{4}-\frac{37}{4}\nu-\frac{\nu^2}{2}\right)\left(C_{QA}+C_{QB}\right)\\
&-\left(\frac{21}{4}+\frac{5}{4}\nu\right)X_{AB}\left(C_{QA}-C_{QB}\right)\Bigg]\hat{S}_*^2\\
&+\frac{1}{1-4\nu}\left[69-227\nu-2\nu^2-(23+\nu)\,\nu\left(C_{QA}+C_{QB}\right)-2\nu X_{AB}\left(C_{QA}-C_{QB}\right)\right]\hat{S}\hat{S}_*\Bigg\}\frac{1}{j^6}\\
&+\left[\left(-\frac{1701}{8}+\frac{3597}{4}\nu-195\nu^2\right)\hat{S}+\left(-\frac{4295}{16}+\frac{411}{8}\nu-\frac{5}{16}\nu^2\right)\hat{S}_*\right]\frac{1}{j^7}\\
&+\Bigg\{\frac{53703}{128}-\left(\frac{989911}{1920}+\frac{128}{5}\gamma-\frac{6581}{512}\pi^2+\frac{256}{5}\log(2)+\frac{128}{5}\log\left(1/j\right)\right)\nu\\
&+\left(\frac{8875}{384}-\frac{41}{64}\pi^2\right)\nu^2-\frac{3}{64}\nu^3+\frac{7}{128}\nu^4+\frac{1}{1-4\nu}\Big[\frac{8013}{14}-\frac{71545}{28}\nu\\
&+\frac{2575}{28}\nu^2-\frac{3}{4}\nu^3+\left(\frac{7449}{112}-\frac{17119}{112}\nu+\frac{975}{112}\nu^2-\frac{3}{8}\nu^3\right)\left(C_{QA}+C_{QB}\right)\\
&+\left(\frac{7449}{112}-\frac{2221}{112}\nu-\frac{5}{16}\nu^2\right)X_{AB}\left(C_{QA}-C_{QB}\right)\Big]\hat{S}^2\\
&+\frac{1}{1-4\nu}\Big[252-\frac{10203}{8}\nu+\frac{2757}{28}\nu^2-\frac{3}{4}\nu^3+\left(\frac{819}{16}-\frac{1473}{16}\nu+\frac{1199}{112}\nu^2-\frac{3}{8}\nu^3\right)\left(C_{QA}+C_{QB}\right)\\
&-\left(\frac{819}{16}+\frac{165}{16}\nu+\frac{11}{16}\nu^2\right)X_{AB}\left(C_{QA}-C_{QB}\right)\Big]\hat{S}_*^2\\
&+\frac{1}{1-4\nu}\Bigg[\frac{4041}{4}-\frac{201927}{56}\nu+\frac{5661}{28}\nu^2-\frac{3}{2}\nu^3-\left(\frac{6591}{28}-\frac{533}{28}\nu+\frac{3}{4}\nu^2\right)\nu\left(C_{QA}+C_{QB}\right)
\end{aligned}
$$

$$- \left(\frac{429}{14} + \nu \right) \nu X_{AB} \left(C_{QA} - C_{QB} \right) \Bigg] \hat{S} \hat{S}_* \Bigg\} \frac{1}{j^8} + \mathcal{O}\left[j^{-9} \right] \Bigg\}. \tag{6.54}$$

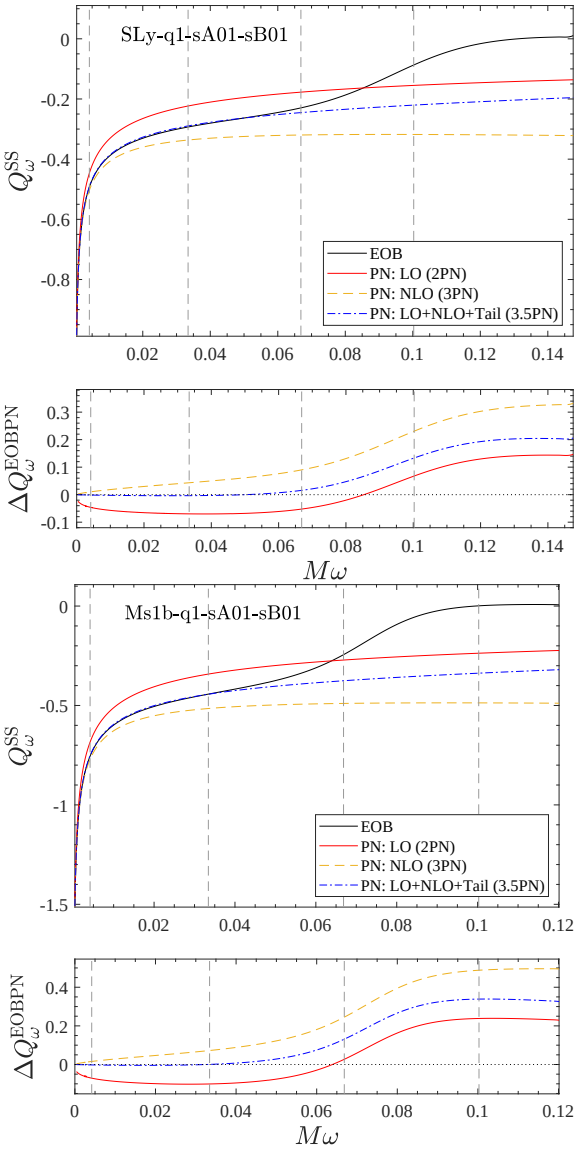

Figure 6.1: Left panel: Sly EOS, $M_A = M_B = 1.35$, $\chi_A = \chi_B = 0.1$ and $C_{QA} = C_{QB} = 5.48$. Right panel: Ms1B EOS, $M_A = M_B = 1.35$, $\chi_A = \chi_B = 0.1$ and $C_{QA} = C_{QB} = 8.40$. The grey vertical lines correspond to 50, 400, 800 and 1200 Hz respectively. The additional $Q_\omega^{\rm SS_{QM,tail}}$ term in TaylorF2 is crucial to get an excellent agreement between the PN-expanded and EOB phasing for most of the inspiral.

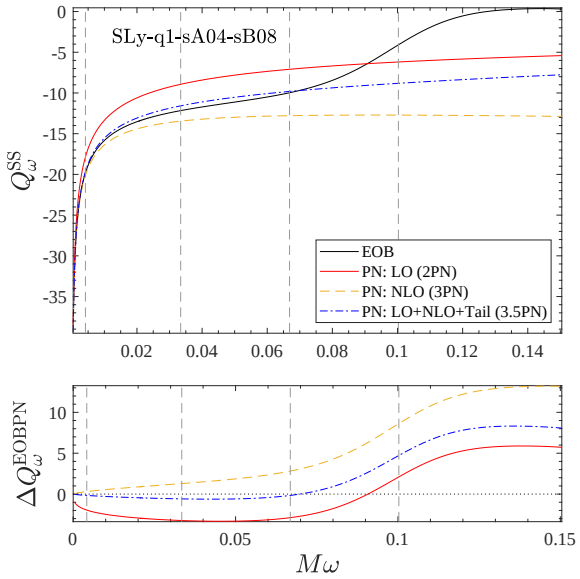

Figure 6.2: Closeness of the tail-completed TaylorF2 description of the phasing to the EOB one, even when rather high values of the individual spins are considered.

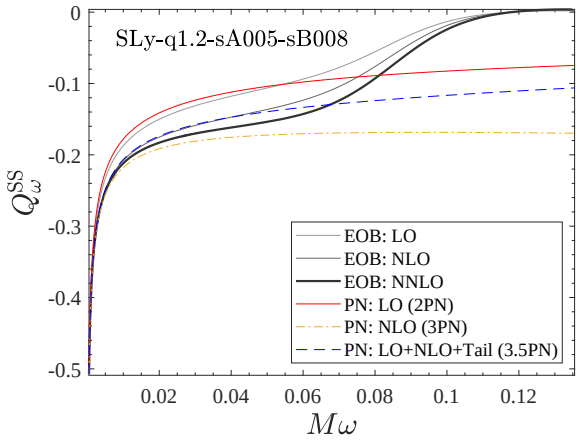

Figure 6.3: The effect of the NNLO self-spin term incorporated in the EOB Hamiltonian for one of the configurations of Table 6.1. Although the NNLO term results in an acceleration of the inspiral with respect to the NLO model, the curve is still above the NLO PN-expanded TaylorF2 one.

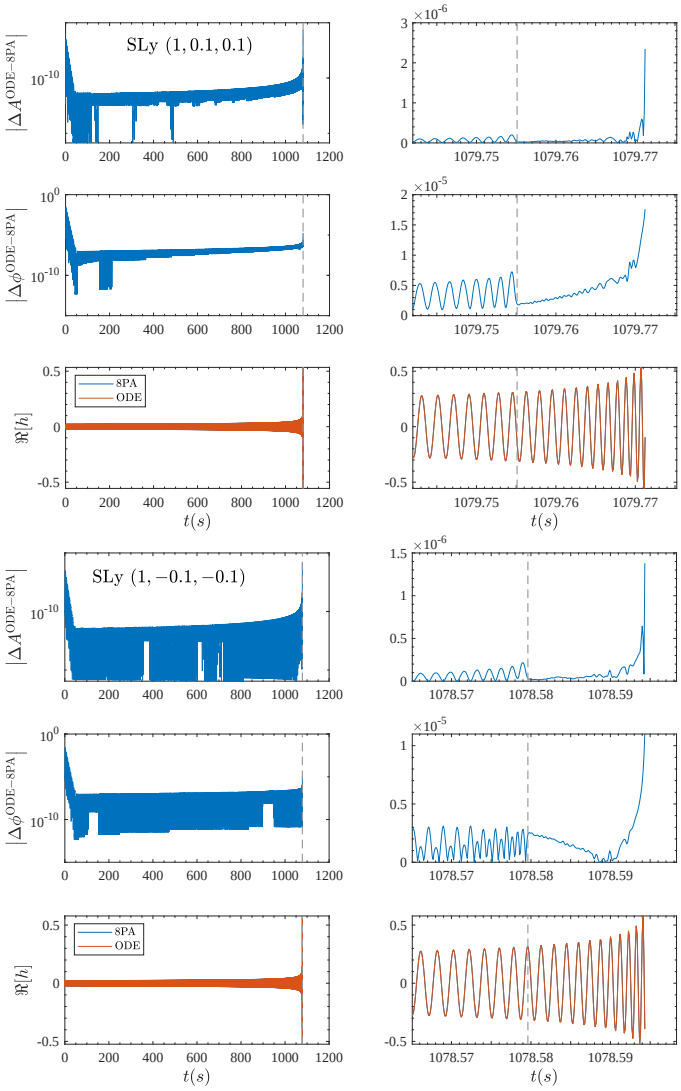

Figure 6.4: Comparison between the waveforms (obtained summing all modes up to $\ell_{\rm max} = 8$, see Eq. (6.49)) computed solving the ODEs with the `GSL rk8` routine with adaptive stepsize and the PA waveform completed with the same ODE solver after $r < r_{\rm min}$. We have considered BNS systems with $1.35M_\odot + 1.35M_\odot$ and SLy EOS (see first row of Table 6.1), starting at initial frequency 10 Hz. Dimensionless spins are $\chi_A = \chi_B = 0.1$ (top) and $\chi_A = \chi_B = -0.1$ (bottom). The parameters used for the PA run are listed in Table 6.3. The dashed grey line marks the stitching point, $r_{\rm min}$, between the PA and ODE-based dynamics. Given the waveform strain as $h \equiv Ae^{-{\rm i}\phi}$, we defined the phase difference as $\Delta\phi^{\rm ODE-8PA} \equiv \phi^{\rm ODE} - \phi^{\rm 8PA}$ and the fractional amplitude difference as $\Delta A^{\rm ODE-8PA} \equiv (A^{\rm ODE} - A^{\rm 8PA})/A^{\rm ODE}$. The larger differences at the beginning of the evolution are partly due to the fact that the complete ODE is started using only 2PA-accurate initial data.

Chapter 7

Quasi-5.5PN TaylorF2 approximant for compact binaries: point-mass phasing and impact on the tidal polarizability inference [3]

7.1 Introduction

The data-analysis of GW170817 [43] relied on gravitational waveform models that incorporate tidal effects. The latter allow one to extract information about the neutron star equation of state (EOS) via the inference of the mass-weighted averaged tidal polarizability parameter $\tilde{\Lambda}$ [243, 237, 211, 210, 299]. The understanding of the systematic uncertainties on the measurement of $\tilde{\Lambda}$ due to the waveform model/approximants have been the subject of intensive investigation in recent years. For example, building on the work of Favata [266], Wade et al. [300] investigated the performance of different PN inspiral approximants within a Bayesian analysis framework for the advanced detectors and found that the choice of approximant significantly biases the recovery of tidal parameters. Later, a similar Bayesian analysis in the case of LIGO and advanced LIGO detectors was carried out by Dudi et al. [301] who concluded that the `TaylorF2` 3.5PN waveform model can be used to place an upper bound on $\tilde{\Lambda}$. The same conclusion was drawn also by the study of

the LIGO-Virgo collaboration [210].

Beside being interesting per se' because done in the precise setup that is relevant for data analysis, these studies collectively stress the paramount need of having an analytically reliable description of the phasing up to merger. The tidal extension of the effective-one-body (EOB) [28, 29] description for coalescing compact binaries was introduced in [157] and developed during the last ten years [206, 212, 213, 1, 6, 2] with the goal of providing robust binary neutron star waveforms to be used in gravitational-wave inference. While analytically more accurate, EOB waveform generation is usually slower than PN. Different routes have been explored to speed up EOB approximants (see Sec. 4.5). However, none of the methods described above provide us with waveform generation algorithms faster than PN. Although it is well known that inspiral PN approximants might be problematic, they retain the advantage of being the most efficient for Bayesian inference.

One important source of systematics in BNS inspiral waveforms resides in the description of the nontidal part (see e.g. [302]). The practice that became common after the observation of GW170817 is to augment standard point-mass model with the tidal part of the phasing. A natural step is thus to improve the accuracy point-mass PN approximant beyond the current available technology. In this chapter we introduce a nonspinning, point-mass, closed-form frequency-domain `TaylorF2` waveform approximant at quasi-5.5PN order (Sec. 7.2). The new approximant is obtained by PN-expanding the adiabatic EOB dynamics along circular orbits. As such, it delivers a phasing representation that improves the currently known 3.5PN one. We show that, when applied in the GW data analysis context, the new phasing description allows one to strongly reduce the biases in the recovery of the tidal parameters that are usually present with the 3.5PN `TaylorF2` point-mass (Sec. 7.3).

7.2 Quasi-5.5PN-accurate orbital phasing

Building upon Damour et al. [243], Ref. [11] illustrated how to formally obtain a high-order PN approximant by PN-expanding the EOB energy $E_{\rm EOB}$ and energy flux $\mathcal{F}_{\rm EOB}$ along circular orbits. Stopping the expansion at 4.5PN, allowed one to obtain a consistent 4.5PN approximant with a few parameters needed to formally take into account the yet uncalculated ν-dependent terms in the waveform amplitudes at 4PN. Here we follow precisely that approach,

but we extend it to 5.5PN accuracy. To get the waveform phase in the frequency domain along circular orbits, we start with the gauge-invariant[1] description of the adiabatic phasing defined by

$$Q_\omega \equiv E_{\rm EOB}(x) \left(\frac{d\mathcal{F}_{\rm EOB}}{dx} \right)^{-1} \ , \tag{7.1}$$

where $x \equiv (M\omega)^{2/3}$, with ω the orbital frequency along circular orbits. The high-order phasing approximant is obtained by Taylor-expanding the above equation and then by solving Eq. (5.34), that we rewrite here in terms of the frequency f as

$$\frac{d^2\Psi_{\rm 5.5PN}}{d^2\hat{f}} = \frac{Q_\omega(\hat{f})}{\hat{f}^2} \ , \tag{7.2}$$

where $\hat{f} \equiv Mf \equiv \omega/2\pi$. The double integration of Eq. (7.2) delivers $\Psi_{\rm 5.5PN}(\hat{f})$ modulo an affine part of the form $p + q\hat{f}$, where (p, q) are two arbitrary integration constants that are fixed to be consistent with the usual conventions adopted in the literature for the 3.5 PN approximant [99].

We consider here only *nonspinning* binaries (the reader is referred Sec. 7.5 for the discussion of the spin case). The corresponding, circularized, EOB Hamiltonian is given by Eq. (4.19), where the effective Hamltonian (4.24) has been rewrited in terms of the orbital angular momentum along circular orbits j, i.e. $\hat{H}_{\rm eff} \equiv H_{\rm eff}/\mu = \sqrt{A(u)(1+u^2j^2)}$, where $A(u)$ is the EOB interaction potential (4.15) plus a 5PN term $\nu(a_6^c + a_6^{\ln} \ln u)u^6$ with a_6^c an analytically unknown coefficient. The orbital angular momentum along circular orbits j is obtained solving $\partial_u \hat{H}_{\rm eff} = 0$. By PN-expanding one of Hamilton's equations, $M\omega = \partial_\varphi H^{\rm EOB}$, one obtains $x(u)$ as a 5PN truncated series in u, that, once inverted, allows to obtain the (formal) 5.5 PN accurate energy flux as function of x by PN-expanding its general EOB expression $\mathcal{F} = \sum_{\ell=2}^{\infty} \sum_{\ell=-m}^{m} F_{\ell m}^{\rm Newt} \hat{F}_{\ell m}$, where $F_{\ell m}^{\rm Newt}$ is the Newtonian (leading-order) contribution and $\hat{F}_{\ell m}$ is the relativistic correction. Each multipolar contribution within the EOB formalism comes written in factorized and resummed form as Eq. (6.32). Here we use the relativistic residual amplitude ($\rho_{\ell m}$) information reported in Eqs (7)-(18) of Ref. [11], where the unknown high-PN coefficients (polynomials in ν) have been parametrized by some coefficients $c_{\ell m}$. We include for consistency all the coefficients to go up to the $\ell = 7$, $m =$ even multipoles.

[1] In the sense that it is independent of time and phase arbitrary shifts.

From Eq. (7.1) one obtains the following PN-expanded expression

$$\hat{Q}_\omega^{\rm PN} = 1 + b_2 x + b_3 x^{3/2} + b_4 x^2 + b_5 x^{5/2} + b_6 x^3 + b_7 x^{7/2} + b_8 x^4 + b_9 x^{9/2} + b_{10} x^5 + b_{11} x^{11/2}. \tag{7.3}$$

The coefficients of this expansion, that are reported in full in Sec. 7.6, have the structure $b_i \equiv b_i^0 + b_i(\nu)$, where b_i^0 is the ν-independent (test-particle) part, fully known analytically, while the $b_i(\nu)$ encode the ν-dependence that is completely known at 3PN, while only partially known at 4PN because the corresponding waveform calculation is not completed yet. The ν-dependence beyond 3PN is formally incorporated by extending the analytically known $\rho_{\ell m}$ function with additional ν-dependent coefficients and then reflects in the coefficients $b_i(\nu)$. Among these coefficients, those that depend on the parameters that we have introduced in the computation are

$$b_8 = b_8(c_{21}^{\rm 3PN}, c_{22}^{\rm 4PN}) \tag{7.4}$$

$$b_{10} = b_{10}(c_{21}^{\rm 3PN}, c_{22}^{\rm 4PN}, c_{22}^{\rm 5PN}) \tag{7.5}$$

$$b_{11} = b_{11}(c_{21}^{\rm 3PN}, c_{22}^{\rm 4PN}) \ . \tag{7.6}$$

In the following analysis, we fix to zero a_6^c as well as all the yet uncalculated, ν-dependent, PN waveform coefficients entering Eq. (7.3) above. This entitles us to use the definition of *quasi-5.5PN* approximant (this PN-order choice is discussed in Sec. 7.4 and resumed in Fig. 7.5). Note however that in the NR-informed EOB model, that we shall use to check the reliability of this quasi-5.5PN approximant, all the waveform coefficients are equally fixed to be zero; on the contrary, a_6^c is informed by NR simulations and, as such, effectively takes into account, to same extent, all this missing analytical information. The importance of the ν-dependent waveform coefficients is, a priori, expected to be low, as suggested in Table II of [4]. This is in accord with the fact that an eventual tuning of some free parameters is better when they tend to be small (see See Sec. 7.4).

7.2.1 Assessing the 5.5PN phasing accuracy

Let us now study the performance of `TaylorF2` at 5.5PN versus the full EOB phasing. We do so by comparing the corresponding Q_ω functions and taking the differences, similarly to what was done in Ref. [209] for isolating the tidal part of the EOB phasing and in Ref. [2] for isolating the quadratic-in-spin

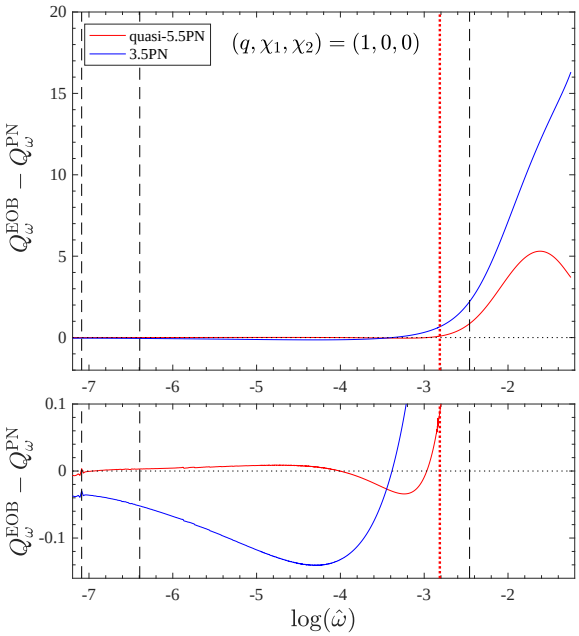

Figure 7.1: Comparison between the point-mass (nonspinning) orbital phasing for $q = 1$ $Q_\omega^{\rm EOB} - Q_\omega^{\rm PN}$ difference up to (approximate) merger time. The vertical lines mark the 10Hz, 20Hz, 718Hz or 1024Hz for a $(1.35 + 1.35)M_\odot$ binary. The quasi-5.5PN curve is always much closer to the EOB one than the standard 3.5PN approximant.

part. Since we have in mind an application to a paradigmatic BNS system, Fig. 7.1 only focuses on the $q = 1$ case. We show our results in terms of differences between the EOB and the PN curves, $Q_\omega^{\rm EOB} - Q_\omega^{\rm PN}$. The top panel of the figure illustrates the full phasing acceleration evolution, up to the peak of the EOB orbital frequency that is identified with the merger. The bottom panel is a close up on the inspiral part. The vertical lines corresponds (from left to right) to 10Hz, 20Hz, 718Hz and 1024Hz for a fiducial equal-mass BNS system with $(1.35 + 1.35)M_\odot$. The 718Hz line corresponds to $\hat{\omega} = 0.06$, that roughly corresponds to the NR contact frequency [240]. The figure highlights that the quasi-5.5PN approximant delivers a rather good representation of the point-mass EOB phasing precisely up to $\hat{\omega} = 0.06$. Table 7.1 reports the phase difference

$$\Delta\phi_{(\hat{\omega}_0,\hat{\omega}_1)} = \int_{\hat{\omega}_0}^{\hat{\omega}_1} \Delta Q_\omega d\log\hat{\omega} \ , \tag{7.7}$$

Table 7.1: EOB/PN phase difference accumulated between $[f_0, f_1]$. It is obtained by integrating the $\Delta Q_\omega^{\rm EOBPN}$'s in Fig. 7.1 between the corresponding values of $\log(\hat{\omega})$. The limits of integration are denoted in Hz as we want to ideally refer to the fiducial $(1.35+1.35)M_\odot$ binary system.

$\hat{\omega}_0 \times 10^4$	$\hat{\omega}_1$	f_0[Hz]	f_1[Hz]	$\Delta\phi^{\rm EOBPN}_{\rm 3.5PN}$	$\Delta\phi^{\rm EOBPN}_{\rm 5.5PN}$
8.35	0.086	10	1024	0.2718	0.1364
8.35	0.060	10	718	-0.1916	1.45×10^{-3}
16.7	0.086	20	1024	0.3009	0.1354
16.7	0.060	20	718	-0.1625	4.54×10^{-4}
20.0	0.086	24	1024	0.3110	0.1348

accumulated between the frequencies $[\hat{\omega}_0, \hat{\omega}_1]$ (or equivalently $[f_0, f_1]$ in physical units) marked by vertical lines in the plots. The numbers in the table illustrate quantitatively how the 5.5PN phasing approximant delivers a phasing description that is, by itself, more EOB compatible than the standarly used 3.5PN one. Note that this is achieved even if the EOB incorporates the effective, NR-informed, $a_c^6(\nu)$ parameter, that is not included in the `TaylorF2` approximant.

7.3 Application to $\tilde{\Lambda}$ inference

We focus now on a BNS system to study the implication of changing the PN-accuracy of the point-mass baseline on the estimate of the tidal polarizability parameter

$$\tilde{\Lambda} = \frac{16}{13}\frac{(m_1+12m_2)m_1^4\Lambda_1 + (m_2+12m_1)m_2^4\Lambda_2}{M^5}, \tag{7.8}$$

where $\Lambda^i \equiv 2/3k_2^i\left[c^2/(G\mathcal{C}_i)\right]^5$ where $\mathcal{C}_i \equiv m_i/R_i$ is the compactness of each star and k_2^i the corresponding quadrupolar Love number [227, 110, 233, 108], see Sec. 3.1.4.

We construct equal-mass EOBNR hybrid BNS waveforms by matching the `TEOBResumS` EOB tidal model [1] to state-of-the-art NR simulations of the `CoRe` collaboration [209]. Note that the version of `TEOBResumS` used here does not incorporate the analytical developments of Refs. [2, 6]. Two fiducial waveforms are considered here corresponding to two nonspinning, equal-mass $(1.35M_\odot + 1.35M_\odot)$ BNS models described by the SLy and H4 EOS. The

Table 7.2: Data behind Figs. 7.2 and 7.3. For each measured quantity, chirp mass $\mathcal{M}$, symmetric mass ratio ν and tidal polarizability $\tilde{\Lambda}$, the columns report: the injected value; the minimum value of frequency considered, either 24Hz or 32Hz; the combination EOS-SNR; finally, the last three columns list the median values measured with the three different waveform approximants with the 90% credible interval. The last row of the table shows the average waveform generation time for each approximant, assuming starting frequency of 24Hz.

	Injected Val.	$f_{\rm min}$	EOS	SNR	`TF2` 3.5PN	`TF2` 5.5PN	`IMRPh.D_NRTidal`
$\mathcal{M}$	1.1752	24 Hz	SLy	30	$1.1753^{1.1755}_{1.1752}$	$1.1753^{1.1755}_{1.1752}$	$1.1753^{1.1755}_{1.1752}$
			H4	30	$1.1753^{1.1755}_{1.1752}$	$1.1753^{1.1755}_{1.1752}$	$1.1753^{1.1755}_{1.1752}$
			SLy	100	$1.1753^{1.1754}_{1.1752}$	$1.1753^{1.1754}_{1.1752}$	$1.1753^{1.1754}_{1.1752}$
			H4	100	$1.1753^{1.1754}_{1.1752}$	$1.1753^{1.1754}_{1.1752}$	$1.1753^{1.1754}_{1.1753}$
		32 Hz	SLy	30	$1.1754^{1.1757}_{1.1752}$	$1.1754^{1.1757}_{1.1752}$	$1.1754^{1.1756}_{1.1752}$
			H4	30	$1.1754^{1.1756}_{1.1751}$	$1.1754^{1.1757}_{1.1752}$	$1.1753^{1.1756}_{1.1751}$
ν	0.25	24 Hz	SLy	30	$0.24649^{0.24996}_{0.23147}$	$0.24558^{0.24995}_{0.23135}$	$0.24636^{0.24997}_{0.23105}$
			H4	30	$0.24729^{0.24997}_{0.2338}$	$0.24581^{0.24995}_{0.23162}$	$0.2459^{0.24996}_{0.23079}$
			SLy	100	$0.24857^{0.24998}_{0.23744}$	$0.24738^{0.24995}_{0.23691}$	$0.24703^{0.24998}_{0.23292}$
			H4	100	$0.24877^{0.24997}_{0.24083}$	$0.24735^{0.24995}_{0.23694}$	$0.24702^{0.24997}_{0.23307}$
		32 Hz	SLy	30	$0.24658^{0.24996}_{0.23107}$	$0.2467^{0.24997}_{0.23247}$	$0.24592^{0.24997}_{0.23054}$
			H4	30	$0.24684^{0.24997}_{0.23282}$	$0.24602^{0.24995}_{0.23194}$	$0.24576^{0.24996}_{0.23051}$
$\tilde{\Lambda}$	392	24 Hz	SLy	30	$935.91^{2547.71}_{245.40}$	$517.88^{971.32}_{162.29}$	$400.47^{761.30}_{135.47}$
	1110		H4	30	$1690.56^{3589.6}_{632.12}$	$987.29^{1575.33}_{422.78}$	$1044.27^{1459.18}_{630.88}$
	392		SLy	100	$452.24^{694.52}_{180.44}$	$301.87^{459.52}_{149.57}$	$295.21^{410.31}_{162.62}$
	1110		H4	100	$1405.42^{1726.90}_{1065.20}$	$894.93^{1069.01}_{711.92}$	$1051.61^{1195.12}_{837.18}$
	392	32 Hz	SLy	30	$1007.47^{2743.87}_{267.25}$	$572.29^{1177.84}_{156.79}$	$419.89^{803.14}_{144.15}$
	1110		H4	30	$1675.67^{3464.08}_{660.31}$	$1042.61^{1713.99}_{416.23}$	$1060.44^{1509.45}_{633.25}$
Average Time					22.9 ms	32.68 ms	60.13 ms

corresponding values of the tidal parameters are $\tilde{\Lambda} = 392.231$ (Sly EOS) and $\tilde{\Lambda} = 1110.5$ (H4 EOS) [For equal masses $\tilde{\Lambda} = \Lambda_1 = \Lambda_2$.] The waveforms are injected at SNR of 30 and 100 into a fiducial data stream of the LIGO detectors [303]. We assume the projected noise curve for the Advanced LIGO detectors in the zero-detuned high-power configuration (ZDHP) [223] and no actual noise is added to the data.

The injected waveform is recovered with three approximants:
(i) `IMRPhenomD_NRTidal` [209], where the point-mass orbital phasing is obtained by a suitable representation of hybridized EOB/NR BBH waveforms, the `PhenomD` approximant [30]; (ii) `TaylorF2` where the 3.5PN orbital phase

is augmented by the 6PN (next-to-leading) tidal phase [242]; (iii) the same as above where the 3.5PN orbital, nonspinning, phase is replaced by the quasi-5.5PN one. The models are implemented in the
`LSC Algorithm Library Suite (LALSuite)`. The LIGO-Virgo parameter-estimation algorithm `LALInference` [45]) is then employed to extract the binary properties from the signal. We use a uniform prior distribution in the interval $[1M_\odot, 3M_\odot]$ for the component masses, and a uniform prior between -1 and 1 for both dimensionless aligned spins. We also pick a uniform prior distribution for the individual tidal parameters $\Lambda_{1,2}$ between 0 and 5000.

The outcome of the analysis is illustrated in Fig. 7.2 for the SLy EOS and and Fig. 7.3 the H4 EOS. We compare the inference of the tidal parameter done on two frequency intervals, $[24, 1024]$ Hz and $[32, 1024]$. Note that we do not extend the analysis interval even further because we know that the orbital part of the `TaylorF2` approximants becomes largely inaccurate at higher frequencies. For SNR = 30 one finds that the 3.5PN orbital baseline induces a clear bias in $\tilde{\Lambda}$, while the quasi-5.5PN one agrees much better with the `PhenomD` model as well as the expected value (vertical line in the plots). Incrementing the SNR to 100, the statement only holds for the softer EOS, since for the H4 case also the 5.5PN approximant is biased, although still less than the 3.5PN one. The two figures are complemented by Table 7.2, that, for each choice of configuration and SNR, lists the recovered values with their 90% credible interval. The last row of the table also reports the time needed to generate a single waveform during the PE process: interestingly, the timing of the quasi-5.5PN `TaylorF2` is comparable to the one of the 3.5PN approximant, i.e. it remains approximately *two times faster* than `PhenomD_NRTidal` being consistent with this latter at SNR $\lesssim 30$. This suggests that, for events similar to GW170817 or quieter, the quasi-5.5PN `TaylorF2` can effectively be used in place of `PhenomD_NRTidal` to get an even faster, yet accurate, estimate of the parameters.

7.3.1 Understanding waveform systematics of the injections via the Q_ω analysis

Let us finally heuristically explain why the effect of the 3.5PN-accurate orbital baseline is to bias the value of $\tilde{\Lambda}$ towards values that are larger than the theoretical expectation. Inspecting Fig. 7.1 one sees that the $Q_\omega^{\rm EOB} - Q_\omega^{\rm 3.5PN}$ is negative. This means that the PN phase accelerates *less* than the EOB

one, namely the inspiral occurs *more slowly* in the 3.5PN phasing description than in the EOB one. Loosely speaking, one may think that the gravitational interaction behind the 3.5PN-accurate orbital phasing is *less attractive* than what predicted by the EOB model. Evidently, this effect might be compensated by an additional part in the total PN phasing that stems for a part of the dynamics that is intrinsically *attractive* and that could compensate for the inaccurate behavior of the 3.5 PN. Since eventually the phase difference is given by an integral, two effects of opposite sign can mutually compensate and thus generate a PN-based frequency phase that is compatible with the EOB one. Since tidal interactions are attractive, the corresponding part of the phasing is naturally able to compensate the repulsive character of the orbital phasing. For this compensation to be effective, it may happen that $\tilde{\Lambda}$ has to be *larger* than the theoretically correct one that accounts for the tidal interaction (at leading order) in the EOB waveform.

Such intuitive explanation is put on more solid ground in Fig. 7.4. The figure refers to the SLy model and compares two EOB-PN Q_ω differences $\Delta Q_\omega^{\rm EOBPN} \equiv Q_\omega^{\rm EOB} - Q_\omega^{\rm PN}$, where the $Q_\omega^{\rm EOB}$ is the complete function, while $Q_\omega^{\rm PN}$ is obtained summing together the 3.5PN orbital phase and the 6PN-accurate tidal phase [230]. When we use the theoretically correct value of $\tilde{\Lambda} = \Lambda_1 = \Lambda_2 = 392.231$ the phase difference in the interval $\hat{\omega} \in [\hat{\omega}_0, \hat{\omega}_1] = [0.002, 0.06]$, corresponding to $f \in [20, 718]$ Hz (dotted vertical line in the figure) for this binary, is $\Delta\phi_{(\hat{\omega}_0,\hat{\omega}_1)} \simeq -0.276$ rad. By contrast, if the value of $\tilde{\Lambda}$ is progressively increased, the accumulated phase difference between $[\hat{\omega}_0, \hat{\omega}_1]$ gets reduced up to $\Delta\phi_{(\hat{\omega}_0,\hat{\omega}_1)} \simeq 2.429 \times 10^{-4}$ for $\tilde{\Lambda} = 442.987$. Note however that such analytically predicted "bias"in $\tilde{\Lambda}$ depends on the frequency interval considered: if we extended the integration up to $\hat{\omega}_1 \simeq 0.08$ (corresponding to 957.4 Hz) one finds that a similarly small accumulated phase difference $\Delta\phi_{0.002,0.08} \simeq 5.0 \times 10^{-5}$ is obtained for $\tilde{\Lambda} = 424.08$, i.e. the analytical bias is *reduced*. This fact looks counterintuitive: a result obtained with a PN approximant is not, a priori, expected to improve when including higher frequencies. By contrast, the fact that the analytic bias is (slightly) reduced increasing $\hat{\omega}_1$ just illustrates the *lack of robustness* as well as the *lack of predictive power* of the approximant in the strong-field regime. Generally speaking, one sees that the combination of 3.5PN orbital phase with 6PN tidal phase may result in a waveform that is *effectual* with respect the EOB one, in the sense that the noise-weighted scalar product will be of order unity, but with an incorrect value of the tidal parameter. This simple example is

Table 7.3: EOB/PN phase difference accumulated between $[f_0, f_1]$. It is obtained by integrating the $\Delta Q_\omega^{\rm EOBPN}$'s in Fig. 7.5 between the corresponding values of $\log(\hat{\omega})$, also listed in the table. The limits of integration denoted in Hz refer to the fiducial $(1.35+1.35)M_\odot$ binary system.

$\hat{\omega}_0\ \times 10^4$	$\hat{\omega}_1$	f_0[Hz]	f_1[Hz]	$\Delta\phi_{\rm 5PN}^{\rm EOBPN}$	$\Delta\phi_{\rm 4.5PN}^{\rm EOBPN}$	$\Delta\phi_{\rm 4PN}^{\rm EOBPN}$
8.35	0.086	10	1024	1.0805	1.0109	1.6306
8.35	0.060	10	718	0.4984	0.469	0.9241
16.7	0.086	20	1024	1.079	1.0094	1.6235
16.7	0.060	20	718	0.4970	0.4675	0.9170
20.0	0.086	24	1024	1.0781	1.0085	1.6203

helpful to intuitively understand how the incorrect behavior of the point-mass nonspinning phasing can eventually result in a bias towards larger values of $\tilde{\Lambda}$. Interestingly, this value is close to the value obtained with SNR=100 (see left-bottom panel of Fig. 7.2). Although the analysis of Fig. 7.4 certainly cannot replace an injection-recovery study, it should be kept in mind as a complementary tool to interpret its outcome within a simple, intuitive but quantitative, framework.

7.4 Why quasi-5.5PN?

Post-Newtonian expansion are truncated asymptotic series, so it is not a priori granted that by increasing the PN order one will automatically get a better approximation to the exact result. The choice of using the quasi-5.5PN `TaylorF2` for the injection study of Sec. 7.3 was made after having carefully analyzed all the previous quasi-PN orders beyond 3.5PN and having compared each PN-truncation of the Q_ω function to the corresponding outcome of `TEOBResumS`. The result of this analysis is shown in Fig. 7.5, that illustrates how the quasi-5.5PN $Q_\omega^{\rm EOB} - Q_\omega^{\rm PN}$ difference remains consistently close to zero for a frequency interval that is much longer than for any other lower-PN truncation. This finding justifies our choice of focussing on the quasi-5.5PN approximant in the main text.

With this PN order, the first natural question that follows is whether there is some simple way to improve the accuracy of the approximant just by tuning some of its (many) free parameters. Before entering this discussion, the simplest thing to do is to incorporate more analytical information, e.g.

instead of using $a_6^c = 0$ incorporating either the analytical gravitational self-force value $a_6^c(0)$, that was obtained in Refs. [152, 304]

$$a_6^c(0) = -\frac{1066621}{1575} - \frac{14008\gamma}{105} + \frac{246367\pi^2}{3072} - \frac{31736\log(2)}{105} + \frac{243\log(3)}{7}, \tag{7.9}$$

or even the numerical-relativity informed one [34]

$$a_{6,\mathrm{NR}}^c(\nu) = 3097.3\nu^2 - 1330.6\nu + 81.38. \tag{7.10}$$

Although these two functions encode physically correct effect (though only effectively for $a_{6,\mathrm{NR}}^c(\nu)$) they turn out, both, to increase the repulsive character of the approximant, without any real advantage. In practice, when the values above are used, one get an acceptable EOB/PN agreement only up to $\hat{\omega} \approx 0.02$.

From the PN point of view, we expect from Table II of [4] that the order of magnitude of the various $c_{\ell m}^{\mathrm{PN}}$ coefficient is small. This is the rational behind our conservative choice of simply setting then to zero. Still, one could think to use some of these coefficients, as well as a_6^c as tunable parameter and investigate whether it is possible to flex the quasi-5.5PN `TaylorF2` approximant so as to reduce the EOB/PN disagreement even to frequencies higher than 0.06.

As a proof of principle, we explored that this is the case considering the $q = 1$ case and flexing, at the same time, both a_6^c and $c_{22}^{4\mathrm{PN}}$, that are, in sense, the lowest-order unknown coefficients in the model. One easily finds that fixing $a_6^c = 49$ and $c_{22}^{4\mathrm{PN}} = 10.45$ the integrated EOB/PN phase difference in the point-mass sector accumulated on the interval $[\hat{\omega}_0, \hat{\omega}_1] = [0.002, 0.08]$ can be reduced from 0.085 rad to $\simeq 10^{-4}$ rad.

7.5 Mass ratio and spin

Increasing the mass ratio or the spins (to mild values) of the binary does not affect the robustness of the quasi-5.5PN, untuned, approximant. In Fig. 7.6 we see that the difference between the "exact" numerical Q_ω and the analytical one is still approximately flat for a qualitatively wide range of frequencies. Beyond that, for what concerns the spin, we show in Figs. 7.7 a

qualitative point-mass BNS case with realistic positive and negative spins. In this case we put to zero the quadrupole-monopole interaction terms, $C_{Q1} = C_{Q2} = 0$, removing the quadratic-in-spin PN corrections both in the numerical `TEOBResumS` model and in the analytical approximant. So contribution of the mixed $\chi_1\chi_2$ terms and the spin-orbit interaction is tested, including for completeness also the new 4PN spin-orbit `Taylor-F2` term computed in Ref. [2], i.e. the Q_ω analogue of Eq. (48) there. While the spin-orbit terms are already contained in `TEOBResumS` in a resummed form, we neglect the spin cube and spin quartic PN corrections (see [2]) for simplicity, since their effect does not affect our preliminary robustness test.

7.6 Quasi-5.5PN phasing coefficients

We report in this section the explicit expressions for the coefficients entering Eq. (7.3). For simplicity, we put to zero all the $c_{\ell m}^{\rm PN}$'s except $c_{22}^{\rm 4PN}$ and $c_{21}^{\rm 3PN}$. We have:

$$b_2 = \frac{11\nu}{4} + \frac{743}{336}$$

$$b_3 = -4\pi \tag{7.11}$$

$$b_4 = \frac{617\nu^2}{144} + \frac{5429\nu}{1008} + \frac{3058673}{1016064} \tag{7.12}$$

$$b_5 = \pi\left(\frac{13\nu}{8} - \frac{7729}{672}\right) \tag{7.13}$$

$$b_6 = \frac{25565\nu^3}{5184} - \frac{15211\nu^2}{6912} + \left(-\frac{451\pi^2}{48} + \frac{3147553127}{12192768}\right)\nu + \frac{856\log(x)}{105} + \frac{3424\log(2)}{105} + \frac{32\pi^2}{3} + \frac{1712\gamma}{105} - \frac{10817850546611}{93884313600} \tag{7.14}$$

$$b_7 = \pi\left(\frac{14809\nu^2}{3024} - \frac{75703\nu}{6048} - \frac{15419335}{1016064}\right) \tag{7.15}$$

$$b_8 = c_{21}^{3\mathrm{PN}}\left(\frac{4}{9}\nu^2 - \frac{1}{9}\nu\right) + \frac{73893895655\nu^4}{14239120896} - \frac{102008296205\nu^3}{11650189824} + \left(\frac{79909\pi^2}{24192} - \frac{300600673165997}{2563041761280}\right)\nu^2 + \left(-4c_{22}^{4\mathrm{PN}} + \frac{332683\log(x)}{2205} - \frac{1860443\pi^2}{48384} + \frac{6252765829282087}{5695648358400}\right)\nu + \gamma\left(\frac{665366\nu}{2205} + \frac{9203}{210}\right) + \frac{9203\log(x)}{420} + \left(\frac{47385}{1568} - \frac{47385\nu}{392}\right)\log(3) + \left(\frac{177586\nu}{245} + \frac{50551}{882}\right)\log(2) + \frac{9049\pi^2}{252} - \frac{2496799162103891233}{3690780136243200} \tag{7.16}$$

$$b_9 = \pi\left[\frac{2064751\nu^3}{399168} + \frac{9058667\nu^2}{254016} + \left(\frac{451\pi^2}{12} - \frac{298583452147}{268240896}\right)\nu - \frac{3424}{105}\log(x) - \frac{13696}{105}\log(2) - \frac{64\pi^2}{3} - \frac{6848\gamma}{105} + \frac{90036665674763}{187768627200}\right], \tag{7.17}$$

$$\begin{aligned} b_{10} = {} & \frac{1}{-1+3\nu}\left[c_{21}^{3\mathrm{PN}}\left(\frac{121}{189}\nu - \frac{2815}{756}\nu^2 + \frac{599}{252}\nu^3 + \frac{191}{21}\nu^4\right) + \left(-12c_{22}^{5\mathrm{PN}} + 54a_6^c + \frac{349c_{22}^{4\mathrm{PN}}}{42}\right. \right. \\ & - \frac{415795517\pi^2}{3612672} + \frac{99239192119\gamma}{18336780} + \frac{359258131018599276889754 9}{292602096577251901440} + \frac{58330935\log(3)}{21952} \\ & \left. + \frac{117340379713\log(2)}{18336780}\right)\nu^2 + \left(-18a_6^c + \frac{311c_{22}^{4\mathrm{PN}}}{42} + 4c_{22}^{5\mathrm{PN}} + \frac{5451429547\pi^2}{32514048}\right. \\ & - \frac{63787407527\gamma}{36673560} - \frac{27492311773558199217812 77}{216742293760927334400} - \frac{8924175\log(3)}{12544} \\ & \left. - \frac{159943397077\log(2)}{73347120}\right)\nu + \left(-\frac{641c_{22}^{4\mathrm{PN}}}{7} + \frac{460519\pi^2}{6144} + \frac{3073896571\gamma}{3056130}\right. \\ & \left. + \frac{655042586669421296014259}{137157232770586828800} - \frac{1279395\log(3)}{392} + \frac{10777949417\log(2)}{1528065}\right)\nu^3 \\ & - \frac{24250665851020529797 97\nu^6}{3428930819264670720} + \frac{12721434740371951621\nu^5}{2705270863325184} \\ & + \left(\frac{9434797\pi^2}{75264} - \frac{11160810800663155149913}{1088549466433228800}\right)\nu^4 - \frac{578223115\pi^2}{12192768} - \frac{6470582647\gamma}{110020680} \\ & \left. + \frac{1412206995432957982751}{505226791983513600} + \frac{5512455\log(3)}{87808} - \frac{53992839431\log(2)}{220041360}\right] \\ & + \left(-\frac{6431890181\nu^2}{18336780} - \frac{2968141499\nu}{12224520} + \frac{6470582647}{220041360}\right)\log(x)\,, \end{aligned} \tag{7.18}$$

$$\begin{aligned} b_{11} = {} & \pi\left[c_{21}^{3\mathrm{PN}}\left(-\frac{8}{3}\nu^2 + \frac{2}{3}\nu\right) + \frac{131525414689\nu^4}{64076044032} - \frac{216119565695\nu^3}{11650189824}\right. \\ & + \left(-\frac{2129581\pi^2}{16128} + \frac{5120314955146397}{1398022778880}\right)\nu^2 \\ & + \left(-\frac{673331\log(x)}{1260} + \frac{9003157\pi^2}{64512} + 16c_{22}^{4\mathrm{PN}} - \frac{471473599592788087}{76891252838400}\right)\nu \\ & + \gamma\left(-\frac{673331\nu}{630} - \frac{3558011}{17640}\right) - \frac{3558011\log(x)}{35280} + \left(\frac{47385\nu}{196} - \frac{47385}{784}\right)\log(3) \\ & \left. + \left(-\frac{10504813\nu}{4410} - \frac{862549}{2520}\right)\log(2) - \frac{9439\pi^2}{126} + \frac{17955051434264337 71}{615130022707200}\right]. \end{aligned} \tag{7.19}$$

The GW phase in the SPA is computed from the Q_ω using (7.2) and it is given by the Taylor series

$$\Psi(f) = \frac{3(\pi M f)^{-5/3}}{128\nu} \sum_i \varphi_i (\pi M f)^i \ ; \tag{7.20}$$

with the coefficients:

$$\varphi_0 = 1$$

$$\varphi_1 = 0 \tag{7.21}$$

$$\varphi_2 = \frac{3715}{756} + \frac{55}{9}\nu \tag{7.22}$$

$$\varphi_3 = -16\pi \tag{7.23}$$

$$\varphi_4 = \frac{3085\nu^2}{72} + \frac{27145\nu}{504} + \frac{15293365}{508032} \tag{7.24}$$

$$\varphi_5 = \pi\left(\frac{38645}{756} - \frac{65\nu}{9}\right)[1 + \log(\pi f M)] \tag{7.25}$$

$$\begin{aligned}\varphi_6 = {} & -\frac{6848}{63}\log(\pi f M) - \frac{127825\nu^3}{1296} + \frac{76055\nu^2}{1728} + \left(\frac{2255\pi^2}{12} - \frac{15737765635}{3048192}\right)\nu \\ & - \frac{640\pi^2}{3} - \frac{6848\gamma}{21} + \frac{11583231236531}{4694215680} - \frac{13696\log(2)}{21}\end{aligned} \tag{7.26}$$

$$\varphi_7 = \pi\left(-\frac{74045\nu^2}{756} + \frac{378515\nu}{1512} + \frac{77096675}{254016}\right) \tag{7.27}$$

$$\begin{aligned}\varphi_8 = {} & [1 - \log(\pi f M)]\left[c_{21}^{3\mathrm{PN}}\left(\frac{40\nu}{81} - \frac{160\nu^2}{81}\right) + \frac{160 c_{22}^{4\mathrm{PN}}\nu}{9}\right. \\ & - \frac{369469478275\nu^4}{16019011008} + \frac{510041481025\nu^3}{13106463552} + \left(\frac{300600673165997}{576684396288} - \frac{399545\pi^2}{27216}\right)\nu^2 \\ & + \left(-\frac{5679872289503527}{1281520880640} - \frac{5322928\gamma}{3969} + \frac{9302215\pi^2}{54432}\right. \\ & \left.\left. - \frac{1420688\log(2)}{441} + \frac{26325\log(3)}{49}\right)\nu - \frac{90490\pi^2}{567} - \frac{36812\gamma}{189} + \frac{2550713843998885153}{830425530654720}\right. \\ & \left. - \frac{26325\log(3)}{196} - \frac{1011020\log(2)}{3969}\right] + \left(\frac{2661464\nu}{11907} + \frac{18406}{567}\right)\log^2(\pi f M)\end{aligned} \tag{7.28}$$

$$\begin{aligned}\varphi_9 = {} & \pi\left[-\frac{13696}{63}\log(\pi f M) + \frac{10323755\nu^3}{199584} + \frac{45293335\nu^2}{127008} + \left(\frac{2255}{6}\pi^2 - \frac{1492917260735}{134120448}\right)\nu\right. \\ & \left. - \frac{640}{3}\pi^2 - \frac{13696\gamma}{21} + \frac{105344279473163}{18776862720} - \frac{27392\log(2)}{21}\right]\end{aligned} \tag{7.29}$$

$$\varphi_{10} = \frac{1}{1-3\nu}\Bigg[a_6^c(72\nu - 216\nu^2) + c_{21}^{3\mathrm{PN}}\left(-\frac{764\nu^4}{21} - \frac{599\nu^3}{63} + \frac{2815\nu^2}{189} - \frac{484\nu}{189}\right)$$
$$+ c_{22}^{4\mathrm{PN}}\left(\frac{2564\nu^3}{7} - \frac{698\nu^2}{21} - \frac{622\nu}{21}\right) + c_{22}^{5\mathrm{PN}}\left(48\nu^2 - 16\nu\right)$$
$$+ \left(\frac{12863780362\nu^3}{4584195} + \frac{13849493129\nu^2}{13752585} - \frac{24279431641\nu}{27505170} + \frac{6470582647}{82515510}\right)\log(\pi f M)$$
$$+ \frac{24250665851020529797\nu^6}{857232704816167680} - \frac{12721434740371951621\nu^5}{676317715831296} + \Bigg(\frac{11160810800663155149913}{272137366608307200}$$
$$- \frac{9434797\pi^2}{18816}\Bigg)\nu^4 + \Bigg(-\frac{857104076559310860540851}{34289308192646707200} - \frac{6147793142\gamma}{1528065} - \frac{460519\pi^2}{1536}$$
$$- \frac{43111797668\log(2)}{1528065} + \frac{1279395\log(3)}{98}\Bigg)\nu^3 + \Bigg(-\frac{18736399363805057301105217}{365752620721564876800} - \frac{99239192119\gamma}{4584195}$$
$$+ \frac{415795517\pi^2}{903168} - \frac{117340379713\log(2)}{4584195} - \frac{58330935\log(3)}{5488}\Bigg)\nu^2 + \Bigg(\frac{569935181259668744781113}{10837114688046366720}$$
$$+ \frac{63787407527\gamma}{9168390} - \frac{5451429547\pi^2}{8128512} + \frac{159943397077\log(2)}{18336780} + \frac{8924175\log(3)}{3136}\Bigg)\nu + \frac{578223115\pi^2}{3048192}$$
$$+ \frac{6470582647\gamma}{27505170} - \frac{1433006523295407126559}{126306697995878400} - \frac{5512455\log(3)}{21952} + \frac{53992839431\log(2)}{55010340}\Bigg] \tag{7.30}$$

$$\varphi_{11} = \pi\Bigg[c_{21}^{3\mathrm{PN}}\left(-\frac{160\nu^2}{27} + \frac{40\nu}{27}\right) + \frac{320c_{22}^{4\mathrm{PN}}\nu}{9} - \left(\frac{1346662\nu}{1701} + \frac{3558011}{23814}\right)\log(\pi f M)$$
$$+ \frac{657627073445\nu^4}{144171099072} - \frac{1080597828475\nu^3}{26212927104} + \frac{5120314955146397\nu^2}{629110250496}$$
$$+ \pi^2\left(-\frac{10647905\nu^2}{36288} + \frac{45015785\nu}{145152} - \frac{94390}{567}\right)$$
$$+ \left(-\frac{1346662\gamma}{567} - \frac{430383707398397047}{34601063777280} + \frac{26325}{49}\log(3) - \frac{21009626\log(2)}{3969}\right)\nu - \frac{3558011\gamma}{7938}$$
$$+ \frac{1857541407236594411}{276808510218240} - \frac{26325\log(3)}{196} - \frac{862549\log(2)}{1134}\Bigg] \tag{7.31}$$

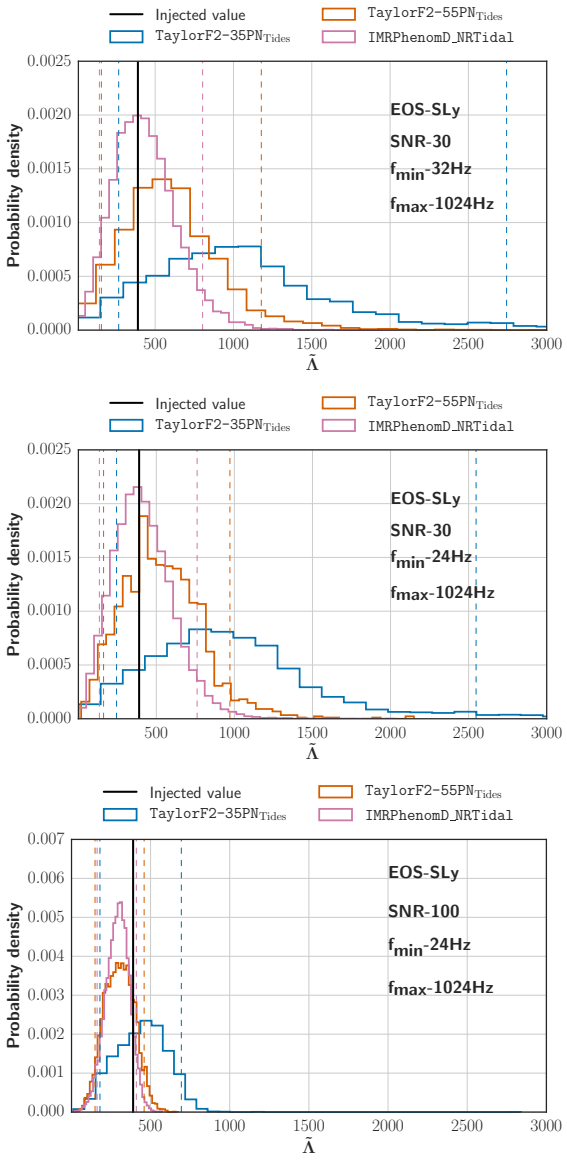

Figure 7.2: $1.35M_\odot + 1.35M_\odot$ binary with Sly EOS. Inference of $\tilde{\Lambda}$ with different waveform model on different frequency intervals $[f_{\rm min}, f_{\rm max}]$ with different SNR. The vertical line corresponds to the injected value $\tilde{\Lambda}^{\rm SLy} = 392.231$. Irrespectively of the value of SNR, the 3.5PN baseline introduces a strong bias (and spread) in the measure of $\tilde{\Lambda}$. By contrast this is practically reabsorbed when using the quasi-5.5PN point-mass baseline. The dashed vertical lines corresponds to 90% confidence level.

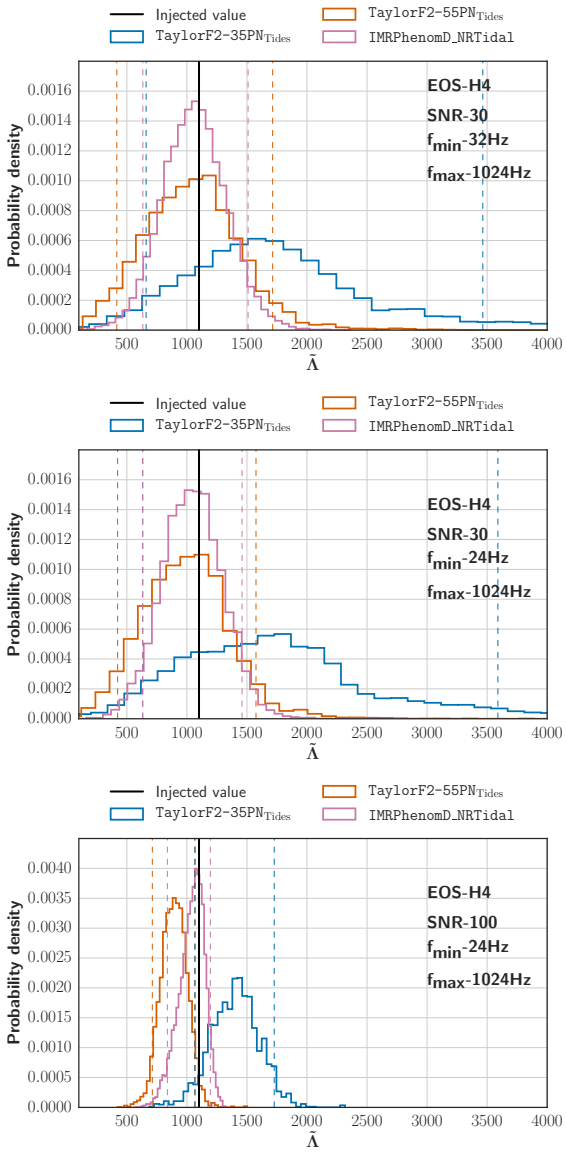

Figure 7.3: $1.35M_\odot + 1.35M_\odot$ binary with Sly EOS. Inference of $\tilde{\Lambda}$ with different waveform model on different frequency intervals $[f_{\rm min}, f_{\rm max}]$ with different SNR. The vertical line corresponds to the injected value $\tilde{\Lambda}^{\rm SLy} = 1020.5$. Irrespectively of the value of SNR, the 3.5PN baseline introduces a strong bias (and spread) in the measure of $\tilde{\Lambda}$. By contrast this is practically reabsorbed when using the quasi-5.5PN point-mass baseline. The dashed vertical lines corresponds to 90% confidence level.

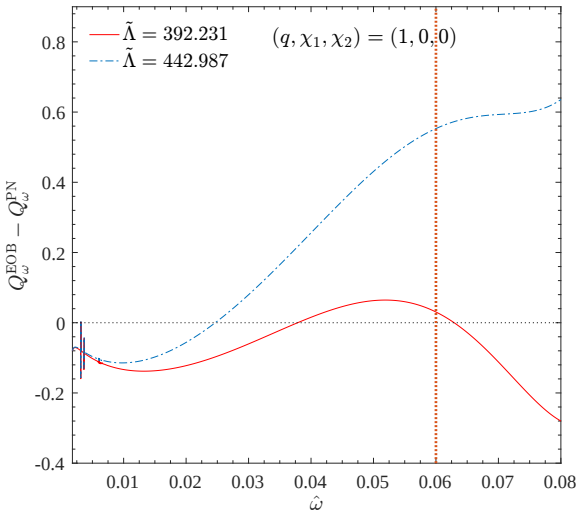

Figure 7.4: Heuristic explanation of the bias on $\tilde{\Lambda}$: $1.35M_\odot + 1.35M_\odot$ binary, Sly EOS, $\tilde{\Lambda} = 392.231$. Shown is the gauge-invariant difference $\Delta Q_\omega^{\rm EOBPN} \equiv Q_\omega^{\rm EOB} - Q_\omega^{\rm PN}$ between the EOB Q_ω and the PN Q_ω with the 3.5PN orbital baseline augmented by the 6PN-accurate tidal phase. Increasing the value of the tidal parameter to $\tilde{\Lambda} = 442.987$ is very effective in reducing the phase difference accumulated between in the interval $\omega \in [0.02, 0.06]$ (dotted vertical line) to a negligible value. Such $\hat{\omega}$ interval correponds to $f \in [24, 718]$ Hz for this binary. The upper frequency limit corresponds to 957.4 Hz.

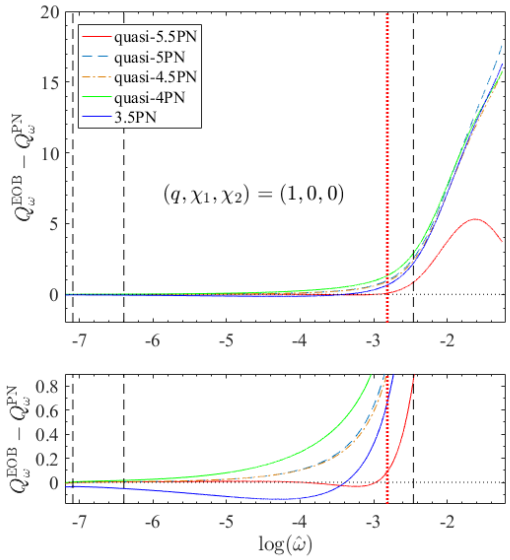

Figure 7.5: Comparison between the point-mass (nonspinning) orbital phasing for $q = 1$ $Q_\omega^{\rm EOB} - Q_\omega^{\rm PN}$ difference up to (approximate) merger time. The vertical lines mark the 10Hz, 20Hz, 718Hz or 1024Hz for a $(1.35 + 1.35)M_\odot$ binary. The quasi-5.5PN curve is always much closer to the EOB one than the other PN order approximants. See Table 7.3 for the accumulated phase differences.

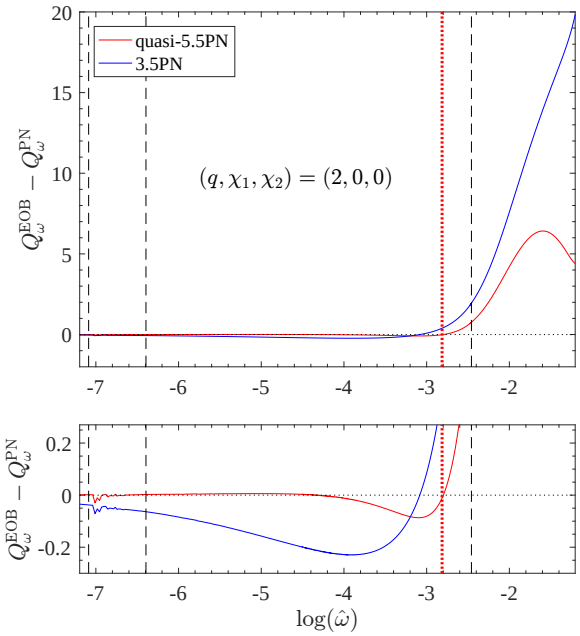

Figure 7.6: Robustness of the quasi-5.5PN `TaylorF2` approximant. The vertical lines correspond to the same four values of $[\hat{\omega}_1, \hat{\omega}_2]$ listed in the first two columns of Table 7.3.

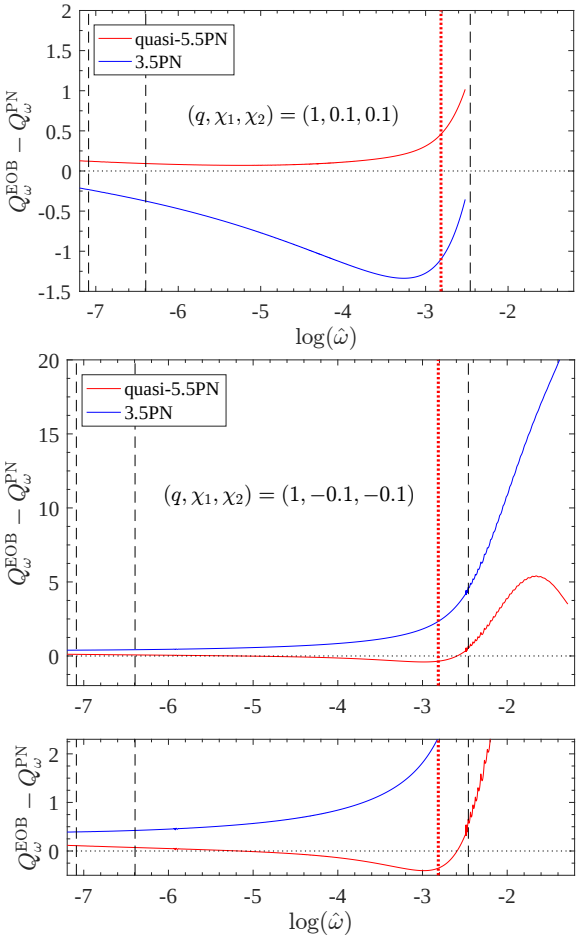

Figure 7.7: Robustness of the quasi-5.5PN `TaylorF2` approximant: spins aligned (top) and spins anti-aligned (bottom) with the orbital angular momentum. The EOB/PN agreement is always improved by the use of the quasi-5.5PN orbital phasing. The vertical lines correspond to the same four values of $[\hat{\omega}_1, \hat{\omega}_2]$ listed in the first two columns of Table 7.3.

Chapter 8

Factorization and resummation: A new paradigm to improve gravitational wave amplitudes. II: the higher multipolar modes [4]

8.1 Introduction

The parameter estimation of gravitational wave events [38, 39, 39, 40, 41, 42, 43] relies on analytical waveform models, possibly calibrated (or informed) by Numerical Relativity simulations [31, 32, 33, 30, 34, 35, 36, 37]. The effective-one-body (EOB) model is currently the only analytical model available that can be consistently used for analyzing both black hole binaries and neutron star binaries [157, 206, 247, 212, 213, 246]. One of the central building blocks of the model is the factorized and resummed (circularized) multipolar post-Newtonian (PN) waveform introduced in [8] for nonspinning binaries. This approach was then straightforwardly generalized in [175] to spinning binaries. Already Ref. [175] pointed out that, in the test-particle limit, the amplitude of such resummed waveform gets inaccurate in the strong-field, fast velocity regime, when the spin of the central black hole is $\gtrsim 0.7$. In the same study, an alternative factorization to improve the test-mass waveform behavior also for larger values of the spin was discussed. More pragmatically, Ref. [305]

finally suggested to improve the analytical multipolar waveform amplitude (and fluxes) of [175] by fitting a few parameters, describing effective high-PN orders, to the highly-accurate fluxes obtained solving numerically the Teukolsky equation [93]. Although this approach is certainly useful to reliably improve the radiation reaction force that drives the transition from quasi-circular inspiral to plunge [226, 61, 306] for a large mass-ratio binary, the question remains whether the domain of validity of purely analytical results can be enlarged in some way. This question makes special sense nowadays, since PN calculations of the fluxes are available at high order [298, 307] and one would like to use them at best. In addition, following for example the seminal attitude of Refs. [167, 8], one has to keep in mind that the test-particle limit should always be seen as a useful *theoretical laboratory* to implement new methods and test new ideas that could be transferred, after suitable modifications, to the case of comparable-mass binaries.

Reference [9] gave a fresh cut to this problem by exploring a new way of treating the residual, PN-expanded, amplitude corrections to the waveforms (i.e., the outcome of the factorization of Refs. [8, 175]) that consists of: (i) factorizing it in a purely orbital and a purely spin-dependent part; (ii) separately resumming each factor in various ways, notably using the inverse Taylor ("iResum") approximant for the spin-dependent factor. Using the test-particle limit to probe the approach, Ref. [9] showed that such factorization–and–resummation paradigm yields a rather good agreement between the $\ell = 2$ numerical and analytical waveform amplitudes up to (and often beyond) the last stable orbit (LSO). The contextual preliminary analysis of the comparable-mass case of [9] also suggests that such improved waveform amplitudes are more robust than the standard ones and may eventually need less important NR-calibration via the next-to-quasi-circular correction factor [167].

The purpose of this chapter is to deepen and refine the investigation of Ref. [9] as well as to generalize it to higher multipoles up to $\ell = 6$. The chapter is organized as follows. In Sec. 8.2 we review and improve the test-particle results of [9] and generalize the procedure up to $\ell = 6$ modes. Section 8.3 brings together all the PN-expanded results currently available for the spin-dependent waveform amplitudes [297, 76, 75], notably written in multipolar form, while Sec. 8.4 explicitly shows the spin-dependent part of the factorized residual amplitudes, both in the standard form of [8, 175], and with the factorization of the orbital terms. The approach to the resummation is undertaken in Sec. (8.5), in particular by discussing the *hybridization* (notably

of the orbital terms) with the test-particle information.

8.2 Test-particle limit: improving the residual multipolar amplitudes

The purpose of this Section is to review and improve the test-particle results of Ref. [9] for the $\ell = 2$ multipole and then generalize them to all multipoles up to $\ell = 6$. Each waveform multipole is written as Eq. (4.36), as explained in Sec. 4.4 and references therein. Such PN correction is then written in factorized form [159] as

$$\hat{h}_{\ell m}(x) = \hat{S}_{\rm eff}^{(\epsilon)} \hat{h}_{\ell m}^{\rm tail} f_{\ell m}(x, S_1, S_2). \tag{8.1}$$

We briefly remind the reader that here the first factor, $\hat{S}_{\rm eff}^{(\epsilon)}$, is the parity-dependent effective source term [8], defined as the EOB effective energy along circular orbits, for $\epsilon = 0$, or the Newton-normalized orbital angular momentum, for $\epsilon = 1$; the second factor, $\hat{h}_{\ell m}^{\rm tail} \equiv T_{\ell m} e^{{\rm i}\delta_{\ell {\rm m}}}$ is a complex factor that accounts for the effect of the tails and other phase-related effects [8, 308, 278]; the third factor, $f_{\ell m}$ is the residual amplitude correction. This latter factor can be further resummed in various ways, that notably depend, when $\nu \neq 0$ and $S_{1,2} \neq 0$, on the parity of m. For example, the original proposal of [8], implemented when the objects are nonspinning, was to first compute from the $f_{\ell m}$ the (Taylor-expanded) functions

$$\rho_{\ell m} \equiv T_n \left[(f_{\ell m})^{1/\ell} \right], \tag{8.2}$$

where $T_n[\dots]$ indicates the Taylor expansion up to x^n and then define the resummed $f_{\ell m}$ by replacing their Taylor expansions with $(\rho_{\ell m})^\ell$. When spins are present, the $\rho_{\ell m}$ functions are naturally written as the sum of an orbital (spin-independent) and a spin-dependent contribution as

$$\rho_{\ell m} = \rho_{\ell m}^{\rm orb} + \rho_{\ell m}^{\rm S}. \tag{8.3}$$

Reference [9] proposed then to improve the strong-field behavior of the $\rho_{\ell m}$'s functions by (i) writing them as the product of a purely orbital and purely spin-dependent factors as

$$\rho_{\ell m} = \rho_{\ell m}^{\rm orb} \hat{\rho}_{\ell m}^{\rm S}, \tag{8.4}$$

where $\hat{\rho}^{\rm S}_{\ell m} \equiv T_n[1+\rho^{\rm S}_{\ell m}/\rho^{\rm orb}_{\ell m}]$, and then resumming each separate factor in a certain way that we detail below [1]. Although there is no first-principle reason for treating the orbital and spin contributions as separate multiplicative factors, such representation proved useful for interpreting the global behavior of the $\rho_{\ell m}$'s as well as for improving it near (or even below) the LSO. For instance, it was argued that a sort of compensation between the spin and orbital factors should occurr in order to guarantee a good agreement between the numerical and analytical functions close to the LSO, especially for large and positive values of the black hole spin. To accomplish such effect, it is necessary to *resum* each factor (or at least the spin-dependent one), that is given by a truncated Taylor series, in a specific way. In particular, it was suggested [9] that a simple and efficient method to temperate the divergent behavior of $\hat{\rho}^{\rm S}_{\ell m}$ towards the LSO is to take its inverse Taylor series (or inverse resummed representation, "iResum") defined as

$$\bar{\rho}^{\rm S}_{\ell m} = \left(T_n\left[\left(\hat{\rho}^{\rm S}_{\ell m}(x)\right)^{-1}\right]\right)^{-1}. \tag{8.5}$$

Reference [9] illustrated that, due to the large amount of PN information available, it is possible to achieve satisfactory numerical/analytical agreement using different truncated PN series as a starting point, though lower-PN orders (e.g. 6PN) are preferable with respect to high-PN orders (e.g. 10PN or 20PN)[2]. The analysis [9] also showed that, once that the factorization and resummation paradigm is assumed, one is free to choose at what PN order to work, provided the resummed amplitude shows a good agreement with the numerical curves. For consistency with previous, EOB-related, works [159], in [9] it was chosen to keep the orbital part at 5PN order, and in Taylor-expanded form, together with the spin-dependent factor truncated at 3.5PN. This choice was made so to be consistent with the spin-dependent information used in the comparable-mass case. For the $\ell = m = 2$ multipole, this yielded rather acceptable analytical/numerical agreement ($\simeq 1\%$) up to the LSO for all spin values between -0.99 and $+0.99$ (see Fig. 4 of [9]).

[1] To simplify the notation, note that we are using here the same symbol $\rho_{\ell m}$, for both the orbital-additive and orbital-factorized amplitudes. By contrast, Ref. [9] was addressing with $\tilde{\rho}_{\ell m}$ the orbital-factorized amplitudes.

[2] It has to be stressed that the impact of high-PN information, i.e. larger than 10 PN, has not been assessed throughly yet, except for preliminary investigations reported in Ref. [9]. We are not going to do this in the current work, but we postpone it to future studies.

Here we relax the constraint of being consistent with previous EOB-related works and present, instead, a new recipe to further improve $\ell = m = 2$ results of Ref. [9] and extend them to higher multipolar modes. To do so, we: (i) generally increase the PN order, possibly requiring it to be the same for both the spin and orbital factors; (ii) resum the orbital factor using some Padé approximant, to be chosen according to the PN order and the multipole; (iii) resum the spin factor taking its inverse Taylor approximant (iResum) as proposed in [9], see Eq. (8.5) above. We find that, modulo a few exceptions to be detailed below, a good compromise is reached by working at *relative* 6PN order for each mode[3] and then taking a Padé P^4_2 approximant[4] for the orbital factor[5]. There are exceptions to this choice (see 2nd column of Table 8.1). For example, the (2,1) mode is better represented using a P^5_1 approximant, the (3,1) using a P^3_2 (i.e. keeping $\rho^{\rm orb}_{32}$ at 5PN accuracy), while for $(4,2)$, $(5,1)$ and $(6,1)$ the orbital factor in Taylor-expanded form is preferable. These choices are made so that the analytical $\rho_{\ell m}$'s remain as close as possible to the numerical one up to the LSO (and possibly beyond). This is illustrated in Fig. 8.1, which displays all $\rho_{\ell m}$'s functions up $\ell = 6$. The figure collects five values of the dimensionless black-hole spin, $\hat{a} = (-0.99, -0.5, 0, +0.5, +0.99)$. The analytical functions are depicted as colored curves, while the numerical data are black. Both curves extend up to the light-ring, while the filled circle mark the LSO location. The $\hat{a} = +0.99$ curves extend up to the highest-frequency (purple, lowest curve) while the $\hat{a} = -0.99$ is at the top of each panel and is depicted red. The information encoded in the figure is complemented by Table 8.1, that lists, for each multipole, the Padé approximant adopted together with the numerical/analytical fractional difference evaluated at the LSO. The figure also highlights that the numerical/analytical agreement looks improvable (for large values of $\hat{a}$) for some subdominant modes, especially ρ_{31} and ρ_{62}, where the analytical

[3]This means that the functions $\hat{h}^{(\epsilon)}_{\ell m}$ in Eq. (4.36) are taken at 6PN, i.e. as 6th-order polynomials in x. This implies that the *global* PN-accuracy we retain is actually higher than $6PN$, because of the presence of the Newtonian prefactors $h^{(N,\epsilon)}_{\ell m}$.

[4]To ease the notation, we indicate with P^n_d the Padé approximant of order (n, d), where n is the highest power of the numerator and d the highest power at the denominator of the rational function.

[5]A priori one would like to use diagonal Padé approximants, since they are known to deliver, in general, the closest approximation to the full function. However, we found that spurious poles are always present in this case. This fact prevents us from making this choice to preserve the simplicity of the approach.

functions are systematically above the numerical ones towards the boundary of the x-domain considered. The reason behind this behavior is that both $P_2^3(\rho_{32}^{\rm orb})$ and $P_2^4(\rho_{62}^{\rm orb})$ develop a spurious pole on the real x-axis, at $x \approx 0.86$ for the former and at $x \approx 0.82$ for the latter. In this respect, we stress that our choices about the PN truncation order and the consequent resummation strategies should be seen as a compromise between simplicity (i.e. using relatively low-order PN-information) and achievable accuracy (i.e. good global agreement with the numerical functions). For example, one finds that the numerical/analytical disagreement for ρ_{31} at the LSO for $\hat{a} = +0.99$ can be reduced to just -0.17% by: (i) taking $\rho_{31}^{\rm orb}$ at only 4PN order and resumming it with a P_1^3 approximant, while (ii) $\hat{\rho}_{31}^{\rm S}$ is taken up to 8PN order and then resummed as usual with its inverse Taylor series. Similarly, one also easily finds that the global behavior of the $(3,3)$, $(4,4)$ and $(5,5)$ modes can be improved by just keeping the orbital factor in Taylor-expanded form instead of replacing it with its $(4,2)$ Padé approximant. To figure out the relevance of any of these improvements, it is convenient to inspect the total energy flux reconstructed using the resummed $\rho_{\ell m}$'s. At a practical level, some analytical/numerical differences that look large on the $\rho_{\ell m}$'s are subdominant within the flux and can be practically ignored. Figure 8.2 compares Newton-normalized energy fluxes, with all multipoles summed together up to $\ell = 6$ included, as follows: (i) the numerical flux, that can be considered as "exact" since its numerical uncertainty is of 10^{-14} [309] (i.e. several orders of magnitude smaller than the relative differences illustrated in Table 8.1); (ii) the analytical flux that is obtained from the $\rho_{\ell m}$'s shown in Fig. 8.1, where the choices for the Padé of the orbital part are listed as non-bold face in Table 8.1 (dot-dashed, orange line); (iii) the analytical flux obtained by taking the $\rho_{33}^{\rm orb}$, $\rho_{44}^{\rm orb}$ and $\rho_{55}^{\rm orb}$ as plain 6PN-accurate Taylor expansions; (iv) the analytical flux where the 6PN-accurate $\rho_{\ell m}$'s are neither further factorized nor resummed, following the original paradigm of Refs. [8, 175]. The vertical line marks the LSO location. The figure illustrates how changing the treatment of the orbital part of the subdominant modes mentioned above allows one to reduce the fractional difference around the LSO from 10% to approximately 5%. It is also to be noticed the good qualitative behavior of the flux also below the LSO, close to the light ring where the flux diverges. By contrast, the flux obtained using the standard, nonresummed, $\rho_{\ell m}$ amplitudes in the form of [8, 175], though pushed to higher PN order as discussed above, is reliable only up to $x \approx 0.2$. We also mention that, even though the choice of $P_1^3(\rho_{31}^{\rm orb})\bar{\rho}_{31}^{\rm S}$ with $\hat{\rho}_{31}^{\rm S}$ taken at 8PN order can strongly reduce the

numerical/analytical differences displayed in Fig. 8.1, in practice this does not have any notable consequence on the total flux. The same statement also holds for the $(6,2)$ mode: the near-LSO behavior of the analytical ρ_{62} can be improved by working at 8PN, both in the spin and orbital factors (with a P_2^6 approximant for this latter), without however producing any important impact on the total flux computation.

Let us finally mention in passing that another way to improve the strong-field behavior of the $\rho_{\ell m}$'s (and thus of the flux) is by including some effective high-PN order parameter that can be *informed* (i.e., calibrated or even fitted) to the numerical data. This approach might be necessary, for example, when dealing with precision calculations that require an accurate representation of the radiation reaction in the near-LSO regime, e.g., estimate of the final recoil velocity when the central black hole is quasi-extremal with the spin aligned with the orbital angular momentum [306]. As an exploratory investigation dealing with just ρ_{22}, we found that it is sufficient to introduce a 6.5PN (effective) parameter at the denominator of $\bar{\rho}^{\rm S}_{22}$ and tune it to reduce by more than an order of magnitude the fractional difference between the analytical and numerical functions up to the LSO. More precisely, we have that $\bar{\rho}^{\rm S}_{22}$ has the structural form $1/(1+\hat{a}x^{3/2}+.....+\hat{a}c_{13/2}x^{13/2})$, where $\hat{a}c_{13/2}x^{13/2}$ is formally the first spin-orbit term beyond what we are using in this work. One easily checks that the value $c_{13/2}=5.1$ is sufficient to obtain a fractional disagreement of the order 0.15% at the LSO for $\hat{a}=+0.99$. This illustrative example suggests that there is a simple, though effective, way to incorporate the information encoded in the numerical data within the analytical description of the waveform amplitudes. More work will be needed to put this approach in a more systematic form. In particular one may hope that a suitable modification of this method, probably with a few more parameters, could be used to obtain an accurate, semi-analytic, representation of the circularized fluxes also up to the light-ring.

8.3 Comparable masses: Post-Newtonian expanded results

8.3.1 Waveform amplitudes: spin-orbit and quadratic-in-spin terms

We start by summarizing here new results for the PN-expanded, nonprecessing, multipolar waveform amplitudes up to: (i) next-to-next-to-leading-order (NNLO) for the spin-orbit terms; (ii) next-to-leading-order (NLO) for the spin-spin terms and (iii) for the leading-order (LO) spin-cube terms. These waveform amplitudes were computed by A. Bohé and S. Marsat [252] as part of a project that aims at obtaining the complete waveform at this PN order (we recall that the corresponding calculation of the PN-expanded energy flux is complete [310, 77, 76, 75]), and kindly shared with us before publication. Here we only list the PN-expanded multipolar waveform amplitudes with their complete, currently known, spin dependence. For completeness, we also include the known, ν-dependent, orbital terms [169]. To start with, let us set the notations and define our choice of spin variables. We denote with $\nu = m_1 m_2/M^2$ the symmetric mass ratio, with $M = m_1 + m_2$ and we adopt the convention that $m_1 \geq m_2$. From the conserved norm, dimensionful, spin vectors $(\mathbf{S}_1, \mathbf{S}_2)$, PN results are usually expressed in terms of the spin combinations $\mathbf{S} \equiv \mathbf{S}_1 + \mathbf{S}_2$ and $\mathbf{\Sigma} \equiv M\left(\mathbf{S}_2/m_2 - \mathbf{S}_1/m_1\right)$. For spin-aligned binaries, where $\boldsymbol{\ell}$ indicates the unit vector normal to the orbital plane (i.e., the direction of the orbital angular momentum), one deals with the projections of the spin-vectors along $\boldsymbol{\ell}$, i.e., $S_\ell = \mathbf{S} \cdot \boldsymbol{\ell}$ and $\Sigma_\ell = \mathbf{\Sigma} \cdot \boldsymbol{\ell}$. Then, it is common practice to work with dimensionless spin variables $\chi_{1,2} \equiv S_{1,2}/(m_{1,2})^2$ and in the PN-expansions the spin vectors always appear divided by the square of the total mass, so that one has

$$\hat{S}_\ell \equiv \frac{S_\ell}{M^2} = (X_1)^2 \chi_1 + (X_2)^2 \chi_2, \tag{8.6}$$

$$\hat{\Sigma}_\ell \equiv \frac{\Sigma_\ell}{M^2} = X_2 \chi_2 - X_1 \chi_1, \tag{8.7}$$

where we introduced the usual convenient notation $X_i \equiv m_i/M$, which yields $X_1 + X_2 = 1$, $X_1 X_2 = \nu$ and, since $X_1 \geq X_2$, we have $X_1 = \left(1 + \sqrt{1-4\nu}\right)/2$. From the dimensionless spin variables, the waveform spin-dependence is sometimes also written via their symmetric and antisymmetric combinations (see e.g. [175, 177, 159, 36]), $\chi_S \equiv (\chi_1 + \chi_2)/2$ and $\chi_A \equiv (\chi_1 - \chi_2)/2$.

Here, we express the waveform spin dependence using the Kerr parameters of the two black holes divided by the total mass of the system, namely via the variables

$$\tilde{a}_i \equiv \frac{a_i}{M} = \frac{S_i}{M m_i} = X_i \chi_i \qquad i = 1, 2. \tag{8.8}$$

This choice is convenient for two reasons: (i) the analytical expression get more compact as several factors $\sqrt{1-4\nu}$ are absorbed in the definitions, and one can more clearly distinguish the sequence of terms that are "even", in the sense that are symmetric under exchange of body 1 with body 2 and are proportional to the "total Kerr dimensionless spin" $\hat{a}_0 \equiv \tilde{a}_1 + \tilde{a}_2$ from those that are "odd", i.e. change sign under the exchange of body 1 with body 2 and are proportional to the factor $\sqrt{1-4\nu}(\tilde{a}_1 - \tilde{a}_2)$; (ii) in addition, one can infer the (spinning) test-particle limit from the general ν-dependent, expressions just by inspecting them visually. In fact, in this limit, $m_2 \ll m_1$, $\tilde{a}_{12} \to 0$ and $\tilde{a}_1$ becomes the dimensionless spin of the massive black hole of mass $m_1 \approx M$, $\tilde{a}_1 \to S_1/(m_1)^2$. Similarly, the *spinning* particle limit around Kerr is simply obtained by putting $\nu = 0$, since $\tilde{a}_2$ just reduces to the usual spin-variable used in PN or numerical calculations [311, 312, 313, 314], $\sigma \equiv S_2/(m_1 m_2)$. To keep the expressions compact, we also define the following combinations of the $\tilde{a}_i$ of Eq. (8.8)

$$\hat{a}_0 \equiv X_1 \chi_1 + X_2 \chi_2 = \tilde{a}_1 + \tilde{a}_2, \tag{8.9}$$

$$\tilde{a}_{12} \equiv \tilde{a}_1 - \tilde{a}_2, \tag{8.10}$$

$$X_{12} \equiv X_1 - X_2 = \sqrt{1-4\nu}. \tag{8.11}$$

Equations (8.6)-(8.7) above then simply read

$$\hat{S}_\ell = \frac{1}{2}\left(\hat{a}_0 + \tilde{a}_{12} X_{12}\right), \tag{8.12}$$

$$\hat{\Sigma}_\ell = -\tilde{a}_{12}. \tag{8.13}$$

We report below the complete modulus of $\hat{h}_{\ell m}$ up to NNLO in the spin-orbit coupling and up to NLO in the spin-spin coupling. Note however that for the $m =$ odd multipoles we defactorized the factor X_{12} (that is usually seen as part of the Newtonian prefactor $h^{(N,\epsilon)}_{\ell m}$) to avoid the appearence of a fictitious singularity when $\nu = 1/4$ in the spin-dependent terms proportional to $\tilde{a}_{12}$ (see also [177]). To have a consistent notation, when $m =$ odd we focus on the quantities

$$\tilde{h}^{(\epsilon)}_{\ell m} = X_{12} \hat{h}^{(\epsilon)}_{\ell m}. \tag{8.14}$$

In conclusion, the modulus of the Newton-normalized PN-expanded, multipolar, waveform we use as starting point reads:

$$
\begin{aligned}
|\hat{h}^{(0)}_{22}| = 1 &+ \left(-\frac{107}{42}+\frac{55}{42}\nu\right)x - \left[-2\pi+\hat{a}_0+\frac{1}{3}\tilde{a}_{12}X_{12}\right]x^{3/2}\\
&+ \left[\hat{a}_0^2-\frac{2173}{1512}-\frac{1069}{216}\nu+\frac{2047}{1512}\nu^2\right]x^2\\
&+ \left[-\pi\left(\frac{107}{21}-\frac{34}{21}\nu\right)-\hat{a}_0\left(\frac{163}{126}+\frac{46}{63}\nu\right)-\tilde{a}_{12}X_{12}\left(\frac{157}{126}+\frac{22}{21}\nu\right)\right]x^{5/2}\\
&+ \left\{\frac{27027409}{646800}-\frac{113}{63}\left(\tilde{a}_1^2+\frac{271}{113}\tilde{a}_1\tilde{a}_2+\tilde{a}_2^2\right)-2\pi\left(\hat{a}_0+\frac{1}{3}\tilde{a}_{12}X_{12}\right)\right.\\
&+ \frac{2}{3}\pi^2+\frac{121}{63}\hat{a}_0\tilde{a}_{12}X_{12}-\frac{856}{105}\mathrm{eulerlog}_2(x)\\
&\left.+ \left[-\frac{278185}{33264}+\frac{20}{21}\left(\tilde{a}_1^2+\frac{24}{5}\tilde{a}_1\tilde{a}_2+\tilde{a}_2^2\right)+\frac{41}{96}\pi^2\right]\nu-\frac{20261}{2772}\nu^2+\frac{114635}{99792}\nu^3\right\}x^3\\
&+ \left[\hat{a}_0\left(\frac{1061}{168}+\frac{4043}{168}\nu+\frac{499}{168}\nu^2\right)+\tilde{a}_{12}X_{12}\left(\frac{241}{216}+\frac{5135}{1512}\nu-\frac{79}{72}\nu^2\right)\right]x^{7/2},
\end{aligned}
\tag{8.15}
$$

$$|\tilde{h}^{(1)}_{21}| = X_{12} - \frac{3}{2}\tilde{a}_{12}x^{1/2} + X_{12}\left(-\frac{17}{28} + \frac{5}{7}\nu\right)x + \left[\tilde{a}_{12}\left(\frac{18}{7} + \frac{33}{14}\nu\right) + X_{12}\left(-\frac{43}{14}\hat{a}_0 + \pi\right)\right]x^{3/2}$$
$$+ \left[\tilde{a}_{12}\left(\hat{a}_0 - \frac{3}{2}\pi\right) + X_{12}\left(-\frac{43}{126} + 2\hat{a}_0^2 - 2\tilde{a}_1\tilde{a}_2 - \frac{509}{126}\nu + \frac{79}{168}\nu^2\right)\right]x^2$$
$$+ \left[\tilde{a}_{12}\left(-\frac{131}{72} + \frac{5483}{504}\nu + \frac{179}{126}\nu^2\right) + \hat{a}_0 X_{12}\left(-\frac{331}{504} + \frac{193}{63}\nu\right)\right]x^{5/2}, \tag{8.16}$$

$$|\tilde{h}^{(0)}_{33}| = X_{12} + X_{12}(-4 + 2\nu)x + \left[\tilde{a}_{12}\left(-\frac{1}{4} + \frac{5}{2}\nu\right) + X_{12}\left(-\frac{7}{4}\hat{a}_0 + 3\pi\right)\right]x^{3/2}$$
$$+ X_{12}\left(\frac{3}{2}\hat{a}_0^2 + \frac{123}{110} - \frac{1838}{165}\nu + \frac{887}{330}\nu^2\right)x^2$$
$$+ \left[\tilde{a}_{12}\left(-\frac{119}{60} + \frac{27}{20}\nu + \frac{241}{30}\nu^2\right) + \hat{a}_0 X_{12}\left(\frac{139}{60} - \frac{83}{60}\nu\right)\right]x^{5/2}, \tag{8.17}$$

$$|\hat{h}^{(1)}_{32}| = 1 + \frac{1}{1-3\nu}\left\{\left(\hat{a}_0 - \tilde{a}_{12}X_{12}\right)x^{1/2} + \left(-\frac{193}{90} + \frac{145}{18}\nu - \frac{73}{18}\nu^2\right)x\right.$$
$$\left. + \frac{1}{6}\left[\hat{a}_0(-39 + 73\nu) + \tilde{a}_{12}X_{12}(23 + 13\nu) + 12\pi(1 - 3\nu)\right]x^{3/2}\right\}, \tag{8.18}$$

$$|\tilde{h}^{(0)}_{31}| = X_{12} - \frac{2}{3}X_{12}(4 + \nu)x + \left[\tilde{a}_{12}\left(-\frac{9}{4} + \frac{13}{2}\nu\right) + X_{12}\left(\frac{1}{4}\hat{a}_0 + \pi\right)\right]x^{3/2}$$
$$+ \left[-4(\tilde{a}_1^2 + \tilde{a}_2^2) + X_{12}\left(\frac{607}{198} - \frac{136}{99}\nu - \frac{247}{198}\nu^2 + \frac{3}{2}\hat{a}_0^2\right)\right]x^2$$
$$+ \left[\tilde{a}_{12}\left(\frac{73}{12} - \frac{641}{36}\nu - \frac{5}{2}\nu^2\right) + X_{12}\hat{a}_0\left(-\frac{79}{36} + \frac{443}{36}\nu\right)\right]x^{5/2}, \tag{8.19}$$

$$|\hat{h}^{(0)}_{44}| = 1 + \frac{1}{1-3\nu}\Bigg\{\frac{1}{330}(-1779+6365\nu-2625\nu^2)x \\ + \frac{1}{15}\Big[\hat{a}_0(-38+114\nu) + 60\pi(1-3\nu) - 2\tilde{a}_{12}X_{12}(1-21\nu)\Big]x^{3/2} \\ + \left(\frac{1068671}{200200} - \frac{1088119}{28600}\nu + \frac{146879}{2340}\nu^2 - \frac{226097}{17160}\nu^3\right)x^2\Bigg\}, \tag{8.20}$$

$$|\tilde{h}^{(1)}_{43}| = X_{12} + \frac{1}{-1+2\nu}\left\{\frac{5}{4}\Big[\tilde{a}_{12}(1-2\nu) - \hat{a}_0 X_{12}\Big]x^{1/2} + X_{12}\left(\frac{39}{11} - \frac{1267}{132}\nu + \frac{131}{33}\nu^2\right)x\right\}, \tag{8.21}$$

$$|\hat{h}^{(0)}_{42}| = 1 + \frac{1}{1-3\nu}\Bigg\{\frac{1}{330}(-1311+4025\nu-285\nu^2)x \\ - \frac{1}{15}\Big[2\hat{a}_0(1-3\nu) + \tilde{a}_{12}X_{12}(38-78\nu) - 30\pi(1-3\nu)\Big]x^{3/2} \\ + \left(\frac{1038039}{200200} - \frac{606751}{28600}\nu + \frac{400453}{25740}\nu^2 + \frac{25783}{17160}\nu^3\right)x^2\Bigg\}, \tag{8.22}$$

$$|\tilde{h}^{(1)}_{41}| = X_{12} + \frac{1}{-1+2\nu}\left\{\frac{5}{4}\Big[\tilde{a}_{12}(1-2\nu) - \hat{a}_0 X_{12}\Big]x^{1/2} + X_{12}\left(\frac{101}{33} - \frac{337}{44}\nu + \frac{83}{33}\nu^2\right)x\right\}. \tag{8.23}$$

8.3.2 Cubic-order spin effects

We are also going to incorporate leading-order spin-cube effects in the waveform amplitudes. To do so, we start from the corresponding energy fluxes, that were recently obtained in Ref. [76]. The analytically fully known spin-dependence of the energy flux has the following structure

$$\mathcal{F}^S = \frac{32}{5}\nu^2 x^5\Big[x^{3/2} f^{\rm LO}_{\rm SO} + x^2 f^{\rm LO}_{\rm SS} + x^{5/2} f^{\rm NLO}_{\rm SO} \\ + x^3 f^{\rm NLO}_{\rm SS} + x^{7/2}\left(f^{\rm NNLO}_{\rm SO} + f^{\rm LO}_{\rm SSS}\right)\Big]. \tag{8.24}$$

All terms, except the cubic ones, can be obtained by multiplying each multipolar amplitude of the previous section by its corresponding "Newtonian"

term, taking the square and finally summing them together. The spin-cube information we shall need in the next section is included in the $f^{\rm LO}_{\rm SSS}$ term above, though one has to remember that $f^{\rm LO}_{\rm SSS}$ is actually given by two independent multipolar contributions, one coming from the cubic-in-spin mass quadrupole and another from the cubic-in-spin current quadrupole. The full term is given in Eq. (6.19) of [76], but, for the purpose of this paper, S. Marsat kindly separated for us the two partial multipolar contributions, that read

$$f^{\rm sss}_{22} = -\frac{2}{3}\left(\hat{a}_0^3 + 3\hat{a}_0^2\tilde{a}_{12}X_{12}\right)x^{7/2}, \tag{8.25}$$

$$f^{\rm sss}_{21} = -\left[\frac{1}{12}\hat{a}_0\tilde{a}_{12}^2 + \left(\frac{5}{24}\tilde{a}_1^2 + \frac{1}{4}\tilde{a}_1\tilde{a}_2 + \frac{5}{24}\tilde{a}_2^2\right)\tilde{a}_{12}X_{12}\right]x^{7/2}. \tag{8.26}$$

It is easy to verify that by taking the sum $f^{\rm SSS}_{22} + f^{\rm SSS}_{21}$ one obtains Eq. (6.19) of [76] once specified to the black-hole case, i.e. with $\kappa_+ = 2 = \lambda_+$, $\kappa_- = 0 = \lambda_-$ and using Eqs. (8.6)-(8.7) above.

8.3.3 PN-expanded energy and angular momentum along circular orbits

To implement the factorization of the waveform amplitudes (and fluxes) in order to extract the $f_{\ell m}$ and $\rho_{\ell m}$ residual amplitude corrections, one needs the PN-expanded effective source $\hat{S}^{(\epsilon)}_{\rm eff}$, namely the effective energy and angular momentum of the system along circular orbits. In addition, also the total, real, energy is needed, since it enters the tail factor. Defined as $\mu \equiv m_1 m_2/M$ the reduced-mass of the system, the μ-normalized PN-expanded energy along circular orbits reads

$$\hat{E}^{\rm tot}(x) \equiv \frac{E^{\rm tot}}{\mu} = \hat{E}^{\rm orb}(x) + \hat{E}^{\rm SO}(x) + \hat{E}^{\rm SS}(x), \tag{8.27}$$

and is written as the sum of an orbital term, a spin-orbit term (SO) and a quadratic-in-spin term (SS). The 3PN-accurate orbital term reads

$$\begin{aligned}\hat{E}^{\rm orb}(x) &= 1 - \frac{1}{2}\nu x\Bigg\{1 - \left(\frac{3}{4} + \frac{\nu}{12}\right)x \\ &+ \left(-\frac{27}{8} + \frac{19}{8}\nu - \frac{\nu^2}{24}\right)x^2 \\ &+ \left[-\frac{675}{64} + \left(\frac{34445}{576} - \frac{205}{96}\pi^2\right)\nu - \frac{155}{96}\nu^2 - \frac{35}{5184}\nu^3\right]x^3\Bigg\},\end{aligned} \tag{8.28}$$

while the spin-orbit term is

$$\begin{aligned}\hat{E}^{\rm SO}(x) &= -\frac{1}{6}(7\hat{a}_0 + \tilde{a}_{12}X_{12})\nu x^{5/2} \\ &+ \frac{1}{4}\left[-(11\hat{a}_0 + 5\tilde{a}_{12}X_{12})\nu + \frac{1}{9}(61\hat{a}_0 + \tilde{a}_{12}X_{12})\nu^2\right]x^{7/2} \\ &+ \frac{1}{16}\Bigg[-(135\hat{a}_0 + 81\tilde{a}_{12}X_{12})\nu \\ &+ (367\hat{a}_0 + 55\tilde{a}_{12}X_{12})\nu^2 + \frac{1}{3}(-29\hat{a}_0 + \tilde{a}_{12}X_{12})\nu^3\Bigg]x^{9/2},\end{aligned} \tag{8.29}$$

and finally the quadratic-in-spin contribution

$$\begin{aligned}\hat{E}^{\rm SS}(x) &= \frac{1}{2}\hat{a}_0^2\nu x^3 \\ &+ \frac{1}{36}\Bigg\{\left[10(\hat{a}_0^2 + \tilde{a}_1\tilde{a}_2) + 55(\tilde{a}_1^2 - \tilde{a}_2^2)X_{12}\right]\nu \\ &- 35\left(\tilde{a}_1^2 - \frac{2}{7}\tilde{a}_1\tilde{a}_2 + \tilde{a}_2^2\right)\nu^2\Bigg\}x^4.\end{aligned} \tag{8.30}$$

The Newton-normalized angular momentum incorporating up to NLO spin-orbit terms reads

$$\begin{aligned}\hat{j}^{\rm tot}(x) &= 1 + \frac{1}{2}\left(3 + \frac{\nu}{3}\right)x - \frac{5}{12}(7\hat{a}_0 + \tilde{a}_{12}X_{12})x^{3/2} \\ &+ \left[\frac{1}{8}\left(27 - 19\nu + \frac{\nu^2}{3}\right) + \hat{a}_0^2\right]x^2 \\ &+ \frac{1}{16}\left[-(77\hat{a}_0 + 35\tilde{a}_{12}X_{12}) + \frac{1}{9}(427\hat{a}_0 + 7\tilde{a}_{12}X_{12})\nu\right]x^{5/2}.\end{aligned} \tag{8.31}$$

Finally, the PN-expanded effective energy along circular orbits is obtained by PN-expanding the usual relation between the real and effective, μ-normalized, energy along circular orbits [28],

$$\hat{E}^{\rm eff} = \frac{E_{\rm eff}}{\mu} = T_n \left[1 + \frac{1}{2\nu} (\hat{E}^2_{\rm tot} - 1) \right] . \tag{8.32}$$

8.4 Factorized waveform amplitudes

8.4.1 Factorizing the source and tail factor: the residual amplitudes

Now that all the necessary analytical elements are introduced, we can finally compute the residual amplitude corrections when $\nu \neq 0$ by factorizing tail and source from Eqs. (8.15)-(8.23), (8.25) and (8.26). Focusing first on the even-m case, the PN-expanded $\rho_{\ell m}$'s functions are obtained as

$$\rho_{\ell m}(x;\nu,\tilde{a}_1,\tilde{a}_2) = T_n \left[\left(\frac{|\hat{h}_{\ell m}(x)|}{|\hat{h}^{\rm tail}_{\ell m}| \hat{S}^{(\epsilon)}_{\rm eff}} \right)^{1/\ell} \right] , \tag{8.33}$$

where $\hat{S}^{(\epsilon)}_{\rm eff}(x)$ is either $\hat{E}_{\rm eff}$ when $\ell + m$ is even, or $\hat{j}^{\rm tot}$ when $\ell + m$ is odd, while $|\hat{h}^{\rm tail}|$ is the modulus of the tail factor introduced in Eq. (4.39) whose explicit expression is given in Eq. (8.37) below. The Taylor expansion $T_n[\dots]$ is truncated at the same n-PN order of the $|h^{(\epsilon)}_{\ell m}|$. The functions $\rho_{\ell m}$ have the form $1 + c_1^{\ell m} x + \dots$ and, like in the test-particle case, are given as the sum of orbital and spin terms as

$$\rho_{\ell m}(x;\nu,\tilde{a}_1,\tilde{a}_2) = \rho^{\rm orb}_{\ell m}(x;\nu) + \rho^{\rm S}_{\ell m}(x;\nu,\tilde{a}_1,\tilde{a}_2) \ . \tag{8.34}$$

For the odd-m case, the same factorization yields the function

$$\delta m f_{\ell m} = X_{12} f^{\rm orb}_{\ell m} + \tilde{f}^{\rm S}_{\ell m}, \tag{8.35}$$

that is obtained as the following Taylor expansion

$$\delta m f_{\ell m} = T_n \left[\frac{|\tilde{h}_{\ell m}|}{|\hat{h}^{\rm tail}_{\ell m}| \hat{S}^{(\epsilon)}_{\rm eff}} \right] , \tag{8.36}$$

where, for consistency with notation used in Ref. [9], we also used $\delta m \equiv X_{12}$. Finally, to perform this calculation, we also need the Taylor expansion of the modulus of the tail factor, that is given by [159]

$$|\hat{h}^{\rm tail}_{\ell m}(x)|^2 = \frac{4\pi E^{\rm tot} m x^{3/2} \prod_{s=1}^{\ell} \left(s^2 + 2E^{\rm tot} m x^{3/2}\right)^2}{(\ell!)^2 \left(1 - e^{-4\pi m E^{\rm tot}}\right)}. \tag{8.37}$$

When factorizing out that tail and effective source factors from the waveform amplitudes of Eqs. (8.15)-(8.23), as well as from the spin-cube flux terms, Eqs. (8.25) and (8.26), one finally finds the following spin-dependent terms:

$$\begin{aligned}
\rho^{\rm S}_{22} = &-\left(\frac{\hat{a}_0}{2} + \frac{1}{6}\tilde{a}_{12}X_{12}\right)x^{3/2} \\
&+ \frac{\hat{a}_0^2}{2}x^2 - \left[\hat{a}_0\left(\frac{52}{63} + \frac{19}{504}\nu\right) + \left(\frac{50}{63} + \frac{209}{504}\nu\right)\tilde{a}_{12}X_{12}\right]x^{5/2} \qquad (8.38)\\
&+ \left[\left(-\frac{11}{21} + \frac{103}{504}\nu\right)\hat{a}_0^2 + \left(-\frac{19}{63} + \frac{10}{9}\nu\right)\tilde{a}_1\tilde{a}_2 + \frac{221}{252}\hat{a}_0\tilde{a}_{12}X_{12}\right]x^3 \\
&+ \left[\hat{a}_0\left(\frac{32873}{21168} + \frac{477563}{42336}\nu + \frac{147421}{84672}\nu^2\right)\right. \\
&\left. - \tilde{a}_{12}X_{12}\left(\frac{23687}{63504} - \frac{171791}{127008}\nu + \frac{50803}{254016}\nu^2\right) + \left(\frac{7}{12}\hat{a}_0^3 - \frac{1}{4}\hat{a}_0^2\tilde{a}_{12}X_{12}\right)\right]x^{7/2}, \qquad (8.39)
\end{aligned}$$

$$\begin{aligned}
\rho^{\rm S}_{32} = &\frac{1}{3(1-3\nu)}\left(\hat{a}_0 - \tilde{a}_{12}X_{12}\right)x^{1/2} \\
&+ \frac{1}{162(1-3\nu)^2}\left[\left(-\frac{1433}{10} + 553\nu - \frac{797}{2}\nu^2\right)\hat{a}_0 - \left(-\frac{1793}{10} + 427\nu + \frac{607}{2}\nu^2\right)\tilde{a}_{12}X_{12}\right]x^{3/2}, \qquad (8.40)
\end{aligned}$$

$$\rho^{\rm S}_{42} = \frac{1}{30}\left(\frac{1}{-1+3\nu}\right)[\hat{a}_0(1-3\nu) + \tilde{a}_{12}X_{12}(19-39\nu)]x^{3/2}, \tag{8.41}$$

$$\rho^{\rm S}_{44} = \frac{1}{30}\left(\frac{1}{-1+3\nu}\right)[\hat{a}_0(19-57\nu) - \tilde{a}_{12}X_{12}(-1+21\nu)]x^{3/2}, \tag{8.42}$$

and similarly

$$\tilde{f}^{\rm S}_{21} = -\frac{3}{2}\tilde{a}_{12}x^{1/2} + \left[\tilde{a}_{12}\left(\frac{110}{21}+\frac{79}{84}\nu\right) - \frac{13}{84}\hat{a}_0 X_{12}\right]x^{3/2} + \left[-\frac{27}{8}(\tilde{a}_1^2-\tilde{a}_2^2) + \frac{3}{8}X_{12}\left(\tilde{a}_1^2+\frac{10}{3}\tilde{a}_1\tilde{a}_2+\tilde{a}_2^2\right)\right]x^2 + \left[\tilde{a}_{12}\left(-\frac{3331}{1008}-\frac{13}{504}\nu+\frac{613}{1008}\nu^2\right) + \hat{a}_0 X_{12}\left(-\frac{443}{252}+\frac{1735}{1008}\nu\right) + \frac{3}{4}\hat{a}_0^2\tilde{a}_{12}\right]x^{5/2}, \tag{8.43}$$

$$\tilde{f}^{\rm S}_{31} = \left[\tilde{a}_{12}\left(-\frac{9}{4}+\frac{13}{2}\nu\right) + \frac{1}{4}\hat{a}_0 X_{12}\right]x^{3/2} + \left[-4(\tilde{a}_1^2-\tilde{a}_2^2) + \frac{3}{2}\hat{a}_0^2 X_{12}\right]x^2 + \left[\tilde{a}_{12}\left(\frac{41}{8}-\frac{137}{9}\nu-\frac{5}{2}\nu^2\right) + \hat{a}_0 X_{12}\left(-\frac{65}{72}+\frac{443}{36}\nu\right)\right]x^{5/2}, \tag{8.44}$$

$$\tilde{f}^{\rm S}_{33} = \left[\tilde{a}_{12}\left(-\frac{1}{4}+\frac{5}{2}\nu\right) - \frac{7}{4}\hat{a}_0 X_{12}\right]x^{3/2} + \frac{3}{2}\hat{a}_0^2 X_{12}x^2 + \left[\tilde{a}_{12}\left(-\frac{233}{120}+\frac{29}{15}\nu+\frac{241}{30}\nu^2\right) + \hat{a}_0 X_{12}\left(\frac{313}{120}-\frac{83}{60}\nu\right)\right]x^{5/2}, \tag{8.45}$$

$$\tilde{f}^{\rm S}_{41} = \tilde{f}^{S}_{43} = \frac{5}{4}\left(\frac{1}{-1+2\nu}\right)[\tilde{a}_{12}(1-2\nu) - \hat{a}_0 X_{12}]x^{1/2}. \tag{8.46}$$

After applying the proper change of variables, one easily checks that the NLO contributions we computed here do coincide with Eqs. (85)-(95) of Ref. [159]. Similarly, the NNLO spin-orbit contribution to ρ_{22}, that was also computed in Ref. [9] is checked with the same term computed in Ref. [36].

8.4.2 Factorization of the orbital part

Likewise the test-particle case above, we now apply the prescription of Ref. [9] of factorizing the orbital parts of $\rho^{\rm S}_{\ell m}$ and $\tilde{f}^{\rm S}_{\ell m}$. After this operation, the factorized residual amplitudes are written as

$$\rho_{\ell m} = \rho^{\rm orb}_{\ell m}\hat{\rho}^{\rm S}_{\ell m} \qquad m = \text{even} \tag{8.47}$$

$$\delta m f_{\ell m} = \left(\rho^{\rm orb}_{\ell m}\right)^{\ell}\hat{f}^{\rm S}_{\ell m} \qquad m = \text{odd} \tag{8.48}$$

where, as in Ref. [9], the $m=$ odd spin factors are written as the sum of two separate terms

$$\hat{f}^{\rm S}_{21} = X_{12}\hat{f}^{{\rm S}_{(0)}}_{21} - \frac{3}{2}\tilde{a}_{12}x^{1/2}\hat{f}^{{\rm S}_{(1)}}_{21}, \tag{8.49}$$

$$\hat{f}^{\rm S}_{33} = X_{12}\hat{f}^{{\rm S}_{(0)}}_{33} + \left(-\frac{1}{4}+\frac{5}{2}\nu\right)\tilde{a}_{12}x^{3/2}\hat{f}^{{\rm S}_{(1)}}_{33}, \tag{8.50}$$

$$\hat{f}^{\rm S}_{31} = X_{12}\hat{f}^{{\rm S}_{(0)}}_{31} + \left(-\frac{9}{4}+\frac{13}{2}\nu\right)\tilde{a}_{12}x^{3/2}\hat{f}^{{\rm S}_{(1)}}_{31}, \tag{8.51}$$

$$\hat{f}^{\rm S}_{43} = X_{12}\hat{f}^{{\rm S}_{(0)}}_{43} - \frac{5}{4}\tilde{a}_{12}x^{1/2}\hat{f}^{{\rm S}_{(1)}}_{43}, \tag{8.52}$$

$$\hat{f}^{\rm S}_{43} = X_{12}\hat{f}^{{\rm S}_{(0)}}_{41} - \frac{5}{4}\tilde{a}_{12}x^{1/2}\hat{f}^{{\rm S}_{(1)}}_{41}. \tag{8.53}$$

As shown in Ref. [9], we recall that the need of separating the $\hat{f}_{\ell m}$'s function into two separate terms, one proportional to X_{12} and another to $\tilde{a}_{12}$ times x is necessary to identify the two functions $\hat{f}^{{\rm S}_{(0)}}_{\ell m}$ and $\hat{f}^{{\rm S}_{(1)}}_{\ell m}$ that can be separately resummed using their inverse Taylor representation. The $\hat{f}^{{\rm S}_{(0),(1)}}_{\ell m}$ functions read

$$\begin{aligned}\hat{f}^{{\rm S}_{(0)}}_{21} &= 1 - \frac{13}{84}\hat{a}_0 x^{3/2} \\ &\quad + \frac{3}{8}\left(\hat{a}_0^2 + \frac{4}{3}\tilde{a}_1\tilde{a}_2\right)x^2 \\ &\quad + \hat{a}_0\left(-\frac{14705}{7056}+\frac{12743}{7056}\nu\right)x^{5/2},\end{aligned} \tag{8.54}$$

$$\begin{aligned}\hat{f}^{{\rm S}_{(1)}}_{21} &= 1 - \left(\frac{349}{252}+\frac{74}{63}\nu\right)x + \frac{9}{4}\hat{a}_0 x^{3/2} \\ &\quad - \left(\frac{3379}{21168} - \frac{4609}{10584}\nu + \frac{39}{392}\nu^2 + \frac{\hat{a}_0^2}{2}\right)x^2,\end{aligned} \tag{8.55}$$

$$\hat{f}^{{\rm S}_{(0)}}_{31} = 1 + \frac{1}{4}\hat{a}_0 x^{3/2} + \frac{3}{2}\hat{a}_0^2 x^2 + \hat{a}_0\left(-\frac{13}{36}+\frac{449}{36}\nu\right)x^{5/2}, \tag{8.56}$$

$$\begin{aligned}\hat{f}^{{\rm S}_{(1)}}_{31} &= 1 - \frac{16}{26\nu-9}\hat{a}_0 x^{1/2} \\ &\quad + \frac{1}{26\nu-9}\left(1 - \frac{95}{9}\nu + \frac{22}{3}\nu^2\right)x,\end{aligned} \tag{8.57}$$

$$\hat{f}_{33}^{\mathrm{S}_{(0)}} = 1 - \frac{7}{4}\hat{a}_0 x^{3/2} + \frac{3}{2}\hat{a}_0^2 x^2 + \hat{a}_0\left(-\frac{211}{60} + \frac{127}{60}\nu\right)x^{5/2}, \tag{8.58}$$

$$\hat{f}_{33}^{\mathrm{S}_{(1)}} = 1 + \frac{1}{15}\left(\frac{-169 + 671\nu + 182\nu^2}{10\nu - 1}\right)x, \tag{8.59}$$

$$\hat{f}_{41}^{\mathrm{S}_{(0)}} = f_{43}^{S_{(0)}} = 1 - \frac{5}{4}\left(\frac{1}{-1 + 2\nu}\right)\hat{a}_0 x^{1/2}, \tag{8.60}$$

$$\hat{f}_{41}^{\mathrm{S}_{(1)}} = f_{43}^{S_{(1)}} = 1. \tag{8.61}$$

Equations (8.49), (8.54) correspond to Eqs. (9)-(10) of [9], while Eq. (8.55) presents an additional term, $\hat{a}_0^2/2$, that is the leading-order spin-cube that

was omitted in [9]. Finally the $m =$ even spin factors read

$$\begin{aligned}
\hat{\rho}^{\rm S}_{22} &= 1 - \left(\frac{\hat{a}_0}{2} + \frac{1}{6}\tilde{a}_{12}X_{12}\right)x^{3/2} + \frac{\hat{a}_0^2}{2}x^2 \\
&+ \left[\left(-\frac{337}{252} + \frac{73}{252}\nu\right)\hat{a}_0 - \left(\frac{27}{28} + \frac{11}{36}\nu\right)\tilde{a}_{12}X_{12}\right]x^{5/2} \\
&+ \left[\frac{221}{252}\hat{a}_0\tilde{a}_{12}X_{12} - \left(\frac{1}{84} + \frac{31}{252}\nu\right)\hat{a}_0^2 \right.\\
&\left. + \left(-\frac{19}{63} + \frac{10}{9}\nu\right)\tilde{a}_1\tilde{a}_2\right]x^3 \\
&+ \left[\left(-\frac{2083}{2646} + \frac{123541}{10584}\nu + \frac{4717}{2646}\nu^2\right)\hat{a}_0 \right.\\
&+ \left(-\frac{13367}{7938} + \frac{22403}{15876}\nu + \frac{25}{324}\nu^2\right)\tilde{a}_{12}X_{12} \\
&\left. + \frac{7}{12}\hat{a}_0^3 - \frac{1}{4}\hat{a}_0^2\tilde{a}_{12}X_{12}\right]x^{7/2}, \qquad (8.62)
\end{aligned}$$

$$\begin{aligned}
\hat{\rho}^{\rm S}_{32} &= 1 + \left(\frac{1}{3(1-3\nu)}\right)(\hat{a}_0 - \tilde{a}_{12}X_{12})\,x^{1/2} \\
&+ \frac{1}{27(1-3\nu)^2}\left[\hat{a}_0\left(-\frac{259}{20} + 55\nu - \frac{223}{4}\nu^2\right)\right. \\
&\left. - \tilde{a}_{12}X_{12}\left(-\frac{379}{20} + 34\nu + \frac{245}{4}\nu^2\right)\right]x^{3/2}, \qquad (8.63)
\end{aligned}$$

$$\hat{\rho}^{\rm S}_{42} = 1 + \rho^{\rm S}_{42}, \qquad (8.64)$$

$$\hat{\rho}^{\rm S}_{44} = 1 + \rho^{\rm S}_{44}. \qquad (8.65)$$

Note that our Eq. (8.62) above corrects an error in the published $\tilde{a}_1\tilde{a}_2$ NLO term of Eq. (8) of Ref. [9].

8.5 Resummation

We now proceed by resumming the orbital and spin factors according to the prescriptions of Ref. [9], basically extending to higher modes the treatment

of the $\ell = 2$ modes discussed there. However, we want to have at least the orbital multipolar factors, $\rho^{\rm orb}_{\ell m}$, consistent with the test-particle ones discussed above, in order to take advantage of the high-order PN-information available and of the robustness of its analytical representation in Padé resummed form. To do so, we follow the, now standard, practice, originally suggested in Ref. [8], of *hybridizing* the low-PN-order ν-dependent information available with the high-PN-order test-mass ($\nu = 0$) one. At the time of Ref. [8], the test-particle orbital fluxes were analytically known up to 5.5PN order, which implied that the, nonresummed, $\rho_{\ell m}$'s functions where available as polynomials of different order, that is $\rho^{\rm orb}_{22} = 1+x+....+x^5$, $\rho^{\rm orb}_{21} = 1+x+....+x^4$ etc., consistent with the global 5.5PN accuracy of the total flux. This prompted, at the time, the construction of what was called the 3^{+2} PN approximation, where the 3PN results were hybridized with two more test-particle PN orders. As we saw above, the availability of PN results of high order [315] allows us to keep more PN terms in each $\rho^{\rm orb}_{\ell m}$'s, notably up to 6PN relative accuracy for each (ℓ, m) as a good compromise between simplicity and accuracy. Since we are working with relative PN truncations, we give here the 3^{+3} PN approximation for the $\rho_{\ell m}(x;\nu)$ a different meaning with respect to [8]. More precisely, working at 3^{+3}PN order here means that each $\rho^{\rm orb}_{\ell m}(x;\nu)$ carries the complete test-mass information up to x^6, but whenever possible, the lower PN terms are augmented by the corresponding ν-dependent information compatible with the ν-dependent 3PN accuracy. For example, $\rho^{\rm orb}_{22}(x;\nu)$ formally reads

$$\begin{aligned}\rho^{\rm orb}_{22}(x;\nu) = 1 &+ c_1(\nu)x + c_2(\nu)x^2 + c_3(\nu;\log(x))x^3 \\ &+ c^0_4(\log(x))x^4 + c^0_5(\log(x))x^5 \\ &+ c^0_6(\log(x),\log^2(x))x^6, \end{aligned} \tag{8.66}$$

where (c^0_4, c^0_5, c^0_6) are test-particle, ν-independent, coefficients with the corresponding dependence on $\log(x)$. The function $\rho^{\rm orb}_{21}(x;\nu)$ shares the same analytical structure, though the ν-dependence of c_3 is currently unknown, since it is a (global) 4PN effect. For higher modes, the ν dependence is progressively reduced, up to only $c_1(\nu)$ for the $\ell = 8$ modes [8]. Choosing the above defined 3^{+3} PN approximation also means that we adopt the same Padé resummation, multipole by multipole, detailed in Table 8.1. In this way we implement, by construction, the consistency with the $\nu = 0$ limit. This choice opens the question of what would be the magnitude of the systematic error done by neglecting such, yet-uncalculated, ν-dependent terms. Refer-

ence [8] analyzed the ν-dependence of a few multipoles and concluded that, working with Taylor-expanded $\rho^{\rm orb}_{\ell m}$, the ν-dependence is mild and that the effect of the missing terms is small enough to be considered of no importance. We shall repeat and update that reasoning to our current choices in the next section, though we anticipate the same conclusion of [8] remains essentially true here for all examined modes.

We turn now to discussing the resummation of the spinning factors, $\hat{\rho}^{\rm S}_{\ell m}$ and $\hat{f}^{\rm S}_{\ell m}$. We do so by applying the resummation recipe of Ref. [9], that is: (i) for even-m, we simply resum $\hat{\rho}^{\rm S}_{\ell m}$ taking its inverse Taylor representation, $\bar{\rho}^{\rm S}_{\ell m}(x;\nu)$, as in Eq. (8.5); (ii) for odd-m, we need to resum separately the two factors $\hat{f}^{\rm S_{(0)}}_{\ell m}$ and $\hat{f}^{\rm S_{(1)}}_{\ell m}$. The analytical representation of the two factors we choose depend on the multipole. More precisely: the factor $\hat{f}^{\rm S_{(0)}}_{21}$ is always resummed taking its inverse Taylor representation. The same choice is also adopted to resum $\hat{f}^{\rm S_{(1)}}_{\ell m}$ for $\ell = 2$, but for $\ell \geq 3$, $m =$ odd case, the $\hat{f}^{\rm S_{(1)}}_{\ell m}$ are kept in Taylor-expanded form because of the presence of spurious poles when taking the inverse. The quality of the resummation is assessed in Figs. 8.3 and 8.4 for a few illustrative binary configurations. Since one does not have at hand the analogous of the test-mass numerical data for circularized, comparable-mass, binaries to compare with, our aim here is only limited to prove the *internal consistency* of the resummed analytical expressions once taken at different PN orders. To do so, by keeping the orbital part unchanged, we contrast the functions obtained using the full NNLO information with the ones truncated at NLO accuracy. The same figures also display the standard representation of the $\rho_{\ell m}$'s, where no additional factorization or resummation is adopted [175]. The plot illustrates how the spread between the NLO and NNLO truncations in PN-expanded form is systematically much larger than the corresponding one obtained with the factorized and resummed functions. Interestingly, this conclusion remains true for any configuration analyzed. This makes us conclude that factorizing and resumming as discussed here is helpful also in the comparable-mass case, although a precise quantification of the improvement brought by this procedure should be assessed through a comprehensive comparison between an EOB model built from iResum waveforms and NR data, in a way analogous, though more detailed, to what briefly analyzed in [9]. However, to better grasp the meaning of this result, it is useful to remind the reader that the merger of a binary black-hole coalescence (defined as the peak of the $\ell = m = 2$ waveform amplitude) will occur at $x \approx 0.3$, with $x = (\omega_{22}/2)^{2/3}$

and ω_{22} the quadrupolar GW frequency[6]. As Figs. 8.3 and 8.4 illustrate, the improvement in the consistency between PN truncations brought by the resummation is evident precisely in a neighborhood of 0.3. Just to pick some random examples, this is the case for $(1, +0.99, +0.99)$ and $(8, +0.50, 0)$, configurations where the frequency parameter at merger is $x \approx 0.38$ and $x \approx 0.32$ respectively [192].

8.5.1 Mild dependence of $\rho^{\rm orb}_{\ell m}$ to uncalculated ν-dependent orbital terms

As mentioned above, the idea of hybridizing test-mass orbital information with the $\nu \neq 0$ one in the waveform amplitudes dates back to Ref. [8]. The rationale behind that choice was to show that the dependence on ν of the coefficients in the $\rho^{\rm orb}_{\ell m}$ is mild when $0 \leq \nu \leq 1/4$, so that one does not introduce a large systematical error in neglecting it. To get to this conclusion, one was comparing the fractional variation of the coefficients when ν is varied between 0 and 1/4 (see Sec. IVA in [8]). Here we follow the same approach and compute the fractional variation in ν for all multipoles up to $\ell = 6$. The 3PN-accurate ν-dependent terms in $\rho^{\rm orb}_{31}$ and $\rho^{\rm orb}_{33}$ that were obtained only in Ref. [278] are also included. The $\log(x)$ terms are evaluated, for simplicity, at $x^{\rm Schw}_{\rm LSO} = 1/6$. The numbers listed in Table 8.2 suggest that, up to $\ell = 3$, the next missing ν-dependent term might be, on average, of the order of 20% larger (or smaller) then the test-mass ($\nu = 0$) one (note however the larger variations of the 2PN coefficient in $\rho^{\rm orb}_{31}$ and $\rho^{\rm orb}_{32}$. One can then investigate the impact on $\rho^{\rm orb}_{\ell m}$ of missing ν-dependent corrections by varying the $\nu = 0$ term by $\pm 30\%$. Clearly, the operation has to be done on the $P^n_d(\rho^{\rm orb}_{\ell m})$ function. To be concrete on one case, let us analyze the effect on $\rho^{\rm orb}_{21}$, whose known ν-dependence stops at 2PN. Schematically, the Taylor-expanded function reads

$$\begin{aligned}\rho^{\rm orb}_{21} &= 1 + (c_0^{\rm 1PN} + c_\nu^{\rm 1PN})x + (c_0^{\rm 2PN} + c_\nu^{\rm 2PN})x^2 \\ &+ \left[c_0^{\rm 3PN}(1+\alpha)\right] x^3 + c_0^{\rm 4PN} x^4 + c_0^{\rm 5PN} x^5 + c_0^{\rm 6PN} x^6, \end{aligned} \tag{8.67}$$

and then one takes its P^5_1 Padé approximant. Here, $c_0^{n\rm PN}$ indicate the $\nu = 0$ coefficients, while $c_\nu^{n\rm PN}$ the corresponding ν-dependent terms. The effect of

[6] Let us recall that in the test-particle limit this frequency approximately corresponds to the crossing of the Schwarzschild light ring [316, 167]

the missing ν-dependent information is parametrized through α. One finds that, even putting $\alpha = \pm 0.20$ with $\nu = 1/4$, the fractional variation in $P_1^5\left(\rho_{21}^{\rm orb}\right)$ is of the order of 0.04% at the Schwarzschild LSO $x_{\rm LSO}^{\rm Schw} = 1/6$, of the order of 0.9% at $x = 1/3$ and of the order of 6% at $x = 1/2$. This value is close to the LSO location of a Kerr black hole with $\hat{a} = +0.99$ and we use here just for illustrative purposes, since a comparable mass binary, with a nonnegligible value of ν, is not expected to reach such a high frequency at merger. Since the waveform amplitude is just $(\rho_{21})^2$, the fractional differences above get a factor two in front, which suggests that, within the current framework, one is expecting the 3PN correction to $\rho_{21}^{\rm orb}$ to yield an amplitude correction around merger of just a few percents. Once the calculation of the waveform will be completed at 4PN accuracy [270, 74, 317, 318, 319], it will be interesting to concretely probe the reasonable assumptions we are adopting here. In addition, inspection of the behavior of higher modes, like $\rho_{44}^{\rm orb}$, shows that a variation of the order 20% with respect to the $\nu = 0$ values has an unnaturally large effect on the global behavior of the function in the strong-field regime ($0.3 \lesssim x \lesssim 0.5$), with variations of order 8% at $x = 1/3$ and $\sim 30\%$ at $x = 1/2$. Though we cannot make strong statements, we are prone to think that the uncalculated ν-dependent terms will provide, on average, a correction of the order of 10% to the current orbital terms, consistently with the ν-variation of the 3PN coefficients in $\rho_{22}^{\rm orb}$ and $\rho_{33}^{\rm orb}$, as in Table 8.2.

8.5.2 Hybridizing test-mass results: the spin information

Now that we have justified our approach of hybridizing $\nu = 0$ and $\nu \neq 0$ information in the $\rho_{\ell m}^{\rm orb}$ functions, one wonders whether an analogous procedure exists for the $\rho_{\ell m}^{\rm S}$ (and in turn for the factorized $\hat{\rho}_{\ell m}^{\rm S}$). This would allow to have EOB waveforms fully consistent and complete all over the parameter space of nonprecessing BBHs[7]. Such hybridization is rather straightforward to do by taking advantage of the structure of the $\rho_{\ell m}^{\rm S}$ and $f_{\ell m}^{\rm S}$ functions and understanding how the spinning test-particle limit builds up. This is especially evident using the $\tilde{a}_i$ variables, that make the limit look apparent. To explain the approach, let us first focus on the spin-orbit terms entering the

[7]Note this is not the case for current EOB waveform models, where the high-order test-mass analytical information is not incorporated [36, 35, 37]

$\rho_{\ell m}$ functions. One sees that, at a given n-PN order of the orbital part, the corresponding spin-orbit term reads like

$$\Bigg(\hat{a}_0(c_0 + c_1\nu + \cdots + c_{n-1}\nu^{n-1}) \\ + \tilde{a}_{12}X_{12}(d_0 + d_1\nu + \cdots + d_{n-1}\nu^{n-1})\Bigg)x^{(2n+1)/2}, \tag{8.68}$$

as it is clear from Eq. (8.38) that corresponds to 3PN orbital dynamics. Note that within our writing, the LO spin-orbit coefficients are ν-independent, the NLO are linear in ν, while the NNLO are quadratic in ν. A similar, though slightly more complicated, structure is found for the quadratic-in-spin terms, that, e.g. for $\rho^{\rm S}_{22}$, are given as the sum of terms proportional to $\hat{a}_0^2$, $\tilde{a}_1\tilde{a}_2$ and $\hat{a}_0\tilde{a}_{12}X_{12}$. As for the SO case above, at LO there is no ν dependence, while it is similarly linear-in-ν at NLO. The ν independent terms in Eq. (8.38) are those that, combined together when $\nu \to 0$, generate the (spinning) test particle results, see e.g. Refs. [311, 298]. Having understood this, one can implement the inverse process, namely incorporate the $\rho^{\rm S}_{\ell m}$'s (and $f^{\rm S}_{\ell m}$) obtained from the perturbative calculations of the fluxes of a spinning particle around a Kerr black hole by imposing the structure given by Eq. (8.68). This means, in particular, replacing the dimensionless Kerr spin as $\hat{a} \to \tilde{a}_1$ and the particle spin as $\sigma \to \tilde{a}_2$. In other words, on the ν-dependent side, the next-to-next-to-next-to-leading-order (NNNLO) spin-orbit term will have the form

$$c_{22}^{{\rm SO}^{\rm NNNLO}_\nu} = \left(c_0^{\rm NNNLO}\hat{a}_0 + X_{12}\tilde{a}_{12}d_0^{\rm NNNLO}\right)x^{9/2}, \tag{8.69}$$

where $\left(c_0^{\rm NNNLO}, d_0^{\rm NNNLO}\right)$ are the unknown ν-independent, coefficients. On the $\nu = 0$ side, the corresponding spin-orbit terms reads

$$c_{22}^{{\rm SO}_0^{\rm 4.5PN}} = \left(c_{\hat{a}}^{\rm 4.5PN}\hat{a} + c_\sigma^{\rm 4.5PN}\sigma\right)x^{9/2}. \tag{8.70}$$

By equating the $\nu = 0$ limit of Eq. (8.70) to this equation, one finds

$$c_{22}^{{\rm SO}^{\rm NNNLO}_\nu} = \Bigg(\frac{c_{\hat{a}}^{\rm 4.5PN} + c_\sigma^{\rm 4.5PN}}{2}\hat{a}_0 \\ + X_{12}\tilde{a}_{12}\frac{c_{\hat{a}}^{\rm 4.5PN} - c_\sigma^{\rm 4.5PN}}{2}\Bigg)x^{9/2}, \tag{8.71}$$

where $c_{\hat{a}}^{4.5\mathrm{PN}}$ is analytically known [298] and reads

$$c_{\hat{a}}^{4.5\mathrm{PN}} = -\frac{8494939}{467775} + \frac{2536}{315}\mathrm{eulerlog}_2(x), \tag{8.72}$$

while the spinning-particle term, $c_{\sigma}^{4.5\mathrm{PN}}$, is currently unknown. The same procedure can be applied to incorporate spinning-particle spin-orbit terms at higher-PN order and can be extended to the other multipoles, with the obvious difference that for m-odd multipoles the hybridization procedure applies to the $f_{\ell m}^{\mathrm{S}}$ functions. The hybridization of the spinning-particle, spin-square terms into ρ_{22}^{S} is done in a similar way. A similar calculation for the NNLO (relative 4PN-accuracy) spin-square term yields

$$\begin{aligned} c_{22}^{\mathrm{SS}_\nu^{\mathrm{NNLO}}} = \Bigg[& \frac{1}{2}\left(c_{\hat{a}^2} + c_{\sigma^2}\right)\hat{a}_0^2 + \left(c_{\hat{a}\sigma} - c_{\hat{a}^2} - c_{\sigma^2}\right)\tilde{a}_1\tilde{a}_2 \\ & + \frac{1}{2}\left(c_{\hat{a}^2} - c_{\sigma^2}\right)\hat{a}_0\tilde{a}_{12}X_{12}\Bigg] x^4, \end{aligned} \tag{8.73}$$

where $(c_{\sigma^2}, c_{\hat{a}\sigma}, c_{\sigma^2})$ are the coefficients entering the spin-square spinning-particle term at 4PN, that will have the structure

$$c_{22}^{\mathrm{SS}_0} = \left(c_{\hat{a}^2}\hat{a}^2 + c_{\hat{a}\sigma}\hat{a}\sigma + c_{\sigma^2}\sigma^2\right) x^4, \tag{8.74}$$

where only $c_{\hat{a}^2}$ is currently analytically known and reads [298]

$$c_{\hat{a}^2} = \frac{18353}{21168}. \tag{8.75}$$

This approach gives us a consistent way of hybridizing the test-mass result above with the low-PN ν-dependent information. Even if the spinning-particle terms are not currently published starting from 4PN order, it could be instructive to investigate the robustness of the results of Fig. 8.3 under the incorporation of the *nonspinning* test-particle terms. To do so, we replicate the procedure done above to incorporate the 4PN and 4.5PN test-particle terms for the spin-square 5PN and 6PN terms as well as for the 5.5PN spin-orbit term, that will have the same relation given in Eqs. (8.69)-(8.73) with the test-particle coefficients. After this is done, we factorize and resum the hybrid ρ_{22} as before. Such, test-particle-improved, $\bar{\rho}_{22}^{\mathrm{S}}$ is consistent with the $\nu = 0$ function discussed in Sec. 8.2 except for the obvious absence of the

spin-cube terms coming beyond the NLO as well as of the terms involving higher powers of the spins up to the sixth-power, that enters at LO in the 6PN term. The effect of the additional $\nu = 0$ terms is illustrated in Fig. 8.5 for $(1, +0.99, +0.99)$ and $(8, +0.50, 0)$, where the hybridized function is contrasted with the NNLO one of Fig. 8.3. The figure shows that the effect is quantitatively important for the case $(8, +0.50, 0)$, notably towards the merger frequency $x \approx 0.32$.

8.6 Multipolar fluxes

In this Section we explicitly report, for completeness, the PN-expanded, complete, Newton-normalized multipoles of the energy flux up to NNLO in the spin-orbit coupling, NLO in the spin-spin coupling and LO in the spin-cube couplings. Though these expressions are obtained as the square of the Newton-normalized waveform multipoles of Eqs. (8.15)-(8.23), it is convenient to have them written down explicitly. Each multipolar contribution to the flux is written as the product of the Newtonian prefactor $F^N_{\ell m}$ and the PN correction $\hat{F}_{\ell m}$ as

$$F_{\ell m} \equiv F^{(N,\epsilon)}_{\ell m} \hat{F}^{(\epsilon)}_{\ell m}, \tag{8.76}$$

where the PN correction factors explicitly read

$$
\begin{aligned}
\hat{F}_{22}^{(0)} &= 1 + \left(-2\hat{a}_0 + 4\pi - \frac{2}{3}\tilde{a}_{12}X_{12}\right)x^{3/2} + \left(-\frac{107}{21} + \frac{55}{21}\nu\right)x \\
&+ \left(\frac{4784}{1323} + 2\hat{a}_0^2 - \frac{87691}{5292}\nu + \frac{5851}{1323}\nu^2\right)x^2 \\
&+ \left[\left(-\frac{428}{21} + \frac{178}{21}\nu\right)\pi + \hat{a}_0\left(\frac{158}{63} - \frac{257}{63}\nu\right) - \tilde{a}_{12}X_{12}\left(\frac{50}{63} + \frac{187}{63}\nu\right)\right]x^{5/2} \\
&+ \left[\frac{99210071}{1091475} + \frac{1650941}{349272}\nu - \frac{669017}{19404}\nu^2 + \frac{255110}{43659}\nu^3 + \left(\frac{16}{3} + \frac{41}{48}\nu\right)\pi^2\right. \\
&- \left(8\hat{a}_0 + \frac{8}{3}\tilde{a}_{12}X_{12}\right)\pi + \frac{257}{63}\nu\left(\tilde{a}_1^2 + \frac{962\tilde{a}_1\tilde{a}_2}{257} + \tilde{a}_1^2\right) + \frac{284}{63}X_{12}\left(\tilde{a}_1^2 - \tilde{a}_2^2\right) \\
&\left.- \frac{53}{7}\left(\tilde{a}_1^2 + \frac{1072\tilde{a}_1\tilde{a}_2}{477} + \tilde{a}_2^2\right) - \frac{1712}{105}\mathrm{eulerlog}_2(x)\right]x^3 \\
&+ \left[\left(\frac{19136}{1323} - \frac{144449}{2646}\nu + \frac{33389}{2646}\nu^2\right)\pi + \hat{a}_0\left(\frac{29234}{1323} + \frac{77212}{1323}\nu + \frac{1747}{1323}\nu^2\right)\right. \\
&\left.+ \tilde{a}_{12}X_{12}\left(\frac{37858}{3969} + \frac{96575}{7938}\nu - \frac{23182}{3969}\nu^2\right) - \frac{2}{3}(\hat{a}_0^3 + 3\hat{a}_0^2\tilde{a}_{12}X_{12})\right]x^{7/2},
\end{aligned}
\tag{8.77}
$$

$$\hat{F}_{21}^{(1)} = 1 - 4\nu - 3\tilde{a}_{12}X_{12}x^{1/2} + \left(-\frac{17}{14} + \frac{44}{7}\nu - \frac{40}{7}\nu^2 + \frac{9}{4}\tilde{a}_{12}^2\right)x$$
$$+ \left[2\pi(1-4\nu) + \hat{a}_0\left(-\frac{43}{7} + \frac{172}{7}\nu\right)\right.$$
$$\left. + \tilde{a}_{12}X_{12}\left(\frac{195}{28} + \frac{18}{7}\nu\right)\right]x^{3/2} + \left\{-\frac{2215}{7056} - \frac{13567}{1764}\nu + \frac{65687}{1764}\nu^2 - \frac{853}{147}\nu^3\right.$$
$$- \frac{26}{7}\left(\tilde{a}_1^2 - \frac{68}{13}\tilde{a}_1\tilde{a}_2 + \tilde{a}_2^2\right) - \frac{323}{14}\left(\tilde{a}_1^2 + \frac{26}{323}\tilde{a}_1\tilde{a}_2 + \tilde{a}_2^2\right)\nu$$
$$\left. + X_{12}\left[\frac{157}{14}(\tilde{a}_1^2 - \tilde{a}_2^2) - 6\pi\tilde{a}_{12}\right]\right\}x^2$$
$$+ \left\{\left(\frac{9}{2}\tilde{a}_{12}^2 - \frac{17}{7} + \frac{81}{7}\nu - \frac{52}{7}\nu^2\right)\pi + \hat{a}_0\left(\frac{2131}{882} - \frac{1165}{147}\nu - \frac{3068}{441}\nu^2\right)\right.$$
$$- \tilde{a}_{12}X_{12}\left(\frac{10121}{1764} - \frac{30595}{882}\nu - \frac{16927}{3528}\nu^2\right)$$
$$\left. + 3\hat{a}_0\tilde{a}_{12}^2 + \frac{3}{2}X_{12}[5(\tilde{a}_1^3 - \tilde{a}_2^3) + \tilde{a}_1(\tilde{a}_1\tilde{a}_2 - \tilde{a}_2^2)]\right\}x^{5/2}, \tag{8.78}$$

$$\hat{F}_{31}^{(0)} = 1 - 4\nu + \left(-\frac{16}{3} + 20\nu + \frac{16}{3}\nu^2\right)x$$
$$+ \left[2\pi(1-4\nu) + \hat{a}_0\left(\frac{1}{2} - 2\nu\right) + \tilde{a}_{12}X_{12}\left(-\frac{9}{2} + 13\nu\right)\right]x^{3/2}$$
$$+ \left[\frac{437}{33} - \frac{5164}{99}\nu - \frac{523}{99}\nu^2 + \frac{812}{99}\nu^3 + 3\hat{a}_0^2(1-4\nu) - 8X_{12}(\tilde{a}_1^2 - \tilde{a}_2^2)\right]x^2$$
$$+ \left[\left(-\frac{32}{3} + 39\nu + \frac{44}{3}\nu^2\right)\pi + \hat{a}_0\left(-\frac{103}{18} + \frac{283}{6}\nu - \frac{874}{9}\nu^2\right)\right.$$
$$\left. + \tilde{a}_{12}X_{12}\left(\frac{145}{6} - \frac{1211}{18}\nu - \frac{41}{3}\nu^2\right)\right]x^{5/2}, \tag{8.79}$$

$$\hat{F}_{32}^{(1)} = 1 + \frac{1}{1-3\nu}\Bigg\{2(\hat{a}_0 - \tilde{a}_{12}X_{12})x^{1/2} + \left(-\frac{193}{45} + \frac{145}{9}\nu - \frac{73}{9}\nu^2\right)x + \frac{1}{(1-3\nu)}\Bigg[4\pi(1-3\nu)^2 + \hat{a}_0\left(-\frac{778}{45} + \frac{715}{9}\nu - \frac{730}{9}\nu^2\right) + \tilde{a}_{12}X_{12}\left(\frac{538}{45} - \frac{313}{9}\nu - \frac{44}{9}\nu^2\right)\Bigg]x^{3/2}\Bigg\}, \tag{8.80}$$

$$\begin{aligned}\hat{F}_{33}^{(0)} &= 1 - 4\nu + (-8 + 36\nu - 16\nu^2)x \\ &+ \left[6\pi(1-4\nu) + \hat{a}_0\left(-\frac{7}{2} + 14\nu\right) + \tilde{a}_{12}X_{12}\left(-\frac{1}{2} + 5\nu\right)\right]x^{3/2} \\ &+ \left[\frac{1003}{55} - \frac{18352}{165}\nu + \frac{8937}{55}\nu^2 - \frac{6188}{165}\nu^3 + 3\hat{a}_0^2(1-4\nu)\right]x^2 \\ &+ \Bigg[(-48 + 213\nu - 84\nu^2)\pi + \hat{a}_0\left(\frac{559}{30} - \frac{843}{10}\nu + \frac{586}{15}\nu^2\right) \\ &+ \tilde{a}_{12}X_{12}\left(-\frac{59}{30} - \frac{183}{10}\nu + \frac{391}{15}\nu^2\right)\Bigg]x^{5/2}\ ,\end{aligned} \tag{8.81}$$

$$\hat{F}^{(1)}_{41} = 1 - 4\nu + \frac{1}{-1+2\nu}\Bigg\{\left[\hat{a}_0\left(-\frac{5}{2}+10\nu\right)+\tilde{a}_{12}X_{12}\left(\frac{5}{2}-5\nu\right)\right]x^{1/2} + \left[\frac{202}{33}-\frac{2627}{66}\nu+\frac{2188}{33}\nu^2-\frac{664}{33}\nu^3\right]x\Bigg\}\,, \tag{8.82}$$

$$\hat{F}^{(0)}_{42} = 1 + \frac{1}{1-3\nu}\Bigg\{\left(-\frac{1311}{165}+\frac{805}{33}\nu-\frac{19}{11}\nu^2\right)x + \left[4\pi(1-3\nu)-\frac{4}{5}\hat{a}_0\left(\frac{1}{3}-\nu\right)-\tilde{a}_{12}X_{12}\left(\frac{76}{15}-\frac{52}{5}\nu\right)\right]x^{3/2} + \frac{1}{(1-3\nu)}\left(\frac{7199152}{275275}-\frac{140762423}{825825}\nu+\frac{37048126}{117975}\nu^2-\frac{3504901}{31460}\nu^3-\frac{65037}{7865}\nu^4\right)x^2\Bigg\}, \tag{8.83}$$

$$\hat{F}^{(1)}_{43} = 1 - 4\nu + \frac{1}{-1+2\nu}\Bigg\{\left[\hat{a}_0\left(-\frac{5}{2}+10\nu\right)+\tilde{a}_{12}X_{12}\left(\frac{5}{2}-5\nu\right)\right]x^{1/2} + \left(\frac{78}{11}-\frac{3139}{66}\nu+\frac{932}{11}\nu^2-\frac{1048}{33}\nu^3\right)x\Bigg\}, \tag{8.84}$$

$$\hat{F}^{(0)}_{44} = 1 + \frac{1}{1-3\nu}\Bigg\{\left(-\frac{1779}{165}+\frac{1273}{33}\nu-\frac{175}{11}\nu^2\right)x + \left[8\pi(1-3\nu)-\hat{a}_0\left(\frac{76}{15}-\frac{76}{5}\nu\right)-\tilde{a}_{12}X_{12}\left(\frac{4}{15}-\frac{28}{5}\nu\right)\right]x^{3/2} + \frac{1}{(1-3\nu)}\left(\frac{2187772}{55055}-\frac{261025727}{825825}\nu+\frac{95748634}{117975}\nu^2-\frac{4466169}{6292}\nu^3+\frac{1119423}{7865}\nu^4\right)x^2\Bigg\}. \tag{8.85}$$

The Newtonian prefactor can be written in closed form as

$$F^{(N,\epsilon)}_{\ell m} = \frac{1}{8\pi}x^3 m^2 (-)^{\ell+\epsilon}\left|\mathcal{R}h^{(N,\epsilon)}_{\ell m}\right|^2\,, \tag{8.86}$$

where the Newtonian waveform multipole $h^{(N,\epsilon)}_{\ell m}$ is given by Eq. (4.35).

The explicit evaluation of Eq. (8.86) for the multipoles of interest here

gives

$$F_{22}^{(N,0)} = \frac{32}{5}\nu^2 x^5 \ , \tag{8.87}$$

$$F_{21}^{(N,1)} = \frac{8}{45}(1-4\nu)\nu^2 x^6 \ , \tag{8.88}$$

$$F_{33}^{(N,0)} = \frac{243}{28}(1-4\nu)\nu^2 x^6 \ , \tag{8.89}$$

$$F_{32}^{(N,1)} = \frac{32}{63}(1-3\nu)^2\nu^2 x^7 \ , \tag{8.90}$$

$$F_{31}^{(N,0)} = \frac{(1-4\nu)\nu^2}{1260} x^6 \ , \tag{8.91}$$

$$F_{44}^{(N,0)} = \frac{8192}{567}(1-3\nu)^2\nu^2 x^7 \ , \tag{8.92}$$

$$F_{43}^{(N,1)} = \frac{729}{700}(1-4\nu)(1-2\nu)^2\nu^2 x^8 \ , \tag{8.93}$$

$$F_{42}^{(N,0)} = \frac{32(1-3\nu)^2\nu^2}{3969} x^7 \ , \tag{8.94}$$

$$F_{41}^{(N,1)} = \frac{(1-4\nu)(1-2\nu)^2\nu^2}{44100} x^8 \ . \tag{8.95}$$

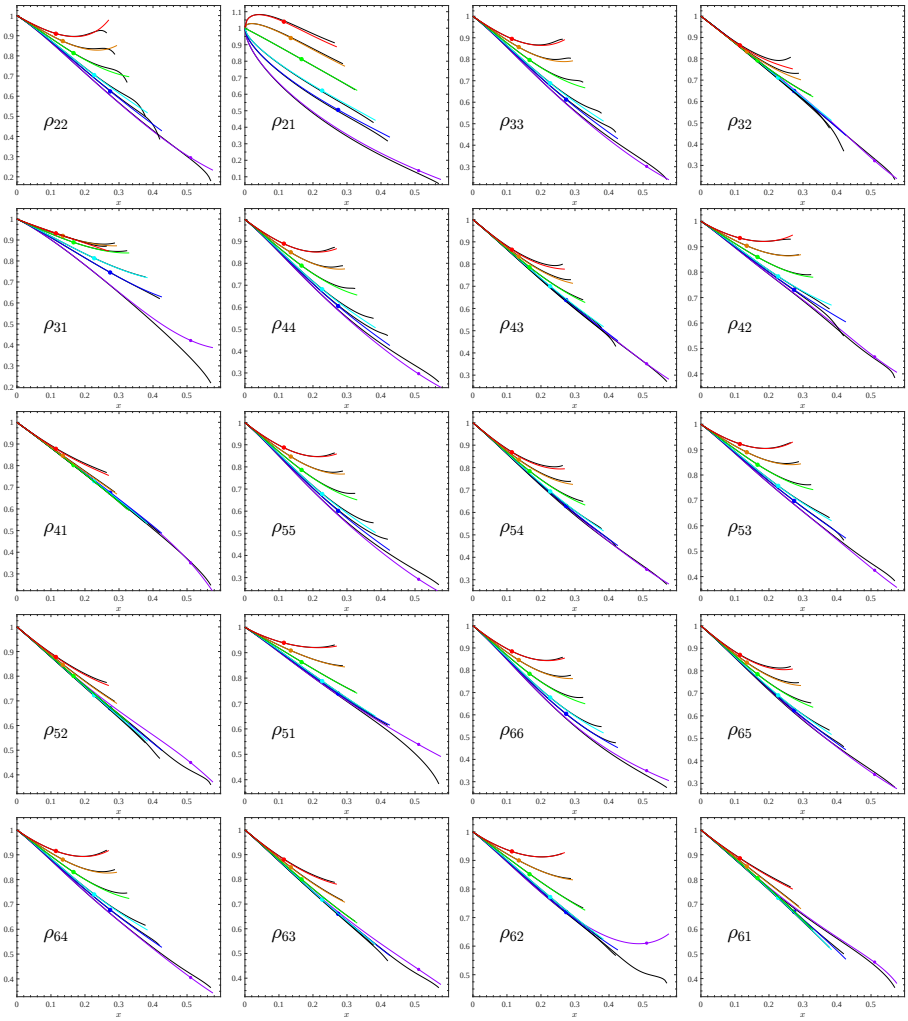

Figure 8.1: Comparison between the factorized and resummed analytical $\rho_{\ell m}$'s (colored online) and the corresponding numerical (exact) functions (black online) up to $\ell = 6$ for values of the BH dimensionless spin $\hat{a} = (-0.99, -0.5, 0, +0.5, +0.99)$ (red, orange, green, cyan, blue and purple respectively). The filled circles mark the LSO location. This plot is obtained using relative 6PN information for all modes except for: ρ_{32} that use to 5PN relative accuracy in $\rho^{\rm orb}_{32}$; ρ_{66} and ρ_{61} that use 5PN relative accuracy for $\hat{\rho}^{\rm S}_{66}$ and $\hat{\rho}^{\rm S}_{61}$. The Padé approximants used on $\rho^{\rm orb}_{\ell m}$ are listed in second column of Table 8.1. The same table also lists the numerical/analytical relative difference at the LSO. The agreement remains good (except for few exceptions, see text for details) also for $\hat{a} = +0.99$.

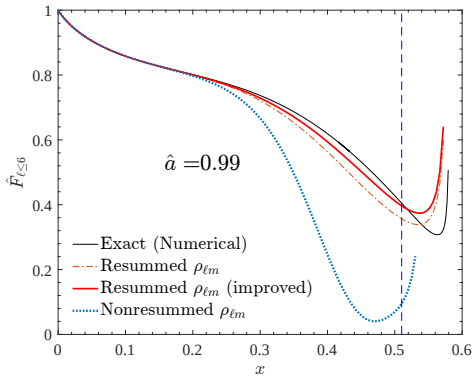

Figure 8.2: Test-particle limit: comparison between analytical and numerical "exact" (see text) fluxes for dimensionless black-hole spin $\hat{a} = +0.99$. The functions $\rho_{33}^{\rm orb}$, $\rho_{44}^{\rm orb}$ and $\rho_{55}^{\rm orb}$ are either resummed using (4,2) Padé approximants (orange, dot-dashed line) or kept in PN-expanded form up to (relative) 6PN order. This second choice improves the agreement with the numerical curve. The dotted line represents the analytical flux where the total 6PN-accurate $\rho_{\ell m}$'s are kept in the standard, nonfactorized, Taylor-expanded form.

Table 8.1: Fractional differences between the resummed and the numerical $\rho_{\ell m}$'s at the LSO. From left to right the columns report: the multipolar order; the Padé approximant chosen for the orbital factor, where the notation P^n_d indicates the approximant of order (n,d); the PN order chosen for the spin-dependent factors; the fractional difference $(\rho^{\rm num}-\rho^{\rm anlyt})/\rho^{\rm num}$ at $x_{\rm LSO}$.

(ℓ,m)	$P^i_j(\rho^{orb}_{\ell m})$	iR(PN)	$\Delta(x)\rho(x)/\rho\|_{x=x_{\rm LSO}}$ for $-0.99\leq\hat{a}\leq+0.99$					
			-0.99	-0.5	0	$+0.5$	$+0.7$	$+0.99$
$(2,2)$	P^4_2	6	-1×10^{-4}	-3×10^{-4}	-6×10^{-4}	-0.002	-0.004	0.026
$(2,1)$	P^5_1	6	-0.006	-0.004	2×10^{-5}	0.010	0.019	0.159
$(3,3)$	P^4_2	6	-4×10^{-5}	-1×10^{-4}	-4×10^{-4}	-0.002	-0.005	-0.058
(3,3)	P^6_0	6	-2×10^{-5}	-6×10^{-5}	-2×10^{-4}	-0.001	-0.002	-0.023
$(3,2)$	P^4_2	6	-0.004	-0.003	-5×10^{-5}	0.006	0.012	-0.026
$(3,1)$	P^3_2	6	-3×10^{-5}	-6×10^{-5}	-1×10^{-4}	-3×10^{-4}	-8×10^{-5}	0.248
(3,1)	P^3_1	8	-2×10^{-5}	-4×10^{-5}	-1×10^{-4}	-8×10^{-4}	-0.002	-0.0017
$(4,4)$	P^4_2	6	-2×10^{-5}	-8×10^{-5}	-3×10^{-4}	-0.002	-0.005	-0.088
(4,4)	P^6_0	6	-4×10^{-6}	-3×10^{-5}	-2×10^{-4}	-0.001	-0.002	-0.046
$(4,3)$	P^4_2	6	-0.003	-0.002	-1×10^{-4}	0.004	0.008	0.004
$(4,2)$	P^6_0	6	-1×10^{-5}	-2×10^{-5}	-5×10^{-5}	6×10^{-4}	0.003	0.015
$(4,1)$	P^4_2	6	-0.003	-0.002	8×10^{-6}	0.005	0.008	-0.013
$(5,5)$	P^4_2	6	-2×10^{-5}	-7×10^{-5}	-3×10^{-4}	-0.002	-0.037	-0.101
(5,5)	P^6_0	6	2×10^{-6}	-2×10^{-5}	-1×10^{-4}	-0.001	-0.034	-0.054
$(5,4)$	P^4_2	6	-0.003	-0.002	-2×10^{-4}	0.003	0.005	-0.013
$(5,3)$	P^4_2	6	-2×10^{-5}	-6×10^{-5}	-2×10^{-4}	-6×10^{-4}	-7×10^{-4}	-0.043
$(5,2)$	P^4_2	6	-0.002	-0.002	8×10^{-6}	0.004	0.009	0.077
$(5,1)$	P^6_0	6	1×10^{-5}	1×10^{-5}	3×10^{-5}	1×10^{-4}	5×10^{-4}	0.101
$(6,6)$	P^4_2	5	-4×10^{-5}	-1×10^{-4}	-3×10^{-4}	-5×10^{-5}	0.002	0.064
$(6,5)$	P^4_2	6	-0.002	-0.001	-2×10^{-4}	0.002	0.003	-0.029
$(6,4)$	P^4_2	6	-2×10^{-5}	-6×10^{-5}	-2×10^{-4}	-8×10^{-4}	-0.001	-0.035
$(6,3)$	P^4_2	6	-0.002	-0.001	-1×10^{-5}	0.003	0.007	0.053
$(6,2)$	P^4_2	6	-4×10^{-6}	-2×10^{-5}	-5×10^{-5}	2×10^{-5}	0.001	0.213
(6,2)	P^6_2	8	-6×10^{-7}	-8×10^{-7}	-7×10^{-7}	8×10^{-5}	9×10^{-4}	0.015
$(6,1)$	P^6_0	5	-0.002	-0.001	7×10^{-6}	0.003	0.003	0.028

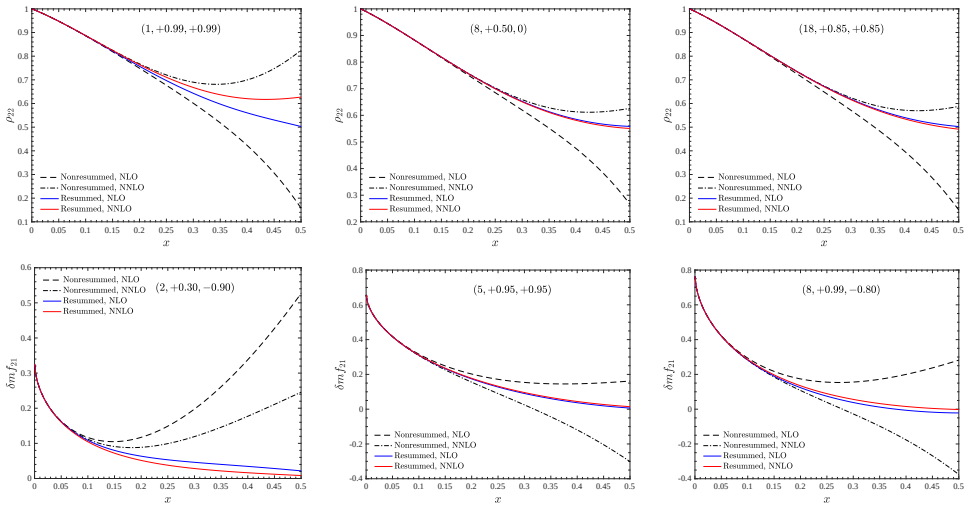

Figure 8.3: Nonresummed (black) and resummed (colored) waveform amplitudes ρ_{22} (top panels) and f_{21} (bottom panels) for a few configurations. The 3PN-accurate orbital factors are hybridized with test-particle information up to relative 6PN order for each mode and then resummed with the Padé approximants of Table 8.1. The consistency between NNLO and NLO truncations of the spin dependence is dramatically improved when the factorization and resummation procedure is applied.

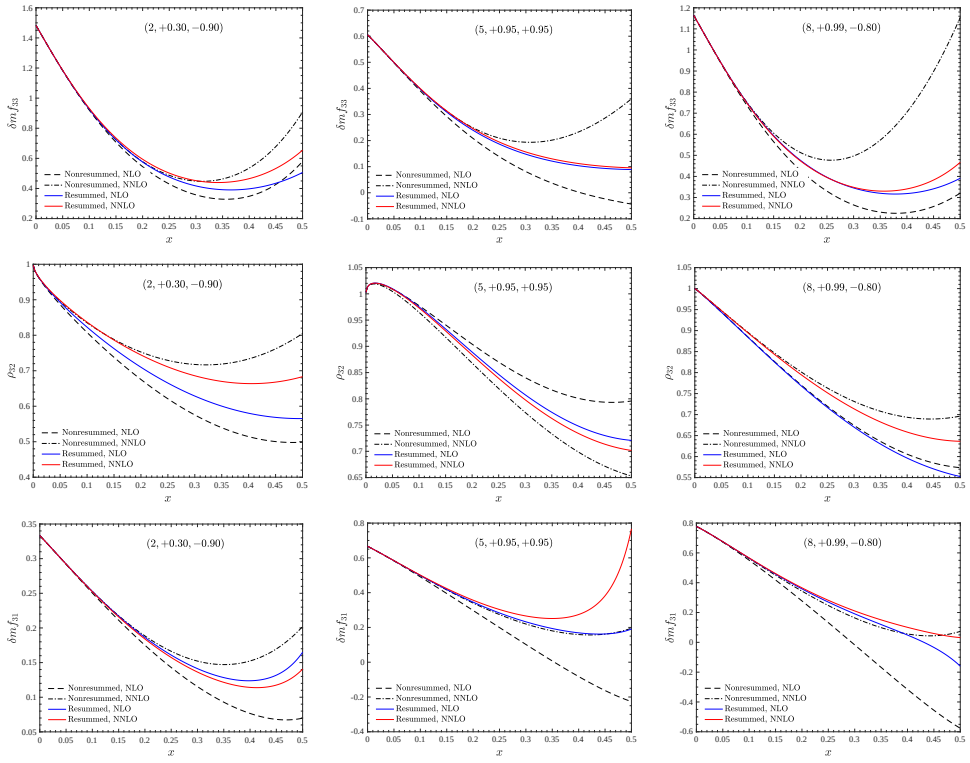

Figure 8.4: Nonresummed (black) and resummed (colored) residual waveform amplitudes for $\ell = 3$ multipoles. The 3PN-accurate orbital factors are hybridized with test-particle information up to relative 6PN order for each mode, except for the $(3, 1)$ mode that is taken at relative 5PN order, and then resummed with the Padé approximants of Table 8.1. Likewise the $\ell = 2$ case of Fig. 8.3, the consistency between NLO and NNLO truncations of the spin dependence is improved by the resummation.

Table 8.2: Analysis of the fractional variation $\triangle c_n^{\rho_{\ell m}^{\rm orb}}(\nu) = c_n^{\rho_{\ell m}^{\rm orb}}(\nu)/c_n^{\rho_{\ell m}^{\rm orb}}(0) - 1$ of the coefficients $c_n^{\rho_{\ell m}^{\rm orb}}(\nu)$.

(ℓ, m)	$\triangle c_1^{\rho_{\ell m}^{\rm orb}}(1/4)$	$\triangle c_2^{\rho_{\ell m}^{\rm orb}}(1/4)$	$\triangle c_1^{\rho_{\ell m}^{\rm orb}}(1/4, \log(1/6))$
$(2,2)$	-0.159884	0.185947	-0.100421
$(2,1)$	-0.649718	0.224005	...
$(3,1)$	0.0769231	-18.7351	-0.28487
$(3,2)$	-0.155488	-0.633264	...
$(3,3)$	-0.142857	0.260344	-0.0970255
$(4,1)$	-0.0905316	...	...
$(4,2)$	-0.0181065	1.05237	...
$(4,3)$	-0.141892	...	...
$(4,4)$	-0.230328	0.46265	...
$(5,1)$	0.219436	...	...
$(5,2)$	-0.117576	...	...
$(5,3)$	-0.0746667	...	...
$(5,4)$	-0.176295	...	...
$(5,5)$	-0.201232	...	...
$(6,1)$	-0.0910973	...	...
$(6,2)$	-0.0168919	...	...
$(6,3)$	-0.118343	...	...
$(6,4)$	-0.119186	...	...
$(6,5)$	-0.165766	...	...
$(6,6)$	-0.238208	...	...

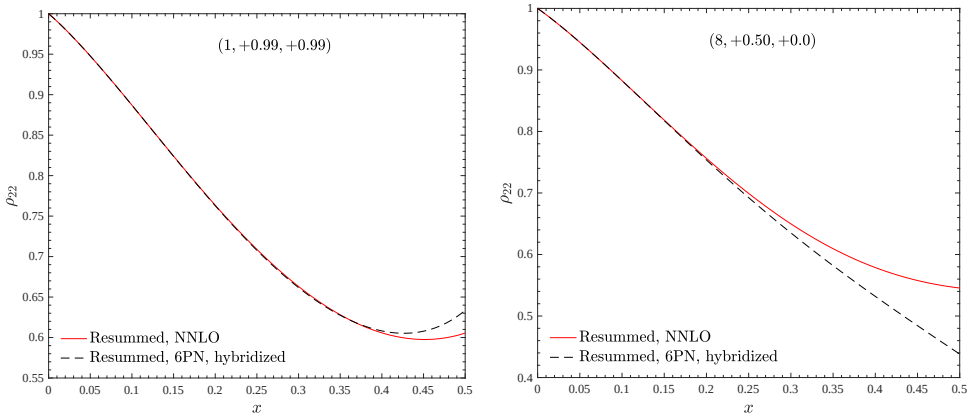

Figure 8.5: Modification of the results of Fig. 8.3 when (nonspinning) test-particle terms up to 6PN are hybridized with the NNLO ν-dependent waveform (see Eqs. (8.71)-(8.73) and text). When $\nu = 0$, one is using here the same spin-orbit and spin-square analytical information used in Fig. (8.1). The frequency parameter approximately corresponding to the BBH merger is $x \approx 0.38$ for $(1, +0.99, +0.99)$ and $x \approx 0.32$ for $(8, +0.50, 0)$. In this latter case, the effect of the additional test-particle terms is important towards merger.

Chapter 9

Factorization and resummation: A new paradigm to improve gravitational wave amplitudes. III: the spinning test-body terms [5]

9.1 Introduction

Test-mass results have been crucial to devise robust resummation techniques for the truncated post-Newtonian expansion that give access to analytical gravitational waveform and fluxes for circularized, nonprecessing, binaries [139, 8, 175, 9, 4]. Such resummed waveform, and related fluxes, are one of the crucial building blocks of effective-one-body (EOB) waveform models for coalescing relativistic binaries [2, 6, 1, 296, 320, 36]. Up to now, resummation of PN-expanded analytical result is the only approach that can be adopted to improve the behavior of the PN-expansions in the strong-field, fast velocity regime up to merger [143]. From the very beginning of this endeavor [139] the development (and testing) of resummation techniques has been driven by comparisons between some analytically resummed waveform and numerical waveforms (or fluxes) generated by a *nonspinning* particle inspiralling and plunging into a Schwarzschild or a Kerr black hole [167, 61]. By contrast, none of the resummation approaches routinely used in state-of-the-

art EOB models [1, 36] has been tested in the special case where the particle (which models a test black-hole) is spinning. This was not done up to now for at least two reasons: (i) on the one hand, robust and accurate numerical computations of the energy fluxes from a spinning particle on circular orbits around a Kerr black became available only recently [314, 313, 312]; (ii) on the other hand, the analytical PN knowledge of the fluxes of a spinning particle around a Kerr black hole was only known at global 2.5PN order [311] and only recently pushed to 3.5PN accuracy [296]. This paper builds on previous works and improves them along two directions: (i) the numerical fluxes of Refs. [312, 313] are recomputed, in the time-domain, at an improved accuracy and increasing the number of multipoles. In addition, they are compared with an analogous calculation performed with a completely independent numerical code in the frequency domain, finding excellent consistency between the two methods once the results are linearized in the particle spin; (ii) though we here only consider the case of a spinning particle around a Schwarzschild black hole, the 2.5PN accurate results of Ref. [311] are pushed to much higher PN order, namely *relative* 5.5PN accuracy for all multipoles of the flux up to $\ell = 7$. The availability of such new PN information, at high order, allows us to extensively test the standard waveform resummation techniques of Refs. [139, 8, 175] in a corner of the binary parameter space that had not been covered before. Similarly, we use these new numerical data to check new resummation approaches proposed recently in Refs. [9, 4] and that are going to be partly incorporated in the next generation of EOB waveform models [321].

9.2 Energy fluxes emitted by a spinning particle around a Schwarzschild black hole

In this section we consider the energy flux radiated in gravitational waves by a spinning particle on a circular orbit of radius r_0 around a Schwarzschild black hole. We will restrict our attention to the case where the particle's spin axis is aligned with the orbital angular momentum. We compute the radiated flux both analytically, via high-order post-Newtonian calculations, and numerically, using two independent approaches.

9.2.1 Post-Newtonian results

Dynamics of a spinning particle

The equations of motion of a spinning test body moving on a curved spacetime background (Schwarzschild) are given by the Mathisson-Papapetrou-Dixon equations (MPD) [322, 323, 324]

$$\frac{\mathrm{D}p^\mu}{d\tau} = -\frac{1}{2} R^\mu{}_{\nu\alpha\beta}\, u^\nu\, S^{\alpha\beta}\,, \tag{9.1}$$

$$\frac{\mathrm{D}S^{\mu\nu}}{d\tau} = 2\, p^{[\mu} u^{\nu]}\,, \tag{9.2}$$

where p^μ is the four-momentum, u^μ is the four-velocity (τ is the proper time), $R^\mu{}_{\nu\alpha\beta}$ is the Riemann tensor of the spacetime and $S^{\alpha\beta}$ is the spin-tensor. From the spin tensor we can define the spin magnitude, $s = (\frac{1}{2} S_{\mu\nu} S^{\mu\nu})^{1/2}$, from which we define the spin variable

$$\sigma \equiv \frac{s}{\mu M}\,. \tag{9.3}$$

As in previous work [314, 313, 312], we consider $-1 \leq \sigma \leq 1$. We will comment in Appendix 9.4 on the meaning of these limits and on the interpretation of the test-mass results presented here as part of the general case where the masses of the two bodies are comparable. The MPD equations do not form a closed systems of evolution equations and a closure, called spin supplementary condition (SSC), is required. The choice of a SSC amounts to choosing a centre of mass for the spinning body [325]. For astrophysically relevant values of the spin, there are strong indications that any physically meaningful quantity will not depend upon the SSC choice [313, 314]. In this paper we choose the Tulczyjew-Dixon condition $S^{\mu\nu} p_\nu = 0$ [326].

Throughout this section, we will work to linear order in σ for which we have $p^\alpha = \mu u^\alpha + \mathcal{O}(\sigma^2)$. The orbital frequency is then given by [311]

$$\Omega = u^{3/2} \left(1 - \frac{3}{2}\sigma u^{3/2}\right) \tag{9.4}$$

where $u = M/r_0$ and r_0 is the radius of a circular orbit expressed in Schwarzschild coordinates.

Calculation of the energy fluxes

In the Teukolsky approach, the problem of computing the energy and angular momentum fluxes at infinity from perturbations to either a Kerr or Schwarzschild black hole has been well laid out in the literature, and it is briefly overviewed in Sec. 2.5.2 of Chapter 2. We now briefly describe the calculation of the $F_{\ell m}$ functions appearing in Eq. (2.160) as a PN expansion, i.e an expansion for large orbital radius and small frequency. This calculation was first presented for a spinning particle on a circular orbit by Tanaka et al. [311], though truncated at 2.5PN order. We will extend their calculation to a higher order in the expansion. To evaluate Eq. (2.159) we first need PN expansions for the homogeneous radial functions $R^{\pm}_{\ell m}$. The well established method for systematically computing these uses the solutions of Mano, Suzuki and Takasugi (MST) [308, 327]. The MST solutions to the homogeneous radial Teukolsky equation are given as infinite series of either hypergeometric ${}_2F_1$ functions or irregular confluent hypergeometric U functions. In the PN limit, restricting the frequencies to the allowed harmonics of the orbital frequency, these infinite series truncate at finite orders and, with modern algebraic software, are methodically Taylor expanded to a desired PN order. For in depth discussion of our calculations see [328]. With these in hand the evaluation of Eq. (2.159) is straightforwardly accomplished by also Taylor expanding the B_i's, thus giving PN expansions for the energy flux modes. At each order in the PN expansion we also work to linear order in the spin σ. In practice, we found it easy to consider modes up to $\ell = 7$ and obtain each multipolar flux at 5.5PN accuracy *beyond* the leading-order contribution. More precisely, each PN-expanded multipolar contribution is factorized as

$$F_{\ell m} = F^{(N,\epsilon)}_{\ell m} \hat{F}_{\ell m} \ , \tag{9.5}$$

where $F^{(N,\epsilon)}_{\ell m}$ is the Newtonian (or leading-order) prefactor, while $\hat{F}_{\ell m}$ is the PN correction. Here, $\epsilon = 0, 1$ depending on the parity of $\ell + m$. For each (ℓ, m), $\hat{F}_{\ell m}$ is given by a 5.5PN-accurate polynomial, i.e. it has the structure $1 + x + x^{3/2} + x^2 + x^{5/2} + \cdots + x^{11/2}$, where $x = (GM\Omega/c^3)^{2/3} = \mathcal{O}(c^{-2})$ is the PN-ordering frequency parameter. The defining formula for the $F^{(N,\epsilon)}_{\ell m}$'s is given by Eq. (8.86); the Newton-normalized PN-expanded multipolar fluxes, $\hat{F}_{\ell m}$, in Sec. 9.5.1.

9.2.2 Numerical results

For computing numerically the radiated fluxes we employ two codes that solve the Teukolsky equation. One is a 2+1 time-domain code of Ref. [312, 313] and the other a frequency domain code [329]. The details of each of these codes are presented elsewhere and so here we will only give a brief overview of each code and show that their results are consistent with one another.

Frequency domain approach

The method employed by the frequency domain (FD) numerical code follows closely the description of the PN calculation given in Sec. 9.2.1 with the exception that the homogeneous solutions are computed numerically. This is done using the semi-analytic MST method (see [62] for a review and [330, 331] for extensions we use). A similar version of the code to compute the homogeneous solutions is publicly available as part of the Black Hole Perturbation Toolkit (`bhptoolkit.org`). With the homogeneous solutions in hand the inhomogeneous solutions are computed by convolving them with the Teukolsky source. From the inhomogeneous solutions we can compute the radiated fluxes per mode from the complex asymptotic amplitudes, $C^{\pm}_{\ell m}$, of the radial Teukolsky solutions via Eq. (2.160).

Both in the source and in the orbital dynamics we linearize with respect to σ. Our resulting fluxes though are not linear in σ. This is because the radial Teukolsky equation contains a term proportional to the square of the mode frequency, $\omega = m\Omega$. In principle it would be possible to solve this equation to linear order in σ but we have not attempted to do so in this work. Instead, at a range of fixed orbital frequencies, we numerically compute the fluxes for various values of σ and fit this data using a polynomial and extract the linear in σ piece. It is important to make this step as the quadratic and higher contributions to the raw frequency-domain flux data are not complete as we are not including, e.g., higher order corrections to the orbital dynamics.

The code is written in C++ and internally (particularly for the MST part of the calculation) it uses extended precision. We have high confidence in the results for three reasons: i) when $\sigma = 0$ we recover known flux results nonspinning bodies to $\sim$14 significant digits ii) for $\sigma \neq 0$ and after extracting the linear in σ contribution we see good agreement with the PN results – see Fig. 9.1 – and iii) we have reconstructed the metric perturbation at the particle using the standard CCK procedure [332, 333, 334] and from this we

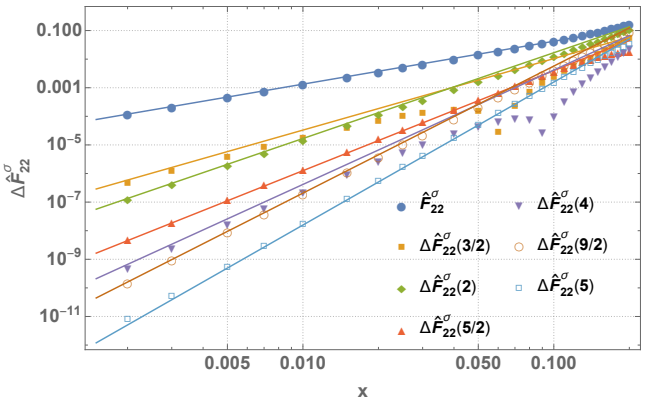

Figure 9.1: Consistency test between FD calculation and PN-expanded fluxes. Comparison of the linear-in-sigma contribution of the $\ell = m = 2$ (Newtonian normalized) flux to infinity between the numerical frequency domain results and the PN series. Here the markers show the difference $\Delta\hat{F}^{\sigma}_{22}(n) = |\hat{F}^{\mathrm{FD}\sigma}_{22} - \hat{F}^{\mathrm{PN}\sigma}_{22}(n)|$ where $\hat{F}^{\mathrm{PN}\sigma}_{22}(n)$ is the $\mathcal{O}(\sigma)$ piece of the PN series truncated at x^n. The full PN series is given by Eq. (9.40) and successively higher order truncations of this are shown by the colored curves. The $\mathcal{O}(\sigma)$ piece of the numerical results is extracted from the numerical data using the method described in the main text. At large radii we observe that subtracting successively higher order PN series improves the agreement with the numerical data, as expected.

have shown that the local self-force experienced by the particle is balanced (to a relative error of 10^{-9}) by the radiated fluxes through the spacetime boundaries. Details on each of these checks will be presented in [329].

Numerical results: time-domain approach with Hamiltonian dynamics

An overview about the TD code used in this work is contained in Sec. 2.5.2 of Chapter 2. It is important to stress that the delta functions in the source can be discretized either using a narrow Gaussian or discrete delta functions; the former option is used in case of circular orbits as discussed in [312]. The code was extensively tested and delivers multipolar waveforms and GW fluxes at null infinity with an accuracy well below the 1% level up to $m = 4$ modes [306, 312, 313, 314]. The data used for this work are produced exactly as

described in [312, 313]. Circular equatorial trajectories for the test body are computed using the Hamiltonian formalism detailed in Sec. III of [313]. The Hamiltonian of a spinning particle at linear order in the spin was originally obtained in Ref. [335]. The same Hamiltonian can be recasted in certain specific effective-one-body (EOB) coordinates as illustrated in Ref. [336]. The EOB coordinates are transformed to the hyperboloidal ones via a transformation linear in σ. The EOB dynamics is compatible with the MPD dynamics with Tulczyjew and the Pirani [337] SSCs across almost the whole spin and frequency range for the Schwarzschild background [313]. One must, however, be aware that that the Hamiltonian circular dynamics and the MPD dynamics described above are fully equivalent and compatible *only* when the spin of the particle is small. We address the reader to Ref. [313] for additional details. Following previous work of some of us [313, 314], we want to accurately compute numerical fluxes for values of the spins that are *large*, i.e., $\sigma \sim 1$ and for orbits that are near the spin-dependent last-stable orbit. Past work [313] suggests that this can be done using the Hamiltonian formalism. Like the FD results mentioned above, our results will not be linear in σ, essentially for the same reasons mentioned above. Thus, to provide a consistent comparison with FD results, we also extracted the linear-in-sigma piece out of the numerical results.

9.2.3 Comparing numerical waveform amplitudes

Since the main aim of the paper is to check resummation procedure for gravitational waveform amplitudes, it is convenient to directly use these quantities for comparing the results obtained with the two numerical approaches. In this respect, the extraction of the linear piece mentioned in the previous section is now performed at the level of the waveform amplitudes (defined below) and not on the fluxes. Likewise for the fluxes, each waveform multipole is factorized in the product of a Newtonian (leading-order) contribution and a relativistic correction

$$h_{\ell m}(x) \equiv h^{(N,\epsilon)}_{\ell m}(x)\hat{h}^{(\epsilon)}_{\ell m}(x), \tag{9.6}$$

where $h^{(N,\epsilon)}_{\ell m}$ is the Newtonian prefactor given by Eq. (4.35). In practice, it is convenient to focus only on the relativistic correction, since it is a function of order unity whose PN expansion has the structure $\hat{h}^{(\epsilon)}_{\ell m} \simeq 1 + x + x^{3/2} + \ldots$. Figure 9.2 offers a comprehensive comparison of the various numerical data

at our disposal for an illustrative sample of multipoles and spins. The top part of each panel of the figure shows 4 curves: (i) the outcome of the time-domain code with Hamiltonian dynamics; (ii) the same quantity where one has subtracted the nonlinar-in-spin part; (iii) the outcome of the frequency-domain code with MPD dynamics: (iv) the same quantity where one has subtracted the nonlinear-in-spin part. The vertical line in the plot marks the location of the σ-dependent frequency of the last-stable-orbit (LSO), as obtained, for example, in Ref. [313]

$$x^{\rm LSO} = \frac{1}{6} + \frac{\sigma}{12\sqrt{6}}. \tag{9.7}$$

As can be seen from Fig. 9.2, the linear-in-spin results from the two codes are in the excellent agreement reaching a fractional accuracy of $\sim 10^{-5}$ (this is limited by the precision of the TD code and the need to extract the linear-in-spin contribution). Note that we do not expect agreement between the nonlinear in spin results as each code effectively includes different pieces of the nonlinear contribution (either through their dynamics or other aspects of the calculation). We emphasize that, to the best of our knowledge, this is the first successful comparison between two completely independent Teukolsky codes with a spinning secondary object. The excellent agreement between the two codes (after linearizing in spin) and the agreement between the FD and PN results presented in Fig. 9.1 gives us a high degree of confidence in our results.

Since the PN results are linear in the spin, we will use the linearized FD data as the target points to verify the accuracy of the various analytical approximations to the waveform amplitudes.

9.3 Comparing analytical and numerical results

We turn now to comparing the "exact" numerical data computed in the previous section to different analytical approximations of $|\hat{h}^{(\epsilon)}_{\ell m}|$. More precisely:

(i) In Sec. 9.3.1, we consider the straightforward PN-expanded expressions of $|\hat{h}^{(\epsilon)}_{\ell m}|$ up to 5.5PN order.

(ii) In Sec. 9.3.2 we consider the, now standard, factorization and resummation of Refs. [8, 175]. Note that this analytical approach is adopted in state-of-the-art EOB waveform models for coalescing binaries [36, 1].

(iii) In Sec. 9.3.3 we explore the performance of a hybrid approach that consists of: implementing the orbital factorization, and subsequent resummation, of Refs. [9, 4] for the $\epsilon = 0$ modes, while the $\epsilon = 1$ only benefit the factorization of the tail contribution.

(iv) In Sec. 9.3.4 we test the special orbital-factorization and resummation of odd-m modes that is adopted in the $\nu \neq 0$ case and that was recently shown to yield excellent consistency between EOB and state-of-the-art NR waveform amplitudes.

9.3.1 PN-expanded waveform amplitudes

The comparison with the plain PN-expanded waveform amplitudes is exhibited in Fig. 9.3. One observes good consistency between the numerical and analytical results at low frequencies, as expected. This progressively worsens towards the LSO, that now is indicated by colored markers on the figure. This worsening is prominent for higher modes. It is, however, interesting to note that the PN-expanded $m = 1$ modes already offer an excellent representation of the numerical data up to the LSO and for any value of ℓ.

9.3.2 Standard resummation: factorized and resummed amplitudes

We start by investigating whether the standard factorization and resummation procedure of waveform amplitudes of Refs. [8, 176] can reduce the gap between the PN-expanded and numerical amplitudes towards the LSO seen in Fig. 9.3. The PN-expanded circularized waveform amplitudes are resummed as (4.36) (See Sec. 4.4 for details). From the PN-expanded Newton-normalized fluxes $\hat{F}_{\ell m}$, as what was done in Chapt. 8, we calculate the PN-expanded residual amplitudes $\rho_{\ell m}$. To do so for a spinning particle problem, we need the energy and angular momentum of a spinning body along circular orbits of Schwarzschild spacetime at linear order in the spin. These were

obtained in Eqs. (81) and (82) of Ref. [313],

$$\begin{aligned}\hat{E}(x) \equiv E/\mu &= \hat{E}^{\rm orb}(x) + \hat{E}^{\sigma}(x) \\ &= \frac{1-2x}{\sqrt{1-3x}} - \frac{x^{5/2}\sigma}{\sqrt{1-3x}}, \qquad (9.8)\\ \hat{j}(x) &= \hat{j}^{\rm orb}(x) + \hat{j}^{\sigma}(x) \\ &= \frac{1}{\sqrt{1-3x}} - \sqrt{x}\left(1 - \frac{1-4x}{\sqrt{1-3x}}\right)\sigma, \qquad (9.9)\end{aligned}$$

where the expression for $\hat{j}$ is obtained multiplying by $\sqrt{x}$ (i.e., the inverse of the Newtonian angular momentum along circular orbits) Eq. (81) of Ref. [313]. The PN-expanded $\rho_{\ell m}$'s are then given by

$$\rho_{\ell m} = T_n\left[\frac{\sqrt{\hat{F}_{\ell m}}}{|\hat{h}^{\rm tail}_{\ell m}(x)|\hat{S}^{(\epsilon)}}\right]^{1/\ell}, \qquad (9.10)$$

where T_n denotes a Taylor-expansion of order n and $\hat{F}_{\ell m}$ are the Newton-normalized PN-expanded energy fluxes. The $\rho_{\ell m}$ functions are here written as the sum of an orbital (spin-independent) and a spin-dependent term

$$\rho_{\ell m} = \rho^{\rm orb}_{\ell m} + \rho^{\sigma}_{\ell m}. \qquad (9.11)$$

The PN knowledge of $\rho^{\sigma}_{\ell m}$ before this work was limited to global 3.5PN (NNLO) and the functions are written explicitly in Ref. [4, 296]. Here the computation of *each* $\rho^{\sigma}_{\ell m}$ is pushed up to *relative* 5.5PN order, i.e., next-to-next-to-next-to-next-to-leading-order, N^{4}LO in the spin-orbit coupling. We list the functions explicitly in Sec. 9.6. One verifies that the 3.5PN-accurate truncation of our results agrees in full with the corresponding formulas of Refs. [4, 296].

The analytical $|\hat{h}_{\ell m}|$'s from Eq. (4.36) are compared with the corresponding numerical ones in Fig. 9.4. The effect of the standard resummation can be summarized as follows. First, the analytically resummed $\ell = m$ modes deliver a rather good approximation to the numerical functions. One can see that this remains true up to $\ell = m = 6$. However, we see that the procedure gives a rather unreliable result (even for small values of x) for the $\ell+m =$ odd modes. This illustrates that the standard resummation approach introduced in Ref. [176] can become highly inaccurate in some corners of the black-hole binary parameter space. As such, it should be replaced by something else that is more robust. One possibility is proposed in the next section.

9.3.3 Improved resummation

References [9, 4] presented an alternative factorization and resummation procedure based on the idea of first factoring out the orbital, spin-independent, contribution to the $\rho_{\ell m}$'s and then independently resumming, in various ways, the orbital and spin factors. The same procedure was implemented in similar ways for the odd-parity and even-parity modes. In the case of a *nonspinning* particle on circular orbits around a Kerr black hole, Refs. [4] illustrated that this procedure yields a remarkable analytical/numerical agreement between the $\rho_{\ell m}$'s (and fluxes) up to the LSO *also* for extremal values of the spin of the black hole (see e.g. Figs. 1 and 2) of [4]). In this Section we test this procedure on the even-parity modes. By contrast, we apply a different factorization, that only concerns the tail factor, to the odd-parity modes. Some of the resummation procedures of Refs. [4] applied to some of the odd-parity modes are instead discussed in Sec. 9.3.4 below.

$\ell + m$=even: orbital factorization

We implement the orbital factorization of the $\rho_{\ell m}$'s of [4] to all even-parity multipoles up to $\ell = 6$ included. Consistently with [4], the orbital factors are taken at 6PN order[1] and Padé resummed according to Table I of [4]. More precisely, we use the standard P^4_2 Padé for all the multipoles except the $(3,1)$ one, that is kept at 5PN with a P^3_2 Padé (the bold values in the table are not considerated). The only exception is the $(4,2)$ multipole, that in this paper is resummed with a P^4_2 Padé instead of a P^6_0 Taylor Series, since the difference between the two choices in this case is minimal. By resumming the spin-dependent factors by taking their inverse-Taylor representation, the resummed residual amplitudes finally read

$$\rho_{\ell m}(x,\sigma) = P^n_d[\rho^{\rm orb}_{\ell m}]\overline{\hat{\rho}^\sigma_{\ell m}}, \tag{9.12}$$

where $\hat{\rho}^\sigma_{\ell m} = T_n\left[1 + \rho^\sigma_{\ell m}/\rho^{\rm orb}_{\ell m}\right]$ and we defined $\overline{\hat{\rho}^\sigma_{\ell m}} \equiv (T_n[(\hat{\rho}^\sigma_{\ell m})^{-1}])^{-1}$. Finally, the even-parity waveform amplitudes read

$$|\hat{h}^{(0)}_{\ell m}(x,\sigma)| = \hat{E}\,|\hat{h}^{\rm tail}_{\ell m}|\,\left[\rho_{\ell m}(x,\sigma)\right]^\ell . \tag{9.13}$$

The analytical/numerical agreement, displayed in Fig. 9.5, is essentially comparable to the standard approach shown in Fig. 9.4 above.

[1] Though the $(3,1)$ mode is taken at 5PN only.

Table 9.1: Fractional differences between the resummed and the numerical $\hat{h}_{\ell m}$'s at the LSO shown in Fig. 9.5. The fractional difference is defined as $|\hat{h}^{\rm num} - \hat{h}^{\rm analyt}|/\hat{h}^{\rm num}$ computed at $x_{\rm LSO}$.

(ℓ, m)	$\Delta(x)\hat{h}(x)/\hat{h}\|_{x=x_{\rm LSO}}$ for $-0.9 \leq \sigma \leq +0.9$			
	-0.9	-0.5	$+0.5$	$+0.9$
$(2,2)$	8×10^{-4}	5×10^{-5}	0.0023	0.0024
$(2,1)$	4×10^{-5}	7×10^{-5}	5×10^{-5}	4×10^{-4}
$(3,3)$	0.0035	0.0012	2×10^{-4}	0.0056
$(3,2)$	9×10^{-4}	5×10^{-4}	0.0041	0.0086
$(3,1)$	0.0057	0.0018	0.0023	0.0091
$(4,4)$	0.0098	0.0046	0.0017	0.0085
$(4,3)$	0.0049	0.0029	0.013	0.029
$(4,2)$	0.0047	0.0013	0.0013	0.007
$(4,1)$	7×10^{-5}	3×10^{-5}	4×10^{-4}	0.001
$(5,5)$	0.014	0.0055	0.0072	0.042
$(5,4)$	0.012	0.0068	0.023	0.05
$(5,3)$	0.0029	6×10^{-4}	10^{-4}	0.0036
$(5,2)$	8×10^{-4}	5×10^{-4}	0.018	0.046
$(5,1)$	0.019	0.0067	0.0097	0.032
$(6,6)$	0.02	0.0087	0.013	0.078

$\ell + m =$**odd: factorizing the tail factor only**

For the odd-parity modes we suggest here to follow a new route: factor out *only* the tail factor spin part of the modulus, $|h^{\sigma}_{\ell m}|$, while keeping the orbital part $|h^{\rm orb}_{\ell m}|$ factorized as usual (9.10), i.e., with the orbital angular momentum $\hat{j}^{\rm orb}$ factored out. Note that for this particular calculation, we keep $\rho^{\rm orb}_{\ell m}$ at 5PN accuracy and in Taylor-expanded form. The rationale behind the choice of not factorizing the orbital angular momentum is that, in the presence of a spinning body, the source of the field is given by the sum of two separate pieces, one proportional to $\hat{j}^{\rm orb}$ and another one to σ. This is in particular the structure of the source of the Regge-Wheeler-Zerilli equation for a spinning test-body. It seems then less sound to factor out $\hat{j}^{\rm orb}$

also from the σ-dependent term. Starting from

$$|\hat{h}^{(1)}_{\ell m}(x,\sigma)| \equiv |\hat{h}^{\rm orb,(1)}_{\ell m}| + \sigma |\hat{h}^{\sigma,(1)}_{\ell m}|, \tag{9.14}$$

we factorize each term separately as

$$\rho^{\rm orb}_{\ell m} = T_n \left[\left(\frac{|\hat{h}^{\rm orb,(1)}_{\ell m}|}{|\hat{h}^{\rm tail}_{\ell m}| \hat{j}^{\rm orb}} \right)^{1/\ell} \right] , \tag{9.15}$$

$$|\tilde{h}|^{\sigma}_{\ell m} = T_n \left[\frac{|\hat{h}^{\sigma,(1)}_{\ell m}|}{|\hat{h}^{\rm tail}_{\ell m}|} \right] . \tag{9.16}$$

The resummed odd-parity waveform amplitudes finally read

$$|\hat{h}^{(1)}_{\ell m}(x,\sigma)| = |\hat{h}^{\rm tail}_{\ell m}| \left\{ \left(\rho^{\rm orb}_{\ell m}\right)^{\ell} \hat{j}^{\rm orb} + \sigma |\tilde{h}^{\sigma,(1)}_{\ell m}| \right\} . \tag{9.17}$$

It is important to stress that, for simplicity, we are here not using Padé approximants of the orbital $\rho^{\rm orb}_{\ell m}$ in Eq. (9.17). The analytical and numerical amplitudes are compared in Fig. 9.5. The agreement between the two is remarkable, and way better than the one obtained with the standard approach shown in Fig. 9.4 above. To better quantify the agreement, we list in Table 9.1 the fractional differences computed at $x_{\rm LSO}$. Although not shown in the table, we have also verified that an analogous quantitative agreement holds for $\sigma = \pm 0.99$,

9.3.4 Resumming the dominant m=odd modes consistently with the comparable-mass case.

Up to this point we have seen that there are different procedures for resumming the waveform amplitudes depending on the parity of $\ell + m$. Actually, detailed studies of the waveform amplitudes for two objects of masses (M_1, M_2) [9, 4] have illustrated that one should also carefully separate the analytic treatment depending on the parity of m only. In particular, Refs. [9, 4] introduced a special analytical treatment of the orbital-factorized spin-dependent functions $\hat{f}^S_{\ell m}$ when $\nu \equiv M_1 M_2/(M_1+M_2)^2 \neq 0$. More precisely, one shows that, when $\nu \neq 0$, these functions are naturally written as the sum of two separate Taylor expansions, one proportional to $X_{12} = X_1 - X_2 = \sqrt{1-4\nu}$ and the other to $\tilde{a}_{12} \equiv X1\chi_1 - X_2\chi_2$, where $X_i \equiv M_i/(M_1+M_2)$

and $\chi_i \equiv S_i/M_i^2$ are the dimensionless spins of the two objects. Each Taylor expansion can eventually be resummed taking its inverse-Taylor representation. This resummation of the m-odd waveform amplitudes has been recently incorporated in a new, multipolar, EOB waveform model. One of the remarkable features of this analytical choice is that the zero in the $(2,1)$ time-domain amplitude, that exists in certain regions of the parameter space, is quantitatively consistent with a similar feature found in state-of-the-art NR simulations. On top of this, Ref. [9], pointed out that the resummation procedure is reliable and accurate also in the special case of a nonspinning particle orbiting a spinning black hole.

In this section we investigate to which extent the m-odd multipoles resummation approach remains robust and stable also in the case of a spinning test-body on a Schwarzschild black hole. To do so, we focus on the same m-odd modes considered in the $\nu \neq 0$ case, $(2,1)$, $(3,3)$, $(3,1)$, $(4,3)$, $(4,1)$. In addition, each mode is truncated at the largest PN order that carries known ν-dependent corrections [2]. Consistently with Ref. [321], the m-odd waveform amplitudes are written as

$$|\hat{h}_{\ell m}| = \hat{j}^{\rm orb} |\hat{h}^{\rm tail}_{\ell m}| (P^m_n[\rho^{\rm orb}_{\ell m}])^\ell (1 + \hat{f}^\sigma_{\ell m}). \tag{9.18}$$

The Padé approximants of the orbital part $P^m_n[\rho^{\rm orb}_{\ell m}]$ are the same, adopted in Ref. [4], that is P^5_1 for $(2,1)$, P^3_2 for $(3,1)$, P^6_0 for $(5,5)$ and P^4_2 for $(3,2)$, $(4,3)$ and $(4,1)$. On the other hand, the spin-dependent terms $\hat{f}^\sigma_{\ell m}$ are given by

$$\hat{f}^\sigma_{21} = \overline{f^{\sigma_{(0)}}_{21}} + \frac{3}{2}\sigma x^{1/2} \overline{f^{\sigma_{(1)}}_{21}}, \tag{9.19}$$

$$\hat{f}^\sigma_{33} = \overline{f^{\sigma_{(0)}}_{33}} + \frac{1}{4}\sigma x^{3/2} f^{\sigma_{(1)}}_{33}, \tag{9.20}$$

$$\hat{f}^\sigma_{31} = \overline{f^{\sigma_{(0)}}_{31}} + \frac{9}{4}\sigma x^{3/2} f^{\sigma_{(1)}}_{31}, \tag{9.21}$$

$$\hat{f}^\sigma_{43} = f^{\sigma_{(0)}}_{43} + \frac{5}{4}\sigma x^{1/2} f^{\sigma_{(1)}}_{43}, \tag{9.22}$$

$$\hat{f}^\sigma_{41} = f^{\sigma_{(0)}}_{41} + \frac{5}{4}\sigma x^{1/2} f^{\sigma_{(1)}}_{41}. \tag{9.23}$$

Following Ref. [4], the overbar indicates that each term is resummed using

[2] Even if we have more spinning-particle terms, we cannot use them since we cannot consistently split each PN order in the two separate series.

its inverse-Taylor representation. The function written above explicitly read

$$\overline{f_{21}^{\sigma_{(0)}}} = \left(1 + \frac{13}{84}x^{3/2}\sigma + \frac{14705}{7056}x^{5/2}\sigma\right)^{-1}, \tag{9.24}$$

$$\overline{f_{21}^{\sigma_{(1)}}} = \left(1 + \frac{349}{252}x + \frac{65969}{31752}x^{2}\right)^{-1}, \tag{9.25}$$

$$\overline{f_{33}^{\sigma_{(0)}}} = \left(1 + \frac{7}{4}x^{3/2}\sigma + \frac{211}{60}x^{5/2}\sigma\right)^{-1}, \tag{9.26}$$

$$f_{33}^{\sigma_{(1)}} = 1 + \frac{169}{15}x, \tag{9.27}$$

$$\overline{f_{31}^{\sigma_{(0)}}} = \left(1 - \frac{1}{4}x^{3/2}\sigma + \frac{13}{36}x^{5/2}\sigma\right)^{-1}, \tag{9.28}$$

$$f_{31}^{\sigma_{(1)}} = 1 - \frac{1}{9}x, \tag{9.29}$$

$$f_{43}^{\sigma_{(0)}} = \left(1 - \frac{5}{4}\right)x^{1/2}\sigma, \tag{9.30}$$

$$f_{43}^{\sigma_{(1)}} = 1, \tag{9.31}$$

$$f_{41}^{\sigma_{(0)}} = \left(1 - \frac{5}{4}\right)x^{1/2}\sigma, \tag{9.32}$$

$$f_{41}^{\sigma_{(1)}} = 1\ . \tag{9.33}$$

The analytical $|\hat{h}_{\ell m}|$ are compared to the numerical ones in Fig. 9.6. The most interesting result displayed in the figure is that both the $(2,1)$ and $(3,3)$ analytical amplitudes deliver a reasonably accurate representation of the numerical data up to the LSO, although this is not as good as the tail-factorized case discussed in Fig. 9.5. Note however that in that case we were using spin information truncated at 5.5PN accuracy. Thus, to produce a meaningful comparison we need to redo the calculation of Fig. 9.5 truncating the $\ell = 2$, $m = 1$ mode at 2.5PN. By contrast, the orbital $\rho_{21}^{\rm orb}$ function is kept at 5PN accuracy and in Taylor-expanded form. This new comparison is displayed in Fig. 9.7. Interestingly, despite the reduced PN information, the analytical/numerical agreement is visibly *better* than the one displayed in the top-left panel of Fig. 9.6. We also performed the same analysis for the $\ell = 4$ modes. Although we found an improvement, the truncation at 1.5PN of the spin information is not sufficient to provide a good agreement up to the LSO location. In conclusion, the result of Fig. 9.7 gives further support

to the need of exploring the performance of the tail-only factorization also for comparable mass binaries.

9.4 Interpreting the spinning-body limit using the EOB dynamics

In the main text we have considered $-1 \leq \sigma \leq 1$. Due to the definition of σ in Eq. (9.3) we can also write

$$\sigma = \frac{\mu}{M}\frac{s}{\mu^2}. \tag{9.34}$$

This parameter, per se, can be thus meaningful also for the equal-mass case, with the understanding that the MPD approach (or the Hamiltonian approach) plus the solution of the Teukolsky equations for the fluxes can only deliver some of the contributions at leading-order in the mass ratio. More precisely, the value $\sigma = \pm 1$ can be interpreted as the case of an extremally spinning black hole, $s/\mu^2 = \pm 1$ in an equal-mass binary, $\mu/M = 1$. Although in this case the perturbative approach we are using is expected to be meaningless, in practice it is useful to compute, and test numerically, some of the terms that enter the complete PN expansion.

The euristic comparable-mass limit suggested by Eq. (9.34) can be put on a more solid ground starting from the complete EOB Hamiltonian for a two-body system with masses (m_1, m_2), with the convention that $m_1 \geq m_2$. We also refer the reader to Sec. III of Ref. [313] for complementary information. The complete EOB Hamiltonian is given by Eq. (4.19) and (4.24). The spin-orbit sector is given by Eq. (4.25). For the case where only the secondary, m_2 is spinning ($S_1 = 0$), the spin-orbit Hamiltonian becomes

$$\hat{H}^{\rm eff}_{\rm SO} = p_\varphi \left\{ G_{S^*} \frac{1}{(m_1+m_2)^2}\frac{m_1}{m_2} S_2 + G_S \frac{S_2}{(m_1+m_2)^2} \right\}. \tag{9.35}$$

After introducing powers of m_2 so to explicitly have a dimensionless spin variable $\chi_2 \equiv S_2/m_2^2$ one obtains

$$\hat{H}_{\rm SO} = p_\varphi \left\{ G_{S_*} \nu \frac{S_2}{m_2^2} + G_S \frac{1}{4}(1-\sqrt{1-4\nu})^2 \frac{S_2}{m_2^2} \right\}. \tag{9.36}$$

The extreme-mass-ratio limit is now defined by the condition $\nu \to 0$. In this limit, one sees that the term proportionalt to G_S is suppressed with respect

to the one proportional to G_{S_*} because of the different ν dependence. In the $\nu \to 0$ limit one finally has that the spin-orbit sector of the *real* spin-orbit Hamiltonian describing a spinning test-body orbiting a Schwarzschild black hole is given by

$$\hat{H}_{\rm SO} = p_\phi G_{S_*} \nu \frac{S_2}{m_2^2}, \tag{9.37}$$

where G_{S_*} is known analytically in closed, non-PN expanded, form [335, 276, 336]. One then defines the dimensionless spin σ as

$$\sigma \equiv \nu \frac{S_2}{m_2^2} = \nu \chi_2. \tag{9.38}$$

Thus, since $-1 \leq \chi_2 \leq +1$, and $0 \leq \nu \leq 1/4$, one concludes, from the EOB (and thus PN) perspective, that $-1/4 \leq \sigma \leq 1/4$. The usual limit $-1 \leq \sigma \leq 1$ is obtained writing σ as

$$\sigma \equiv \frac{m_1 m_2}{(m_1+m_2)^2} \frac{S_2}{m_2^2} \tag{9.39}$$

and then addtionally expanding the symmetric mass ratio in powers of the mass ratio $m_2/m_1 \approx \mu/M \ll 1$.

9.5 Spinning particle on Schwarzschild background: PN-expanded multipolar energy fluxes

9.5.1 Newton-normalized PN fluxes

The PN-expanded fluxes up to $\ell = 7$ are presented below. For completeness and future reference we also keep all the nonspinning terms. All of the series given below can be found digitally in the `PostNewtonianSelfForce` package in the Black Hole Perturbation Toolkit (`bhptoolkit.org`).

$$
\begin{aligned}
\hat{F}_{22} = 1 &- \frac{107}{21}x + \frac{4784}{1323}x^2 + \left(4\pi - \frac{4\sigma}{3}\right)x^{3/2} + \left(-\frac{428\pi}{21} + \frac{208\sigma}{63}\right)x^{5/2} \\
&+ \left(-\frac{16\pi\sigma}{3} - \frac{856\log(x)}{105} + \frac{16\pi^2}{3} - \frac{1712\gamma}{105} + \frac{99210071}{1091475} - \frac{3424\log(2)}{105}\right)x^3 \\
&+ \left(\frac{19136\pi}{1323} + \frac{49844\sigma}{3969}\right)x^{7/2} \\
&+ \left(\frac{832\pi\sigma}{63} + \frac{91592\log(x)}{2205} - \frac{1712\pi^2}{63} + \frac{183184\gamma}{2205} - \frac{27956920577}{81265275} + \frac{366368\log(2)}{2205}\right)x^4 \\
&+ \left[\sigma\left(\frac{3424\log(x)}{315} - \frac{64\pi^2}{9} + \frac{6848\gamma}{315} - \frac{46815716}{363825} + \frac{13696\log(2)}{315}\right)\right. \\
&\left.+ \pi\left(-\frac{3424\log(x)}{105} - \frac{6848\gamma}{105} + \frac{396840284}{1091475} - \frac{13696\log(2)}{105}\right)\right]x^{9/2} \\
&\left(\frac{199376\pi\sigma}{3969} - \frac{4095104\log(x)}{138915} + \frac{76544\pi^2}{3969} - \frac{8190208\gamma}{138915}\right. \\
&\left.+ \frac{187037845924}{6257426175} - \frac{16380416\log(2)}{138915}\right)x^5 \\
&+ \left[\sigma\left(-\frac{178048\log(x)}{6615} + \frac{3328\pi^2}{189} - \frac{356096\gamma}{6615} + \frac{123621054016}{893918025} - \frac{712192\log(2)}{6615}\right)\right. \\
&\left.+ \pi\left(\frac{366368\log(x)}{2205} + \frac{732736\gamma}{2205} - \frac{111827682308}{81265275} + \frac{1465472\log(2)}{2205}\right)\right]x^{11/2}
\end{aligned}
\tag{9.40}
$$

$$\begin{aligned}
\hat{F}_{21} &= 1 + 3\sigma x^{1/2} - \frac{17}{14}x + \left(2\pi - \frac{367\sigma}{28}\right)x^{3/2} \\
&+ \left(6\pi\sigma - \frac{2215}{7056}\right)x^2 + \left(-\frac{17\pi}{7} + \frac{14383\sigma}{1764}\right)x^{5/2} \\
&\left(-\frac{367\pi\sigma}{14} - \frac{214\log(x)}{105} + \frac{4\pi^2}{3} - \frac{428\gamma}{105} + \frac{15707221}{727650} - \frac{428\log(2)}{105}\right)x^3 \\
&+ \left[\sigma\left(-\frac{214\log(x)}{35} + 4\pi^2 - \frac{428\gamma}{35} + \frac{3602793}{53900} - \frac{428\log(2)}{35}\right) - \frac{2215\pi}{3528}\right]x^{7/2} \\
&\left(\frac{14383\pi\sigma}{882} + \frac{1819\log(x)}{735} - \frac{34\pi^2}{21} + \frac{3638\gamma}{735} - \frac{6435768121}{1589187600} + \frac{3638\log(2)}{735}\right)x^4 \\
&+ \left[\sigma\left(\frac{39269\log(x)}{1470} - \frac{367\pi^2}{21} + \frac{39269\gamma}{735} - \frac{344524801603}{1589187600} + \frac{39269\log(2)}{735}\right) + \right. \\
&\left.\pi\left(-\frac{428\log(x)}{105} - \frac{856\gamma}{105} + \frac{15707221}{363825} - \frac{856\log(2)}{105}\right)\right]x^{9/2} \\
&+ \left[\pi\sigma\left(-\frac{428\log(x)}{35} - \frac{856\gamma}{35} + \frac{3602793}{26950} - \frac{856\log(2)}{35}\right)\right. \\
&\left.+ \frac{47401\log(x)}{74088} - \frac{2215\pi^2}{5292} + \frac{47401\gamma}{37044} + \frac{113031526373}{11124313200} + \frac{47401\log(2)}{37044}\right]x^5 \\
&+ \left[\sigma\left(-\frac{1538981\log(x)}{92610} + \frac{14383\pi^2}{1323} - \frac{1538981\gamma}{46305} + \frac{19389238559}{1112431320} - \frac{1538981\log(2)}{46305}\right)\right. \\
&\left.+ \pi\left(\frac{3638\log(x)}{735} + \frac{7276\gamma}{735} - \frac{6435768121}{794593800} + \frac{7276\log(2)}{735}\right)\right]x^{11/2} \quad (9.41)
\end{aligned}$$

$$\begin{aligned}
\hat{F}_{31} = 1 &- \frac{16}{3}x + (2\pi + 5\sigma)x^{3/2} + \frac{437}{33}x^2 + \left(-\frac{32\pi}{3} - \frac{269\sigma}{9}\right)x^{5/2} \\
&+ \left(10\pi\sigma - \frac{26\log(x)}{21} + \frac{4\pi^2}{3} - \frac{52\gamma}{21} - \frac{1137077}{6306300} - \frac{52\log(2)}{21}\right)x^3 \\
&+ \left(\frac{35839\sigma}{594} + \frac{874\pi}{33}\right)x^{7/2} \\
&+ \left(-\frac{538\pi\sigma}{9} + \frac{416\log(x)}{63} - \frac{64\pi^2}{9} + \frac{832\gamma}{63} - \frac{38943317051}{624323700} + \frac{832\log(2)}{63}\right)x^4 \\
&+ \left[\sigma\left(-\frac{130\log(x)}{21} + \frac{20\pi^2}{3} - \frac{260\gamma}{21} + \frac{358636417}{11351340} - \frac{260\log(2)}{21}\right)\right. \\
&\left.+ \pi\left(-\frac{52\log(x)}{21} - \frac{104\gamma}{21} - \frac{1137077}{3153150} - \frac{104\log(2)}{21}\right)\right]x^{9/2} \\
&+ \left(\frac{35839\pi\sigma}{297} - \frac{11362\log(x)}{693} + \frac{1748\pi^2}{99} - \frac{22724\gamma}{693} + \frac{806092611133}{4548644100} - \frac{22724\log(2)}{693}\right)x^5 \\
&+ \left[\sigma\left(\frac{6994\log(x)}{189} - \frac{1076\pi^2}{27} + \frac{13988\gamma}{189} - \frac{21000333479}{48024900} + \frac{13988\log(2)}{189}\right)\right. \\
&\left.+ \pi\left(\frac{832\log(x)}{63} + \frac{1664\gamma}{63} - \frac{38943317051}{312161850} + \frac{1664\log(2)}{63}\right)\right]x^{11/2} \quad (9.42)
\end{aligned}$$

$$
\begin{aligned}
\hat{F}_{32} = 1 &+ 4\sigma x^{1/2} - \frac{193}{45}x + \left(4\pi - \frac{1316\sigma}{45}\right)x^{3/2} + \left(16\pi\sigma + \frac{86111}{22275}\right)x^2 \\
&+ \left(\frac{92498\sigma}{1485} - \frac{772\pi}{45}\right)x^{5/2} \\
&+ \left(-\frac{5264\pi\sigma}{45} - \frac{104\log(x)}{21} + \frac{16\pi^2}{3} - \frac{208\gamma}{21} + \frac{960188809}{14189175} - \frac{416\log(2)}{21}\right)x^3 \\
&+ \left[\sigma\left(-\frac{416\log(x)}{21} + \frac{64\pi^2}{3} - \frac{832\gamma}{21} + \frac{3402129202}{14189175} - \frac{1664\log(2)}{21}\right) + \frac{344444\pi}{22275}\right]x^{7/2} \\
&+ \left(\frac{369992\pi\sigma}{1485} + \frac{20072\log(x)}{945} - \frac{3088\pi^2}{135} + \frac{40144\gamma}{945} - \frac{185796488947}{780404625} + \frac{80288\log(2)}{945}\right)x^4 \\
&+ \left[\sigma\left(\frac{19552\log(x)}{135} - \frac{21056\pi^2}{135} + \frac{39104\gamma}{135} - \frac{65791391422}{37162125} + \frac{78208\log(2)}{135}\right)\right. \\
&\left. + \pi\left(-\frac{416\log(x)}{21} - \frac{832\gamma}{21} + \frac{3840755236}{14189175} - \frac{1664\log(2)}{21}\right)\right]x^{9/2} \\
&+ \left[\pi\sigma\left(-\frac{1664\log(x)}{21} - \frac{3328\gamma}{21} + \frac{13608516808}{14189175} - \frac{6656\log(2)}{21}\right)\right. \\
&\left. - \frac{8955544\log(x)}{467775} + \frac{1377776\pi^2}{66825} - \frac{17911088\gamma}{467775} + \frac{3746014222817}{27554286375} - \frac{35822176\log(2)}{467775}\right]x^5 \\
&+ \left[\sigma\left(-\frac{1374256\log(x)}{4455} + \frac{1479968\pi^2}{4455} - \frac{2748512\gamma}{4455}\right.\right. \\
&\left.\left. + \frac{367939750486582}{119401907625} - \frac{5497024\log(2)}{4455}\right)\right. \\
&\left. + \pi\left(\frac{80288\log(x)}{945} + \frac{160576\gamma}{945} - \frac{743185955788}{780404625} + \frac{321152\log(2)}{945}\right)\right]x^{11/2}
\end{aligned}
\tag{9.43}
$$

$$
\begin{aligned}
\hat{F}_{33} = {} & 1 - 8x + (6\pi - 3\sigma)x^{3/2} + \frac{1003}{55}x^2 + \left(-48\pi + \frac{103\sigma}{5}\right)x^{5/2} \\
& + \left(-18\pi\sigma - \frac{78\log(x)}{7} + 12\pi^2 - \frac{156\gamma}{7} + \frac{103033003}{700700} - \frac{156\log(3)}{7} - \frac{156\log(2)}{7}\right)x^3 \\
& + \left(\frac{6018\pi}{55} - \frac{587\sigma}{22}\right)x^{7/2} \\
& + \left(\frac{618\pi\sigma}{5} + \frac{624\log(x)}{7} - 96\pi^2 + \frac{1248\gamma}{7}\right. \\
& \left. - \frac{8538500227}{7707700} + \frac{1248\log(3)}{7} + \frac{1248\log(2)}{7}\right)x^4 \\
& + \left[\sigma\left(\frac{234\log(x)}{7} - 36\pi^2 + \frac{468\gamma}{7} - \frac{350580603}{700700} + \frac{468\log(3)}{7} + \frac{468\log(2)}{7}\right)\right. \\
& \left. + \pi\left(-\frac{468\log(x)}{7} - \frac{936\gamma}{7} + \frac{309099009}{350350} - \frac{936\log(3)}{7} - \frac{936\log(2)}{7}\right)\right]x^{9/2} \\
& + \left(-\frac{1761\pi\sigma}{11} - \frac{78234\log(x)}{385} + \frac{12036\pi^2}{55}\right. \\
& \left. - \frac{156468\gamma}{385} + \frac{1337469126533}{655154500} - \frac{156468\log(3)}{385} - \frac{156468\log(2)}{385}\right)x^5 \\
& + \left[\sigma\left(-\frac{8034\log(x)}{35} + \frac{1236\pi^2}{5} - \frac{16068\gamma}{35}\right.\right. \\
& \left.\left. + \frac{107744864609}{38538500} - \frac{16068\log(3)}{35} - \frac{16068\log(2)}{35}\right)\right. \\
& \left. + \pi\left(\frac{3744\log(x)}{7} + \frac{7488\gamma}{7} - \frac{25615500681}{3853850} + \frac{7488\log(3)}{7} + \frac{7488\log(2)}{7}\right)\right]x^{11/2}
\end{aligned}
\tag{9.44}
$$

$$
\begin{aligned}
\hat{F}_{41} = {} & 1 + 5\sigma x^{1/2} - \frac{202}{33}x + \left(2\pi - \frac{1432\sigma}{33}\right)x^{3/2} \\
& + \left(10\pi\sigma + \frac{7478267}{495495}\right)x^2 + \left(\frac{24367582\sigma}{165165} - \frac{404\pi}{33}\right)x^{5/2} \\
& + \left(-\frac{2864\pi\sigma}{33} - \frac{3142\log(x)}{3465} + \frac{4\pi^2}{3} - \frac{6284\gamma}{3465} - \frac{1847674847}{624323700} - \frac{6284\log(2)}{3465}\right)x^3 \\
& + \left[\sigma\left(-\frac{3142\log(x)}{693} + \frac{20\pi^2}{3} - \frac{6284\gamma}{693} - \frac{22314389969}{124864740} - \frac{6284\log(2)}{693}\right)\right. \\
& \left. + \frac{14956534\pi}{495495}\right]x^{7/2} \\
& + \left(\frac{48735164\pi\sigma}{165165} + \frac{634684\log(x)}{114345} - \frac{808\pi^2}{99} + \frac{1269368\gamma}{114345}\right. \\
& \left. - \frac{6373046696371}{91063854882} + \frac{1269368\log(2)}{114345}\right)x^4 \\
& + \left[\sigma\left(\frac{4499344\log(x)}{114345} - \frac{5728\pi^2}{99} + \frac{8998688\gamma}{114345} - \frac{831081952398961}{2276596372050} + \frac{8998688\log(2)}{114345}\right)\right. \\
& \left. + \pi\left(-\frac{6284\log(x)}{3465} - \frac{12568\gamma}{3465} - \frac{1847674847}{312161850} - \frac{12568\log(2)}{3465}\right)\right]x^{9/2} \\
& + \left[\pi\sigma\left(-\frac{6284\log(x)}{693} - \frac{12568\gamma}{693} - \frac{22314389969}{62432370} - \frac{12568\log(2)}{693}\right)\right. \\
& - \frac{23496714914\log(x)}{1716890175} + \frac{29913068\pi^2}{1486485} - \frac{46993429828\gamma}{1716890175} \\
& \left. + \frac{348496299110928742}{1921534899409125} - \frac{46993429828\log(2)}{1716890175}\right]x^5 \\
& + \left[\sigma\left(-\frac{76562942644\log(x)}{572296725} + \frac{97470328\pi^2}{495495} - \frac{153125885288\gamma}{572296725}\right.\right. \\
& \left.\left. + \frac{116422245347531790853}{66613209846183000} - \frac{153125885288\log(2)}{572296725}\right)\right. \\
& \left. + \pi\left(\frac{1269368\log(x)}{114345} + \frac{2538736\gamma}{114345} - \frac{6373046696371}{45531927441} + \frac{2538736\log(2)}{114345}\right)\right]x^{11/2}
\end{aligned}
\tag{9.45}
$$

$$
\begin{aligned}
\hat{F}_{42} = 1 &- \frac{437}{55}x + \left(4\pi + \frac{24\sigma}{5}\right)x^{3/2} + \frac{7199152}{275275}x^2 + \left(-\frac{11504\sigma}{275} - \frac{1748\pi}{55}\right)x^{5/2} \\
&+ \left(\frac{96\pi\sigma}{5} - \frac{12568\log(x)}{3465} + \frac{16\pi^2}{3} - \frac{25136\gamma}{3465} + \frac{9729776708}{780404625} - \frac{50272\log(2)}{3465}\right)x^3 \\
&+ \left(\frac{187271932\sigma}{1376375} + \frac{28796608\pi}{275275}\right)x^{7/2} \\
&+ \left(-\frac{46016\pi\sigma}{275} + \frac{5492216\log(x)}{190575} - \frac{6992\pi^2}{165} + \frac{10984432\gamma}{190575}\right. \\
&\left. - \frac{3621954717305192}{9485818216875} + \frac{21968864\log(2)}{190575}\right)x^4 \\
&+ \left[\sigma\left(-\frac{100544\log(x)}{5775} + \frac{128\pi^2}{5} - \frac{201088\gamma}{5775} + \frac{18538641488}{260134875} - \frac{402176\log(2)}{5775}\right)\right. \\
&\left. + \pi\left(-\frac{50272\log(x)}{3465} - \frac{100544\gamma}{3465} + \frac{38919106832}{780404625} - \frac{201088\log(2)}{3465}\right)\right]x^{9/2} \\
&+ \left[\frac{749087728\pi\sigma}{1376375} - \frac{90478942336\log(x)}{953827875} + \frac{115186432\pi^2}{825825} - \frac{180957884672\gamma}{953827875}\right. \\
&\left. + \frac{17759046991305753284}{13877752051288125} - \frac{361915769344\log(2)}{953827875}\right]x^5 \\
&+ \left[\sigma\left(\frac{144582272\log(x)}{952875} - \frac{184064\pi^2}{825} + \frac{289164544\gamma}{952875}\right.\right. \\
&\left.\left. - \frac{20087730595257316}{9485818216875} + \frac{578329088\log(2)}{952875}\right)\right. \\
&\left. + \pi\left(\frac{21968864\log(x)}{190575} + \frac{43937728\gamma}{190575} - \frac{14487818869220768}{9485818216875} + \frac{87875456\log(2)}{190575}\right)\right]x^{11/2}
\end{aligned}
\tag{9.46}
$$

$$
\begin{aligned}
\hat{F}_{43} = {} & 1 + 5\sigma x^{1/2} - \frac{78}{11}x + \left(6\pi - \frac{556\sigma}{11}\right)x^{3/2} + \left(30\pi\sigma + \frac{850587}{55055}\right)x^2 \\
& + \left(\frac{9743466\sigma}{55055} - \frac{468\pi}{11}\right)x^{5/2} \\
& + \left(-\frac{3336\pi\sigma}{11} - \frac{3142\log(x)}{385} + 12\pi^2 - \frac{6284\gamma}{385}\right. \\
& \left. + \frac{8495997793}{69369300} - \frac{6284\log(3)}{385} - \frac{6284\log(2)}{385}\right)x^3 \\
& + \left[\sigma\left(-\frac{3142\log(x)}{77} + 60\pi^2 - \frac{6284\gamma}{77} + \frac{5881588639}{13873860} - \frac{6284\log(3)}{77}\right.\right. \\
& \left.\left. - \frac{6284\log(2)}{77}\right) + \frac{5103522\pi}{55055}\right]x^{7/2} \\
& + \left(\frac{58460796\pi\sigma}{55055} + \frac{245076\log(x)}{4235} - \frac{936\pi^2}{11} + \frac{490152\gamma}{4235}\right. \\
& \left. - \frac{23942096774363}{28106128050} + \frac{490152\log(3)}{4235} + \frac{490152\log(2)}{4235}\right)x^4 \\
& + \left[\sigma\left(\frac{1746952\log(x)}{4235} - \frac{6672\pi^2}{11} + \frac{3493904\gamma}{4235} - \frac{520642287162973}{84318384150}\right.\right. \\
& \left. + \frac{3493904\log(3)}{4235} + \frac{3493904\log(2)}{4235}\right) \\
& \left. + \pi\left(-\frac{18852\log(x)}{385} - \frac{37704\gamma}{385} + \frac{8495997793}{11561550} - \frac{37704\log(3)}{385} - \frac{37704\log(2)}{385}\right)\right]x^{9/2} \\
& + \left[\pi\sigma\left(-\frac{18852\log(x)}{77} - \frac{37704\gamma}{77} + \frac{5881588639}{2312310} - \frac{37704\log(3)}{77} - \frac{37704\log(2)}{77}\right)\right. \\
& - \frac{2672544354\log(x)}{21196175} + \frac{10207044\pi^2}{55055} - \frac{5345088708\gamma}{21196175} + \frac{164198437359891442}{102798163342875} \\
& \left. - \frac{5345088708\log(3)}{21196175} - \frac{5345088708\log(2)}{21196175}\right]x^5 \\
& + \left[\sigma\left(-\frac{30613970172\log(x)}{21196175} + \frac{116921592\pi^2}{55055} - \frac{61227940344\gamma}{21196175}\right.\right. \\
& \left. + \frac{16347298755161569813}{822385306743000} - \frac{61227940344\log(3)}{21196175} - \frac{61227940344\log(2)}{21196175}\right) \\
& \left. + \pi\left(\frac{1470456\log(x)}{4235} + \frac{2940912\gamma}{4235} - \frac{23942096774363}{4684354675}\right.\right. \\
& \left.\left. + \frac{2940912\log(3)}{4235} + \frac{2940912\log(2)}{4235}\right)\right]x^{11/2} \qquad (9.47)
\end{aligned}
$$

$$
\begin{aligned}
\hat{F}_{44} = 1 &- \frac{593}{55}x + \left(8\pi - \frac{24\sigma}{5}\right)x^{3/2} + \frac{2187772}{55055}x^2 + \left(\frac{13236\sigma}{275} - \frac{4744\pi}{55}\right)x^{5/2} \\
&+ \left(-\frac{192\pi\sigma}{5} - \frac{50272\log(x)}{3465} + \frac{64\pi^2}{3} - \frac{100544\gamma}{3465} + \frac{143850002468}{780404625} - \frac{100544\log(2)}{1155}\right)x^3 \\
&+ \left(\frac{17502176\pi}{55055} - \frac{205853488\sigma}{1376375}\right)x^{7/2} \\
&+ \left(\frac{105888\pi\sigma}{275} + \frac{29811296\log(x)}{190575} - \frac{37952\pi^2}{165} + \frac{59622592\gamma}{190575}\right. \\
&\left. - \frac{461493531002948}{193588126875} + \frac{59622592\log(2)}{63525}\right)x^4 \\
&+ \left[\sigma\left(\frac{402176\log(x)}{5775} - \frac{512\pi^2}{5} + \frac{804352\gamma}{5775} - \frac{269452289384}{260134875} + \frac{804352\log(2)}{1925}\right)\right. \\
&\left. + \pi\left(-\frac{402176\log(x)}{3465} - \frac{804352\gamma}{3465} + \frac{1150800019744}{780404625} - \frac{804352\log(2)}{1155}\right)\right]x^{9/2} \\
&+ \left(-\frac{1646827904\pi\sigma}{1376375} - \frac{109983673984\log(x)}{190765575} + \frac{140017408\pi^2}{165165} - \frac{219967347968\gamma}{190765575}\right. \\
&\left. + \frac{110876948362954366588}{13877752051288125} - \frac{219967347968\log(2)}{63588525}\right)x^5 \\
&+ \left[\sigma\left(-\frac{221800064\log(x)}{317625} + \frac{282368\pi^2}{275} - \frac{443600128\gamma}{317625}\right.\right. \\
&\left.\left. + \frac{33963566444720392}{3161939405625} - \frac{443600128\log(2)}{105875}\right)\right. \\
&\left. + \pi\left(\frac{238490368\log(x)}{190575} + \frac{476980736\gamma}{190575} - \frac{3691948248023584}{193588126875} + \frac{476980736\log(2)}{63525}\right)\right]x^{11/2}
\end{aligned}
\tag{9.48}
$$

$$\begin{aligned}\hat{F}_{51} = 1 &- \frac{358}{39}x + \left(2\pi + \frac{28\sigma}{3}\right)x^{3/2} + \frac{290803}{7605}x^2 + \left(-\frac{54892\sigma}{585} - \frac{716\pi}{39}\right)x^{5/2} \\ &+ \left(\frac{56\pi\sigma}{3} - \frac{1546\log(x)}{2145} + \frac{4\pi^2}{3} - \frac{3092\gamma}{2145} - \frac{70678556867}{884458575} - \frac{3092\log(2)}{2145}\right)x^3 \\ &+ \left(\frac{1818512\sigma}{4563} + \frac{581606\pi}{7605}\right)x^{7/2} \\ &+ \left(-\frac{109784\pi\sigma}{585} + \frac{553468\log(x)}{83655} - \frac{1432\pi^2}{117} + \frac{1106936\gamma}{83655}\right. \\ &\left. + \frac{30751133534746}{946665494775} + \frac{1106936\log(2)}{83655}\right)x^4 \\ &+ \left[\sigma\left(-\frac{43288\log(x)}{6435} + \frac{112\pi^2}{9} - \frac{86576\gamma}{6435} - \frac{4023624605818}{4927697775} - \frac{86576\log(2)}{6435}\right)\right. \\ &\left. + \pi\left(-\frac{3092\log(x)}{2145} - \frac{6184\gamma}{2145} - \frac{141357113734}{884458575} - \frac{6184\log(2)}{2145}\right)\right]x^{9/2} \\ &+ \left(\frac{3637024\pi\sigma}{4563} - \frac{449581438\log(x)}{16312725} + \frac{1163212\pi^2}{22815} - \frac{899162876\gamma}{16312725}\right. \\ &\left. + \frac{71365115368720132}{237342563332875} - \frac{899162876\log(2)}{16312725}\right)x^5 \\ &+ \left[\sigma\left(\frac{84863032\log(x)}{1254825} - \frac{219568\pi^2}{1755} + \frac{169726064\gamma}{1254825} + \frac{21412695417260944}{127799841794625}\right.\right. \\ &\left. + \frac{169726064\log(2)}{1254825}\right) \\ &\left. + \pi\left(\frac{1106936\log(x)}{83655} + \frac{2213872\gamma}{83655} + \frac{61502267069492}{946665494775} + \frac{2213872\log(2)}{83655}\right)\right]x^{11/2}\end{aligned} \tag{9.49}$$

$$
\begin{aligned}
\hat{F}_{52} = {} & 1 + 6\sigma x^{1/2} - \frac{3911}{455}x + \left(4\pi - \frac{30458\sigma}{455}\right)x^{3/2} \\
& + \left(24\pi\sigma + \frac{18688127}{621075}\right)x^2 + \left(\frac{5403626\sigma}{17745} - \frac{15644\pi}{455}\right)x^{5/2} \\
& + \left(-\frac{121832\pi\sigma}{455} - \frac{6184\log(x)}{2145} + \frac{16\pi^2}{3} - \frac{12368\gamma}{2145} - \frac{3565375256}{2299592295} - \frac{24736\log(2)}{2145}\right)x^3 \\
& + \left[\sigma\left(-\frac{12368\log(x)}{715} + 32\pi^2 - \frac{24736\gamma}{715}\right.\right. \\
& \left.\left. - \frac{225656637512}{547521975} - \frac{49472\log(2)}{715}\right) + \frac{74752508\pi}{621075}\right]x^{7/2} \\
& + \left(\frac{21614504\pi\sigma}{17745} + \frac{24185624\log(x)}{975975} - \frac{62576\pi^2}{1365} + \frac{48371248\gamma}{975975}\right. \\
& \left. - \frac{37120039834250764}{99399876951375} + \frac{96742496\log(2)}{975975}\right)x^4 \\
& + \left[\sigma\left(\frac{188352272\log(x)}{975975} - \frac{487328\pi^2}{1365} + \frac{376704544\gamma}{975975}\right.\right. \\
& \left. - \frac{237272216817464212}{99399876951375} + \frac{753409088\log(2)}{975975}\right) \\
& \left. + \pi\left(-\frac{24736\log(x)}{2145} - \frac{49472\gamma}{2145} - \frac{14261501024}{2299592295} - \frac{98944\log(2)}{2145}\right)\right]x^{9/2} \\
& + \left[\pi\sigma\left(-\frac{49472\log(x)}{715} - \frac{98944\gamma}{715} - \frac{902626550048}{547521975} - \frac{197888\log(2)}{715}\right)\right. \\
& - \frac{115567377368\log(x)}{1332205875} \\
& \left. + \frac{299010032\pi^2}{1863225} - \frac{231134754736\gamma}{1332205875} + \frac{2962795414725501668}{2153664000613125} - \frac{462269509472\log(2)}{1332205875}\right]x^5 \\
& + \left[\sigma\left(-\frac{33416023184\log(x)}{38063025} + \frac{86458016\pi^2}{53235} - \frac{66832046368\gamma}{38063025} + \frac{209759979290346544}{15202334121975}\right.\right. \\
& \left. - \frac{133664092736\log(2)}{38063025}\right) + \pi\left(\frac{96742496\log(x)}{975975} + \frac{193484992\gamma}{975975}\right. \\
& \left.\left. - \frac{148480159337003056}{99399876951375} + \frac{386969984\log(2)}{975975}\right)\right]x^{11/2} \qquad (9.50)
\end{aligned}
$$

$$
\begin{aligned}
\hat{F}_{53} = 1 &- \frac{138}{13}x + (6\pi + 4\sigma)x^{3/2} + \frac{823943}{17745}x^2 + \left(-\frac{20844\sigma}{455} - \frac{828\pi}{13}\right)x^{5/2} \\
&+ \left(24\pi\sigma - \frac{4638\log(x)}{715} + 12\pi^2 - \frac{9276\gamma}{715} + \frac{4687046283}{425850425} - \frac{9276\log(3)}{715} - \frac{9276\log(2)}{715}\right)x^3 \\
&+ \left(\frac{3663136\sigma}{17745} + \frac{1647886\pi}{5915}\right)x^{7/2} \\
&+ \left(-\frac{125064\pi\sigma}{455} + \frac{640044\log(x)}{9295} - \frac{1656\pi^2}{13} + \frac{1280088\gamma}{9295}\right. \\
&\left. - \frac{28614963763754}{27047585565} + \frac{1280088\log(3)}{9295} + \frac{1280088\log(2)}{9295}\right)x^4 \\
&+ \left[\sigma\left(-\frac{18552\log(x)}{715} + 48\pi^2 - \frac{37104\gamma}{715} + \frac{4975310434}{425850425} - \frac{37104\log(3)}{715} - \frac{37104\log(2)}{715}\right)\right. \\
&\left. + \pi\left(-\frac{27828\log(x)}{715} - \frac{55656\gamma}{715} + \frac{28122277698}{425850425} - \frac{55656\log(3)}{715} - \frac{55656\log(2)}{715}\right)\right]x^{9/2} \\
&+ \left(\frac{7326272\pi\sigma}{5915} - \frac{1273815878\log(x)}{4229225} + \frac{3295772\pi^2}{5915} - \frac{2547631756\gamma}{4229225}\right. \\
&\left. + \frac{2096233487612758084}{430732800122625} - \frac{2547631756\log(3)}{4229225} - \frac{2547631756\log(2)}{4229225}\right)x^5 \\
&+ \left[\sigma\left(\frac{96674472\log(x)}{325325} - \frac{250128\pi^2}{455} + \frac{193348944\gamma}{325325}\right.\right. \\
&\left.\left. - \frac{51479627364210592}{11044430772375} + \frac{193348944\log(3)}{325325} + \frac{193348944\log(2)}{325325}\right)\right. \\
&\left. + \pi\left(\frac{3840264\log(x)}{9295} + \frac{7680528\gamma}{9295} - \frac{57229927527508}{9015861855}\right.\right. \\
&\left.\left. + \frac{7680528\log(3)}{9295} + \frac{7680528\log(2)}{9295}\right)\right]x^{11/2} \qquad (9.51)
\end{aligned}
$$

$$
\begin{aligned}
\hat{F}_{54} = {} & 1 + 6\sigma x^{1/2} - \frac{4451}{455}x + \left(8\pi - \frac{35018\sigma}{455}\right)x^{3/2} \\
& + \left(48\pi\sigma + \frac{20952707}{621075}\right)x^2 + \left(\frac{6596234\sigma}{17745} - \frac{35608\pi}{455}\right)x^{5/2} \\
& + \Bigg(-\frac{280144\pi\sigma}{455} - \frac{24736\log(x)}{2145} + \frac{64\pi^2}{3} - \frac{49472\gamma}{2145} \\
& + \frac{1919077079981}{11497961475} - \frac{49472\log(2)}{715}\Bigg)x^3 \\
& + \Bigg[\sigma\Bigg(-\frac{49472\log(x)}{715} + 128\pi^2 - \frac{98944\gamma}{715} \\
& + \frac{1797855496834}{3832653825} - \frac{296832\log(2)}{715}\Bigg) + \frac{167621656\pi}{621075}\Bigg]x^{7/2} \\
& + \Bigg(\frac{52769872\pi\sigma}{17745} + \frac{110099936\log(x)}{975975} - \frac{284864\pi^2}{1365} + \frac{220199872\gamma}{975975} \\
& - \frac{193747438701841261}{99399876951375} + \frac{220199872\log(2)}{325325}\Bigg)x^4 \\
& + \Bigg[\sigma\Bigg(\frac{866205248\log(x)}{975975} - \frac{2241152\pi^2}{1365} + \frac{1732410496\gamma}{975975} \\
& - \frac{1489526042743253458}{99399876951375} + \frac{1732410496\log(2)}{325325}\Bigg) \\
& + \pi\left(-\frac{197888\log(x)}{2145} - \frac{395776\gamma}{2145} + \frac{15352616639848}{11497961475} - \frac{395776\log(2)}{715}\right)\Bigg]x^{9/2} \\
& + \Bigg[\pi\sigma\left(-\frac{395776\log(x)}{715} - \frac{791552\gamma}{715} + \frac{14382843974672}{3832653825} - \frac{2374656\log(2)}{715}\right) \\
& - \frac{518286160352\log(x)}{1332205875} + \frac{1340973248\pi^2}{1863225} - \frac{1036572320704\gamma}{1332205875} \\
& + \frac{13465702596429393907}{2153664000613125} - \frac{1036572320704\log(2)}{444068625}\Bigg]x^5 \\
& + \Bigg[\sigma\Bigg(-\frac{163164444224\log(x)}{38063025} + \frac{422158976\pi^2}{53235} - \frac{326328888448\gamma}{38063025} \\
& + \frac{92163273485725245586}{1292198400367875} - \frac{326328888448\log(2)}{12687675}\Bigg) \\
& + \pi\Bigg(\frac{880799488\log(x)}{975975} + \frac{1761598976\gamma}{975975} \\
& - \frac{1549979509614730088}{99399876951375} + \frac{1761598976\log(2)}{325325}\Bigg)\Bigg]x^{11/2} \qquad (9.52)
\end{aligned}
$$

$$\begin{aligned}\hat{F}_{55} &= 1 - \frac{526}{39}x + \left(10\pi - \frac{20\sigma}{3}\right)x^{3/2} + \frac{722993}{10647}x^2 + \left(\frac{70324\sigma}{819} - \frac{5260\pi}{39}\right)x^{5/2} \\ &+ \left(-\frac{200\pi\sigma}{3} - \frac{7730\log(x)}{429} + \frac{100\pi^2}{3} - \frac{15460\gamma}{429} + \frac{6552129589}{35378343}\right. \\ &\left. - \frac{15460\log(5)}{429} - \frac{15460\log(2)}{429}\right)x^3 + \left(\frac{7229930\pi}{10647} - \frac{12610048\sigma}{31941}\right)x^{7/2} \\ &+ \left(\frac{703240\pi\sigma}{819} + \frac{4065980\log(x)}{16731} - \frac{52600\pi^2}{117} + \frac{8131960\gamma}{16731}\right. \\ &\left. - \frac{477890910720122}{113599859373} + \frac{8131960\log(5)}{16731} + \frac{8131960\log(2)}{16731}\right)x^4 \\ &+ \left[\sigma\left(\frac{154600\log(x)}{1287} - \frac{2000\pi^2}{9} + \frac{309200\gamma}{1287}\right.\right. \\ &\left. - \frac{302007543634}{197107911} + \frac{309200\log(5)}{1287} + \frac{309200\log(2)}{1287}\right) \\ &\left. + \pi\left(-\frac{77300\log(x)}{429} - \frac{154600\gamma}{429} + \frac{65521295890}{35378343} - \frac{154600\log(5)}{429} - \frac{154600\log(2)}{429}\right)\right]x^{9/2} \\ &+ \left(-\frac{126100480\pi\sigma}{31941} - \frac{5588735890\log(x)}{4567563} + \frac{72299300\pi^2}{31941} - \frac{11177471780\gamma}{4567563}\right. \\ &\left. + \frac{1907636757769320236}{93038284826487} - \frac{11177471780\log(5)}{4567563} - \frac{11177471780\log(2)}{4567563}\right)x^5 \\ &+ \left[\sigma\left(-\frac{543604520\log(x)}{351351} + \frac{7032400\pi^2}{2457} - \frac{1087209040\gamma}{351351}\right.\right. \\ &\left. + \frac{195345738616319360}{7156791140499} - \frac{1087209040\log(5)}{351351} - \frac{1087209040\log(2)}{351351}\right) \\ &+ \pi\left(\frac{40659800\log(x)}{16731} + \frac{81319600\gamma}{16731} - \frac{4778909107201220}{113599859373} + \frac{81319600\log(5)}{16731}\right. \\ &\left.\left. + \frac{81319600\log(2)}{16731}\right)\right]x^{11/2} \end{aligned} \tag{9.53}$$

$$\begin{aligned}\hat{F}_{61} &= 1+7\sigma x^{1/2}-\frac{125}{12}x+\left(2\pi-\frac{2147\sigma}{24}\right)x^{3/2}+\left(14\pi\sigma+\frac{180021689}{3769920}\right)x^2\\
&+\left(\frac{78074681\sigma}{157080}-\frac{125\pi}{6}\right)x^{5/2}\\
&+\left(-\frac{2147\pi\sigma}{12}-\frac{1802\log(x)}{3003}+\frac{4\pi^2}{3}-\frac{3604\gamma}{3003}-\frac{24598440919576}{218461268025}-\frac{3604\log(2)}{3003}\right)x^3\\
&+\left[\sigma\left(-\frac{1802\log(x)}{429}+\frac{28\pi^2}{3}-\frac{3604\gamma}{429}\right.\right.\\
&\left.\left.-\frac{186251710369819}{124835010300}-\frac{3604\log(2)}{429}\right)+\frac{180021689\pi}{1884960}\right]x^{7/2}\\
&+\left(\frac{78074681\pi\sigma}{78540}+\frac{112625\log(x)}{18018}-\frac{125\pi^2}{9}+\frac{112625\gamma}{9009}\right.\\
&\left.+\frac{707729869694513}{8643122167680}+\frac{112625\log(2)}{9009}\right)x^4\\
&+\left[\sigma\left(\frac{1934447\log(x)}{36036}-\frac{2147\pi^2}{18}+\frac{1934447\gamma}{18018}+\frac{39883212208000103}{19014868768896}+\frac{1934447\log(2)}{18018}\right)\right.\\
&\left.+\pi\left(-\frac{3604\log(x)}{3003}-\frac{7208\gamma}{3003}-\frac{49196881839152}{218461268025}-\frac{7208\log(2)}{3003}\right)\right]x^{9/2}\\
&+\left[\pi\sigma\left(-\frac{3604\log(x)}{429}-\frac{7208\gamma}{429}-\frac{186251710369819}{62417505150}-\frac{7208\log(2)}{429}\right)\right.\\
&\left.-\frac{9541149517\log(x)}{332972640}+\frac{180021689\pi^2}{2827440}-\frac{9541149517\gamma}{166486320}+\frac{1443709506661055325611}{4457029313344608000}\right.\\
&\left.-\frac{9541149517\log(2)}{166486320}\right]x^5\\
&+\left[\sigma\left(-\frac{4137958093\log(x)}{13873860}+\frac{78074681\pi^2}{117810}-\frac{4137958093\gamma}{6936930}\right.\right.\\
&\left.\left.+\frac{4849567930889021794613}{3157062430285764000}-\frac{4137958093\log(2)}{6936930}\right)\right.\\
&\left.+\pi\left(\frac{112625\log(x)}{9009}+\frac{225250\gamma}{9009}+\frac{707729869694513}{4321561083840}+\frac{225250\log(2)}{9009}\right)\right]x^{11/2}\end{aligned}\tag{9.54}$$

$$
\begin{aligned}
\hat{F}_{62} = 1 &- \frac{81}{7}x + \left(4\pi + \frac{68\sigma}{7}\right)x^{3/2} + \frac{8221522}{137445}x^2 + \left(-\frac{88714\sigma}{735} - \frac{324\pi}{7}\right)x^{5/2} \\
&+ \left(\frac{272\pi\sigma}{7} - \frac{7208\log(x)}{3003} + \frac{16\pi^2}{3} - \frac{14416\gamma}{3003} - \frac{161484749374217}{1223383100940} - \frac{28832\log(2)}{3003}\right)x^3 \\
&+ \left(\frac{7295384\sigma}{11319} + \frac{32886088\pi}{137445}\right)x^{7/2} \\
&+ \left(-\frac{354856\pi\sigma}{735} + \frac{194616\log(x)}{7007} - \frac{432\pi^2}{7}\right. \\
&\left. + \frac{389232\gamma}{7007} - \frac{138951395311225087}{727912945059300} + \frac{778464\log(2)}{7007}\right)x^4 \\
&+ \left[\sigma\left(-\frac{490144\log(x)}{21021} + \frac{1088\pi^2}{21} - \frac{980288\gamma}{21021} - \frac{2244361964428541}{1529228876175} - \frac{1960576\log(2)}{21021}\right)\right. \\
&\left. + \pi\left(-\frac{28832\log(x)}{3003} - \frac{57664\gamma}{3003} - \frac{161484749374217}{305845775235} - \frac{115328\log(2)}{3003}\right)\right]x^{9/2} \\
&+ \left[\frac{29181536\pi\sigma}{11319} - \frac{3485925328\log(x)}{24279255} + \frac{131544352\pi^2}{412335} - \frac{6971850656\gamma}{24279255}\right. \\
&\left. + \frac{69009387572205137581}{30693662516667150} - \frac{13943701312\log(2)}{24279255}\right]x^5 \\
&+ \left[\sigma\left(\frac{639450512\log(x)}{2207205} - \frac{1419424\pi^2}{2205} + \frac{1278901024\gamma}{2207205}\right.\right. \\
&\left.\left. - \frac{51564217241617}{25040004990} + \frac{2557802048\log(2)}{2207205}\right)\right. \\
&\left. + \pi\left(\frac{778464\log(x)}{7007} + \frac{1556928\gamma}{7007} - \frac{138951395311225087}{181978236264825} + \frac{3113856\log(2)}{7007}\right)\right]x^{11/2}
\end{aligned}
\tag{9.55}
$$

$$\hat{F}_{63} = 1 + 7\sigma x^{1/2} - \frac{133}{21}x + \left(6\pi - \frac{2299\sigma}{24}\right)x^{3/2} + \left(42\pi\sigma + \frac{191999369}{3769920}\right)x^2$$
$$+ \left(\frac{86132401\sigma}{157080} - \frac{133\pi}{2}\right)x^{5/2} + \left(-\frac{2299\pi\sigma}{4} - \frac{5406\log(x)}{1001} + 12\pi^2 - \frac{10812\gamma}{1001}\right.$$
$$\left. - \frac{8318725110259}{582563381400} - \frac{10812\log(3)}{1001} - \frac{10812\log(2)}{1001}\right)x^3$$
$$+ \left[\sigma\left(-\frac{5406\log(x)}{143} + 84\pi^2 - \frac{10812\gamma}{143} - \frac{6435219971227}{6935278350}\right.\right.$$
$$\left.\left. - \frac{10812\log(3)}{143} - \frac{10812\log(2)}{143}\right) + \frac{191999369\pi}{628320}\right]x^{7/2}$$
$$\left(\frac{86132401\pi\sigma}{26180} + \frac{17119\log(x)}{286} - 133\pi^2 + \frac{17119\gamma}{143} - \frac{158600290311609547}{158457239740800}\right.$$
$$\left. + \frac{17119\log(3)}{143} + \frac{17119\log(2)}{143}\right)x^4$$
$$+ \left[\sigma\left(\frac{188309\log(x)}{364} - \frac{2299\pi^2}{2} + \frac{188309\gamma}{182} - \frac{59571165214052209}{8339854723200}\right.\right.$$
$$\left. + \frac{188309\log(3)}{182} + \frac{188309\log(2)}{182}\right)$$
$$\left. + \pi\left(-\frac{32436\log(x)}{1001} - \frac{64872\gamma}{1001} - \frac{8318725110259}{97093896900} - \frac{64872\log(3)}{1001} - \frac{64872\log(2)}{1001}\right)\right]x^{9/2}$$
$$+ \left[\pi\sigma\left(-\frac{32436\log(x)}{143} - \frac{64872\gamma}{143} - \frac{6435219971227}{1155879725} - \frac{64872\log(3)}{143} - \frac{64872\log(2)}{143}\right)\right.$$
$$- \frac{10175966557\log(x)}{36996960} + \frac{191999369\pi^2}{314160} - \frac{10175966557\gamma}{18498480} + \frac{42300157953961348695307}{8418833147428704000}$$
$$\left. - \frac{10175966557\log(3)}{18498480} - \frac{10175966557\log(2)}{18498480}\right]x^5$$
$$+ \left[\sigma\left(-\frac{4565017253\log(x)}{1541540} + \frac{86132401\pi^2}{13090} - \frac{4565017253\gamma}{770770} + \frac{6208405960475571319531}{116928238158732000}\right.\right.$$
$$\left. - \frac{4565017253\log(3)}{770770} - \frac{4565017253\log(2)}{770770}\right)$$
$$+ \pi\left(\frac{51357\log(x)}{143} + \frac{102714\gamma}{143} - \frac{158600290311609547}{26409539956800}\right.$$
$$\left.\left. + \frac{102714\log(3)}{143} + \frac{102714\log(2)}{143}\right)\right]x^{11/2} \qquad (9.56)$$

$$
\begin{aligned}
\hat{F}_{64} = 1 &- \frac{93}{7}x + \left(8\pi + \frac{20\sigma}{7}\right)x^{3/2} + \frac{2028464}{27489}x^2 + \left(-\frac{5996\sigma}{147} - \frac{744\pi}{7}\right)x^{5/2} \\
&+ \left(\frac{160\pi\sigma}{7} - \frac{28832\log(x)}{3003} + \frac{64\pi^2}{3} - \frac{57664\gamma}{3003} - \frac{7473136770797}{305845775235} - \frac{57664\log(2)}{1001}\right)x^3 \\
&+ \left(\frac{45679300\sigma}{192423} + \frac{16227712\pi}{27489}\right)x^{7/2} \\
&+ \left(-\frac{47968\pi\sigma}{147} + \frac{893792\log(x)}{7007} - \frac{1984\pi^2}{7} + \frac{1787584\gamma}{7007}\right. \\
&\left. - \frac{389504245584812167}{181978236264825} + \frac{5362752\log(2)}{7007}\right)x^4 \\
&+ \left[\sigma\left(-\frac{576640\log(x)}{21021} + \frac{1280\pi^2}{21} - \frac{1153280\gamma}{21021} - \frac{9680228679908}{61169155047} - \frac{1153280\log(2)}{7007}\right)\right. \\
&\left. + \pi\left(-\frac{230656\log(x)}{3003} - \frac{461312\gamma}{3003} - \frac{59785094166376}{305845775235} - \frac{461312\log(2)}{1001}\right)\right]x^{9/2} \\
&+ \left(\frac{365434400\pi\sigma}{192423} - \frac{3440274944\log(x)}{4855851} + \frac{129821696\pi^2}{82467} - \frac{6880549888\gamma}{4855851}\right. \\
&\left. + \frac{200984978531762355824}{15346831258333575} - \frac{6880549888\log(2)}{1618617}\right)x^5 \\
&+ \left[\sigma\left(\frac{172876672\log(x)}{441441} - \frac{383744\pi^2}{441} + \frac{345753344\gamma}{441441} - \frac{79666062343153756}{12131882417655}\right.\right. \\
&\left.\left. + \frac{345753344\log(2)}{147147}\right)\right. \\
&\left. + \pi\left(\frac{7150336\log(x)}{7007} + \frac{14300672\gamma}{7007} - \frac{3116033964678497336}{181978236264825} + \frac{42902016\log(2)}{7007}\right)\right]x^{11/2}
\end{aligned}
\tag{9.57}
$$

$$\hat{F}_{65} = 1 + 7\sigma x^{1/2} - \frac{149}{12}x + \left(10\pi - \frac{2603\sigma}{24}\right)x^{3/2} + \left(70\pi\sigma + \frac{44119381}{753984}\right)x^2$$
$$+ \left(\frac{20910829\sigma}{31416} - \frac{745\pi}{6}\right)x^{5/2} + \left(-\frac{13015\pi\sigma}{12} - \frac{45050\log(x)}{3003}\right.$$
$$\left. + \frac{100\pi^2}{3} - \frac{90100\gamma}{3003} + \frac{12846599702749}{69907605768} - \frac{90100\log(5)}{3003} - \frac{90100\log(2)}{3003}\right)x^3$$
$$+ \left[\sigma\left(-\frac{45050\log(x)}{429} + \frac{700\pi^2}{3} - \frac{90100\gamma}{429} + \frac{198692130113}{1248350103}\right.\right.$$
$$\left.\left. - \frac{90100\log(5)}{429} - \frac{90100\log(2)}{429}\right) + \frac{220596905\pi}{376992}\right]x^{7/2} + \left(\frac{104554145\pi\sigma}{15708} + \frac{3356225\log(x)}{18018}\right.$$
$$\left. - \frac{3725\pi^2}{9} + \frac{3356225\gamma}{9009} - \frac{9734336137180063}{2716409824128} + \frac{3356225\log(5)}{9009} + \frac{3356225\log(2)}{9009}\right)x^4$$
$$+ \left[\sigma\left(\frac{58632575\log(x)}{36036} - \frac{65075\pi^2}{18} + \frac{58632575\gamma}{18018} - \frac{562883137821630721}{19014868768896}\right.\right.$$
$$\left.\left. + \frac{58632575\log(5)}{18018} + \frac{58632575\log(2)}{18018}\right)\right.$$
$$\left. + \pi\left(-\frac{450500\log(x)}{3003} - \frac{901000\gamma}{3003} + \frac{64232998513745}{34953802884}\right.\right.$$
$$\left.\left. - \frac{901000\log(5)}{3003} - \frac{901000\log(2)}{3003}\right)\right]x^{9/2}$$
$$+ \left[\pi\sigma\left(-\frac{450500\log(x)}{429} - \frac{901000\gamma}{429} + \frac{1986921301130}{1248350103}\right.\right.$$
$$\left.\left. - \frac{901000\log(5)}{429} - \frac{901000\log(2)}{429}\right) - \frac{58458179825\log(x)}{66594528}\right.$$
$$\left. + \frac{1102984525\pi^2}{565488} - \frac{58458179825\gamma}{33297264} + \frac{10003750718547616854575}{606155986614866688}\right.$$
$$\left. - \frac{58458179825\log(5)}{33297264} - \frac{58458179825\log(2)}{33297264}\right]x^5$$
$$+ \left[\sigma\left(-\frac{27706848425\log(x)}{2774772} + \frac{522770725\pi^2}{23562}\right.\right.$$
$$\left.\left. - \frac{27706848425\gamma}{1387386} + \frac{4801663674782405880901}{25256499442286112} - \frac{27706848425\log(5)}{1387386}\right.\right.$$
$$\left.\left. - \frac{27706848425\log(2)}{1387386}\right) + \pi\left(\frac{16781125\log(x)}{9009} + \frac{33562250\gamma}{9009} - \frac{48671680685900315}{1358204912064}\right.\right.$$
$$\left.\left. + \frac{33562250\log(5)}{9009} + \frac{33562250\log(2)}{9009}\right)\right]x^{11/2} \qquad (9.58)$$

$$\begin{aligned}\hat{F}_{66} &= 1 - \frac{113}{7}x + \left(12\pi - \frac{60\sigma}{7}\right)x^{3/2} + \frac{134290}{1309}x^2 + \left(\frac{6554\sigma}{49} - \frac{1356\pi}{7}\right)x^{5/2} \\ &+ \left(-\frac{720\pi\sigma}{7} - \frac{21624\log(x)}{1001} + 48\pi^2 - \frac{43248\gamma}{1001} + \frac{18044070358903}{135931455660}\right. \\ &\left. - \frac{43248\log(3)}{1001} - \frac{86496\log(2)}{1001}\right)x^3 + \left(\frac{1611480\pi}{1309} - \frac{51347864\sigma}{64141}\right)x^{7/2} \\ &+ \left(\frac{78648\pi\sigma}{49} + \frac{2443512\log(x)}{7007} - \frac{5424\pi^2}{7} + \frac{4887024\gamma}{7007}\right. \\ &\left. - \frac{530645101377839167}{80879216117700} + \frac{4887024\log(3)}{7007} + \frac{9774048\log(2)}{7007}\right)x^4 \\ &+ \left[\sigma\left(\frac{1297440\log(x)}{7007} - \frac{2880\pi^2}{7} + \frac{2594880\gamma}{7007} - \frac{3745245301351}{2265524261}\right.\right. \\ &\left. + \frac{2594880\log(3)}{7007} + \frac{5189760\log(2)}{7007}\right) \\ &+ \pi\left(-\frac{259488\log(x)}{1001} - \frac{518976\gamma}{1001} + \frac{18044070358903}{11327621305}\right. \\ &\left.\left. - \frac{518976\log(3)}{1001} - \frac{1037952\log(2)}{1001}\right)\right]x^{9/2} \\ &+ \left[-\frac{616174368\pi\sigma}{64141} - \frac{13139760\log(x)}{5929} + \frac{6445920\pi^2}{1309} - \frac{26279520\gamma}{5929}\right. \\ &\left. + \frac{656585911003784857}{15431705639350} - \frac{26279520\log(3)}{5929} - \frac{52559040\log(2)}{5929}\right]x^5 \\ &+ \left[\sigma\left(-\frac{141723696\log(x)}{49049} + \frac{314592\pi^2}{49} - \frac{283447392\gamma}{49049}\right.\right. \\ &\left. + \frac{450585773170908589}{8087921611770} - \frac{283447392\log(3)}{49049} - \frac{566894784\log(2)}{49049}\right) \\ &+ \pi\left(\frac{29322144\log(x)}{7007} + \frac{58644288\gamma}{7007} - \frac{530645101377839167}{6739934676475}\right. \\ &\left.\left. + \frac{58644288\log(3)}{7007} + \frac{117288576\log(2)}{7007}\right)\right]x^{11/2} \end{aligned} \tag{9.59}$$

$$\hat{F}_{71} = 1 - \frac{223}{17}x + \left(2\pi + \frac{27\sigma}{2}\right)x^{3/2} + \frac{39565047}{499681}x^2 + \left(-\frac{90301\sigma}{476} - \frac{446\pi}{17}\right)x^{5/2}$$
$$+ \left(27\pi\sigma - \frac{11948\log(x)}{23205} + \frac{4\pi^2}{3} - \frac{23896\gamma}{23205} - \frac{900375181510781}{3241170812880} - \frac{23896\log(2)}{23205}\right)x^3$$
$$+ \left(\frac{9523157277\sigma}{7994896} + \frac{79130094\pi}{499681}\right)x^{7/2}$$
$$+ \left(-\frac{90301\pi\sigma}{238} + \frac{2664404\log(x)}{394485} - \frac{892\pi^2}{51} + \frac{5328808\gamma}{394485} + \frac{272158571374959377057}{481573159377710400}\right.$$
$$\left. + \frac{5328808\log(2)}{394485}\right)x^4$$
$$+ \left[\sigma\left(-\frac{53766\log(x)}{7735} + 18\pi^2 - \frac{107532\gamma}{7735} - \frac{204661562601577}{48017345376} - \frac{107532\log(2)}{7735}\right)\right.$$
$$\left. + \pi\left(-\frac{23896\log(x)}{23205} - \frac{47792\gamma}{23205} - \frac{900375181510781}{1620585406440} - \frac{47792\log(2)}{23205}\right)\right]x^{9/2}$$
$$+ \left(\frac{9523157277\pi\sigma}{3997448} - \frac{157574393852\log(x)}{3865032535} + \frac{52753396\pi^2}{499681} - \frac{315148787704\gamma}{3865032535}\right.$$
$$\left. - \frac{235741151452316569687157}{620828064631098324000} - \frac{315148787704\log(2)}{3865032535}\right)x^5$$
$$+ \left[\sigma\left(\frac{269729087\log(x)}{2761395} - \frac{90301\pi^2}{357} + \frac{539458174\gamma}{2761395} + \frac{29113672696708980165059}{3371012115643972800}\right.\right.$$
$$\left.\left. + \frac{539458174\log(2)}{2761395}\right)\right.$$
$$\left. + \pi\left(\frac{5328808\log(x)}{394485} + \frac{10657616\gamma}{394485} + \frac{272158571374959377057}{240786579688855200} + \frac{10657616\log(2)}{394485}\right)\right]x^{11/2} \tag{9.60}$$

$$\begin{aligned}\hat{F}_{72} = {} & 1 + 8\sigma x^{1/2} - \frac{13619}{1071}x + \left(4\pi - \frac{129320}{1071}\right)x^{3/2} + \left(32\pi\sigma + \frac{20288614207}{283319127}\right)x^2 \\ & + \left(\frac{3613352872\sigma}{4497129} - \frac{54476\pi}{1071}\right)x^{5/2} \\ & + \left(-\frac{517280\pi\sigma}{1071} - \frac{47792\log(x)}{23205} + \frac{16\pi^2}{3} - \frac{95584\gamma}{23205}\right. \\ & \left. - \frac{469120756856}{2500903405} - \frac{191168\log(2)}{23205}\right)x^3 \\ & + \left[\sigma\left(-\frac{382336\log(x)}{23205} + \frac{128\pi^2}{3} - \frac{764672\gamma}{23205} - \frac{110775486737506}{40514635161}\right.\right. \\ & \left.\left. - \frac{1529344\log(2)}{23205}\right) + \frac{81154456828\pi}{283319127}\right]x^{7/2} \\ & + \left(\frac{14453411488\pi\sigma}{4497129} + \frac{650879248\log(x)}{24852555} - \frac{217904\pi^2}{3213} + \frac{1301758496\gamma}{24852555}\right. \\ & \left. - \frac{5565093875687384492}{67721225537490525} + \frac{2603516992\log(2)}{24852555}\right)x^4 \\ & + \left[\sigma\left(\frac{1236092288\log(x)}{4970511} - \frac{2069120\pi^2}{3213} + \frac{2472184576\gamma}{4970511}\right.\right. \\ & \left. + \frac{153689215630344417094}{67721225537490525} + \frac{4944369152\log(2)}{4970511}\right) \\ & \left. + \pi\left(-\frac{191168\log(x)}{23205} - \frac{382336\gamma}{23205} - \frac{1876483027424}{2500903405} - \frac{764672\log(2)}{23205}\right)\right]x^{9/2} \\ & + \left[\pi\sigma\left(-\frac{1529344\log(x)}{23205} - \frac{3058688\gamma}{23205} - \frac{443101946950024}{40514635161} - \frac{6117376\log(2)}{23205}\right)\right. \\ & - \frac{969633450180944\log(x)}{6574420342035} + \frac{324617827312\pi^2}{849957381} - \frac{1939266900361888\gamma}{6574420342035} \\ & \left. + \frac{26804007745506705831944402}{11000297270182273428375} - \frac{3878533800723776\log(2)}{6574420342035}\right]x^5 \\ & + \left[\sigma\left(-\frac{172689360458624\log(x)}{104355878445} + \frac{57813645952\pi^2}{13491387} - \frac{345378720917248\gamma}{104355878445}\right.\right. \\ & \left. + \frac{11711346651047295703868141}{523823679532489210875} - \frac{690757441834496\log(2)}{104355878445}\right) \\ & + \pi\left(\frac{2603516992\log(x)}{24852555} + \frac{5207033984\gamma}{24852555} - \frac{22260375502749537968}{67721225537490525}\right. \\ & \left.\left. + \frac{10414067968\log(2)}{24852555}\right)\right]x^{11/2} \end{aligned} \tag{9.61}$$

$$\hat{F}_{73} = 1 - \frac{239}{17}x + \left(6\pi + \frac{19}{2}\right)x^{3/2} + \frac{131958599}{1499043}x^2 + \left(-\frac{201767\sigma}{1428} - \frac{1434\pi}{17}\right)x^{5/2}$$
$$+ \left(57\pi\sigma - \frac{35844\log(x)}{7735} + 12\pi^2 - \frac{71688\gamma}{7735} - \frac{78766297655021}{360130090320}\right.$$
$$\left. - \frac{71688\log(3)}{7735} - \frac{71688\log(2)}{7735}\right)x^3 + \left(\frac{1154491277\sigma}{1262352} + \frac{263917198\pi}{499681}\right)x^{7/2}$$
$$+ \left(-\frac{201767\pi\sigma}{238} + \frac{8566716\log(x)}{131495} - \frac{2868\pi^2}{17} + \frac{17133432\gamma}{131495} - \frac{79572683467659663}{121333625441600}\right.$$
$$\left. + \frac{17133432\log(3)}{131495} + \frac{17133432\log(2)}{131495}\right)x^4 + \left[\sigma\left(-\frac{340518\log(x)}{7735} + 114\pi^2 - \frac{681036\gamma}{7735}\right.\right.$$
$$\left. - \frac{344989969285499}{144052036128} - \frac{681036\log(3)}{7735} - \frac{681036\log(2)}{7735}\right)$$
$$+ \pi\left(-\frac{215064\log(x)}{7735} - \frac{430128\gamma}{7735} - \frac{78766297655021}{60021681720}\right.$$
$$\left.\left. - \frac{430128\log(3)}{7735} - \frac{430128\log(2)}{7735}\right)\right]x^{9/2}$$
$$+ \left(\frac{1154491277\pi\sigma}{210392} - \frac{1576641340852\log(x)}{3865032535} + \frac{527834396\pi^2}{499681} - \frac{3153282681704\gamma}{3865032535}\right.$$
$$\left. + \frac{4609993098496362230956667}{620828064631098324000} - \frac{3153282681704\log(3)}{3865032535} - \frac{3153282681704\log(2)}{3865032535}\right)x^5$$
$$+ \left[\sigma\left(\frac{602678029\log(x)}{920465} - \frac{201767\pi^2}{119} + \frac{1205356058\gamma}{920465} - \frac{20019219044238975311}{3112661233281600}\right.\right.$$
$$\left. + \frac{1205356058\log(3)}{920465} + \frac{1205356058\log(2)}{920465}\right)$$
$$+ \pi\left(\frac{51400296\log(x)}{131495} + \frac{102800592\gamma}{131495} - \frac{238718050402978989}{60666812720800} + \frac{102800592\log(3)}{131495}\right.$$
$$\left.\left. + \frac{102800592\log(2)}{131495}\right)\right]x^{11/2} \qquad (9.62)$$

$$\hat{F}_{74} = 1 + 8\sigma x^{1/2} - \frac{14543}{1071}x + \left(8\pi - \frac{139064\sigma}{1071}\right)x^{3/2}$$
$$+ \left(64\pi\sigma + \frac{22046072455}{283319127}\right)x^2 + \left(\frac{4041717718\sigma}{4497129} - \frac{116344\pi}{1071}\right)x^{5/2}$$
$$+ \left(-\frac{1112512\pi\sigma}{1071} - \frac{191168\log(x)}{23205} + \frac{64\pi^2}{3} - \frac{382336\gamma}{23205}\right.$$
$$\left. - \frac{3897310139143}{67524391935} - \frac{382336\log(2)}{7735}\right)x^3$$
$$+ \left[\sigma\left(-\frac{1529344\log(x)}{23205} + \frac{512\pi^2}{3} - \frac{3058688\gamma}{23205} - \frac{79565406120562}{40514635161}\right.\right.$$
$$\left.\left. - \frac{3058688\log(2)}{7735}\right) + \frac{176368579640\pi}{283319127}\right]x^{7/2}$$
$$+ \left(\frac{32333741744\pi\sigma}{4497129} + \frac{2780156224\log(x)}{24852555} - \frac{930752\pi^2}{3213} + \frac{5560312448\gamma}{24852555}\right.$$
$$\left. - \frac{19342673411957889689}{9674460791070075} + \frac{5560312448\log(2)}{8284185}\right)x^4$$
$$+ \left[\sigma\left(\frac{26584586752\log(x)}{24852555} - \frac{8900096\pi^2}{3213} + \frac{53169173504\gamma}{24852555}\right.\right.$$
$$\left. - \frac{1052245252615435125134}{67721225537490525} + \frac{53169173504\log(2)}{8284185}\right)$$
$$\left.+ \pi\left(-\frac{1529344\log(x)}{23205} - \frac{3058688\gamma}{23205} - \frac{31178481113144}{67524391935} - \frac{3058688\log(2)}{7735}\right)\right]x^{9/2}$$
$$+ \left[\pi\sigma\left(-\frac{12234752\log(x)}{23205} - \frac{24469504\gamma}{23205} - \frac{636523248964496}{40514635161} - \frac{24469504\log(2)}{7735}\right)\right.$$
$$- \frac{842900715815488\log(x)}{1314884068407} + \frac{1410948637120\pi^2}{849957381} - \frac{1685801431630976\gamma}{1314884068407}$$
$$\left. + \frac{14386207722530860607103 4793}{11000297270182273428375} - \frac{1685801431630976\log(2)}{438294689469}\right]x^5$$
$$+ \left[\sigma\left(-\frac{772647092714624\log(x)}{104355878445} + \frac{258669933952\pi^2}{13491387} - \frac{1545294185429248\gamma}{104355878445}\right.\right.$$
$$\left. + \frac{769629802386104927041343 54}{523823679532489210875} - \frac{1545294185429248\log(2)}{34785292815}\right)$$
$$+ \pi\left(\frac{22241249792\log(x)}{24852555} + \frac{44482499584\gamma}{24852555}\right.$$
$$\left.\left. - \frac{154741387295663117512}{9674460791070075} + \frac{44482499584\log(2)}{8284185}\right)\right]x^{11/2} \qquad (9.63)$$

$$\hat{F}_{75} = 1 - \frac{271}{17}x + \left(10\pi + \frac{3\sigma}{2}\right)x^{3/2} + \frac{161912939}{1499043}x^2 + \left(-\frac{37511\sigma}{1428} - \frac{2710\pi}{17}\right)x^{5/2}$$
$$+ \left(15\pi\sigma - \frac{59740\log(x)}{4641} + \frac{100\pi^2}{3} - \frac{119480\gamma}{4641} - \frac{72708277771009}{648234162576}\right.$$
$$\left. - \frac{119480\log(5)}{4641} - \frac{119480\log(2)}{4641}\right)x^3 + \left(\frac{4609070647\sigma}{23984688} + \frac{1619129390\pi}{1499043}\right)x^{7/2}$$
$$+ \left(-\frac{187555\pi\sigma}{714} + \frac{16189540\log(x)}{78897} - \frac{27100\pi^2}{51} + \frac{32379080\gamma}{78897}\right.$$
$$\left. - \frac{69798849954372148039}{19262926375108416} + \frac{32379080\log(5)}{78897} + \frac{32379080\log(2)}{78897}\right)x^4$$
$$+ \left[\sigma\left(-\frac{29870\log(x)}{1547} + 50\pi^2 - \frac{59740\gamma}{1547} - \frac{139128548929393}{432156108384}\right.\right.$$
$$\left. - \frac{59740\log(5)}{1547} - \frac{59740\log(2)}{1547}\right)$$
$$\left. + \pi\left(-\frac{597400\log(x)}{4641} - \frac{1194800\gamma}{4641} - \frac{363541388855045}{324117081288}\right.\right.$$
$$\left.\left. - \frac{1194800\log(5)}{4641} - \frac{1194800\log(2)}{4641}\right)\right]x^{9/2}$$
$$+ \left[\frac{23045353235\pi\sigma}{11992344} - \frac{9672678975860\log(x)}{6957058563} + \frac{16191293900\pi^2}{4497129} - \frac{19345357951720\gamma}{6957058563}\right.$$
$$\left. + \frac{1275474878427485531926255}{44699620653439079328} - \frac{19345357951720\log(5)}{6957058563} - \frac{19345357951720\log(2)}{6957058563}\right]x^5$$
$$+ \left[\sigma\left(\frac{560226785\log(x)}{1656837} - \frac{937775\pi^2}{1071} + \frac{1120453570\gamma}{1656837} - \frac{210794710578688517173}{36774677625206976}\right.\right.$$
$$\left. + \frac{1120453570\log(5)}{1656837} + \frac{1120453570\log(2)}{1656837}\right)$$
$$\left. + \pi\left(\frac{161895400\log(x)}{78897} + \frac{323790800\gamma}{78897} - \frac{348994249771860740195}{9631463187554208}\right.\right.$$
$$\left.\left. + \frac{323790800\log(5)}{78897} + \frac{323790800\log(2)}{78897}\right)\right]x^{11/2} \qquad (9.64)$$

$$\begin{aligned}
\hat{F}_{76} &= 1 + 8\sigma x^{1/2} - \frac{1787}{119}x + \left(12\pi - \frac{17256\sigma}{119}\right)x^{3/2} + \left(96\pi\sigma + \frac{313730895}{3497767}\right)x^2 \\
&+ \left(\frac{538436792\sigma}{499681} - \frac{21444\pi}{119}\right)x^{5/2} + \left(-\frac{207072\pi\sigma}{119} - \frac{143376\log(x)}{7735} + 48\pi^2 - \frac{286752\gamma}{7735}\right. \\
&\left. + \frac{69080576624}{441335895} - \frac{286752\log(3)}{7735} - \frac{573504\log(2)}{7735}\right)x^3 \\
&+ \left[\sigma\left(-\frac{1147008\log(x)}{7735} + 384\pi^2 - \frac{2294016\gamma}{7735} - \frac{1179430181126}{1500542043}\right.\right. \\
&\left.\left. - \frac{2294016\log(3)}{7735} - \frac{4588032\log(2)}{7735}\right) + \frac{3764770740\pi}{3497767}\right]x^{7/2} \\
&+ \left(\frac{6461241504\pi\sigma}{499681} + \frac{256212912\log(x)}{920465} - \frac{85776\pi^2}{119} + \frac{512425824\gamma}{920465}\right. \\
&\left. - \frac{535457980021354132}{92896056978725} + \frac{512425824\log(3)}{920465} + \frac{1024851648\log(2)}{920465}\right)x^4 \\
&+ \left[\sigma\left(\frac{2474096256\log(x)}{920465} - \frac{828288\pi^2}{119} + \frac{4948192512\gamma}{920465}\right.\right. \\
&\left.\left. - \frac{14231093283367007518}{278688170936175} + \frac{4948192512\log(3)}{920465} + \frac{9896385024\log(2)}{920465}\right)\right. \\
&\left. + \pi\left(-\frac{1720512\log(x)}{7735} - \frac{3441024\gamma}{7735} + \frac{276322306496}{147111965}\right.\right. \\
&\left.\left. - \frac{3441024\log(3)}{7735} - \frac{6882048\log(2)}{7735}\right)\right]x^{9/2} \\
&+ \left[\pi\sigma\left(-\frac{13764096\log(x)}{7735} - \frac{27528192\gamma}{7735} - \frac{4717720724504}{500180681}\right.\right. \\
&\left.\left. - \frac{27528192\log(3)}{7735} - \frac{55056384\log(2)}{7735}\right)\right. \\
&\left. - \frac{8996296160304\log(x)}{5411045549} + \frac{15059082960\pi^2}{3497767} - \frac{17992592320608\gamma}{5411045549}\right. \\
&\left. + \frac{530642810226274540730842}{15089571015339195375} - \frac{17992592320608\log(3)}{5411045549} - \frac{35985184641216\log(2)}{5411045549}\right]x^5 \\
&+ \left[\sigma\left(-\frac{77198913489792\log(x)}{3865032535} + \frac{25844966016\pi^2}{499681} - \frac{154397826979584\gamma}{3865032535}\right.\right. \\
&\left.\left. + \frac{303009886036669594783701}{718551000730437875} - \frac{154397826979584\log(3)}{3865032535} - \frac{308795653959168\log(2)}{3865032535}\right)\right. \\
&\left. + \pi\left(\frac{3074554944\log(x)}{920465} + \frac{6149109888\gamma}{920465} - \frac{6425495760256249584}{92896056978725}\right.\right. \\
&\left.\left. + \frac{6149109888\log(3)}{920465} + \frac{12298219776\log(2)}{920465}\right)\right]x^{11/2} \qquad (9.65)
\end{aligned}$$

$$\hat{F}_{77} = 1 - \frac{319}{17}x + \left(14\pi - \frac{21\sigma}{2}\right)x^{3/2} + \frac{30773287}{214149}x^2 + \left(\frac{39119\sigma}{204} - \frac{4466\pi}{17}\right)x^{5/2}$$
$$+ \left(-147\pi\sigma - \frac{83636\log(x)}{3315} + \frac{196\pi^2}{3} - \frac{167272\gamma}{3315} + \frac{699898468579}{66146343120}\right.$$
$$\left. - \frac{167272\log(7)}{3315} - \frac{167272\log(2)}{3315}\right)x^3 + \left(\frac{430826018\pi}{214149} - \frac{4813117711\sigma}{3426384}\right)x^{7/2}$$
$$+ \left(\frac{273833\pi\sigma}{102} + \frac{26679884\log(x)}{56355} - \frac{62524\pi^2}{51} + \frac{53359768\gamma}{56355}\right.$$
$$\left. - \frac{92269694194596106543}{9828023660769600} + \frac{53359768\log(7)}{56355} + \frac{53359768\log(2)}{56355}\right)x^4$$
$$+ \left[\sigma\left(\frac{292726\log(x)}{1105} - 686\pi^2 + \frac{585452\gamma}{1105}\right.\right.$$
$$\left. - \frac{8231923476353}{8819512416} + \frac{585452\log(7)}{1105} + \frac{585452\log(2)}{1105}\right)$$
$$+ \pi\left(-\frac{1170904\log(x)}{3315} - \frac{2341808\gamma}{3315} + \frac{4899289280053}{33073171560}\right.$$
$$\left.\left. - \frac{2341808\log(7)}{3315} - \frac{2341808\log(2)}{3315}\right)\right]x^{9/2}$$
$$+ \left(-\frac{33691823977\pi\sigma}{1713192} - \frac{2573754631532\log(x)}{709903935} + \frac{6031564252\pi^2}{642447} - \frac{5147509263064\gamma}{709903935}\right.$$
$$\left. + \frac{66286435739816234692759}{857365748301348000} - \frac{5147509263064\log(7)}{709903935} - \frac{5147509263064\log(2)}{709903935}\right)x^5$$
$$+ \left[\sigma\left(-\frac{817939171\log(x)}{169065} + \frac{1916831\pi^2}{153} - \frac{1635878342\gamma}{169065}\right.\right.$$
$$\left. + \frac{2911813721908485052367}{29484070982308800} - \frac{1635878342\log(7)}{169065} - \frac{1635878342\log(2)}{169065}\right)$$
$$+ \pi\left(\frac{373518376\log(x)}{56355} + \frac{747036752\gamma}{56355} - \frac{645887859362172745801}{4914011830384800}\right.$$
$$\left.\left. + \frac{747036752\log(7)}{56355} + \frac{747036752\log(2)}{56355}\right)\right]x^{11/2} \tag{9.66}$$

9.6 Multipolar 5.5PN EOB relativistic residual amplitudes derived from the new spinning particle on Schwartzschild fluxes results

The spin-dependent part of the PN-expanded residual relativistic amplitudes obtained from the fluxes of Sec. 9.5.1 read

$$\rho_{22}^{\sigma} = -\frac{1}{3}\sigma x^{3/2} - \frac{2}{63}\sigma x^{5/2} + \frac{61153\sigma}{31752}x^{7/2} + \sigma\left(\frac{214\log(x)}{315} + \frac{428\gamma}{315} - \frac{14661629}{8731800} + \frac{856\log(2)}{315}\right)x^{9/2} + \sigma\left(\frac{428\log(x)}{6615} + \frac{856\gamma}{6615} - \frac{90273995723}{88994505600} + \frac{1712\log(2)}{6615}\right)x^{11/2} \tag{9.67}$$

$$\rho_{21}^{\sigma} = \frac{3\sigma}{4}x^{1/2} + -\frac{61\sigma}{32}x^{3/2} + -\frac{137839\sigma}{225792}x^{5/2} + \sigma\left(-\frac{107\log(x)}{280} - \frac{107\gamma}{140} + \frac{8865471731}{3477196800} - \frac{107\log(2)}{140}\right)x^{7/2} + \sigma\left(\frac{6527\log(x)}{6720} + \frac{6527\gamma}{3360} - \frac{79695561168973}{18226074746880} + \frac{6527\log(2)}{3360}\right)x^{9/2} + \sigma\left(\frac{14748773\log(x)}{47416320} + \frac{14748773\gamma}{23708160} - \frac{3969300389840021}{729042989875200} + \frac{14748773\log(2)}{23708160}\right)x^{11/2} \tag{9.68}$$

$$\rho_{31}^{\sigma} = \frac{5\sigma}{6}x^{3/2} - \frac{29\sigma}{36}x^{5/2} - \frac{129079\sigma}{42768}x^{7/2} + \sigma\left(-\frac{65\log(x)}{378} - \frac{65\gamma}{189} - \frac{1842715099}{668697120} - \frac{65\log(2)}{189}\right)x^{9/2} + \sigma\left(\frac{377\log(x)}{2268} + \frac{377\gamma}{1134} - \frac{1848295232183}{359610451200} + \frac{377\log(2)}{1134}\right)x^{11/2} \tag{9.69}$$

$$\rho_{32}^{\sigma} = \frac{2\sigma}{3}x^{1/2} - \frac{1613\sigma}{810}x^{3/2} - \frac{363103\sigma}{962280}x^{5/2} + \sigma\left(-\frac{104\log(x)}{189} - \frac{208\gamma}{189} + \frac{2565868645267}{496507611600} - \frac{416\log(2)}{189}\right)x^{7/2} + \sigma\left(\frac{41938\log(x)}{25515} + \frac{83876\gamma}{25515} - \frac{10180707438904003}{1179702085161600} + \frac{167752\log(2)}{25515}\right)x^{9/2} + \sigma\left(\frac{4720339\log(x)}{15155910} + \frac{4720339\gamma}{7577955} - \frac{55888392652159222117}{7962989074840800000} + \frac{9440678\log(2)}{7577955}\right)x^{11/2} \tag{9.70}$$

$$\rho_{33}^{\sigma} = -\frac{\sigma}{2}x^{3/2} + \frac{7\sigma}{20}x^{5/2} + \frac{15247\sigma}{7920}x^{7/2} + \sigma\left(\frac{13\log(x)}{14} + \frac{13\gamma}{7} - \frac{2131142749}{454053600} + \frac{13\log(3)}{7} + \frac{13\log(2)}{7}\right)x^{9/2} + \sigma\left(-\frac{13\log(x)}{20} - \frac{13\gamma}{10} + \frac{97710564283}{28540512000} - \frac{13\log(3)}{10} - \frac{13\log(2)}{10}\right)x^{11/2} \tag{9.71}$$

$$\begin{aligned}\rho_{41}^{\sigma} &= \frac{5\sigma}{8}x^{1/2} - \frac{1187\sigma}{704}x^{3/2} - \frac{29908639\sigma}{169128960}x^{5/2} \\ &+ \sigma\left(-\frac{1571\log(x)}{22176} - \frac{1571\gamma}{11088} + \frac{1310663510743}{2812952862720} - \frac{1571\log(2)}{11088}\right)x^{7/2} \\ &+ \sigma\left(\frac{1864777\log(x)}{9757440} + \frac{1864777\gamma}{4878720} - \frac{30823552696653631}{19893202645155840} + \frac{1864777\log(2)}{4878720}\right)x^{9/2} \\ &+ \sigma\Bigg(\frac{46986471869\log(x)}{2344127385600} + \frac{46986471869\gamma}{1172063692800} \\ &- \frac{26722270856299940280173}{17462253281917796352000} + \frac{46986471869\log(2)}{1172063692800}\Bigg)x^{11/2} \end{aligned} \tag{9.72}$$

$$\begin{aligned}\rho_{42}^{\sigma} &= \frac{3\sigma}{5}x^{3/2} - \frac{403\sigma}{550}x^{5/2} - \frac{83093993\sigma}{44044000}x^{7/2} \\ &+ \sigma\left(-\frac{1571\log(x)}{5775} - \frac{3142\gamma}{5775} - \frac{10890814807}{57229672500} - \frac{6284\log(2)}{5775}\right)x^{9/2} \\ &+ \sigma\left(\frac{633113\log(x)}{1905750} + \frac{633113\gamma}{952875} - \frac{61976095519654871}{13876396934400000} + \frac{1266226\log(2)}{952875}\right)x^{11/2}\end{aligned} \tag{9.73}$$

$$\begin{aligned}\rho_{43}^{\sigma} &= \frac{5\sigma}{8}x^{1/2} - \frac{1443\sigma}{704}x^{3/2} - \frac{11933877\sigma}{56376320}x^{5/2} \\ &+ \sigma\Bigg(-\frac{1571\log(x)}{2464} - \frac{1571\gamma}{1232} + \frac{423522768659}{62510063616} - \frac{1571\log(3)}{1232} - \frac{1571\log(2)}{1232}\Bigg)x^{7/2} \\ &+ \sigma\Bigg(\frac{2266953\log(x)}{1084160} + \frac{2266953\gamma}{542080} - \frac{9259292611008173}{736785283153920} \\ &+ \frac{2266953\log(3)}{542080} + \frac{2266953\log(2)}{542080}\Bigg)x^{9/2} \\ &+ \sigma\Bigg(\frac{18748120767\log(x)}{86819532800} + \frac{18748120767\gamma}{43409766400} - \frac{7723130549892884353}{975490379415552000} \\ &+ \frac{18748120767\log(3)}{43409766400} + \frac{18748120767\log(2)}{43409766400}\Bigg)x^{11/2}\end{aligned} \tag{9.74}$$

$$\rho_{44}^{\sigma} = -\frac{3\sigma}{5}x^{3/2} + \frac{146\sigma}{275}x^{5/2} + \frac{87298781\sigma}{44044000}x^{7/2} + \sigma\left(\frac{6284\log(x)}{5775} + \frac{12568\gamma}{5775} - \frac{6129600606719}{915674760000} + \frac{12568\log(2)}{1925}\right)x^{9/2} + \sigma\left(-\frac{917464\log(x)}{952875} - \frac{1834928\gamma}{952875} + \frac{576017315427752921}{97134778540800000} - \frac{1834928\log(2)}{317625}\right)x^{11/2} \tag{9.75}$$

$$\rho_{51}^{\sigma} = \frac{14\sigma}{15}x^{3/2} - \frac{4034\sigma}{2925}x^{5/2} - \frac{5744501\sigma}{2281500}x^{7/2} + \sigma\left(-\frac{10822\log(x)}{160875} - \frac{21644\gamma}{160875} - \frac{16213030784959}{6406007107500} - \frac{21644\log(2)}{160875}\right)x^{9/2} + \sigma\left(\frac{3118282\log(x)}{31370625} + \frac{6236564\gamma}{31370625} - \frac{2272557953476553377}{531647341865640000} + \frac{6236564\log(2)}{31370625}\right)x^{11/2} \tag{9.76}$$

$$\rho_{52}^{\sigma} = \frac{3\sigma}{5}x^{1/2} - \frac{39413\sigma}{22750}x^{3/2} - \frac{5349527\sigma}{47775000}x^{5/2} + \sigma\left(-\frac{3092\log(x)}{17875} - \frac{6184\gamma}{17875} + \frac{4330589662282661}{2491224986250000} - \frac{12368\log(2)}{17875}\right)x^{7/2} + \sigma\left(\frac{5539318\log(x)}{11090625} + \frac{11078636\gamma}{11090625} - \frac{796581754627562940017}{2349451637032500000000} + \frac{22157272\log(2)}{11090625}\right)x^{9/2} + \sigma\Bigg(\frac{4135184371\log(x)}{128096718750} + \frac{4135184371\gamma}{64048359375} - \frac{6099355932458608484088427}{309447511667043750000000000} + \frac{8270368742\log(2)}{64048359375}\Bigg)x^{11/2} \tag{9.77}$$

$$\rho_{53}^{\sigma} = \frac{2\sigma}{5}x^{3/2} - \frac{1182\sigma}{2275}x^{5/2} - \frac{300929\sigma}{253500}x^{7/2} + \sigma\left(-\frac{4638\log(x)}{17875} - \frac{9276\gamma}{17875} + \frac{181745950091}{237259522500} - \frac{9276\log(3)}{17875} - \frac{9276\log(2)}{17875}\right)x^{9/2} + \sigma\Bigg(\frac{2741058\log(x)}{8133125} + \frac{5482116\gamma}{8133125} - \frac{844630470658099711}{229724160065400000} + \frac{5482116\log(3)}{8133125} + \frac{5482116\log(2)}{8133125}\Bigg)x^{11/2} \tag{9.78}$$

$$\rho_{54}^{\sigma} = \frac{3\sigma}{5}x^{1/2} - \frac{47633\sigma}{22750}x^{3/2} - \frac{4565087\sigma}{47775000}x^{5/2} + \sigma\left(-\frac{12368\log(x)}{17875} - \frac{24736\gamma}{17875} + \frac{19650484510197881}{2491224986250000} - \frac{74208\log(2)}{17875}\right)x^{7/2} + \sigma\Bigg(\frac{294562472\log(x)}{121996875} + \frac{589124944\gamma}{121996875} - \frac{41115919165624337072107}{2584396800735750000000} + \frac{589124944\log(2)}{40665625}\Bigg)x^{9/2} + \sigma\Bigg(\frac{7057624502\log(x)}{64048359375} + \frac{14115249004\gamma}{64048359375} - \frac{48855778575018486818308321 3}{587950272167383125000000 00} + \frac{14115249004\log(2)}{21349453125}\Bigg)x^{11/2} \tag{9.79}$$

$$\rho_{55}^{\sigma} = -\frac{2\sigma}{3}x^{3/2} + \frac{514\sigma}{819}x^{5/2} + \frac{929219\sigma}{456300}x^{7/2} + \sigma\left(\frac{1546\log(x)}{1287} + \frac{3092\gamma}{1287} - \frac{73675207595933}{8968409950500} + \frac{3092\log(5)}{1287} + \frac{3092\log(2)}{1287}\right)x^{9/2} + \sigma\Bigg(-\frac{397322\log(x)}{351351} - \frac{794644\gamma}{351351} + \frac{27897212127015034469}{3721531393059480000} - \frac{794644\log(5)}{351351} - \frac{794644\log(2)}{351351}\Bigg)x^{11/2} \tag{9.80}$$

$$\rho_{61}^{\sigma} = \frac{7\sigma}{12}x^{1/2} - \frac{2789\sigma}{1728}x^{3/2} - \frac{50175395\sigma}{651442176}x^{5/2} + \sigma\left(-\frac{901\log(x)}{30888} - \frac{901\gamma}{15444} + \frac{6036361379999233}{49700712452751360} - \frac{901\log(2)}{15444}\right)x^{7/2} + \sigma\left(\frac{2512889\log(x)}{31135104} + \frac{2512889\gamma}{15567552} - \frac{331771917464745022019}{347620983098100940800} + \frac{2512889\log(2)}{15567552}\right)x^{9/2} + \sigma\Bigg(\frac{2659295935\log(x)}{690452066304} + \frac{2659295935\gamma}{345226033152} - \frac{24629161414638634093562509 9}{22862805189931024326328320 0} + \frac{2659295935\log(2)}{345226033152}\Bigg)x^{11/2} \tag{9.81}$$

$$\rho_{62}^{\sigma} = \frac{17\sigma}{21}x^{3/2} - \frac{1819\sigma}{1470}x^{5/2} - \frac{574085\sigma}{271656}x^{7/2} + \sigma\left(-\frac{30634\log(x)}{189189} - \frac{61268\gamma}{189189} - \frac{16770732413683}{15112379482200} - \frac{122536\log(2)}{189189}\right)x^{9/2} + \sigma\left(\frac{1638919\log(x)}{6621615} + \frac{3277838\gamma}{6621615} - \frac{2006995067160111247}{431609558011632000} + \frac{6555676\log(2)}{6621615}\right)x^{11/2} \tag{9.82}$$

$$\rho_{63}^{\sigma} = \frac{7\sigma}{12}x^{1/2} - \frac{3085\sigma}{1728}x^{3/2} - \frac{35390867\sigma}{651442176}x^{5/2} + \sigma\left(-\frac{901\log(x)}{3432} - \frac{901\gamma}{1716} + \frac{145753300581274073}{49700712452751360} - \frac{901\log(3)}{1716} - \frac{901\log(2)}{1716}\right)x^{7/2} + \sigma\left(\frac{2779585\log(x)}{3459456} + \frac{2779585\gamma}{1729728} - \frac{94487187434422183760819}{17033428171806946099200} + \frac{2779585\log(3)}{1729728} + \frac{2779585\log(2)}{1729728}\right)x^{9/2} + \sigma\left(\frac{1875715951\log(x)}{76716896256} + \frac{1875715951\gamma}{38358448128} - \frac{10689835353210782026889725049}{434393298608689462200238080 0} + \frac{1875715951\log(3)}{38358448128} + \frac{1875715951\log(2)}{38358448128}\right)x^{11/2} \tag{9.83}$$

$$\rho_{64}^{\sigma} = \frac{5\sigma}{21}x^{3/2} - \frac{46\sigma}{147}x^{5/2} - \frac{21617\sigma}{31416}x^{7/2} + \sigma\left(-\frac{36040\log(x)}{189189} - \frac{72080\gamma}{189189} + \frac{5008174606007}{5709121137720} - \frac{72080\log(2)}{63063}\right)x^{9/2} + \sigma\left(\frac{331568\log(x)}{1324323} + \frac{663136\gamma}{1324323} - \frac{3751539084367382743}{1467472497239548800} + \frac{663136\log(2)}{441441}\right)x^{11/2} \tag{9.84}$$

$$\rho_{65}^{\sigma} = \frac{7\sigma}{12}x^{1/2} - \frac{3677\sigma}{1728}x^{3/2} - \frac{8157683\sigma}{651442176}x^{5/2} + \sigma\left(-\frac{22525\log(x)}{30888} - \frac{22525\gamma}{15444} + \frac{86699363941370165}{9940142490550272} - \frac{22525\log(5)}{15444} - \frac{22525\log(2)}{15444}\right)x^{7/2} + \sigma\left(\frac{82824425\log(x)}{31135104} + \frac{82824425\gamma}{15567552} - \frac{1160763233925296604961}{61939738806570713088} + \frac{82824425\log(5)}{15567552} + \frac{82824425\log(2)}{15567552}\right)x^{9/2} + \sigma\left(\frac{10808929975\log(x)}{690452066304} + \frac{10808929975\gamma}{345226033152} - \frac{14714771556418553595742 05745}{17375731944347578488009523 2} + \frac{10808929975\log(5)}{345226033152} + \frac{10808929975\log(2)}{345226033152}\right)x^{11/2} \tag{9.85}$$

$$\rho_{66}^{\sigma} = -\frac{5\sigma}{7}x^{3/2} + \frac{67\sigma}{98}x^{5/2} + \frac{9605147\sigma}{4618152}x^{7/2} + \sigma\left(\frac{9010\log(x)}{7007} + \frac{18020\gamma}{7007} - \frac{9897759433831}{1048614086520} + \frac{18020\log(3)}{7007} + \frac{36040\log(2)}{7007}\right)x^{9/2} + \sigma\Bigg(-\frac{60367\log(x)}{49049} - \frac{120734\gamma}{49049} + \frac{1394113205906052901}{163052499693283200} - \frac{120734\log(3)}{49049} - \frac{241468\log(2)}{49049}\Bigg)x^{11/2} \tag{9.86}$$

$$\rho_{71}^{\sigma} = \frac{27\sigma}{28}x^{3/2} - \frac{10617\sigma}{6664}x^{5/2} - \frac{1800329721\sigma}{783499808}x^{7/2} + \sigma\left(-\frac{26883\log(x)}{758030} - \frac{26883\gamma}{379015} - \frac{9712009819849013}{3999844869820800} - \frac{26883\log(2)}{379015}\right)x^{9/2} + \sigma\left(\frac{10570993\log(x)}{180411140} + \frac{10570993\gamma}{90205570} - \frac{61582104147771940639}{16457454020990062080} + \frac{10570993\log(2)}{90205570}\right)x^{11/2} \tag{9.87}$$

$$\rho_{72}^{\sigma} = \frac{4\sigma}{7}x^{1/2} - \frac{57473\sigma}{34986}x^{3/2} - \frac{10380062389\sigma}{259142561496}x^{5/2} + \sigma\left(-\frac{95584\log(x)}{1137045} - \frac{191168\gamma}{1137045} + \frac{34452124473358455517}{41672883756836732400} - \frac{382336\log(2)}{1137045}\right)x^{7/2} + \sigma\Bigg(\frac{52822108\log(x)}{218575035} + \frac{105644216\gamma}{218575035} - \frac{24152743930278491015878137 7}{12135843854437971331984320 0} + \frac{211288432\log(2)}{218575035}\Bigg)x^{9/2} + \sigma\Bigg(\frac{31005246355943\log(x)}{5261727747075345} + \frac{62010492711886\gamma}{5261727747075345} - \frac{14394488640643641362199805810 1657}{11827714778973791239865238115 2000} + \frac{124020985423772\log(2)}{5261727747075345}\Bigg)x^{11/2} \tag{9.88}$$

$$\rho_{73}^{\sigma} = \frac{19\sigma}{28}x^{3/2} - \frac{20843\sigma}{19992}x^{5/2} - \frac{217718161\sigma}{123710496}x^{7/2} + \sigma\left(-\frac{170259\log(x)}{758030} - \frac{170259\gamma}{379015} - \frac{12906790690613}{631554453129600} - \frac{170259\log(3)}{379015} - \frac{170259\log(2)}{379015}\right)x^{9/2} + \sigma\left(\frac{62258041\log(x)}{180411140} + \frac{62258041\gamma}{90205570} - \frac{1918909190748718903547}{394112714713183065600} + \frac{62258041\log(3)}{90205570} + \frac{62258041\log(2)}{90205570}\right)x^{11/2} \tag{9.89}$$

$$\rho_{74}^{\sigma} = \frac{4\sigma}{7}x^{1/2} - \frac{64193\sigma}{34986}x^{3/2} - \frac{1192699477\sigma}{259142561496}x^{5/2} + \sigma\left(-\frac{382336\log(x)}{1137045} - \frac{764672\gamma}{1137045} + \frac{165797414938111965193}{41672883756836732400} - \frac{764672\log(2)}{379015}\right)x^{7/2} + \sigma\left(\frac{3067911856\log(x)}{2841475455} + \frac{6135823712\gamma}{2841475455} - \frac{941107749182924698786607473}{12135843854437971331984 3200} + \frac{6135823712\log(2)}{947158485}\right)x^{9/2} + \sigma\left(\frac{14250373351196\log(x)}{5261727747075345} + \frac{28500746702392\gamma}{5261727747075345} - \frac{34384968557096673594048269896 0253}{11827714778973791239865238115 2000} + \frac{28500746702392\log(2)}{1753909249025115}\right)x^{11/2} \tag{9.90}$$

$$\rho_{75}^{\sigma} = \frac{3\sigma}{28}x^{3/2} - \frac{2795\sigma}{19992}x^{5/2} - \frac{717495539\sigma}{2350499424}x^{7/2} + \sigma\left(-\frac{14935\log(x)}{151606} - \frac{14935\gamma}{75803} + \frac{792909572981707}{1439944153135488} - \frac{14935\log(5)}{75803} - \frac{14935\log(2)}{75803}\right)x^{9/2} + \sigma\left(\frac{3211025\log(x)}{24980004} + \frac{3211025\gamma}{12490002} - \frac{3461511047071262080289}{2695730968638172168704} + \frac{3211025\log(5)}{12490002} + \frac{3211025\log(2)}{12490002}\right)x^{11/2} \tag{9.91}$$

$$\rho^{\sigma}_{76} = \frac{4\sigma}{7}x^{1/2} - \frac{25131\sigma}{11662}x^{3/2} + \frac{466355089\sigma}{9597872648}x^{5/2}$$
$$+ \sigma\left(-\frac{286752\log(x)}{379015} - \frac{573504\gamma}{379015} + \frac{1608805429614769871}{171493348793566800}\right.$$
$$\left. - \frac{573504\log(3)}{379015} - \frac{1147008\log(2)}{379015}\right)x^{7/2}$$
$$+ \sigma\left(\frac{900795564\log(x)}{315719495} + \frac{1801591128\gamma}{315719495} - \frac{3523335266452814138505897}{16647248085648794694080 0}\right.$$
$$\left. + \frac{1801591128\log(3)}{315719495} + \frac{3603182256\log(2)}{315719495}\right)x^{9/2}$$
$$+ \sigma\left(-\frac{4179007952529\log(x)}{64959601815745} - \frac{8358015905058\gamma}{64959601815745} - \frac{460728741621406041051059518219}{5408191485584723932265769600 0}\right.$$
$$\left. - \frac{8358015905058\log(3)}{64959601815745} - \frac{16716031810116\log(2)}{64959601815745}\right)x^{11/2} \qquad (9.92)$$

$$\rho^{\sigma}_{77} = -\frac{3\sigma}{4}x^{3/2} + \frac{293\sigma}{408}x^{5/2} + \frac{709636883\sigma}{335785632}x^{7/2}$$
$$+ \sigma\left(\frac{2987\log(x)}{2210} + \frac{2987\gamma}{1105} - \frac{53784383538559963}{5142657689769600} + \frac{2987\log(7)}{1105} + \frac{2987\log(2)}{1105}\right)x^{9/2}$$
$$+ \sigma\left(-\frac{875191\log(x)}{676260} - \frac{875191\gamma}{338130} + \frac{89536447352345626970969}{9627610602279186316800}\right.$$
$$\left. - \frac{875191\log(7)}{338130} - \frac{875191\log(2)}{338130}\right)x^{11/2} \qquad (9.93)$$

9.7 Orbital factorization

Let us finally compute the orbital-factorized residual amplitudes via the usual formula

$$\hat{\rho}^{\sigma}_{\ell m} = T_n\left[1 + \rho^{\sigma}_{\ell m}/\rho^{\mathrm{orb}}_{\ell m}\right], \qquad (9.94)$$

that give

$$\hat{\rho}^{\sigma}_{22} = 1 - \frac{\sigma}{3}x^{3/2} - \frac{47\sigma}{126}x^{5/2} + \frac{3559\sigma}{3969}x^{7/2} + \frac{12651734\sigma}{4584195}x^{9/2} + \frac{28149619976\sigma}{3754455705}x^{11/2} \tag{9.95}$$

$$\hat{\rho}^{\sigma}_{21} = 1 + \frac{3\sigma}{4}x^{1/2} - \frac{125\sigma}{112}x^{3/2} - \frac{32789\sigma}{28224}x^{5/2} - \frac{77944927\sigma}{43464960}x^{7/2} - \frac{428533338559\sigma}{142391208960}x^{9/2} - \frac{62955838520401\sigma}{11960861552640}x^{11/2} \tag{9.96}$$

$$\hat{\rho}^{\sigma}_{31} = 1 + \frac{5\sigma}{6}x^{3/2} - \frac{11\sigma}{54}x^{5/2} - \frac{11323\sigma}{3564}x^{7/2} - \frac{717713\sigma}{108108}x^{9/2} - \frac{1064675011\sigma}{107026920}x^{11/2} \tag{9.97}$$

$$\hat{\rho}^{\sigma}_{32} = 1 + \frac{2\sigma}{3}x^{1/2} - \frac{319\sigma}{270}x^{3/2} - \frac{648019\sigma}{534600}x^{5/2} - \frac{6638464687\sigma}{4378374000}x^{7/2} - \frac{33146739061679\sigma}{17338361040000}x^{9/2} - \frac{60503098348345699\sigma}{26527692391200000}x^{11/2} \tag{9.98}$$

$$\hat{\rho}^{\sigma}_{33} = 1 - \frac{\sigma}{2}x^{3/2} - \frac{7\sigma}{30}x^{5/2} + \frac{177\sigma}{220}x^{7/2} + \frac{871951\sigma}{300300}x^{9/2} + \frac{17852323\sigma}{2202200}x^{11/2} \tag{9.99}$$

$$\hat{\rho}^{\sigma}_{41} = 1 + \frac{5\sigma}{8}x^{1/2} - \frac{257\sigma}{264}x^{3/2} - \frac{16757891\sigma}{15855840}x^{5/2} - \frac{229249343\sigma}{149497920}x^{7/2} - \frac{17887683247311111\sigma}{712321709299200}x^{9/2} - \frac{246270710769267027 49\sigma}{5517141144907392000}x^{11/2} \tag{9.100}$$

$$\hat{\rho}^{\sigma}_{42} = 1 + \frac{3\sigma}{5}x^{3/2} - \frac{233\sigma}{1100}x^{5/2} - \frac{2550686\sigma}{1376375}x^{7/2} - \frac{10879637\sigma}{2595450}x^{9/2} - \frac{438353771264176\sigma}{57968889103125}x^{11/2} \tag{9.101}$$

$$\hat{\rho}^{\sigma}_{43} = 1 + \frac{5\sigma}{8}x^{1/2} - \frac{111\sigma}{88}x^{3/2} - \frac{2098731\sigma}{1761760}x^{5/2} - \frac{49844891\sigma}{38758720}x^{7/2} - \frac{33317029019173\sigma}{26382285529600}x^{9/2} - \frac{19612189638842587\sigma}{29690218253696000}x^{11/2} \tag{9.102}$$

$$\hat{\rho}^{\sigma}_{44} = 1 - \frac{3\sigma}{5}x^{3/2} - \frac{223\sigma}{1100}x^{5/2} + \frac{1054688\sigma}{1376375}x^{7/2} + \frac{1353843731\sigma}{454203750}x^{9/2} + \frac{992355473557843\sigma}{115937778206250}x^{11/2} \tag{9.103}$$

$$\hat{\rho}^{\sigma}_{51} = 1 + \frac{14\sigma}{15}x^{3/2} - \frac{1801\sigma}{2925}x^{5/2} - \frac{66704\sigma}{22815}x^{7/2} - \frac{286905117\sigma}{51354875}x^{9/2} - \frac{133827846344194\sigma}{15411854761875}x^{11/2} \tag{9.104}$$

$$\hat{\rho}^{\sigma}_{52} = 1 + \frac{3\sigma}{5}x^{1/2} - \frac{4717\sigma}{4550}x^{3/2} - \frac{25745627\sigma}{24843000}x^{5/2} - \frac{5732338755709\sigma}{4227533310000}x^{7/2} - \frac{17511367939735839 97\sigma}{877128611158800000}x^{9/2} - \frac{11961162624065972919 37\sigma}{378088596073188000000}x^{11/2} \tag{9.105}$$

$$\hat{\rho}^{\sigma}_{53} = 1 + \frac{2\sigma}{5}x^{3/2} - \frac{307\sigma}{2275}x^{5/2} - \frac{96296\sigma}{88725}x^{7/2} - \frac{6666572173\sigma}{2516388875}x^{9/2} - \frac{148115323552418\sigma}{27969662345625}x^{11/2} \tag{9.106}$$

$$\hat{\rho}^{\sigma}_{54} = 1 + \frac{3\sigma}{5}x^{1/2} - \frac{6037\sigma}{4550}x^{3/2} - \frac{28942427\sigma}{24843000}x^{5/2} - \frac{4810921567549\sigma}{4227533310000}x^{7/2} - \frac{75541258132680255 7\sigma}{877128611158800000}x^{9/2} + \frac{26655736215015454051 97\sigma}{7183683325390572000000}x^{11/2} \tag{9.107}$$

$$\hat{\rho}^{\sigma}_{55} = 1 - \frac{2\sigma}{3}x^{3/2} - \frac{839\sigma}{4095}x^{5/2} + \frac{23336\sigma}{31941}x^{7/2} + \frac{8156376169\sigma}{2717699985}x^{9/2} + \frac{4839706866014\sigma}{549222460605}x^{11/2} \tag{9.108}$$

$$\hat{\rho}^{\sigma}_{61} = 1 + \frac{7\sigma}{12}x^{1/2} - \frac{277\sigma}{288}x^{3/2} - \frac{44433049\sigma}{45239040}x^{5/2} - \frac{371051135027\sigma}{268177029120}x^{7/2} - \frac{10542121763613631\sigma}{4680583081574400}x^{9/2} - \frac{14271837079733762037 97\sigma}{358098305938628935680}x^{11/2} \tag{9.109}$$

$$\hat{\rho}^{\sigma}_{62} = 1 + \frac{17\sigma}{21}x^{3/2} - \frac{1156\sigma}{2205}x^{5/2} - \frac{268757\sigma}{113190}x^{7/2} - \frac{21065590229\sigma}{4403373975}x^{9/2} - \frac{417535804117937\sigma}{51876148799475}x^{11/2} \tag{9.110}$$

$$\hat{\rho}^{\sigma}_{63} = 1 + \frac{7\sigma}{12}x^{1/2} - \frac{317\sigma}{288}x^{3/2} - \frac{46104169\sigma}{45239040}x^{5/2} - \frac{29627725649\sigma}{24379729920}x^{7/2} - \frac{66489059319263639\sigma}{42125247734169600}x^{9/2} - \frac{3720872775185061088913\sigma}{1790491529693144678400}x^{11/2}$$

$$\hat{\rho}^{\sigma}_{64} = 1 + \frac{5\sigma}{21}x^{3/2} - \frac{61\sigma}{882}x^{5/2} - \frac{112912\sigma}{192423}x^{7/2} - \frac{4568593831\sigma}{2994294303}x^{9/2} - \frac{575938803081179\sigma}{176378905918215}x^{11/2} \tag{9.111}$$

$$\hat{\rho}^{\sigma}_{65} = 1 + \frac{7\sigma}{12}x^{1/2} - \frac{397\sigma}{288}x^{3/2} - \frac{10344629\sigma}{9047808}x^{5/2} - \frac{55766903119\sigma}{53635405824}x^{7/2} - \frac{333153630992549\sigma}{561669969788928}x^{9/2} + \frac{5921133406562379283\sigma}{5509204706748137472}x^{11/2} \tag{9.112}$$

$$\hat{\rho}^{\sigma}_{66} = 1 - \frac{5\sigma}{7}x^{3/2} - \frac{32\sigma}{147}x^{5/2} + \frac{89149\sigma}{128282}x^{7/2} + \frac{994661431\sigma}{332699367}x^{9/2} + \frac{583804341345 01\sigma}{6532552071045}x^{11/2} \tag{9.113}$$

$$\hat{\rho}^{\sigma}_{71} = 1 + \frac{27\sigma}{28}x^{3/2} - \frac{5055\sigma}{6664}x^{5/2} - \frac{314399559\sigma}{111928544}x^{7/2} - \frac{347816889471\sigma}{66597483680}x^{9/2} - \frac{32891164408304279241\sigma}{3961979671719829760}x^{11/2} \tag{9.114}$$

$$\hat{\rho}^{\sigma}_{72} = 1 + \frac{4\sigma}{7}x^{1/2} - \frac{15013\sigma}{14994}x^{3/2} - \frac{15283693519\sigma}{15865871112}x^{5/2} - \frac{217904503299487\sigma}{169923479609520}x^{7/2} - \frac{358420203298401950614 57\sigma}{18196184038307662138752}x^{9/2} - \frac{41562145193596080980127845387\sigma}{126672735182678789978922048 00}x^{11/2} \tag{9.115}$$

$$\hat{\rho}^{\sigma}_{73} = 1 + \frac{19\sigma}{28}x^{3/2} - \frac{8189\sigma}{19992}x^{5/2} - \frac{11131789\sigma}{5890976}x^{7/2} - \frac{127060305413\sigma}{31546176480}x^{9/2} - \frac{13578207003592742947\sigma}{1876727212919919360}x^{11/2} \tag{9.116}$$

$$\hat{\rho}^{\sigma}_{74} = 1 + \frac{4\sigma}{7}x^{1/2} - \frac{17365\sigma}{14994}x^{3/2} - \frac{15963282247\sigma}{15865871112}x^{5/2} - \frac{1881655577289 43\sigma}{169923479609520}x^{7/2} - \frac{1135653519725655063196 37\sigma}{90980920191538310693760}x^{9/2} - \frac{151923208214188436595220043 63\sigma}{126672735182678789978922048 00}x^{11/2} \tag{9.117}$$

$$\hat{\rho}^{\sigma}_{75} = 1 + \frac{3\sigma}{28}x^{3/2} - \frac{509\sigma}{19992}x^{5/2} - \frac{81873157\sigma}{335785632}x^{7/2} - \frac{80098504867\sigma}{119875470624}x^{9/2} - \frac{321737899854962906 87\sigma}{21394690227287080704}x^{11/2} \tag{9.118}$$

$$\hat{\rho}^{\sigma}_{76} = 1 + \frac{4\sigma}{7}x^{1/2} - \frac{2365\sigma}{1666}x^{3/2} - \frac{220684127\sigma}{195874952}x^{5/2} - \frac{226470388407\sigma}{233091192880}x^{7/2} - \frac{168327747745750230 71\sigma}{41600786553058212480}x^{9/2} + \frac{338509237739925055727213\sigma}{21452138932527018235520 0}x^{11/2} \tag{9.119}$$

$$\hat{\rho}^{\sigma}_{77} = 1 - \frac{3\sigma}{4}x^{3/2} - \frac{667\sigma}{2856}x^{5/2} + \frac{4527163\sigma}{6852768}x^{7/2} + \frac{36227099497\sigma}{12232190880}x^{9/2} + \frac{400325034129853661\sigma}{44553707262155520}x^{11/2} \tag{9.120}$$

for the $m =$ even case read

For the $m =$ odd case, the best choice is to factorize the $f^{\sigma}_{\ell m} = (\rho^{\sigma}_{\ell m})^{\ell}$'s:

$$\hat{f}^{\sigma}_{21} = 1 + \frac{3\sigma}{2}x^{1/2} - \frac{125\sigma}{56}x^{3/2} - \frac{32789\sigma}{14112}x^{5/2} - \frac{77944927\sigma}{21732480}x^{7/2} - \frac{428533338559\sigma}{71195604480}x^{9/2} - \frac{62955838520401\sigma}{5980430776320}x^{11/2} \tag{9.121}$$

$$\hat{f}^{\sigma}_{31} = 1 + \frac{5\sigma}{2}x^{3/2} - \frac{11\sigma}{18}x^{5/2} - \frac{11323\sigma}{1188}x^{7/2} - \frac{717713\sigma}{36036}x^{9/2} - \frac{1064675011\sigma}{35675640}x^{11/2} \tag{9.122}$$

$$\hat{f}^{\sigma}_{33} = 1 - \frac{3\sigma}{2}x^{3/2} - \frac{7\sigma}{10}x^{5/2} + \frac{531\sigma}{220}x^{7/2} + \frac{871951\sigma}{100100}x^{9/2} + \frac{53556969\sigma}{2202200}x^{11/2} \tag{9.123}$$

$$\hat{f}^{\sigma}_{41} = 1 + \frac{5\sigma}{2}x^{1/2} - \frac{257\sigma}{66}x^{3/2} - \frac{16757891\sigma}{3963960}x^{5/2} - \frac{229249343\sigma}{37374480}x^{7/2} - \frac{1788768324731111\sigma}{178080427324800}x^{9/2} - \frac{246270710769267027 49\sigma}{1379285286226848000}x^{11/2} \tag{9.124}$$

$$\hat{f}^{\sigma}_{43} = 1 + \frac{5\sigma}{2}x^{1/2} - \frac{111\sigma}{22}x^{3/2} - \frac{2098731\sigma}{440440}x^{5/2} - \frac{49844891\sigma}{9689680}x^{7/2} - \frac{33317029019173\sigma}{6595571382400}x^{9/2} - \frac{196121896388425 87\sigma}{7422554563424000}x^{11/2} \tag{9.125}$$

$$\hat{f}^{\sigma}_{51} = 1 + \frac{14\sigma}{3}x^{3/2} - \frac{1801\sigma}{585}x^{5/2} - \frac{66704\sigma}{4563}x^{7/2} - \frac{286905117\sigma}{10270975}x^{9/2} - \frac{1338278463441 94\sigma}{3082370952375}x^{11/2} \tag{9.126}$$

$$\hat{f}^{\sigma}_{53} = 1 + 2\sigma x^{3/2} - \frac{307\sigma}{455}x^{5/2} - \frac{96296\sigma}{17745}x^{7/2} - \frac{6666572173\sigma}{503277775}x^{9/2} - \frac{1481153235524 18\sigma}{5593932469125}x^{11/2} \tag{9.127}$$

$$\hat{f}^{\sigma}_{55} = 1 - \frac{10\sigma}{3}x^{3/2} - \frac{839\sigma}{819}x^{5/2} + \frac{116680\sigma}{31941}x^{7/2} + \frac{8156376169\sigma}{543539997}x^{9/2} + \frac{4839706866014\sigma}{109844492121}x^{11/2} \tag{9.128}$$

$$\hat{f}^{\sigma}_{61} = 1 + \frac{7\sigma}{2}x^{1/2} - \frac{277\sigma}{48}x^{3/2} - \frac{44433049\sigma}{7539840}x^{5/2} - \frac{371051135027\sigma}{44696171520}x^{7/2} - \frac{10542121763613631\sigma}{780097180262400}x^{9/2} - \frac{1427183707973376203797\sigma}{59683050989771489280}x^{11/2} \quad (9.129)$$

$$\hat{f}^{\sigma}_{63} = 1 + \frac{7\sigma}{2}x^{1/2} - \frac{317\sigma}{48}x^{3/2} - \frac{46104169\sigma}{7539840}x^{5/2} - \frac{29627725649\sigma}{4063288320}x^{7/2} - \frac{66489059319263639\sigma}{7020874622361600}x^{9/2} - \frac{37208727751850610889 13\sigma}{298415254948857446400}x^{11/2} \quad (9.130)$$

$$\hat{f}^{\sigma}_{65} = 1 + \frac{7\sigma}{2}x^{1/2} - \frac{397\sigma}{48}x^{3/2} - \frac{10344629\sigma}{1507968}x^{5/2} - \frac{55766903119\sigma}{8939234304}x^{7/2} - \frac{333153630992549\sigma}{93611661631488}x^{9/2} + \frac{5921133406562379283\sigma}{918200784458022912}x^{11/2} \quad (9.131)$$

$$\hat{f}^{\sigma}_{71} = 1 + \frac{27\sigma}{4}x^{3/2} - \frac{5055\sigma}{952}x^{5/2} - \frac{314399559\sigma}{15989792}x^{7/2} - \frac{347816889471\sigma}{9513926240}x^{9/2} - \frac{32891164408304279241\sigma}{565997095959975680}x^{11/2} \quad (9.132)$$

$$\hat{f}^{\sigma}_{73} = 1 + \frac{19\sigma}{4}x^{3/2} - \frac{5055\sigma}{952}x^{5/2} - \frac{11131789\sigma}{841568}x^{7/2} - \frac{127060305413\sigma}{4506596640}x^{9/2} - \frac{13578207003592742947\sigma}{268103887559988480}x^{11/2} \quad (9.133)$$

$$\hat{f}^{\sigma}_{75} = 1 + \frac{3\sigma}{4}x^{3/2} - \frac{509\sigma}{2856}x^{5/2} - \frac{81873157\sigma}{47969376}x^{7/2} - \frac{80098504867\sigma}{17125067232}x^{9/2} - \frac{32173789985496290687\sigma}{3056384318183868672}x^{11/2} \quad (9.134)$$

$$\hat{f}^{\sigma}_{77} = 1 - \frac{21\sigma}{4}x^{3/2} - \frac{667\sigma}{408}x^{5/2} + \frac{31690141\sigma}{6852768}x^{7/2} + \frac{36227099497\sigma}{1747455840}x^{9/2} + \frac{28022752389089756 27\sigma}{44553707262155520}x^{11/2} \quad (9.135)$$

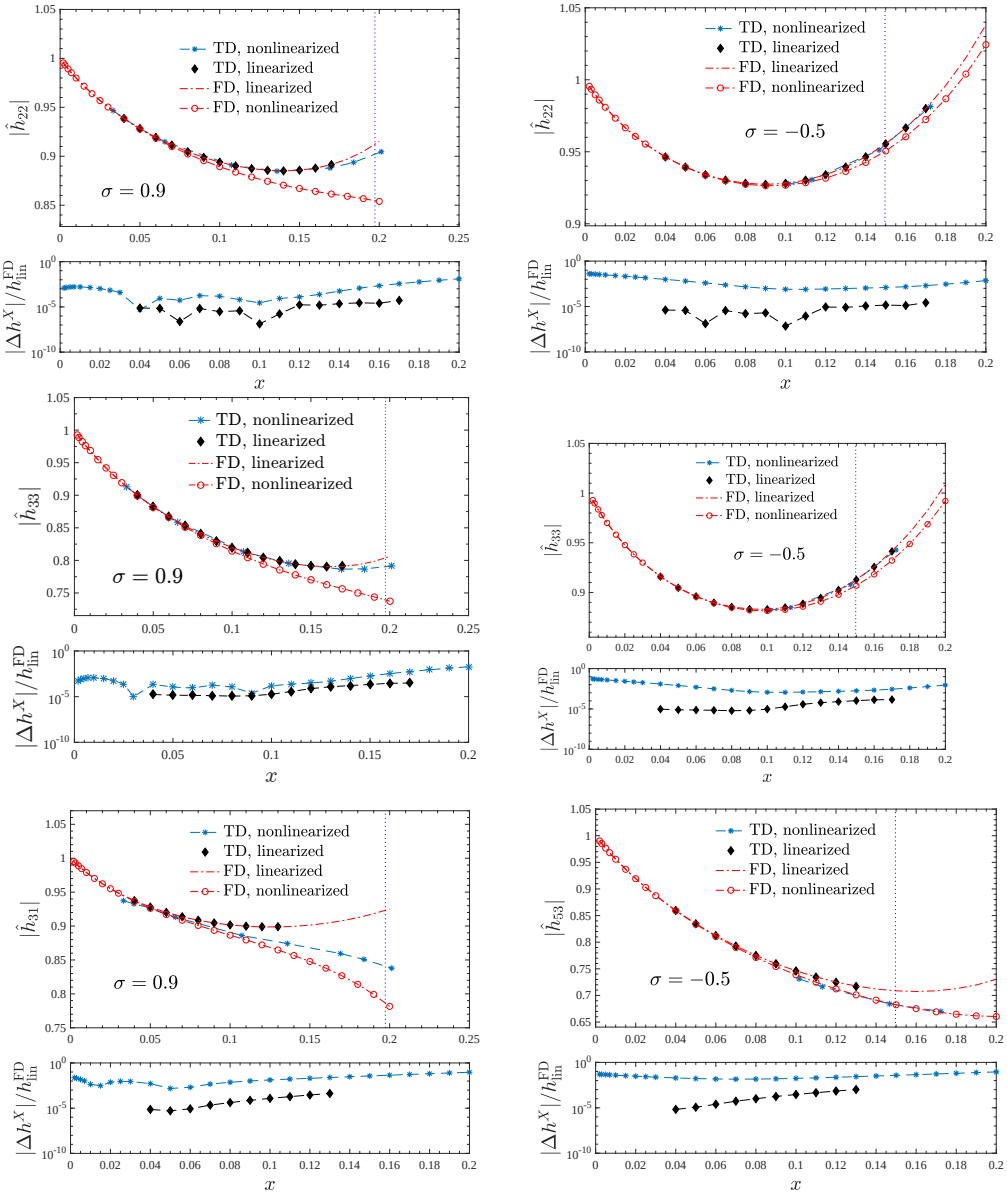

Figure 9.2: Comparing FD (with MPD dynamics) and TD calculation (with Hamiltonian dynamics) for a few multipoles and values of the particle spin. Each plot shows four curves: the TD and FD result with all the contributions nonlinear in the particle spin and the same data linearized in σ. In the latter case, the agreement between TD and FD results is excellent. The bottom part of each panel illustrate the fractional difference between: X =TD-nonlinearized and FD-linearized and the fractional difference between X =TD-linearized and FD-linearized. The vertical line marks the location of the LSO, Eq. (9.7).

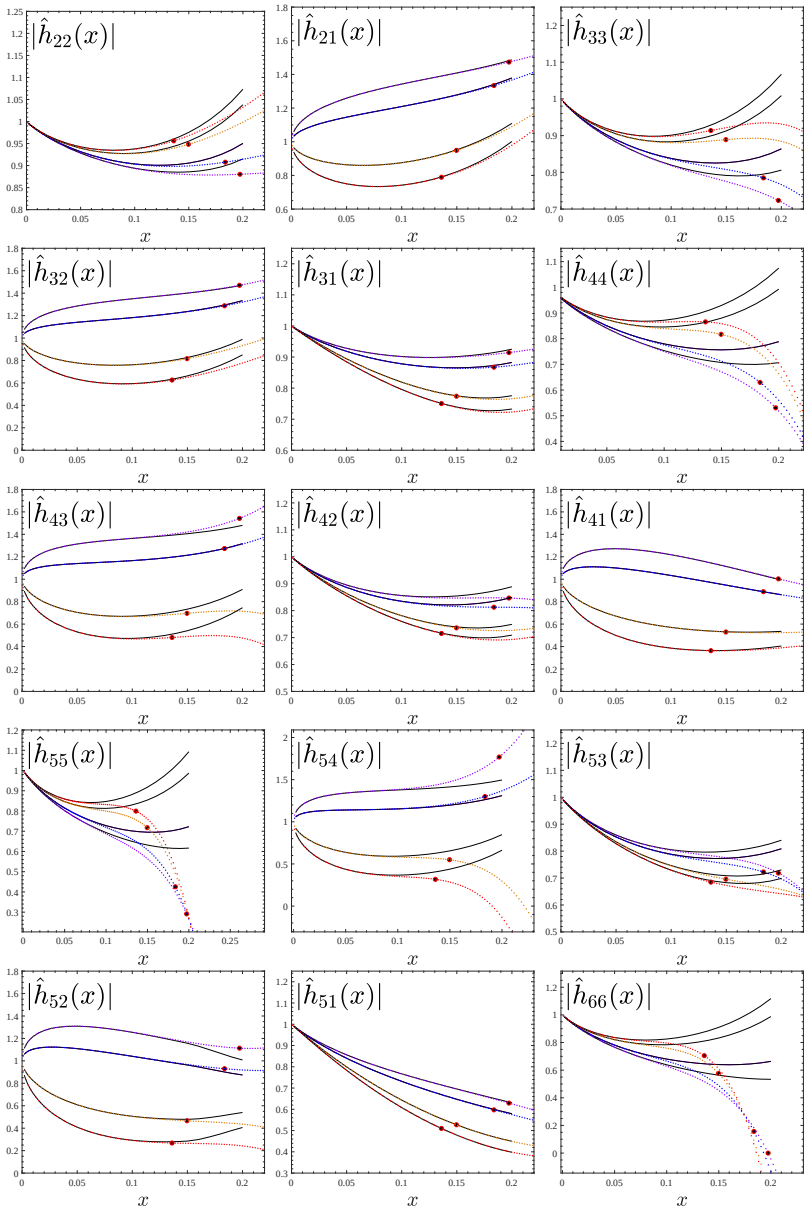

Figure 9.3: Comparison between the PN-expanded, Newton-normalized, waveform amplitudes (dotted lines) and the corresponding numerical ones (black lines). The values of the particle spin $\sigma = (-0.90, -0.5, +0.5, +0.90)$ are respectively indicated by the colors red, orange, blue and purple. The colored markers indicate the location of the LSO, Eq. (9.7).

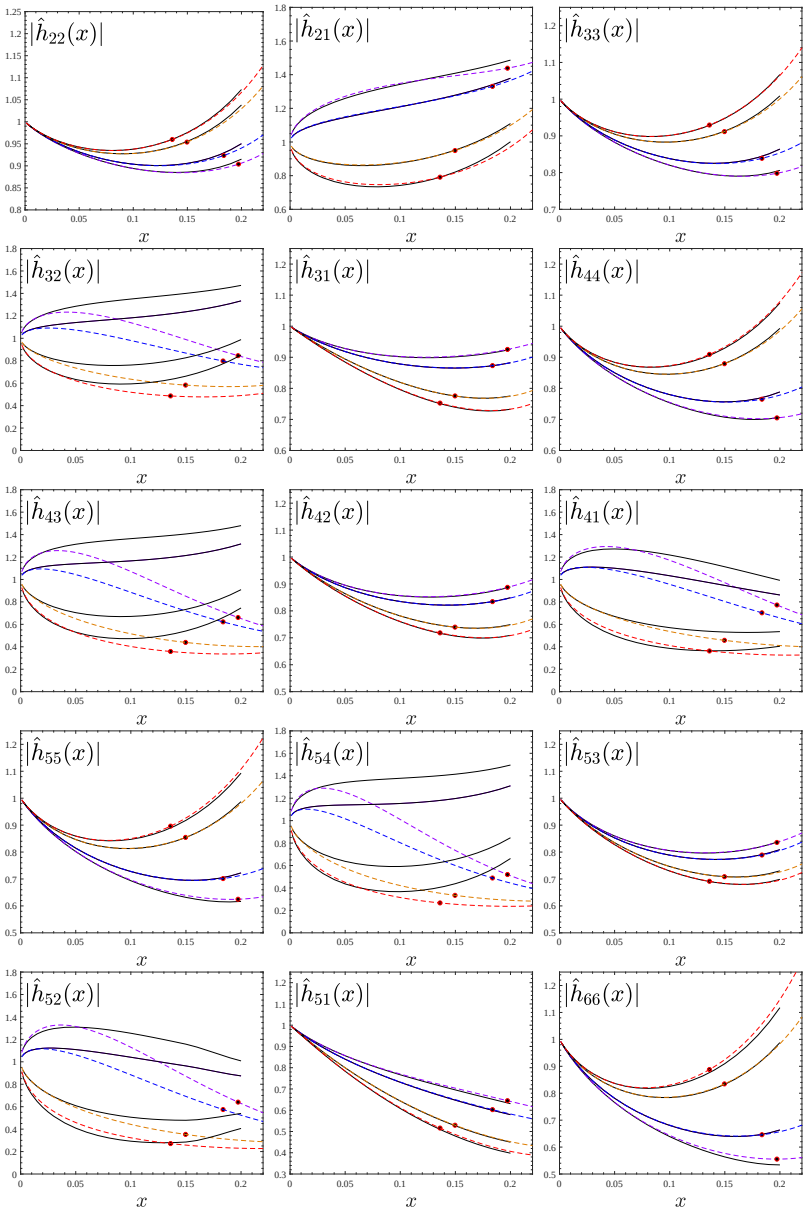

Figure 9.4: Comparison between the factorized and resummed, Newton-normalized, waveform amplitudes (dotted lines) following the standard procedure of Ref. [176] and the corresponding numerical ones (black lines). The values of the particle spin $\sigma = (-0.90, -0.5, +0.5, +0.90)$ are respectively indicated by the colors red, orange, blue and purple. The colored markers indicate the location of the LSO, Eq. (9.7). The analytical approximation is, in general, rather inaccurate for $\ell + m =$ odd modes.

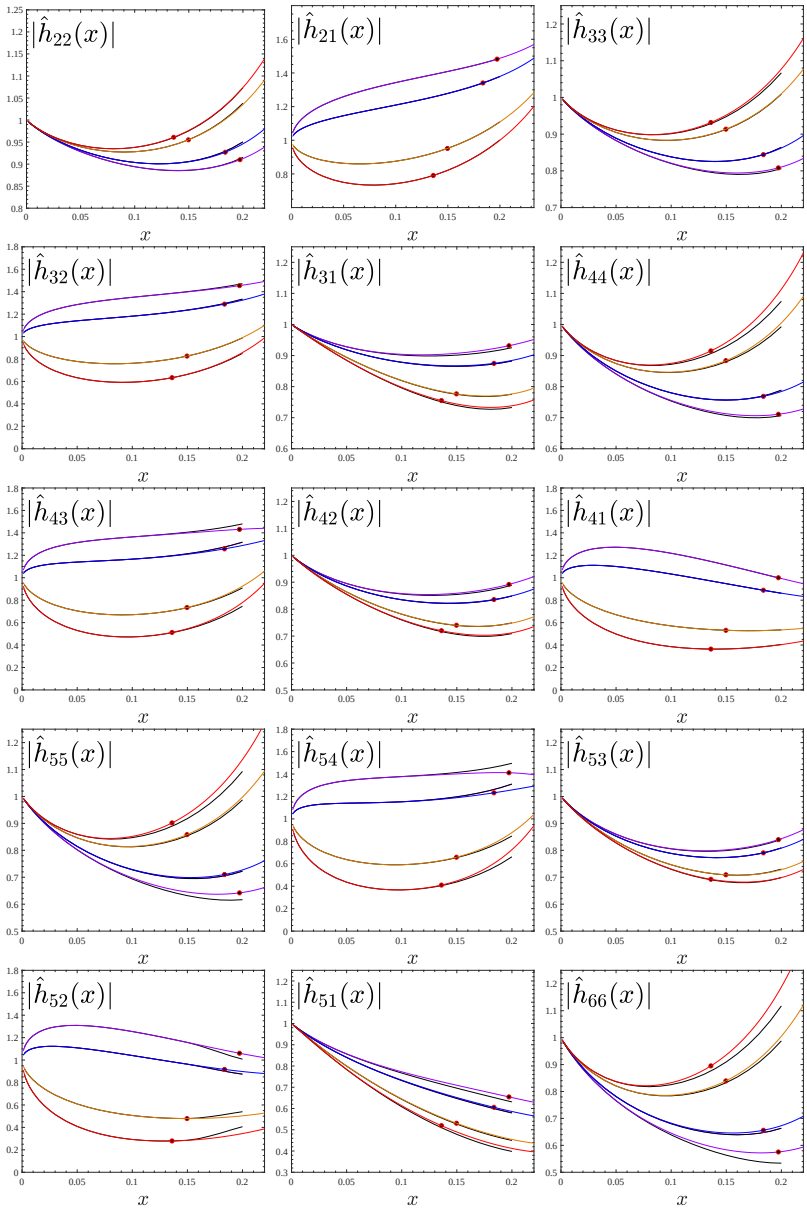

Figure 9.5: Alternative resummation: the $\ell+m=$ even modes are resummed using Eq. (9.13), while the $\ell+m=$ odd rely on Eq. (9.17), where only the tail factor is overall factorized. The values of the particle spin are $\sigma = (-0.90, -0.5, +0.5, +0.90)$, and are respectively indicated by the colors red, orange, blue and purple. The colored markers indicate the location of the LSO, Eq. (9.7). The improvement in the $\ell+m=$ odd modes with respect to Fig. 9.4 is evident. By contrast, the behavior of the $\ell+m=$ even modes is similar to those of Fig. 9.4, though slightly worse.

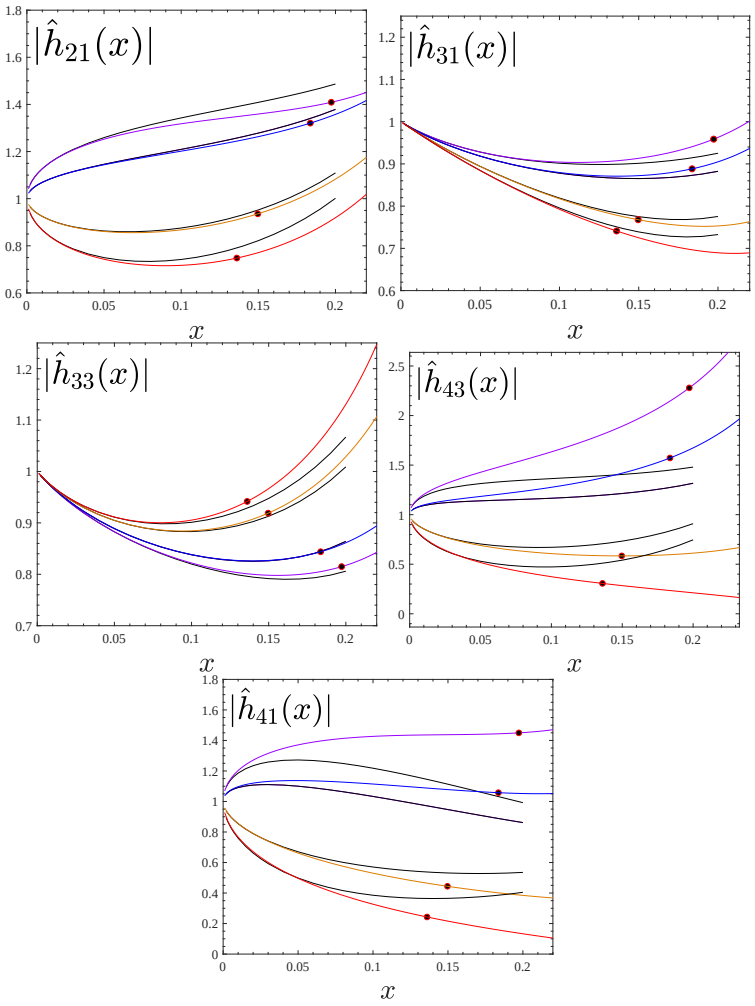

Figure 9.6: Testing the resummation of the $m =$ odd modes suggested in the comparable-mass case. The analytical/numerical agreement is rather good for the $(2, 1)$ and $(3, 3)$ mode, while it is largely inaccurate for the other multipoles.

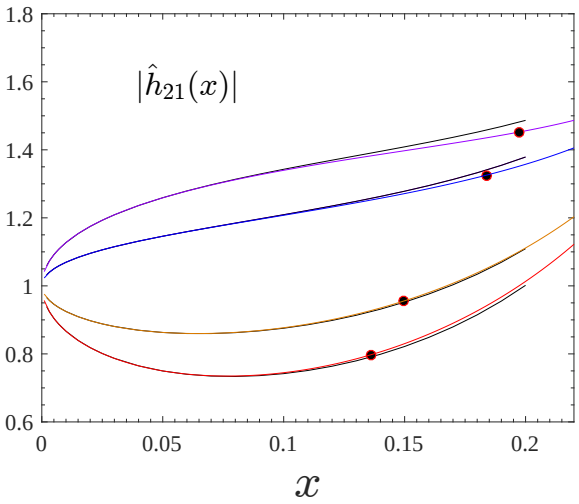

Figure 9.7: Analytical/numerical agreement with the tail-factorized $\ell = 2$, $m = 1$ amplitude truncated at 2.5PN in the spin sector, consistently with Eq. (9.19). Despite the reduced amount of spin-dependent information reduced amount of PN information the tail-factorized analytical amplitude does not look especially better than the orbital-factorized and resummed one displayed in Fig. 9.6.

Chapter 10

Conclusions

10.1 Ref. [1] (Chapter 5)

This paper has introduced and detailed `TEOBResumS`, a state-of-the-art effective-one-body model that generates time-domain gravitational waveforms for non-precessing, coalescing relativistic binaries. Our main results are as follows.

(i) After correcting a minor coding error in the numerical implementation of the BBH sector of the model, we obtained a new determination of the NNNLO spin-orbit effective parameter c_3 with respect to Ref. [37]. In addition, the merger and postmerger part was updated with respect of Ref. [37] thanks to new effective fits that combine together NR information with test-particle results [338]. The parameter c_3 is determined by comparing EOB waveforms with 27, spin-dependent, NR waveforms from the SXS catalog. The model is then validated by computing the unfaithfulness (or mismatch) $\bar{F}$ over 135 NR waveforms from the SXS catalog obtained with the `SpEC` code and 19 NR waveforms from the `BAM` code. Over the SXS catalog, $\max(\bar{F}) \lesssim 2.5 \times 10^{-3}$ except for a single outlier, $(3, +0.85, +0.85)$ where $\max(\bar{F}) \lesssim 7.1 \times 10^{-3}$. By incorporating more flexibility in the global fit for c_3, notably allowing c_3 to depend *quadratically* on the individual spin variables also away from the equal-mass, equal-spin regime, one finds that $\max(\bar{F}) \lesssim 2.5 \times 10^{-3}$ *all over* the SXS waveform catalog. By contrast, $\bar{F}$ over the `BAM` NR waveform is always well below the 1% level except for the single outlier $(8, +0.85, +0.85)$, that shoots up to 5.2%. We have identified the cause of this discrepancy to be the strength of the EOB-predicted spin-orbit

interaction to be too small (i.e., resulting in a dynamics plunging too fast with respect to the NR prediction) in that corner of the parameter space. We have shown that the problem can be fixed by a new, NR-driven, choice for c_3. For simplicity, we have however decided not to provide a new fit of c_3 that also incorporates this strong-field information. This will be done in a forthcoming study that implements the factorized and resummed waveform amplitudes of Refs. [9, 4] that are expected to be more robust for large mass ratios and large, positive spins.

(ii) We comprehensively explored the behavior of `TEOBResumS` waveform amplitude and frequencies outside the NR-covered portion of the parameter space. Thanks to the robustness of the merger and postmerger fits of Ref. [338], the waveforms look sane and consistent among themselves even for large mass ratios ($q \leq 20$) and high-spins ($\chi_1 = \chi_2 = \pm 0.95$).

(iii) Building on previous work [206], the matter-dependent sector of `TEOBResumS` blends together, in resummed form, spin-orbit, spin-spin and tidal effects. Notably, the EOS-dependent self-spin effects are also incorporated in the model (at leading order) in a similar fashion to the BBH case [159]. We showed that `TEOBResumS` waveforms are compatible with state-of-the-art, long-end, error-controlled, NR simulations of coalescing, spinning BNSs for an illustrative choice of EOS.

(iv) We have produced selected comparisons with the EOB-based models `SEOBNRv4` and its tidal counterpart, `SEOBNRv4T`. In particular, for the case of spinning BNS, we computed the faithfulness (or match) between `SEOBNRv4T` and `TEOBResumS`, starting from 40Hz, with $M_A/M_B \in [1, 2]$, the heaviest mass $M_A \in [1, 3]M_\odot$, dimensionless spins $\chi_{A,B} \in [-0.15, +0.15]$ and tidal parameters $\Lambda_{A,B} \in [2, 1600]$. We found excellent compatibility between the two models, with minimum match equal to 0.9898 for more than 17,000 events.

(v) Finally, we tested the performance of `TEOBResumS` in a realistic setting by performing a parameter estimation study on the publicly available data for GW150914. Our posteriors, listed in Table 5.4, are fully compatible with those inferred by the LVC analysis of Refs. [44, 275], that are based on other NR-calibrated EOB waveform models.

While this paper was being finalized, a computationally efficient version of `TEOBResumS` based on the post-adiabatic approximation appeared [191]. In addition, `TEOBResumS` is being used to test the RIFT algorithm to perform Rapid parameter (RapidPE) inference of gravitational wave sources via Iterative Fitting [339]. In particular, RapidPE results obtained using `TEOBResumS` on GW170817 data are reported in Ref. [210].

10.2 Ref. [2] (Chapter 6)

We have incorporated the EOS-dependent self-spin terms (or monopole-quadrupole effects) in `TEOBResumS` at NLO (i.e., at 3PN order, in both the Hamiltonian and the flux) and at NNLO (4PN order, though only in the Hamiltonian, since the corresponding information in the flux is not available yet). Following previous work [1], this was done through a modification of the centrifugal radius function $r_c(r, \tilde{a}_i)$, which now depends on the spin-induced quadrupole moments.

Our main findings can be summarized as follows:

(i) Using the Q_ω gauge-invariant description of the phasing, we have found that, once incorporated in the EOB formalism, NLO self-spin effects during the late inspiral are *more phase accelerating* than the LO ones (consistent with the corresponding PN behavior) but at the same time different and *less phase accelerating* than the corresponding PN description at NLO expressed through the TaylorF2 approximant. We have verified this to be the case for a few (though illustrative) EOS choices and binary parameters

(ii) The resummed EOB self-spin phasing during the inspiral can be well approximated by augmenting the TaylorF2 approximant by the LO self-spin tail term. The resulting approximant delivers a simple phasing expression that is consistent with the EOB one up to dimensionless frequency up to $M\omega \simeq 0.06$

(iii) In general, the fact that the PN prediction is always more phase accelerating than the EOB one may have consequences on the estimate of these effects on real data, especially in the case of fast spinning BNS [135] made by recycled NS. This also indicates that current waveform models, notably `PhenomPv2_NRTidal` [209], that incorporate self-spin effects

and that have been used for the analysis of GW170817, should be updated accordingly. This may eventually affect the evaluation of the systematics due to waveform models in the analysis of GW170817.

(iv) Similarly, it will also be interesting to repeat the parameter estimation of GW170817 performed in Ref. [210] using `TEOBResumS` using the current version of the model that incorporates up to NNLO, EOS-dependent, self-spin effects. Note that this will also imply incorporating more, point-mass, spin-dependent terms than those currently present in the model.

(v) We have illustrated how to consistently compare the EOB and TaylorF2 phasing, notably in the low-frequency regime, using the $Q_\omega(\omega)$ function. In the present paper this comparison was restricted to the quadrupole-monopole part of the phasing. It would be interesting to generalize it to the other parts, so to have in hands precise comparisons between the orbital, spin-orbit or spin-spin parts. We postpone such a comparison to future work.

10.3 Ref. [3] (Chapter 7)

Our results can be summarized as follows:

1. Starting from the EOB resummed expressions for the energy flux and energy along circular orbits, we have computed a `TaylorF2` point-mass, nonspinning, approximant at formal 5.5PN order. Such quasi-5.5PN approximant depends on some, yet uncalculated, ν-dependent, PN parameters that are set to zero.

2. Among various truncations of the 5.5PN approximant (3.5PN, 4PN, 4.5PN, 5PN, see Sec. 7.4), we have found that the 5.5PN phasing performs best when compared with the complete point-mass phasing obtained with `TEOBResumS`. Such phasing comparison was done exploiting its gauge-invariant description through the $Q_\omega = \hat{\omega}^2/\dot{\hat{\omega}}$ function. The main outcome of this analysis is that the EOB-derived quasi-5.5PN approximant is *remarkably close* to the complete EOB phasing up to the late inspiral (e.g. $\hat{\omega} \simeq 0.06$) and performs better than the standard (analytically complete) 3.5PN one. We tested that the performances

remain robust for unequal masses up to $q = 2$ and aligned spin cases with dimensionless spin magnitudes up to $\chi \sim \pm 0.1$.

3. To assess the use of the 5.5PN approximant in GW parameter estimations, we considered injection studies with hybrid waveforms of GW170817-like sources. The improved `TaylorF2` point-mass baseline reduces (or even eliminates) the biases on the measurability of the tidal polarizability parameter $\tilde{\Lambda}$ instead produced by the use the standard 3.5PN point-mass baseline. Therefore, the new 5.5PN approximant can be faithfully and effectively used in matched filtered searches and Bayesian parameter estimation.

We recommend the use of the new quasi-5.5PN approximant to improve the performance of the `TaylorF2` and substitute it to the 3.5PN in searches/parameter estimation. To ease this task, we have implemented all the new PN terms up to 5.5PN in the `LSC Algorithm Library Suite (LALSuite)`.

The performances of the 5.5PN approximant could be further improved towards higher frequencies by carefully tuning some of the free parameters. A preliminary investigation based on a equal masses nonspinning BNS is presented at the end of Sec. 7.4. We find that by tuning the 5PN parameter a_6^c and the 4PN coefficient $c_{22}^{4\mathrm{PN}}$ entering the $\ell = m = 2$ waveform amplitude, the phase difference between such flexed PN approximant and the EOB phasing is negligible essentially up to merger. This indicates that, while the PN series keeps oscillating even when high order terms come into play, future work might be devoted to effectively minimize such oscillations by suitably tuning such parameters.

10.4 Ref. [4] (Chapter 8) and the Multipolar TEOBResum code [7]

In this paper we have improved and generalized the factorization and resummation procedure of waveform amplitudes introduced in Ref. [9]. The key conceptual step of the approach relies on factorizing the orbital and the spin-dependence into two separate factors that can then be resummed separately in various ways. Our results can be summarized as follows:

(i) Concerning a circularized, (nonspinning) particle orbiting around a Kerr black hole, we have shown that the (relative) 6PN-accurate $\rho_{\ell m}$

functions can be factorized and resummed in a form that yields a more than satisfactory agreement (of the order of a few %) with the corresponding numerical (exact) function up to the last-stable-orbit. This is notably true for the case of a quasi-extremal black hole with dimensionless spin parameter $\hat{a} = +0.99$. One of the novelties with respect to previous work [9] is that the 6PN-accurate orbital function $\rho_{22}^{\rm org}$ is resummed with a Padé approximant (typically P_2^4). The same recipe proved to work essentially the same way for all subdominant modes up to $\ell = 6$, modulo a few exceptions where working at either higher or lower PN-information proved a better choice (see Table 8.1). More concretely, the factorization-resummation procedure allows us to obtain an analytic flux, summed over all multipoles up to $\ell = 6$, that is consistent at the 5% fractional level up to the LSO, for the most demanding case of $\hat{a} = +0.99$. This result is accomplished relying only on purely analytical information, without any additional fit to the numerical fluxes. We recall that this route was followed instead in Ref. [305] , where several higher-PN terms, unknown at the time, were calibrated to the same Teukolsky data we are using here. The fits were able to improve the standard $\rho_{\ell m}$-nonresummed flux so to have a fractional difference at the LSO of the order (or below) 1%. We have briefly illustrated (for the $\ell = m = 2$ mode only, see end of Sec. 8.2) that an analogous route can be followed also in our framework and that it is easy to reach analytical/numerical fractional differences in ρ_{22} of the order of 0.1% at the LSO for $\hat{a} = +0.99$ by just choosing one effective parameter entering at 6.5PN order in the resummed spin factor $\bar{\rho}_{22}^{\rm S}$. Alternatively, we want to remind that we have explored only a few of the many possibile choices. Focusing on the $(2, 2)$ mode only for definitess, the logic driving our approach is: first (i), to simplify things we choose to keep the same PN-order for both the orbital and PN factors; then (ii), as a similarly simple choice to reduce the growth of the spin factor in the strong-field regime (see discussion in Ref. [9]), we resummed it with its inverse-Taylor approximant; (iii) finally, we found that a good match with the exact numerical data was found by taking the P_2^4 Padé approximant of the orbital factor. Once the factorization paradigm is accepted, any of the points (i)-(iii) above could be, in principle, changed. For example, for $(3, 1)$ we found that the numerical/analytical agreement gets improved by keeping the spin factor at 8PN accuracy and the orbital factor just at 4PN accuracy resummed with a $(3, 1)$ Padé approximant.

Similarly, for some multipoles like $(3,3)$ and $(4,4)$ things are such that the straightforward, Taylor-expanded, form of the orbital factor yields a better agreement with the numerical results. These facts suggest that it might be possible that there are some special combinations of Padé approximant for the orbital part and PN-truncation of the spin factor that could further reduce the analytical/numerical disagreement in the near-LSO regime. Seen the large amount of PN-knowledge that is available (up to 20PN [307]), this would require a specific, dedicated study depending on the spin regime where one would like to use the resummed flux.

(ii) We have extended the factorization and resummation procedure to all the existing ν-dependent spin terms. This means that we go up to NNLO in the spin-orbit coupling, up to NLO in the spin-spin coupling and up to LO in the spin-cube coupling. This is done consistently for all multipoles currently known above the LO contributions ($\ell = 4$). In doing so, we propose to use the orbital part of the waveform in hybridized form, where currently known, ν-dependent orbital terms are hybridized with the test-mass term, as proposed long ago in [8]. The novelty here is that, to maintain the consistency with the choices done in the test-particle limit, each $\rho_{\ell m}$ is kept up to relative 6PN order (modulo a few exceptions), with the Padé-approximant that was chosen in the test-particle limit, however maintaining the full ν-dependence that is currently available in the low-order terms. By contrast, as a first choice, the spin-dependent factor is not hybridized with high-order test-particle results, but it is inverse resummed at the currently available ν-dependent PN order. We have explored the robustness of this choice on an indicative sample of binary configurations, contrasting the resummed amplitude with the plain, Taylor-expanded, $\rho_{\ell m}$. Since we do not have circularized comparable-mass BH data to compare with, the only effect that we could investigate for is the *consistency* between NNLO and NLO truncations of the waveform, as an indication of the analytical robustness of the resummed expressions. Our Figs. 8.3 (for $\ell = 2$) and 8.4 (for $\ell = 3$) show that, for the same binary, differences that are large for the Taylor-expanded $\rho_{\ell m}$ or $\delta m f_{\ell m}$ are either very much reduced, or practically negligible, in the resummed representation of the same functions. This effect is very striking on $\delta m f_{21}$, where not only one can see this effect, but the function is also qualitatively close

to the numerical one (see for example Fig. 5 of Ref. [9]).

These findings suggest that the resummed waveform amplitudes should be incorporated within the EOB approach as a new, state-of-the-art, analytical waveform paradigm. This was pointed out already in Ref. [9]. In particular, we expect that next-to-quasi-circular corrections [167] to the waveforms will generically have a smaller impact than in current EOB models [37], because they will hopefully have to bring just small corrections to the already good strong-field behavior of the analytical waveform. This was briefly pointed out already in Ref. [37], and has been recently confirmed in Ref. [7] (see Table I and Fig. 8 there, that we report here, for completeness, in Table 10.1 and Fig. 10.1 respectively).

(iii) Following Ref. [9], we wrote all spin-dependent expressions using as spin variables the Kerr parameters of the individual black holes divided by the total mass of the system, $\tilde{a}_i \equiv a_i/M = S_i/(m_i M)$. The use of these quantities to parametrize a spin-dependent function was already suggested in Ref. [34] in the context of informing a next-to-next-to-next-to-leading order spin-orbit effective parameter using NR simulations; similarly, the same spin variables allow for a simple recasting of the NLO correction to the centrifugal radius, that has rather complicated coefficients when written using the dimensionless spin variables $\chi_i = S_i/m_i^2$, see Eq. (58)-(65) of [34]. When using $\tilde{a}_i$, Eq. (58) of [34] reduces to the following very compact form

$$\delta a^2 = \frac{M^3}{r}\left\{\frac{5}{4}\tilde{a}_{12}\hat{a}_0 X_{12} - \left(\frac{5}{4}+\frac{\nu}{2}\right)\hat{a}_0^2 + \left(\frac{1}{2}+2\nu\right)\tilde{a}_1\tilde{a}_2\right\}. \tag{10.1}$$

The use of the $\tilde{a}_i$'s in our context, on top of providing similar simplifications in writing the formulas, is extremely convenient since these variables are natuarally connected to the (spinning) test-particle limit, that can be obtained straightforwardly by just putting $\nu = 0$ in the equations. On top of this, since our analytical writing of the fluxes makes absolutely transparent which terms combine to generate the (spinning) test-particle limit, it is technically clear how to hybridize the $\nu = 0$ information with $\nu \neq 0$ one *also* in the presence of spin, in order to have a

waveform model that is fully consistent with the test-mass results discussed at point (i) above. Though stating whether such test-particle information will have any important impact on LIGO/Virgo targeted waveform models requires deeper investigations, it will certainly allow us to improve their self-consistency all over the binary parameter space.

10.5 Ref. [5] (Chapter 9)

In this paper we have collected several new results concerning the gravitational waveform fluxes and amplitudes emitted by a spinning particle (i.e., a spinning test-black hole) on circular orbits around a Schwarzschild black hole at linear order in the particle spin. Our main findings are summarized as follows:

(i) We have analytically computed the PN-expanded multipolar energy fluxes up to $\ell = 7$. Each multipole is obtained at 5.5 PN order beyond the leading, Newtonian, contribution. This improves our current analytical knowledge of the fluxes in this corner of the parameter space, that was previously known only up to *global* 3.5PN order.

(ii) We have computed numerically the multipolar energy fluxes (and waveform amplitudes) up to $\ell = 6$ using two different, and independent, numerical codes. One is a frequency-domain code; the other uses a time-domain approach. We demonstrated the excellent mutual consistency between the two numerical approaches once the numerical data are suitably linearized in the spin of the particle. This allows us to provide accurate, circularized, waveform amplitudes up to the LSO for different values of the particle spin.

(iii) We compared to these numerical data, considered as exact, the PN-expanded analytical amplitudes as well as different flavors of their resummation. In particular, we could show that the standard resummation approach of Ref. [176], that is implemented in state-of-the-art waveform models for coalescing black-hole binaries, such as `SEOBNRv4` [36] or `TEOBResumS` [1], is *inaccurate* for $\ell + m$ odd modes and provides nonnegligible differences with the numerical data already in the early inspiral. This indicates that the procedure of Ref. [176] should be improved to construct a waveform model robust and accurate all over the BBH parameter space.

(iv) The most important result of this work is that the factorization of *only* the tail factor in the $\ell + m =$ odd modes allows one to obtain an excellent analytical/numerical agreement up to the LSO (and even below), for $-0.9 \leq \sigma \leq +0.9$, and for *all* odd-parity modes analyzed up to $\ell = 5$, see Fig. 9.5. This result opens at least two questions. First of all, one wonders whether the only-tail factorization would be helpful also to resumming the fluxes emitted by a nonspinning particle orbiting a Kerr black hole. Resumming that PN series has always been a challenge [176] that was solved, to a certain extent, only through the orbital factorization (and additional resummation) procedure of Refs. [9, 4]. Hopefully the only-tail factorization approach might be useful in that case *at least* for what concerns the terms linear in the black-hole spin. On the other hand, our findings also suggest that it might be worth investigating the performance of the only-tail factorization procedure *also* in the $\nu \neq 0$ case. The accuracy of such odd-parity waveform amplitudes should then be carefully evaluated by performing extensive comparisons between a so-constructed EOB waveform model and state-of-the-art NR simulations.

(v) We also explored the accuracy of the orbital-factorization/resummation approach of Ref. [9, 4], notably in the form developed for the odd-m modes in the $\nu \neq 0$ case. We do so by truncating the PN information at the same PN order where ν-dependent corrections are known. This approach has been recently used to improve the behavior of the $\ell = 2$, $m = 1$ waveform amplitude in a new, EOB-based, multipolar waveform model [321]. For this mode, we found (see top-left panel of Fig. 9.6) that the numerical/analytical agreement is rather good, though not at the level of the only-tail factorized case mentioned above. The situation is even worse for the subdominant modes (except the $\ell = m = 3$ one). Our results seem to suggest that the resummation of Ref. [9, 4] should be replaced by the only-tail factorization one, since it is simpler and more accurate. More investigations, notably when both objects are spinning, will be needed to confirm this preliminary conclusion.

Table 10.1: Resummation choices used to build the multipolar EOB waveform of Ref. [7]. The bar denotes resummation using the inverse Taylor expansion, as described by Eq. (5) of Ref. [9]. The PN-order should be intended relative to the leading-order term and also indicates the order of the additional (spinning) test-particle terms. For example, 3.5PN means that we take a polynomial of the form $1+x^{3/2}+x^2+x^{5/2}+...+x^{7/2}$, with the known ν dependence in the coefficients. Instead, 1.5^{+1}PN means that we add to the ν-dependent 1.5PN-accurate polynomial an additional term proportional to $x^{5/2}$ obtained by suitably incorporating spinning p article terms as illustrated in Sec. 8.5.2 of Chapt. 8. We denote Padé resummation by P^n_d, where $N=n+d$ is the PN order. These choices, motived by the work done in Ref. [4], have reduced the impact of NQC corrections as indicatively showed in Fig. 10.1 for some multipoles.

(ℓ,m)	Resummation choices		Relative PN order	
	orbital	spin	orbital	spin
$(2,2)$	$P^5_0[\rho^{\rm orb}_{22}]$	$T[\rho^{\rm S}_{22}]$	3^{+2}PN	3.5PN without NNLO SO term
$(2,1)$	$P^5_1[\rho_{21}]$	$\hat{f}^{\rm S}_{21}=X_{12}\overline{\hat{f}^{\rm S_{(0)}}_{21}}-\frac{3}{2}\tilde{a}_{12}x^{1/2}\overline{\hat{f}^{\rm S_{(1)}}_{21}}$	3^{+3}PN	2.5PN
$(3,3)$	$P^4_2[\rho_{33}]$	$\hat{f}^{\rm S}_{33}=X_{12}\overline{\hat{f}^{\rm S_{(0)}}_{33}}+\left(-\frac{1}{4}+\frac{5}{2}\nu\right)\tilde{a}_{12}x^{3/2}\hat{f}^{\rm S_{(1)}}_{33}$	3^{+3}PN	2.5PN
$(3,2)$	$P^4_2[\rho_{32}]$	$T[\rho^{\rm S}_{32}]$	2^{+2}PN	1.5^{+1}PN (SO only)
$(3,1)$	$P^3_2[\rho^{\rm orb}_{31}]$	$\hat{f}^{\rm S}_{31}=X_{12}\overline{\hat{f}^{\rm S_{(0)}}_{31}}+\left(-\frac{9}{4}+\frac{13}{2}\nu\right)\tilde{a}_{12}x^{3/2}\hat{f}^{\rm S_{(1)}}_{31}$	3^{+2}PN	2.5PN
$(4,4)$	$P^6_0[\rho^{\rm orb}_{44}]$	$T[\rho^{\rm S}_{44}]$	2^{+4}PN	1.5^{+2}PN (SO only)
$(4,3)$	$P^4_2[\rho^{\rm orb}_{43}]$	$\hat{f}^{\rm S}_{43}=X_{12}\hat{f}^{\rm S_{(0)}}_{43}-\frac{5}{4}\tilde{a}_{12}x^{1/2}$	1^{+5}PN	0.5PN (SO only)
$(4,2)$	$P^6_0[\rho^{\rm orb}_{42}]$	$T[\rho^{\rm S}_{42}]$	2^{+4}PN	1.5^{+3}PN (SO only)
$(4,1)$	$P^4_2[\rho^{\rm orb}_{41}]$	$\hat{f}^{\rm S}_{41}=X_{12}\hat{f}^{\rm S_{(0)}}_{41}-\frac{5}{4}\tilde{a}_{12}x^{1/2}$	1^{+5}PN	0.5PN (SO only)
$(5,5)$	$P^6_0[\rho^{\rm orb}_{55}]$	$\hat{f}^{\rm S}_{55}=X_{12}\overline{\hat{f}^{\rm S_{(0)}}_{55}}+10\nu\frac{(1-3\nu)}{3-6\nu}\tilde{a}_{12}x^{3/2}$	1^{+5}PN	2PN

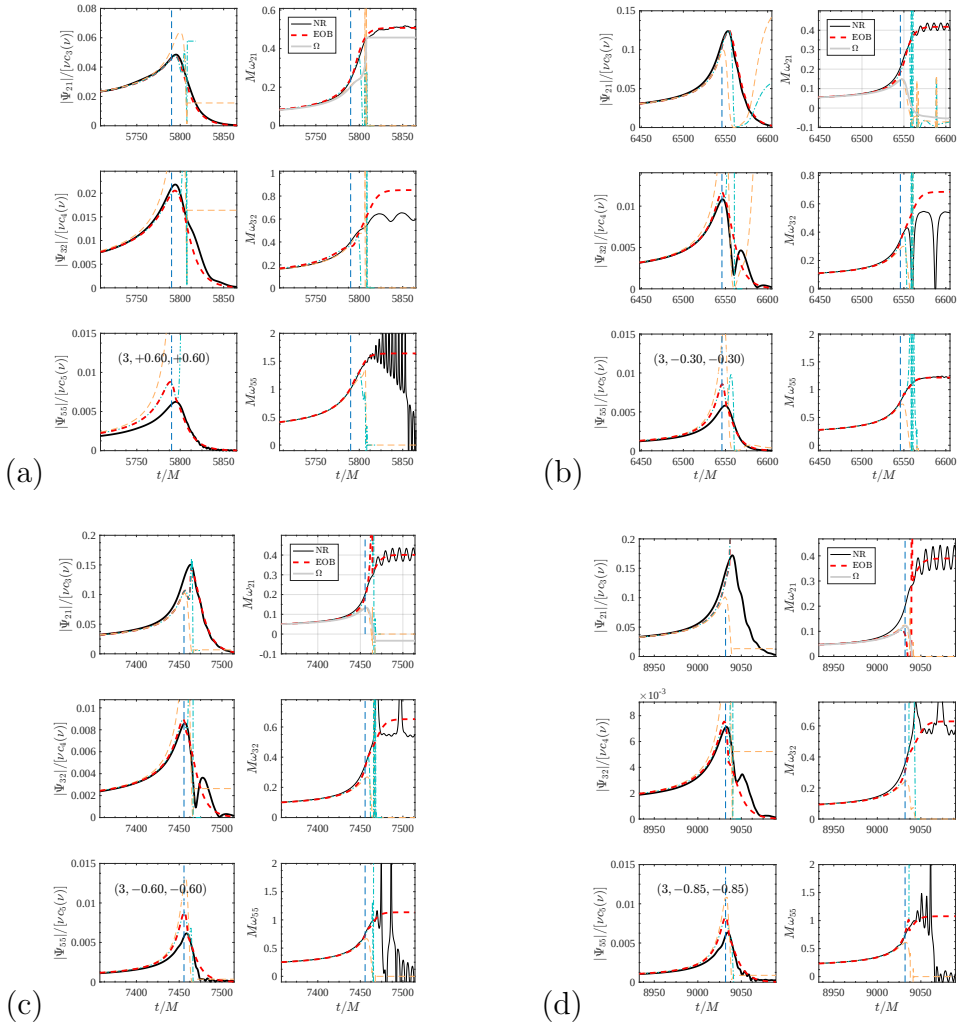

Figure 10.1: Fig. 8 of Ref. [7]. Frequency and amplitude for the $(2,1)$, $(3,2)$ and $(5,5)$ modes for some illustrative BBH configurations. On top of the NR (black) and complete EOB curves (red, dashed), the plots also show: (i) the analytical EOB waveform, without NQC corrections and ringdown (orange online) and (ii) the NQC-augmented EOB waveform (light-blue online). The dashed, vertical, line marks the merger location, i.e. the peak of the $\ell = m = 2$ waveform amplitude. The $(2,1)$ frequency plots also incorporate the orbital frequency Ω (grey online). The construction of the $(2,1)$ mode through merger and ringdown cannot be accomplished correctly for large values of the spins anti-aligned with the orbital angular momentum [see panel (c) and (d) of Ref. [7]].

Bibliography

[1] Alessandro Nagar et al. Time-domain effective-one-body gravitational waveforms for coalescing compact binaries with nonprecessing spins, tides and self-spin effects. *Phys. Rev.*, D98(10):104052, 2018. doi: 10.1103/PhysRevD.98.104052.

[2] Alessandro Nagar, Francesco Messina, Piero Rettegno, Donato Bini, Thibault Damour, Andrea Geralico, Sarp Akcay, and Sebastiano Bernuzzi. Nonlinear-in-spin effects in effective-one-body waveform models of spin-aligned, inspiralling, neutron star binaries. *Phys. Rev.*, D99:044007, 2019. doi: 10.1103/PhysRevD.99.044007.

[3] Francesco Messina, Reetika Dudi, Alessandro Nagar, and Sebastiano Bernuzzi. Quasi-5.5PN TaylorF2 approximant for compact binaries: point-mass phasing and impact on the tidal polarizability inference. *Phys. Rev.*, D99:124051, 2019. doi: 10.1103/PhysRevD.99.124051.

[4] Francesco Messina, Alberto Maldarella, and Alessandro Nagar. Factorization and resummation: A new paradigm to improve gravitational wave amplitudes. II: the higher multipolar modes. *Phys. Rev.*, D97(8): 084016, 2018. doi: 10.1103/PhysRevD.97.084016.

[5] Alessandro Nagar, Francesco Messina, Chris Kavanagh, Georgios Lukes-Gerakopoulos, Niels Warburton, Sebastiano Bernuzzi, and Enno Harms. Factorization and resummation: A new paradigm to improve gravitational wave amplitudes. III: the spinning test-body terms. *Phys. Rev.*, D100(10):104056, 2019. doi: 10.1103/PhysRevD.100.104056.

[6] Sarp Akcay, Sebastiano Bernuzzi, Francesco Messina, Alessandro Nagar, Néstor Ortiz, and Piero Rettegno. Effective-one-body multipolar

waveform for tidally interacting binary neutron stars up to merger. *Phys. Rev.*, D99(4):044051, 2019. doi: 10.1103/PhysRevD.99.044051.

[7] Alessandro Nagar, Gunnar Riemenschneider, Geraint Pratten, Piero Rettegno, and Francesco Messina. A multipolar effective one body waveform model for spin-aligned black hole binaries. 2020.

[8] Thibault Damour, Bala R. Iyer, and Alessandro Nagar. Improved resummation of post-Newtonian multipolar waveforms from circularized compact binaries. *Phys. Rev.*, D79:064004, 2009. doi: 10.1103/PhysRevD.79.064004.

[9] Alessandro Nagar and Abhay Shah. Factorization and resummation: A new paradigm to improve gravitational wave amplitudes. *Phys. Rev.*, D94(10):104017, 2016. doi: 10.1103/PhysRevD.94.104017.

[10] B. P. Abbott et al. GWTC-1: A Gravitational-Wave Transient Catalog of Compact Binary Mergers Observed by LIGO and Virgo during the First and Second Observing Runs. 2018.

[11] Francesco Messina and Alessandro Nagar. Parametrized-4.5PN TaylorF2 approximants and tail effects to quartic nonlinear order from the effective one body formalism. *Phys. Rev.*, D95(12):124001, 2017. doi: 10.1103/PhysRevD.95.124001,10.1103/PhysRevD.96.049907. [Erratum: Phys. Rev.D96,no.4,049907(2017)].

[12] Albert Einstein. The Foundation of the General Theory of Relativity. *Annalen Phys.*, 49(7):769–822, 1916. doi: 10.1002/andp.200590044,10.1002/andp.19163540702. [Annalen Phys.14,517(2005); ,65(1916); Annalen Phys.354,no.7,769(1916)].

[13] Albert Einstein. Über Gravitationswellen. *Sitzungsber. Preuss. Akad. Wiss. Berlin (Math. Phys.)*, 1918:154–167, 1918.

[14] J. Weber. Detection and Generation of Gravitational Waves. *Phys. Rev.*, 117:306–313, 1960. doi: 10.1103/PhysRev.117.306.

[15] J. Weber. Observation of the Thermal Fluctuations of a Gravitational-Wave Detector. *Phys. Rev. Lett.*, 17:1228–1230, 1966. doi: 10.1103/PhysRevLett.17.1228.

[16] J. Weber. Gravitational-Wave-Detector Events. *Phys. Rev. Lett.*, 20 (23):1307, 1968. doi: 10.1103/PhysRevLett.20.1307.

[17] LLuis Bel, T. Damour, N. Deruelle, J. Ibanez, and J. Martin. Poincaré-invariant gravitational field and equations of motion of two pointlike objects: The postlinear approximation of general relativity. *Gen. Rel. Grav.*, 13:963–1004, 1981. doi: 10.1007/BF00756073.

[18] Thibault Damour and Nathalie Deruelle. Radiation Reaction and Angular Momentum Loss in Small Angle Gravitational Scattering. *Phys. Lett.*, A87:81, 1981. doi: 10.1016/0375-9601(81)90567-3.

[19] R.A. Hulse and J.H. Taylor. Discovery of a pulsar in a binary system. *Astrophys.J.*, 195:L51–L53, 1975. doi: 10.1086/181708.

[20] R.A. Hulse and J.H. Taylor. A High-Sensitivity Pulsar Survey. *Astrophys. J. Lett.*, 191:L59, 1974. doi: 10.1086/181548.

[21] Luc Blanchet and Thibault Damour. Méthode d'itération post-Minkowskienne et structure des champs gravitationnels radiatifs. *Compt. Rend. Acad. Sci. Ser. II*, 298(10):431–434, 1984.

[22] Luc Blanchet and Thibault Damour. Multipolar radiation reaction in general relativity. *Phys. Lett.*, A104:82–86, 1984. doi: 10.1016/0375-9601(84)90967-8.

[23] L. Blanchet and T. Damour. Postnewtonian generation of gravitational waves. *Annales Poincare Phys.Theor.*, 50:377–408, 1989.

[24] Luc Blanchet and Thibault Damour. Hereditary effects in gravitational radiation. *Phys. Rev.*, D46:4304–4319, 1992.

[25] Luc Blanchet, Thibault Damour, Bala R. Iyer, Clifford M. Will, and Alan.G. Wiseman. Gravitational radiation damping of compact binary systems to second postNewtonian order. *Phys.Rev.Lett.*, 74:3515–3518, 1995. doi: 10.1103/PhysRevLett.74.3515.

[26] T. Damour and Bala R. Iyer. Multipole analysis for electromagnetism and linearized gravity with irreducible cartesian tensors. *Phys. Rev.*, D43:3259–3272, 1991. doi: 10.1103/PhysRevD.43.3259.

[27] Frans Pretorius. Evolution of binary black hole spacetimes. *Phys. Rev. Lett.*, 95:121101, 2005. doi: 10.1103/PhysRevLett.95.121101.

[28] A. Buonanno and T. Damour. Effective one-body approach to general relativistic two-body dynamics. *Phys. Rev.*, D59:084006, 1999. doi: 10.1103/PhysRevD.59.084006.

[29] Alessandra Buonanno and Thibault Damour. Transition from inspiral to plunge in binary black hole coalescences. *Phys. Rev.*, D62:064015, 2000. doi: 10.1103/PhysRevD.62.064015.

[30] Sebastian Khan, Sascha Husa, Mark Hannam, Frank Ohme, Michael Pürrer, Xisco Jiménez Forteza, and Alejandro Bohé. Frequency-domain gravitational waves from nonprecessing black-hole binaries. II. A phenomenological model for the advanced detector era. *Phys. Rev.*, D93 (4):044007, 2016. doi: 10.1103/PhysRevD.93.044007.

[31] Andrea Taracchini, Alessandra Buonanno, Yi Pan, Tanja Hinderer, Michael Boyle, et al. Effective-one-body model for black-hole binaries with generic mass ratios and spins. *Phys.Rev.*, D89(6):061502, 2014. doi: 10.1103/PhysRevD.89.061502.

[32] Mark Hannam, Patricia Schmidt, Alejandro Bohé, Le¨ila Haegel, Sascha Husa, Frank Ohme, Geraint Pratten, and Michael Pürrer. Simple Model of Complete Precessing Black-Hole-Binary Gravitational Waveforms. *Phys. Rev. Lett.*, 113(15):151101, 2014. doi: 10.1103/PhysRevLett.113.151101.

[33] Patricia Schmidt, Frank Ohme, and Mark Hannam. Towards models of gravitational waveforms from generic binaries II: Modelling precession effects with a single effective precession parameter. *Phys. Rev.*, D91 (2):024043, 2015. doi: 10.1103/PhysRevD.91.024043.

[34] Alessandro Nagar, Thibault Damour, Christian Reisswig, and Denis Pollney.

[35] Stanislav Babak, Andrea Taracchini, and Alessandra Buonanno. Validating the effective-one-body model of spinning, precessing binary black holes against numerical relativity. *Phys. Rev.*, D95(2):024010, 2017. doi: 10.1103/PhysRevD.95.024010.

[36] Alejandro Bohé et al. Improved effective-one-body model of spinning, nonprecessing binary black holes for the era of gravitational-wave astrophysics with advanced detectors. *Phys. Rev.*, D95(4):044028, 2017. doi: 10.1103/PhysRevD.95.044028.

[37] Alessandro Nagar, Gunnar Riemenschneider, and Geraint Pratten. Impact of Numerical Relativity information on effective-one-body waveform models. *Phys. Rev.*, D96(8):084045, 2017. doi: 10.1103/PhysRevD.96.084045.

[38] B. P. Abbott et al. Observation of Gravitational Waves from a Binary Black Hole Merger. *Phys. Rev. Lett.*, 116(6):061102, 2016. doi: 10.1103/PhysRevLett.116.061102.

[39] B. P. Abbott et al. GW151226: Observation of Gravitational Waves from a 22-Solar-Mass Binary Black Hole Coalescence. *Phys. Rev. Lett.*, 116(24):241103, 2016. doi: 10.1103/PhysRevLett.116.241103.

[40] B. P. Abbott et al. GW170814: A Three-Detector Observation of Gravitational Waves from a Binary Black Hole Coalescence. *Phys. Rev. Lett.*, 119(14):141101, 2017. doi: 10.1103/PhysRevLett.119.141101.

[41] Benjamin P. Abbott et al. GW170104: Observation of a 50-Solar-Mass Binary Black Hole Coalescence at Redshift 0.2. *Phys. Rev. Lett.*, 118 (22):221101, 2017. doi: 10.1103/PhysRevLett.118.221101.

[42] B.. P.. Abbott et al. GW170608: Observation of a 19-solar-mass Binary Black Hole Coalescence. *Astrophys. J.*, 851(2):L35, 2017. doi: 10.3847/2041-8213/aa9f0c.

[43] Benjamin P. Abbott et al. GW170817: Observation of Gravitational Waves from a Binary Neutron Star Inspiral. *Phys. Rev. Lett.*, 119(16): 161101, 2017. doi: 10.1103/PhysRevLett.119.161101.

[44] B. P. Abbott et al. Properties of the Binary Black Hole Merger GW150914. *Phys. Rev. Lett.*, 116(24):241102, 2016. doi: 10.1103/PhysRevLett.116.241102.

[45] J. Veitch et al. Parameter estimation for compact binaries with ground-based gravitational-wave observations using the LALInference software

library. *Phys. Rev.*, D91(4):042003, 2015. doi: 10.1103/PhysRevD.91.042003.

[46] J. Veitch and A. Vecchio. Bayesian coherent analysis of in-spiral gravitational wave signals with a detector network. *Phys.Rev.*, D81:062003, 2010. doi: 10.1103/PhysRevD.81.062003.

[47] Thibault Damour. Gravitational Self Force in a Schwarzschild Background and the Effective One Body Formalism. *Phys. Rev.*, D81: 024017, 2010. doi: 10.1103/PhysRevD.81.024017.

[48] Eric Poisson. The Gravitational self-force. In *General relativity and gravitation. Proceedings, 17th International Conference, GR17, Dublin, Ireland, July 18-23, 2004*, pages 119–141, 2004. doi: 10.1142/9789812701688_0012.

[49] Yasushi Mino, Misao Sasaki, and Takahiro Tanaka. Gravitational radiation reaction to a particle motion. *Phys.Rev.*, D55:3457–3476, 1997. doi: 10.1103/PhysRevD.55.3457.

[50] Theodore C. Quinn and Robert M. Wald. An Axiomatic approach to electromagnetic and gravitational radiation reaction of particles in curved space-time. *Phys.Rev.*, D56:3381–3394, 1997. doi: 10.1103/PhysRevD.56.3381.

[51] B. Bertotti and J. Plebanski. Numerical Simulations of Driven Relativistic MHD Turbulence. *Ann. Phys. (N.Y.)*, II:169, year =.

[52] T. Damour. Advances in mathematics and theoretical physics, accademia nazionale dei lincei, roma, italy. `http://www.mat.uniroma2.it/tlc/17SIMP/Slides/damour.pdf`, 2017.

[53] K. S. Thorne. Multipole Expansions of Gravitational Radiation. *Rev. Mod. Phys.*, 52:299–339, 1980.

[54] Luc Blanchet and Thibault Damour. Radiative gravitational fields in general relativity I. general structure of the field outside the source. *Phil. Trans. Roy. Soc. Lond.*, A320:379–430, 1986. doi: 10.1098/rsta.1986.0125.

[55] Richard A. Isaacson. Gravitational Radiation in the Limit of High Frequency. I. The Linear Approximation and Geometrical Optics. *Phys. Rev.*, 166:1263–1271, 1968. doi: 10.1103/PhysRev.166.1263.

[56] Richard A. Isaacson. Gravitational Radiation in the Limit of High Frequency. II. Nonlinear Terms and the Ef fective Stress Tensor. *Phys. Rev.*, 166:1272–1279, 1968. doi: 10.1103/PhysRev.166.1272.

[57] Tullio Regge and John A. Wheeler. Stability of a Schwarzschild singularity. *Phys. Rev.*, 108:1063–1069, 1957.

[58] Frank J. Zerilli. Effective potential for even parity Regge-Wheeler gravitational perturbation equations. *Phys. Rev. Lett.*, 24:737–738, 1970. doi: 10.1103/PhysRevLett.24.737.

[59] Saul A. Teukolsky. Perturbations of a rotating black hole. 1. Fundamental equations for gravitational electromagnetic and neutrino field perturbations. *Astrophys. J.*, 185:635–647, 1973. doi: 10.1086/152444.

[60] Enno Harms, Sebastiano Bernuzzi, and Bernd Brügmann. Numerical solution of the 2+1 Teukolsky equation on a hyperboloidal and horizon penetrating foliation of Kerr and application to late-time decays. *Class.Quant.Grav.*, 30:115013, 2013. doi: 10.1088/0264-9381/30/11/115013.

[61] Enno Harms, Sebastiano Bernuzzi, Alessandro Nagar, and Anil Zenginoglu. A new gravitational wave generation algorithm for particle perturbations of the Kerr spacetime. *Class.Quant.Grav.*, 31:245004, 2014. doi: 10.1088/0264-9381/31/24/245004.

[62] Misao Sasaki and Hideyuki Tagoshi. Analytic black hole perturbation approach to gravitational radiation. *Living Rev.Rel.*, 6:6, 2003.

[63] Robert A. Eisenstein. Numerical Relativity and the Discovery of Gravitational Waves. *Annalen Phys.*, 531(8):1800348, 2019. doi: 10.1002/andp.201800348.

[64] Luc Blanchet. Gravitational Radiation from Post-Newtonian Sources and Inspiralling Compact Binaries. *Living Rev. Relativity*, 17:2, 2014. doi: 10.12942/lrr-2014-2.

[65] Lev D. Landau and Evgenij M. Lifsits. *Teoria dei campi*. Editori Riuniti Mir, Roma, 3rd edition, 1999.

[66] P. C. Peters and J. Mathews. Gravitational radiation from point masses in a Keplerian orbit. *Phys. Rev.*, 131:435–439, 1963. doi: 10.1103/PhysRev.131.435.

[67] P. C. Peters. Gravitational Radiation and the Motion of Two Point Masses. *Phys. Rev.*, 136:B1224–B1232, 1964. doi: 10.1103/PhysRev.136.B1224.

[68] Curt Cutler and Eanna E. Flanagan. Gravitational waves from merging compact binaries: How accurately can one extract the binary's parameters from the inspiral wave form? *Phys.Rev.*, D49:2658–2697, 1994. doi: 10.1103/PhysRevD.49.2658.

[69] Curt Cutler et al. The Last three minutes: issues in gravitational wave measurements of coalescing compact binaries. *Phys. Rev. Lett.*, 70: 2984–2987, 1993. doi: 10.1103/PhysRevLett.70.2984.

[70] L. Blanchet and Gerhard Schaefer. Gravitational wave tails and binary star systems. *Class. Quant. Grav.*, 10:2699–2721, 1993. doi: 10.1088/0264-9381/10/12/026.

[71] F., J. Dyson. *Gravitational Machines, in A.G.W. Cameron, ed., Interstellar Communication*. New York: Benjamin Press, 1963.

[72] John D. Jackson. *Classical Electrodynamics*. New York: John Wiley & Sons, 3rd edition, 1999.

[73] B.R Iyer. *Multipole expansion techniques for gravitational radiation problems*. IUCAA, 1993.

[74] Tanguy Marchand, Luc Blanchet, and Guillaume Faye. Gravitational-wave tail effects to quartic non-linear order. *Class. Quant. Grav.*, 33 (24):244003, 2016. doi: 10.1088/0264-9381/33/24/244003.

[75] Alejandro Bohé, Guillaume Faye, Sylvain Marsat, and Edward K. Porter. Quadratic-in-spin effects in the orbital dynamics and gravitational-wave energy flux of compact binaries at the 3PN order. *Class. Quant. Grav.*, 32(19):195010, 2015. doi: 10.1088/0264-9381/32/19/195010.

[76] Sylvain Marsat. Cubic order spin effects in the dynamics and gravitational wave energy flux of compact object binaries. *Class. Quant. Grav.*, 32(8):085008, 2015. doi: 10.1088/0264-9381/32/8/085008.

[77] Sylvain Marsat, Alejandro Bohé, Luc Blanchet, and Alessandra Buonanno. Next-to-leading tail-induced spin?orbit effects in the gravitational radiation flux of compact binaries. *Class. Quant. Grav.*, 31: 025023, 2014. doi: 10.1088/0264-9381/31/2/025023.

[78] V. Moncrief. Gravitational perturbations of spherically symmetric systems. I. The exterior problem. *Ann. Phys.*, 88:323–342, 1974.

[79] C. Flammer. *Spheroidal Wave Functions*. Stanford University Press, 1957.

[80] J. N. Goldberg, A. J. MacFarlane, E. T. Newman, F. Rohrlich, and E. C. G. Sudarshan. Spin s spherical harmonics and edth. *J. Math. Phys.*, 8:2155, 1967.

[81] T. Damour. Ondes gravitationnelles et trous noirs binaires, institut henri poincaré, paris. `http://www.bourbaphy.fr/december2016.html`, 2016.

[82] Y. Foures-Bruhat. Theoreme d'existence pour certains systemes derivees partielles non lineaires. *Acta Mat.*, 88:141–225, 1952.

[83] David Garfinkle. Harmonic coordinate method for simulating generic singularities. *Phys.Rev.*, D65:044029, 2002. doi: 10.1103/PhysRevD.65.044029.

[84] Helmut Friedrich. Conformal Einstein evolution. *Lect. Notes Phys.*, 604:1–50, 2002. [,1(2002)].

[85] Othmar Brodbeck, Simonetta Frittelli, Peter Hubner, and Oscar A. Reula. Einstein's equations with asymptotically stable constraint propagation. *J.Math.Phys.*, 40:909–923, 1999. doi: 10.1063/1.532694.

[86] Carsten Gundlach, Jose M. Martin-Garcia, Gioel Calabrese, and Ian Hinder. Constraint damping in the Z4 formulation and harmonic gauge. *Class. Quant. Grav.*, 22:3767–3774, 2005. doi: 10.1088/0264-9381/22/17/025.

[87] Manuela Campanelli, C. O. Lousto, P. Marronetti, and Y. Zlochower. Accurate Evolutions of Orbiting Black-Hole Binaries Without Excision. *Phys. Rev. Lett.*, 96:111101, 2006. doi: 10.1103/PhysRevLett.96.111101.

[88] John G. Baker, Joan Centrella, Dae-Il Choi, Michael Koppitz, and James van Meter. Gravitational wave extraction from an inspiraling configuration of merging black holes. *Phys. Rev. Lett.*, 96:111102, 2006. doi: 10.1103/PhysRevLett.96.111102.

[89] Bernd Brügmann, Wolfgang Tichy, and Nina Jansen. Numerical simulation of orbiting black holes. *Phys. Rev. Lett.*, 92:211101, 2004. doi: 10.1103/PhysRevLett.92.211101.

[90] Lee Lindblom, Mark A. Scheel, Lawrence E. Kidder, Robert Owen, and Oliver Rinne. A New generalized harmonic evolution system. *Class.Quant.Grav.*, 23:S447–S462, 2006. doi: 10.1088/0264-9381/23/16/S09.

[91] Mark A. Scheel, Harald P. Pfeiffer, Lee Lindblom, Lawrence E. Kidder, Oliver Rinne, and Saul A. Teukolsky. Solving Einstein's equations with dual coordinate frames. *Phys. Rev.*, D74:104006, 2006. doi: 10.1103/PhysRevD.74.104006.

[92] Lee Lindblom, Keith D. Matthews, Oliver Rinne, and Mark A. Scheel. Gauge Drivers for the Generalized Harmonic Einstein Equations. *Phys.Rev.*, D77:084001, 2008. doi: 10.1103/PhysRevD.77.084001.

[93] Scott A. Hughes, Steve Drasco, Eanna E. Flanagan, and Joel Franklin. Gravitational radiation reaction and inspiral waveforms in the adiabatic limit. *Phys. Rev. Lett.*, 94:221101, 2005. doi: 10.1103/PhysRevLett.94.221101.

[94] William Krivan, Pablo Laguna, Philippos Papadopoulos, and Nils Andersson. Dynamics of perturbations of rotating black holes. *Phys. Rev.*, D56:3395–3404, 1997. doi: 10.1103/PhysRevD.56.3395.

[95] Anil Zenginoğlu. Hyperboloidal foliations and scri-fixing. *Class. Quant. Grav.*, 25:145002, 2008. doi: 10.1088/0264-9381/25/14/145002.

[96] Sebastiano Bernuzzi, Alessandro Nagar, and Anil Zenginoglu. Binary black hole coalescence in the large-mass-ratio limit: the hyperboloidal layer method and waveforms at null infinity. *Phys.Rev.*, D84:084026, 2011. doi: 10.1103/PhysRevD.84.084026.

[97] Ian Hinder, Alessandra Buonanno, Michael Boyle, Zachariah B. Etienne, James Healy, et al. Error-analysis and comparison to analytical models of numerical waveforms produced by the NRAR Collaboration. *Class.Quant.Grav.*, 31:025012, 2013. doi: 10.1088/0264-9381/31/2/025012.

[98] S.W. Hawking and J.B. Hartle. Energy and angular momentum flow into a black hole. *Commun.Math.Phys.*, 27:283–290, 1972. doi: 10.1007/BF01645515.

[99] Thibault Damour, Bala R. Iyer, and B. S. Sathyaprakash. A Comparison of search templates for gravitational waves from binary inspiral. *Phys. Rev.*, D63:044023, 2001. doi: 10.1103/PhysRevD.63.044023,10.1103/PhysRevD.72.029902. [Erratum: Phys. Rev.D72,029902(2005)].

[100] K. S. Thorne. *Gravitomagnetism, Jets in Quasars, and the Stanford Gyroscope Experiment*. From the book "Near Zero: New Frontiers of Physics, Editors, J. D. Fairbank, B. S. DeiIVW, Jr., C. W. F. Everitt, P. F. Michelson, Copyright 1988 by W. H. Freeman 2nd Company, New York.

[101] Ruffini Remo Ohanian, Hans C. *Gravitation and Spacetime*. Norton, 2rd edition, 1994.

[102] Matteo Luca Ruggiero and Angelo Tartaglia. Gravitomagnetic effects. *Nuovo Cim.*, B117:743–768, 2002.

[103] Gerhard Schaefer. Gravitomagnetic effects. *Gen. Rel. Grav.*, 36:2223, 2004. doi: 10.1023/B:GERG.0000046180.97877.32.

[104] Thibault Damour, Michael Soffel, and Chong-ming Xu. General relativistic celestial mechanics. 1. Method and definition of reference systems. *Phys. Rev.*, D43:3273–3307, 1991. doi: 10.1103/PhysRevD.43.3273.

[105] Thibault Damour, Michael Soffel, and Chong-ming Xu. General relativistic celestial mechanics. 2. Translational equations of motion. *Phys. Rev.*, D45:1017–1044, 1992. doi: 10.1103/PhysRevD.45.1017.

[106] Thibault Damour, Michael Soffel, and Chong-ming Xu. General relativistic celestial mechanics. 3. Rotational equations of motion. *Phys. Rev.*, D47:3124–3135, 1993. doi: 10.1103/PhysRevD.47.3124.

[107] Thibault Damour, Michael Soffel, and Chong-ming Xu. General relativistic celestial mechanics. 4: Theory of satellite motion. *Phys. Rev.*, D49:618–635, 1994. doi: 10.1103/PhysRevD.49.618.

[108] Thibault Damour and Alessandro Nagar. Relativistic tidal properties of neutron stars. *Phys. Rev.*, D80:084035, 2009. doi: 10.1103/PhysRevD.80.084035.

[109] Eanna E. Flanagan and Tanja Hinderer. Constraining neutron star tidal Love numbers with gravitational wave detectors. *Phys. Rev.*, D77:021502, 2008. doi: 10.1103/PhysRevD.77.021502.

[110] Tanja Hinderer. Tidal Love numbers of neutron stars. *Astrophys.J.*, 677:1216–1220, 2008. doi: 10.1086/533487.

[111] Marc Favata. Are neutron stars crushed? gravitomagnetic tidal fields as a mechanism for binary-induced collapse. *Phys. Rev.*, D73:104005, 2006. doi: 10.1103/PhysRevD.73.104005.

[112] Kip S. Thorne and James B. Hartle. Laws of motion and precession for black holes and other bodies. *Phys. Rev.*, D31:1815–1837, 1984. doi: 10.1103/PhysRevD.31.1815.

[113] Thibault Damour and Orchidea Maria Lecian. On the gravitational polarizability of black holes. *Phys. Rev.*, D80:044017, 2009. doi: 10.1103/PhysRevD.80.044017.

[114] Lee Lindblom, Gregory Mendell, and James R. Ipser. Relativistic stellar pulsations with near - zone boundary conditions. *Phys. Rev.*, D56:2118–2126, 1997. doi: 10.1103/PhysRevD.56.2118.

[115] C. T. Cunningham, R. H. Price, and V. Moncrief. Radiation from collapsing relativistic stars. I - Linearized odd-parity radiation. *Astrophys. J.*, 224:643, 1978. doi: 10.1086/156413.

[116] Zeferino Andrade and Richard H. Price. Excitation of the odd parity quasinormal modes of compact objects. *Phys. Rev.*, D60:104037, 1999. doi: 10.1103/PhysRevD.60.104037.

[117] Jocelyn S. Read, Benjamin D. Lackey, Benjamin J. Owen, and John L. Friedman. Constraints on a phenomenologically parameterized neutron- star equation of state. *Phys. Rev.*, D79:124032, 2009. doi: 10.1103/PhysRevD.79.124032.

[118] Jocelyn S. Read, Charalampos Markakis, Masaru Shibata, Koji Uryu, Jolien D.E. Creighton, et al. Measuring the neutron star equation of state with gravitational wave observations. *Phys.Rev.*, D79:124033, 2009. doi: 10.1103/PhysRevD.79.124033.

[119] Chris Vuille and Jim Ipser. On the maximum mass of neutron stars. *AIP Conf. Proc.*, 493(1):60, 1999. doi: 10.1063/1.1301564.

[120] J. L. Zdunik, Michal Bejger, P. Haensel, and E. Gourgoulhon. Phase transitions in rotating neutron stars cores: back bending, stability, corequakes and pulsar timing. *Astron. Astrophys.*, 450:747–758, 2006. doi: 10.1051/0004-6361:20054260.

[121] Michal Bejger, P. Haensel, and J. L. Zdunik. Mixed-phase induced core-quakes and the changes in neutron star parameters. *Mon. Not. Roy. Astron. Soc.*, 359:699–706, 2005. doi: 10.1111/j.1365-2966.2005.08933.x.

[122] P. Haensel and Alexander Y. Potekhin. Analytical representations of unified equations of state of neutron-star matter. *Astron. Astrophys.*, 428:191–197, 2004.

[123] Masaru Shibata, Keisuke Taniguchi, and Koji Uryu. Merger of binary neutron stars with realistic equations of state in full general relativity. *Phys. Rev.*, D71:084021, 2005. doi: 10.1103/PhysRevD.71.084021.

[124] M. Prakash, T. L. Ainsworth, and J. M. Lattimer. Equation of state and the maximum mass of neutron stars. *Phys. Rev. Lett.*, 61:2518–2521, 1988. doi: 10.1103/PhysRevLett.61.2518.

[125] F. Douchin and P. Haensel. A unified equation of state of dense matter and neutron star structure. *Astron. Astrophys.*, 380:151–167, 2001.

[126] A. Akmal, V. R. Pandharipande, and D. G. Ravenhall. The equation of state for nucleon matter and neutron star structure. *Phys. Rev.*, C58: 1804–1828, 1998. doi: 10.1103/PhysRevC.58.1804.

[127] B. Friedman and V. R. Pandharipande. Hot and cold, nuclear and neutron matter. *Nucl. Phys.*, A361:502–520, 1981. doi: 10.1016/0375-9474(81)90649-7.

[128] Robert B. Wiringa, V. Fiks, and A. Fabrocini. Equation of state for dense nucleon matter. *Phys. Rev.*, C38:1010–1037, 1988.

[129] M. Baldo, I. Bombaci, and G. F. Burgio. Microscopic nuclear equation of state with three-body forces and neutron star structure. *Astron. Astrophys.*, 328:274–282, 1997.

[130] W. Zuo, I. Bombaci, and U. Lombardo. Asymmetric nuclear matter from extended Brueckner-Hartree-Fock approach. *Phys. Rev.*, C60: 024605, 1999. doi: 10.1103/PhysRevC.60.024605.

[131] L. Engvik, G. Bao, M. Hjorth-Jensen, E. Osnes, and E. Ostgaard. Asymmetric nuclear matter and neutron star properties. *Astrophys. J.*, 469:794, 1996. doi: 10.1086/177827.

[132] H. Müther, M. Prakash, and T. L. Ainsworth. The nuclear symmetry energy in relativistic Brueckner-Hartree-Fock calculations. *Phys. Lett.*, B199:469–474, 1987. doi: 10.1016/0370-2693(87)91611-X.

[133] Horst Müller and Brian D. Serot. Relativistic mean field theory and the high density nuclear equation of state. *Nucl. Phys.*, A606:508–537, 1996. doi: 10.1016/0375-9474(96)00187-X.

[134] Eric Poisson. Gravitational waves from inspiraling compact binaries: The Quadrupole moment term. *Phys. Rev.*, D57:5287–5290, 1998. doi: 10.1103/PhysRevD.57.5287.

[135] Ian Harry and Tanja Hinderer. Observing and measuring the neutron-star equation-of-state in spinning binary neutron star systems. *Class. Quant. Grav.*, 35(14):145010, 2018. doi: 10.1088/1361-6382/aac7e3.

[136] Michele Levi and Jan Steinhoff. Complete conservative dynamics for inspiralling compact binaries with spins at fourth post-Newtonian order. *arXiv*, 1607.04252, 2016.

[137] Kent Yagi and Nicolas Yunes. I-Love-Q Relations in Neutron Stars and their Applications to Astrophysics, Gravitational Waves and Fundamental Physics. *Phys.Rev.*, D88:023009, 2013. doi: 10.1103/PhysRevD.88.023009.

[138] Patrick R. Brady, Jolien D. E. Creighton, and Kip S. Thorne. Computing the merger of black hole binaries: The IBBH problem. *Phys. Rev.*, D58:061501, 1998. doi: 10.1103/PhysRevD.58.061501.

[139] Thibault Damour, Bala R. Iyer, and B. S. Sathyaprakash. Improved filters for gravitational waves from inspiralling compact binaries. *Phys. Rev.*, D57:885–907, 1998. doi: 10.1103/PhysRevD.57.885.

[140] Alessandra Buonanno and Thibault Damour. Binary black holes coalescence: Transition from adiabatic inspiral to plunge. In *Recent developments in theoretical and experimental general relativity, gravitation and relativistic field theories. Proceedings, 9th Marcel Grossmann Meeting, MG'9, Rome, Italy, July 2-8, 2000. Pts. A-C*, pages 1637–1638, 2000.

[141] Thibault Damour, Piotr Jaranowski, and Gerhard Schaefer. On the determination of the last stable orbit for circular general relativistic binaries at the third postNewtonian approximation. *Phys. Rev.*, D62: 084011, 2000. doi: 10.1103/PhysRevD.62.084011.

[142] E. Brezin, C. Itzykson, and Jean Zinn-Justin. Relativistic balmer formula including recoil effects. *Phys. Rev.*, D1:2349–2355, 1970. doi: 10.1103/PhysRevD.1.2349.

[143] Thibault Damour and Alessandro Nagar. An improved analytical description of inspiralling and coalescing black-hole binaries. *Phys. Rev.*, D79:081503, 2009. doi: 10.1103/PhysRevD.79.081503.

[144] M. Davis, R. Ruffini, and J. Tiomno. Pulses of gravitational radiation of a particle falling radially into a schwarzschild black hole. *Phys. Rev.*, D60:124004, 1999. doi: 10.1103/PhysRevD.60.124004.

[145] Richard H. Price and Jorge Pullin. Colliding black holes: The Close limit. *Phys. Rev. Lett.*, 72:3297–3300, 1994. doi: 10.1103/PhysRevLett.72.3297.

[146] Piotr Jaranowski and Gerhard Schäfer. Derivation of local-in-time fourth post-Newtonian ADM Hamiltonian for spinless compact binaries. *Phys. Rev.*, D92(12):124043, 2015. doi: 10.1103/PhysRevD.92.124043.

[147] Thibault Damour, Piotr Jaranowski, and Gerhard Schäfer. Nonlocal-in-time action for the fourth post-Newtonian conservative dynamics of two-body systems. *Phys. Rev.*, D89(6):064058, 2014. doi: 10.1103/PhysRevD.89.064058.

[148] T. Damour and Gerhard Schäfer. HIGHER ORDER RELATIVISTIC PERIASTRON ADVANCES AND BINARY PULSARS. *Nuovo Cim.*, B101:127, 1988. doi: 10.1007/BF02828697.

[149] Thibault Damour, Piotr Jaranowski, and Gerhard Schaefer. Dynamical invariants for general relativistic two-body systems at the third postNewtonian approximation. *Phys. Rev.*, D62:044024, 2000. doi: 10.1103/PhysRevD.62.044024.

[150] Piotr Jaranowski and Gerhard Schaefer. Third postNewtonian higher order ADM Hamilton dynamics for two-body point mass systems. *Phys. Rev.*, D57:7274–7291, 1998. doi: 10.1103/PhysRevD.57.7274,10.1103/PhysRevD.63.029902. [Erratum: Phys. Rev.D63,029902(2001)].

[151] Thibault Damour, Piotr Jaranowski, and Gerhard Schaefer. Dimensional regularization of the gravitational interaction of point masses. *Phys. Lett.*, B513:147–155, 2001. doi: 10.1016/S0370-2693(01)00642-6.

[152] Enrico Barausse, Alessandra Buonanno, and Alexandre Le Tiec. The complete non-spinning effective-one-body metric at linear order in the mass ratio. *Phys.Rev.*, D85:064010, 2012. doi: 10.1103/PhysRevD.85.064010.

[153] Luc Blanchet, Steven L. Detweiler, Alexandre Le Tiec, and Bernard F. Whiting. High-Order Post-Newtonian Fit of the Gravitational Self-Force for Circular Orbits in the Schwarzschild Geometry. *Phys.Rev.*, D81:084033, 2010. doi: 10.1103/PhysRevD.81.084033.

[154] Luc Blanchet and Thibault Damour. Tail transported temporal correlations in the dynamics of a gravitating system. *Phys. Rev.*, D37:1410, 1988.

[155] Donato Bini and Thibault Damour. Analytical determination of the two-body gravitational interaction potential at the fourth post-Newtonian approximation. *Phys.Rev.*, D87(12):121501, 2013. doi: 10.1103/PhysRevD.87.121501.

[156] Piotr Jaranowski and Gerhard Schäfer. Dimensional regularization of local singularities in the 4th post-Newtonian two-point-mass Hamiltonian. *Phys. Rev.*, D87:081503, 2013. doi: 10.1103/PhysRevD.87.081503.

[157] Thibault Damour and Alessandro Nagar. Effective One Body description of tidal effects in inspiralling compact binaries. *Phys. Rev.*, D81: 084016, 2010. doi: 10.1103/PhysRevD.81.084016.

[158] Thibault Damour. Coalescence of two spinning black holes: An effective one- body approach. *Phys. Rev.*, D64:124013, 2001. doi: 10.1103/PhysRevD.64.124013.

[159] Thibault Damour and Alessandro Nagar. New effective-one-body description of coalescing nonprecessing spinning black-hole binaries. *Phys.Rev.*, D90(4):044018, 2014. doi: 10.1103/PhysRevD.90.044018.

[160] Johannes Hartung and Jan Steinhoff. Next-to-leading order spin-orbit and spin(a)-spin(b) Hamiltonians for n gravitating spinning compact objects. *Phys. Rev.*, D83:044008, 2011. doi: 10.1103/PhysRevD.83.044008.

[161] Simone Balmelli and Philippe Jetzer. Effective-one-body Hamiltonian with next-to-leading order spin-spin coupling. *Phys. Rev.*, D91:064011, 2015. doi: 10.1103/PhysRevD.91.064011.

[162] Alessandro Nagar. Effective one body Hamiltonian of two spinning black-holes with next-to-next-to-leading order spin-orbit coupling. *Phys.Rev.*, D84:084028, 2011. doi: 10.1103/PhysRevD.84.084028.

[163] Johannes Hartung and Jan Steinhoff. Next-to-next-to-leading order post-Newtonian spin-orbit Hamiltonian for self-gravitating binaries. *Annalen Phys.*, 523:783–790, 2011. doi: 10.1002/andp.201100094.

[164] Thibault Damour, Piotr Jaranowski, and Gerhard Schäfer. Effective one body approach to the dynamics of two spinning black holes with

next-to-leading order spin-orbit coupling. *Phys.Rev.*, D78:024009, 2008. doi: 10.1103/PhysRevD.78.024009.

[165] Enrico Barausse and Alessandra Buonanno. Extending the effective-one-body Hamiltonian of black-hole binaries to include next-to-next-to-leading spin-orbit couplings. *Phys.Rev.*, D84:104027, 2011. doi: 10.1103/PhysRevD.84.104027.

[166] Thibault Damour and Alessandro Nagar. Comparing Effective-One-Body gravitational waveforms to accurate numerical data. *Phys. Rev.*, D77:024043, 2008. doi: 10.1103/PhysRevD.77.024043.

[167] Thibault Damour and Alessandro Nagar. Faithful Effective-One-Body waveforms of small-mass-ratio coalescing black-hole binaries. *Phys. Rev.*, D76:064028, 2007. doi: 10.1103/PhysRevD.76.064028.

[168] Luc Blanchet, Thibault Damour, Gilles Esposito-Farese, and Bala R. Iyer. Gravitational radiation from inspiralling compact binaries completed at the third post-Newtonian order. *Phys.Rev.Lett.*, 93:091101, 2004. doi: 10.1103/PhysRevLett.93.091101.

[169] Lawrence E. Kidder. Using Full Information When Computing Modes of Post- Newtonian Waveforms From Inspiralling Compact Binaries in Circular Orbit. *Phys. Rev.*, D77:044016, 2008. doi: 10.1103/PhysRevD.77.044016.

[170] Emanuele Berti et al. Inspiral, merger and ringdown of unequal mass black hole binaries: A multipolar analysis. *Phys. Rev.*, D76:064034, 2007. doi: 10.1103/PhysRevD.76.064034.

[171] Luc Blanchet, Guillaume Faye, Bala R. Iyer, and Siddhartha Sinha. The third post-Newtonian gravitational wave polarisations and associated spherical harmonic modes for inspiralling compact binaries in quasi-circular orbits. *Class. Quant. Grav.*, 25:165003, 2008. doi: 10.1088/0264-9381/25/16/165003.

[172] Hideyuki Tagoshi and Misao Sasaki. PostNewtonian expansion of gravitational waves from a particle in circular orbit around a Schwarzschild black hole. *Prog. Theor. Phys.*, 92:745–772, 1994. doi: 10.1143/PTP.92.745.

[173] Takahiro Tanaka, Hideyuki Tagoshi, and Misao Sasaki. Gravitational waves by a particle in circular orbits around a Schwarzschild black hole: 5.5 postNewtonian formula. *Prog. Theor. Phys.*, 96:1087–1101, 1996. doi: 10.1143/PTP.96.1087.

[174] Hideki Asada and Toshifumi Futamase. Propagation of gravitational waves from slow motion sources in Coulomb type potential. *Phys. Rev.*, D56:R6062–R6066, 1997. doi: 10.1103/PhysRevD.56.R6062.

[175] Yi Pan, Alessandra Buonanno, Ryuichi Fujita, Etienne Racine, and Hideyuki Tagoshi. Post-Newtonian factorized multipolar waveforms for spinning, non-precessing black-hole binaries. *Phys.Rev.*, D83:064003, 2011. doi: 10.1103/PhysRevD.83.064003.

[176] Yi Pan, Alessandra Buonanno, Michael Boyle, Luisa T. Buchman, Lawrence E. Kidder, et al. Inspiral-merger-ringdown multipolar waveforms of nonspinning black-hole binaries using the effective-one-body formalism. *Phys.Rev.*, D84:124052, 2011. doi: 10.1103/PhysRevD.84.124052.

[177] Andrea Taracchini, Yi Pan, Alessandra Buonanno, Enrico Barausse, Michael Boyle, et al. Prototype effective-one-body model for nonprecessing spinning inspiral-merger-ringdown waveforms. *Phys.Rev.*, D86:024011, 2012. doi: 10.1103/PhysRevD.86.024011.

[178] Ryuichi Fujita and Bala R. Iyer. Spherical harmonic modes of 5.5 post-Newtonian gravitational wave polarizations and associated factorized resummed waveforms for a particle in circular orbit around a Schwarzschild black hol. *Phys. Rev.*, D82:044051, 2010. doi: 10.1103/PhysRevD.82.044051.

[179] Ryuichi Fujita. Gravitational radiation for extreme mass ratio inspirals to the 14th post-Newtonian order. *Prog.Theor.Phys.*, 127:583–590, 2012. doi: 10.1143/PTP.127.583.

[180] S. Marsat. Post-newtonian higher order order spin effects in inspiraling compact binaries. In *Proceedings, 50th Rencontres de Moriond Gravitation : 100 years after GR: La Thuile, Italy, March 21-28, 2015*, pages 339–342, 2015.

[181] Sylvain Marsat, Luc Blanchet, Alejandro Bohe, and Guillaume Faye. Gravitational waves from spinning compact object binaries: New post-Newtonian results. 2013.

[182] Alessandra Buonanno, Gregory B. Cook, and Frans Pretorius. Inspiral, merger and ring-down of equal-mass black-hole binaries. *Phys. Rev.*, D75:124018, 2007. doi: 10.1103/PhysRevD.75.124018.

[183] Yi Pan, Alessandra Buonanno, John G. Baker, Joan Centrella, Bernard J. Kelly, Sean T. McWilliams, Frans Pretorius, and James R. van Meter. A Data-analysis driven comparison of analytic and numerical coalescing binary waveforms: Nonspinning case. *Phys. Rev.*, D77: 024014, 2008. doi: 10.1103/PhysRevD.77.024014.

[184] Thibault Damour, Eric Gourgoulhon, and Philippe Grandclement. Circular orbits of corotating binary black holes: Comparison between analytical and numerical results. *Phys. Rev.*, D66:024007, 2002. doi: 10.1103/PhysRevD.66.024007.

[185] Piero Rettegno, Fabio Martinetti, Alessandro Nagar, Donato Bini, Gunnar Riemenschneider, and Thibault Damour. Comparing Effective One Body Hamiltonians for spin-aligned coalescing binaries. 2019.

[186] Thibault Damour, Alessandro Nagar, Ernst Nils Dorband, Denis Pollney, and Luciano Rezzolla. Faithful Effective-One-Body waveforms of equal-mass coalescing black-hole binaries. *Phys. Rev.*, D77:084017, 2008. doi: 10.1103/PhysRevD.77.084017.

[187] Thibault Damour, Alessandro Nagar, Mark Hannam, Sascha Husa, and Bernd Brügmann. Accurate Effective-One-Body waveforms of inspiralling and coalescing black-hole binaries. *Phys. Rev.*, D78:044039, 2008. doi: 10.1103/PhysRevD.78.044039.

[188] Alessandra Buonanno, Yi Pan, Harald P. Pfeiffer, Mark A. Scheel, Luisa T. Buchman, and Lawrence E. Kidder. Effective-one-body waveforms calibrated to numerical relativity simulations: Coalescence of non-spinning, equal-mass black holes. *Phys. Rev.*, D79:124028, 2009. doi: 10.1103/PhysRevD.79.124028.

[189] Sebastiano Bernuzzi, Alessandro Nagar, and Anil Zenginoglu. Binary black hole coalescence in the extreme-mass-ratio limit: testing and improving the effective-one-body multipolar waveform. *Phys.Rev.*, D83: 064010, 2011. doi: 10.1103/PhysRevD.83.064010.

[190] Michael Pürrer. Frequency domain reduced order models for gravitational waves from aligned-spin compact binaries. *Class. Quant. Grav.*, 31(19):195010, 2014. doi: 10.1088/0264-9381/31/19/195010.

[191] Alessandro Nagar and Piero Rettegno. Efficient effective one body time-domain gravitational waveforms. *Phys. Rev.*, D99(2):021501, 2019. doi: 10.1103/PhysRevD.99.021501.

[192] `https://data.black-holes.org/waveforms/index.html`. SXS Gravitational Waveform Database.

[193] Luisa T. Buchman, Harald P. Pfeiffer, Mark A. Scheel, and Bela Szilagyi. Simulations of non-equal mass black hole binaries with spectral methods. *Phys. Rev.*, D86:084033, 2012. doi: 10.1103/PhysRevD.86.084033.

[194] Tony Chu, Harald P. Pfeiffer, and Mark A. Scheel. High accuracy simulations of black hole binaries:spins anti-aligned with the orbital angular momentum. *Phys. Rev.*, D80:124051, 2009. doi: 10.1103/PhysRevD.80.124051.

[195] Daniel A. Hemberger, Geoffrey Lovelace, Thomas J. Loredo, Lawrence E. Kidder, Mark A. Scheel, Béla Szilágyi, Nicholas W. Taylor, and Saul A. Teukolsky. Final spin and radiated energy in numerical simulations of binary black holes with equal masses and equal, aligned or anti-aligned spins. *Phys. Rev.*, D88:064014, 2013. doi: 10.1103/PhysRevD.88.064014.

[196] Mark A. Scheel, Matthew Giesler, Daniel A. Hemberger, Geoffrey Lovelace, Kevin Kuper, Michael Boyle, B. Szilágyi, and Lawrence E. Kidder. Improved methods for simulating nearly extremal binary black holes. *Class. Quant. Grav.*, 32(10):105009, 2015. doi: 10.1088/0264-9381/32/10/105009.

[197] Jonathan Blackman, Scott E. Field, Chad R. Galley, Béla Szilágyi, Mark A. Scheel, Manuel Tiglio, and Daniel A. Hemberger. Fast and

Accurate Prediction of Numerical Relativity Waveforms from Binary Black Hole Coalescences Using Surrogate Models. *Phys. Rev. Lett.*, 115 (12):121102, 2015. doi: 10.1103/PhysRevLett.115.121102.

[198] Geoffrey Lovelace, Michael Boyle, Mark A. Scheel, and Bela Szilagyi. Accurate gravitational waveforms for binary-black-hole mergers with nearly extremal spins. *Class. Quant. Grav.*, 29:045003, 2012. doi: 10.1088/0264-9381/29/4/045003.

[199] Geoffrey Lovelace, Mark.A. Scheel, and Bela Szilagyi. Simulating merging binary black holes with nearly extremal spins. *Phys.Rev.*, D83: 024010, 2011. doi: 10.1103/PhysRevD.83.024010.

[200] Geoffrey Lovelace et al. Nearly extremal apparent horizons in simulations of merging black holes. *Class. Quant. Grav.*, 32(6):065007, 2015. doi: 10.1088/0264-9381/32/6/065007.

[201] Abdul H. Mroue, Mark A. Scheel, Bela Szilagyi, Harald P. Pfeiffer, Michael Boyle, et al. A catalog of 174 binary black-hole simulations for gravitational-wave astronomy. *Phys.Rev.Lett.*, 111:241104, 2013. doi: 10.1103/PhysRevLett.111.241104.

[202] Prayush Kumar, Kevin Barkett, Swetha Bhagwat, Nousha Afshari, Duncan A. Brown, Geoffrey Lovelace, Mark A. Scheel, and Béla Szilágyi. Accuracy and precision of gravitational-wave models of inspiraling neutron star-black hole binaries with spin: Comparison with matter-free numerical relativity in the low-frequency regime. *Phys. Rev.*, D92(10):102001, 2015. doi: 10.1103/PhysRevD.92.102001.

[203] Tony Chu, Heather Fong, Prayush Kumar, Harald P. Pfeiffer, Michael Boyle, Daniel A. Hemberger, Lawrence E. Kidder, Mark A. Scheel, and Bela Szilagyi. On the accuracy and precision of numerical waveforms: Effect of waveform extraction methodology. *Class. Quant. Grav.*, 33 (16):165001, 2016. doi: 10.1088/0264-9381/33/16/165001.

[204] Bernd Bruegmann, Jose A. Gonzalez, Mark Hannam, Sascha Husa, Ulrich Sperhake, and Wolfgang Tichy. Calibration of Moving Puncture Simulations. *Phys. Rev.*, D77:024027, 2008. doi: 10.1103/PhysRevD.77.024027.

[205] Sascha Husa, Jose A. González, Mark Hannam, Bernd Brügmann, and Ulrich Sperhake. Reducing phase error in long numerical binary black hole evolutions with sixth order finite differencing. *Class. Quant. Grav.*, 25:105006, 2008. doi: 10.1088/0264-9381/25/10/105006.

[206] Sebastiano Bernuzzi, Alessandro Nagar, Tim Dietrich, and Thibault Damour. Modeling the Dynamics of Tidally Interacting Binary Neutron Stars up to the Merger. *Phys.Rev.Lett.*, 114(16):161103, 2015. doi: 10.1103/PhysRevLett.114.161103.

[207] Kenta Kiuchi, Kyohei Kawaguchi, Koutarou Kyutoku, Yuichiro Sekiguchi, Masaru Shibata, and Keisuke Taniguchi. Sub-radian-accuracy gravitational waveforms of coalescing binary neutron stars in numerical relativity. *Phys. Rev.*, D96(8):084060, 2017. doi: 10.1103/PhysRevD.96.084060.

[208] Kyohei Kawaguchi, Kenta Kiuchi, Koutarou Kyutoku, Yuichiro Sekiguchi, Masaru Shibata, and Keisuke Taniguchi. Frequency-domain gravitational waveform models for inspiraling binary neutron stars. *Phys. Rev.*, D97(4):044044, 2018. doi: 10.1103/PhysRevD.97.044044.

[209] Tim Dietrich et al. Matter imprints in waveform models for neutron star binaries: Tidal and self-spin effects. *Phys. Rev.*, D99(2):024029, 2019. doi: 10.1103/PhysRevD.99.024029.

[210] B. P. Abbott et al. Properties of the binary neutron star merger GW170817. *Phys. Rev.*, X9(1):011001, 2019. doi: 10.1103/PhysRevX.9.011001.

[211] B. P. Abbott et al. GW170817: Measurements of neutron star radii and equation of state. *Phys. Rev. Lett.*, 121(16):161101, 2018. doi: 10.1103/PhysRevLett.121.161101.

[212] Tanja Hinderer et al. Effects of neutron-star dynamic tides on gravitational waveforms within the effective-one-body approach. *Phys. Rev. Lett.*, 116(18):181101, 2016. doi: 10.1103/PhysRevLett.116.181101.

[213] Jan Steinhoff, Tanja Hinderer, Alessandra Buonanno, and Andrea Taracchini. Dynamical Tides in General Relativity: Effective Action and Effective-One-Body Hamiltonian. *Phys. Rev.*, D94(10):104028, 2016. doi: 10.1103/PhysRevD.94.104028.

[214] . J. Vines and S. Marsat, (private communication, LIGODocument T1800028-v1, 2018).

[215] Thibault Damour, Alessandro Nagar, and Sebastiano Bernuzzi. Improved effective-one-body description of coalescing nonspinning black-hole binaries and its numerical-relativity completion. *Phys.Rev.*, D87: 084035, 2013. doi: 10.1103/PhysRevD.87.084035.

[216] Alessandro Nagar and Luciano Rezzolla. Gauge-invariant non-spherical metric perturbations of Schwarzschild black-hole spacetimes. *Class. Quant. Grav.*, 22:R167, 2005. doi: 10.1088/0264-9381/22/16/R01.

[217] Thibault Damour and Alessandro Nagar. A new analytic representation of the ringdown waveform of coalescing spinning black hole binaries. *Phys.Rev.*, D90:024054, 2014. doi: 10.1103/PhysRevD.90.024054.

[218] Walter Del Pozzo and Alessandro Nagar. Analytic family of post-merger template waveforms. *Phys. Rev.*, D95(12):124034, 2017. doi: 10.1103/PhysRevD.95.124034.

[219] Michael Boyle. Transformations of asymptotic gravitational-wave data. *Phys. Rev. D*, 93(8):084031, 2016. doi: 10.1103/PhysRevD.93.084031.

[220] Xisco Jiménez-Forteza, David Keitel, Sascha Husa, Mark Hannam, Sebastian Khan, and Michael Pürrer. Hierarchical data-driven approach to fitting numerical relativity data for nonprecessing binary black holes with an application to final spin and radiated energy. *Phys. Rev.*, D95 (6):064024, 2017. doi: 10.1103/PhysRevD.95.064024.

[221] Emanuele Berti, Vitor Cardoso, and Clifford M. Will. On gravitational-wave spectroscopy of massive black holes with the space interferometer LISA. *Phys. Rev.*, D73:064030, 2006. doi: 10.1103/PhysRevD.73.064030.

[222] Emanuele Berti, Vitor Cardoso, and Andrei O. Starinets. Quasinormal modes of black holes and black branes. *Class. Quant. Grav.*, 26:163001, 2009. doi: 10.1088/0264-9381/26/16/163001.

[223] David Shoemaker. URL `https://dcc.ligo.org/cgi-bin/DocDB/ShowDocument?docid=2974`.

[224] Sascha Husa, Sebastian Khan, Mark Hannam, Michael Pürrer, Frank Ohme, Xisco Jiménez Forteza, and Alejandro Bohé. Frequency-domain gravitational waves from nonprecessing black-hole binaries. I. New numerical waveforms and anatomy of the signal. *Phys. Rev.*, D93(4): 044006, 2016. doi: 10.1103/PhysRevD.93.044006.

[225] David Keitel et al. The most powerful astrophysical events: Gravitational-wave peak luminosity of binary black holes as predicted by numerical relativity. *Phys. Rev.*, D96(2):024006, 2017. doi: 10.1103/PhysRevD.96.024006.

[226] Andrea Taracchini, Alessandra Buonanno, Gaurav Khanna, and Scott A. Hughes. Small mass plunging into a Kerr black hole: Anatomy of the inspiral-merger-ringdown waveforms. *Phys.Rev.*, D90:084025, 2014. doi: 10.1103/PhysRevD.90.084025.

[227] T. Damour. Gravitational radiation and the motion of compact bodies. In N. Deruelle and T. Piran, editors, *Gravitational Radiation*, pages 59–144. North-Holland, Amsterdam, 1983.

[228] Etienne Racine and Eanna E. Flanagan. Post-1-Newtonian equations of motion for systems of arbitrarily structured bodies. *Phys. Rev.*, D71: 044010, 2005. doi: 10.1103/PhysRevD.71.044010,10.1103/PhysRevD.88.089903. [Erratum: Phys. Rev.D88,no.8,089903(2013)].

[229] Eanna E. Flanagan and Tanja Hinderer. Constraining neutron star tidal Love numbers with gravitational wave detectors. *Phys.Rev.*, D77: 021502, 2008. doi: 10.1103/PhysRevD.77.021502.

[230] Justin Vines, Eanna E. Flanagan, and Tanja Hinderer. Post-1-Newtonian tidal effects in the gravitational waveform from binary inspirals. *Phys. Rev.*, D83:084051, 2011. doi: 10.1103/PhysRevD.83.084051.

[231] Tanja Hinderer, Benjamin D. Lackey, Ryan N. Lang, and Jocelyn S. Read. Tidal deformability of neutron stars with realistic equations of state and their gravitational wave signatures in binary inspiral. *Phys. Rev.*, D81:123016, 2010. doi: 10.1103/PhysRevD.81.123016.

[232] Sebastiano Bernuzzi, Alessandro Nagar, Simone Balmelli, Tim Dietrich, and Maximiliano Ujevic. Quasi-universal properties of neu-

tron star mergers. *Phys.Rev.Lett.*, 112:201101, 2014. doi: 10.1103/PhysRevLett.112.201101.

[233] Taylor Binnington and Eric Poisson. Relativistic theory of tidal Love numbers. *Phys. Rev.*, D80:084018, 2009. doi: 10.1103/PhysRevD.80.084018.

[234] Donato Bini and Thibault Damour. Gravitational self-force corrections to two-body tidal interactions and the effective one-body formalism. *Phys.Rev.*, D90(12):124037, 2014. doi: 10.1103/PhysRevD.90.124037.

[235] Sebastiano Bernuzzi, Tim Dietrich, and Alessandro Nagar. Modeling the complete gravitational wave spectrum of neutron star mergers. *Phys. Rev. Lett.*, 115:091101, 2015. doi: 10.1103/PhysRevLett.115.091101.

[236] Francesco Zappa, Sebastiano Bernuzzi, David Radice, Albino Perego, and Tim Dietrich. Gravitational-wave luminosity of binary neutron stars mergers. *Phys. Rev. Lett.*, 120(11):111101, 2018. doi: 10.1103/PhysRevLett.120.111101.

[237] Walter Del Pozzo, Tjonnie G. F. Li, Michalis Agathos, Chris Van Den Broeck, and Salvatore Vitale. Demonstrating the feasibility of probing the neutron star equation of state with second-generation gravitational wave detectors. *Phys. Rev. Lett.*, 111(7):071101, 2013. doi: 10.1103/PhysRevLett.111.071101.

[238] Michalis Agathos, Jeroen Meidam, Walter Del Pozzo, Tjonnie G. F. Li, Marco Tompitak, John Veitch, Salvatore Vitale, and Chris Van Den Broeck. Constraining the neutron star equation of state with gravitational wave signals from coalescing binary neutron stars. *Phys. Rev.*, D92(2):023012, 2015. doi: 10.1103/PhysRevD.92.023012.

[239] Donato Bini, Thibault Damour, and Guillaume Faye. Effective action approach to higher-order relativistic tidal interactions in binary systems and their effective one body description. *Phys.Rev.*, D85:124034, 2012. doi: 10.1103/PhysRevD.85.124034.

[240] Sebastiano Bernuzzi, Alessandro Nagar, Marcus Thierfelder, and Bernd Brügmann. Tidal effects in binary neutron star coalescence. *Phys.Rev.*, D86:044030, 2012. doi: 10.1103/PhysRevD.86.044030.

[241] Sam R. Dolan, Patrick Nolan, Adrian C. Ottewill, Niels Warburton, and Barry Wardell. Tidal invariants for compact binaries on quasicircular orbits. *Phys. Rev.*, D91(2):023009, 2015. doi: 10.1103/PhysRevD.91.023009.

[242] Justin E. Vines and Eanna E. Flanagan. Post-1-Newtonian quadrupole tidal interactions in binary systems. *Phys. Rev.*, D88:024046, 2010. doi: 10.1103/PhysRevD.88.024046.

[243] Thibault Damour, Alessandro Nagar, and Loic Villain. Measurability of the tidal polarizability of neutron stars in late-inspiral gravitational-wave signals. *Phys.Rev.*, D85:123007, 2012. doi: 10.1103/PhysRevD.85.123007.

[244] Kenta Hotokezaka, Koutarou Kyutoku, Hirotada Okawa, and Masaru Shibata. Exploring tidal effects of coalescing binary neutron stars in numerical relativity. II. Long-term simulations. *Phys. Rev.*, D91(6):064060, 2015. doi: 10.1103/PhysRevD.91.064060.

[245] Kenta Hotokezaka, Koutarou Kyutoku, Yu-ichiro Sekiguchi, and Masaru Shibata. Measurability of the tidal deformability by gravitational waves from coalescing binary neutron stars. *Phys. Rev.*, D93 (6):064082, 2016. doi: 10.1103/PhysRevD.93.064082.

[246] Tim Dietrich and Tanja Hinderer. Comprehensive comparison of numerical relativity and effective-one-body results to inform improvements in waveform models for binary neutron star systems. *Phys. Rev.*, D95(12):124006, 2017. doi: 10.1103/PhysRevD.95.124006.

[247] Benjamin D. Lackey, Sebastiano Bernuzzi, Chad R. Galley, Jeroen Meidam, and Chris Van Den Broeck. Effective-one-body waveforms for binary neutron stars using surrogate models. *Phys. Rev.*, D95(10):104036, 2017. doi: 10.1103/PhysRevD.95.104036.

[248] Michele Levi and Jan Steinhoff. Equivalence of ADM Hamiltonian and Effective Field Theory approaches at next-to-next-to-leading order spin1-spin2 coupling of binary inspirals. *JCAP*, 1412(12):003, 2014. doi: 10.1088/1475-7516/2014/12/003.

[249] Simone Balmelli and Thibault Damour. New effective-one-body Hamiltonian with next-to-leading order spin-spin coupling. *Phys. Rev.*, D92 (12):124022, 2015. doi: 10.1103/PhysRevD.92.124022.

[250] Rafael A. Porto and Ira Z. Rothstein. Spin(1)Spin(2) Effects in the Motion of Inspiralling Compact Binaries at Third Order in the Post-Newtonian Expansion. *Phys. Rev.*, D78:044012, 2008. doi: 10.1103/PhysRevD.78.044012,10.1103/PhysRevD.81.029904. [Erratum: Phys. Rev.D81,029904(2010)].

[251] Noah Sennett, Tanja Hinderer, Jan Steinhoff, Alessandra Buonanno, and Serguei Ossokine. Distinguishing Boson Stars from Black Holes and Neutron Stars from Tidal Interactions in Inspiraling Binary Systems. *Phys. Rev.*, D96(2):024002, 2017. doi: 10.1103/PhysRevD.96.024002.

[252] . S. Marsat, private communication, 2017.

[253] Kent Yagi and Nicolas Yunes. I-Love-Q. *Science*, 341:365–368, 2013. doi: 10.1126/science.1236462.

[254] Wolfgang Tichy. Initial data for binary neutron stars with arbitrary spins. *Phys.Rev.*, D84:024041, 2011. doi: 10.1103/PhysRevD.84.024041.

[255] Wolfgang Tichy. Constructing quasi-equilibrium initial data for binary neutron stars with arbitrary spins. *Phys. Rev. D*, 86:064024, 2012. doi: 10.1103/PhysRevD.86.064024.

[256] Tim Dietrich, Niclas Moldenhauer, Nathan K. Johnson-McDaniel, Sebastiano Bernuzzi, Charalampos M. Markakis, Bernd Brügmann, and Wolfgang Tichy. Binary Neutron Stars with Generic Spin, Eccentricity, Mass ratio, and Compactness - Quasi-equilibrium Sequences and First Evolutions. *Phys. Rev.*, D92(12):124007, 2015. doi: 10.1103/PhysRevD.92.124007.

[257] Bernd Brügmann, Jose A. Gonzalez, Mark Hannam, Sascha Husa, Ulrich Sperhake, et al. Calibration of Moving Puncture Simulations. *Phys.Rev.*, D77:024027, 2008. doi: 10.1103/PhysRevD.77.024027.

[258] Marcus Thierfelder, Sebastiano Bernuzzi, and Bernd Bruegmann. Numerical relativity simulations of binary neutron stars. *Phys. Rev. D*, 84:044012, 2011. doi: 10.1103/PhysRevD.84.044012.

[259] Sebastiano Bernuzzi and Tim Dietrich. Gravitational waveforms from binary neutron star mergers with high-order weighted-essentially-nonoscillatory schemes in numerical relativity. *Phys. Rev.*, D94(6): 064062, 2016. doi: 10.1103/PhysRevD.94.064062.

[260] Tim Dietrich, Sebastiano Bernuzzi, and Wolfgang Tichy. Closed-form tidal approximants for binary neutron star gravitational waveforms constructed from high-resolution numerical relativity simulations. *Phys. Rev.*, D96(12):121501, 2017. doi: 10.1103/PhysRevD.96.121501.

[261] Tim Dietrich, Sebastiano Bernuzzi, Bernd Brügmann, and Wolfgang Tichy. High-resolution numerical relativity simulations of spinning binary neutron star mergers. In *2018 26th Euromicro International Conference on Parallel, Distributed and Network-based Processing (PDP)*, pages 682–689, 2018. doi: 10.1109/PDP2018.2018.00113. URL `https://inspirehep.net/record/1663472/files/1803.07965.pdf`.

[262] David Radice, Luciano Rezzolla, and Filippo Galeazzi. High-Order Fully General-Relativistic Hydrodynamics: new Approaches and Tests. *Class.Quant.Grav.*, 31:075012, 2014. doi: 10.1088/0264-9381/31/7/075012.

[263] David Radice, Luciano Rezzolla, and Filippo Galeazzi. Beyond second-order convergence in simulations of binary neutron stars in full general-relativity. *Mon.Not.Roy.Astron.Soc.*, 437:L46–L50, 2014. doi: 10.1093/mnrasl/slt137.

[264] Luca Baiotti, Thibault Damour, Bruno Giacomazzo, Alessandro Nagar, and Luciano Rezzolla. Accurate numerical simulations of inspiralling binary neutron stars and their comparison with effective-one-body analytical models. *Phys. Rev.*, D84:024017, 2011. doi: 10.1103/PhysRevD.84.024017.

[265] M. Kramer and N. Wex. The double pulsar system: A unique laboratory for gravity. *Class. Quant. Grav.*, 26:073001, 2009. doi: 10.1088/0264-9381/26/7/073001.

[266] Marc Favata. Systematic parameter errors in inspiraling neutron star binaries. *Phys.Rev.Lett.*, 112:101101, 2014. doi: 10.1103/PhysRevLett.112.101101.

[267] Hee-Suk Cho and Chang-Hwan Lee. Gravitational Wave Searches for Aligned-Spin Binary Neutron Stars Using Nonspinning Templates. *J. Korean Phys. Soc.*, 72(1):1–5, 2018. doi: 10.3938/jkps.72.1.

[268] Tim Dietrich, Sebastiano Bernuzzi, Maximiliano Ujevic, and Wolfgang Tichy. Gravitational waves and mass ejecta from binary neutron star mergers: Effect of the stars' rotation. *Phys. Rev.*, D95(4):044045, 2017. doi: 10.1103/PhysRevD.95.044045.

[269] Laura Bernard, Luc Blanchet, Alejandro Bohé, Guillaume Faye, and Sylvain Marsat. Energy and periastron advance of compact binaries on circular orbits at the fourth post-Newtonian order. *Phys. Rev.*, D95 (4):044026, 2017. doi: 10.1103/PhysRevD.95.044026.

[270] Thibault Damour, Piotr Jaranowski, and Gerhard Schäfer. Conservative dynamics of two-body systems at the fourth post-Newtonian approximation of general relativity. *Phys. Rev.*, D93(8):084014, 2016. doi: 10.1103/PhysRevD.93.084014.

[271] Thibault Damour, Piotr Jaranowski, and Gerhard Schäfer. Fourth post-Newtonian effective one-body dynamics. *Phys. Rev.*, D91(8): 084024, 2015. doi: 10.1103/PhysRevD.91.084024.

[272] Luca Baiotti, Thibault Damour, Bruno Giacomazzo, Alessandro Nagar, and Luciano Rezzolla. Analytic modelling of tidal effects in the relativistic inspiral of binary neutron stars. *Phys. Rev. Lett.*, 105:261101, 2010. doi: 10.1103/PhysRevLett.105.261101.

[273] `https://losc.ligo.org/about/`. LIGO Open Science Center.

[274] `https://github.com/johnveitch/cpnest`. Parallel nested sampling algorithm in python.

[275] Thomas D. Abbott et al. Improved analysis of GW150914 using a fully spin-precessing waveform Model. *Phys. Rev.*, X6(4):041014, 2016. doi: 10.1103/PhysRevX.6.041014.

[276] Enrico Barausse and Alessandra Buonanno. An Improved effective-one-body Hamiltonian for spinning black-hole binaries. *Phys.Rev.*, D81: 084024, 2010. doi: 10.1103/PhysRevD.81.084024.

[277] James Healy, Carlos O. Lousto, and Yosef Zlochower. Nonspinning binary black hole merger scenario revisited. *Phys. Rev.*, D96(2):024031, 2017. doi: 10.1103/PhysRevD.96.024031.

[278] Guillaume Faye, Luc Blanchet, and Bala R. Iyer. Non-linear multipole interactions and gravitational-wave octupole modes for inspiralling compact binaries to third-and-a-half post-Newtonian order. *Class. Quant. Grav.*, 32(4):045016, 2015. doi: 10.1088/0264-9381/32/4/045016.

[279] Alessandra Buonanno, Yanbei Chen, and Thibault Damour. Transition from inspiral to plunge in precessing binaries of spinning black holes. *Phys. Rev.*, D74:104005, 2006. doi: 10.1103/PhysRevD.74.104005.

[280] Ian Hinder, Larry Kidder, Harald Pfeiffer, Mark Scheel, Michael Boyle, Dan Hemberger, Geoffrey Lovelace, and Bela Szilagyi. Binary black-hole simulation sxs:bbh:1375, April 2018. URL `https://doi.org/10.5281/zenodo.1215769`.

[281] Sebastiano Bernuzzi and Alessandro Nagar. Binary black hole merger in the extreme-mass-ratio limit: a multipolar analysis. *Phys. Rev.*, D81:084056, 2010. doi: 10.1103/PhysRevD.81.084056.

[282] N. V. Krishnendu, K. G. Arun, and Chandra Kant Mishra. Testing the binary black hole nature of a compact binary coalescence. *Phys. Rev. Lett.*, 119(9):091101, 2017. doi: 10.1103/PhysRevLett.119.091101.

[283] N. V. Krishnendu, Chandra Kant Mishra, and K. G. Arun. Spin-induced deformations and tests of binary black hole nature using third-generation detectors. 2018.

[284] Sebastiano Bernuzzi, Marcus Thierfelder, and Bernd Brügmann. Accuracy of numerical relativity waveforms from binary neutron star mergers and their comparison with post-Newtonian waveforms. *Phys.Rev.*, D85:104030, 2012. doi: 10.1103/PhysRevD.85.104030.

[285] David Radice, Luciano Rezzolla, and Filippo Galeazzi. High-Order Numerical-Relativity Simulations of Binary Neutron Stars. *ASP Conf. Ser.*, 498:121–126, 2015.

[286] David Radice, Sebastiano Bernuzzi, and Christian D. Ott. One-armed spiral instability in neutron star mergers and its detectability in gravitational waves. *Phys. Rev.*, D94(6):064011, 2016. doi: 10.1103/PhysRevD.94.064011.

[287] Sebastiano Bernuzzi, Tim Dietrich, Wolfgang Tichy, and Bernd Brügmann. Mergers of binary neutron stars with realistic spin. *Phys.Rev.*, D89:104021, 2014. doi: 10.1103/PhysRevD.89.104021.

[288] Michele Levi and Jan Steinhoff. Next-to-next-to-leading order gravitational spin-squared potential via the effective field theory for spinning objects in the post-Newtonian scheme. *JCAP*, 1601:008, 2016. doi: 10.1088/1475-7516/2016/01/008.

[289] Michele Levi and Jan Steinhoff. Next-to-next-to-leading order gravitational spin-orbit coupling via the effective field theory for spinning objects in the post-Newtonian scheme. *JCAP*, 1601:011, 2016. doi: 10.1088/1475-7516/2016/01/011.

[290] Gerhard Schaefer and Piotr Jaranowski. Hamiltonian formulation of general relativity and post-Newtonian dynamics of compact binaries. *Living Rev. Rel.*, 21(1):7, 2018. doi: 10.1007/s41114-018-0016-5.

[291] William G. Laarakkers and Eric Poisson. Quadrupole moments of neutron stars. *Astrophys. J.*, 512:282, 1998.

[292] George Pappas and Theocharis A. Apostolatos. Revising the multipole moments of numerical spacetimes, and its consequences. *Phys. Rev. Lett.*, 108:231104, 2012. doi: 10.1103/PhysRevLett.108.231104.

[293] George Pappas and Theocharis A Apostolatos. Multipole Moments of numerical spacetimes. 2012.

[294] Kent Yagi, Koutarou Kyutoku, George Pappas, Nicolás Yunes, and Theocharis A. Apostolatos. Effective No-Hair Relations for Neutron Stars and Quark Stars: Relativistic Results. *Phys. Rev.*, D89(12): 124013, 2014. doi: 10.1103/PhysRevD.89.124013.

[295] T. Hinderer, private communication, 2018.

[296] Roberto Cotesta, Alessandra Buonanno, Alejandro Bohé, Andrea Taracchini, Ian Hinder, and Serguei Ossokine. Enriching the Symphony of Gravitational Waves from Binary Black Holes by Tuning Higher Harmonics. *Phys. Rev.*, D98(8):084028, 2018. doi: 10.1103/PhysRevD.98.084028.

[297] Alejandro Bohé, Sylvain Marsat, and Luc Blanchet. Next-to-next-to-leading order spin–orbit effects in the gravitational wave flux and orbital phasing of compact binaries. *Class. Quant. Grav.*, 30:135009, 2013. doi: 10.1088/0264-9381/30/13/135009.

[298] Ryuichi Fujita. Gravitational Waves from a Particle in Circular Orbits around a Rotating Black Hole to the 11th Post-Newtonian Order. *PTEP*, 2015(3):033E01, 2015. doi: 10.1093/ptep/ptv012.

[299] B. P. Abbott et al. GWTC-1: A Gravitational-Wave Transient Catalog of Compact Binary Mergers Observed by LIGO and Virgo during the First and Second Observing Runs. 2018.

[300] Leslie Wade, Jolien D. E. Creighton, Evan Ochsner, Benjamin D. Lackey, Benjamin F. Farr, Tyson B. Littenberg, and Vivien Raymond. Systematic and statistical errors in a bayesian approach to the estimation of the neutron-star equation of state using advanced gravitational wave detectors. *Phys. Rev.*, D89(10):103012, 2014. doi: 10.1103/PhysRevD.89.103012.

[301] Reetika Dudi, Francesco Pannarale, Tim Dietrich, Mark Hannam, Sebastiano Bernuzzi, Frank Ohme, and Bernd Bruegmann. Relevance of tidal effects and post-merger dynamics for binary neutron star parameter estimation. 2018.

[302] Anuradha Samajdar and Tim Dietrich. Waveform systematics for binary neutron star gravitational wave signals: effects of the point-particle baseline and tidal descriptions. *Phys. Rev.*, D98(12):124030, 2018. doi: 10.1103/PhysRevD.98.124030.

[303] J. Aasi et al. Advanced LIGO. *Class. Quant. Grav.*, 32:074001, 2015. doi: 10.1088/0264-9381/32/7/074001.

[304] Donato Bini and Thibault Damour. High-order post-Newtonian contributions to the two-body gravitational interaction potential from analytical gravitational self-force calculations. *Phys.Rev.*, D89(6):064063, 2014. doi: 10.1103/PhysRevD.89.064063.

[305] Andrea Taracchini, Alessandra Buonanno, Scott A. Hughes, and Gaurav Khanna. Modeling the horizon-absorbed gravitational flux for equatorial-circular orbits in Kerr spacetime. *Phys.Rev.*, D88:044001, 2013. doi: 10.1103/PhysRevD.88.044001.

[306] Alessandro Nagar, Enno Harms, Sebastiano Bernuzzi, and Anil Zenginoglu. The antikick strikes back: recoil velocities for nearly-extremal binary black hole mergers in the test-mass limit. *Phys. Rev.*, D90(12):124086, 2014. doi: 10.1103/PhysRevD.90.124086.

[307] Abhay G Shah. Gravitational-wave flux for a particle orbiting a Kerr black hole to 20th post-Newtonian order: a numerical approach. 2014.

[308] Shuhei Mano, Hisao Suzuki, and Eiichi Takasugi. Analytic solutions of the Teukolsky equation and their low frequency expansions. *Prog.Theor.Phys.*, 95:1079–1096, 1996. doi: 10.1143/PTP.95.1079.

[309] Nicolas Yunes, Alessandra Buonanno, Scott A. Hughes, Yi Pan, Enrico Barausse, et al. Extreme Mass-Ratio Inspirals in the Effective-One-Body Approach: Quasi-Circular, Equatorial Orbits around a Spinning Black Hole. *Phys.Rev.*, D83:044044, 2011. doi: 10.1103/PhysRevD.83.044044.

[310] Alejandro Bohe, Sylvain Marsat, Guillaume Faye, and Luc Blanchet. Next-to-next-to-leading order spin-orbit effects in the near-zone metric and precession equations of compact binaries. *Class. Quant. Grav.*, 30: 075017, 2013. doi: 10.1088/0264-9381/30/7/075017.

[311] Takahiro Tanaka, Yasushi Mino, Misao Sasaki, and Masaru Shibata. Gravitational waves from a spinning particle in circular orbits around a rotating black hole. *Phys.Rev.*, D54:3762–3777, 1996. doi: 10.1103/PhysRevD.54.3762.

[312] Enno Harms, Georgios Lukes-Gerakopoulos, Sebastiano Bernuzzi, and Alessandro Nagar. Asymptotic gravitational wave fluxes from a spin-

ning particle in circular equatorial orbits around a rotating black hole. *Phys. Rev.*, D93(4):044015, 2016. doi: 10.1103/PhysRevD.93.044015.

[313] Enno Harms, Georgios Lukes-Gerakopoulos, Sebastiano Bernuzzi, and Alessandro Nagar. Spinning test body orbiting around a Schwarzschild black hole: Circular dynamics and gravitational-wave fluxes. *Phys. Rev.*, D94(10):104010, 2016. doi: 10.1103/PhysRevD.94.104010.

[314] Georgios Lukes-Gerakopoulos, Enno Harms, Sebastiano Bernuzzi, and Alessandro Nagar. Spinning test-body orbiting around a Kerr black hole: circular dynamics and gravitational-wave fluxes. *Phys. Rev.*, D96 (6):064051, 2017. doi: 10.1103/PhysRevD.96.064051.

[315] Ryuichi Fujita. Gravitational Waves from a Particle in Circular Orbits around a Schwarzschild Black Hole to the 22nd Post-Newtonian Order. *Prog.Theor.Phys.*, 128:971–992, 2012. doi: 10.1143/PTP.128.971.

[316] Alessandro Nagar, Thibault Damour, and Angelo Tartaglia. Binary black hole merger in the extreme mass ratio limit. *Class. Quant. Grav.*, 24:S109–S124, 2007. doi: 10.1088/0264-9381/24/12/S08.

[317] Thibault Damour and Piotr Jaranowski. Four-loop static contribution to the gravitational interaction potential of two point masses. *Phys. Rev. D*, 95(8):084005, 2017. doi: 10.1103/PhysRevD.95.084005.

[318] Tanguy Marchand, Laura Bernard, Luc Blanchet, and Guillaume Faye. Ambiguity-Free Completion of the Equations of Motion of Compact Binary Systems at the Fourth Post-Newtonian Order. *Phys. Rev. D*, 97(4):044023, 2018. doi: 10.1103/PhysRevD.97.044023.

[319] Laura Bernard, Luc Blanchet, Guillaume Faye, and Tanguy Marchand. Center-of-Mass Equations of Motion and Conserved Integrals of Compact Binary Systems at the Fourth Post-Newtonian Order. *Phys. Rev.*, D97(4):044037, 2018. doi: 10.1103/PhysRevD.97.044037.

[320] Tanja Hinderer and Stanislav Babak. Foundations of an effective-one-body model for coalescing binaries on eccentric orbits. *Phys. Rev.*, D96 (10):104048, 2017. doi: 10.1103/PhysRevD.96.104048.

[321] Gunnar Riemenschneider, Alessandro Nagar, Geraint Pratten, and Francesco Messina. A multipolar effective one body model for black hole binaries. ii: The spinning case. To be published.

[322] Myron Mathisson. Neue mechanik materieller systemes. *Acta Phys. Polon.*, 6:163–2900, 1937.

[323] Achille Papapetrou. Spinning test particles in general relativity. 1. *Proc. Roy. Soc. Lond.*, A209:248–258, 1951. doi: 10.1098/rspa.1951.0200.

[324] W. G. Dixon. Dynamics of extended bodies in general relativity. I. Momentum and angular momentum. *Proc. Roy. Soc. Lond.*, A314: 499–527, 1970. doi: 10.1098/rspa.1970.0020.

[325] L. Filipe O. Costa and José Natário. Center of mass, spin supplementary conditions, and the momentum of spinning particles. *Fund. Theor. Phys.*, 179:215–258, 2015. doi: 10.1007/978-3-319-18335-0_6.

[326] W. Tulczyjew. Equations of motion. In *Proceedings, International Conference on Relativistic Theories of Gravitation: London, United Kingdom, July 1965*, volume 2, 1965.

[327] Shuhei Mano, Hisao Suzuki, and Eiichi Takasugi. Analytic solutions of the Regge-Wheeler equation and the postMinkowskian expansion. *Prog. Theor. Phys.*, 96:549–566, 1996. doi: 10.1143/PTP.96.549.

[328] Chris Kavanagh, Adrian C. Ottewill, and Barry Wardell. Analytical high-order post-Newtonian expansions for spinning extreme mass ratio binaries. *Phys. Rev.*, D93(12):124038, 2016. doi: 10.1103/PhysRevD.93.124038.

[329] Sarp Akcay, Sam. R. Dolan, Jordan Moxon, Niels Warburton, and Barry Wardell. Dissipation in extreme-mass ratio binaries with a spinning secondary. In preparation.

[330] Marc Casals and Adrian C. Ottewill. High-order tail in Schwarzschild spacetime. *Phys. Rev.*, D92(12):124055, 2015. doi: 10.1103/PhysRevD.92.124055.

[331] Marc Casals, Chris Kavanagh, and Adrian C. Ottewill. High-order late-time tail in a Kerr spacetime. *Phys. Rev.*, D94(12):124053, 2016. doi: 10.1103/PhysRevD.94.124053.

[332] P. L. Chrzanowski. Vector Potential and Metric Perturbations of a Rotating Black Hole. *Phys. Rev.*, D11:2042–2062, 1975. doi: 10.1103/PhysRevD.11.2042.

[333] J. M. Cohen and L. S. Kegeles. Electromagnetic fields in curved spaces - a constructive procedure. *Phys. Rev.*, D10:1070–1084, 1974. doi: 10.1103/PhysRevD.10.1070.

[334] L. S. Kegeles and J. M. Cohen. CONSTRUCTIVE PROCEDURE FOR PERTURBATIONS OF SPACE-TIMES. *Phys. Rev.*, D19:1641–1664, 1979. doi: 10.1103/PhysRevD.19.1641.

[335] Enrico Barausse, Etienne Racine, and Alessandra Buonanno. Hamiltonian of a spinning test-particle in curved spacetime. *Phys. Rev.*, D80: 104025, 2009. doi: 10.1103/PhysRevD.80.104025.

[336] Donato Bini, Thibault Damour, and Andrea Geralico. Spin-dependent two-body interactions from gravitational self-force computations. *Phys. Rev.*, D92(12):124058, 2015. doi: 10.1103/PhysRevD.93.109902,10.1103/PhysRevD.92.124058. [Erratum: Phys. Rev.D93,no.10,109902(2016)].

[337] F. A. E. Pirani. On the Physical significance of the Riemann tensor. *Acta Physica Polonica*, 15:389–405, Jan 1956.

[338] A. Nagar and R. Gunnar. ??? In preparation.

[339] Jacob Lange, Richard O'Shaughnessy, and Monica Rizzo. Rapid and accurate parameter inference for coalescing, precessing compact binaries. 2018.